Synthesis and Complete Characterisation of new Oxide Materials by full and Congruent Crystallisation from Glass or the Molten liquid

Haytem Bazzaoui

UNIVERSITÉ D'ORLÉANS

ÉCOLE DOCTORALE ÉNERGIE MATÉRIAUX SCIENCES DE LA TERRE ET DE L'UNIVERS

CEMHTI - CNRS

THÈSE présentée par :

Haytem BAZZAOUI

soutenue le : **18 Novembre 2022**

pour obtenir le grade de : **Docteur de l'Université d'Orléans**

Discipline/ Spécialité : Sciences des Matériaux

Synthesis and Complete Characterisation of new Oxide Materials by full and Congruent Crystallisation from Glass or the Molten liquid

THÈSE dirigée par :

M. Mathieu Allix	Directeur de Recherche, CEMHTI CNRS
M. Michael J. Pitcher	Chargé de Recherche, CEMHTI CNRS

RAPPORTEURS :

Mme. Gwenaelle Rousse	Maître de Conférences, CSE Sorbonne Université
M. Pascal Roussel	Directeur de Recherche, UCCS Université de Lille

---

JURY :

M. Vincent Maisonneuve	Professeur des Universités, IMMM Le Mans Université, Président du jury
Mme. Gwenaelle Rousse	Maître de Conférences, CSE Sorbonne Université
M. Pascal Roussel	Directeur de Recherche, UCCS Université de Lille
M. Matthew Dyer	Maître de Conférences, Université de Liverpool
M. Mathieu Allix	Directeur de Recherche, CEMHTI CNRS
M. Michael J. Pitcher	Chargé de Recherche, CEMHTI CNRS

« It’s not the load that breaks you down, it’s the way you carry it. »

Lou Holtz

« Passion is energy. Feel the power that comes from focusing on what excites you. »

Oprah Winfrey

Acknowledgements

I would like first to acknowledge the Region Centre Val-de-Loire, Agence National de la Recherche (ANR) and the CEMHTI laboratory for the provided financial support over three years of my PhD.

Many thanks to Dr. Gwenaelle Rousse (CSE, Paris) and Dr. Pascal Roussel (UCCS, Lille) for accepting to review in details my work. I would like to also thank the examiners Prof. Vincent Maisonneuve (IMMM, Le Mans) and Dr. Matthew Dyer (University of Liverpool) for taking part of my PhD defence committee.

My deepest respect and gratitude to Dr. Mathieu Allix and Dr. Michael J. Pitcher for first giving me this opportunity in joining the CERAM group and work as a part of the team, also for their supervision and their presence in tough times when I needed their help the most. My sincere recognition to the CEMHTI laboratory director Catherine Bessada for welcoming as a PhD student in the CEMHTI lab. Special thanks go to all the lab and CERAM group members who made my time much enjoyable.

- To Emmanuel Veron: Merci beaucoup for all the things you thought me about X-ray diffraction. Merci beaucoup for the time you took explaining to me the different software I used over my PhD. Merci beaucoup for all the laughs we had together about stupid stuff. Merci for cheering me up when I needed encouragements. Just thank you for being you.
- To Cécile Genevois: I miss the days we shared the same office, which we named "the office of stressed people". Thank you for operating all the TEM measurements, your top-notch experience was really handy in bringing the most information possible to complete the analysis of my different materials especially the amazing STEM-EDS maps you provided for the lanagsite materials project. Thank very much you for your continuous support.
- To Sandra Ory: Thank you for operating all the DSC measurements even in short notice times 😳. Having nearby offices was a hell of an experience that made my stay at CEMHTI a very memorable one.
- To Weiwei Cao: Or Dr. Cao I should say. I can't thank you enough for all the advices you gave me about how to optimise my synthesis using the ADL given your wide experience. I wish you all the best in your future career whatever you end up doing.

- To Alessio Zandona: Grazie mille for all the knowledge you brought to the team, and the project we shared together, it was an enjoyable experience working with you. I much liked your human side as you were always there to hear me out.
- To Xue Fang, Renaud Valois, Euan Duncun and Jan Baborak: Thank you for sharing your time with me and reminding me every day how stupid my jokes can be, really appreciate it guys 👍😂. I'm pretty sure you all will be doctors of philosophy in the near future.

I would like to give special thanks to: Yannick Ledemi, Sébastien Chenu, Olivier Hernandez, Alberto José Fernandez-Carrion, Přemysl Beran, Matthew Dyer, Stanislav Savvin, Emmanuelle Suard, Dominique Massiot, Vincent Sarou-Kanian, Franck Fayon and Leire Del-Campo for paying attention to my questions and being part of my research work. Many thanks also to all the other PhD students in the CEMHTI laboratory for the many laughs we had together and the time spent arguing about dumb stuff.

I present my sincere gratitude and appreciation to my mother Assia, my father Hassan, my sister Chaymae and my brother Youness for always being by my side and their endless support and never-ending love, even though they are far from me.

To my best mates Yassine Hbiriq (H), Babacar Diallo (babou), Salah Eddine EL Abbadi (momo), Houssine El Barkali, Othmane Noussair (Hit-man). I could not of done this without your tremendous support.

After three years of hard work, dedication, pure passion, sacrifices, my story as a PhD student in the CEMHTI laboratory has reached its final chapter. Many memories are crossing my mind while writing this, obviously there were highs and lows, but I can't express how much I loved the experience and would definitely do it all over again if I had the chance to, with the same energy, conviction and most importantly the same passion.

Scientific communications

Publications

- **Emergence of A-Site Cation Order in the Small Rare-Earth Melilites $SrREGa_3O_7$ (RE = Dy–Lu, Y).**
C. Genevois, H. Bazzaoui, M. Boyer, S. Ory, Y. Ledemi, Y. Messaddeq, M. J. Pitcher, and M. Allix, *Inorg. Chem.*, 60, 12339, 2021.
- **Stabilization of the Trigonal Langasite Structure in $Ca_3Ga_{2-2x}Zn_xGe_{4+x}O_{14}$ ($0 \leq x \leq 1$) with Partial Ordering of Three Isoelectronic Cations Characterized by a Multitechnique Approach.**
H. Bazzaoui, C. Genevois, D. Massiot, V. Sarou-Kanian, E. Veron, S. Chenu, P. Beran, M. J. Pitcher, and M. Allix, *Inorg. Chem.*, 61, 9339, 2022.
- **Towards New Zero-Thermal-Expansion Materials: Li-Free Quartz Solid Solutions Stuffed with Transition Metal Cations.**
H. Bazzaoui, C. Genevois, E. Véron, M. J. Pitcher, M. Allix, A. Zandona (Submitted to: Journal of the European Ceramic Society).
- **Prediction and Synthesis of La-doped $Ca_5Ga_6O_{14}$ Melilite-like Structure for New Interstitial Oxide Ion Conductors.**
H. Bazzaoui, C. Genevois, O. Hernandez, M. Dyer, S. Chenu, L. Del-Campo, M. Allix, and M. J. Pitcher (In preparation).
- **Extended Doping Limits in the $La_{1+x}Ba_{1-x}Ga_3O_{7+x/2}$ Solid Solution with the Highest Interstitial Oxides Concentration in a Tetragonal $P\bar{4}2_1m$ Melilite.**
H. Bazzaoui, L. Babicova, A. J. Fernández-Carrión, M. Allix, and M. J. Pitcher (In preparation).

Oral and poster presentations

- **Cationic Ordering in $SrREGa_3O_7$ (RE =Dy, Ho, Er, Tm, Yb, Lu) melilites: Structure, Stability.** (Poster)
H. Bazzaoui, C. Genevois, M. Boyer, S. Ory, Y. Ledemi, Y. Messaddeq, M. J. Pitcher, and M. Allix *Ecole de Cristallographie et Grands Equipements* (CGE), 12 – 16 October 2020, Synchrotron Soleil, France.
- **Cationic ordering in $SrREGa_3O_7$ (RE =Dy, Ho, Er, Tm, Yb, Lu) Melilites: Structure, Stability** (Oral)
H. Bazzaoui, C. Genevois, M. Boyer, S. Ory, Y. Ledemi, Y. Messaddeq, M. J. Pitcher, and M. Allix *Journée des jeunes chercheures* (J2C), 24 – 26 march 2021, Orleans, France.
- **Emergence of A-Site Cation Order in the Small Rare-Earth Melilites $SrREGa_3O_7$ (RE = Dy – Lu, Y).** (Poster)
H. Bazzaoui, C. Genevois, M. Boyer, S. Ory, Y. Ledemi, Y. Messaddeq, M. J. Pitcher, and M. Allix *15th International conference on materials chemistry (MC15)*, 12 – 14 July 2021, Visio-conference.
- **New Materials by Direct Crystallisation from Glass or Molten Liquid.** (Oral)
H. Bazzaoui, C. Genevois, E. Véron, S. Ory, M. J. Pitcher, and M. Allix
Journée des Doctorants (JDD), 7, 14 et 21 September 2021, Orleans, France.

- **Emergence of A-Site Cation Order in the Small Rare-Earth Melilites $SrREGa_3O_7$ (RE = Dy – Lu, Y).** (Oral)
H. Bazzaoui, C. Genevois, M. Boyer, S. Ory, Y. Ledemi, Y. Messaddeq, M. J. Pitcher, and M. Allix

Journées de la Division Chimie du Solide de la SCF, 15 – 19 November, visio-conference.

- **$Ca_3Ga_{2-2x}Zn_xGe_{4+x}O_{14}$ Structural and Cationic Disorder Characterisation.** (Poster)
  H. Bazzaoui, C. Genevois, D. Massiot, V. Sarou-Kanian, P. Beran, S. Chenu, M. J. Pitcher and M. Allix
  14e Colloque Rayons X et Matière, 23 – 26 November 2021, Aix-en-Provence, France.
- **Prediction and Synthesis of La-doped $Ca_5Ga_6O_{14}$ Melilite-like Structure for New Interstitial Oxide Ion Conductors.** (Oral)
  H. Bazzaoui, C. Genevois, O. Hernandez, M. Dyer, S. Chenu, L. Del-Campo, M. Allix, and M. J. Pitcher
  Journée des jeunes chercheures (J2C), 28 - 29 march 2022, Orleans, France.
- **Prediction and Synthesis of La-doped $Ca_5Ga_6O_{14}$ Melilite-like Structure for New Interstitial Oxide Ion Conductors.** (Poster)
  H. Bazzaoui, C. Genevois, O. Hernandez, M. Dyer, S. Chenu, L. Del-Campo, M. Allix, and M. J. Pitcher
  17th European Powder Diffraction Conference (EPDIC17), 31 May – 3 June, Šibenik, Croatia.

Table of contents

General introduction

Design and development of new materials is much needed in today's society for various different application types: medical [1]–[6], energy storage and conversion [7]–[10], industrial [11], [12] and security [13]. Recent works have demonstrated the possibility of computationally probing a particular property and then synthesising the material itself [14]–[17]. However, one of the major obstacles relates to the synthesis approach to achieve these materials. At the CEMHTI laboratory, a unique synthesis path of metastable materials is approached: crystallisation from glass or the under-cooled melt. The use of aerodynamic levitation coupled to two CO_2 lasers (described in appendices Chapter A.I section A.I.1.1.2) at high temperatures allows samples to be melted at temperatures as high as 3000°C; the setup also affords rapid cooling rates reaching almost 1000°C/s (depending on the material and the carrier gas). This process grants the occurrence of either glass or the direct crystallisation of materials from an under-cooled melt. Additionally, in the case of achieving glass samples, crystallisation can be induced by an appropriate heat treatment at relatively low temperatures. This can produce new materials, for example glass crystallisation allowed the discovery of the first fully crystallised $BaAl_4O_7$ transparent ceramic material with two new polymorphs, unattainable by conventional ceramic methods [18].

The context of the present work follows previous PhD student projects in the CEMHTI laboratory who used aerodynamic levitation to develop new polycrystalline transparent ceramic materials in different systems, including aluminates, strontium aluminosilicates, rare earth gallates…etc., where precursor glasses can be formed by the aerodynamic levitation method.

This thesis will focus on the synthesis and multi-scale characterisation of two main materials classes:

(i) Materials for optics: Chapter II and Chapter III.

(ii) Ionic conducting materials for energy application such as solid oxide fuel cells: Chapter IV and Chapter V.

Chapter I sets the state of the art for the discussed materials in the following chapters. This chapter also describes different alternative synthesis pathways to the conventional ceramic routes to reach for new metastable materials. Several examples of new materials made at the CEMHTI laboratory by crystallisation from glass or an under-cooled melt are given.

Chapter II follows on from Marina Boyer's thesis work (University of Orléans, 2016) on the Sr*RE*Ga_3O_7 (*RE* for rare earth) melilite compounds, during which she discovered a new melilite superstructure crystallising in an orthorhombic supercell for small rare earths *RE*= [Ho - Yb]. She was also able to synthesise some of these melilite materials as bulk transparent ceramics. This chapter reports investigations on extending the synthesis limits of this new melilite polymorph but also for the parent tetragonal melilite subcell to small lanthanides, with a detailed structural study of both polymorphs. Additionally, the stability of both melilite structures against temperature is also reported. Finally, the photoluminescence properties are investigated and compared between the glass, parent and superstructured melilites of the same composition.

In Chapter III, a new solid solution $Ca_3Ga_{2-2x}Zn_xGe_{4+x}O_{14}$ crystallising in the langasite structure family (S.G. *P*321), which is a melilite related mineral, is investigated by two synthesis processes: glass and melt crystallisation. By refining the synthesis route via a metastable precursor (i.e. glass or melt), the trigonal langasite structure is stabilised all the way to the $Ca_3ZnGe_5O_{14}$ (x = 1) compound previously reported to crystallise in a distorted monoclinic *C*2 cell by single crystal growth methods. The interest of investigating this solid solution is motivated by previous works at the CEMTI laboratory on the $Zn_{1+x}Ga_{2-2x}Ge_xO_4$ spinel solid solution, which exhibited interesting long-lasting red luminescence when functionalised by Cr^{3+} [19], but also nanoscale phase separation in the parent glass leading to transparent ceramic materials by controlled crystallisation in the $Na_2O{-}ZnO{-}Ga_2O_3{-}GeO_2$ phase system [20]. Moreover, one of the main interests in this work is the characterisation of crystallographic ordering between three isoelectronic cations Zn^{2+}, Ga^{3+} and Ge^{4+} over three different crystallographic sites. To fulfil this task, a combined analysis against SPD, NPD and ss-NMR data was first adopted for the x = 0 and 1 end members. Furthermore, to build a chemically justified model for intermediate compositions such as x = 0.5, an innovative and unique approach was adapted by quantifying the cationic sites occupancies from a full two-dimensional signal refinement of acquired atomic resolution STEM-EDS maps for each cation.

Both Chapters IV and V focus on the synthesis of new doped melilite materials with ionic conduction properties for potential SOFC applications. The discovery by J. Fan *et al.* [21], of the alkali free $La_2Ga_3O_{7.5}$ (x = 1) end member which crystallises from an under-cooled melt using the ADL apparatus, and adopts a melilite *Ima*2 super cell ($\sqrt{2}a \times \sqrt{2}b \times 2c$), suggested the possibility of increasing the lanthanum doping amounts in the $La_{1+x}Ba_{1-x}Ga_3O_{7+x/2}$ solid solution, previously set at x = 0.35 attainable by solid state reaction, and motivated the work

presented in Chapter IV. Therefore, by crystallising an under-cooled melt of $La_{1+x}Ba_{1-x}Ga_3O_{7+x/2}$ ($0.3 \leq x < 1$) composition, the synthesis of the whole solid solution series is investigated, while setting the x stability limits between the parent tetragonal ($P\bar{4}2_1m$) and orthorhombic (*Ima*2) melilites. The structural trend is studied by SPD measurement across the whole solid solution compositions, while the cationic and anionic distribution are characterised by NPD measurements at room and high temperatures. To study the electric properties of these materials, AC impedance spectroscopy measurements were used, revealing the high ionic conductivity of these materials, almost equalling the best known melilite conductors [22], [23].

Chapter V on the other hand presents the study of a melilite-like material, $Ca_5Ga_6O_{14}$, which possesses the same melilite $[GaO_4]_n$ infinite 2D framework layers stacked antiparallel with different positioning of the A-sites. In this chapter, the study consists of first defining the most energetically favourable doping aliovalent cation by DFT calculation, then synthesising the doped compound and defining its doping limits by multiple synthesis approaches. The structural characterisation of both doped and parent compounds is reported by coupling SPD, NPD and TEM characterisation techniques. One of the strongest aspects of this work is exploiting the characterisation techniques to their sensitivity limits, as of due to the quite low doping amounts, with only 0.89% of introduced interstitial oxides (to keep a charge balanced composition), makes the determination of their position in the cell particularly hard to resolve with diffraction techniques. Therefore, DFT calculations were used to identify the most energetically favourable position of the interstitial oxide, which helps to interpret the observed results from previous analysis techniques. Ionic conductivity investigations by AC-impedance on SPS-densified pellets of the maximally-doped and parent samples, showed an increase of two orders of magnitude over the parent material. Nevertheless, even by retaining the same melilite framework, the structural constraints imposed by the $[GaO_4]_n$ sheets stacking and A-sites positioning limited the interstitial oxide distribution over the five-fold pentagonal channels, as opposed to the complete disordered $P\bar{4}2_1m$ melilite interstitial oxides framework, which inhibits its ionic conductivity and showed much lower values compared the best melilite conductors.

References:

[1] C. Greskovich, S. Duclos, *Annual Review of Materials Science*, 1997, **27**, 69.

[2] S.J. Duclos *et al.*, *Nuclear Instruments and Methods in Physics Research Section A: Accelerators, Spectrometers, Detectors and Associated Equipment*, 2003, **505**, 68.

[3] L.S. Bass, *et al.*, *Lasers in Surgery and Medicine*, 1995, **17**, 315.

[4] S. Balasubramanian, *et al.*, *International Journal of Pharmaceutical Sciences and Research*, 2017, **8**, 4950-4959.

[5] M. Vallet-Regí, *Dalton Transactions*, 2006, 5211.

[6] E. Meechoowas *et al.*, *Materials Today: Proceedings*, 2022, **65**, 2407.

[7] J.L. Black, *Glassy Metals I*, 1981, 167.

[8] J.H. Campbell, *et al.*, *Journal of Non-Crystalline Solids*, 2000, **263**, 318-341.

[9] S. Supriya, *Journal of Inorganic and Organometallic Polymers and Materials*, 2022, 1-18.

[10] J. Lin *et al.*, *Chemical Engineering Journal*, 2022, **444**, 136538.

[11] C.B. Carter, *et al.*, Ceramic Materials. Springer New York, 2013, 766.

[12] Y. Lakhdar *et al.*, *Progress in Materials Science*, 2021, **116**, 100736.

[13] R. Klement *et al.*, *Journal of the European Ceramic Society*, 2008, **28**, 1091.

[14] A.R. Oganov *et al.*, *Nature Reviews Materials*, 2019, **4**, 331.

[15] S. Chibani, F.-X. Coudert, *APL Materials*, 2020, **8**, 080701.

[16] B. Civalleri *et al.*, *CrystEngComm*, 2006, **8**, 364.

[17] P.G. Boyd *et al.*, *The Journal of Physical Chemistry Letters*, 2017, **8**, 357.

[18] M. Allix *et al.*, *Advanced Materials*, 2012, **24**, 5570.

[19] M. Allix *et al.*, *Chemistry of Materials*, 2013, **25**, 1600.

[20] S. Chenu *et al.*, *Advanced Optical Materials*, 2014, **2**, 364.

[21] J. Fan *et al.*, *Chemistry of Materials*, 2020, **32**, 9016.

[22] X. Kuang *et al.*, *Nature Materials*, 2008, **7**, 498.

[23] M. R. Li *et al.*, *Angewandte Chemie International Edition*, 2010, **49**, 2362.

Chapter I: State of the Art

I.1. Introduction.

Materials science is one of the largest research fields ranging from the synthesis, structural determination to properties characterisation of solids, but most importantly the understanding of the link between these three main axes. This is even more important as the demand of novel high performing materials keep on increasing. Materials science therefore includes aspects of engineering, physics and chemistry, related to fulfil these desired aims [1]. Extended inorganic oxides are one of the many materials science subsets and are usually known to be synthesisable by the oldest, simplest and widely used solid state reactions. For instance, this synthesis route has seen its usage in making a large number of high-T_c superconductor materials [1]. Although this method is quite simple to set up, i.e. mixing the starting materials powder and sinter them for long times at high temperatures, in most cases it leads to the thermodynamically stable products. Hence, reaching for metastable new materials can be facilitated by the development of new synthesis routes. In the following chapter, the state of art is described, considering different alternative synthesis approaches to the conventional ceramic routes. Particular attention is given to crystallisation methods from glass or under-cooled molten liquid precursors, as these two synthesis paths are heavily used in this thesis work. Some key material examples obtained by these two methods are also given for optical applications. A small review of new ionic conducting materials is given at the end of the chapter.

I.2. Synthesis of metastable inorganic materials.

The conventional ceramic materials synthesis routes by solid-state reaction are widely spread due to their simplicity and effectiveness in making solids react with each other. They usually operate at high temperatures ranging from 900°C to 1600°C with long sintering times and require sometimes multiple heat treatments with intermediate grinding of the powder mixture, leading to the most thermodynamically stable reaction products [2]. Classic manual powder mixing usually leads to precursors grain size at the micron scale, meaning that atoms from the grains core will need high activation energy to diffuse all the way to the interface and react, which can explain the required high temperatures to reach for full precursors reactions in the solid-state. These synthesis procedures have brought to light many key materials with desirable properties, for example thermal, optical and energy properties [3]–[9]. Despite the wide usage of these synthesis paths, the reactions remain limited by the low diffusion rates of the reactants within a solid even at high temperatures. Nonetheless, demands for high-performing novel materials by consumers, industries, and governments continue to increase; for example, nowadays new materials for energy applications and CO_2 storage are highly desirable to reduce

the negative impact of energy extraction on the environment. Discovery of inorganic materials with new compositions and crystal structures faces two fundamental problems: (i) how to synthesise materials that may be metastable and thus easily missed by conventional ceramic approaches, and (ii) which compositions to target in the first place. The second problem is approachable by prediction of materials properties and crystal structures, shown to be achievable by computational methods narrowing the targeted compositions and facilitating the heavy task of synthesis exploration in the quest of discovering new materials with more efficient or equally performing properties [10]–[18]. Yet, the ultimate challenge lies in synthesising these compounds, which is not always achievable by conventional routes. Formerly, many new materials were discovered with the intention of systems exploration [19]. Soft chemistry is one of the main known approaches to synthesise both stable and metastable materials at low temperatures. This approach involves two alternative pathways: (i) topochemical, which consists of preparing the parent compound by classic routes and then converting it to a descendant phase by cation exchange, hydrolysis or even redox reactions (see Figure I.1). (ii) Non-topochemical, which on the other hand does not involve any intermediate stage (e.g. a parent compound) and the final material is synthesised directly [2] (see Figure I.1).

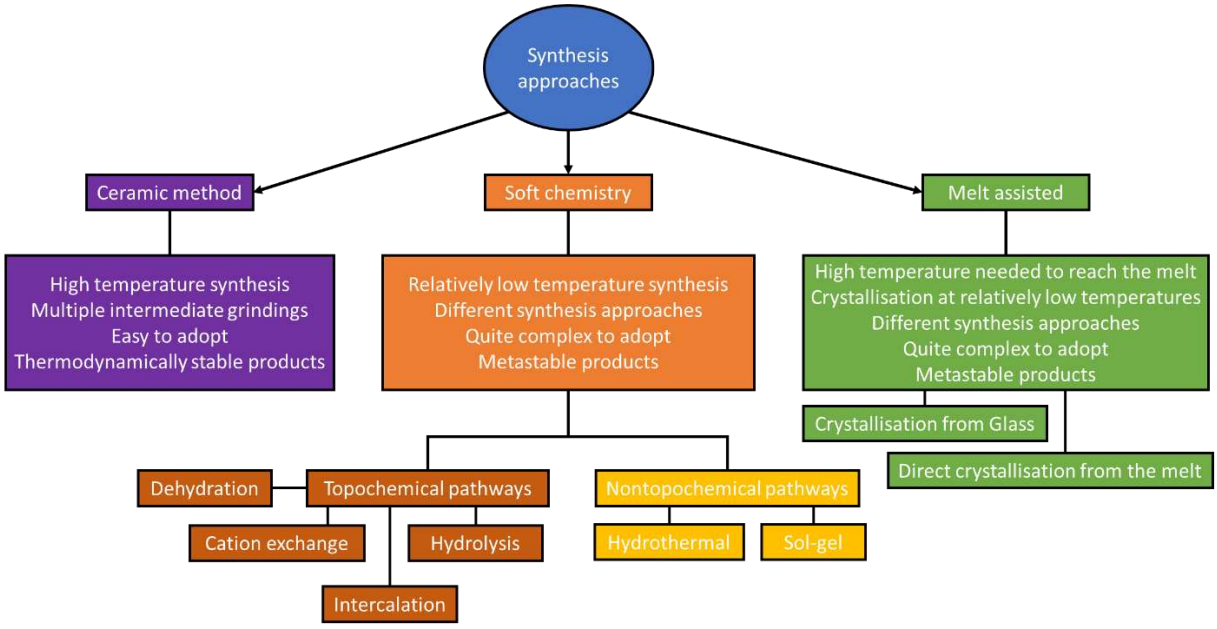

***Figure I.1**. Comparison between conventional and soft chemistry synthesis approaches, redrawn and adapted from [2].*

The metastable state of matter by definition is a state whose free energy lies at a local minimum and can be converted to the most thermodynamically stable state when energetically

disturbed [20], [21] (see Figure I.2). The key points in making new metastable materials are the initial mixture homogeneity and the diffusion distance that atoms will have to travel within the sample mixture to react and form the target compound, as ensuring a good homogeneity of the mixture while reducing the atoms diffusion distance can considerably lower the synthesis temperature. In fact, this allows to reach for energy local minima, thus probing metastable structures. This can be fulfilled by ball milling the mixture, which helps to substantially reduce the grain size to the nanometre scale. Far better procedures can be adopted by making a gel or glass from the initial composition or even melting the mixture (few compound examples are given in section I.3 and section I.4 of this Chapter). These latter approaches strongly depend on the mixture composition, as they can also be phase separated, in which case crystallisation will result in a multi-phase product.

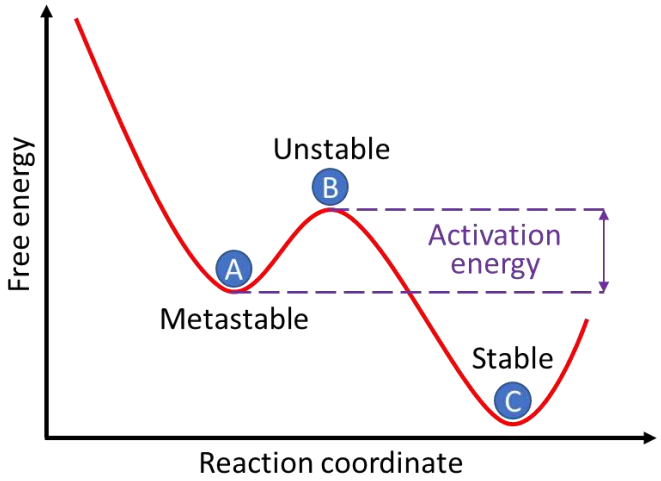

Figure I.2. *Energy curve of a system comparing its metastable, unstable and stable states.*

I.2.1. Crystallisation from glass: An innovative concept for achieving new metastable materials.

Commonly the word glass has been linked to inorganic oxides which were successfully cooled from their liquid to solid state without crystallising, hence retaining their amorphous structure [22]. Moreover, different definitions have been given to glass materials in order to best describe the glassy state of this category of compounds [23]–[25]; the latest one to date is as follows: *"Glass is a nonequilibrium, non-crystalline condensed state of matter that exhibits a glass transition. The structure of glasses is similar to that of their parent supercooled liquids (SCL), and they spontaneously relax toward the SCL state. Their ultimate fate, in the limit of infinite time, is to crystallize"* designated by E. D. Zanotto *et. al.* [22]. Considering this

definition, the metastable state of glass is the major motivation behind choosing it as precursor for crystallisation to reach for new metastable materials.

Oxide glasses are usually synthesised by conventional melt quench approaches, which involve melting at high temperatures and then air or water quenching. However, to prevent the emergence of devitrification, i.e. long-range order, during glass synthesis, the melt cooling rate needs to be high enough to "freeze" or suspend atomic movement going from the liquid to solid state of matter. Moreover, the required cooling rates differ from one composition to another, for example borosilicate glasses are very hard to crystallise [25]. Nevertheless, even with sufficient cooling rates, more than one parameter enters the complex equation of accomplishing oxide glass compounds. The crucial parameter in making glass is the starting composition ability to form a covalently bonded network [25], [26]. Glass-making compositions must contain a network former element (e.g. SiO_2) which ensures the formation of strongly bonded long atomic chains [25]. Other components can be found in glass composition such as network modifiers (e.g. B, Ca, Ba, Sr…etc) and network intermediaries (e.g. Al, Ga, Ge…etc). The first ones are usually introduced to modify the glass properties, wheras the latter ones role sits in between network formers and modifer, and can play the role of both [25], [26].

The amorphous state of matter represents a long-range non-periodicity in terms of atomic positions, which is usually linked with topological or chemical disorder. The opposite of crystals which show long-range periodicity of atomic positions (but not always chemical ordering). In oxide glasses, even in the absence of long-range order, local order can be discerned on the length scale of several Angstroms, for example SiO_4 tetrahedral units taking part of the SiO_2 glass network (see Figure I.3).

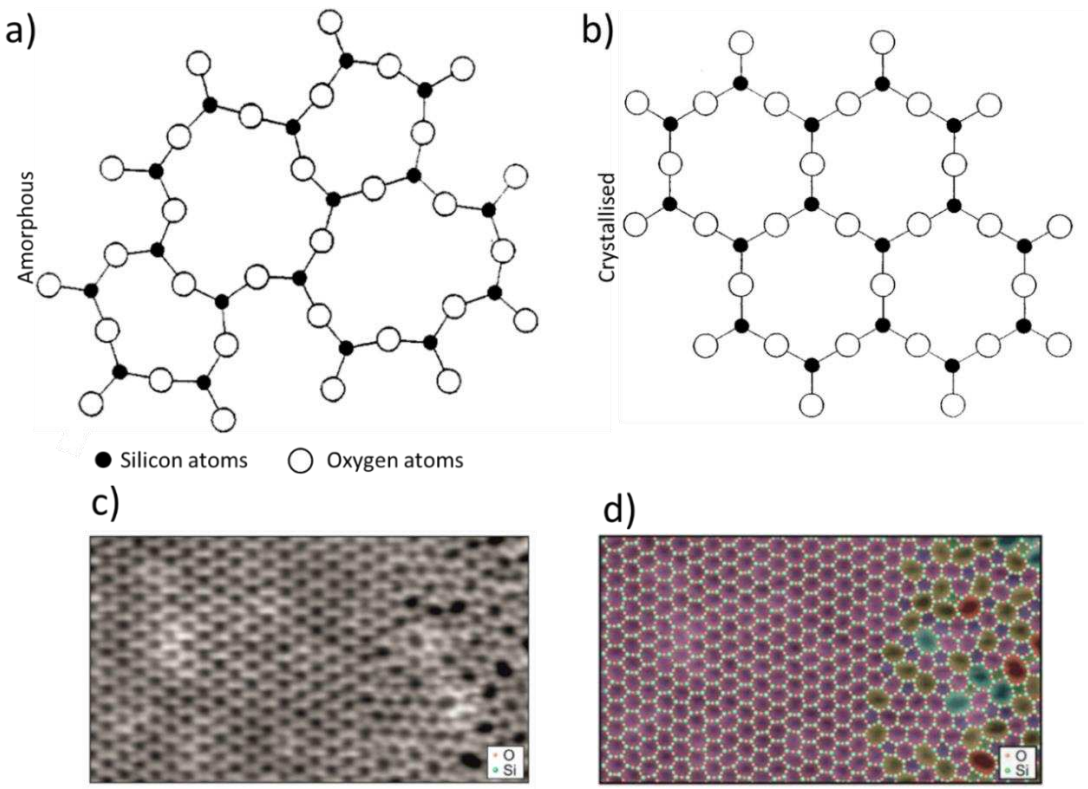

***Figure I.3**. a), b) Planar projection of quartz network in its both amorphous and crystalline states respectively, drawn from [24]. c) STM image of a partially crystallised SiO_2 film. d) coloured STM image (showed in (c)) highlighting the random distribution of $[SiO_4]_n$ rings in the amorphous SiO_2 vs the well-defined $[SiO_4]_6$ rings in the crystallised quartz, from [27].*

Glass-ceramic materials are usually attained by partial crystallisation of glass compounds, i.e. a significant fraction of the material remains amorphous. The crystallisation task is usually a two-step process: (i) nucleation (homogeneous or heterogeneous), which typically occurs slightly above the glass transition temperature "T_g", (ii) crystal growth at temperatures superior to T_c ($T_c > T_g$). These steps are illustrated in Figure I.4. Ideally, to control the crystallite growth and size, homogeneous nucleation is highly desired, as it induces volume crystallisation. However, this phenomenon is rarely observed in glass-ceramic materials and heterogeneous nucleation is the dominant process, being thermodynamically favoured, i.e. surface crystallisation [25]. Surface or bulk crystallisation mechanisms are highly relevant when it comes to the materials related properties, as they both can lead to different performance of the same material. For a controlled nucleation, the addition of nucleating agents (like TiO_2, ZrO_2, …etc) have shown to help achieving a volume crystallisation instead of the expected surface crystallisation [28], [29]. This discovery marked a milestone and the start of the glass-ceramic era, as soon after commercial glass-ceramics starting emerging with managed crystallite numbers and sizes.

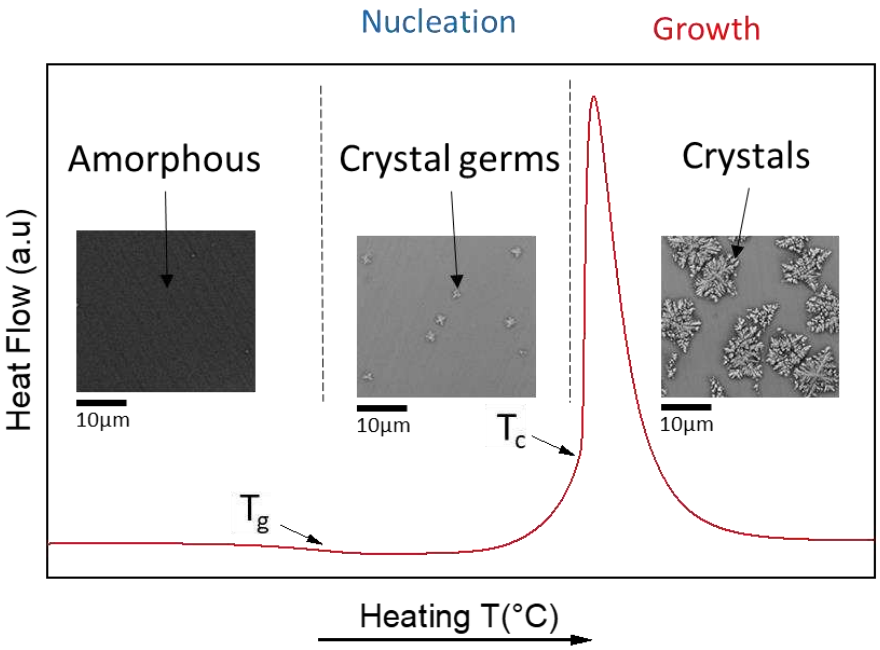

Figure I.4. *Illustration of the crystallisation process evidencing the temperature depending phenomena of nucleation and crystals growth using a DSC curve. The insert SEM images were taken from [30].*

I.2.2. Direct crystallisation from under-cooled melts.

Glass synthesis is not always a successful process, as for some compositions crystallisation might occur on the cooling. Taking advantage of a melt homogeneity in its liquid state and metastable aspect, it is possible to reach for new materials by operating a direct crystallisation from the under-cooled melt. In different words, it means that crystallisation of the melt occurs at temperatures far below the liquidus point on the phase diagram. In this aspect, this procedure can be perceived as an alternative synthesis process to the previously described glass crystallisation process in the hunt for new out of equilibrium materials. Direct crystallisation from the under-cooled liquid operates by heating a sample until reaching its liquid state, then cooling to room temperature using an appropriate (rapid) cooling rate to secure a crystalline compound directly. Moreover, using the ADL apparatus offer the possibility to control the melt's cooling rates, by controlling the lasers power. This was demonstrated in several works as a promising strategy to reach for new metastable crystalline compounds, with new and interesting properties (discussed in the next sections). It is feasible by this approach to synthesise millimetre sized single crystalline domains in certain cases [31]. Nevertheless, it is rather different to conventional single crystal synthesis approaches from the melt (i.e. crystal pulling, directional solidification floating zone, Verneuil technique) [32] in the sense that the crystallisation occurs under conditions that are far from equilibrium.

I.3. New materials for optical ceramics.

New materials with optical properties, especially new transparent ceramics, are one of the major research axes of the CERAM group at the CEMHTI laboratory. The aerodynamic levitation coupled to two CO_2 lasers offers the possibility to melt samples with melting temperatures as high as 3000°C while levitated by a carrier gas of choice (argon, oxygen, …) in a contactless process. This procedure allows to reach very high cooling rates (1000°C/s in some cases), but most importantly it prevents impurity contamination that may come from the sample holder, or the formation of crystal nucleation centres from contact points between the sample and the sample holder leading to heterogeneous crystallisation, which permits the family of glass-forming compositions to be enlarged. Operating crystallisation from glass or melt precursors offers a certain degree of control of the crystallised sample microstructure, which is essential in seeking for new transparent ceramic materials as light scattering needs to be minimized. Regarding this aspect, many glass and melt crystallised materials have been reported as transparent ceramics, and even functionalised by rare earth doping, which unveiled interesting emission, scintillation and luminescence properties.

In the BaO-Al_2O_3 binary system, the $BaAl_4O_7$ compound was found to be non-synthesisable by conventional solid state routes [33]. Glass of $BaAl_4O_7$ composition was successfully synthesised using aerodynamic levitation coupled to two CO_2 lasers. Interestingly, by adopting the right heat treatment it is possible to crystallise this glass sample under two new phase pure α or β orthorhombic polymorphs [33]. Moreover, this composition was also reported as the first highly transparent polycrystalline ceramic (see Figure I.5), achieved by full and congruent crystallisation from a bulk glass [33], with potential optical applications (scintillators, optical lenses, high energy lasers, …). Since this finding, many works have been conducted on polycrystalline ceramic materials crystallised from glass for potential use in optics, photonic or energy fields. Additionally, by substituting Al_2O_3 for Ga_2O_3 in the initial mixture, the $BaGa_4O_7$ material was reported to be uniquely attainable by a direct crystallisation from the melt route. This previously unreported compound was described in a monoclinic structure (S.G. *I*2/*m*), and displayed strong luminescence in the orange-red region when doped with Eu^{3+} and excited under a 393 nm wavelength [34].

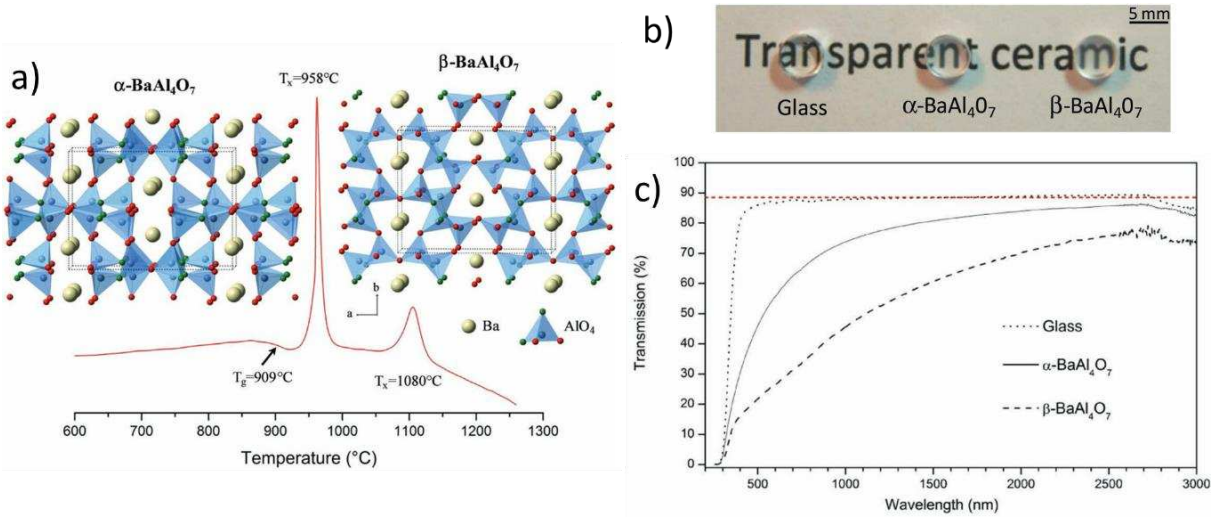

Figure I.5. *a) Differential scanning calorimetry curve upon heating of the $BaAl_4O_7$ glass composition and the crystal structure projection of the two synthesisable polymorphs in inserts. b) Photograph of polished glass and crystallised beads of the same composition. c) Transmittance measurements comparison between glass and the two polymorphs. All from [33].*

Other interesting systems could be the strontium aluminate system, where the glass crystallised $Sr_3Al_2O_6$ compound exhibits high transparency in the visible range, thanks to its cubic symmetry (S.G. $Pa\bar{3}$), no birefringence effects were found (optical isotropy). Moreover, scintillation and emission properties in the visible and infrared ranges were observed when doped with Ce^{3+}, Er^{3+} and Er^{3+}+Ho^{3+} respectively [35]. Furthermore, studied solid solutions of strontium alumino-silicates $Sr_{1-x/2}Al_{2-x}Si_xO_4$ and $Sr_{1+x/2}Al_{2+x}Si_{2-x}O_8$, reported large scale fully transparent bulk ceramics (Figure I.6a and Figure I.6b) with tunable luminescent properties controlled by the related chemical disorder of their crystal structures [36], [37]. The $Bi_{0.8}Nb_{0.8}Te_{2.4}O_8$ compound was successfully crystallised in a large-scale (discs of 60 mm diameter) transparent ceramic by full and congruent crystallisation from a $75TeO_2$-$12.5Nb_2O_5$-$12.5Bi_2O_3$ parent glass precursor composition (see Figure I.6c). The same study of this compound has revealed its crystallisation in a new cubic cell (S.G. $Fm\bar{3}m$) with a transparency in a wider range (3–7 µm) compared to that from the earlier described alumino-silicates solid solutions (4.2 µm) [38].

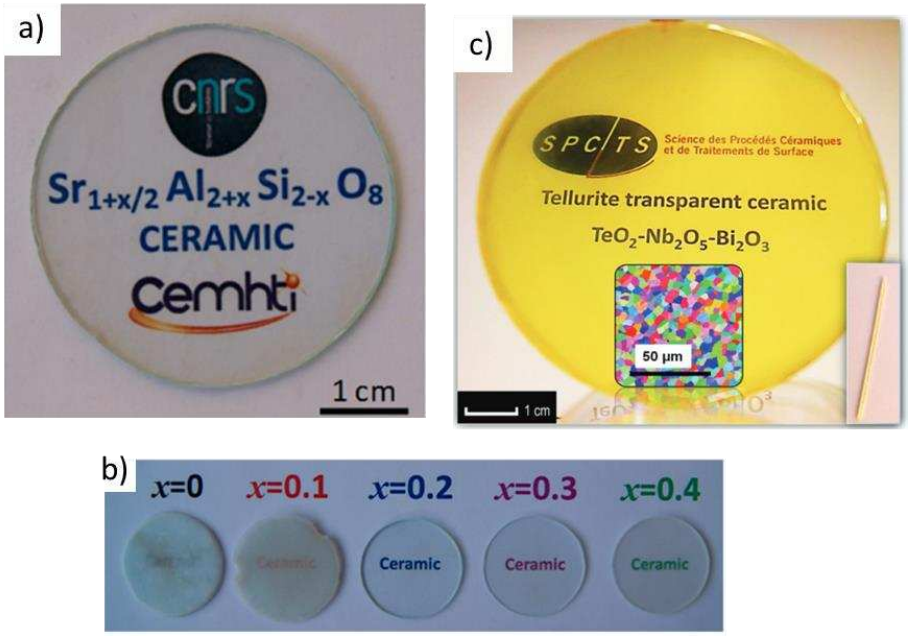

Figure I.6. *a) Photograph of a large crystallised bulk ceramic of $Sr_{1+x/2}Al_{2+x}Si_{2-x}O_8$ (x =0.2) composition. b) Photograph of different $Sr_{1+x/2}Al_{2+x}Si_{2-x}O_8$ ($0 \leq x \leq 0.2$) bulk crystallised compositions evidencing the evolution of transparency as a function of disorder. c)Photograph of a glass crystallised $Bi_{0.8}Nb_{0.8}Te_{2.4}O_8$ compound in the form of large disc (60 mm in diameter). The insert inside the disc shows an EBSD-SEM map of the material evidencing crystalline domains sizes. The insert at the bottom right shows a ceramic fibre of the same composition. These figures were taken from [37] and [38].*

More recently, in the CEMHTI laboratory, Weiwei Cao former PhD student has operated direct and full crystallisation from the under-cooled liquid as an approach to synthesise highly non-stoichiometric YAG (yttrium aluminium garnet) materials. In the literature the $Y_{3+x}Al_{5-x}O_{12}$ solid solution was reported with a maximum value of x = 0.03, synthesisable by solid-state reaction [39]. Moreover, this amount was extended to the value of x = 0.40 by W. Cao in her thesis work [40]. The increase of non-stoichiometry in this compound induced a significant population of Y^{3+} (< 20 %) on the 6-coordinated 16a sites of the garnet structure (S.G. $Ia\bar{3}d$) which usually host Al^{3+} exclusively. This was detected directly by crystallography rather than the previous indirect analyses of the cell parameters trend and energy calculations [39]–[41]. Interestingly, when non-stoichiometry is introduced, the luminescence properties can be strongly modified compared to the stoichiometric YAG garnet, depending on the coordination preference of the rare earth dopant ions [40].

The melilite compounds have also been studied as potential transparent ceramics by aerodynamic levitation methods. They have a general formula of $A_2B'(B_2O_7)$ which actually groups the åkermanite, Gehlénite, Okayamalite, Hardystonite and Gugiaïteare minerals that crystallise under the same structure family, adopting a tetragonal cell with a symmetry

following the $P\bar{4}2_1m$ space group (n°113) (Figure I.7). Their structure can be described as stacked sheets along the *c*-axis, which are formed by corner sharing (B',B)O_4 tetrahedra, creating edge-sharing $[(B',B)O_4]_5$ pentagonal channels where the A-site cations are held in the centre and in between the structure layers. Since their discovery, the melilite compounds attracted a lot of researchers interest due to their remarkable underlaying B'(B_2O_7) framework ability to distort, which led to the development of new synthetic melilite compositions, hence enlarging the field of compositions that takes part of this family. In the last century, newly developed melilite compounds showed different phase transitions from their parent tetragonal $P\bar{4}2_1m$ structure, with both modulations and supercells [42]–[48]. One of the leading motivations behind developing new melilite compound (especially the ABC_3O_7 compositions) is because of their impressive properties, with potential applications in the optical, piezoelectric and energy fields [49]–[52]. The (*AE*,*RE*)C_3O_7 melilite compositions where *AE* is an alkaline earth and *RE* a rare earth, were reported to manifest interesting transparency in the NIR range. Moreover, Marina Boyer a former PhD student in the CEMHTI laboratory, reported for the first time the stabilisation of a Sr*RE*Ga_3O_7 melilite series with *RE*= [Eu - Yb] as fully transparent bulk ceramics (Figure I.7c) achieved by congruent crystallisation from glass [53], [54]. However, one of the major limiting transparency factors of these materials is the sample colouration arising from the *RE* nature. Nevertheless, both $SrGdGa_3O_7$ and $SrYGa_3O_7$ compositions were also obtained as colourless bulk ceramic samples, showing very high transparency reaching a transmittance of 80% in the NIR region at ~ 2700 nm (Figure I.7d) [53], [54]. These (*AE*,*RE*)C_3O_7 composition-type, single-crystal materials, were also reported with promising piezoelectric and elastic properties at high temperatures [51].

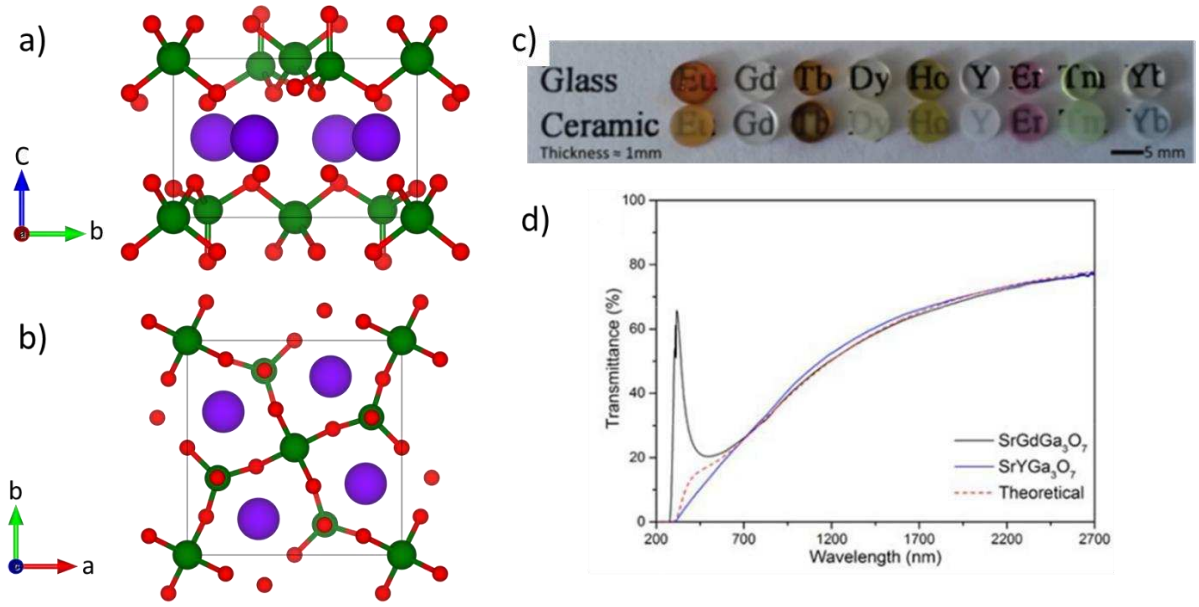

Figure I.7. *a), b) Crystal structure projection of the $A_2B'(B_2O_7)$ $P\bar{4}2_1m$ melilite compounds within the a-axis and c-axis respectively. c) Photograph of the $SrREGa_3O_7$ polished glass and ceramic materials. d) Transmittance curves after thickness normalization at 1 mm from both the $SrGdGa_3O_7$ (black) and $SrYGa_3O_7$ (blue) ceramics. The red dot curve corresponds to the transmittance fit based on the theoretical model. Both c) and d) panels were taken from [53].*

Highly transparent glass-ceramic materials were also obtained by a controlled crystallisation from $Na_2O–ZnO–Ga_2O_3–GeO_2$ systems, where $ZnGa_2O_4$ spinel nano-crystals can be found embedded in a GeO_2-rich glassy matrix [55]. In this system, the size of nano-crystals is fairly controlled by tuning the amount of Na_2O, which is found to not interfere in the crystals compositions but remains in the amorphous matrix. These materials can be easily functionalised by Cr^{3+} doping as demonstrated for $Zn_{1+x}Ga_{2-2x}(Ge/Sn)_xO_4:Cr^{3+}$ ($0 \leq x \leq 0.5$) solid solution in [56], leading to a considerable improvements of their long-lasting luminescence properties. Therefore, the occurrence of a high symmetry phase in the same system to potentially play the role of $ZnGa_2O_4$ spinels are of interest to investigate for new optically active materials.

Attempts to expand this study and develop new glass-ceramic compounds at nearby compositions has revealed the crystallisation of new langasite-type materials [57]. The $A_3BC_3D_2O_{14}$ langasite materials family which counts more than 250 members, is a melilite-related mineral. This structure family crystallises in a trigonal *P*321 cell, where A is an 8-coordinated, B 6-coordinated, C and D 4-coordinted sites. Its crystal structure can be described as a layered structure with an ABAB stacking along the *c*-axis. The langasites underlaying framework is formed by open $[(C,D)O_4]_5$ pentagons (A-layer at z_A=0.5), linked by BO_6 octahedra (B-layer z_B=z_A+0.5). The A-site cations sits in the B-layers filling the $[(C,D)O_4]_5$

pentagons centre, similar to the melilite structure (see Figure I.8). These structures were first reported in the $CaCO_3$-Ga_2O_3-GeO_2 ternary system, with the discovery of the $Ca_3Ga_2Ge_4O_{14}$ compound in 1980 [58], which can be readily produced as transparent materials by single crystals growth methods [59], [60]. Moreover, a few langasite compositions crystallise under a monoclinic *C*2 polymorph, or undergo a phase transition at high pressure/temperature (*P*321 → *C*2) [61]–[63]. Furthermore, langasite compounds have also been reported with compelling luminescence properties, as in the Eu^{3+} doped $La_3Ga_5MO_{14}$ *M*= [Zr, Hf, Sn] compound, assumingly promising red-emitting LED phosphors due to their high colour purity and thermal stability [64].

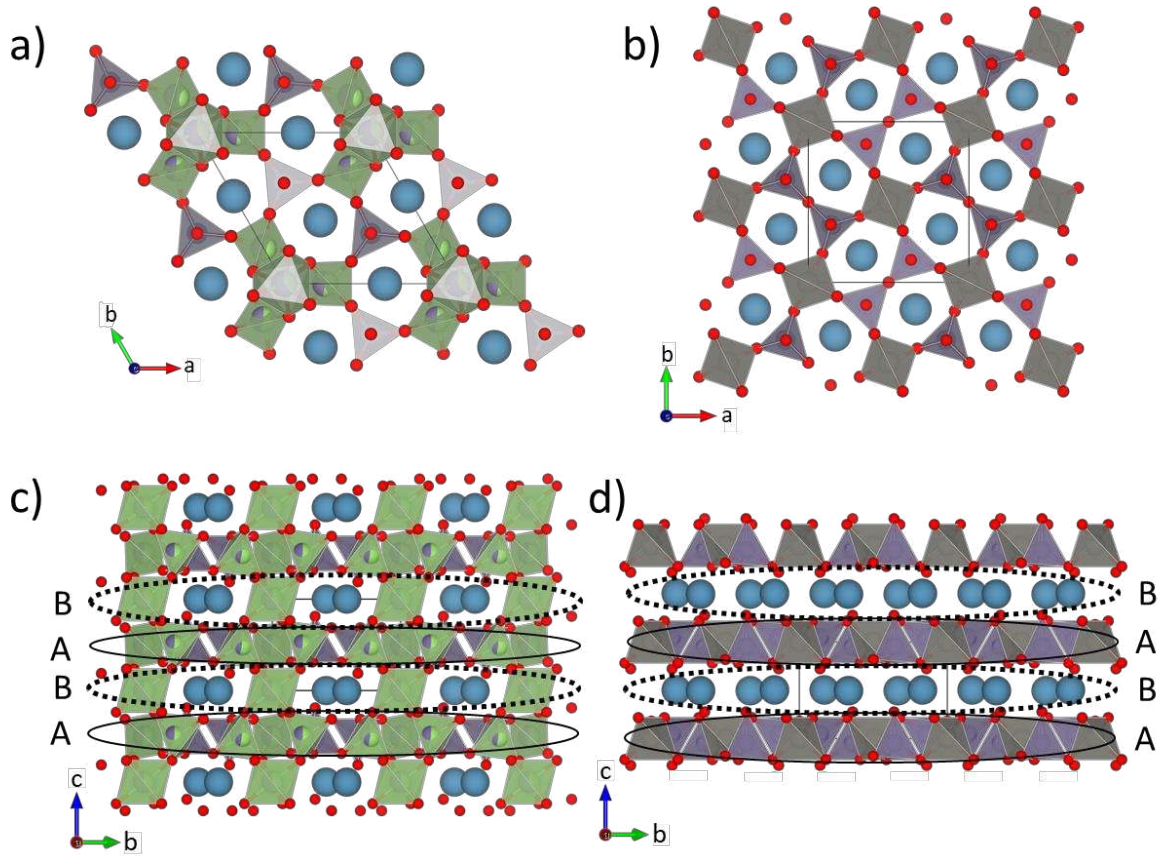

Figure I.8. *Langasite and melilite crystal structure projection respectively within, a) and b) c-axis, c) and d) a-axis, evidencing the similarities between these two structure types.*

I.4. New oxide ion conductor materials.

Research for new renewable energy sources as clean technologies is driven by the motivation of future decarbonisation and limiting planet pollution. In this aspect fuel cells are of interest [65]. Among the existing fuel cells types (e.g. alkaline fuel cells "AFC", molten carbonate fuel cells "MCFC", …) [66], here we focus on solid oxide fuel cells (SOFCs). In SOFCs, the

electrolyte is a dense ceramic material with O^{2-} anions taking the role of mobile charge carriers. SOFCs usually operate at temperatures around 1000°C due to the slow oxide ion migration at intermediate temperatures (500°C – 750°C). However, at these temperatures their functioning cost is high [67]. Developing new better performing oxide ion conductor materials (i.e. fast ion conduction) at intermediate temperatures will strongly benefit SOFCs in reducing their working temperature, and consequently lowering their functioning cost [67], [68].

SOFCs are composed of a dense solid electrolyte (ceramic), sandwiched between the cathode and the anode, as illustrated in Figure I.9. Oxygen from the atmosphere is reduced at the cathode surface (Equation I.1), and diffuses through the cathode and electrolyte until it reaches the anode, where it is oxidised to H_2O (Equation I.2). For all three components the materials choice is crucial for an operating SOFC [69]–[73]. SOFCs can also operate by proton or dual oxide-proton conduction [74]–[76]; these will not be further discussed, as only oxide ion conductors will be addressed in this thesis.

$$\frac{1}{2}O_2 + 2e^- \rightarrow 2O^{2-} \qquad \text{(Equation I.1)}$$

$$O^{2-} + H_2^- \rightarrow H_2O + 2e^- \qquad \text{(Equation I.2)}$$

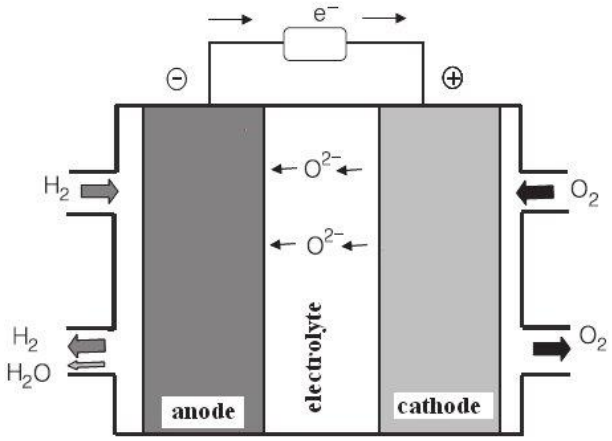

Figure I.9. *Schematic of a solid oxide fuel cell (SOFC) showing its different components, from [73].*

I.4.1. Electrolyte materials.

Development of new oxide electrolyte materials operating at intermediate temperature has tremendously increased in the last century. It has been proven that introducing oxygen defects while leaving the crystal structure as undisturbed as possible is highly preferable in making

good oxide ion conductors electrolytes [77]. In the following, a few important oxide-conductors structure-types will be addressed.

Fluorite structured oxides: Since early works of W. Nerst (1900s) on the fluorite structured oxide materials, many studies have been reported on these structure-type materials as potential candidates for oxide ion conductor electrolytes [77], [78]. AO_2 fluorite-type oxides crystallise in a cubic motif with the highest symmetry space group ($Fm\bar{3}m$) where the cations sit in a 4a site and are 8-coordinated, whereas the oxygens are held in the centre of an OA_4 tetrahedron (8c site) (see Figure I.10). These materials are usually doped with rare earth or alkaline cations substituting the host A cation, which introduce vacancies into the oxide sublattice, allowing the oxygen to migrate to adjacent (vacant) sites, thus enhancing the ionic conduction mechanism. Ytrria-stabilized zirconia $Zr_{1-x}Y_xO_{2-\delta}$ (YSZ) are among the best oxygen ion conductors [78] at elevated temperatures, besides the δ-Bi_2O_3 (i.e. $Bi_{0.75}Y_{0.25}O_{1.5}$) which exhibits an oxide ion conductivity of ~ 1 S cm^{-1}at 750°C [79] but is only stable in the temperature range 730°C – 824°C [80]. Moreover, $Ce_{1-x}M_xO_{2-\delta}$ M= [Gd, Sm] (GDC and SDC) are strong candidates for use at temperatures as low as 550°C [77] (see Figure I.12).

Perovskite oxides: Perovskite oxides are of interest materials, thanks to their ABO_3 structure-type which offers two distinct cation sites that can be both substituted with lower valence cations, thus leading to a wide range of possible perovskite-based oxide ion conducting materials [77] (excluding interstitial oxide containing perovskites). The typical perovskite crystal structure consists on a simple small cubic lattice where the A- and B-sites are 12- and 6-coordinated respectively (see Figure I.10). However, only few oxides crystallise under this cell-type and other distorted perovskite variants are often observed [81]. Ishihara *et al*[82] first reported fast oxide-ion conduction in the $La_{1-x}Sr_xGa_{1-y}Mg_yO_{3-\delta}$ (LSGM) which crystallise in a perovskite cell and reach impressive conductivity values of 8.10^{-2}S.cm^{-1} at 600°C for x = 0.2 (see Figure I.12).

BiMeVOx: The $Bi_4V_2O_{11}$ is the parent compound of this solid solution family and represent two reversable structural phase transitions $\alpha \leftrightarrow \beta$ and $\beta \leftrightarrow \gamma$, with an ionic conductivity of 0.1 S.cm^{-1} at T > 550°C attained under the γ polymorph [77], [83]. The γ- $Bi_4V_2O_{11}$ structure can be described as an alternated stacking between an A layer, i.e. $[Bi_2O_2]^{2+}$, and a B layer, i.e. $[VO_{3.5}\square_{0.5}]^{2-}$, with $\square$ representing oxide ion vacancies (see Figure I.10d). As in the fluorite-based and perovskite-based conductors, oxide vacancies provide fast charge transport at high temperature. To stabilise the γ polymorph at room temperature, usually vanadium substitution

is considered by lower valence cations to introduce oxygen vacancies, hence increase the material conductivity at low temperature. For example, the $Bi_2V_{1.9}Cu_{0.1}O_{5.35}$ (BICUVOX.10) compound is stabilised at room temperature under an incommensurate supercell of the disordered tetragonal γ polymorph, noted γ'. It is only at higher temperatures (~ T > 400°C) that the γ'↔γ phase transition occurs [84]–[86]. The BICUVOX.10 compound showed a considerable increase of its ionic conductivity by almost three orders of magnitude at low temperatures over the $Bi_4V_2O_{11}$ parent compound, i.e. 0.5×10^{-2} S.cm^{-1} *vs* 10^{-5} S.cm^{-1} respectively at 300°C [83].

Apatites: The $A(1)_2A(2)_3(MO_4)_6X_2$ *A*= [Ln, Na, K, Ca, Sr Ba, Mn, Cd, Pb] *M*= [Si, Ge, P, V] and *X*= [O, OH, F, Cl, Br, I] [87] apatite compounds structure can be described as isolated MO_4 tetrahedra stacked along the *c*-axis creating three distinct channels. Two are fully occupied by independently stacked *A*(1) and *A*(2) atoms, while the third one consists of an oxygen atom row (see Figure I.10). Contrary to what has been stated above for fluorite and perovskite conductors, relying on the introduction of oxygen vacancies to achieve fast oxide ion conduction, the apatite materials depend on introducing interstitial oxygens to act as mobile charge carriers. Lanthanum-based silicates or germanates oxide apatites, were found to be good ionic conductors at intermediate temperatures. In this aspect, the $Ln_{9.75}Sr_{0.25}(SiO_4)_6O_{2.895}$ and $La_{9.5}(Ge_{5.5}Al_{0.5}O_{24})O_2$ alkaline doped apatites show an increase of their conductivity by an order of magnitude compared to their $La_{10}(SiO_4)_6O_3$ analogue at 700°C [88] (see Figure I.12).

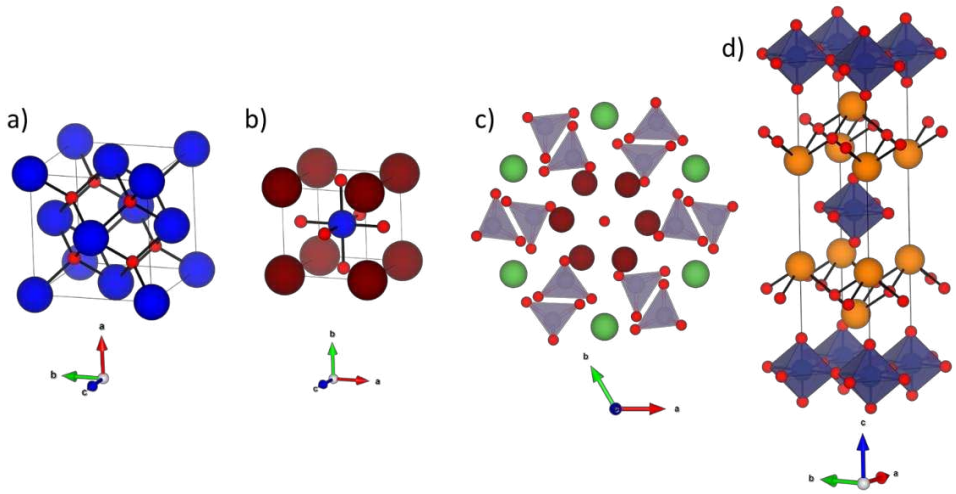

Figure I.10. *a) AO_2 fluorite structure, where the blue and red spheres represent the A cations and oxygen atoms respectively. b) simple ABO_3 perovskite cell, with A and B atoms corresponding to the blue and brown spheres respectively, while the red spheres correspond to the oxygen atoms. c) Apatite crystal structure projection within the* c*-axis, evidencing the three channels type, with brown, green and red spheres corresponding to the A(1), A(2) and oxygen atoms. d) Simplified γ-type BIMEVOX structure, where blue spheres represent V and the dopant element (held in an octahedral site), orange and red spheres correspond to Bi and oxygen atoms.*

Melilite and melilite-related oxides: The melilite layered structure was already described in section I.3. The ionic conductivity in these compounds family is enhanced by the introduction of interstitial oxides (O_{int}), which is usually fulfilled by aliovalent atoms substitution; for example, in the $RE_{1+x}AE_{1-x}Ga_3O_{7+x/2}$ melilite solid solution the alkali earth metal (AE^{2+}) is exchanged by a rare earth cation (RE^{3+}); therefore, interstitial oxides are introduced to the structure in the right stoichiometry to keep a charge balanced composition. The interstitial oxides are held in the GaO_4 infinite framework pentagons centre at the $[GaO_4]_n$ sheets level by local expansion of the gallium coordination into GaO_5 units, forming an O_{int} two-dimensional network over the *ab*-plane (see Figure I.11a), which allows fast conduction mechanism by a knock-on process between nearby charge carrier oxides [89], [90]. Previous studies have reported ionic conductivity of the $La_{1.54}Sr_{0.46}Ga_3O_{7.27}$ and $La_{1.64}Ca_{0.36}Ga_3O_{7.32}$ melilites revealing a value of 0.1 $S.cm^{-1}$ at 800°C [49], [91], [92], which is still the best observed conductivity of a melilite compound to date (see Figure I.12). The barium analogue of these melilite solid solutions was also reported, but with a far smaller limit of O_{int}, i.e. $La_{1.35}Ba_{0.65}Ga_3O_{7.175}$, hence its conductivity is one order of magnitude lower 1.6×10^{-3} $S.cm^{-1}$ at 600°C than the best-performing Ca and Sr melilites . Moreover, an alkali earth-free $La_2Ga_3O_{7.5}$ melilite with the highest concentration of interstitial oxides was successfully synthesised by J. Fan *et. al.* [42] using direct crystallisation from the under-cooled melt as a synthesis route, as it is unreachable by conventional solid state reactions. The high concentration of interstitial oxides leads to their ordering in a one-dimensional chain-like arrangement (see Figure I.11b), hence an *Ima*2 orthorhombic melilite superstructure is stabilised instead of the tetragonal $P\bar{4}2_1m$ structure. The interstitial oxides ordering is driven by their local environment relaxation, as in order minimise repulsion between two close oxides the Ga-O-Ga angles are distorted pushing these oxides outside the five-membered rings. In fact, this relaxation causes even more constraints on the surrounding edge-sharing pentagons which are better suited being interstitial oxide free. The ordering of these oxides has a limiting effect on the ionic conduction of this compound, as even with such high interstitial oxides concentration, the sample reaches 0.01 $S.cm^{-1}$ at 800°C, which is one order of magnitude less than the previously described Sr-based and Ca-based melilites.

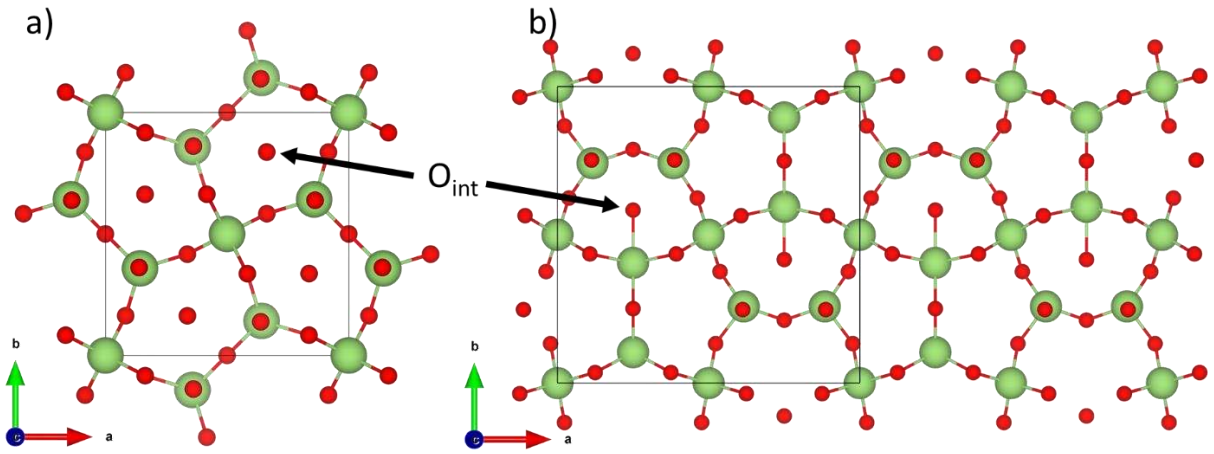

Figure I.11. *Crystal structure projection along the c-axis of both: a) fully disordered $P\bar{4}2_1m$ and b) ordered Ima2 melilites.*

The langasite structure as described above (section I.3), can be described as a melilite related mineral, due to the similarities between their structures. In previous works langasite oxide ion conductors were reported with quite high interstitial oxide concentration, as in $La_3Ga_{5-x}Ge_{1+x}O_{14+x/2}$ ($0 < x \leq 1.5$) [93]. This solid solution was reported with x = 0.3 as a Ga substitution limit when synthesised by solid-state reactions. Nevertheless, the maximum x amount was substantially extended to x = 1.5 when a sol-gel synthesis approach was adopted [93]. In contrast with the melilite structures which host the interstitial oxide in the framework five-membered rings centre, the langasites accommodate these additional oxides by forming framework bridging $(Ga,Ge)_2O_8$ units, allowed by (Ga,Ge)-O-(Ga,Ge) angles distortion. The $La_3Ga_{5-x}Ge_{1+x}O_{14+x/2}$ solid solution conductivity was also studied and indicated a maximum value of 0.01 $S.cm^{-1}$ at 800°C for x = 0.5 composition. Hence, these two families in general are of interest in synthesising new electrolyte materials due to their capacity to host high interstitial oxides concentration and their fast charge transport mechanism.

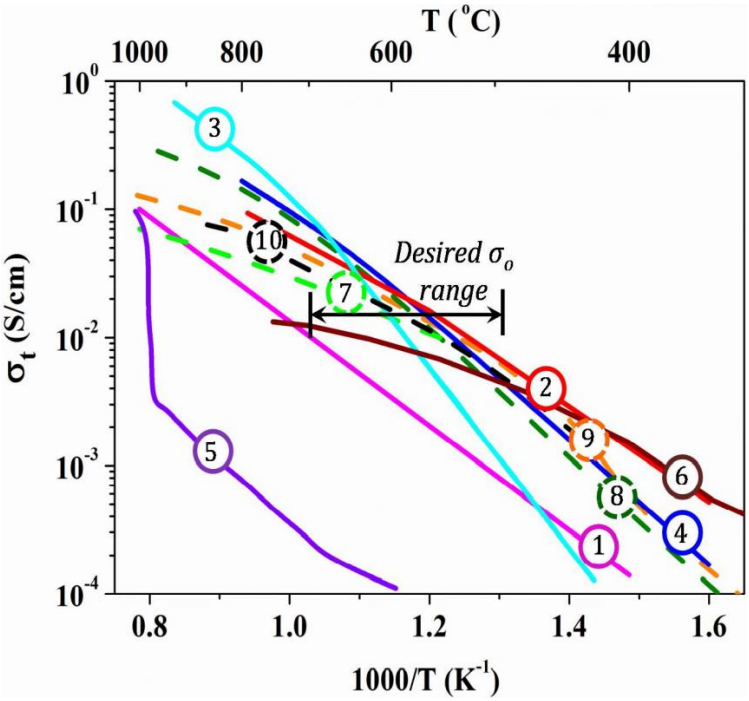

Figure I.12. *Arrhenius plots of the total conductivity of, (1) $Zr_{0.9}Y_{0.1}O_{1.95}$ (YSZ), (2) $Ce_{0.9}Gd_{0.1}O_{1.95}$ (GDC), (3) $Bi_{0.75}Y_{0.25}O_{1.5}$ (Stabilized δ-Bi_2O_3), (4) $La_{0.8}Sr_{0.2}Ga_{0.83}Mg_{0.17}O_{2.815}$ (LSGM), (5) $Ba_2In_2O_5$ (Brownmillerite), (6) $Bi_4Cu_{0.15}Ti_{0.15}V_{1.7}O_{11-\delta}$ (BICUTIVOX), (7) $La_{9.75}Sr_{0.25}(SiO_4)_6O_{2.895}$ (Si-apatite), (8) $La_{9.5}(Ge_{5.5}Al_{0.5}O_{24})O_2$ (Ge-apatite), (9) $La_{1.54}Sr_{0.46}Ga_3O_{7.27}$ (Sr-melilite) and (10) $La_{1.64}Ca_{0.36}Ga_3O_{7.32}$ (Ca-melilite). Solid and dashed lines correspond to vacancies and interstitial conductor materials. This figure was taken from [94].*

I.5. References.

[1] A.R. West, Solid State Chemistry and its Applications. John Wiley & Sons, 2014.

[2] I.P. Parkin, *Encyclopedia of Materials: Science and Technology*, 2001, 8675-8679.

[3] F. Kaiser *et al.*, *Chemistry of Materials*, 2020, **32**, 2025.

[4] D. Dini *et al.*, *Chemical Reviews*, 2016, **116**, 13043.

[5] P.S. Halasyamani *et al.*, *Inorganic Chemistry*, 2017, **56**, 12077.

[6] G. Bodländer *et al.*, *Zeitschrift für Elektrochemie und angewandte physikalische Chemie*, 1905, **11**, 161.

[7] H. Nozaki *et al.*, *Journal of Solid State Chemistry*, 1991, **91**, 306.

[8] T. Takahashi *et al.*, *Journal of The Electrochemical Society*, 1979, **126**, 1654.

[9] T.E. Warner *et al.*, Properties and Mineralogy of Important Inorganic Materials. John Wiley & Sons, 2011.

[10] C. Collins *et al.*, *Nature*, 2017, **546**, 280.

[11] M.S. Dyer *et al.*, *Science*, 2013, **340**, 847.

[12] A.R. Oganov *et al.*, *Nature Reviews Materials*, 2019, **4**, 331.

[13] J. Gamon *et al.*, *Chemistry of Materials*, 2019, **31**, 9699.

[14] C.M. Collins *et al.*, *Angewandte Chemie International Edition*, 2021, **60**, 16457.

[15] S. Chibani *et al.*, *APL Materials*, 2020, **8**, 080701.

[16] J.M. Rondinelli *et al.*, *Annual Review of Materials Research*, 2015, **45**, 491.

[17] A.R. Oganov *et al.*, *Accounts of Chemical Research*, 2011, **44**, 227.

[18] A.G. Kvashnin *et al.*, *The Journal of Physical Chemistry Letters*, 2017, **8**, 755.

[19] A. Stein *et al.*, *Science*, 1993, **259**, 1558.

[20] F. Leyvraz *et al.*, *The European Physical Journal B - Condensed Matter and Complex Systems*, 2006, **50**, 57.
[21] C.X. Wang *et al.*, *Materials Science and Engineering: R: Reports*, 2005, **49**, 157.
[22] E.D. Zanotto *et al.*, *Journal of Non-Crystalline Solids*, 2017, **471**, 490.
[23] G. Tammann, *Leopold Voss*, 1933.
[24] W.H. Zachariasen, *Journal of the American Chemical Society*, 1932, **54**, 3841.
[25] J.D. Musgraves, J. Hu, L. Calvez, Springer Handbook of Glass. Springer International Publishing, 2019. 326.
[26] K.-H. Sun, *Journal of the American Ceramic Society*, 1947, **30**, 277.
[27] H.-J. Freund, *Accounts of Chemical Research*, 2017, **50**, 446.
[28] S.D. Stookey, *Industrial & Engineering Chemistry*, 1959, **51**, 805.
[29] N. Lahl *et al.*, *Journal of materials science*, 2000, **35**, 3089.
[30] C.-Z. Liao *et al.*, *Crystal Growth & Design*, 2017, **17**, 1079.
[31] W. Wisniewski *et al.*, *CrystEngComm*, 2018, **20**, 3455.
[32] J. Friedrich, in *Reference Module in Materials Science and Materials Engineering*, Elsevier, 2016.
[33] M. Allix *et al.*, *Advanced Materials*, 2012, **24**, 5570.
[34] M. Boyer *et al.*, *CrystEngComm*, 2015, **17**, 6127.
[35] S. Alahraché *et al.*, *Chemistry of Materials*, 2013, **25**, 4017.
[36] A.J. Fernandez-Carrion *et al.*, *Inorganic Chemistry*, 2017, **56**, 14446.
[37] K. Al Saghir *et al.*, *Chemistry of Materials*, 2015, **27**, 508.
[38] A. Bertrand *et al.*, *Advanced Optical Materials*, 2016, **4**, 1482.
[39] A.P. Patel *et al.*, *Applied Physics Letters*, 2008, **93**, 191902.
[40] W. Cao, Synthesis and characterization of highly non-stoichiometric garnet oxides, PhD thesis, Orleans 2021.
[41] C. Milanese *et al.*, *Chemistry of Materials*, 2004, **16**, 1232.
[42] J. Fan *et al.*, *Chemistry of Materials*, 2020, **32**, 9016.
[43] F. Wei *et al.*, *Inorganic Chemistry*, 2012, **51**, 5941.
[44] F. Wei *et al.*, *Journal of the American Chemical Society*, 2011, **133**, 15200.
[45] Z.H. Jia *et al.*, *Acta Crystallographica Section B Structural Science*, 2006, **62**, 547.
[46] A. Sazonov *et al.*, *Acta Crystallographica Section B Structural Science, Crystal Engineering and Materials*, 2016, **72**, 126.
[47] C. Van Heurck, G. Van Tendeloo, S. Amelinckx, *Physics and Chemistry of Minerals*, 1992, **18**, 441.
[48] J. Barbier *et al.*, *Chemistry of Materials*, 2005, **17**, 3130.
[49] L. Zhou *et al.*, *The Chemical Record*, 2020, **20**, 1117.
[50] R.-L. Tang *et al.*, *Inorganic Chemistry Frontiers*, 2019, **6**, 2304.
[51] Y. Zhang *et al.*, *Crystal Growth & Design*, 2012, **12**, 622.
[52] C. Jiang *et al.*, *Journal of Crystal Growth*, 2018, **496–497**, 57.
[53] M. Boyer *et al.*, *Journal of Materials Chemistry C*, 2016, **4**, 3238.
[54] M. Boyer, Synthèse de nouvelles céramiques polycristallines transparentes par cristallisation complète du verre, PhD thesis, Orleans, 2016.
[55] S. Chenu *et al.*, *Advanced Optical Materials*, 2014, **2**, 364.
[56] M. Allix *et al.*, *Chemistry of Materials*, 2013, **25**, 1600.

[57] H. Bazzaoui *et al.*, *Inorganic Chemistry*, 2022, **61**, 9339.
[58] E.L. Belokoneva *et al.*, in *Sov. Phys. Dokl*, 1980, **25**, 954.
[59] A.P. Dudka *et al.*, *Crystallography Reports*, 2013, **58**, 594.
[60] A.A. Kaminskii *et al.*, *Physica Status Solidi (a)*, 1984, **86**, 345.
[61] G.J. Redhammer, *Acta Crystallographica Section C Structural Chemistry*, 2015, **71**, 80.
[62] A. Pavlovska *et al.*, *Acta Crystallographica Section B Structural Science*, 2002, **58**, 939.
[63] B.A. Maksimov *et al.*, *Crystallography Reports*, 2004, **49**, 585.
[64] A. Reinhardt *et al.*, *Journal of Luminescence*, 2020, **218**, 116833.
[65] J.T.S. Irvine, P. Connor, Solid Oxide Fuels Cells: Facts and Figures: Past Present and Future Perspectives for SOFC Technologies. Springer London, 2013.
[66] J. Larminie, A. Dicks, M.S. McDonald, Fuel cell systems explained. J. Wiley, 2003.
[67] E.D. Wachsman, K.T. Lee, *Science*, 2011, **334**, 935.
[68] J.A. Kilner *et al.*, *Annual Review of Materials Research*, 2014, **44**, 31.
[69] S.P.S. Badwal, *Solid State Ionics*, 2001, **143**, 39.
[70] D.Z. de Florio *et al.*, *Cerâmica*, 2004, **50**, 275.
[71] S.C. Singhal, K. Kendall, High-temperature Solid Oxide Fuel Cells: Fundamentals, Design and Applications. Elsevier, 2003.
[72] C. Sun *et al.*, *Journal of Solid State Electrochemistry*, 2010, **14**, 1125.
[73] H.A. Taroco *et al.*, Ceramic Materials for Solid Oxide Fuel Cells. *Advances in Ceramics - Synthesis and Characterization, Processing and Specific Applications*, IntechOpen, 2011.
[74] Y. Lu *et al.*, *Nature Materials*, 2014, **13**, 961.
[75] H. Shi *et al.*, *Progress in Natural Science: Materials International*, 2020, **30**, 764.
[76] F. Wang *et al.*, *Materials Science and Technology*, 2019, **35**, 1551.
[77] S.J. Skinner *et al.*, *Materials Today*, 2003, **6**, 30.
[78] K. Huang, J.B. Goodenough, Solid Oxide Fuel Cell Technology: Principles, Performance and Operations. Elsevier, 2009.
[79] T. Takahashi *et al.*, *Materials Research Bulletin*, 1978, **13**, 1447.
[80] H.A. Harwig, *Zeitschrift für anorganische und allgemeine Chemie*, 1978, **444**, 151.
[81] I. Tatsumi., Perovskite Oxide for Solid Oxide Fuel Cells. Springer US, 2009.
[82] T. Ishihara *et al.*, *Journal of Materials Science*, 2001, **36**, 1125.
[83] G. Mairesse, *Comptes Rendus de l'Académie des Sciences - Series IIC - Chemistry*, 1999, **2**, 651.
[84] S.P. Simner *et al.*, *Journal of the American Ceramic Society*, 2005, **80**, 2563.
[85] Y. Yue *et al.*, *Journal of Materials Chemistry A*, 2022, **10**, 3793.
[86] P. Fuierer *et al.*, *Journal of Materials Science*, 2011, **46**, 5447.
[87] T.J. White *et al.*, *Acta Crystallographica Section B: Structural Science*, 2003, **59**, 1.
[88] H. Arikawa *et al.*, *Solid State Ionics*, 2000, **136–137**, 31.
[89] J. Schuett *et al.*, *Chemistry of Materials*, 2020, **32**, 4442.
[90] C. Tealdi *et al.*, *Advanced Functional Materials*, 2010, **20**, 3874.
[91] M.-R. Li *et al.*, *Angewandte Chemie International Edition*, 2010, **49**, 2362.
[92] X. Kuang *et al.*, *Nature Materials*, 2008, **7**, 498.
[93] M. Diaz-Lopez *et al.*, *Chemistry of Materials*, 2019, **31**, 5742.
[94] M. Diaz-Lopez, A Study of Novel Electrolyte Materials with Interstitial Oxides as Mobile Species, PhD thesis, Liverpool, 2016.

Chapter II: Cationic Ordering and Structural Stability in the Sr*RE*Ga_3O_7 *RE* = [Dy-Lu / Y] Small Rare Earth Melilite Structure

II.1. Introduction.

Transparent ceramics are usually obtained by powder sintering processes at high temperatures and high pressures routes [1]–[3]. However, full and congruent crystallisation from a bulk glass was shown to be an alternative path to achieve crack-less, dense transparent ceramics without porosity when both the amorphous and crystalline phases have similar densities [4]–[12]. Crystallisation from glass precursors was also demonstrated as a way to synthesise new metastable structures, as demonstrated in the BaO-Al_2O_3 [4], Bi_2O_3-Nb_2O_5-TeO [13] and SrO-SiO_2-Al_2O_3 [5], [14], [15] systems.

The melilite compositions were shown to yield transparent ceramic materials when synthesised by glass crystallisation [10], [12]. The ABC_3O_7 melilites crystallise in a tetragonal (S.G. $P\bar{4}2_1m$) cell and adopt a layered structure stacked along the *c*-axis, and formed by 3- and 4- vertex linked MO_4 tetrahedra, creating pentagonal channels accommodating different sized A-site cations sandwiched between the MO_4 layers, thanks to their network strong flexibility (Figure II.1a) [16]. These compounds are of interest due to their well-known piezoelectric, optical and ionic conductivity properties [12], [17]–[26]. The melilite structures with general formula $(AE,RE)C_3O_7$ where *AE* and *RE* represents an alkali earth and rare earth elements and C = [Al, Ga], have been reported for *RE* = [La - Er, Y] to be synthesisable by ceramic routes, whereas for the smallest rare earth cations *RE* = [Tm, Yb, Lu] their synthesis by classic solid-state reaction was shown to be unsuccessful [16]. In some cases, the melilite compounds do not only crystallise in the parent tetragonal structure, but exhibit different modulations or supercells due to the MO_4 layered framework distortion, which are usually linked to an ordering of the A/B-site cations or intercalation of interstitial oxides. Such behaviour can be noticed in the $CaREGa_3O_7$ *RE*= [La, Nd] melilites [27], [28] or the $Ca_2MC_2O_7$ *M* = [Mg^{2+}, Co^{2+}, Zn^{2+}] C = [Si^{4+}, Ge^{4+}] ackermanites [29]–[32] crystallising in *5D* modulated incommensurate structures, or exhibiting fully commensurate superstructure cell as seen for $Bi_2ZnB_2O_7$ [33] and $La_2Ga_3O_{7.5}$ [34].

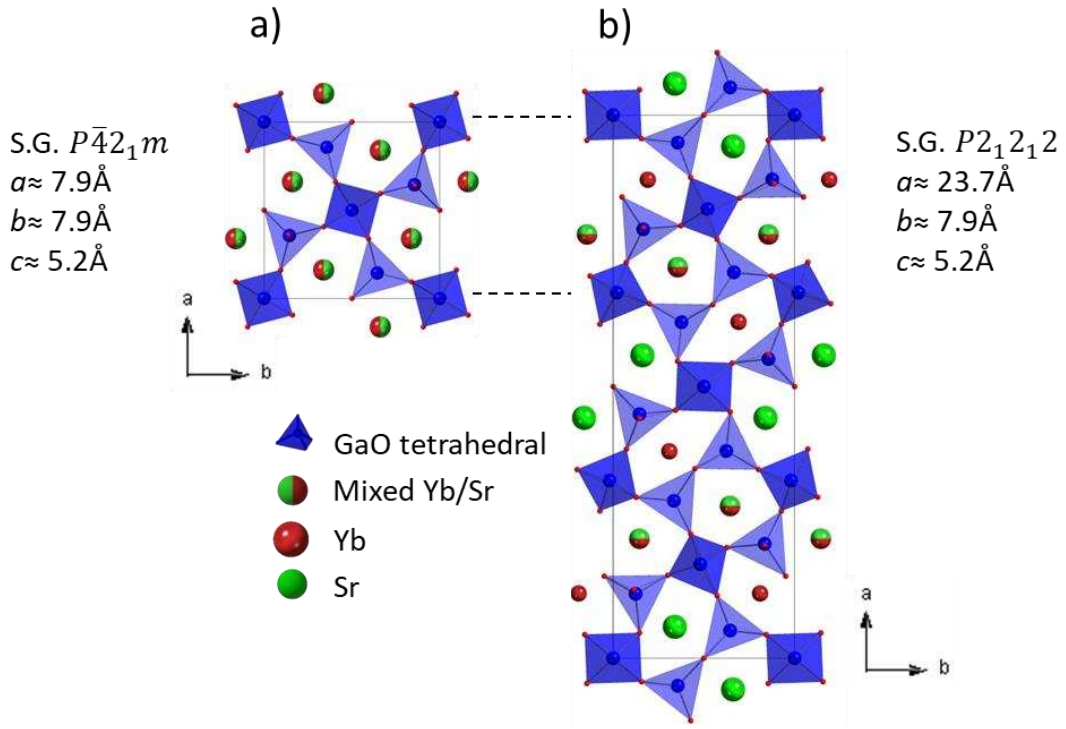

Figure II.1. *$SrYbGa_3O_7$ melilite structure projection within the c-axis of both, a) disordered and b) ordered polymorphs.*

During Marina Boyer's PhD [35], she reported for the first time the synthesis of Sr*RE*Ga_3O_7 *RE* = [Eu, Gd, Tb, Dy, Ho, Er, Tm, Yb and Y] melilites by full and congruent crystallisation from bulk glass precursors; hence, achieving the stabilisation of the melilite structure with small rare earths [12]. However, from her study the Ho, Er, Tm and Yb compositions exhibit more Bragg diffraction peaks by PXRD, compared to the larger rare earth compositions [12], [35]. By using selected area electron diffraction (SAED), the patterns were indexed in a $P2_12_12$ (3**a, b, c*) supercell of the original $P\bar{4}2_1$m structure. From structure solution using the charge flipping method implemented in JANA2006 [36], the *a* parameter tripling was assigned to an ordering of the A-site cations, with 3 distinct crystallographic A-sites: 1 fully occupied by *RE*, 1 fully occupied by Sr and one 50%/50% mixed *RE*/Sr [35], [37] (see Figure II.1). This superstructure retains the same layered framework, with three different types of distorted $[GaO_4]_5$ pentagonal channels, in order to accommodate the rare earth, strontium and mixed A-sites. The *RE* cation being smaller than the Sr atom, its local structure is the most distorted of the three as it adopts a [6+1] coordination defined by six short *RE*-O distances in the range 2.2 – 2.5 Å that form a triangular-prismatic first coordination sphere, and one long distance of 2.9 Å. The Sr and *RE*/Sr sites are less distorted and remain 8-coordinated with moderately

similar cation-oxide first neighbour bond distances to the $SrLaGa_3O_7$ parent $P\bar{4}2_1m$ melilite (see Figure II.2).

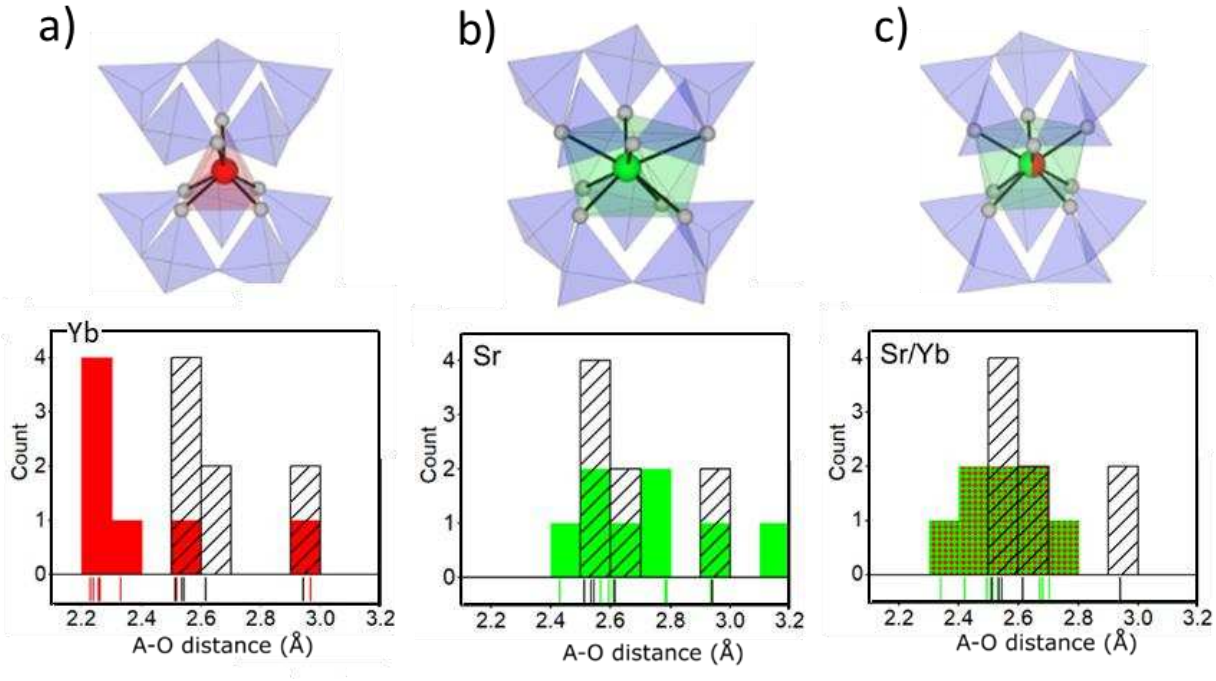

Figure II.2. *Local coordination and their A-O bond distances of a) Yb site (red histogram), b) Sr site (green histogram) and c) mixed Yb/Sr site (patterned red/green histogram). The black dashed histograms are given from A-O distances of the parent disordered $SrLaGa_3O_7$ melilite.*

The current chapter will address the following points: (i) exploration of stabilising this new ordered melilite polymorph to other rare earths, with a fine structural study of these compounds, (ii) explore the possibility of isolating the parent disordered melilite structure for the compositions crystallising under the ordered polymorph, studying the thermal stability of these structures and their phase transitions, (iii) explain the ordering origin and why different ordering types are disfavoured, (iv) the ordering effect on these compounds optical properties.

II.2. Synthesis by full and congruent glass crystallisation.

First, stoichiometric amounts of $SrCO_3$, Ga_2O_3 and RE_2O_3 *RE* = [Dy, Ho, Er, Tm, Yb, Lu and Y] (all from Strem Chemicals, purity > 99.9 %) were weighed according to the nominal chemical formula $Sr\mathit{RE}Ga_3O_7$ and mixed together in an agate mortar using ethanol to ensure a better homogeneity of the sample. The resulting powder mixtures were left to dry on the bench for a couple of minutes and pressed to pellets, then broken into small pieces of ~ 60mg each. The pellet chunks were levitated (using argon gas) and melted individually using the aerodynamic levitation coupled to two CO_2 lasers apparatus (as described in the appendices

Chapter A.I section A.I.1.1.2). The samples melted around 1650°C, were held for several seconds at that temperature and then subsequently quenched by turning the lasers off (estimated cooling rates of 300°C/s); hence, achieving glass samples in the form of spherical beads. The amorphous state of the beads was confirmed by laboratory PXRD (see Figure II.3), and only $SrLuGa_3O_7$ showed a very small amount of crystallised melilite, distinct to what Marina Boyer reported in her PhD, as she obtained mainly crystalline beads at this composition [35].

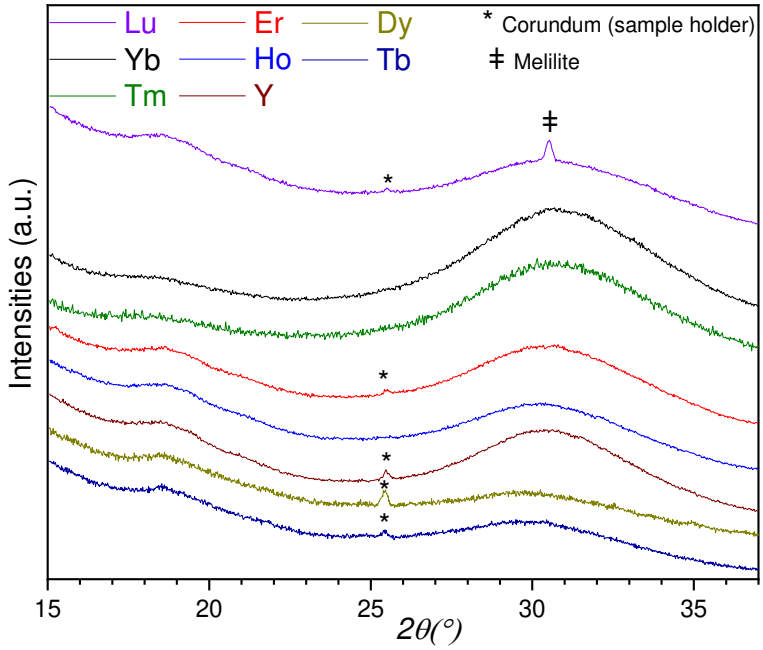

Figure II.3. *Laboratory X-ray powder diffraction data of $SrREGa_3O_7$ (RE = Tb-Lu, Y) glass samples synthesized by aerodynamic levitation coupled to laser heating (ADL).*

In order to determine the glass precursors transition and crystallisation temperatures (i.e. "T_g" and "T_c" respectively), DSC measurements were performed from room temperature to 920°C, upon heating and cooling using 10°C/min rates. In Figure II.4a, showing the DSC results, a clear decreasing trend in T_g (from 788°C for Lu to 761°C for Tb) can be observed as the rare-earth size increases, indicative of the glass network rigidity decline [38]. As shown in Figure II.5 the PXRDs of the post-DSC samples contain peaks from the $P2_12_12$ supercell for all rare-earths, except Tb which express no sign of superstructure peaks. Moreover, due to the absence of X-ray scattering contrast between strontium and yttrium ions (Z_{Sr}= 38, Z_Y= 39), it might be expected that the superstructure peaks would have very weak intensities, i.e. arising purely from the Ga_3O_7 framework distortion; hence, hard to resolve from a noisy pattern. Following this, a longer scan (in the 5°-50° (2θ) range using a 0.015° step and 5s/step as a measuring time) was performed to improve the signal to noise ratio (see Figure A. 9), evidencing the low angle small intensity supercell melilite peaks. This sets the synthesisability

limits of the ordered melilite between *RE* = Dy and Lu + Y. More details about the synthesis of both ordered and disordered polymorph are indicated in section II.3.

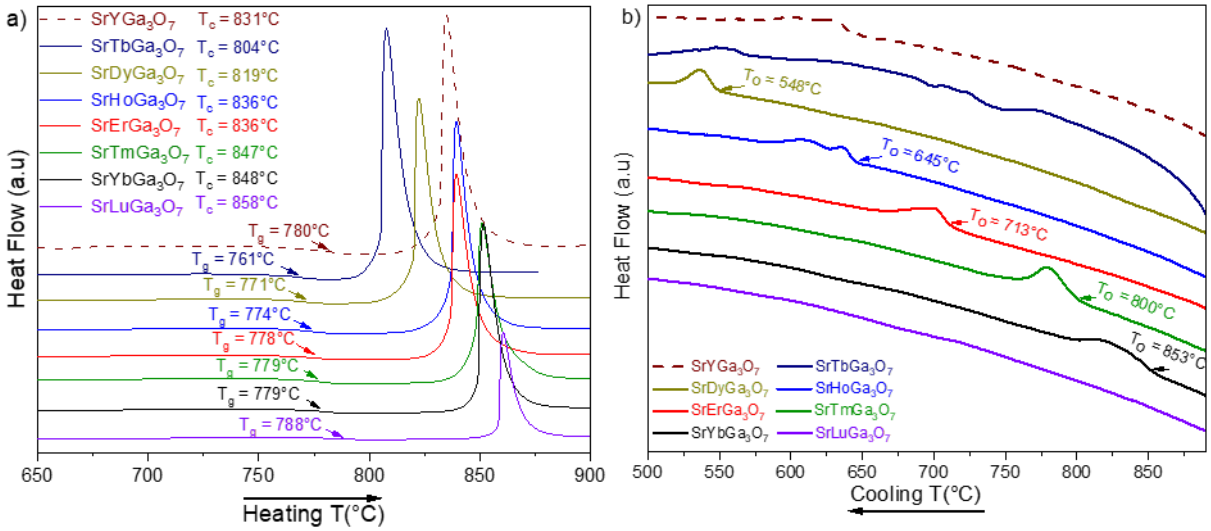

Figure II.4. *Differential scanning calorimetry (DSC) measurements of $SrREGa_3O_7$ (RE = Tb – Lu, Y) glass composition, where T_g, T_c and T_o are glass transition, crystallization and ordering temperatures respectively. a) Heating plots using a 10°C/min heating rates from room temperatures to 925°C. b) Cooling plots using a 10°C/min cooling rates from 925°C to room temperatures.*

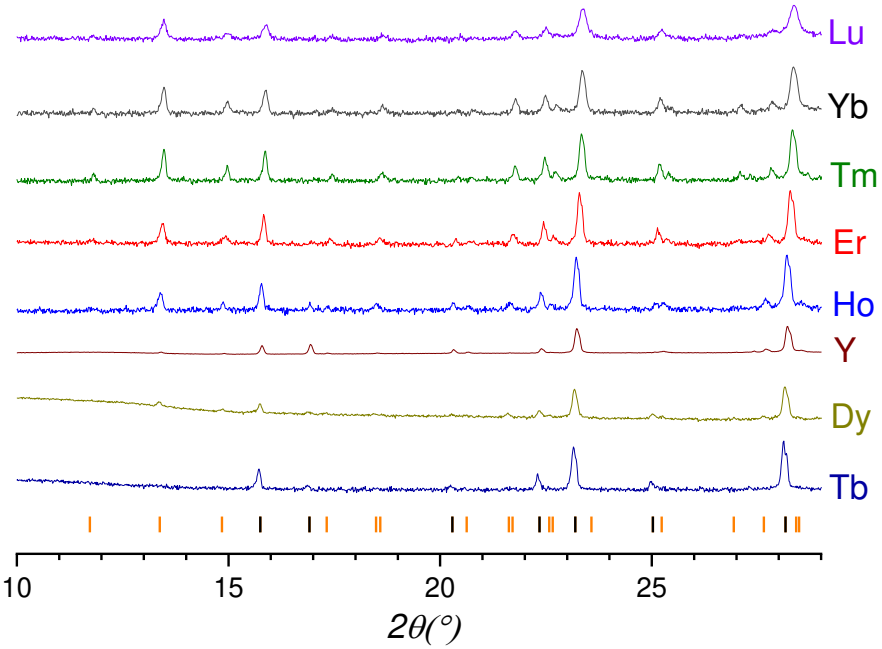

Figure II.5. *Post DSC PXRD data (in natural logarithm scale) of $SrREGa_3O_7$ (RE = Tb – Lu, Y) compounds, where black tick marks correspond to the $SrDyGa_3O_7$ $P\bar{4}2_1m$ disordered melilite phase, while the orange tick marks represents the additional $P2_12_12$ ordered melilite reflections.*

II.3. Structures stability versus temperature (T°C).

To investigate the thermal stability of the $P2_12_12$ melilite supercell, *in situ* VT-PXRD measurements were performed on glass precursors across the series of compositions Sr*RE*Ga_3O_7 *RE* = [Tb-Lu, Y], from room temperature to 740°C in one step and then to the point where the melilite starts to decompose into RE_2O_3 and garnet type oxides (900°C for *RE* = [Ho-Lu], 1000°C for *RE* = Dy and 1100°C for *RE* = Tb) using a 5°C step, in the angular rage of 10°-40° (2θ) with a 0.024 step size and a measuring time of 1s/step. In Figure II.6, the first thing to notice is the very small temperature domain of stability for the Lu compound (over ~ 25°C), as it crystallises and decomposes at 800°C and 825°C respectively, which explains why its phase pure synthesis is challenging. The other rare earth cations display a wider temperature range between their crystallisation and decomposition temperatures, Yb over 90°C, Tm 100°C, Er 110°C, Ho 105°C, Y 115°C, Dy 225°C, Tb 270°C.

The reported results in Figure II.6 can be divided in three distinct categories:

(i) Category 1: smallest rare-earths (*RE* = Yb, Lu) crystallising directly in the ordered polymorph upon heating with no phase transition observed on cooling.

(ii) Category 2: intermediate-size rare-earths (*RE* = Er, Tm) crystallising into the parent $P\bar{4}2_1m$ melilite and then undergoes a phase transition to the $P2_12_12$ ordered melilite on cooling at 720°C and 790°C respectively.

(iii) Category 3: the largest-sized rare-earths (*RE* = Tb-Ho, Y) crystallising in the disordered melilite upon heating and retaining the $P\bar{4}2_1m$ structure whether on heating or on cooling with no sign of supercell peaks.

The VT-PXRD results for Dy, Ho and Y contrast with the thermal analysis described in section II.2, which showed that following a suitable heat treatment, the ordered melilite could be obtained for these compositions. To study the reversibility of the observed phase transition, a Tm glass melilite sample was subject to two heating/cooling cycles measured by *in situ* VT-PXRD (see Figure II.7). From this figure the appearance of the ordered melilite is completely reversible, as it gets disordered on heating at slightly higher ordering temperature (~ 820°C > 790°C), which then on the cooling forms again the $P2_12_12$ melilite polymorph at 790°C.

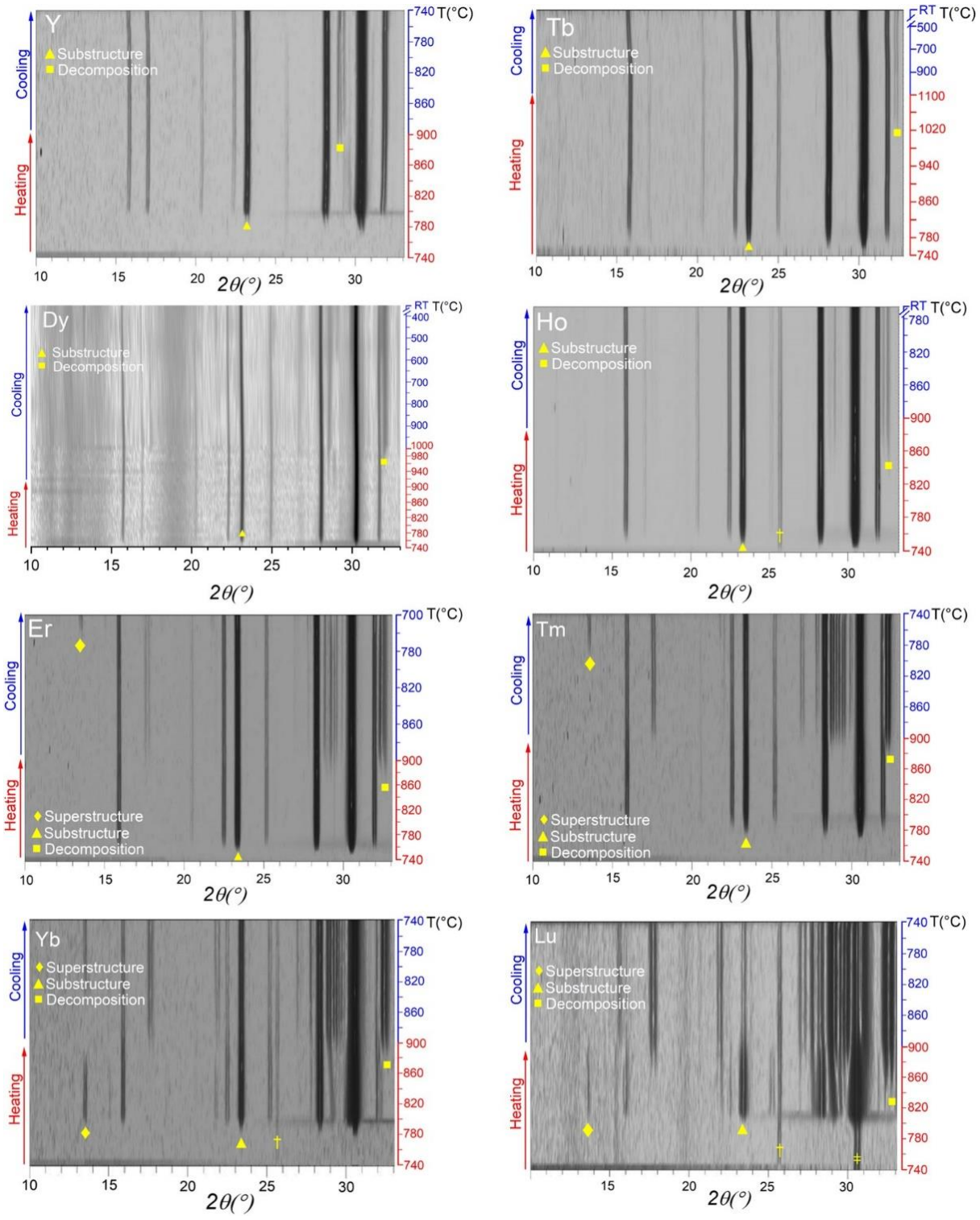

Figure II.6. *Variable temperature powder X-Ray diffraction (VT-PXRD) on $SrREGa_3O_7$ (RE= Tb – Lu, Y), starting from the glass precursors. Peaks representing the initial melilite (substructure) crystallization, the 3x1x1 structural ordering (superstructure), and the onset of decomposition are indicated by symbols described in the Yb panel. Peaks labelled † arise from the alumina sample holder. The precursor glass for RE = Lu contained a small amount of crystallized melilite, indicated by ǂ.*

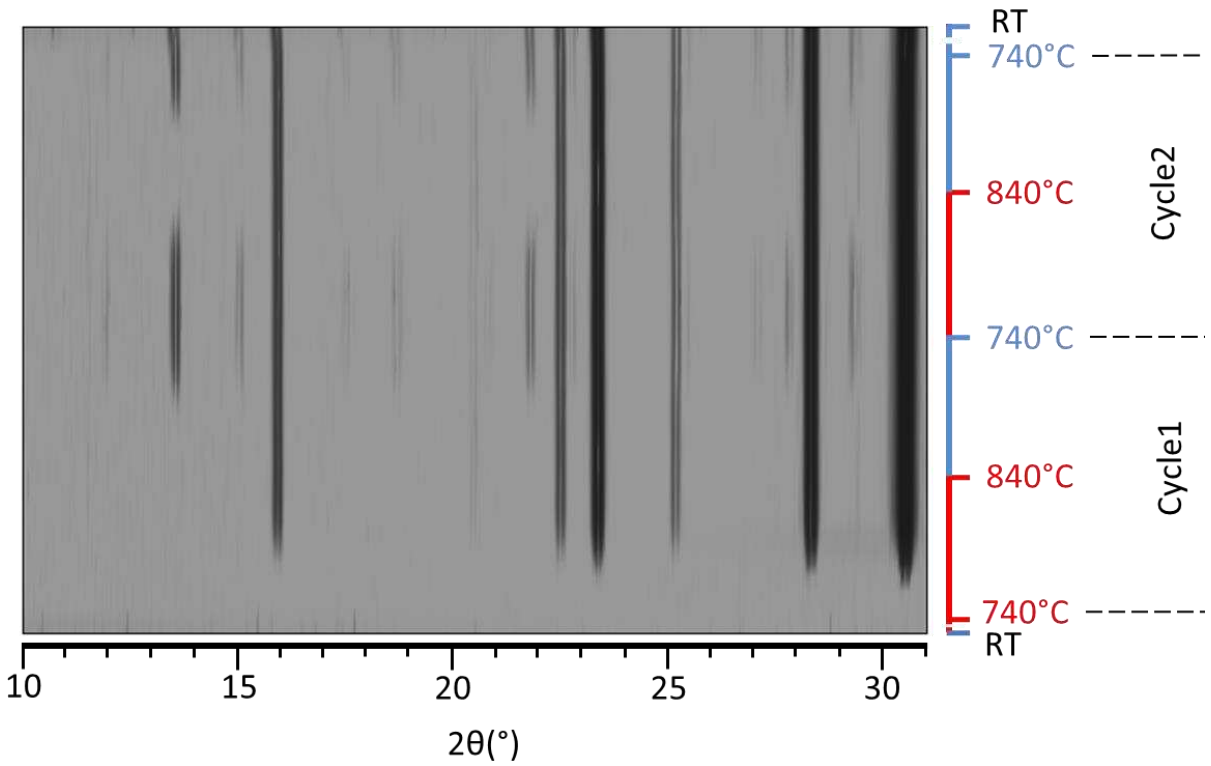

Figure II.7. *Two heating/cooling cycles in situ VT-PXRD measurements on the $SrTmGa_3O_7$ glass sample.*

Comparing the crystallisation temperatures extracted from both DSC and *in situ* VT-PXRD measurements (Figure II.4 and Figure II.6), a clear difference can be noticed, as the DSC temperatures are higher by ~ 50°C to 100°C than the ones from VT-PXRD. This can be attributed to the different heating and cooling kinetics in both techniques, as faster heating rates (10°C/min) from the DSC induce a delayed crystallisation, whereas the slowest heating rates (estimated ~0.15°C/min) from VT-PXRD gives more time for the sample temperature to equilibrate. The DSC acquired cooling curves (Figure II.4b) were found to exhibit a small exothermic peak for all the measured rare earths, except Tb and Lu. The onset temperatures of this peak follow a near-monotonic increase as the rare-earth size increases, with values between 548°C and 853°C (extracted from the onsets) for Dy and Yb respectively, consistent with the ordering temperatures of Er and Tm found by VT-PXRD. This indicates the possibility of stabilising the disordered polymorph for the whole studied *RE* series at room temperature by rapid cooling of the high temperature disordered state. Furthermore, powder glass samples of compositions $Sr\mathit{RE}Ga_3O_7$ *RE* = [Dy-Yb, Y] were annealed in an open-air atmosphere furnace for 2h at their T_c (from DSC) then quenched in air by removing the platinum crucible from the furnace. This produced fully disordered melilites crystallising in the tetragonal parent cell, hence, the first example of the $SrYbGa_3O_7$ $P\bar{4}2_1m$ melilite. Additionally, to synthesise the

ordered melilite polymorph for the Sr*RE*Ga$_3$O$_7$ *RE* = [Dy-Yb, Y] compositions, powder glass samples were heat treated at 815°C for 2h in an open-air atmosphere furnace and left to cool inside the furnace. As for the Lu melilite, its synthesis as a phase pure sample was more difficult to achieve due to the crystallisation of the Lu$_3$Ga$_5$O$_{12}$ garnet as a secondary phase. In this perspective, the crystallisation temperature was reduced to 805°C for 2h then the sample was quenched by placing the Pt crucible into a dish of water, which produced only the ordered melilite.

To map the thermal stability and bring a full picture of all the studied compositions, data from DSC and VT-PXRD were combined with previous results from [16] and drawn in phase diagram-like graph (Figure II.8).

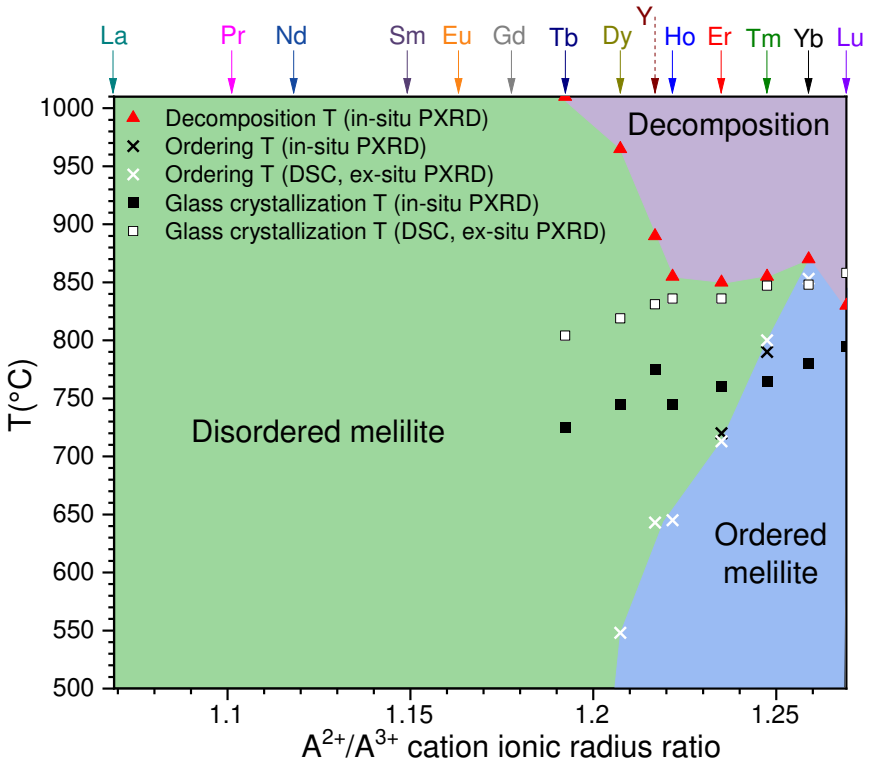

Figure II.8. *SrREGa$_3$O$_7$ (RE= Tb – Lu) melilites stability diagram drawn from DSC and VT-PXRD resumes, coupled to previous results from Jan Skakle et al [16] (RE=La – Gd). The ordering region was drawn according to the highest stability temperature of each compound from both DSC and VT-PXRD.*

II.4. Structural investigation and Rietveld refinements of the Sr*RE*Ga$_3$O$_7$ *RE* = [Dy-Lu / Y] compositions.

II.4.1. Synchrotron powder diffraction analysis.

To explore the cationic ordering over the compositions with different *RE*, synchrotron powder diffraction (SPD) and laboratory PXRD measurements were acquired on Sr*RE*Ga$_3$O$_7$

ordered and disordered samples (see Table II.1 for the measurement conditions of each rare earth).

Table II.1. Powder diffraction measurement conditions of the different synthesised melilite compositions.

RE	Dy, Y		Ho		Er	
Polymorph	Ordered	Disordered	Ordered	Disordered	Ordered	Disordered
Technique	Lab	Lab	SPD	Lab	SPD	SPD
Wavelength(Å)	1.5406	1.5406	0.414225	1.5406	0.414225	0.457874
RE	Tm		Yb		Lu	
Polymorph	Ordered	Disordered	Ordered	Disordered	Ordered	Disordered
Technique	SPD	SPD	SPD	Lab	SPD	--
Wavelength(Å)	0.414225	0.414225	0.414225	1.5406	0.457874	--

Rietveld refinements were carried out using Topas academic (V6) software [39], with the following constraints and conditions:

- Each of the three A-sites to be fully occupied: Occ*RE*1* + OccSr1 = 1, Occ*RE*2 + OccSr2 = 1, Occ*RE*3 + OccSr3 = 1. For the $P2_12_12$ melilite only.
- Constrained A-site 3 partial occupancies to A-site 1 and A-site 2 as follow: Occ*RE*3= 1.5 – Occ*RE*1 – Occ*RE*2. For the $P2_12_12$ melilite only.
- An overall composition constrained to the nominal: $\frac{(\mathrm{Occ}RE1+\mathrm{Occ}RE2+\mathrm{Occ}RE3)\times 4}{\mathrm{Z}} = 1$, $\frac{(\mathrm{OccSr1}+\mathrm{OccSr2}+\mathrm{OccSr3})\times 4}{\mathrm{Z}} = 1$, with: 4 the A-sites multiplicity, and Z=6. For the $P2_12_12$ melilite only
- Isotropic thermal parameters for all atoms. For both melilites.
- Isotropic thermal parameters of O atoms constrained to have the same (refined) value. For both melilites.

This led to a total of 94 independently refined parameters (15 background terms, sample height for lab data or zero shift for SPD data, axial divergence, 6 profile parameters from TCHZ function + 4 peak broadening parameters added to the (310) peak, 67 atomic parameters) for the ordered melilite, and 43 independently refined parameter (15 background terms, sample height for lab data or zero shift for SPD data, axial divergence, 6 profile parameters from TCHZ function, 16 atomic parameters) for the disordered melilite. All these refinements led to satisfactory reliability factors as displayed in Table II.2. For the $SrYbGa_3O_7$ ordered melilite refinements, the initial refined A-site cations partial occupancies converged to: 0.498(1)/0.501(1) Yb1/Sr1, 0.977(1)/0.023(1) Yb2/Sr2, 0.025(2)/0.975(2) Yb3/Sr3. A final

**: The OccX1 notation means the occupation of X in site 1.*

Rietveld refinement of this composition was run with fixed A-sites occupancies to 0.5/0.5 Yb1/Sr1, 1/0 Yb2/Sr2, 0/1 Yb3/Sr3, which did not affect the reliability factors. These occupation constraints were applied to the Tm sample as its refined occupancies were close to the ideal ordered model (as in the Yb compound). Moreover, the refined partial occupancies of the other *RE* ordered melilites were quite far from the ideal model (A-sites disorder > 7%), hence the Sr/*RE* occupancies were not fixed as in the Yb and Tm compounds (see Table II.3). The $SrLuGa_3O_7$ composition diffraction pattern had the broadest peak profile of all compositions and was found to be the most difficult to refine, as some *hkl*-independent peak broadening was observed and the refined structure was shown to be physically non-meaningful with oxygens moving far from their initial positions, breaking the GaO_4 infinite framework. To solve the problem of oxygen atoms moving too far away from their initial position, soft restraints were added to the Lu refinement, by setting dummy oxygen atoms (site occupation = 0) positioned from the $SrYbGa_3O_7$ refined model, and constraining the oxygens to not move too far from these dummy atoms while the refinement runs. The allowance degree of the constraint was adjusted until a stable refinement was reached. Moreover, a large B_{iso} value was noticed for the mixed site Lu3/Sr3 site, doubling the value of the other two A-sites (Lu3/Sr3 0.0272(9) Å^2 *vs* Lu2/Sr2 0.0111(4) Å^2 *vs* Lu1/Sr1 0.0118(4) Å^2). the Lu3/Sr3 site was therefore split into two sites with a maximum occupancy of 50% each. The final refined plots and structural parameters are represented in Figure II.9, Table II.4 to Table II.6 in the main text, and Figure A. 10 to Figure A. 14 and Table A. 1 to Table A. 9 in the appendices Chapter A.II.

Table II.2. Final Rietveld refinements relibility factors for all Sr*RE*Ga3O7 *RE*= [Dy - Lu] compositions measured under both melilite polymorphs, except Lu.

RE	Dy		Ho		Er	
melilite	$P\bar{4}2_1m$	$P2_12_12$	$P\bar{4}2_1m$	$P2_12_12$	$P\bar{4}2_1m$	$P2_12_12$
R_p	2.62%	1.66%	1.41%	4.85%	6.72%	6.70%
R_{wp}	3.35%	2.21%	2.08%	6.30%	8.71 %	8.60%
GOF	1.19	1.73	5.16*	1.11	1.22	1.32
RE	Tm		Yb		Lu	
melilite	$P\bar{4}2_1m$	$P2_12_12$	$P\bar{4}2_1m$	$P2_12_12$	$P2_12_12$	
R_p	6.36%	5.28%	2.87%	4.09	6.87%	
R_{wp}	8.32%	7.06%	3.83%	5.36	9.18%	
GOF	1.26	1.06	1.64	0.96	1.65	

*high GOF values are due to over counted data (i.e. R_{exp}= 0.40%)

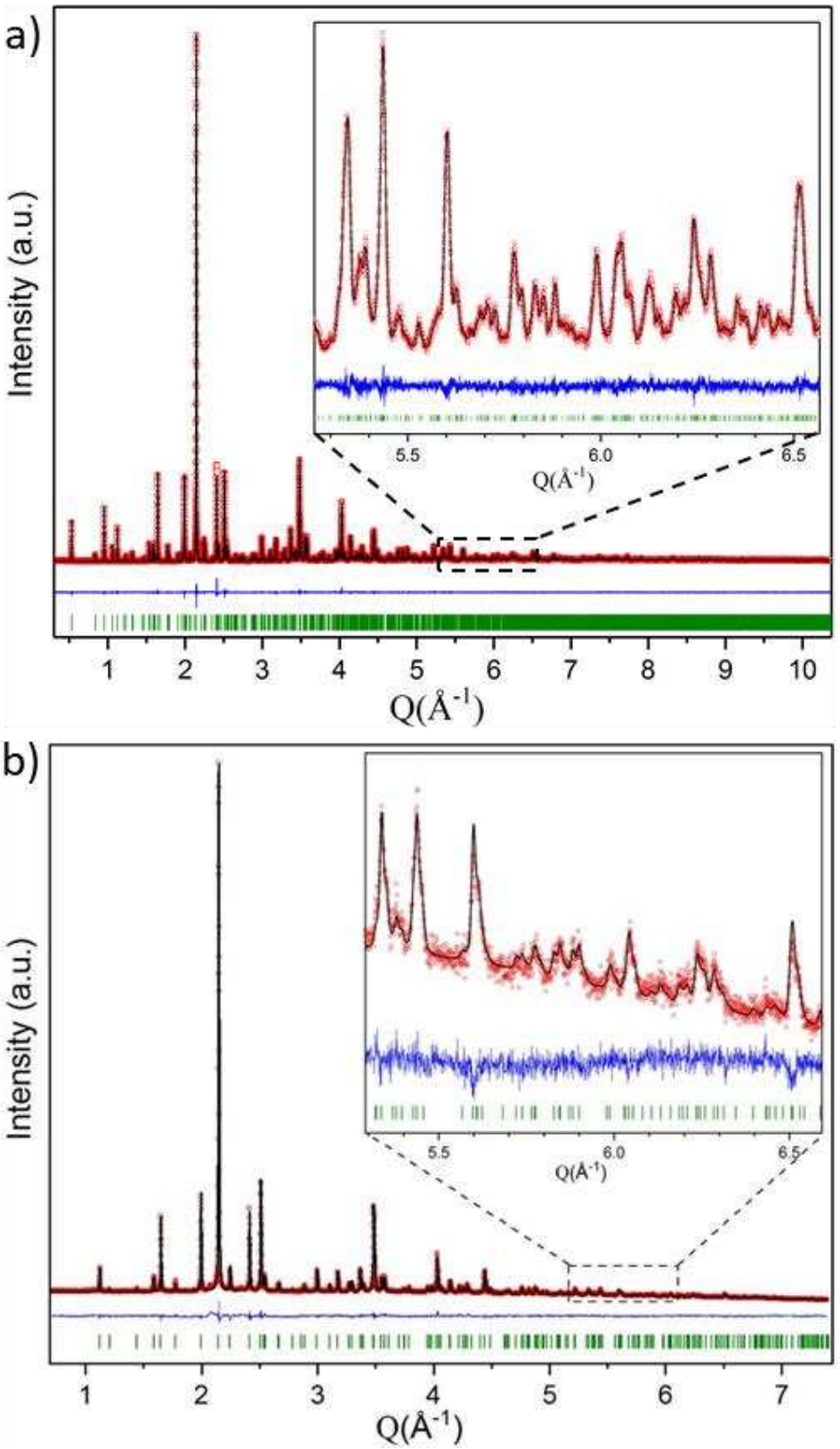

Figure II.9. *Rietveld refinement of a) $SrYbGa_3O_7$ ordered melilite (R_p= 4.09% R_{wp}= 5.36%) (SPD data) and b) $SrYbGa_3O_7$ disordered melilite (R_p= 2.87% R_{wp}= 3.83%) (lab data). Observed (black dot), calculated (red line), and difference (blue line) profiles are shown. The set of green vertical lines corresponds to reflection positions.*

Table II.3. Summarised refined occupancies of all Sr*RE*Ga$_3$O$_7$ *RE*= [Dy - Lu] compositions.

RE	melilite	Occupancy A-site1	Occupancies A-site2	Occupancies A-site3
Dy	$P2_12_12$	0.50(1)Dy/0.50(1)Sr	0.90(1)Dy/0.10(1)Sr	0.10(1)Dy/0.90(1)Sr
Ho	$P2_12_12$	0.499(2)Ho/0.501(2)Sr	0.924(2)Ho/0.076(2)Sr	0.076(3)Ho/0.924(3)Sr
Er	$P2_12_12$	0.504(3)Er/0.496(3)Sr	0.863(3)Er/0.137(3)Sr	0.132(4)Er/0.868(4)Sr
Tm	$P2_12_12$	0.5Tm/0.5Sr	1Tm	1Sr
Yb	$P2_12_12$	0.5Yb/0.5Sr	1Yb	1Sr
Lu	$P2_12_12$	0.520(4)Lu/0.480(4)Sr	0.891(3)Lu/0.109(3)Sr	0.045(2)Sr/0.455(2)Lu ×2[a]

[a]: the ×2 means two sites with the same occupancies (split site model).

Table II.4. Final refined structural parameters obtained from SPD data collected at room temperature on the SrYbGa$_3$O$_7$ superstructure melilite ($P2_12_12$ space group, a = 23.70181(6) Å, b = 7.92117(3) Å and c = 5.21167(1) Å).

Atom	Site	x	y	z	Occ	B_{iso}
Yb1/Sr1	4c	0.71965(3)	0.35610(7)	0.50561(11)	0.5/0.5	0.47(3)[a]
Yb2	4c	0.61899(2)	0.69067(6)	0.45533(9)	1	0.77(2)[a]
Sr3	4c	0.05797(4)	0.33969(11)	0.50854(18)	1	0.66(5)[a]
Ga1	4c	0.94935(4)	0.35511(13)	0.9867(2)	1	0.31(2)
Ga2	2a	0	0	-0.0245(4)	1	0.39(3)
Ga3	4c	0.82689(5)	0.52010(13)	1.0016(3)	1	0.28(2)
Ga4	4c	0.71054(4)	0.66505(13)	0.9532(2)	1	0.34(2)
Ga5	4c	0.11862(5)	0.12302(12)	0.03042(19)	1	0.38(2)
O1	4c	-0.0427(2)	0.1575(9)	-0.2062(12)	1	0.82(4)[b]
O2	4c	0.8850(3)	0.4297(8)	0.8111(11)	1	0.82(4)[b]
O3	4c	0.7083(2)	0.6649(9)	0.2992(10)	1	0.82(4)[b]
O4	4c	0.9412(3)	0.3542(8)	0.3226(11)	1	0.82(4)[b]
O5	4c	0.1275(3)	0.1117(7)	-0.3145(9)	1	0.82(4)[b]
O6	2b	0	0.5	0.8478(16)	1	0.82(4)[b]
O7	4c	0.7711(3)	0.5734(8)	0.7784(14)	1	0.82(4)[b]
O8	4c	-0.0464(2)	-0.1451(8)	0.1539(11)	1	0.82(4)[b]
O9	4c	0.7966(3)	0.3709(9)	0.2280(14)	1	0.82(4)[b]
O10	4c	0.8481(2)	0.7003(8)	0.2033(11)	1	0.82(4)[b]
O11	4c	0.6527(3)	0.5512(8)	0.7981(10)	1	0.82(4)[b]

[a] Calculated from anisotropic refined values

[b] Constrained to refine to the same value

Table II.5. Refined anisotropic thermal parameters from SPD data of the A-sites cations in the SrYbGa$_3$O$_7$ superstructure melilite compound.

	B_{11}	B_{22}	B_{33}	B_{12}	B_{13}	B_{23}
Yb1/Sr1	0.00024(1)	0.00233(9)	0.0027(3)	0.00025(3)	0.00024(5)	-0.0003(1)
Yb2	0.00034(1)	0.00513(9)	0.0023(2)	0.00096(2)	0.00050(3)	0.0028(1)
Sr3	0.00055(2)	0.0017(2)	0.0028(4)	0.00073(4)	-0.00026(8)	0.0003(3)

Table II.6. Final refined structural parameter of $SrYbGa_3O_7$ disordered melilite ($P\bar{4}2_1m$ space group, a= 7.91986(9) Å, and c = 5.21070(7) Å).

Atom	Site	x	y	z	Occ	B_{iso}
Yb1/Sr1	4e	0.33863(9)	0.16137(9)	0.5123(4)	0.5/0.5	2.78(4)
Ga1	2a	0	0	0	1	2.00(7)
Ga2	4e	0.14503(15)	0.35497(15)	0.9698(5)	1	2.28(6)
O1	2c	0.5	0	0.179(2)	1	3.97(2)[a]
O2	4e	0.1438(9)	0.3562(9)	0.2990(14)	1	3.97(2)[a]
O3	8f	0.0932(7)	0.1615(8)	0.7782(15)	1	3.97(2)[a]

[a] Constrained to refine to the same value

Across the *RE* compositions series, the refined cell volumes show a clear decreasing trend going from Dy to Lu end members, which is coherent with the rare-earth size decrease (Figure II.10a). Moreover, Figure II.10b indicates notable differences in the cell parameters evolution as a function of the rare earth, as a matter of fact the contrast between $a_{ordered}/3$ and $a_{disordered}$ gets narrower toward bigger sized *RE*s, evidencing the tendency to stabilise the parent polymorph at the expense of the ordered melilite, also compatible with the observed slope change in the $b_{ordered}$ trend. Furthermore, the ordering trend shows to be slightly deviated from the perfect Yb model as the rare earths size increases (from Er to Dy compositions), where both strontium and rare earth cations can be found in small amounts on each other's dedicated cationic site. This can be best seen in the $SrErGa_3O_7$ compound, as it shows the most disorder over its three cationic A-sites observed in the synthesised *RE*'s series, where their refined occupancies deviate from: 0.5/0.5 for *RE*1/Sr1 site 1, 1/0 for *RE*2/Sr2 site 2 and 1/0 for Sr3/*RE*3 site 3, to: 0.504(3)/0.496(3) for Er1/Sr1 site 1, 0.863(3)/0.137(3) for Er2/Sr2 site 2 and 0.868(4)/0.132(4) for Sr3/Er3 site 3. Even though these rare-earths (Dy-Er) keep a strong ordering tendency, the refined partial disorder is coherent with the weakening stability of the $P2_12_12$ melilite supercell as the rare earth size increases, as seen in the ordering temperatures provided by differential scanning calorimetry indicating a decrease with the increase of the *RE* size to the point where the delivered thermal energy is no longer sufficient to induce A-site ordering (case of Tb).

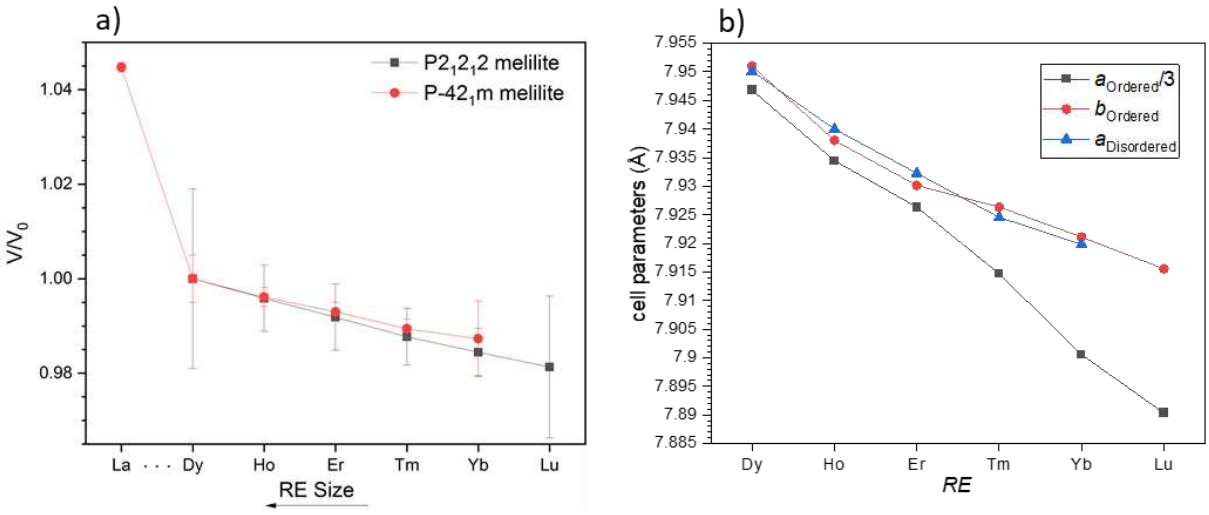

Figure II.10. *a) Normalised (to Dy) cell volumes from both refined $P2_12_12$ and $P\bar{4}2_1m$ structures coupled to RE = La for comparison. b) comparison between the refined ordered melilite tripled parameter and the disordered melilite analogue parameter.*

Another explanation could be the coexistence of both ordered and disordered melilites structures at the microstructure level, which is manifested in the averaged structure by the partial occupations of the ordered sites. This point is supported by the HRTEM study performed on the $SrYGa_3O_7$ compound (Figure II.11), where the sample oriented along the [001] direction indicates the copresence of both parent and superstructured melilites in large nanodomains (~ 20 – 30 nm), as indicated by the related regions FFT's (Fourier Fast Transform). Moreover, to approximate the amount of disordered melilite in Er and Ho compositions (Y and Dy were not considered for the phase quantification due to the low lab data peak resolution compared to the SPD data resolution for Er and Ho compounds), Rietveld refinements were performed using only the disordered model first, after convergence the scale factor was fixed to its refined value and the ordered melilite was added as a secondary phase with fixed occupancies as follows: 0.5/0.5 for *RE*1/Sr1 site1, 1/0 for *RE*2/Sr2 site2 and 0/1 for *RE*3/Sr3 site3 (R_p= 9.32% R_{wp}= 11.37% for Er and R_p= 7.56% R_{wp}= 9.17% for Ho). It resulted in a 60.6(2) wt% / 39.4(2) wt% for Er and 89.48(4) wt% / 10.52(4) wt% for Ho mixed ordered / disordered melilites respectively. The calculated average partial occupancies of the Sr and *RE* from the refined weight% of each of the two polymorphs falls in the same range as the initial refined ones using only the $P2_12_12$ model to describe the whole pattern (see Table II.7).

Table II.7. Comparison between calculated and refined occupancies of Ho and Er melilites.

	Refinement of both ordered/disorder[1]	Refined[2]	Refinement of both ordered/disorder[1]	Refined[2]
RE / site	Ho	Ho	Er	Er
*RE*2/Sr2	0.947(1)/0.053(1)	0.924(2)/0.076(2)	0.803(3)/0.197(3)	0.863(3)/0.137(3)
Sr3/*RE*3	0.947(1)/0.053(1)	0.924(3)/0.076(3)	0.803(3)/0.197(3)	0.868(4)/0.132(4)

[1]Calculated from the refined wt% of each polymorph from the both ideally ordered + disordered melilites refonements.

[2]From Table A. 4 "Er" and Table A. 6 "Ho".

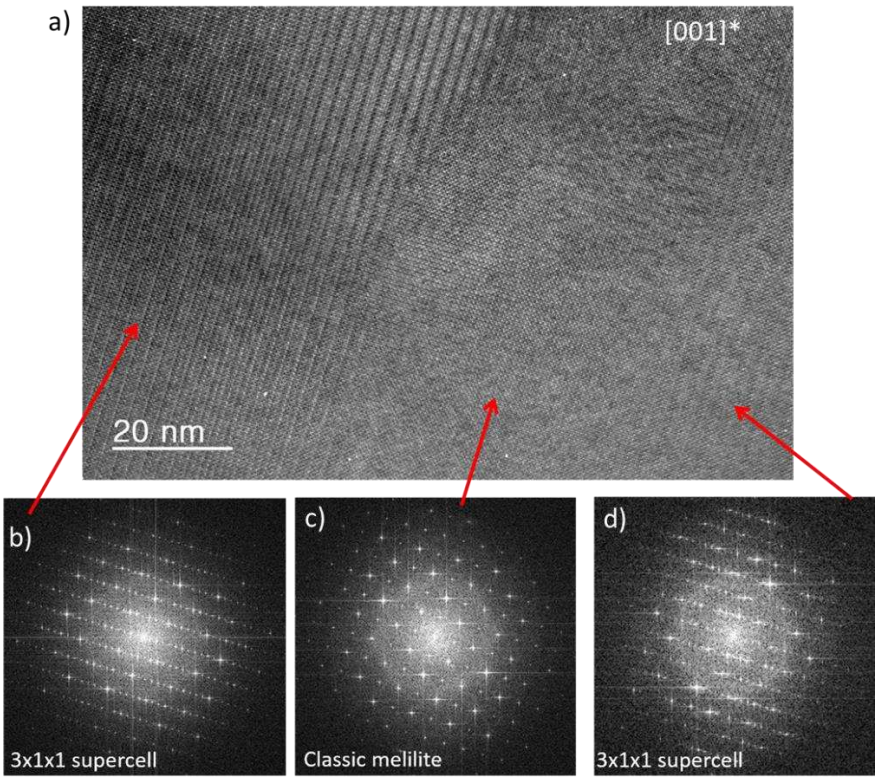

Figure II.11. *a) [001]* HRTEM image and b), c), d) associated FFTs of the $SrYGa_3O_7$ melilite parent synthesised by full crystallization from glass showing the coexistence of both cation-ordered and cation-disordered domains.*

In studies reported by Wei *et. al.* [27], [28] on the Ca*RE*Ga_3O_7 *RE* = [La, Nd] tetragonal melilites, they revealed a five-dimensional structural modulation of these structures, and also mapped the 5D modulated parent melilite region by relating it to the A/B cations radius ratio. The calculated (Sr,*RE*)/Ga ratios of Sr*RE*Ga_3O_7 *RE* = [Dy – Yb] compositions lie just at the edge of incommensurate structure region of this map (see Figure II.12). To test this possibility, and plausible appearance of an incommensurate modulated structure of the original disordered synthesised melilite, SAED measurements were conducted on A-site disordered $SrTmGa_3O_7$ as a representative composition for the series. As shown in Figure II.13, electron diffraction

measurements show a complete absence of satellite reflections and the pattern was fully indexed with the classic $P\bar{4}2_1m$ melilite.

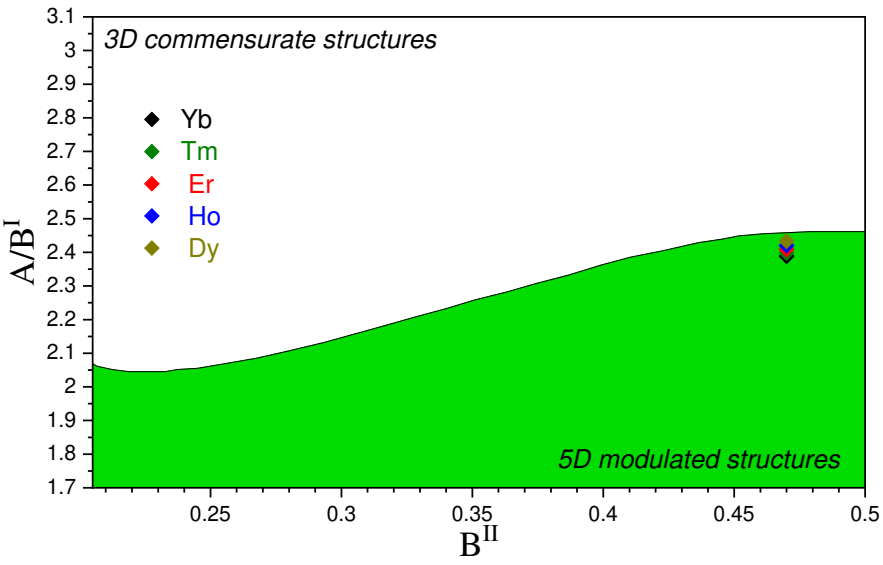

Figure II.12. *Redrawn phase diagram from [27], showing the boundary between commensurate and incommensurate $[A_2]_2[B^I]_2[B^{II}{}_2O_7]_2$ melilite structure domains correlated to the ionic radius ratio of the between the A and B cations. With the coloured solid points represent our study.*

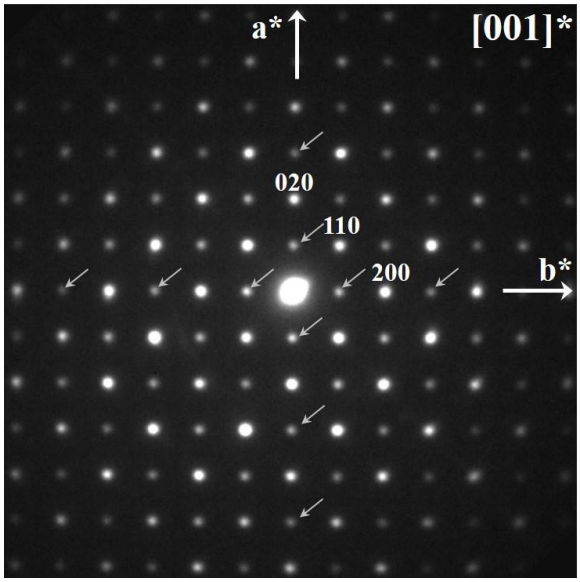

Figure II.13. *[001]* Selected Area Electron Diffraction (SAED) pattern of the $SrTmGa_3O_7$ parent melilite synthesised by full crystallisation from glass, with the indexation of its tetragonal structure (a=7.9 Å, c = 5.2 Å, $P\bar{4}2_1m$). Evidencing a total absence of satellite peaks. The arrows point the reflections assigned to double diffraction.*

II.4.2. Atomic scale observation of the super structured melilite.

To provide an accurate picture of the local structure and the arrangement (distribution) between strontium and rare earth cations at the nanometre scale, not obtainable from the

Rietveld refinement as the structure is averaged across the whole measured sample, atomic-scale STEM-EDS measurements were conducted on the $SrYbGa_3O_7$ compound. First a glass bead of $SrYbGa_3O_7$ composition was annealed at 815°C for 2h in an open atmosphere furnace, and cooled inside the furnace to room temperature (ordered melilite synthesis procedure as described in section II.3). The bead was optically polished to a disk of 50µm, a thin foil of this sample was then prepared by argon ion milling (PIPS GATAN). The sample was oriented along the [001] direction, within this axis each "atom" shown in the 2D projection of the samples structure corresponds to a column of atoms from individual crystallographic sites. As shown in Figure II.14, the Yb and Sr exhibits a pure site each, with a third mixed Sr/Yb site, consistent with the refined disorder from SPD data and the one reported by Marina Boyer in her PhD [35].

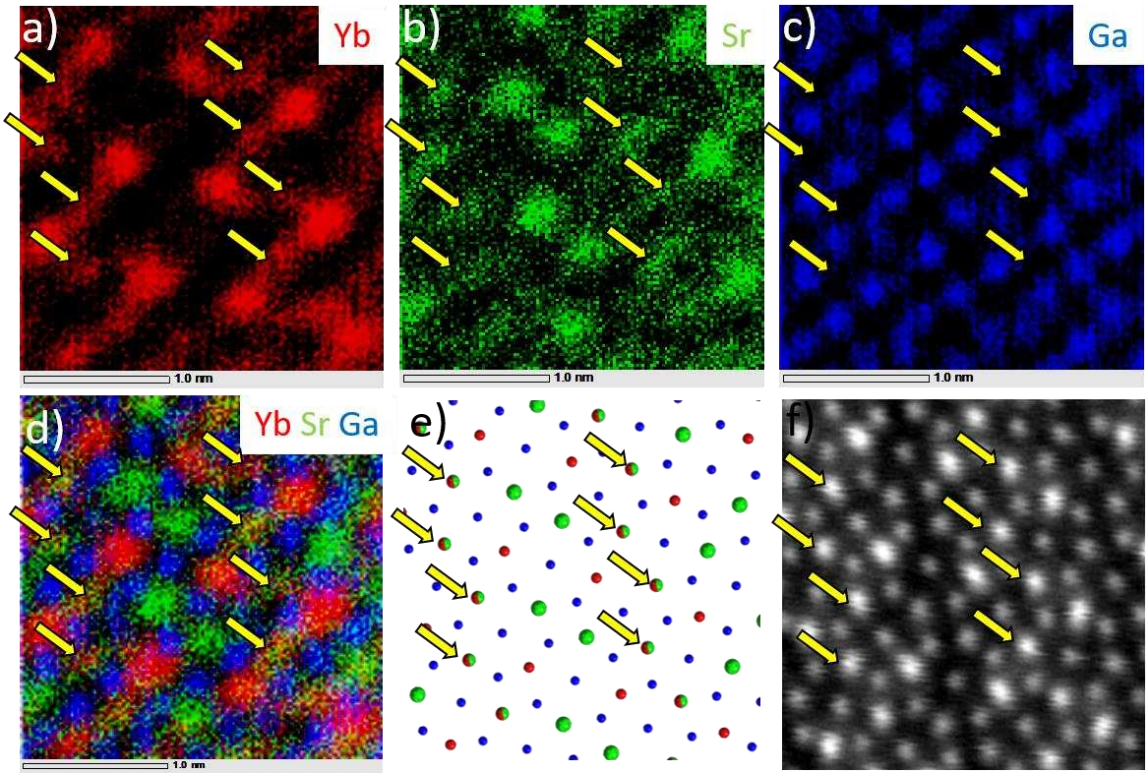

Figure II.14. *Atomic-scale STEM-EDS elemental maps of the cations (a) Yb (red), (b) Sr (green), (c) Ga (blue) and (d) the overlaid EDS maps showing the mixed sites (50/50 Yb1/Sr1) in red/green highlighted by yellow arrows. (e) $SrYbGa_3O_7$ superstructure projection of the cationic sites along the [001] axis. Ga atoms are drawn in blue, Sr3 sites in green, Yb2 sites in red and the mixed sites (50/50 Yb1/Sr1) in red/green. (f) STEM-HAADF image of the $SrYbGa_3O_7$ superstructure along the [001] zone axis. On all the images the yellow arrows highlight the mixed Yb1/Sr1 sites (50/50 average occupancy).*

II.5. Cationic ordering mechanism in the Sr*RE*Ga$_3$O$_7$ *RE* = [Dy-Lu / Y] melilites.

II.5.1. Origin of the *P*2$_1$2$_1$2 melilite superstructure.

In the Sr*RE*Ga$_3$O$_7$ *RE* = [Dy - Lu] compounds, both strontium and rare earth atoms occupy the A-sites of the melilite structure. Due to their different size, larger Sr and smaller *RE*, they tend to prefer different coordination types, which triggers the *P*2$_1$2$_1$2 orthorhombic supercell of the parent tetragonal melilite, induced by an ordering of the A-site cations. Even though this superstructure exhibits three distinct sites with a Sr-dedicated, *RE*-dedicated and 50%/50% mixed Sr/*RE* sites, it does not exhibit a complete ordered framework, where only full Sr and full *RE* sites would be found.

To illustrate why a fully ordered melilite is disfavoured in this case, understanding of the underlying arrangement of the A-site cations is needed. By expanding the *P*2$_1$2$_1$2 melilite cell and showing its projection along the *c*-axis, the mixed Sr/*RE* and the Sr-only sites can be described as one-dimensional chain-like and step-like ordered respectively, with edge-sharing [GaO$_4$]$_5$ pentagons (Figure II.15a). The *RE*-only site on the other hand, shows to be the most spread over the cationic framework in a two-dimensional pseudo-hexagonal sublattice (Figure II.15b), bypassing the edge-sharing configuration of the *RE*-only sites, which are disfavoured due to the its extremely distorted local environment.

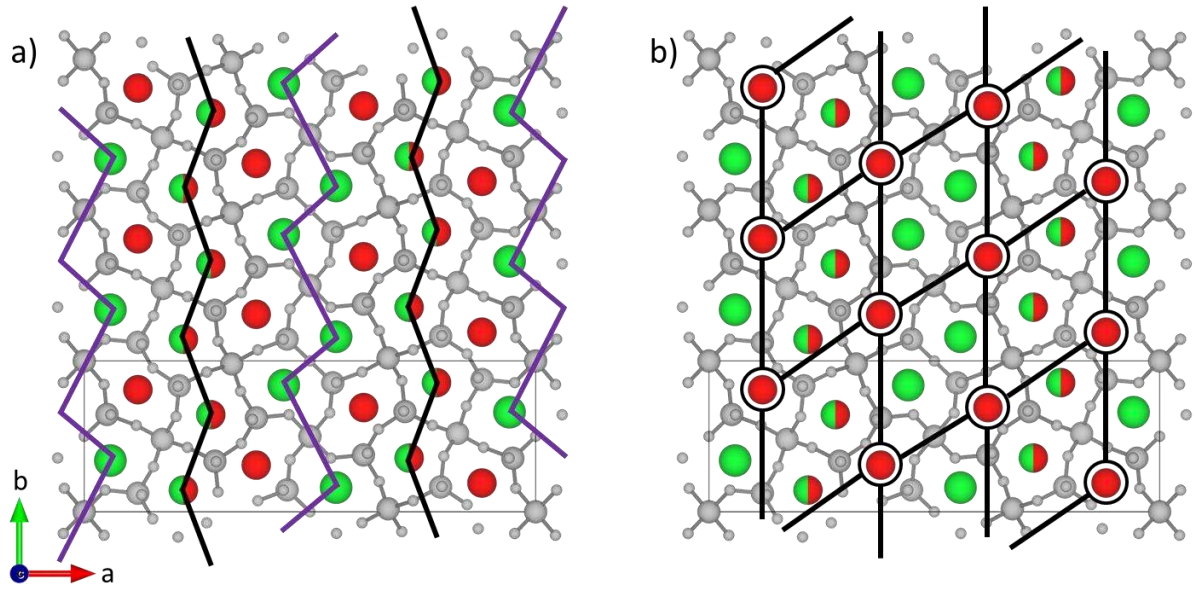

Figure II.15. *The cationic substructure of the P2$_1$2$_1$2 ordered melilite, where a) shows the chain-like and stripe-like arrangement of mixed Sr/RE and Sr-only sites, while b) shows the pseudo-hexagonal sub-cell of the RE-only sites.*

Considering the hexagonal tiling appearance of the underlying melilite structure in “Cairo pentagonal tiling” or “MacMahon’s net” [40] (Figure II.16a), the ordered polymorph can be deconstructed to two tiling types: **A** and **B** (see Figure II.16), as the combination of **A**, **B** and **A**' (corresponding to a 180° rotation of A tile), are needed to describe the whole structure. Tile **A** is half ordered with two mixed sites and two Sr and *RE* dedicated sites (one each), where tile **B** is fully ordered containing only two single natured site types, Sr and *RE*.

The combination of only **A** tiling (= combination of only **A**' tiling) or a combination of both **A** and **A**' (**AA**') tiling (see Figure II.16c and Figure II.16d), supports a wider separation of the distorted *RE* sites, providing a *RE* distorted pentagons edge-sharing free framework. However, it minimises the amount of *RE*-only populated sites (1/4), leading to a half-ordered melilite. The **BB** tiles grouping on the other hand, would result in a fully ordered structure with the maximum amount of *RE*-only sites (1/2). Nevertheless, the disfavoured edge-sharing distorted *RE* sites would be outcome from this configuration (indicated by the black outline in Figure II.16e). This is also seen in the **ABA** tiling combination, which also consequence edge-sharing distorted *RE* sites. The compromise of maximising the amount of *RE* sites while keeping a GaO_4 framework with no edge-sharing *RE* distorted sites, was found by the arrangement of **ABA**' tiling. The $P2_12_12$ melilite structure thus retains 1/3 of its A-sites as mixed sites, which are larger and less distorted than *RE*2, as a buffer between the fully-ordered fragments. This maximizes the *RE*2 [6+1] population, whilst keeping the Ga_3O_7 framework strain to within acceptable limits.

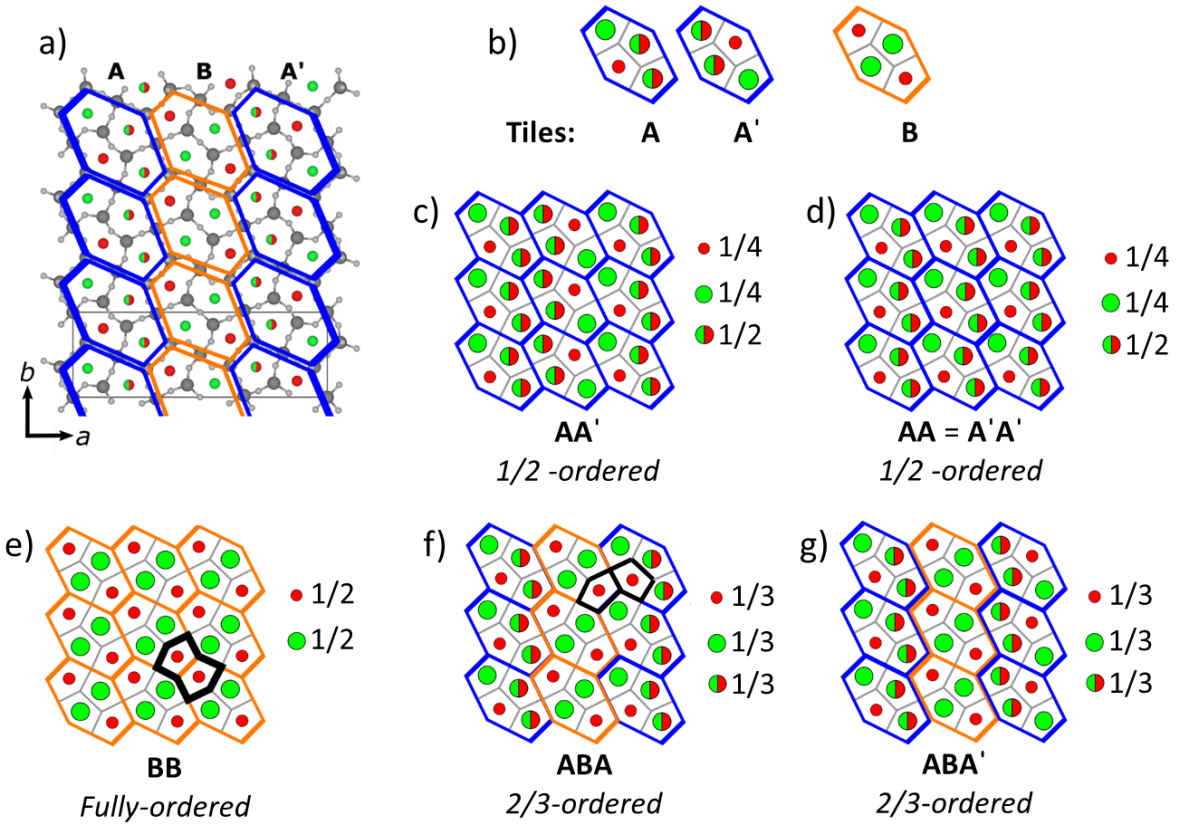

Figure II.16. *a) Observation of the structural ordering of the ordered melilites projected within the c-axis with ABA' tiling. The A, A' and B tiles in b) are combined in c), d), e), f) and g) to create the possible ordering combinations.*

II.5.2. Competition between ordered and disordered polymorphs.

The melilite $[GaO_4]_n$ framework distortion in the Sr*RE*Ga_3O_7 *RE* = [Dy – Lu] compounds, as described above, was assigned to the size mis-match between strontium and rare earth atoms, inducing long range order between these two atoms. However, in other mixed alkaline earth and rare earth gallate melilite compounds (*AE* = Ba) with similar A-site cations ionic radius ratio to the one in $SrYbGa_3O_7$ $r_{Sr}/r_{Yb} = 1.28$ (i.e. $BaNdGa_3O_7$ $r_{Ba}/r_{Nd} = 1.28$, $BaSmGa_3O_7$ $r_{Ba}/r_{Sm} = 1.32$), their structure was reportedly assigned to the parent $P\bar{4}2_1m$ disordered melilite. This could be explained by the fact that the distorted *RE*-only site offering a [6+1] coordination in the ordered structure, is not tolerated by the larger Sm/Nd rare earths (usually found in an 8-fold coordination), with a mean *RE*-O distance of 2.305(2) Å (*RE* = Yb) in the [6+1] coordination *vs* 2.591(4) Å in their respective 8-coordinated site found in the disordered polymorph. Calcium-based gallate melilites as indicated in section II.4.1 showed an alternative way to distort the GaO_4 framework, as the $CaLaGa_3O_7$ and $CaNdGa_3O_7$ structures were described as incommensurate, displaying a pair of modulation vectors parallel to the *ab* plane

[27], [28]. While these compounds still show cationic disorder over the A-sites, Ca shows a slight preference for the smallest 6-coordinated sites, where 54% of that site is occupied by Ca atoms in $CaLaGa_3O_7$, and slightly above 60% in $CaNdGa_3O_7$. However, the low contrast in ionic radii between Ca/La and Ca/Nd, 0.97 and 1.01 respectively, does not supply adequate driving force for full long range cationic ordering to take place. In our synthesised $SrREGa_3O_7$ compounds, both conditions of (i) size contrast between Sr and *RE*, and (ii) small enough rare earth cations to be stable in 6 coordinated sites, are gathered, finding the sweet spot for stabilisation of the $P2_12_12$ ordered melilite.

All of the $(AE,RE)Ga_3O_7$ gallate melilite published structures, which were synthesised by ceramic methods, are summarised in Figure II.17. From this figure, Ba melilites shows the biggest unexplored compositions, while the parent $P\bar{4}2_1m$ Ca-based melilites were reported prior the discovery of the 5D modulation in the La and Nd calcium melilites. This makes both Ba and Ca-based compositions interesting to investigate for new melilite structures.

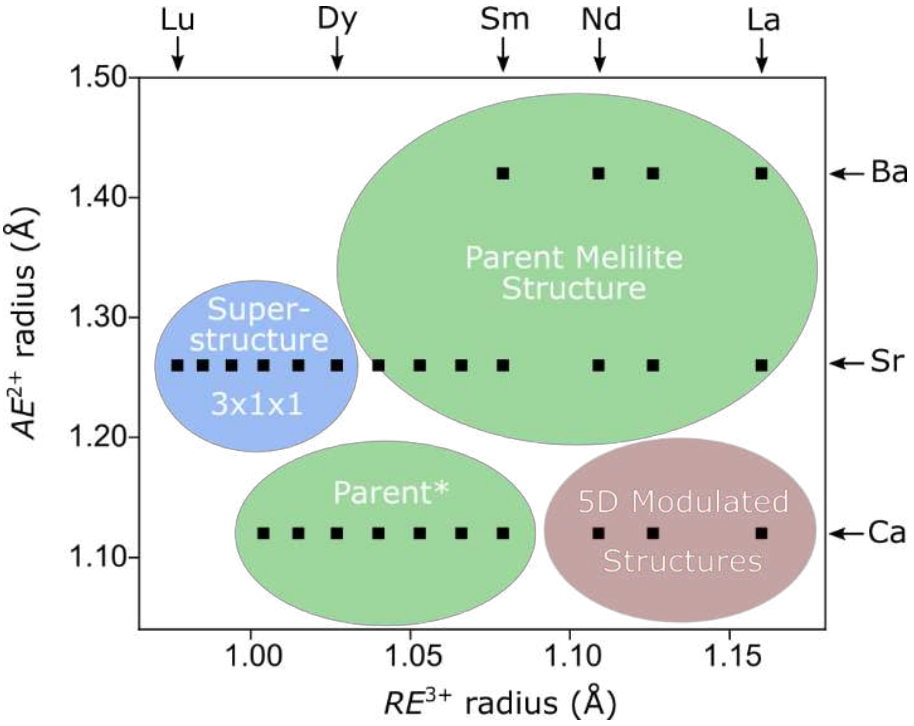

Figure II.17. *Phase diagram indicating the different structural orderings reported for the $(AE,RE)Ga_3O_7$ melilite family, according to the ionic radii of their A site cations. The parent structure and 5D-modulated structure regions have been compiled from the literature[16], [27], [28]. Note that the parent structure region for AE = Ca is marked with an asterisk, as it was reported prior to the discovery of structural modulation in $CaLaGa_3O_7$ and $CaNdGa_3O_7$.*

II.6. Optical properties of the $SrErGa_3O_7$ compound.

It is well known from the literature that *RE*-doped glass-ceramics exhibit interesting optical photoluminescence properties [41]–[44]. In this section, the optical properties (luminescence / photoluminescence) of the ordered melilite were measured on the $SrErGa_3O_7$ composition, as the Er^{3+} spectroscopy is well known and has been exploited in numerous applications[45], [46]. Another point is that this study will allow to probe the effect on the properties of local ordering of the A-sites in glass, disordered and ordered melilites.

To visualise the ordering impact on the optical properties of the crystallised melilite ceramics, photoluminescence spectra were recorded by Yannick Ledemi at Université Laval (Quebec, Canada), on both bulk and powder samples at room temperature in the 1400 – 1650 nm region under excitation at 520 nm using a Xe lamp source. Full attention was given to collect data of ceramic and glass compounds under the exact same experimental conditions to pursue an accurate comparison. In Figure II.18a showing the bulk emission spectrum collected on both glass and ordered melilites of the $SrErGa_3O_7$ composition, a clear peak restructuration and strong emission intensity increase can be noticed for the ceramic material compared to its glass analogue. The peaks structuration (narrower and more well defined) on the ceramic sample can be related to the long range structural order of the crystals in ceramic samples *vs* the amorphous state (short range structural order) of the glass, similarly seen in single crystal materials [41], [44], [47]. The strong increase of the main peak intensity on the other hand is the signature of the local ordering and the designation of the *RE*-only site which is fully occupied by Er^{3+} cations (in this case), favouring a more efficient energy transfer between the *RE* ions of the crystalline phase. One can also notice that the intensity difference of the main Er^{3+} emission band is not as significant on powder samples as it is observed on polished beads bulk samples, which is mainly due to light scattering phenomena induced by grain boundaries (more present in powder samples *vs* bulk) (Figure II.18b). On the other hand, the parent melilite Er^{3+} emission bands show a very similar intensity to the glass compound, which is consistent with the local cationic disorder of the *RE* that can be comparable in both these compounds. Comparing the parent disordered to the ordered melilite Er^{3+} ion emission band, the intensity is almost doubled in the ordered compound, which as indicated above is arising from the local ordering of the A-sites.

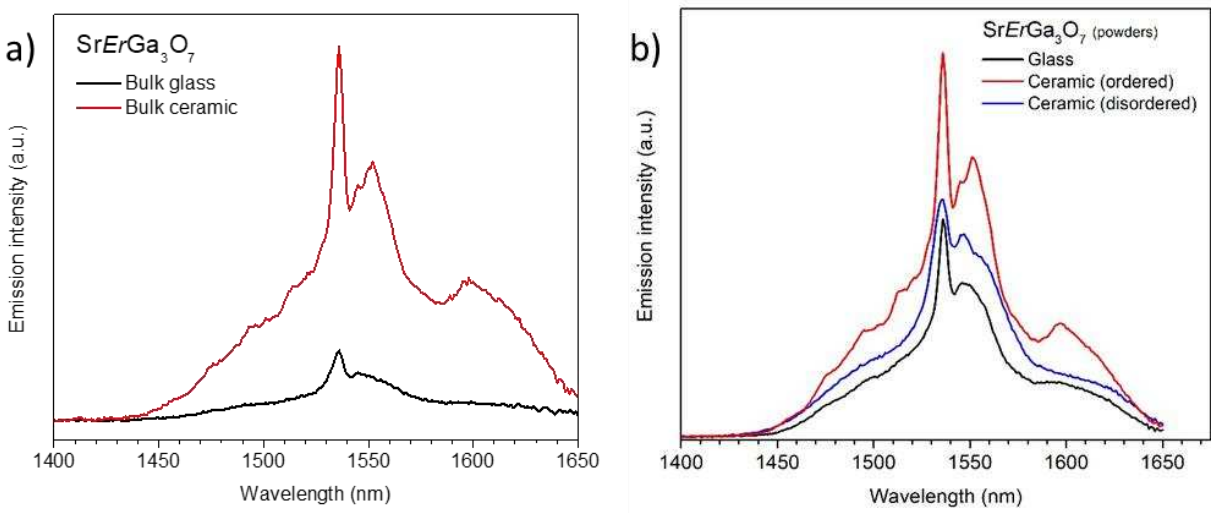

Figure II.18. *Near infrared emission band of the $SrErGa_3O_7$ glass, ordered and disordered ceramics measure on a) bulk, b) powdered samples, under excitation at 520 nm (Xe lamp source).*

II.7. Conclusion and perspectives.

In this chapter, the synthesis of the newly reported Sr*RE*Ga_3O_7 $P2_12_12$ ordered melilite was investigated, revealing the possibility of synthesising this new structure for Lu and Dy rare earths as the *RE*s stability limit of this superstructure, with a precise and controlled heating/cooling protocol of glass precursors. Furthermore, the synthesis of the Sr*RE*Ga_3O_7 disordered $P\bar{4}2_1m$ melilite with small rare-earths was also studied by glass crystallisation, demonstrating the attainability of the parent tetragonal melilite structure for the whole *RE* series except Lu. Hence, the $P\bar{4}2_1m$ $SrYbGa_3O_7$ compound is reporting here for the first time. The stability and occurrence of both melilite polymorphs *vs* temperature was studied using both *in situ* VT-PXRD and DSC techniques. This combined approach unfolded the existence of three distinct Sr*RE*Ga_3O_7 compositions categories with different ordering/disordering mechanisms. First the *RE* = [Yb, Lu] compositions which crystallise in and retain the ordered melilite until they decompose (from VT-PXRD); however, DSC has shown with fast enough heating rates, the disordered ytterbium polymorph also exists, which was successfully stabilised phase pure at room temperature and its crystal structure refined. Second, *RE* = [Er, Tm] both crystallise in the disordered melilite structure and undergo ordering while cooling. The last category contains the Dy and Ho rare earths, as they crystallise in the disordered polymorph and do not order on cooling in a furnace; however, the controlled synthesis parameters in the DSC offer the possibility to stabilise the $P2_12_12$ ordered melilite for these compositions also. The competition between both melilite structures was assigned here to two crucial parameters: (i) the size mis-match between strontium and rare earth atoms, (ii) the ionic radii of the rare earth on its own,

as the eventuality of the ordered melilite was assigned to a combination of both these parameters. Namely, the Lu compound could not be crystallised in the tetragonal melilite due to the its big size difference with Sr atoms and its low decomposition temperature, while on the other extreme of the superstructure limits, Tb could not be achieved in the $P2_12_12$ ordered cell as it is too big to be held in a [6+1] coordination type. The discovery of this new ordered melilite also comes with interesting optical properties compared to their disordered image and corresponding glasses. As described in section II.6, the superstructured melilite photoluminescence spectrum shows a clear band restructuration and significant increase of the *RE* main emission band intensity compared to its glass and tetragonal melilite analogues in the near infrared, which makes it a potential candidate for the development of compact sources for remote sensing, environment, surgery and security and defence [48]–[52].

This family of compounds still shows a wide variety of compositions to be studied especially the B-based and Ca-based melilite compositions which have either never been reported before or reported before the discovery of the incommensurate *5D*-modulation region of the melilite compounds. Moreover, it could be interesting to seek different melilite ordering types by mixing large and small rare-earths natures according to the formula $Sr*RE*1_{1-x}*RE*2_{1+x}Ga_3O_7$, which could offer different optical properties.

II.8. References.

[1] A. Krell *et al.*, *Optical Materials*, 2009, **31**, 1144.

[2] R. Apetz *et al.*, *Journal of the American Ceramic Society*, 2003, **86**, 480.

[3] G.L. Messing *et al.*, *Science*, 2008, ,**322**, 382.

[4] M. Allix *et al.*, *Advanced Materials*, 2012, **24**, 5570.

[5] K. Al Saghir *et al.*, *Chemistry of Materials*, 2015, **27**, 508.

[6] K.A. Saghir, Céramiques Transparentes par Cristallisation Complète du Verre : Application Aux Aluminosilicates de Strontium, PhD thesis, Orleans, 2014.

[7] A. Bertrand *et al.*, *Advanced Optical Materials*, 2016, **4**, 1482.

[8] T. Irifune *et al.*, *Nature Communications*, 2016, **7**, 13753.

[9] X. Ma *et al.*, *Nature Communications*, 2018, **9**, 1175.

[10] M. Boyer *et al.*, *Journal of Materials Chemistry A*, 2018, **6**, 5276.

[11] S. Alahraché *et al.*, *Chemistry of Materials*, 2013, **25**, 4017.

[12] M. Boyer *et al.*, *Journal of Materials Chemistry C*, 2016, **4**, 3238.

[13] G. Rousse *et al.*, *Inorganic Chemistry*, 2014, **53**, 6034.

[14] W. Wisniewski *et al.*, *CrystEngComm*, 2018, **20**, 3455.

[15] A.J. Fernandez-Carrion *et al.*, *Inorganic Chemistry*, 2017, **56**, 14446.

[16] J.M.S. Skakle *et al.*, *Powder Diffr.*, 1999, **14**, 8.

[17] R.-L. Tang *et al.*, *Inorganic Chemistry Frontiers*, 2019, **6**, 2304.

[18] K. Igashira *et al.*, *Optical Materials*, 2021, **112**, 110782.

[19] Y. Chi *et al.*, *Dalton Transactions*, 2018, **47**, 13434.

[20] Y. Zhang *et al.*, *Crystal Growth & Design*, 2012, **12**, 622.

[21] C. Jiang *et al.*, *Journal of Crystal Growth*, 2018, **496–497**, 57.

[22] C. Shen *et al.*, *Journal of Alloys and Compounds*, 2015, **647**, 1069.

[23] J. Xu *et al.*, *Journal of Solid State Chemistry*, 2015, **230**, 309.

[24] J. Xu *et al.*, *Inorganic Chemistry*, 2017, **56**, 6897.

[25] X. Kuang *et al.*, *Nature Materials*, 2008, **7**, 498.

[26] M.-R. Li *et al.*, *Angewandte Chemie International Edition*, 2010, **49**, 2362.

[27] F. Wei *et al.*, *Inorganic Chemistry*, 2012, **51**, 5941.

[28] F. Wei *et al.*, *Journal of the American Chemical Society*, 2011, **133**, 15200.

[29] F. Seifert *et al.*, *Physics and Chemistry of Minerals*, 1987, **14**, 26.

[30] K. Kusaka *et al.*, *Physics and Chemistry of Minerals*, 2001, **28**, 150.

[31] Z.H. Jia *et al.*, *Acta Crystallographica Section B Structural Science*, 2006, **62**, 547.

[32] C. Van Heurck *et al.*, *Physics and Chemistry of Minerals*, 1992, **18**, 441.

[33] J. Barbier, N. Penin, L.M. Cranswick, *Chemistry of Materials*, 2005, **17**, 3130.

[34] J. Fan *et al.*, *Chemistry of Materials*, 2020, **32**, 9016.

[35] M. Boyer, Synthèse de nouvelles céramiques polycristallines transparentes par cristallisation complète du verre, PhD thesis, 2016.

[36] V. Petricek *et al.*, *Institute of Physics, Academy of Sciences of the Czech Republic*, 2006, **162**, 53.

[37] C. Genevois *et al.*, *Inorganic Chemistry*, 2021, **60**, 12339.

[38] A. Rosenflanz *et al.*, *Nature*, 2004, **430**, 761.

[39] A.A. Coelho, *Journal of Applied Crystallography*, 2018, **51**, 210.

[40] M. O'Keeffe, B.G. Hyde, *Philosophical Transactions of the Royal Society of London. Series A, Mathematical and Physical Sciences*, 1980.

[41] A. de Pablos-Martín, A. Durán, M.J. Pascual, *International Materials Reviews*, 2012, **57**, 165.

[42] P.P. Fedorov, A.A. Luginina, A.I. Popov, *Journal of Fluorine Chemistry*, 2015, **172**, 22.

[43] X. Liu *et al.*, *Progress in Materials Science*, 2018, **97**, 38.

[44] D.R. Neuville *et al.*, From glass to crystal: Nucleation, growth and phase separation: from research to applications. *From glass to crystal*, EDP Sciences, 2021.

[45] M. Nakazawa *et al.*, *Applied Physics Letters*, 1989, **54**, 295.

[46] A.C. Lira *et al.*, *Optical Materials*, 2010, **32**, 1266.

[47] H. Yang *et al.*, *High Power Laser Science and Engineering*, 2013, **1**, 138.

[48] A.S. Affan *et al.*, *Defence Technology journal*, 2022, **17**, 583.

[49] A.R. Adams *et al.*, *Philosophical Transactions of the Royal Society of London. Series A: Mathematical, Physical and Engineering Sciences*, 2001, **359**, 635.

[50] B.M. Walsh *et al.*, *Journal of Luminescence*, 2016, **169**, 400.

[51] S.K. Verma *et al.*, *National Journal of Maxillofacial Surgery*, 2012, **3**, 124.

[52] P. Werle *et al.*, *Optics and Lasers in Engineering*, 2002, **37**, 101.

Chapter III: Synthesis and Cationic Order/Disorder Characterisation Between Three Isoelectronic Cations in $Ca_3Ga_{2-2x}Zn_xGe_{4+x}O_{14}$ ($0 \leq x \leq 1$) by a Multi-technique Approach

III.1. Introduction.

In the general introduction and Chapter I, the interests in researching systems with potential nano-crystallised products from glass precursors for new transparent functionalisable ceramic materials was described. In this context, the existence of stable phases in the CaO-ZnO-Ga_2O_3-GeO_2 system such as $Ca_3Ga_2Ge_4O_{14}$ and $Ca_3ZnGe_5O_{14}$ crystallising in the lanagasite [1] and taikanite [2] structures respectively, and capable of hosting multiple cations is of interest to study [3].

The langasite structures family with a general formula $A_3BC_3D_2O_{14}$ are much of interest materials due to their piezoelectric [4], wide transparency up to 7 μm and high laser damage threshold (LDT) [5], [6], low temperature multiferroic 3*d* cations behaviour [7], [8] and ionic conductivity properties [9]. Their structure can be described as a melilite-related family compound, their layered framework thus offers four different crystallographic sites, where A is an 8-coordinated (Wyk. Pos. 3f), B 6-coordinated (1a), C and D both 4-coordinated sites (3f and 2d respectively), organised in channels of the same site nature along the *c*-axis "stacking axis" (see Figure III.1). The variety of the crystallographic sites in this structure can accommodate many cation types, offering the potential for complex cation ordering schemes.

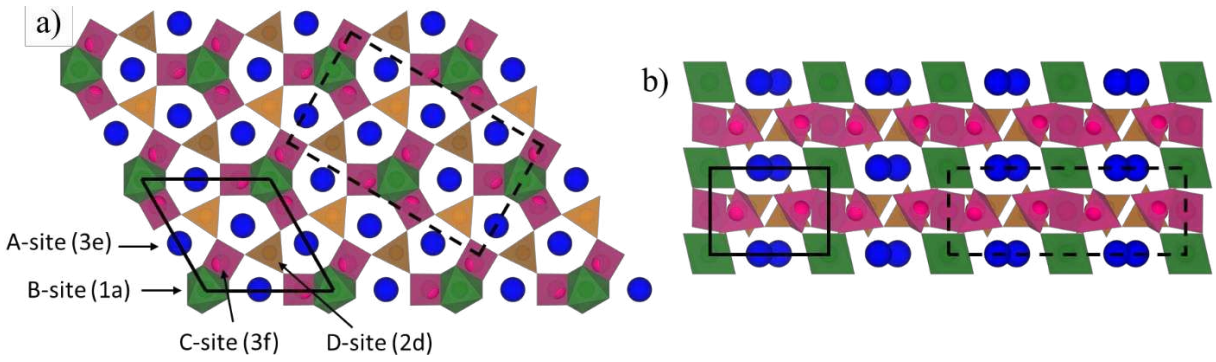

Figure III.1. *Crystal structure projection of the $A_3BC_3D_2O_{14}$ langasite structure family along the a) c-axis, b) b-axis, showing both the P*321 *cell (straight black lines) and C*2 *cell (dashed black lines).*

The $Ca_3Ga_2Ge_4O_{14}$ compound was first discovered and reported by E. L. Belokoneva *et al* [1] in 1980, and was identified as the first member of the langasite family. Its structure was proposed to crystallise in a trigonal cell with the *P*3 space group symmetry, but this was soon after revised to the *P*321 space group [10]. Its crystal structure is as described above, where the A-sites host the Ca atoms, B- and C-sites accommodate Ga and Ge in a disordered scheme, while the D-site remains fully occupied by Ge atoms [9], [10]. The cationic disorder between Ga and Ge over the B- C- and D-sites in the $Ca_3Ga_2Ge_4O_{14}$ compound, was characterised by

single crystal X-ray diffraction, and their occupancies were assigned according to the cation-oxide first neighbours distance analysis [11]. Moreover, recent work characterised the cationic disorder by anomalous diffraction indicating dominant population of the 1a site by Ge atoms (0.2Ga/0.8Ge) [12], [13]; however results were far from the previously reported ones in [11] which declared an almost equal distribution between Ga and Ga over the 1a site (0.4Ga/0.6Ge). The $Ca_3ZnGe_5O_{14}$ phase was reported to be a theoretical phase which can't be synthesised by conventional single crystal growth methods [14]. Nevertheless, it was recently obtained as a by-product from sintering attempts of a phase pure $CaCu_{0.95}Zn_{0.05}Ge_2O_6$ compound in an open platinum tube [2], as single crystal form. Its structure was related to the taikanite family [15], adopting a monoclinic cell (S.G. *C*2, a = 13.938(5) Å, b = 7.941(3) Å, c = 5.0560(17) Å) (see Figure III.1), with a completely ordered langasite framework, where Zn^{2+} fully occupies the octahedral sites, while the tetrahedral framework sites are entirely formed by Ge^{4+} atoms. In this case, the cationic distribution between Zn^{2+} and Ge^{4+} was also investigated only based on single crystal X-ray diffraction *via* a bond valence sum analysis. Several works demonstrated that the langasite family can also adopt a monoclinic cell, going through a high pressure phase transition (*P*321→*C*2) (e.g. $La_3Nb_{0.5}Ga_{5.5}O_{14}$) [16], [17], or a reversed phase transition at high temperatures (*C*2→*P*321) (e.g. $La_3SbZn_3Si_2O_{14}$) [17], [18], which would suggest the possibility to synthesise the trigonal polymorph of the $Ca_3ZnGe_5O_{14}$ phase.

Characterisation of the atomic disorder in complex systems containing neighbouring elements from the periodic table, can be a tough task to answer because of the close X-ray scattering factors and multiple possible solutions when a crystallographic site hosts more than two cations. However, it is sometimes important to resolve the element distributions in the cell, especially where cation ordering controls structural polarity [19], suppresses thermal conductivity [20], or influences lithium battery cyclability [21]. In this chapter the possibility to synthesise the $Ca_3Ga_{2-2x}Zn_xGe_{4+x}O_{14}$ solid solution from x = 0 all the way to x = 1 is investigated by full and congruent crystallisation from glass or molten liquid, while retaining the trigonal polymorph across the whole solid solution series, thus successfully achieving the stabilisation of the first trigonal *P*321 $Ca_3ZnGe_5O_{14}$ phase. Characterisation of their structure and related cationic distribution between three successive elements from the periodic table was challenging, due to the absence of X-ray scattering contrast, or close neutron scattering lengths and the possibility of more than two cation types sharing a single crystallographic site. Using a combined approach between SPD and NPD data, the ordering between Ge/Ga and Ge/Zn for x = 0 and x = 1 compositions was determined. As for intermediate compositions, combination

between SPD, NPD and quantitative analysis of atomic scale STEM-EDS maps, by a new two-dimensional fitting approach, brings insight to the changes in cation arrangement in the layered framework across the solid solution series.

III.2. $Ca_3Ga_{2-2x}Zn_xGe_{4+x}O_{14}$ ($0 \leq x \leq 1$) solid solution synthesis investigations.

III.2.1. Solid-state reaction.

First, a mixture with stoichiometric amounts of high purity precursors $CaCO_3$ 99.95%, Ga_2O_3 99.998%, ZnO 99.999%, GeO_2 99.9% (all from Strem Chemicals) were weighed according to the nominal composition for $0 \leq x \leq 1$, then ground together for several minutes in an agate mortar in presence of ethanol for a better homogeneity of the sample. The resulting powder was then dried at 100°C for 20 minutes to evaporate the remaining ethanol, and pressed into pellets of 16 mm each.

In order to investigate the synthesis of the $Ca_3Ga_{2-2x}Zn_xGe_{4+x}O_{14}$ ($0 \leq x \leq 1$) solid solution compounds, initial attempts were conducted by solid-state reactions, starting from the prepared mixture described above. *In situ* VT-PXRD measurements were conducted from room temperature (RT) to 50°C in one heating step, and then to 1200°C (50°C/step) in an angular range of 10°-50° (2θ) using a step of 0.016° and a measuring time of 0.7 s/step, on the $Ca_3Ga_2Ge_4O_{14}$ (x =0) parent compound. In Figure III.2, it is visible that the main $Ca_3Ga_2Ge_4O_{14}$ (x =0) langasite starts forming at 950°C along with the $CaGeO_3$ perovskite. At 1200°C both phases are still present with unreacted Ga_2O_3, which indicates that either higher temperatures are required or a longer reaction time is needed to achieve a full reaction of the mixture and obtain a langasite phase pure sample. However, the sample mixture melts around 1250°C, which excludes the possibility of raising the ceramic synthesis temperature to higher values. Following this, the initial mixture was left to react for 48 hours at 1200°C with intermediate grinding each 12h, which resulted still in a mixed sample between $Ca_3Ga_2Ge_4O_{14}$ (x =0) langasite, $CaGeO_3$ perovskite and Ga_2O_3. Different synthesis routes were then considered.

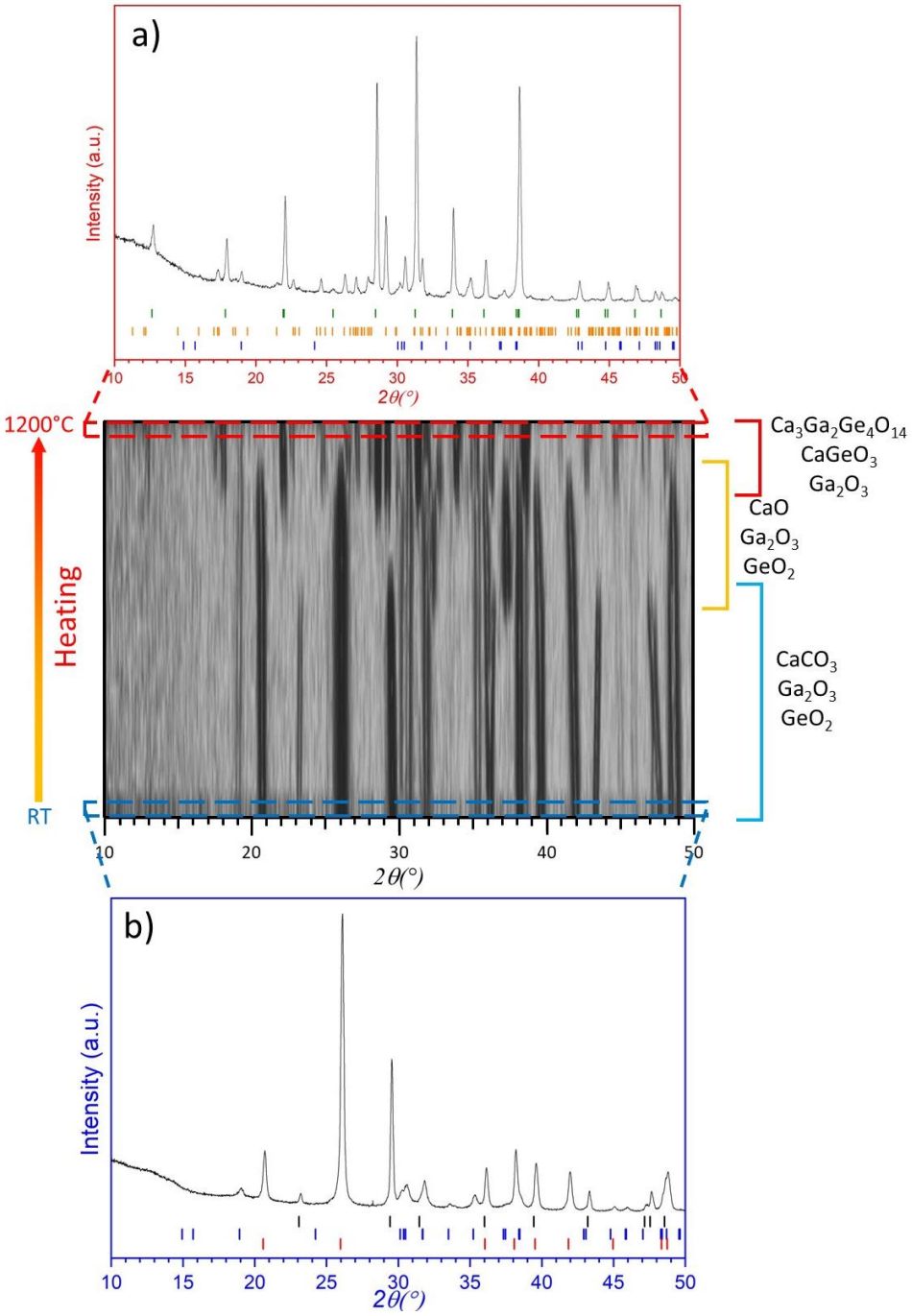

Figure III.2. *In situ powder X-ray diffraction (VT-PXRD) data of a $CaCO_3$-Ga_2O_3-GeO_2 mixture, with respect of $Ca_3Ga_2Ge_4O_{14}$ nominal composition, between room temperature and 1200°C. a), b) Inserts show the indexed diffraction patterns at room temperature and 1200°C, with the different colour tickmarks corresponding to, $CaCO_3$ (black), Ga_2O_3 (blue), GeO_2 (red), $Ca_3Ga_2Ge_4O_{14}$ (green) and $CaGeO_3$ (orange).*

III.2.2. Crystallisation from glass and under-cooled melt.

In order to achieve a phase pure sample, crystallisation from glass or under-cooled melt was considered as an alternate synthesis route. The initial mixture pellets of compositions $Ca_3Ga_{2-2x}Zn_xGe_{4+x}O_{14}$ ($0 \leq x \leq 1$) (described in section III.2.1) were broken into small fragments

of ~ 35 mg each, then melted individually using the ADL apparatus coupled to two CO_2 lasers [22], [23]. These samples reached liquid state between 1250°C – 1350°C (depending on the composition), and were further heated up to 1500°C to ensure their homogeneity, then subsequently quenched by turning the lasers off, reaching high cooling rates (estimated around 300°C/s) in order to achieve vitrification [24], and leading to glass precursors in the form of spherical beads. The synthesised glass beads were checked by laboratory PXRD. As shown in Figure III.3 no Bragg diffraction peaks were observed, confirming the amorphous state of the synthesised samples.

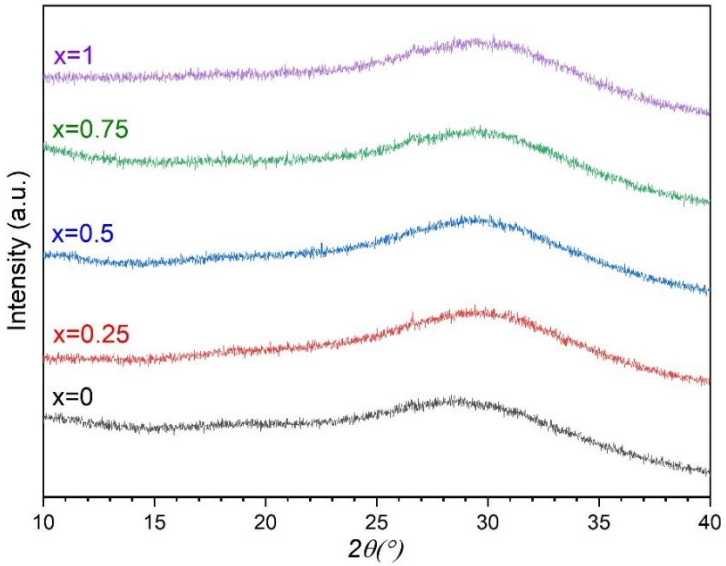

Figure III.3. *Laboratory X-ray powder diffraction data of $Ca_3Ga_{2-x}Zn_xGe_{4+x}O_{14}$ (x = 0, 0.25, 0.5, 0.75, 1) glass samples synthesized by aerodynamic levitation coupled to laser heating (ADL).*

III.2.3. Differential scanning calorimetry (DSC) and *in-situ* Variable Temperature PXRD (VT-PXRD).

As illustrated in Figure III.4a and Figure III.5 the conducted VT-PXRD measurements on the $Ca_3Ga_{2-2x}Zn_xGe_{4+x}O_{14}$ (x = 0 and 1) end members composition shows a crystallisation of mainly the langasite phase with two other minor impurities ($Ca_3Ga_2Ge_3O_{12}$ garnet + $Ca_2Ga_2GeO_7$ melilite and $CaZnGe_2O_6$ clinopyroxene + $Ca_2ZnGe_2O_7$ melilite for x =0 and 1 respectively). Comparing the impurities compositions to the nominal ones, a Ge deficiency can clearly be spotted in both cases, indicating a Ge loss to evaporation during the melting process. Following to this, a new ADL glass synthesis attempts with GeO_2 excess "3CaO $1Ga_2O_3$ $4.5GeO_2$", which corresponds to an additional ~ 2 % (wt%) of GeO_2, showed the crystallisation of a phase pure langasite $Ca_3Ga_2Ge_4O_{14}$ (x = 0) sample (see Figure III.4b). As for the

$Ca_3ZnGe_5O_{14}$ (x = 1) compound, multiple attempts with different excess amounts of GeO_2 resulted in the same multi-phase crystallised sample with the same impurities.

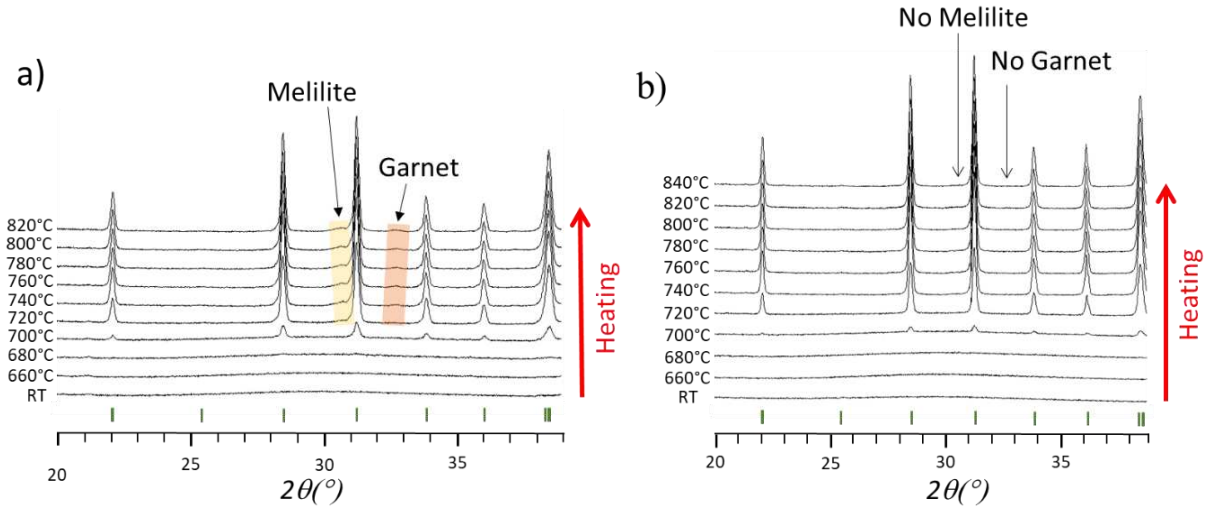

Figure III.4. *Variable temperature powder X-ray diffraction (VT-PXRD) measurements of, a) glass of composition $Ca_3Ga_2Ge_4O_{14}$ (x = 0), b) glass of a slightly deviated composition from $Ca_3Ga_2Ge_4O_{14}$ (x = 0) with an excess of ~ 2% (%wt) of GeO_2 added in the nominal composition. Green tickmarks represent the $Ca_3Ga_2Ge_4O_{14}$ indexation.*

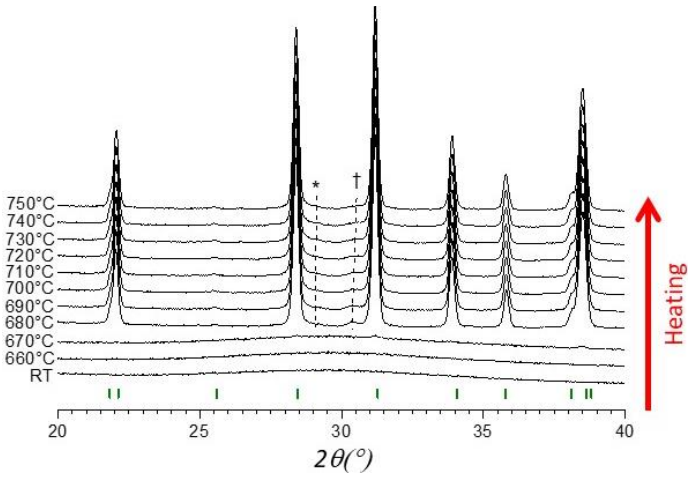

Figure III.5. *Variable temperature PXRD measurements on the $Ca_3ZnGe_5O_{14}$ x =1 glass composition showing its crystallisation upon heating, where * and † represent the clinopyroxene $CaZnGe_2O_6$ and melilite $Ca_2ZnGe_2O_7$ impurities respectively. Green tick marks represent the P*321 *$Ca_3ZnGe_5O_{14}$ indexation.*

DSC measurements were conducted on a single glass bead of each composition to extract the glass transition "T_g" and glass crystallisation "T_c" temperatures (see Figure III.6) of each composition. Comparing the DSC and VT-PXRD measurements for both $Ca_3Ga_{2-2x}Zn_xGe_{4+x}O_{14}$ (x =0 and 1) end members, DSC shows a much higher T_c by 47°C and 150°C for x = 0 and 1 respectively over VT-PXRD. This can be either related to the different heating kinetics from the measuring conditions (DSC: 10°C/min *vs* VT-PXRD: 0.5°C/min), or

due to surface crystallisation mechanism enhanced in the measured powder samples on VT-PXRD. In Figure III.7a, a comparison of the $Ca_3ZnGe_5O_{14}$ (x = 1) DSC measurements under powder and bulk form is shown, where the powder sample clearly exhibits a lower T_c, thus confirming the hypothesis of surface crystallisation mechanisms being favoured. The samples were then crystallised under bulk form to minimise their surface. This helped to isolate phase pure langasite.

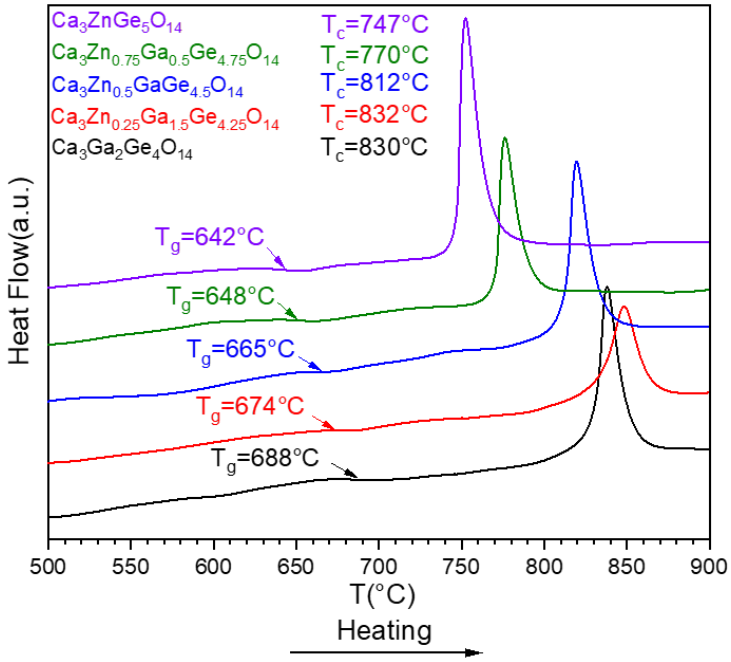

Figure III.6. *Conducted DSC measurements on $Ca_3Ga_{2-2x}Zn_xGe_{4+x}O_{14}$ x = 0 (black), 0.25 (red), 0.5 (blue), 0.75 (green) and 1 (purple) powder samples, using a 10°C/min rates upon heating.*

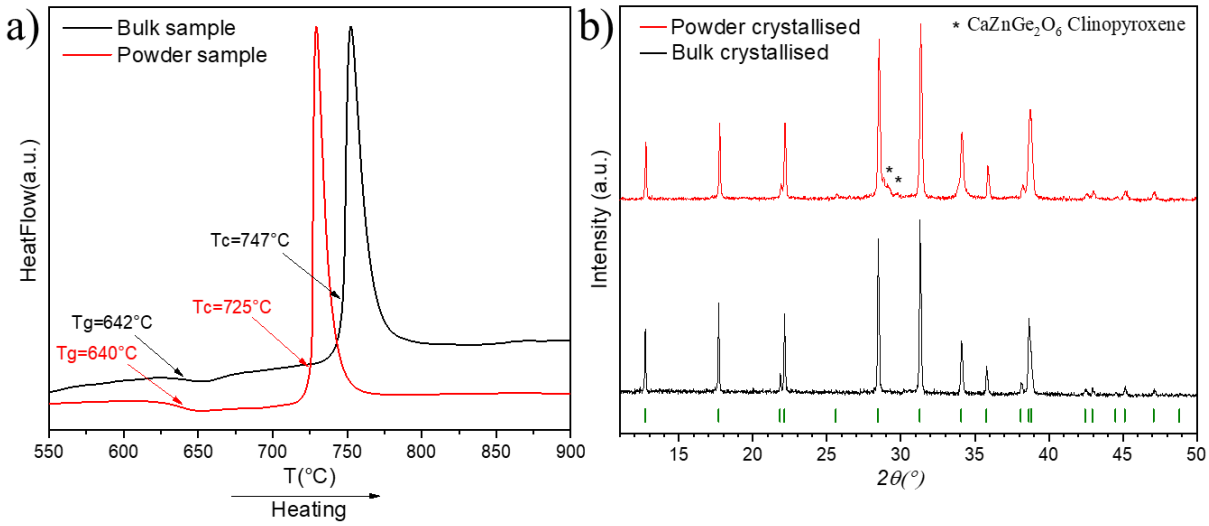

Figure III.7. *a) Comparison between a) DSC measurements of $Ca_3ZnGe_5O_{14}$ (x = 1) under bulk (black) and powder form (red). b) laboratory PXRD measurements of post DSC measured samples in a). Green tickmarks represent the LeBail refined $Ca_3Ga_2Ge_4O_{14}$ P321 structure*

Furthermore, direct crystallisation of the melt was shown to help achieve a better crystallinity for the $Ca_3Ga_{2-2x}Zn_xGe_{4+x}O_{14}$ x = 0 sample (see Figure III.8), whereas (x > 0) compositions favoured multi-phase samples between the main langasite and melilite impurity. Crystallisation of the melt was achieved by adjusting the carrier gas flow (argon in this case) so that the levitating molten bead touches the nozzle while cooling. The contact surface thus acts as a nucleation centre for crystallisation of the entire bead when the lasers are turned off.

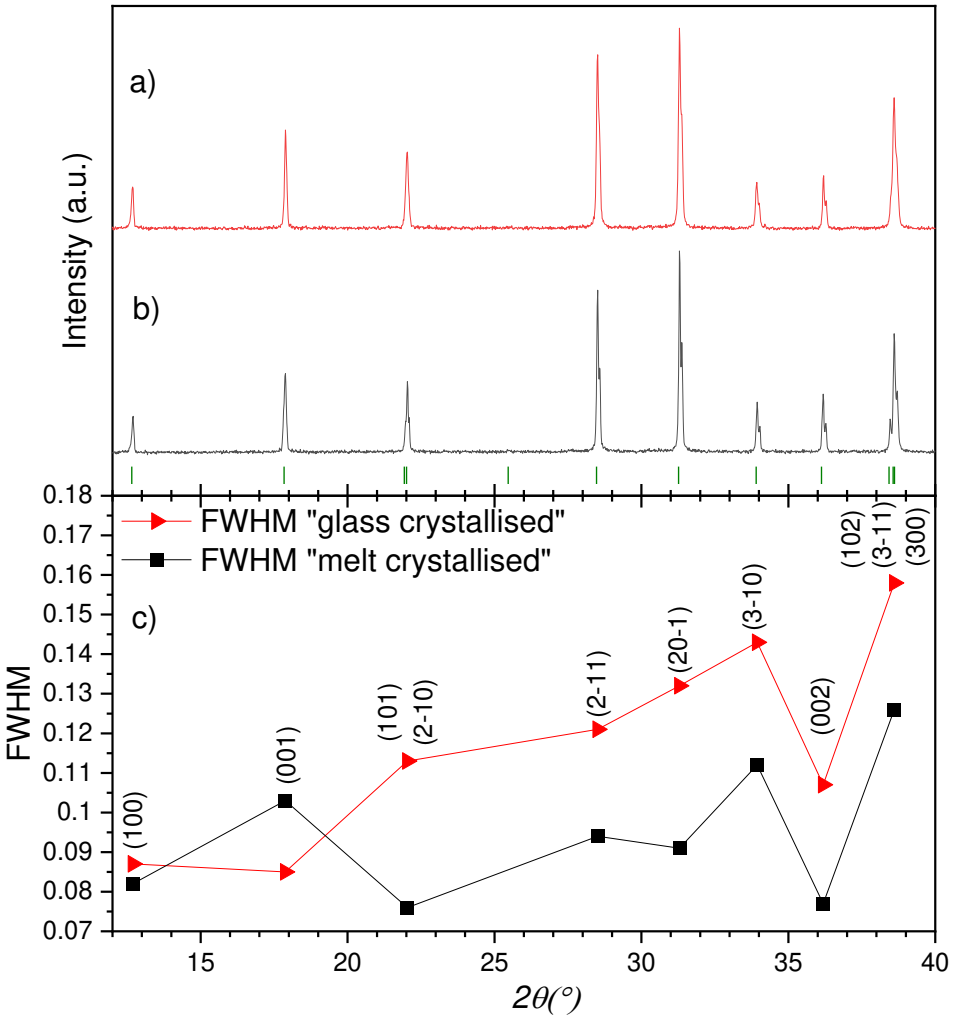

Figure III.8. *Crystallised $Ca_3Ga_2Ge_4O_{14}$ (x = 0) sample from a) glass at 820°C in an open atmosphere furnace, b) molten liquid on the ADL equipment, by turning the lasers off while the droplet is touching the nozzle. Green tick marks represent $Ca_3Ga_2Ge_4O_{14}$ indexation. c) the extracted FWHM's for each peak from a) and b), extracted by individual peak fitting.*

To summarise the final synthesis conditions of the $Ca_3Ga_{2-2x}Zn_xGe_{4+x}O_{14}$ ($0 \leq x \leq 1$) solid solution compounds, crystallisation from the melt was used to achieve a phase pure and highly crystalline $Ca_3Ga_2Ge_4O_{14}$ (x = 0) langasite. Crystallisation from bulk glass samples on the other hand was used to synthesise a single phase langasite for $Ca_3Ga_{2-2x}Zn_xGe_{4+x}O_{14}$ (x = 0.25, 0.5,

0.75 and 1) compounds, where (x = 0.25, 0.5, 0.75) and (x = 1) samples were annealed at 815°C for 2h, and 800°C for 3h respectively.

III.3.Structural analysis across the $Ca_3Ga_{2-2x}Zn_xGe_{4+x}O_{14}$ ($0 \leq x \leq 1$) solid solution series from SPD data.

The $Ca_3ZnGe_5O_{14}$ was reported by G. J. Redhammer to crystallise in a monoclinic langasite structure (SG. *C*2, *a*= 13.938(5) Å, *b*= 7.941(3) Å, *c*= 5.0560(17) Å, *β*= 90.817(4)°) [2] (see Figure III.1 for a comparison between the monoclinic *C*2 and the trigonal *P*321 cells), it can be described as a fully ordered structure where Zn^{2+} cations only occupy the octahedral B-sites, whilst the Ge^{4+} fully occupies the remaining tetrahedral C- and D-sites.

The direct melt crystallised (x = 0) and glass crystallised ($0.25 \leq x \leq 1$) samples were first analysed by laboratory PXRD. As shown in Figure III.9a across the solid solution, all diffraction patterns were indexed with the parent *P*321 $Ca_3Ga_2Ge_4O_{14}$ langasite structure. However, for composition near x = 1 "$Ca_3Ga_{2-2x}Zn_xGe_{4+x}O_{14}$" Bragg diffraction peaks became broader, which could be hinting at atomic disorder, peak splitting with a possible phase transition to *C*2 symmetry, or even microstructural strain (see Figure III.9b). To further investigate this observed peak broadening in lab data and the possibility of a monoclinic distortion for compositions near x = 1 "$Ca_3Ga_{2-2x}Zn_xGe_{4+x}O_{14}$", synchrotron powder diffraction (SPD) measurements were conducted on samples of composition x = 0, 0.25, 0.5, 0.75, 1. First a bead of each sample composition was synthesised and crushed into fine powder, then loaded into 8 mm diameter Kapton capillaries. The prepared samples were sent to the APS Argonne laboratory for the SPD measurement to be conducted on the 11BM beamline.

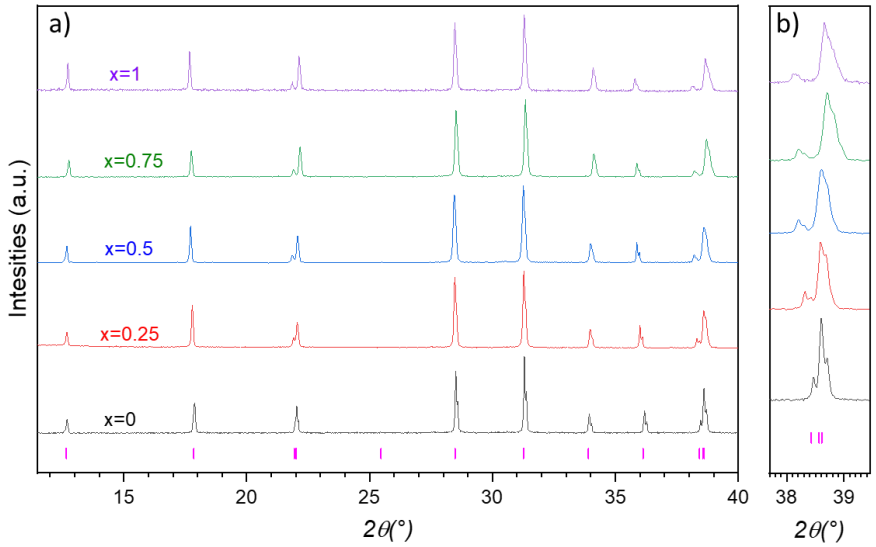

Figure III.9. *a) Normalised stacked diffraction patterns of $Ca_3Ga_{2-2x}Zn_xGe_{4+x}O_{14}$ (x = 0, 0.25, 0.5, 0.75, 1) compositions measured by laboratory powder X-ray diffraction. b) Zoom on the 37.7°-39.5°(2θ) region evidencing the observed peak broadening as x values increases. Pink tick marks correspond to the $Ca_3Ga_2Ge_4O_{14}$ indexation.*

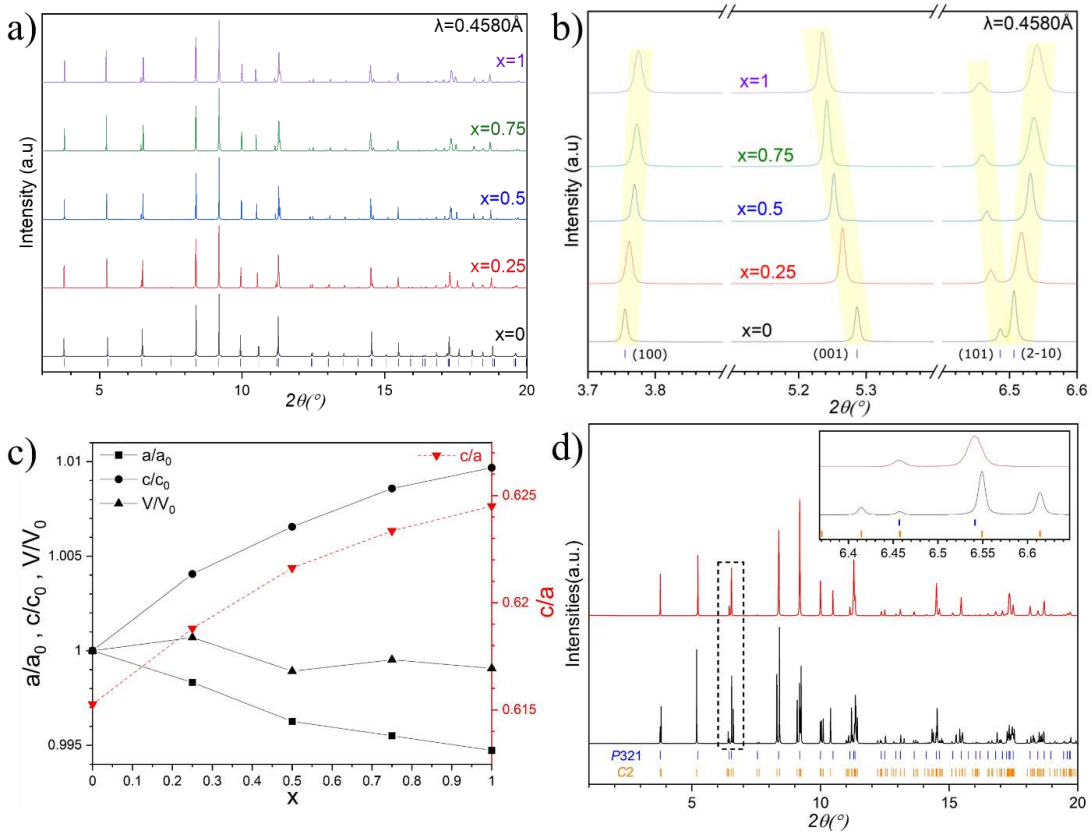

Figure III.10. *a) SPD data of $Ca_3Ga_{2-2x}Zn_xGe_{4+x}O_{14}$ x = 0 (black), 0.25 (red), 0.5 (blue), 0.75 (green) and 1 (purple) compositions, with dark blue tickmarks corresponding to $Ca_3Ga_2Ge_4O_{14}$ indexation. b) Zoom view on the (100), (001), (101) and (2$\bar{1}$0) (S.G P321) peaks shown in (a), highl the peaks shift. c) Normalised simulated monoclinic $Ca_3ZnGe_5O_{14}$ C2 [2] (in black) and measured $Ca_3ZnGe_5O_{14}$ glass crystallised sample (in red), synchrotron powder diffraction (SPD) plots, with their respective cell indexations in orange and blue tick marks. d) Normalised refined cell parameters (from SPD data) of the P321 langasite structure across the solid solution series to the parent $Ca_3Ga_2Ge_4O_{14}$ cell parameters.*

In Figure III.10a and Figure III.10b, SPD measurements shows that across the solid solution series, the same diffraction pattern was retained and fully indexed with the trigonal *P*321 $Ca_3Ga_2Ge_4O_{14}$ parent langasite, and no apparent monoclinic extra peaks was observed for the x = 1 compound.

Rietveld refinements against SPD data were carried out using the $Ca_3Ga_2Ge_4O_{14}$ structure reported by Mill *et. al.* [11] (SG *P*321, a= 8.076 Å, c= 4.974 Å) as a starting model for all compositions, keeping the same number of total refined parameters for each samples (15 background terms, zero shift, scale factor, 6 profile parameters "TCHZ function", axial divergence, 17 atomic parameters, resulting in 41 independently refined parameters), in the absence of X-ray scattering contrast between Ge^{4+}, Ga^{3+} and Zn^{2+} (Z_{Ge}= 32, Z_{Ga}= 31, Z_{Zn}= 30) refining the partial occupancies of each cation against only PXRD data is an impossible task to address, hence the B- C- and D-sites were set as fully-occupied without refining each of the three cations (Ga, Ge and Zn) partial occupancies. The SPD refined cell parameters show an opposing trend in *a* and *c*, giving a very weak decrease in the unit cell volume but a marked increase in *c/a* ratio with increasing x (Figure III.10c). This is consistent with the substitution of Ga^{3+} (ionic radius of 0.62 and 0.47 Å in 6- and 4-coordination respectively) by a mixture of smaller Ge^{4+} (0.53 Å and 0.39 Å) and larger Zn^{2+} (0.74 Å and 0.60 Å) [25], which is also seen in other langasite-type solid solutions such as $La_3Ga_{5-x}Ge_{1+x}O_{14+x/2}$ [9]. The refinements led to satisfactory reliability factors for the entire measured series (see Figure III.12 and Figure A. 15, Figure A. 16 in the appendices Chapter A.III for SPD Rietveld refined plots and Table III.1, Table III.2 and Table A. 10, Table A. 11, Table A. 12 in the appendices Chapter A.III for refined structural parameters). As shown in Figure III.10d, the simulated SPD pattern of the $Ca_3ZnGe_5O_{14}$ *C*2 structure produces many more Bragg peaks compared to our $Ca_3ZnGe_5O_{14}$ (x = 1) sample synthesised by glass crystallisation. Therefore, comparing the Rietveld fits obtained from both structural models, for the two structures refinements, misfits can be detected due to *hkl*-dependent peak broadening in the measured pattern. The *hkl*-dependent peak broadening was then modelled in TopasV6 [26] using the Stephens description [27]: R_{wp} and χ^2 values dropped from [8.98%, 2.01] to [7.36%, 1.35] for the *P*321 model, and from [8.93%, 1.99] to [6.68%, 1.10] for the *C*2 model (see Figure III.12b, Figure A. 17 and Figure A. 18, Table III.2, Table A. 13 to Table A. 15 in the appendices Chapter A.III for refined SPD plots and structural parameters). The refined *C*2 structure showed a huge decrease of the β angle (from 90.817(4)° [2] to 89.955(1)°), making the (*hkl*) and ($hk\bar{l}$) peaks families overlap, hence leading to a metrically orthorhombic cell. The slightly better fit provided by the *C*2 model after using

Stephens broadening functions can be explained by its lower symmetry than the *P*321 space group, hence allowing more refinable parameters (*C*2: 68 + 10 parameters from Stephens description *vs* *P*321: 41 + 5 parameters from Stephens description), the final *C*2 and *P*321 refined models showed to be almost indistinguishable, see Figure III.11 for the overlay of both structures. From these two key points: (i) the complete absence of extra diffraction peaks arising from the monoclinic distortion on the measured $Ca_3ZnGe_5O_{14}$ SPD pattern despite its excellent signal to noise ratio, and (ii) the almost undistinguishable Rietveld refined models *P*321 and *C*2, the trigonal cell *P*321 was then kept to describe the structure of this composition.

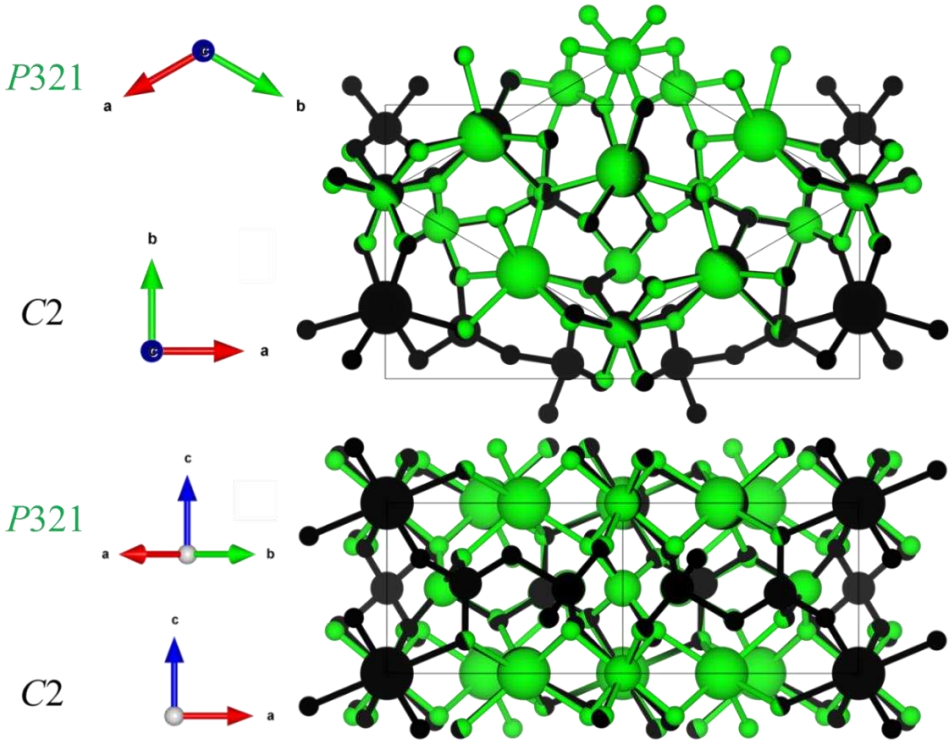

Figure III.11. *Overlay between Rietveld refined C2 (black atoms) and P321 (green atoms) structures for the $Ca_3ZnGe_5O_{14}$ (x = 1) composition against SPD data, along, a) c-axis, b) b-axis of the C2 structure.*

Table III.1. Refined structural parameters obtained from SPD data collected at room temperature on $Ca_3Ga_2Ge_4O_{14}$ (x = 0) (*P*321 space group, *a*= 8.072032(6) Å and *c*= 4.966435(5) Å) sample.

Atom	Position	x	y	z	Occ	B_{iso}
Ca	3e	0.42012(7)	0	0	1	0.96(1)
Ga1/Ge1	1a	0	0	0	0.4/0.6*	0.608(7)
Ga2/Ge2	3f	0.76255(3)	0	0.5	0.47/0.53*	0.679(5)
Ge3	2d	1/3	2/3	0.53090(8)	1	0.593(6)
O1	2d	1/3	2/3	0.1914(4)	1	1.21(2)[a]
O2	6g	0.4652(2)	0.3154(2)	0.3180(2)	1	1.21(2)[a]
O3	6g	0.2144(2)	0.0795(2)	0.7626(3)	1	1.21(2)[a]

*Fixed occupancy from [11]

[a]: constrained to refine to the same Biso values.

Table III.2. Refined structural parameters obtained from SPD data collected at room temperature on $Ca_3ZnGe_5O_{14}$ (x = 1) (*P*321 space group, *a*= 8.02916(2) Å and *c*= 5.014362(17) Å) sample. Modelled strain.

Atom	Position	x	y	z	Occ	B_{iso}
Ca	3e	0.41841(8)	0	0	1	1.16(1)
Zn1/Ge1	1a	0	0	0	0.5/0.5*	1.48(1)
Zn2/Ge2	3f	0.76499(4)	0	0.5	0.17/0.83*	1.154(7)
Ge3	2d	1/3	2/3	0.52849(11)	1	1.009(9)
O1	2d	1/3	2/3	0.1919(6)	1	1.95(3)[a]
O2	6g	0.4671(2)	0.3189(2)	0.3233(3)	1	1.95(3)[a]
O3	6g	0.22055(19)	0.0773(2)	0.7504(3)	1	1.95(3)[a]

*Site was set to be fully occupied without refining each atom occupancy

[a]: constrained to refine to the same Biso values.

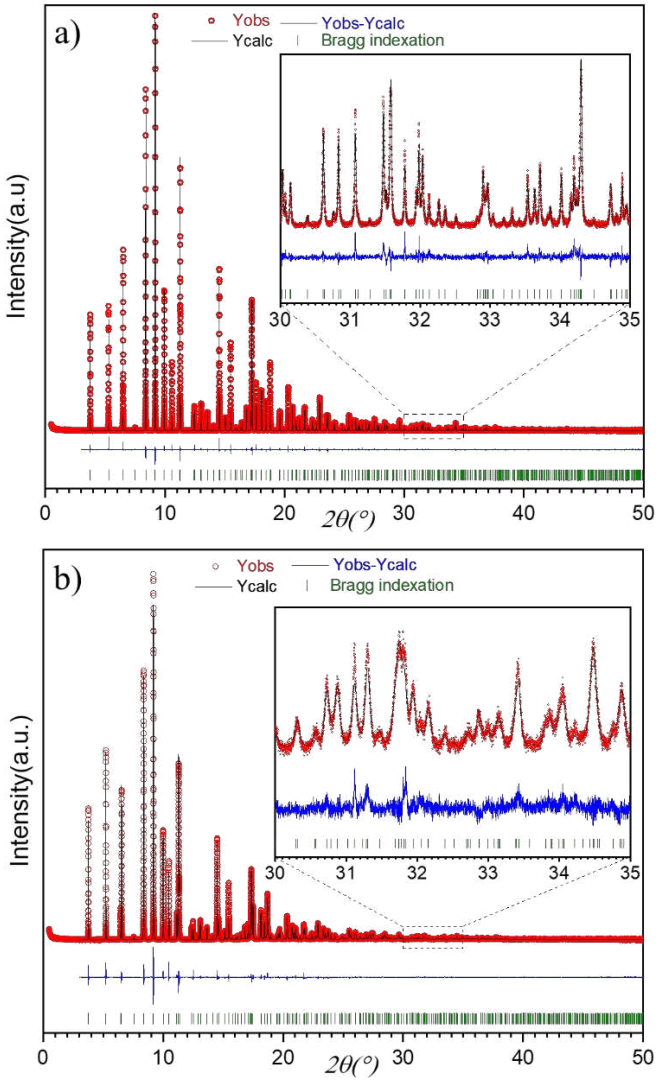

Figure III.12. *Rietveld refinement of a) $Ca_3Ga_2Ge_4O_{14}$ (x = 0) (SPD data, R_p= 7.617% R_{wp}= 9.506%) and b) $Ca_3ZnGe_5O_{14}$ (x = 1) (SPD data, modelled strain R_p= 7.02% R_{wp}= 8.75%). Observed (red dot), calculated (black line), and difference (blue line) profiles are shown. The set of green vertical lines corresponds to reflection positions.*

Metastable structures achieved by glass crystallisation can show a high temperature phase transition to the more thermodynamically stable polymorph. For example, in the Al_2O_3-SrO-SiO_2 ternary diagram, the glass $Sr_{1+x/2}Al_{2+x}Si_{2-x}O_8$ (x = 0) composition was shown to crystallise first in an intermediate metastable hexagonal *P*6$_3$/*mcm* polymorph, and then goes through a phase transition to a more thermodynamically stable monoclinic *I*2/*m* structure [28], [29]. Similar behaviour was noticed by solid state reaction where only the monoclinic polymorph could be stabilised as phase pure [30], [31]. In the langasite structures family, some compositions (e.g. $La_3Nb_{0.5}Ga_{5.5}O_{14}$ [17]) also show phase transition going from the trigonal *P*321 to a monoclinic *C*2 structure under high pressure/temperature. This phase transition was determined by an abrupt slope change in the trigonal cell parameters trend *vs* T(°C) or *vs* P(GPa). In our glass crystallised $Ca_3ZnGe_5O_{14}$ (x = 1) compound, to test the stability of the *P*321 trigonal polymorph and a possible monoclinic phase transition at high temperatures, VT-PXRD measurement were conducted on a previously glass crystallised sample from room temperature to 850°C (sample's decomposition temperature from VT-PXRD). The extracted cell parameters from the measured patterns *vs* T(°C) by Pawley refinements, shows a linear trend and no slope change was noticed until the sample decomposition. This trend was further confirmed by the *a*/*c* ratio which showed a monotonic decreasing tendency (see Figure III.13), with no appearance of *C*2 peaks on their related diffraction patterns. Therefore, the glass crystallised $Ca_3ZnGe_5O_{14}$ (x =1) sample was assumed to retain its trigonal polymorph until it decomposes, with no apparent *C*2 phase transition.

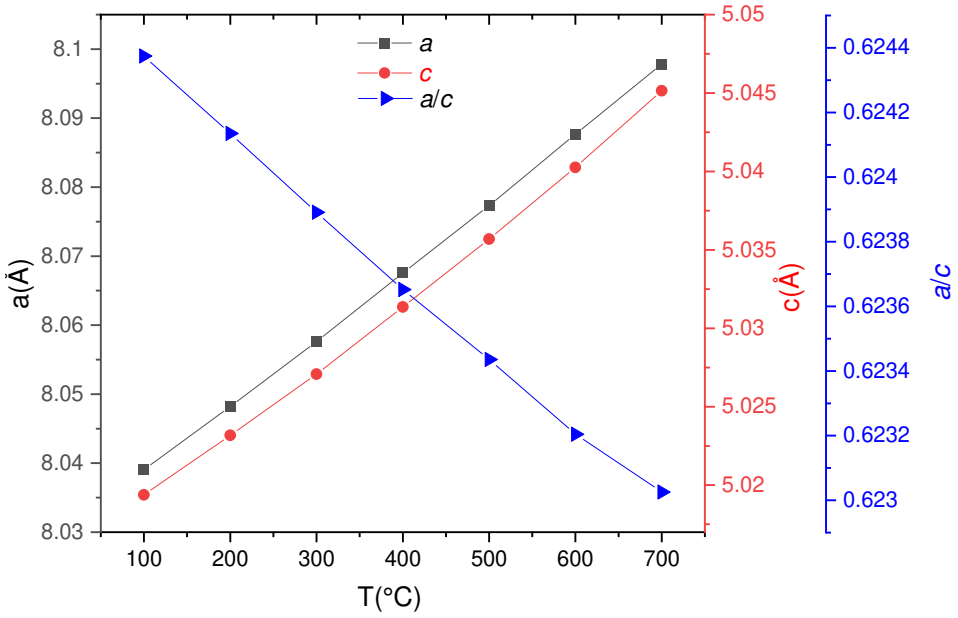

Figure III.13. *Cell parameters evolution of the $Ca_3ZnGe_5O_{14}$ sample vs temperatures on heating.*

III.4. Cationic order/disorder characterisation for $Ca_3Ga_2Ge_4O_{14}$ (x = 0) and $Ca_3ZnGe_5O_{14}$ (x = 1) end members by solid state nuclear magnetic resonance (ss-NMR) and neutron powder diffraction (NPD).

III.4.1. ^{71}Ga and ^{67}Zn SS-NMR.

^{71}Ga solid-state NMR (ss-NMR) is a powerful tool to probe the local structure in terms of coordination and also to provide a quantification of its different environments [32], [33]. ^{71}Ga solid state NMR spectroscopy was performed on the x = 0 member only ($Ca_3Ga_2Ge_4O_{14}$) at 20 T with a Bruker Avance Neo spectrometer equipped with a 0.7 mm magic angle spinning (MAS) double resonance Bruker probehead. The powder sample was spun at a MAS frequency of 100 kHz. Given the wide spectral broadening of the ^{71}Ga NMR environments, a radiofrequency field of 125 kHz was used, which corresponds to 90° and 180° central-transition selective pulses of 1 µs and 2 µs, respectively. A spin echo experiment was recorded using a full echo acquisition (interpulse delay of 150 µs), a recycling delay of 2 s, and with 26000 scans. Furthermore, a two-dimensional QPASS (Quadrupolar Phase-Adjusted Spinning Sidebands) [34] experiment was performed in order to improve the spectral resolution of the Ga environments by separating the overlapping spinning sidebands. Eight sets of timings (constant full duration of seven rotor periods) were needed for a proper separation, with a recycling delay of 2 s, and 8000 scans per set of timings. The spectra were referenced to a 1 M gallium nitrate solution.

As shown in Figure III.14, the spectrum obtained from the spin echo experiment lacks of resolution because of overlapping spinning sidebands, even at ultra-high MAS frequency (100 kHz). Moreover, one can hardly distinguish two Ga environments indicated by the intense peak at 0 ppm and the shouldering at the left side of this peak. Attempts to quantify these two environments by fitting the signal using the Dmfit software [35] and defining two contributions revealed unsuccessful, as the spinning side bands intensity could not be fitted.

The “spinning sidebands-free” QPASS spectrum allows to achieve ultimate spectral resolution, and clearly identifies these two contributions located at ca. 0 ppm and 100 ppm corresponding to 6-coordinated and 4-coordinated Ga respectively. However, the complexity of the QPASS experiment does not allow a precise quantification the two Ga environments. The observed ^{71}Ga lineshapes have smoothed profiles as opposed to singularities of the quadripolar signal expected for fully ordered crystalline phases [36], indicative of geometrical and chemical disorder of both Ga environments in the second coordination sphere [37].

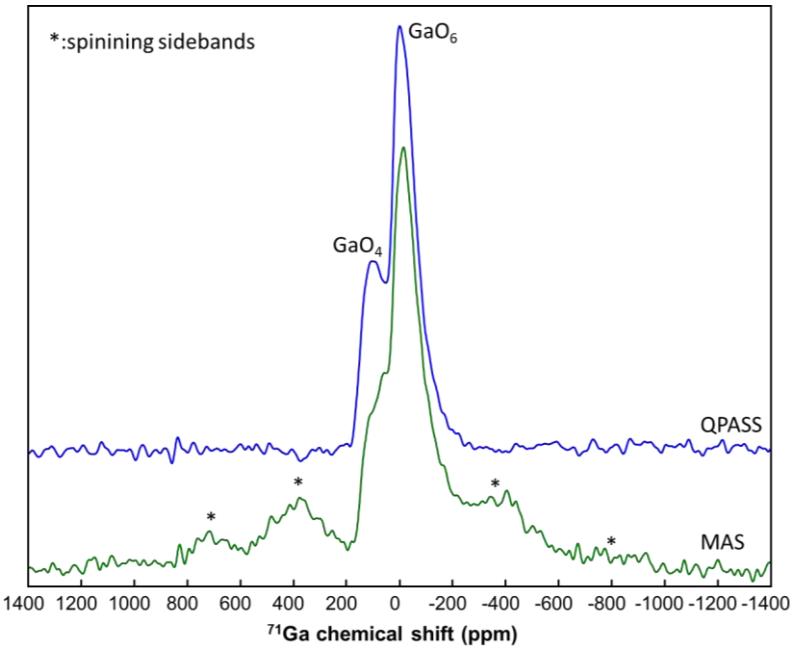

Figure III.14. *^{71}Ga NMR spectra acquired on a sample of composition $Ca_3Ga_2Ge_4O_{14}$ (x = 0) by a MAS spin-echo (green) and a QPASS (blue) experiments, showing the two coordination types of Ga in the sample.*

^{67}Zn ss-NMR remains a challenging task to accomplish due the nucleus low natural abundance (4.1%), weak gyromagnetic ratio (2.667 MHz/T) and potentially large quadrupolar effects (nuclear spin = 5/2). To elucidate the Zn^{2+} cations ordering type in the $Ca_3ZnGe_5O_{14}$ (x = 1) compound, ^{67}Zn ss-NMR spectrum was recorded at a high magnetic field of 17.6 T (^{67}Zn Larmor frequency of 46.9 MHz) using a 4 mm magic angle spinning (MAS) probehead. Moreover, a CPMG echo-train acquisition was used to improve the measurement sensitivity [38]–[42]. Furthermore, a radio frequency field of ~15 kHz, selective of the ^{67}Zn central transition, was adopted (corresponding 90° and 180° selective-pulse durations of 5.6 and 11.2 µs) and a spinning frequency st at 14 kHz. 128 rotor-synchronized echoes spaced by 1 ms (corresponding to 14 rotor periods) have been recorded and 25,600 transients were co-added with a recycle delay of 3 s, which led to 21 hours of total experiment time.

A ^{67}Zn spikelet spectrum was obtained by applying a direct Fourier transform to the whole acquired echo train, and is shown in Figure III.15a. This spectrum discretisation processing distributes the whole spectrum intensity in a limited number of narrow spikes that reproduce the spectral envelope, thus allowing the improvement of the signal to noise ratio [41], [42]. The signal obtained from ^{67}Zn central-transition shows to extends over a large chemical shift range (900 ppm), and exhibits a maximum intensity in the +50 to -50 ppm region. The signal shape suggests a partial overlapping of two resonance with asymmetric line shapes, characteristic of a distribution of the quadripolar interactions, indicative of local disorder between Zn^{2+} and Ge^{4+}

cations. Accordingly, attempt to reconstruct the ^{67}Zn spectrum with a single contribution affected by second-order quadripolar effects were unsuccessful. Moreover, two contributions with distribution of the quadrupolar coupling (Czjezk Gaussian Isotropic Model [43], [44]) were deployed at 60 ppm and 360 ppm isotropic chemical shifts and average quadripolar coupling constants of 7.3 MHz and 9.3 MHz (see Figure III.15b). From the ^{67}Zn NMR reported literature, these contributions placed at 60 ppm and 360 ppm can be assigned to 4- and 6-coordinated Zn atoms [45]–[47] in the $Ca_3ZnGe_5O_{14}$ (x = 1) compound. However, direct quantification of these two Zn coordination types could not be possible from this CPMG spectrum with low signal to noise ratio.

Despite the down sides of unquantified ^{71}Ga and ^{67}Zn spectrum, solid state NMR of these two nuclei informs us about the local disorder occurring among the B- C- and D-sites of this langasite structure, which are key information in building a starting Rietveld model for neutron data refinement presented in the next section.

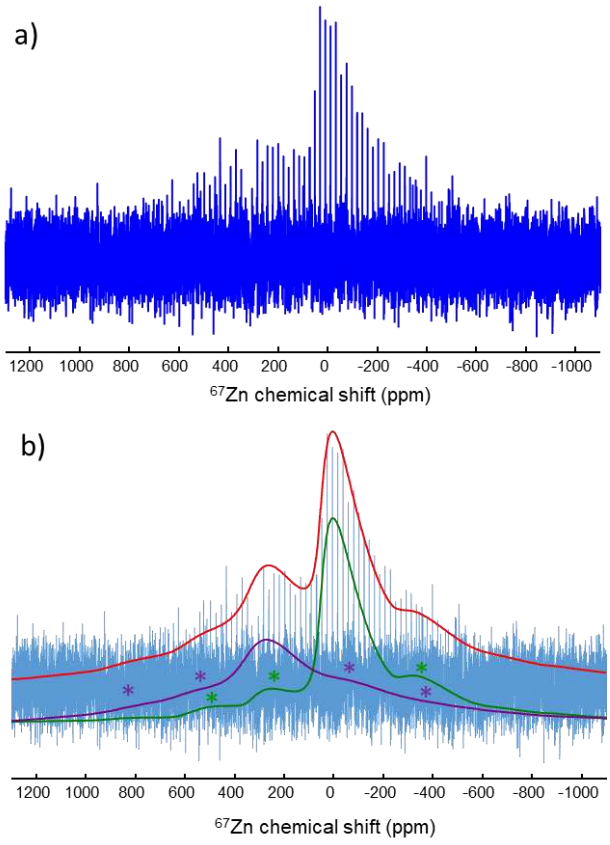

Figure III.15. *a) ^{67}Zn CPMG MAS spectrum recorded at 17.6 T with a spinning frequency of 14 kHz. b) Simulation of the experimental spectrum considering two ^{67}Zn resonance with distribution of the quadrupolar interactions (average coupling of 7.3 MHz and 9.3 MHz), with green purple and red signals corresponding to the 6-coordinated Zn, 4-coordianted Zn and the sum of both contributions. The noted signal with asterisks indicates the spinning sidebands of the central transition.*

III.4.2. $Ca_3Ga_2Ge_4O_{14}$ (x = 0) and $Ca_3ZnGe_5O_{14}$ (x = 1) NPD refinement.

Due to the close atomic number between Ga, Zn and Ge (same Z number), it is not possible to characterise the chemical disorder between these cations over the 1a, 3f, 2d sites using only PXRD. However, from ^{71}Ga and ^{67}Zn ss-NMR, these two elements were found to be present in both four and six coordination types offered by the cell. The end member compositions $Ca_3Ga_{2-2x}Zn_xGe_{4+x}O_{14}$ (x = 0, 1) host only two cation species on the framework (B, C, D) sites, with different neutron scattering lengths (8.185(20) fm, 7.288(2) fm and 5.680(5) fm for Ge, Ga and Zn respectively) [48], allowing the use of NPD to refine the Ga/Ge and Zn/Ge ratios directly. Large sample batches ~3.5 g of $Ca_3Ga_{2-2x}Zn_xGe_{4+x}O_{14}$ (x = 0, 0.5 and 1) compositions were prepared by combining multiple synthesised beads (~70 beads) of each composition. Each individual bead was ground into powder and measured by laboratory PXRD to check its purity. Phase pure samples of the mentioned compositions were then sent to the Nuclear Physics Institute (Czech Republic) for neutron measurements at the MEREDIT instrument. The measurements conditions are described in the appendices Chapter A.III section A.I.2.2.3. Rietveld refinements of the acquired NPD data of $Ca_3Ga_{2-2x}Zn_xGe_{4+x}O_{14}$ (x = 0 and 1) compounds were carried out using two major constraints: (i) keep each of the 1a, 3f and 2d sites to be fully occupied by cations (i.e. $OccGe_{1a}$*+ $OccGa_{1a}$+ $OccZn_{1a}$=1, $OccGe_{3f}$+ $OccGa_{3f}$+ $OccZn_{3f}$=1, $OccGe_{2d}$+ $OccGa_{2d}$+ $OccZn_{2d}$=1); and (ii) the overall refined composition to match the nominal one (i.e. for x = 0 composition: $OccGa_{1a}$+ 3×$OccGa_{3f}$+ 2×$OccGa_{2d}$=2, $OccGe_{1a}$+ 3$OccGe_{3f}$+ 2$OccGe_{2d}$=4, for x = 1 composition: $OccZn_{1a}$+ 3×$OccZn_{3f}$+ 2×$OccZn_{2d}$=1, $OccGe_{1a}$+ 3×$OccGe_{3f}$+ 2×$OccGe_{2d}$=5) "Z=1", see Figure III.16 for refined plots, Table III.3 and Table III.4 for refined parameters.

Table III.3. Refined structural parameters obtained from NPD data collected at room temperature on $Ca_3Ga_2Ge_4O_{14}$ (*P*321 space group, *a*= 8.0712(2) Å and *c*= 4.9680(2) Å).

Atom	Position	x	y	z	Occ	B_{iso}
Ca	3e	0.4183(7)	0	0	1	0.91(10)
Ga1/Ge1	1a	0	0	0	0.51(8)/0.49(8)	0.92(5)[a]
Ga2/Ge2	3f	0.7635(4)	0	1/2	0.50(3)/0.50(3)	0.92(5)[a]
Ge3	2d	1/3	2/3	0.5273(9)	1*	0.92(5)[a]
O1	2d	1/3	2/3	0.1843(11)	1	1.18(4)[b]
O2	6g	0.4616(5)	0.3144(4)	0.3113(6)	1	1.18(4)[b]
O3	6g	0.2174(4)	0.0793(4)	0.7667(6)	1	1.18(4)[b]

[a,b]: constrained to refine to the same B_{iso} values.
*: Fixed at 1 after its initial refined value converged to almost 1.

** Note that $OccX_n$ notation means the occupancy of the atom X in the site n*

Table III.4. Refined structural parameters obtained from NPD data collected at room temperature on $Ca_3ZnGe_5O_{14}$ (*P*321 space group, *a*= 8.0308(3) Å and *c*= 5.0164(4) Å).

Atom	Position	x	y	z	Occ	B_{iso}
Ca	3e	0.4198(8)	0	0	1	1.18(13)
Zn1/Ge1	1a	0	0	0	0.52(4)/0.48(4)	1.09(8)[a]
Zn2/Ge2	3f	0.7674(5)	0	1/2	0.16(1)/0.84(1)	1.09(8)[a]
Ge3	2d	1/3	2/3	0.5295(12)	1[*]	1.09(8)[a]
O1	2d	1/3	2/3	0.1854(17)	1	2.17(7)[b]
O2	6g	0.4617(7)	0.3173(5)	0.3139(10)	1	2.17(7)[b]
O3	6g	0.2227(6)	0.0785(6)	0.7585(10)	1	2.17(7)[b]

[a,b]: constrained to refine to the same B_{iso} values.
[*]: Fixed at 1 after its initial refined value converged to almost 1.

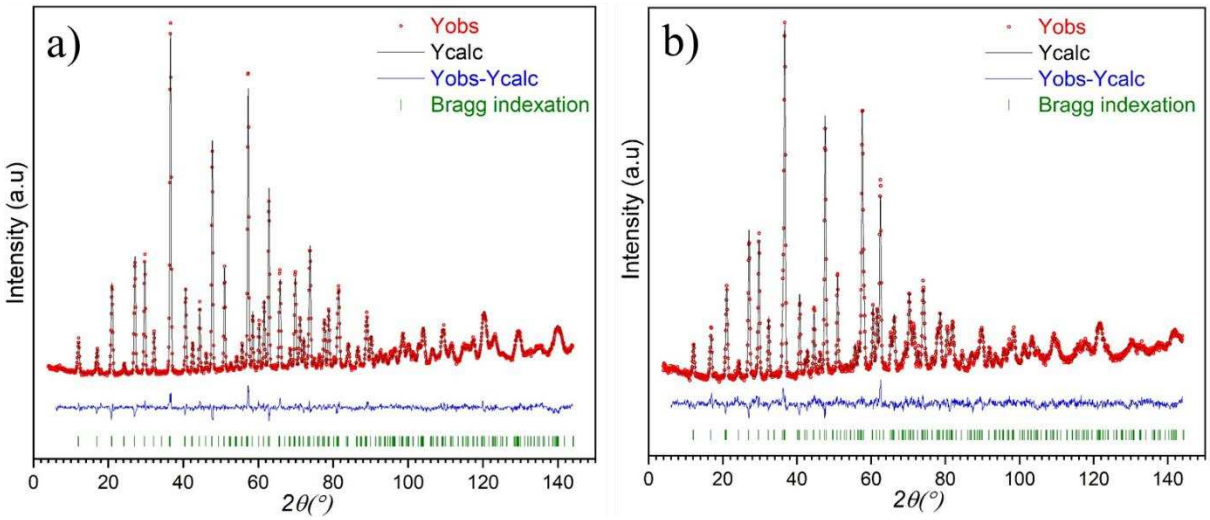

Figure III.16. *NPD Rietveld refinements plots of a) $Ca_3Ga_2Ge_4O_{14}$ (x = 0) R_p= 3.04% R_{wp}= 3.83%, b) $Ca_3ZnGe_5O_{14}$ (x = 1) R_p= 3.43% R_{wp}= 4.35%. Observed (red dot), calculated (black line), and difference (blue line) profiles are shown. The green tick marks correspond to allowed reflection positions.*

For both end member compositions (x = 0 and 1) the cationic distribution was shown to occur only among the 1a and 3f sites, while the 2d sites remains fully occupied by Ge atoms (as previously reported for $Ca_3Ga_2Ge_4O_{14}$ single crystals synthesised by the Czochralski method in [10], [11]). The refined occupancies for x = 0 composition led to a distribution of 0.51(8)Ga/0.49(8)Ge on the 1a site and 0.50(3)Ga/0.50(3)Ge on the 3f site, which displays a complete disorder over the two crystallographic sites, consistent with the ^{71}Ga MAS and QPASS NMR collected spectrum showing signal arising from the two coordination types of the structural gallium. Taking into account each site multiplicity only 25(4)% of the total Ga amount is held in the 6-coordinated B-sites(1a), whereas the remaining 75(4)% goes to the 4-coordinated C-sites(3f). However, in the latest structural study of the $Ca_3Ga_2Ge_4O_{14}$ compound reported by A. Dudka *et. al.* [12] our results are far different from theirs. In [12], the structural

disorder was characterised by anomalous scattering on single crystals grown by the Czochralski method [12], [13]. They showed that only 10% of the Ga^{3+} cations are held in the 1a sites with the remainder present in the 3f sites (see Table III.5). In both materials, our melt crystallised and the single crystals reported in [12], even though the cationic distribution is different between the 1a and the 3f sites, the tetrahedral 2d sites are exclusively occupied by Ge^{4+}. This suggests that the synthesis route can influence the extent of Ga^{3+}/Ge^{4+} ordering in these structures, with melt-crystallisation favouring a higher degree of disorder in this case, compared to the single crystals reported in [12].

Table III.5. Comparison between the refined occupancies of Ga and Ge in the 1a, 3f and 2d sites from this work and Dudka's work [12] on the $Ca_3Ga_2Ge_4O_{14}$ (x = 0) compound.

	This Work			Dudka *et. al.* [11]		
Site / Atom	1a	3f	2d	1a	3f	2d
Ga	0.51(8)	0.50(3)	0	0.2	0.6	0
Ge	0.49(8)	0.50(3)	1	0.8	0.4	1

The strontium and barium analogues ($Sr_3Ga_2Ge_4O_{14}$ and $Ba_3Ga_2Ge_4O_{14}$) were also reported [11], [14], [49] to crystallise isostructural to the parent $Ca_3Ga_2Ge_4O_{14}$ langasite, synthesised by Czochralski and flux-growth single crystal routes. In the Ba compound the Ga was assigned to only the tetrahedral sites, occupying ⅔ of the 3f site [14]. Moreover, in other studies, it was pointed out that Ga was only held in the 2d site [49] with a different synthesis approach as mentioned above. In both these studies, analyses were based on single crystal laboratory X-ray diffraction data, with cation-oxide distance analysis to quantify each site disorder. Which is another example of different synthesis routes leading to different cationic ordering.

On the other extreme of the solid solution $Ca_3ZnGe_5O_{14}$ (x = 1), Rietveld refined NPD data also confirmed that the cationic disorder occurs only between the 1a and 3f sites, with the 2d sites remaining fully occupied by Ge atoms. The refined occupancies over the mixed sites, 0.52(4)Zn/0.48(4)Ge on the 1a and 0.16(1)Zn/0.84(1)Ge on the 3f, show that the total amount of Zn is almost equally dispersed over the two coordination types, 52(4)% on the 1a 6-coordinated site and 48(1)% on the 3f 4-coordinated site. Moreover, the B- and C-site cation-oxide bonds show notable differences going from the $Ca_3Ga_2Ge_4O_{14}$ langasite to the full Ga substituted compound $Ca_3ZnGe_5O_{14}$ (Table III.6 and Table III.7), which also could be interpreted as a difference in the average site cation radii due to the different ordering type between the x = 0 and 1 compounds.

Table III.6. Cation oxide interatomic distances and bond valence sums calculated for all Ga and Ge sites of $Ca_3Ga_2Ge_4O_{14}$.

site	bond	length (Å)	site	bond	length (Å)	site	bond	length (Å)
B(1a)	Ga1/Ge1-O3 x6	1.926(3)	C(3f)	Ga2/Ge2-O3 x2	1.787(4)	D(2d)	Ge3-O1 x1	1.704(7)
				Ga2/Ge2-O2 x2	1.853(5)		Ge3-O2 x3	1.776(4)
	*BVS (Ga)	3.53(2)		*BVS (Ga)	3.37(2)		*BVS (Ga)	3.72(3)
	*BVS (Ge)	3.71(2)		*BVS (Ge)	3.49(2)		*BVS (Ge)	3.91(3)

*Calculated with a distance cut-off at 3Å

Table III.7. Cation oxide interatomic distances and bond valence sums calculated for all Zn and Ge sites of $Ca_3ZnGe_5O_{14}$.

site	bond	length (Å)	site	bond	length (Å)	site	bond	length (Å)
B(1a)	Zn1/Ge1-O3 x6	1.984(6)	C(3f)	Zn2/Ge2-O3 x2	1.767(6)	D(2d)	Ge3-O1 x1	1.73(1)
				Zn2/Ge2-O2 x2	1.862(6)		Ge3-O2 x3	1.770(6)
	*BVS (Zn)	2.74(2)		*BVS (Zn)	3.06(2)		*BVS (Zn)	3.29(3)
	*BVS (Ge)	3.17(2)		*BVS (Ge)	3.58(2)		*BVS (Ge)	3.89(4)

*Calculated with a distance cut-off at 3Å

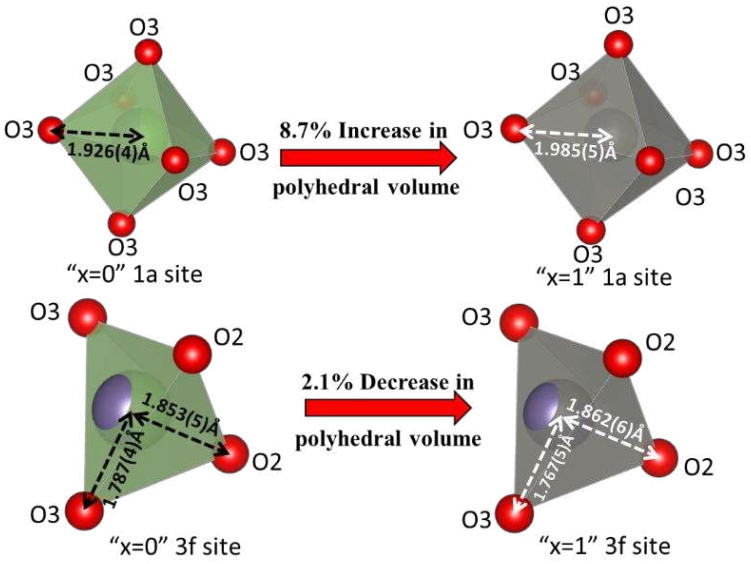

Figure III.17. *Cationic 1a and 3f site coordinations and their nearby interatomic distances for both x = 0 and x = 1 compounds from NPD refined structures.*

The B-O3 bond length increases from 1.926(3)Å (Ga1/Ge1-O3) to 1.984(6)Å (Zn1/Ge1-O3), which allows an 8.7% increase of the polyhedral volume (Figure III.17), whilst both C-site *M*-O3 and *M*-O2 bonds lengths decrease from 1.787(4)Å (Ga2/Ge2-O3) and 1.853(5)Å

(Ga2/Ge2-O2), to 1.767(6)Å (Zn2/Ge2-O3) and 1.862(6)Å (Zn2/Ge2-O2) respectively, leading to a volume decrease of the 3f site tetrahedron of 2.1% (Figure III.17). These results are consistent with the refined occupancies of each site for both end members, where Ga is fully exchanged by a larger Zn cation on the 1a site, and only ⅓ by the same larger cation on the 3f site, while the other ⅔ are substituted by a smaller Ge cation . The hypothesis of a fully ordered trigonal langasite structure for both end members was considered by Rietveld refinement with different fixed Ga/Ge and Zn/Ge occupancies on both 1a and 3f sites against NPD data, while always matching the nominal composition. On Figure III.18a and Figure III.18b, a clear χ^2 minima can be detected when Ga and Zn occupies 50% of the 1a sites for x = 0 and 1 compositions respectively. Moreover, subtle peak intensity misfits at low angle can be spotted when Ga or Zn scattering density is focused on one of the two cationic disordered sites, inducing over- or under-calculated peaks intensities (Figure III.18c and Figure III.18d). The intensity misfits are much more visible for the Zn compound, compared to the Ga parent one due to their close neutron scattering lengths [48]. Furthermore, bond valence sum (BVS) calculations (Table III.6 and Table III.7), indicate that only the 2d site is suitable for Ge^{4+}, BVS = 3.91(3) and 3.89(4) with a mean Ge3-O distance of 1.758(4)Å and 1.759(3)Å for both x = 0 and x = 1 compounds respectively. As for the 1a and 3f sites, refined occupancies indicated that full ordering is disfavoured, as both sites had mixed occupancies between Ga/Ge (x = 0) and Zn/Ge (x = 1). This is better seen in the calculated BVS values indicating that all three cations “Zn, Ge, Ga” are either under- or over-bonded in the two different coordination types (B- C- and D-sites).

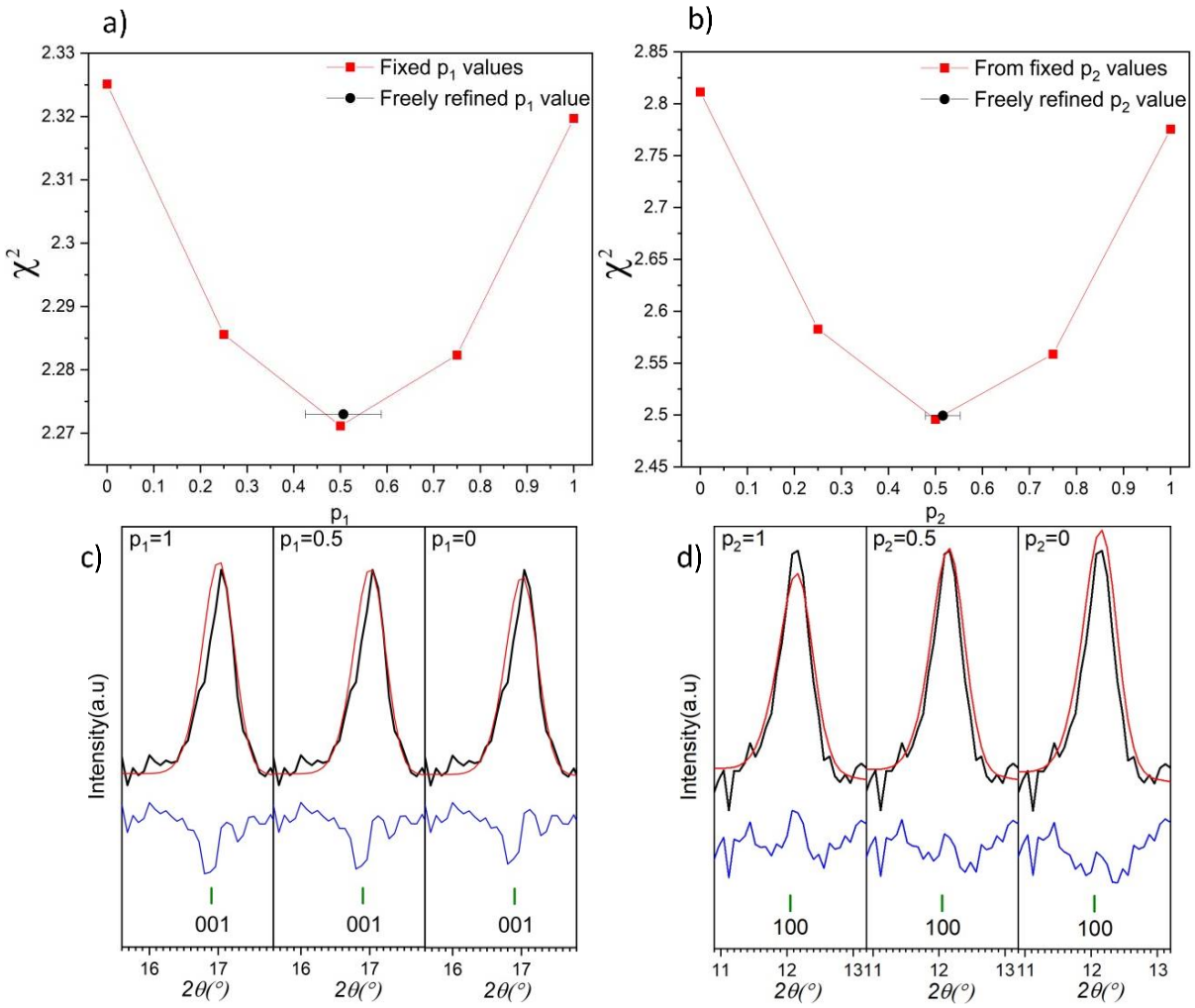

Figure III.18. *a), b) χ^2 evolution as a function of p_1 (Ga occupancy on the 1a site for x = 0 compound), p_2 (Zn occupancy on the 1a site for x = 1 compound). c), d) Rietveld fits (measured "black line", calculated "red line, difference "blue line" and indexation in green tick marks) zoomed view on the (001) and (100) for x = 0 and x = 1 compounds respectively for different fixed p_1 and p_2 values.*

The differences between the reported single-crystal $Ca_3ZnGe_5O_{14}$ monoclinic *C*2 [2] and the glass crystallised $Ca_3ZnGe_5O_{14}$ (x = 1) trigonal *P*321 structures was described in section III.3. In Table III.8 a comparaison between the octahedral (1a), tetrahedral (3f and 2d) *M*-O bond distances between the reported *C*2 against the NPD refined x = 1 *P*321 structures is illustated. For the 1a site (notted Zn1 octa site in Table III.8) a significant decrease representing 6.4% of the polyhedral volume can be spotted due to the shorter *M*-O bonds, consistent with a partial occupancy of the smaller Ge^{4+}. As for the 3f site (notted Ge1 and Ge3 tetra sites in Table III.8) a slight increase of the tetrahedral volume can be noticed, also coherent with the refined partial occupancy of the bigger cations Zn^{2+}. The 2d sites (notted Ge2 tetra site in Table III.8) on the other hand shows almost no polyhedral volume change, confirming their full occupancy by Ge^{4+} cations in both structures.

Table III.8. Comparison between the reported *C*2 [2] and NPD refined *P*321 M-O bond of the $Ca_3ZnGe_5O_{14}$ (x = 1) composition.

		Reported *C*2	Refined *P*321
Bond lengths (Å)	Zn1-O1* x2	2.10(1)	1.985(2)
	Zn1-O4* x2	2.008(9)	1.985(2)
	Zn1-O6* x2	1.992(8)	1.985(2)
V ($Å^3$)	Zn1* octa site	10.77(2)	10.08(2)
Bond lengths (Å)	Ge1-O6* x1	1.731(8)	1.740(1)
	Ge1-O2* x1	1.830(7)	1.862(6)
	Ge1-O1* x1	1.718(10)	1.740(1)
	Ge1-O7* x1	1.830(7)	1.862(6)
V ($Å^3$)	Ge1* tetra site	2.74(2)	2.86(2)
Bond lengths (Å)	Ge3-O4* x2	1.749(9)	1.862(6)
	Ge3-O3* x2	1.852(7)	1.767(6)
V ($Å^3$)	Ge3* tetra site	2.77(2)	2.86(2)
Bond lengths (Å)	Ge2-O7* x1	1.768(6)	1.770(7)
	Ge2-O5* x1	1.714(8)	1.727(11)
	Ge2-O3* x1	1.767(7)	1.770(7)
	Ge2-O2* x1	1.769(7)	1.770(7)
V ($Å^3$)	Ge2* tetra site	2.71(2)	2.74(2)

**M*-O atoms notation taken from *C*2 model, see Table III.9 for the *P*321 analogue atoms.

Table III.9. Atomic Wyckoff positions in the hexagonal *P*321 structure and their images in the monoclinic *C*2 cell.

Origin in *P*321		Analogue in *C*2	
Atom	Wyk. Pos.	Atom	Wyk. Pos.
Ca1	3f	Ca1	2a
		Ca2	4c
Ge1/Zn1	1a	Zn1	2a
Ge2/Zn2	3f	Ge1	4c
		Ge3	4c
Ge3	2d	Ge2	2b
O1	2d	O5	4c
O2	6g	O2	4c
		O3	4c
		O7	4c
O3	6g	O1	4c
		O4	4c
		O6	4c

III.5. Cationic disorder characterisation between Ga, Ge and Zn in the intermediate composition $Ca_3GaZn_{0.5}Ge_{4.5}O_{14}$ (x = 0.5).

Characterisation of the cationic distribution in compounds containing multiple elements with close atomic and neutron scattering factors is a problem that is usually addressed by coupling multiple techniques. In the $Zn_{1+x}Ga_{2-2x}Ge_xO_4$ ($0 \leq x \leq 0.5$) solid solution, the cationic disorder was characterised by coupling NPD and ^{71}Ga NMR [3]. In a different recent study of a more complex oxide system, the high entropy oxide "HEO" material of composition $(Cr_{0.2}Mn_{0.2}Fe_{0.2}Co_{0.2}Ni_{0.2})_3O_4$ crystallises in a spinel structure, and contains several successive first row transition metal cations. The cationic disorder characterisation between Cr, Mn, Fe, Co and Ni over the two possible crystallographic sites offered by the spinel structures, was achieved by coupling X-ray absorption near edge spectroscopy (XANES), soft X-ray magnetic circular dichroism (XMCD) and ^{57}Fe Mössbauer spectroscopy (both in presence and absence of an external magnetic field), complemented with SPD, NPD and TEM techniques [50].

For the $Ca_3GaZn_{0.5}Ge_{4.5}O_{14}$ (x = 0.5) intermediate composition, where Ga^{3+}, Ge^{4+} and Zn^{2+} cation compete for the langasite's layered framework sites (B- C- and D-sites with their 1a, 3f and 2d respective Wykoff positions), characterisation of this simultaneous disorder of three cations is an impossible task to resolve relying only on neutron diffraction. Hence, to construct a suitable Rietveld model for the $Ca_3GaZn_{0.5}Ge_{4.5}O_{14}$ (x = 0.5) sample NPD refinement, another characterisation technique is needed. From x = 0 and 1 samples we know that ^{71}Ga and ^{67}Zn ss-NMR is not an option due to the high disorder present in the material and how challenging it is to extract quantitative information in this solid solution study.

P. Lu *et al* [51], [52] has demonstrated the use of two-dimensionally fitted STEM-EDS maps to extract direct information from $SrTiO_3$ films, thus quantifying the chemical distribution of the different elements present in the measured sample. In this section, the possibility of quantifying the cationic disorder between three isoelectronic (Zn^{2+}, Ga^{3+}, Ge^{4+}) cations is investigated by a one-dimensional "1D" STEM-EDS profile elements refinement approach, and for the first time, a two-dimensional "2D" STEM-EDS maps fitting on powder measured samples.

III.5.1. $Ca_3GaZn_{0.5}Ge_{4.5}O_{14}$ (x = 0.5) STEM-HAADF and STEM-EDS maps analysis.

Transmission electron microscopy measurements were conducted on powder samples deposited on a TEM amorphous holey carbon-coated copper grid. The powder sample was first

finely ground and dispersed in ethanol, droplets from this mixture were then deposited on the grid mentioned above and let to dry. The sample's observation at the atomic scale in STEM-HAADF mode, each observed atom represents in reality a column of atoms (structure projection). To visualise the 2D projection of the $Ca_3GaZn_{0.5}Ge_{4.5}O_{14}$ (x = 0.5) crystal structure, the sample was oriented along the [001]* direction (see Figure III.19a). This particular direction was chosen because it represents the stacking direction of the structure, with each column being composed of the same crystallographic site (Figure III.19b and Figure III.19c). The measured sample thickness (60 nm, representing 120 superimposed cells) by Electron Energy Loss Spectroscopy (EELS), was estimated to be unchanged over the whole imaged area (≈ 5 nm × 5 nm). Knowing that the acquired intensity in STEM-HAADF mode is proportional to the sample's thickness (e), density (ρ) and the mean atomic number ($\bar{Z}$) of the observed crystallographic site "$I \propto e\rho Z^n$", the acquired intensity in STEM-HAADF, is essentially due to the column's mean atomic number ($\bar{Z}$). Hence, the darkest and brightest spots will represent the lightest "Ca" and heaviest "Ge, Ga, Zn" elements respectively.

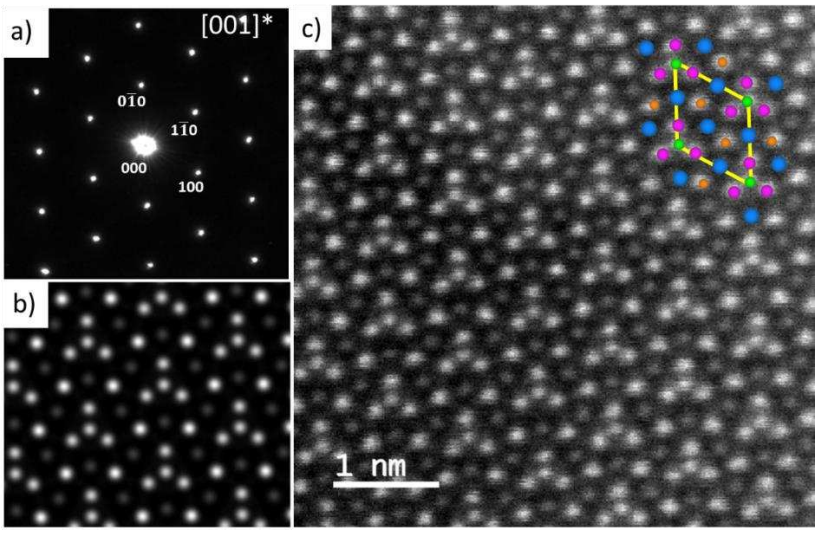

Figure III.19. *a) Selected area electron diffraction (SAED) pattern of the $Ca_3GaZn_{0.5}Ge_{4.5}O_{14}$ (x = 0.5) sample oriented along the [001]* direction, with b) and c) showing simulated (using JEMS software) [53] and measured STEM-HAADF images respectively. The corresponding crystal structure projection is overlaid on the top-right corner of the image, where blue, green, pink and orange points represent the 3e, 1a, 3f and 2d crystallographic sites respectively.*

Due to the isoelectronicity of the three (Zn^{2+}, Ga^{3+}, Ge^{4+}) cations, it is not possible to distinguish between them by their STEM-HAADF intensities. Consequently, EDS maps at the atomic scale of the three cations were cumulated over different regions of the same grain for a total time of 40 minutes of tracking, due to the sample's deterioration under the beam after a certain amount of time. In Figure III.20 showing the atomic scale resolution acquired STEM-EDS maps, Ca can clearly be seen occupying only the A-sites (3e). Ge on the other hand is the

only cation observed at all three sites (1a, 3f and 2d), consistent with structural distribution noticed in the x = 0 and x = 1 end member compounds from the $Ca_3Ga_{2-2x}Zn_xGe_{4+x}O_{14}$ solid solution. For Ga and Zn STEM-EDS maps, the data were noisier due to their relatively low abundance and concentration, so in order to highlight their atomic positions a Wiener filter [55], [56] was applied to enhance the signal to noise ratio. The Ga signal shows individual triangular forms, leading to think that it is present in both coordination types (6-coordinated 1a and 4-coordinated 3f). The Zn cations appear to be only present on the central 1a sites, however due to its very low concentration in the cell (2.22%), and its broad circularly shaped signal on the EDS map diffused over both neighbouring site types, it is hard to say if it is only held on the 1a site or on both 1a and 3f sites.

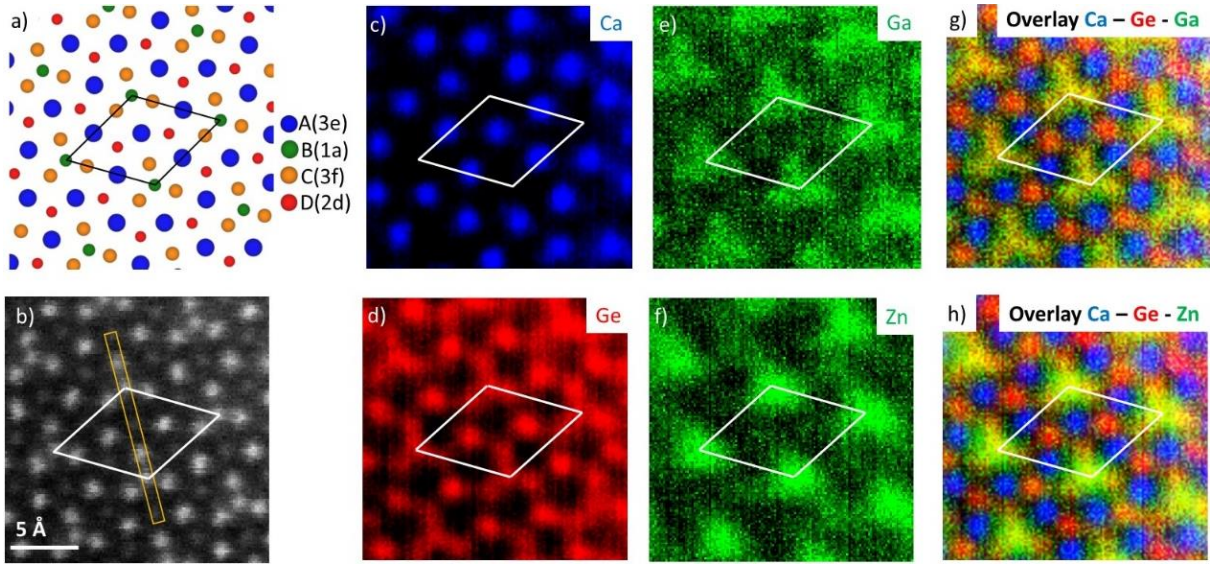

Figure III.20. *a) Scheme of the trigonal P*321 *structure projected along [001], b) its corresponding atomic resolution STEM-HAADF image for the $Ca_3GaZn_{0.5}Ge_{4.5}O_{14}$ (x = 0.5) composition. Atomic-scale STEM-EDS maps of the cations c) Ca in blue, d) Ge in red, e) Ga in green (Wiener filtered image) and f) Zn in green (Wiener strong filtered image). The overlaid EDS maps of "Ca, Ga, Ge" and "Ca, Zn, Ge" are shown in g) and h) respectively. The crystallographic unit cell is outlined in white in panels (b) – (h). The orange rectangle overlaid on (b) is the region used for 1D profile fitting presented in Figure III.21.*

III.5.1.1. One-dimensional fitting approach (1D).

From STEM-EDS maps we know that the A-sites (3e) are only occupied by Ca atoms, the D-sites(2d) sites also shows to be completely inhabited by Ge atoms. Therefore, the sites of interest here are the central B-site(1a) and the neighbouring C-sites(3f). In Figure III.20b, the marked area by a yellow rectangle was integrated to extract a 1D profile intensity "Wiener filtered EDS maps" (Figure III.21a). The width of the yellow rectangle was adjusted to maximise the signal, while taking care to minimise parasitic signals from the adjacent sites. A

one-dimensional refinement approach was then proceeded on the data, in order to extract quantifications of each cation partial occupancy in the different crystallographic sites. As shown in Figure III.21b, the germanium map shows the best signal to noise ratio, thanks to its high abundance. It was thus first refined using two Gaussian contributions. The refined Gaussian peak positions from the Ge profile were then fixed for the Ga and Zn profile fitting (see Figure III.21b). The Zn profile was initially fitted using one Gaussian at the 3f position (see Figure I22c), however a subtle asymmetric profile shape could still be noticed. Hence, a second Gaussian contribution was added at the 3f which improved the overall fit of the profile, indicating a small amount of Zn present also on that site. Assuming that the refined Gaussian area is proportional to the element content on the site, partial occupancies were calculated using the following two equations:

(i) $\frac{\mathrm{OccGe_{1a}}}{\mathrm{OccGe_{3f}}} = \frac{\text{Ge fitted area on the 1a}}{\text{Ge fitted area on the 3f}}$, same equation for Zn and Ge.

(ii) $\mathrm{OccGe_{1a}}+3*\mathrm{OccGe_{3f}}+2*\mathrm{OccGe_{2d}} = 4.5$, $\mathrm{OccGa_{1a}}+3*\mathrm{OccGa_{3f}} = 1$, $\mathrm{OccZn_{1a}}+3*\mathrm{OccZn_{3f}} = 0.5$.

Results from the 1D refinement were as follow: $\frac{\mathrm{OccGe_{1a}}}{\mathrm{OccGe_{3f}}} = 0.9$, $\frac{\mathrm{OccGa_{1a}}}{\mathrm{OccGa_{3f}}} = 1.17$ and $\frac{\mathrm{OccZn_{1a}}}{\mathrm{OccZn_{3f}}} = 2.6$, which leads to the following occupancies 0.23(10)Zn/0.57(5)Ge / 0.28(8)Ga and 0.09(4)Zn/0.64(2)Ge/0.24(3)Ga on the 1a and 3f respectively. Despite the possibility of quantifying the cationic disorder by one-dimensionally fitting the extracted intensity profile from the STEM-EDS maps. This method has certain limitations that can induce biases to the targeted information.

- The use of a Wiener filter affects not only the noise but the actual signal also.
- Parasitic signal coming from neighbouring sites when the interatomic distances are very small.
- Not taking advantage of the whole measured signal.

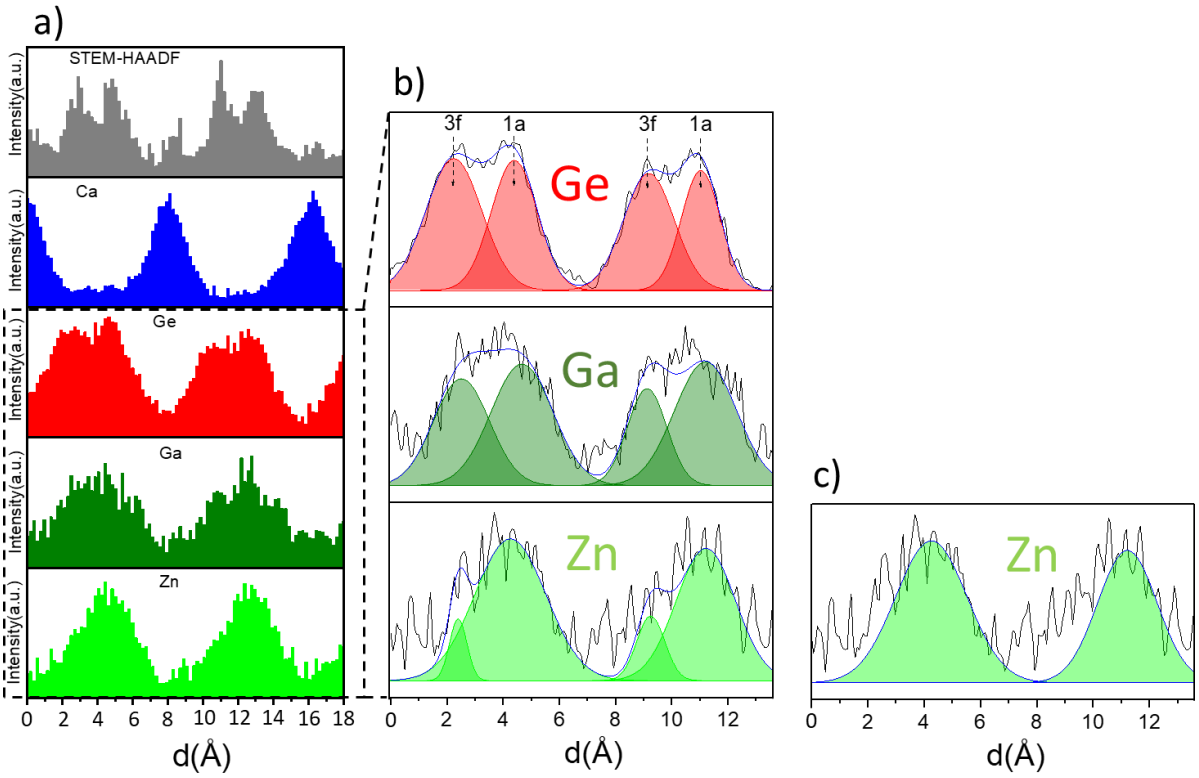

Figure III.21. *a) STEM-HAADF intensity profile in grey and EDS profiles of Ca, Ge, Ga and Zn (in blue, red, dark green and light green respectively). The signal was integrated from the drawn orange rectangle in Figure III.20b. b) In black, EDS profiles of Ge, Ga and Zn extracted from the STEM-EDS raw maps. The signals are integrated through the yellow strip on two neighbouring 1a and 3f sites (Figure III.20b). The calculated signals decomposed in Gaussian curves (blue), difference in orange and the integrated areas (red for Ge, dark and light green for Ga and Zn respectively) under the calculated curves have been overlaid.*

III.5.1.2. Two-dimensional fitting approach (2d).

As stated above in section III.5, P. Lu *et al* [51], [52] demonstrated the use of the two-dimensional aspect of the EDS maps to reduce the 1D refinement approach related issues. However, only nicely crystallised and well oriented thin specimens of $SrTiO_3$ were used in the previously reported studies [51], [52] as examples, and has never been done for powder samples, where recording STEM data is even harder due to the sample thickness inhomogeneities, size limitation of the grains and orientation problems. This approach has the advantage of considering the actual 2D nature of the signal, offering the possibility to reduce the associated errors of the: (i) 1D signal integration, (ii) side signal from the integrated area boundaries, especially when the sites of interest does not line on a straight column. Our approach here was to analyse two different zones from the central part of the 2D elemental images to minimize possible errors or deformation at the borders (see Figure III.22). These regions contain one central 1a site, three and six first neighbours 3f and 2d sites respectively.

The refinements were carried out using the simplest model possible, composed of: (i) background offset (ii) sum of two-dimensional Gaussian lines for each site, where each Gaussian is characterised by its x and y position components. The three 3f sites surrounding the 1a, were constrained to have the same peak width for each cation and each of the two zones independently. Germanium data (with the best signal to noise ratio due to its high concentration on the cell) were refined first to extract the 1a and 3f peaks positions, width and amplitudes. Ga and Zn data were then refined with fixed peak positions and widths from the Ge data fit, hence extracting only the amplitudes as a refined value. The fitted plots are shown in Figure III.23 Figure III.24.

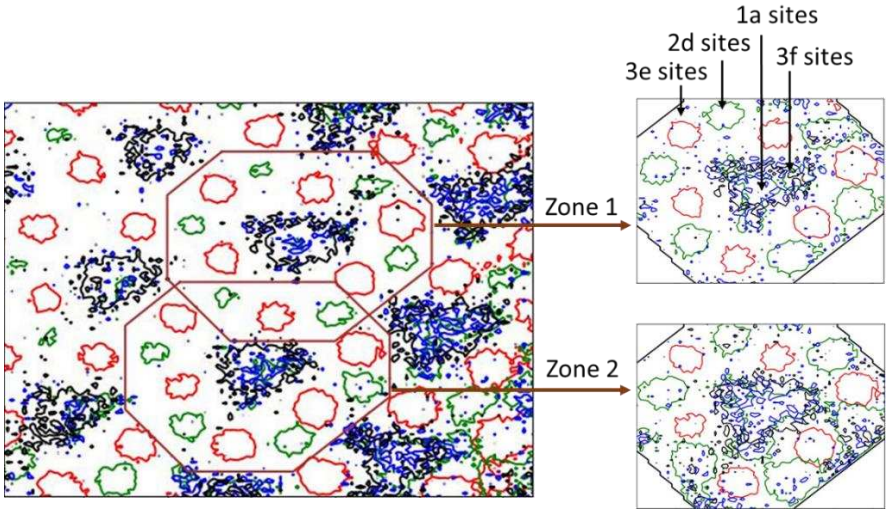

Figure III.22. *Overlay contour map of Ca (red), Ga (black), Ge (green) and Zn (blue) extracted from STEM-EDS raw data after the mask application.*

First, a mean value of the Gaussian areas under the three 3f sites was calculated (for each cation), then the same occupancy calculation logic employed in the 1D approach was used here for the 2D approach, with normalisation so that each site maximum content equals 1. Nevertheless, the obtained results were very close to the 1D fitting procedure (see Figure III.12). Here, the Zn signal is demonstrated to not only arise from the 1a sites but also from the neighbouring 3f, as the fit could not converge with the given constraints (fixed 1a position and peak width). The final refined occupancies from both zones are represented in Table III.10.

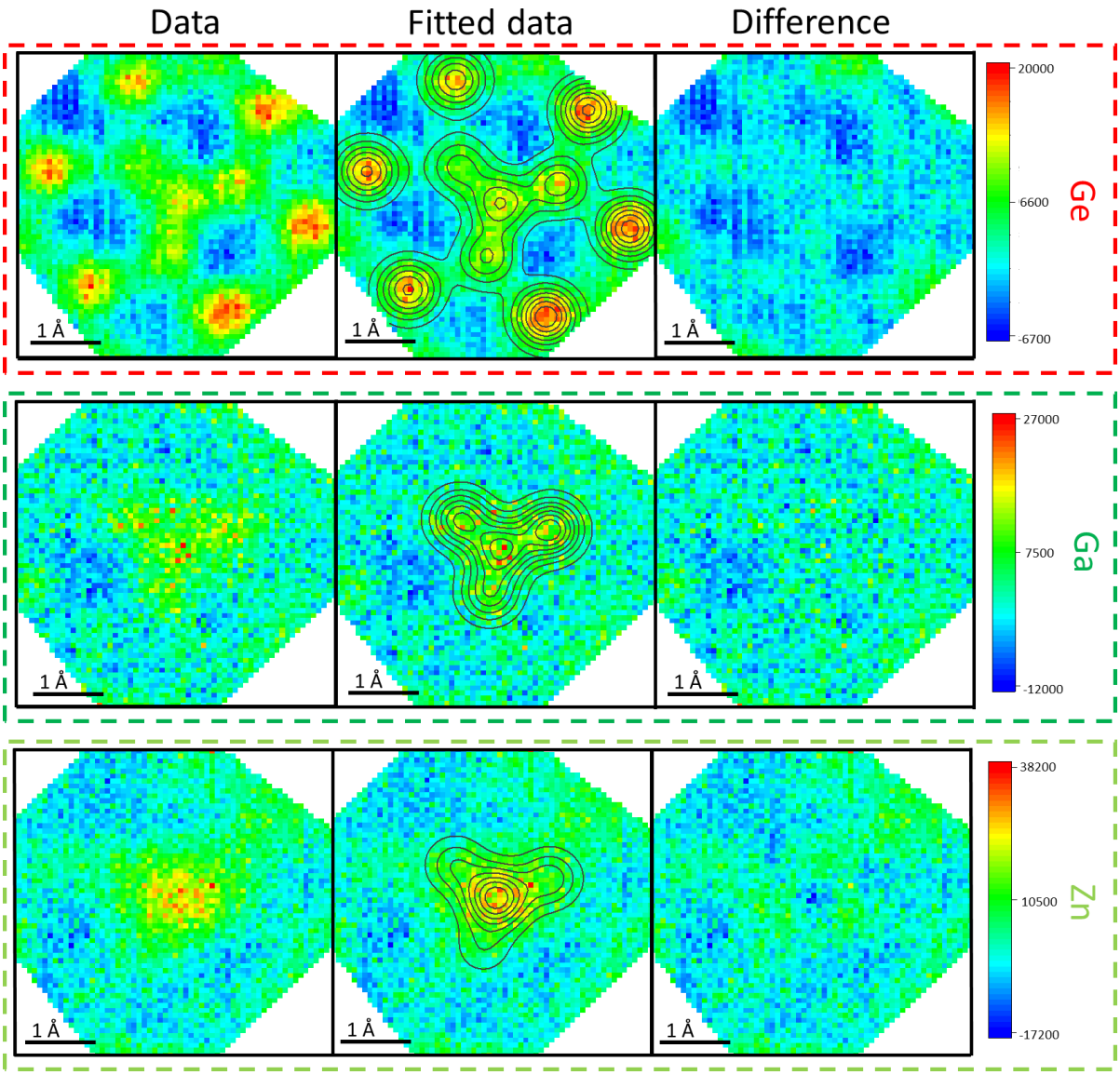

Figure III.23. *STEM-EDS 2D refinement plots of Ge, Ga and Zn from zone1, where the left column represents the data (after processing), middle column fitted data (fit in black contours) and the difference plots in the right column.*

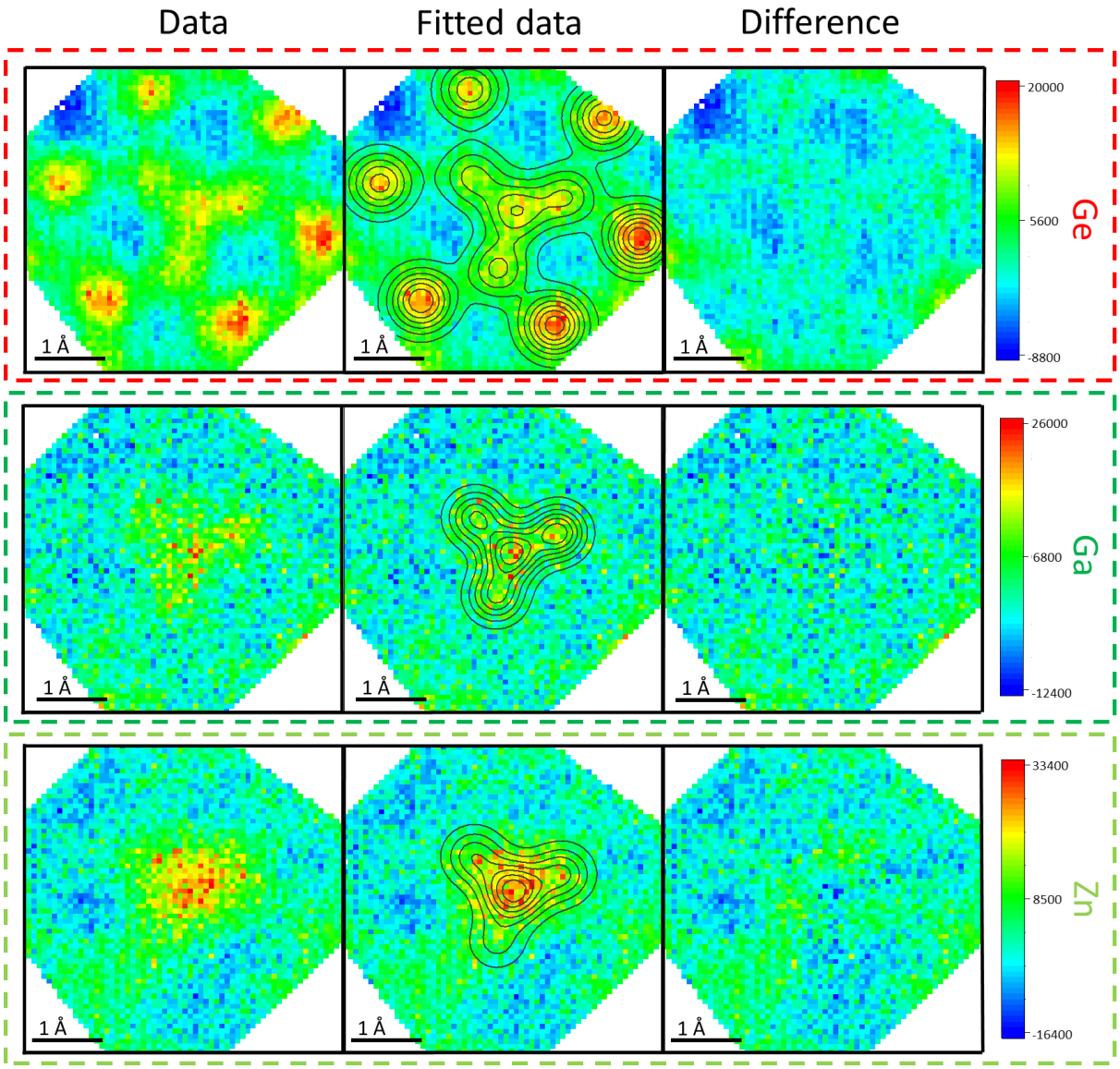

Figure III.24. *STEM-EDS 2D refinement plots of Ge, Ga and Zn from zone2, where the left column represents the data (after processing), middle column fitted data (fit in black contours) and the difference plots in the right column.*

Table III.10. Extracted (refined) occupancies from the 2D EDS maps refinements in both zone1 and zone2, for the $Ca_3GaZn_{0.5}Ge_{4.5}O_{14}$ (x = 0.5) composition.

	Site / Atom	1a	3f	2d
Zone1	Zn	0.19(6)	0.10(6)	0
	Ga	0.22(3)	0.26(3)	0
	Ge	0.59(3)	0.64(3)	1
Zone2	Zn	0.16(6)	0.11(6)[a]	0
	Ga	0.25(3)	0.25(3)	0
	Ge	0.59(3)	0.64(3)	1

III.5.2. $Ca_3GaZn_{0.5}Ge_{4.5}O_{14}$ (x = 0.5) NPD refinement.

Knowing from STEM-EDS quantitative analysis that the 2d sites remain occupied solely by Ge atoms, and that Ga and Zn are distributed in a similar way to their related parent compounds (Ga atoms almost dispersed in a 1:1 disposal between the 1a and 3f, and Zn in 1:3 disposal), the starting occupancies were fixed as follow:

- 1a site: 0.25Ga/0.25Zn/0.5Ge
- 3f site: 0.25Ga/0.083Zn/0.667Ge
- 2d site: 1Ge

Rietveld refinements were then carried out using the described starting model, with the constraints of keeping each site full, and an overall composition matching the nominal one. The gallium occupancies were also fixed for the first runs to maximise the neutron scattering difference between our cations. Hence, only the Ge occupancy on the 1a site was freely refined, while the Zn one was deduced by the deployed constraints. After convergence was reached, Ga were allowed to refine freely among Ge. See Figure III.25 and Table III.11 for the refined plot and structural parameters.

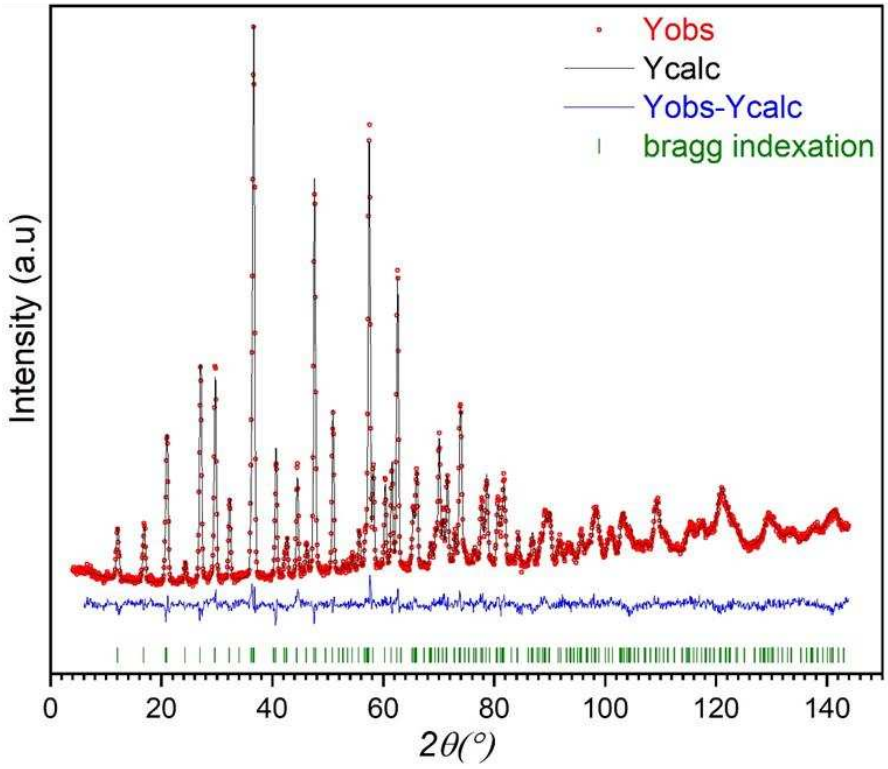

Figure III.25. *NPD Rietveld refinements plot of $Ca_3GaZn_{0.5}Ge_{4.5}O_{14}$ (x = 0.5) R_p= 2.97% R_{wp}= 3.80%. Observed (red dot), calculated (black line), and difference (blue line) profiles are shown. The green tick marks correspond to allowed reflection positions.*

Table III.11. Refined structural parameters obtained from NPD data collected at room temperature on $Ca_3GaZn_{0.5}Ge_{4.5}O_{14}$ (x = 0.5) (*P*321 space group, *a*= 8.0460(2) Å and *c*= 4.9994(2) Å) sample.

Atom	Position	x	y	z	Occ	Biso
Ca	3e	0.4198(7)	0	0	1	1.12(11)
Ga1/Ge1/Zn1	1a	0	0	0	0.25(2)/0.531(15)/0.22(3)	0.98(6)[a]
Ga2/Ge2/Zn2	3f	0.7648(4)	0	1/2	0.250(8)/0.656(5)/0.094(10)	0.98(6)[a]
Ge3	2d	1/3	2/3	0.5283(9)	1	0.98(6)[a]
O1	2d	1/3	2/3	0.1874(13)	1	1.66(5)[b]
O2	6g	0.4629(5)	0.3175(4)	0.3120(7)	1	1.66(5)[b]
O3	6g	0.2208(5)	0.0788(4)	0.7631(7)	1	1.66(5)[b]

[a,b]: Constrained to refine to the same Biso values.

Table III.12. Refined occupancies for Zn, Ga and Ge on the 1a, 3f and 2d sites, extracted from NPD data and STEM-EDS maps.

	Site / Atom	1a	3f	2d
NPD Refinement	Zn	0.22(3)	0.094(10)	0
	Ga	0.25(2)	0.250(8)	0
	Ge	0.531(15)	0.656(5)	1
1D Refinement	Zn	0.23(10)[a]	0.09(4)[a]	0
	Ga	0.28(8)[a]	0.24(3)[a]	0
	Ge	0.57(5)[a]	0.64(2)[a]	1
2D Refinement	Zn	0.18(6)[b]	0.11(6)[b]	0
	Ga	0.24(3)[b]	0.26(3)[b]	0
	Ge	0.59(3)[b]	0.64(3)[b]	1

[a] Errors were estimated by calculating standard deviation from the fitted areas of the 1D EDS profiles over the averaged 4 (1a, 3f sites) on the cell corners, shown in Figure III.20e, d and f.
[b] Mean values from zone 1 and zone 2 refinements. See Table III.10 for zone1 and zone2 individual refined occupancies.

As demonstrated in Table III.12, the Rietveld refined model (constructed from the 2D quantitative analysis of STEM-EDS maps) against NPD data shows little variation from the initial given occupancy values of the different cations and produces a good fit to the acquired data. This illustrates the complementary of the two techniques in this study. The characterised disorder in the $Ca_3GaZn_{0.5}Ge_{4.5}O_{14}$ (x = 0.5) compound follows the same trend found in the x = 0 and 1 end members, where gallium atoms do not show a preference between the two coordination types and the 1:1 ratio is respected in the x = 0.5 compound, as seen for x = 0. Zinc on the other hand appears to be out-competed by germanium for the tetrahedral sites, consistent with the x = 1 compound refined structure. Moreover, this behaviour is also observed

in the $Zn_{1+x}Ga_{2-2x}Ge_xO_4$ spinel solid-solutions, where Zn atoms are out-competed by Ga and Ge atoms in the 6-coordinated sites. The disorder trend of the $Ca_3Ga_{2-2x}Zn_xGe_{4+x}O_{14}$ solid-solution can also be noticed in the polyhedral volume change at the 1a and 3f sites. As illustrated in Figure III.26, the Rietveld refined *M*-O distances at the 1a (octahedral), 3f (tetrahedral) framework sites, as Zn^{2+} is substituted into the structure, illustrate a marked increase of the MO_6 octahedra volume, which goes against the overall decreasing trend observed in unit cell volume, indicating that the 1a site is becoming preferentially populated by larger cations. As the solid solution is traversed, the oxygens thermal parameters show a notable increase, going from B_{iso}= 1.18(4) $Å^2$ (x = 0), 1.66(5) $Å^2$ (x = 0.5) to 2.17(7) $Å^2$ (x = 1), consistent with the increase of the cationic size mismatch due to the Ga substitution by Zn and Ge inducing local static disorder of their coordinating oxides.

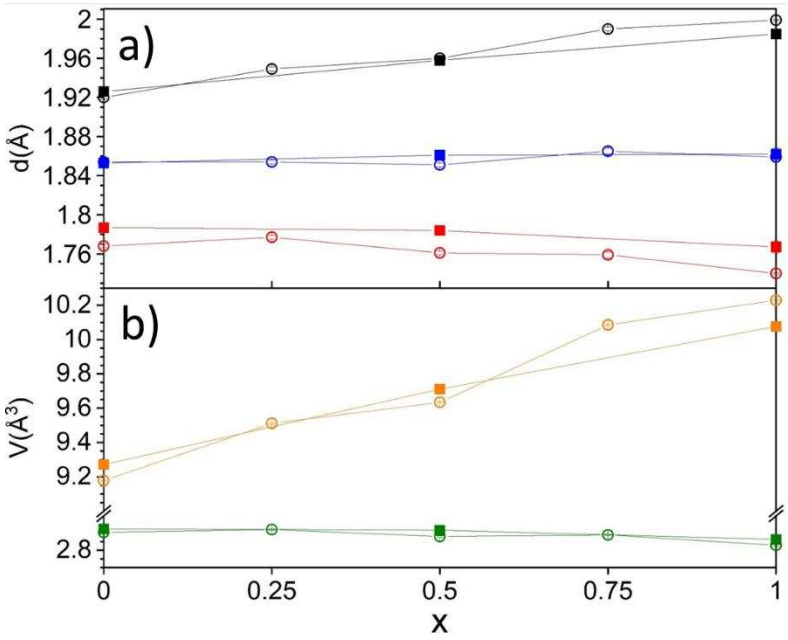

Figure III.26. *a), b) Comparison between SPD (hollow circle) and NPD (full box) refined bond distances "B-O3 in black, C-O2 in blue and C-O3 in red" and mixed sites volumes "B-site (1a) in orange, C-site (3f) in green" respectively for x = 0, 0.25, 0.5, 0.75, 1 compositions.*

III.6.Conclusion and perspectives.

In this chapter the synthesis of the new $Ca_3Ga_{2-2x}Zn_xGe_{4+x}O_{14}$ ($0 \leq x \leq 1$) solid solution was investigated for the first time by crystallisation from glass or under-cooled melt. The (x = 0) sample showed to reach higher crystallinity rates when crystallised directly from the melt, while the ($0.25 \leq x \leq 1$) compositions were achieved phase pure by congruent crystallisation from

glass. The related structures and cationic disorder were fully characterised by combining SPD, NPD and atomic-resolution STEM-EDS. Across the solid solution, all samples retained the same *P*321 trigonal structure; hence, the $Ca_3ZnGe_5O_{14}$ langasite is reported for the first time to crystallise in the trigonal *P*321 structure, in contrast to the previous report of a fully ordered monoclinic *C*2 structure. For compositions x = 0 and x = 1, the presence of only two cations allowed the use of neutron diffraction to quantify the cationic distribution over the layered framework (B, C and D) sites. As for the intermediate x = 0.5 composition, the presence of three cations with close atomic numbers and neutron scattering lengths, a 1D and 2D fitting approach of atomic scale STEM-EDS maps allowed to quantify its related cationic disorder and construct a chemically justified starting structural model for NPD data Rietveld refinement. Furthermore, the cationic disorder between Ge^{4+}/Ga^{3+} (x = 0) and Ge^{4+}/Zn^{2+} (x = 1) was found to occur only at the 1a and 3f sites (B- and C-sites respectively), while the 2d "D-sites" showed a full domination by germanium atoms. Consistent with previous studies of the $Ca_3Ga_2Ge_4O_{14}$ (x = 0) single crystals showing a different cationic distribution of Ga within the same 1a and 3f sites. On the other hand, our results for the $Ca_3ZnGe_5O_{14}$ (x = 1) showing a partial occupancy of Zn atoms in both coordination types, are far from the reported fully ordered $Ca_3ZnGe_5O_{14}$ where Zn is only held in the 1a 6-coordinated site. The difference in the ordering between Ge^{4+}, Ga^{3+} and Zn^{2+} compared to the literature could be assigned to the different synthesis routes employed here, favouring metastable structures. The study of the x = 0.5 composition for the first time, revealed the same ordering trend for Ga and Zn as the x = 0 and 1 compounds respectively, while Ge retained its full occupancy of the 2d sites. The approach to fully characterise this complex composition, was to first quantify the disorder using quantitative fits to 2D atomic-scale STEM-EDS maps to build a structural model for NPD refinements using chemically justified constraints. In principle, this 2D EDS maps refinements procedure can be applied for a wide range of materials, containing multiple elements with close atomic numbers (poor scattering contrast), distributed over different crystallographic sites.

The langasite structure's layered framework can be attractive for different types of studies. For example, its kagomé lattice formed by the B-sites, is usually linked with magnetic frustration and spin liquid focused properties. In this context iron-doped $Ca_3Ga_{2-x}Fe_xGe_4O_{14}$ compositions can be of much interest to investigate. The $A_3TeZn_2Ge_3O_{14}$ (*A* = Sr, Ba, and Pb) compositions adopting also the langasite structure [54], where only the C-sites are mixed between Zn and Ge, while the B- and D-sites are fully occupied by Te and Ge atoms respectively, showed a great SHG "second harmonic generation" response (13×KDP for

A = Pb). The mixed $(Zn,Ge)O_4$ and GeO_4 sites was related to make a considerable contribution to the SHG effect of these compounds. In contrast with the synthesised and described $Ca_3ZnGe_5O_{14}$ compound in this work, exhibiting Zn/Ge disorder over the B- and C-sites, it could be interesting to study the SHG response of this material with Ca^{2+} substitution for Pb^{2+} cations.

III.7.References.

[1] E.L. Belokoneva *et al.*, *Soviet Physics Doklady* 1980, **25**, 954.

[2] G.J. Redhammer, *Acta Crystallographica Section C Structural Chemistry*, 2015, **71**, 80.

[3] M. Allix *et al.*, *Chemistry of Materials*, 2013, **25**, 1600.

[4] S. Zhang *et al.*, *Journal of the American Ceramic Society*, 2011, **94**, 3153.

[5] D. Lu *et al.*, *Optics Express*, 2016, **24**, 17603.

[6] H. Lan *et al.*, *International Journal of Optics*, 2017, **2017**, 1.

[7] A. Zorko *et al.*, *Physical Review Letters*, 2008, **100**, 147201.

[8] K. Marty *et al.*, *Physical Review B*, 2010, **81**, 054416.

[9] M. Diaz-Lopez *et al.*, *Chemistry of Materials*, 2019, **31**, 5742.

[10] E.L. Belokoneva *et al.*, *Doklady Akademii Nauk*, Russian Academy of Sciences, 1981, **260**, 1363.

[11] B.V. Mill *et al.*, *Crystallography Reports*, 2007, **52**, 785.

[12] A.P. Dudka *et al.*, *Crystallography Reports*, 2013, **58**, 594.

[13] A. Dudka, *Journal of Applied Crystallography*, 2008, **41**, 83.

[14] B.V. Mill *et al.*, *INORGANIC MATERIALS*, 1983, **19**, 1516.

[15] T. Armbruster *et al.*, *American Mineralogist*, 1993, **78**, 1088.

[16] A. Pavlovska *et al.*, *Acta Crystallographica Section B Structural Science*, 2002, **58**, 939.

[17] B.V. Mill *et al.*, *Crystallography Reports*, 2004, **49**, 60.

[18] B.A. Maksimov *et al.*, *Crystallography Reports*, 2004, **49**, 585.

[19] H.J. Niu *et al.*, *Journal of the American Chemical Society*, 33.

[20] S. Roychowdhury *et al.*, *Science*, 2021, **371**, 722.

[21] D. Mohanty *et al.*, *Physical Chemistry Chemical Physics*, 2013, **15**, 19496.

[22] C.J. Benmore *et al.*, *Advances in Physics: X*, 2017, **2**, 717.

[23] D.A. Winborne *et al.*, *Metallurgical Transactions B*, 1976, **7**, 711.

[24] J.K.R. Weber, *International Journal of Applied Glass Science*, 2010, **1**, 248.

[25] R.D. Shannon, *Acta crystallographica section A: crystal physics, diffraction, theoretical and general crystallography*, 1976, **32**, 751.
[26] A.A. Coelho, *Journal of Applied Crystallography*, 2018, **51**, 210.
[27] P.W. Stephens, *Journal of Applied Crystallography*, 1999, **32**, 281.
[28] C.H. Drummond *et al.*, *NASA Technical Memorandum*, 1992, 44135.
[29] N.P. Bansal *et al.*, *Journal of the American Ceramic Society*, 1993, **76**, 1321.
[30] K. Al Saghir *et al.*, *Chemistry of Materials*, 2015, **27**, 508.
[31] K.A. Saghir, Céramiques Transparentes par Cristallisation Complète du Verre : Application Aux Aluminosilicates de Strontium, PhD thesis, Orleans, 2014.
[32] D. Massiot *et al.*, *Solid State Nuclear Magnetic Resonance* ,1999, **15**,11.
[33] J. Fan *et al.*, *Chemistry of Materials*, 2020, **32**, 9016.
[34] D. Massiot *et al.*, *Chemical Physics Letters*, 1997, **272**, 295.
[35] D. Massiot *et al.*, *Magnetic Resonance in Chemistry*, 2002, **40**, 70.
[36] J.T. Ash *et al.*, *Magnetic Resonance in Chemistry*, 2006, **44**, 823.
[37] H.Y. Playford *et al.*, *The Journal of Physical Chemistry C*, 2014, **118**, 16188.
[38] H.Y. Carr *et al.*, *Physical Review*, 1954, **94**, 630.
[39] S. Meiboom *et al.*, *Review of Scientific Instruments*, 1958, **29**, 688.
[40] J.S. Waugh, *Journal of Molecular Spectroscopy*, 1970, **35**, 298.
[41] F.H. Larsen *et al.*, *Journal of Magnetic Resonance*, 1998, **131**, 144.
[42] F.H. Larsen *et al.*, *Journal of the American Chemical Society*, 2000, **122**, 7080.
[43] G. Czjzek *et al.*, *Physical Review B*, 1981, **23**, 2513.
[44] G. Le Caër *et al.*, *Journal of Physics: Condensed Matter*, 2010, **22**, 065402.
[45] G. Wu, *Chemical Physics Letters*, 1998, **298**, 375.
[46] S. Sham *et al.*, *Canadian Journal of Chemistry*, 1999, **77**, 1782.
[47] Y. Zhang *et al.*, *Journal of the American Chemical Society*, 2005, **127**, 2370.
[48] V.F. Sears, *Neutron News*, 1992, **3**, 26.
[49] L.N. Bezmaternykh *et al.*, *Crystallography Reports*, 2004, **49**, 271.
[50] A. Sarkar *et al.*, *arXiv:2107.04274 [cond-mat]*, 2021.
[51] P. Lu *et al.*, *Microscopy and Microanalysis*, 2014, **20**, 1782.
[52] P. Lu *et al.*, *Scientific Reports*, 2014, **4**, 3945.
[53] P. Stadelmann, https://www.jems-swiss.ch/ (checked the 03/01/2022).
[54] K. Chen *et al.*, *Chemistry of Materials*, 2021, **33**, 6012.
[55] D.R.G. Mitchell, www.dmscripting.com, v4.0, 2019.
[56] R. Kilaas, Journal of Microscopy, 1998, 190, 45.

Chapter IV: New Oxide ion Conductors by Extending the Doping Range in $La_{1+x}Ba_{1-x}Ga_3O_{7+x/2}$ ($0.3 \leq x \leq 0.9$) Melilites

IV.1. Introduction.

Development of new ceramics exhibiting high oxide ion conductivities at moderate temperatures is of interest for solid oxide fuel cells, electrocatalysers, and sensors [1]. In this context, as mentioned in Chapter I the La*AE*Ga_3O_7 melilites (*AE** = Ca, Sr, Ba) are a well-known structural family that exhibits excellent oxide ion conduction properties in the 500 – 900°C temperature range [2]–[6]. As previously described in Chapter II, these melilites crystallise under the $P\bar{4}2_1m$ space group (n°113) with a layered framework formed by edge sharing five-membered GaO_4 tetrahedra pentagons, stacked along the *c*-axis. The A-site cations are positioned in the $[GaO_4]_5$ pentagons centre sandwiched between the framework layers. Conductivity properties of these melilite materials are mainly due to the ability of the host network to accommodate interstitial oxides by local expansion of the Ga coordination environment to GaO_5 [4]. Usually this is achieved by substitution of the alkali earth metal by an aliovalent cation, i.e lanthanum in the $La_{1+x}AE_{1-x}Ga_3O_{7+x/2}$ solid solution. Charge transport then occurs by a cooperative two-dimensional [7] local migration involving rapid exchange of the interstitial oxide with those of the host framework [8], [9] by a knock-on mechanism. The maximum conductivity values depend strongly on two factors: (i) the material composition, increasing progressively with interstitial oxide (O_{int}) concentration (Figure IV.1a), (ii) the crystal structure of the host framework, as at high O_{int} concentrations a phase transition from the parent tetragonal melilite to an orthorhombic or pseudo-orthorhombic (triclinic) phases with partially-ordered interstitial oxides occurs. This has a limiting effect on ionic conductivity due to the increase of the energy barrier for oxide migration within certain directions. Further increases in O_{int} concentration lead to a decomposition of the phase, as shown in both $La_{1+x}Ca_{1-x}Ga_3O_{7+x/2}$ and $La_{1+y}Sr_{1-y}Ga_3O_{7+y/2}$: in both cases, the maximum conductivities were found for x = 0.64 and y= 0.54 compositions respectively, reaching 10^{-1} S.cm^{-1} at 800°C. Interestingly, the Ca and Sr analogues adopts a pseudo-orthorhombic *P*1 cell at room temperature for doping amounts exceeding x = 0.54 and 0.6 respectively (Figure IV.1b). The high conductivity values reached by the Ca and Sr melilites at 800°C were found to be attainable under the tetragonal $P\bar{4}2_1m$ melilite polymorph [5], [10], as the disordered small tetragonal melilite cell is stabilised at the expense of the *P*1 polymorph for the Ca compound (this is also true for Sr melilite compositions stable under the orthorhombic polymorph at room temperature). In the Ba analogue $La_{1+x}Ba_{1-x}Ga_3O_{7+x/2}$, the melilite stability range was found to be much lower, as the maximum substitution amount was reported at x = 0.35 attainable by conventional solid-state reaction. Across this solid solution all compounds retained the small

cell $P\bar{4}2_1m$ tetragonal melilite structure, and had comparable conductivity values as the Ca and Sr analogues at the same O_{int} concentration (x = 0.35) (see Figure IV.1b).

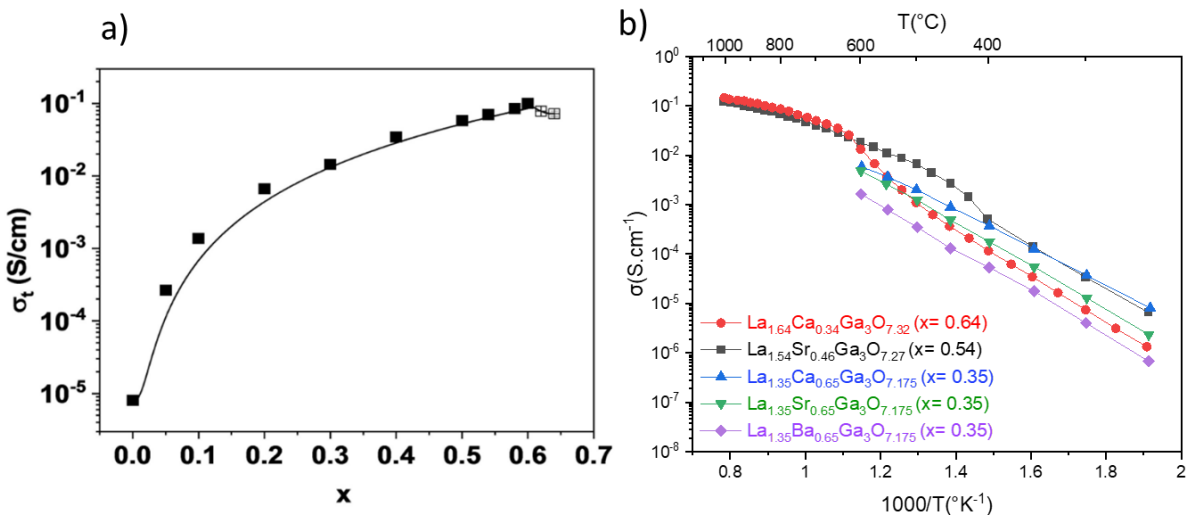

Figure IV.1. *a) Conductivity at 800°C of the $La_{1+x}Sr_{1-x}Ga_3O_{7+x/2}$ solid-solution as a function of x, where the filled and hollow symbols represent the tetragonal and orthorhombic starting room temperature polymorphs. b) Arrhenius plots of the $La_{1+x}AE_{1-x}Ga_3O_{7+x/2}$ melilites bulk conductivities at different x values with AE= Ca, Sr and Ba. (a) panel was adapted from [10], (b) panel was adapted from [3], [5], [6].*

In the CEMHTI laboratory, an alkali earth free melilite (i.e. $La_2Ga_3O_{7.5}$ x = 1) with the maximum interstitial oxide (O_{int}) concentration possible in this solid solution was synthesised by direct crystallisation of the melt at high temperature [11]. $La_2Ga_3O_{7.5}$ crystallises in the *Ima*2 symmetry and adopts an orthorhombic melilite structure with three distinct A-sites: La1, La2 and La3, arranged in the same way as the tetragonal polymorph (Figure IV.2a). Moreover, it is worth noting that the A-site channels can be divided into two types: La1 and La2/La3 hosting channels (Figure IV.2a and Figure IV.2b). The interstitial oxides (O_{int}) network of the $La_2Ga_3O_{7.5}$ melilite is fully ordered into chains within the *a* direction over corner sharing $[GaO_4]_5$ pentagons (see Figure IV.2c). This means that its oxide ion conductivity also has 1D character, as indicated by molecular dynamic calculations in [12], and is ~10x lower at 800°C than that of near-optimal compositions such as $La_{1.54}Sr_{0.46}Ga_3O_{7.27}$ and $La_{1.64}Ca_{0.36}Ga_3O_{7.32}$, but still ~ 10^3× greater than its opposing (x = 0) end member $LaAEGa_3O_7$ *AE*= Ca, Sr [2]. The retention of the melilite structure by $La_2Ga_3O_{7.5}$ implies the existence of a new range of $La_{1+x}AE_{1-x}Ga_3O_{7+x/2}$ compositions between the previously defined limits (x = 0.64, 0.54 and 0.35 for *AE*= Ca, Sr and Ba respectively), which have not yet been explored.

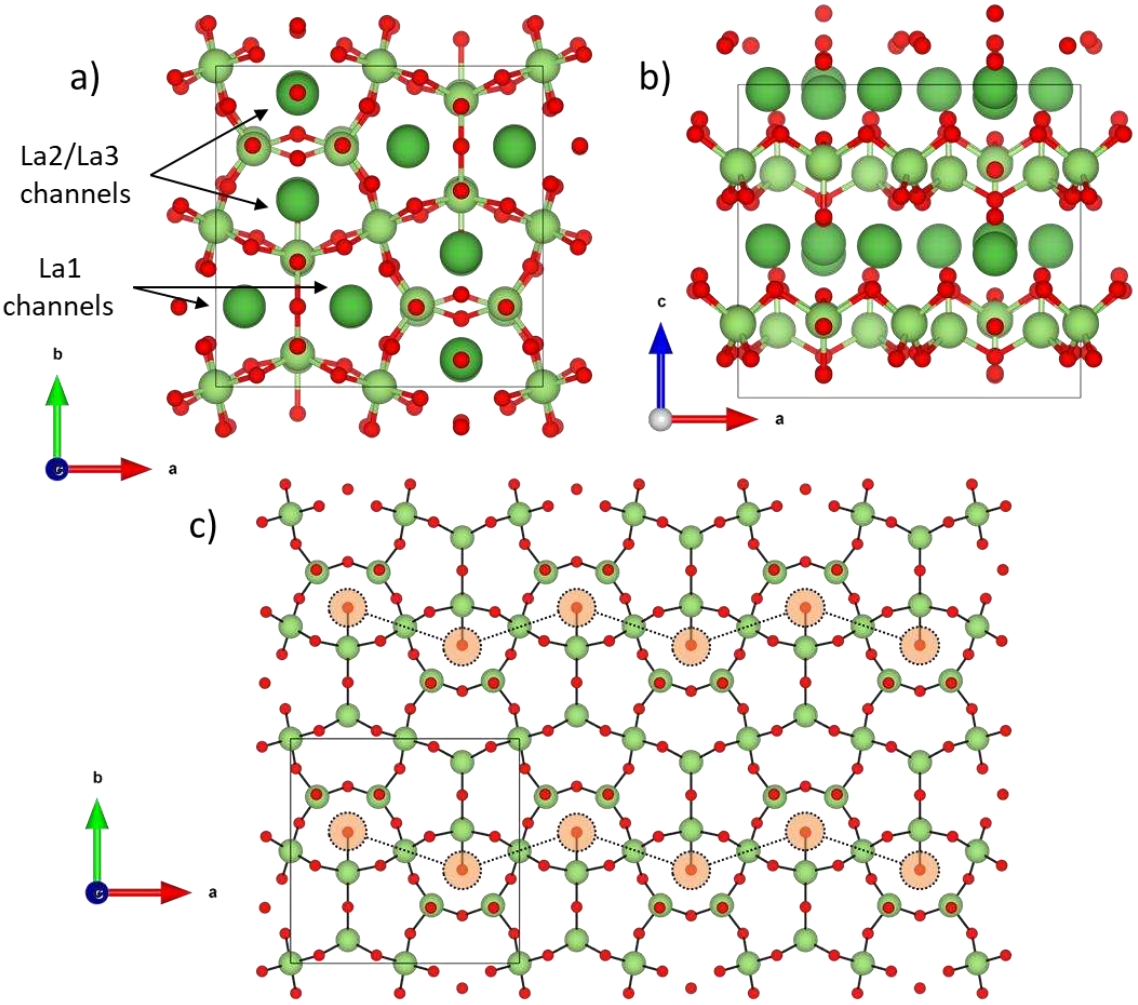

Figure IV.2. *$La_2Ga_3O_{7.5}$ crystal structure projection along (a) the c-axis, (b) the b-axis. Panel (c) shows a single $[GaO_4]_n$ sheet projected along the c-axis evidencing the 1D chain-like ordered O_{int} network. With dark green, light green and red spheres corresponding to La, Ga and oxygen atoms.*

In this chapter, the melilite Ba-containing series $La_{1+x}Ba_{1-x}Ga_3O_{7+x/2}$ solid solution synthesis is investigated by direct crystallisation of the under-cooled melt, as it has the broadest range of unknown super-excess compositions, and an unknown structural transition point. A structural study is also conducted, characterising the tetragonal melilite stability and its transition to the O_{int} ordered orthorhombic melilite as a function of the Ba substituted amount. The related cationic and anionic disorder is also mapped by combining SPD and NPD measurements. Finally, the ionic conductivity of these solid solution samples is determined by AC impedance spectroscopy. The main interest here is to look for the highest O_{int} concentration containing $La_{1+x}Ba_{1-x}Ga_3O_{7+x/2}$ tetragonal melilite compound, and compare its conductivity to the Ca and Sr analogues.

IV.2. Synthesis by direct crystallisation from the melt.

To extend the dopant limits and increase the O_{int} concentration in the $La_{1+x}Ba_{1-x}Ga_3O_{7+x/2}$ solid solution, direct crystallisation from the melt was performed using the ADL apparatus using a similar protocol to that reported for $La_2Ga_3O_{7.5}$ [11]. Regardless of the barium amount all compositions were prepared following the same protocol. First, stoichiometric amounts of $BaCO_3$ (STREM chemicals, 99.999% purity), La_2O_3 (STREM chemicals, 99.9% purity) and Ga_2O_3 (STREM chemicals, 99.998% purity) were weighed and ground together in an agate mortar, with ethanol to improve the homogenisation of the mixture. The resulting powder was dried at 100°C in a conventional laboratory oven for 10 min. The obtained dry sample was pressed into pellets of 13 mm each and broken into small fragments of ~50 mg each. Pellet chunks were levitated and melted using the ADL apparatus (described in the appendices Chapter A.I section A.I.1.1.2). The beads melted between 1800°C and 1850°C and were further heated to 1950°C for few seconds, then subsequently quenched by turning the lasers off. This procedure resulted in a direct crystallisation from the melt of the beads as indicated by a flash occurring on the cooling. The samples were obtained in the form of small beads (diameter of ~3mm) that appeared to be highly transparent, as reported for the $La_2Ga_3O_{7.5}$ superstructured melilite bead samples [11].

The synthesised $La_{1+x}Ba_{1-x}Ga_3O_{7+x/2}$ ($0.3 \leq x \leq 0.9$) beads were first checked by laboratory PXRD, to detect the dopant limit for which the tetragonal $P\bar{4}2_1m$ melilite is no longer stable. To do so, a bead of each composition was crushed and ground in an agate mortar into fine powder and measured using a Bruker D8 advance in a (θ-θ) Bragg Brentano geometry, equipped with a Cu anode (λ= 1.5459 Å) and LynxEye XE detector. On the stacked diffraction patterns shown in Figure IV.3, all $x < 0.8$ compositions were indexed with the tetragonal $P\bar{4}2_1m$ cell. Moreover, for $La_{1+x}Ba_{1-x}Ga_3O_{7+x/2}$ ($x \geq 0.8$) compositions, their related diffraction pattern was observed with a splitting of the $P\bar{4}2_1m$ *hkl*s Bragg peaks. These diffraction patterns could be indexed with both (i) the $La_2Ga_3O_{7.5}$ (x = 1) *Ima*2 melilite, and (ii) the $La_{1.64}Ca_{0.36}Ga_3O_{7.32}$ (x = 0.64) melilite, which crystallise in a pseudo-orthorhombic *P*1 cell, also induced by the ordering of interstitial oxides. Furthermore, the best match was obtained with the $La_2Ga_3O_{7.5}$ (x = 1) *Ima*2 melilite.

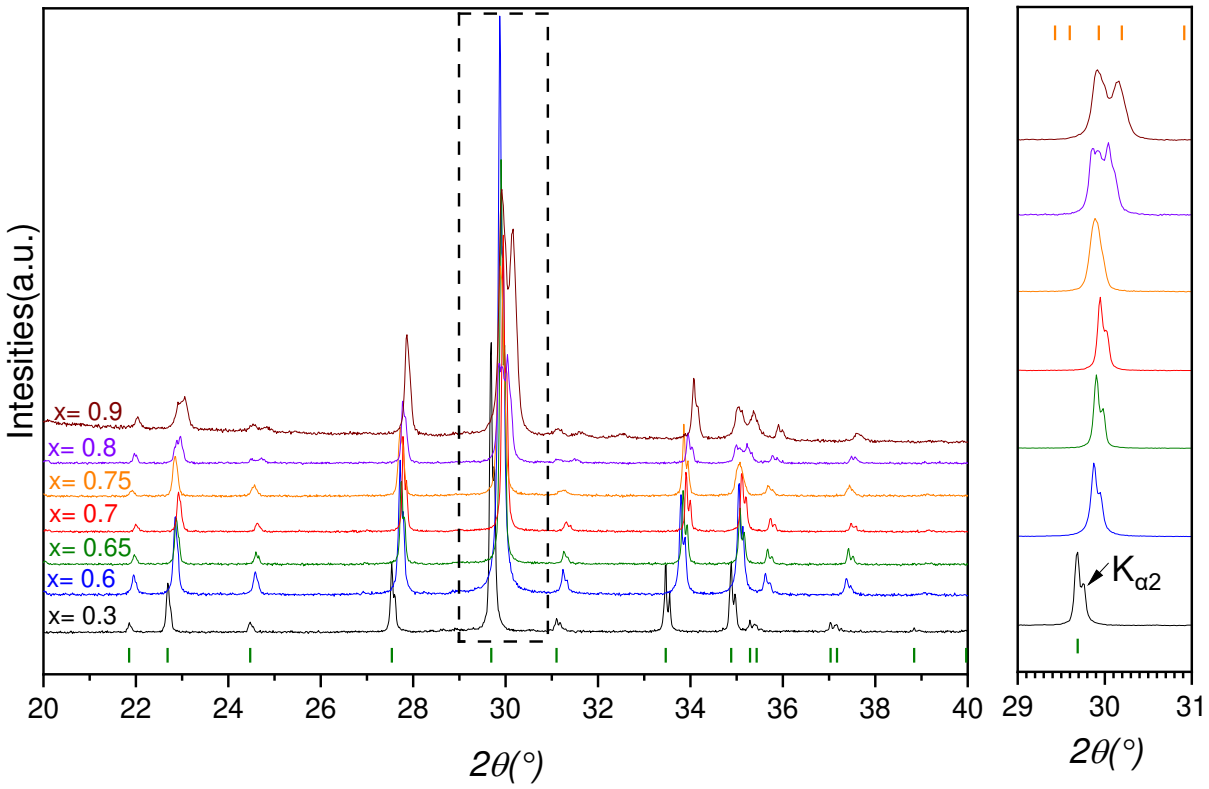

Figure IV.3. *Stacked measured diffraction patterns by laboratory PXRD of the $La_{1+x}Ba_{1-x}Ga_3O_{7+x/2}$ compositions, with the insert showing a zoom of the main peak positioned in the 29-31 (2θ°) range. The green and orange tick marks corresonds to the $P\bar{4}2_1m$ tetragonal and Ima2 orthorhombic melilites indexations.*

IV.3. Structural analysis against SPD and NPD (at RT and HT) data.

IV.3.1. SPD Rietveld refinements and analysis of $La_{1+x}Ba_{1-x}Ga_3O_{7+x/2}$ $0.3 \leq x \leq 0.9$ compositions.

For a better precision of the overall structural trend characterisation over the synthesised compositions of the $La_{1+x}Ba_{1-x}Ga_3O_{7+x/2}$ solid solution, and precise identification at which x value the phase transition from $P\bar{4}2_1m$ to *Ima*2 occurs, high resolution synchrotron X-ray powder diffraction (SPD) measurements were conducted in the 11BM beamline at the APS Argonne laboratory in the United States. To proceed these measurements a bead of each composition was crushed into fine powder and loaded into Kapton capillaries of 0.8 mm in diameter. Due to the absence of X-ray scattering contrast between La and Ba atoms (i.e. similar Z number), it is not possible to characterise the cationic disorder of these two elements over the A-sites. Moreover, due to the light oxygen electron number compared to La and Ba, it was also not possible to investigate the ionic disorder of the interstitial oxides (O_{int}) among the $[GaO_4]_5$ free channels, hence O_{int} occupations were fixed to the nominal composition on their reported positions.

For the x = 0.3, 0.675, 0.8 and 0.9 compositions SPD measured diffraction patterns, few extra peaks were noticed, which were indexed with different impurities: $LaBa_2Ga_{11}O_{20}$ (S.G. *I*2/*m*) (0.472(6)%wt) + $LaGaO_3$ (S.G. *Pbnm*) (0.069(2)%wt) for x = 0.3. $La_{1.3}Ba_{0.7}Ga_3O_{7.15}$ for x = 0.675 (0.162(2)%wt) and 0.8 (0.088(3)%wt). $LaGaO_3$ (S.G. *Pbnm*) (0.082(2)%wt) for x = 0.9.

In Figure IV.4 showing stacked SPD data of the measured compositions, Pawley refinements of these data revealed that the tetragonal melilite is retained for $0.3 \leq x < 0.75$ compositions while the x = 0.9 sample is fully orthorhombic. Moreover, the compositions between x = 0.75 and 0.85 exhibit a peak broadening, which was better modelled in Pawley fits by using both tetragonal and orthorhombic melilite structures. This suggests a stability limit of the $P\bar{4}2_1m$ melilite and the beginning of its phase transition to the *Ima*2 superstructure starting at x = 0.75.

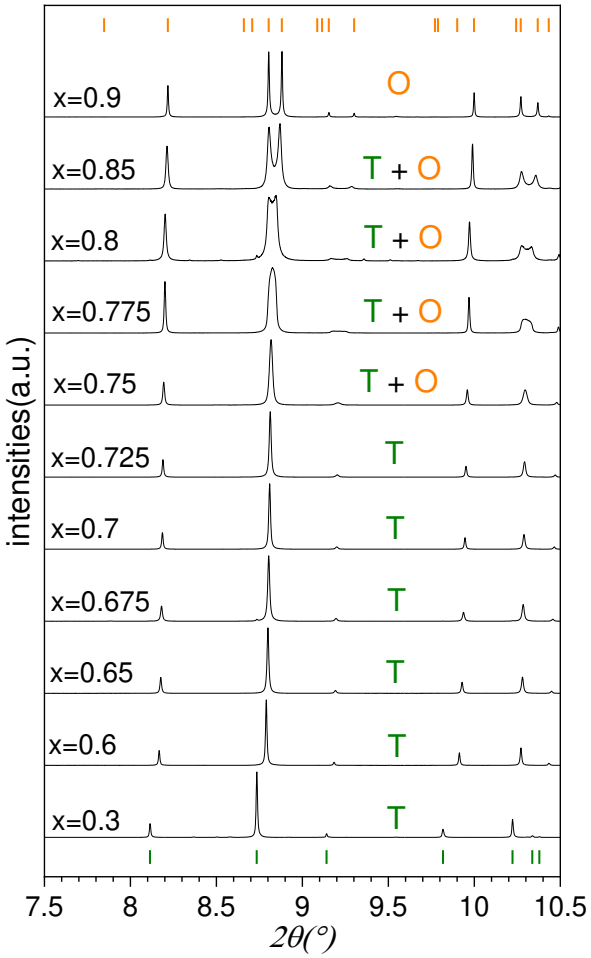

Figure IV.4. *Zoomed stacked diffraction patterns of the SPD measured $La_{1+x}Ba_{1-x}Ga_3O_{7+x/2}$ solid solution compositions on the 7.5°-10° (2θ) region. The bottom green and top orange tick marks represent the indexation of both $P\bar{4}2_1m$ and Ima2 melilite structures respectively. T and O stands for tetragonal and orthorhombic.*

Rietveld refinements of the acquired data were performed using Topas (V6) programme [13]. As mentioned above La, Ba and O_{int} occupancies were fixed to the nominal composition. For patterns containing T or O phases, all the oxide displacement parameters were constrained to refine to a common value, whereas this constraint was applied to both structures independently for patterns containing both melilite polymorphs. An absorption correction was applied to all patterns Rietveld refinements, with μR values ranging from 1.34230(1) for x = 0.3 to 1.40990(1) for x = 0.9. In the following, Rietveld refinement conditions will be described separately in four compositions sections: (i) $0.3 \leq x \leq 0.725$, (ii) x = 0.75, 0.8 and 0.85, (iii) x = 0.775, (iv) x = 0.9.

$La_{1+x}Ba_{1-x}Ga_3O_{7+x/2}$ ($0.3 \leq x \leq 0.725$): For these compositions, the tetragonal $P\bar{4}2_1m$ cell was the only model used to describe the whole diffraction pattern. Moreover, for x = 0.3 and 0.675 the impurities structures were included in Rietveld the refinements to achieve the best possible fit. The total number of independently refined parameters reached 42 (zero shift, scale factor, 15 background terms, 6 profile parameters from a TCHZ profile function, axial divergence correction, 18 structural parameters) for x = 0.6, 0.65, 0.7 and 0.725 composition. On the other hand, for x = 0.3 and 0.675 compositions the total amount of refined parameters accounts 60 and 51 independently refined parameters respectively. These extra parameters come from the impurities cell and profile function parameters.

$La_{1+x}Ba_{1-x}Ga_3O_{7+x/2}$ x = 0.75, 0.8 and 0.85: These compositions were refined using both the tetragonal $P\bar{4}2_1m$ and orthorhombic *Ima*2 melilite structures. The x = 0.75 composition refinement was constraint free, which led to 109 independently refined parameters (zero shift, 1*2 scale factor, 15 background terms, 6*2 profile parameters from a TCHZ profile function, axial divergence correction, 18+62 structural parameters). However, for x = 0.8 composition and due to the small amounts of the tetragonal melilite (2.32(6)% wt%) (see Figure IV.7), the metal oxide "*M*-O" distances were constrained to keep a minimum value of 1.7 Å and 2.5 Å for *M*= Ga, La/Ba respectively (111 independently refined parameters). The x = 0.85 composition on the other hand, contain only 1.14% (wt%) of the tetragonal melilite (Figure IV.7); to avoid non-physical refined values only the cell parameters of the $P\bar{4}2_1m$ melilite were refined, while fixing the related structural parameters. Moreover, the refined profile showed a non-fitted peak broadening noticed on the measured diffraction pattern of this composition. A better refinement with considerably lower R_{wp} and GOF values (from R_{wp}= 12.6%, GOF= 1.97 to R_{wp}= 10.38%, GOF= 1.64) was secured by using Stephens peak broadening description of the main phase peak shapes, i.e. the orthorhombic melilite (98 independently refined parameters).

$La_{1.775}Ba_{0.225}Ga_3O_{7.3875}$ (x = 0.775): The diffraction pattern of this composition was particularly challenging to refine due to unusual peak profiles, as displayed in Figure IV.5. To perform the best possible fit while keeping physically meaningful values/models, three approaches were attempted: (a) Stephens peak broadening description [14] which considers the space group symmetry and describes the sample strain and anisotropic crystallite size within the allowed *hkl* directions. This produced a relatively mediocre fit as seen in Figure IV.6a, and reliability factors of R_{wp}= 12.96% GOF= 2.28. (b) Spherical harmonics (eighth order) was used in second place to describe the anisotropic peak broadening; this allowed to achieve a better description of the measured profile (Figure IV.6b) with lower reliability factors of R_{wp}= 10.13% GOF = 1.78. Finally, a multi-cell approach was considered by using five orthorhombic and one tetragonal melilite cells, with only one profile function for all cells. The number of used cells was determined by having first a tetragonal cell and then orthorhombic cells were added one by one and refined, until an overlap of the *Ima*2 cells *hkl* peaks gave a near-continuous fit to the observed peaks. Four of the five *Ima*2 melilite cells parameters were constrained to refine with respect to a "reference" orthorhombic cell by the addition of a refinable shift parameter, defined in Table IV.2. In fact, by modelling different cells of the same compound it actually describes a possible composition gradient among the sample which could be easily induced by the direct crystallisation from the molten liquid synthesis procedure in the case of a not completely homogeneous melt. Moreover, this refinement strategy accomplished the best graphical fit (Figure IV.6c) and the lowest reliability factors (R_{wp}= 10.01% GOF= 1.07) over the three tested approaches and therefore was retained as the final description of the measured pattern. This led to a total of 125 independently refined parameters (zero shift, 1*6 scale factor, 18 background term, axial divergence correction, 6 profile parameters from a TCHZ profile function, 93 structural parameters).

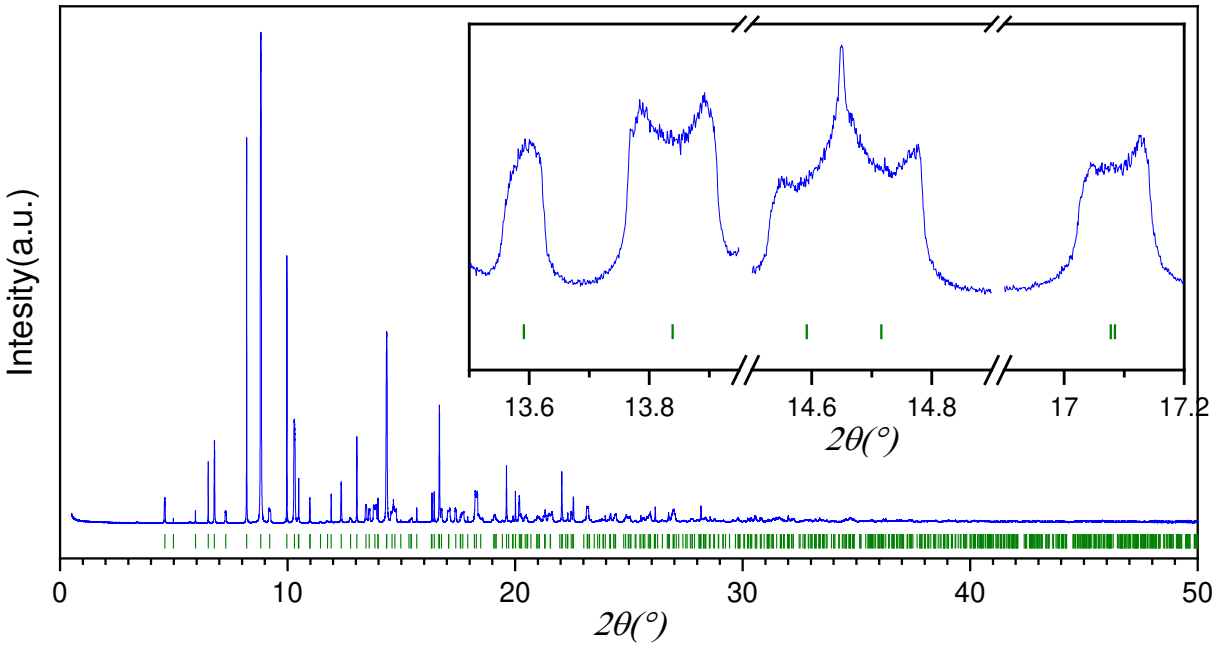

Figure IV.5. *SPD acquired pattern for the $La_{1.775}Ba_{0.225}Ga_3O_{7.3875}$ (x = 0.775) composition, with the insert showing a zoom on the 13.5°-17.2° (2θ) range. Green tick marks correspond to the tetragonal $P\bar{4}2_1m$ melilite indexation.*

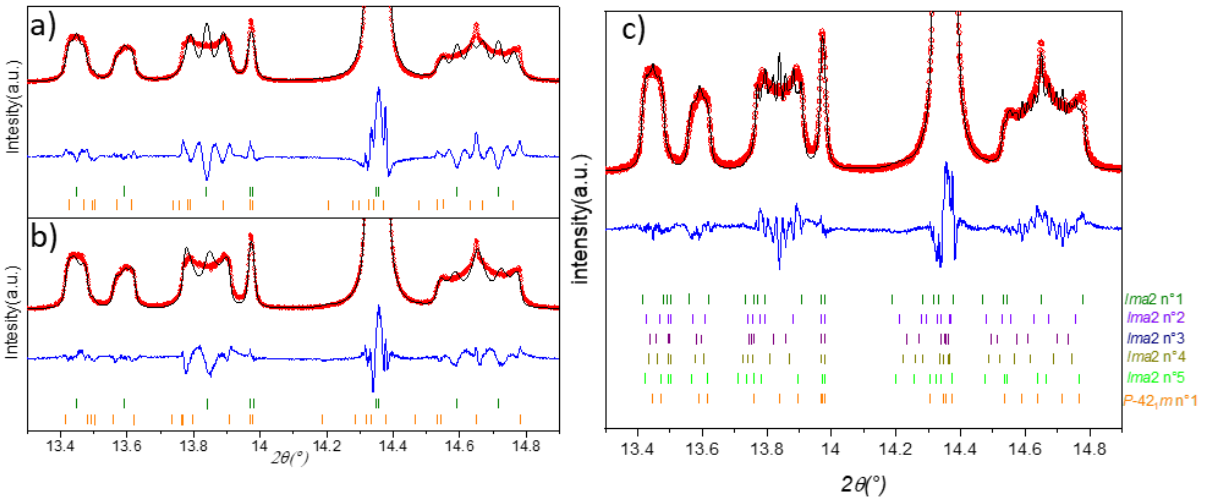

Figure IV.6. *Zoom on the 13.3° - 14.9° (2θ) region from Rietveld refinements of the x = 0.775 compound using different strategies: (a) Stephens broadening description. (b) Spharical harmonic. (c) Multi-cells approach. In all panels red symbols, black and blue lines corresponds to Y_{obs}, Y_{calc} and Y_{obs}-Y_{calc} respectively. In (a) and (b) pannels green and orange tickmarks correspnds tp the $P\bar{4}2_1m$ and Ima2 melilites respectively.*

<u>$La_{1.9}Ba_{0.1}Ga_3O_{7.45}$ (x = 0.9)</u>: This composition was refined using only one orthorhombic cell and the $LaGaO_3$ phase as an impurity. The total number of independently refined parameters of this composition is 82 (zero shift, 1*2 scale factor, axial divergence correction, 15 background term, 6*2 profile parameters from a TCHZ profile function, 49+3 structural parameters).

All the refinements described above led to satisfactory (in the same range) reliability factors, and are summarised in Table IV.1. Their related refined plots and structural parameters are shown in Figure IV.8, Figure IV.9 in the main text and from Figure A. 19 to Figure A. 22, and from Table A. 16 to Table A. 34 in the appendices. The extracted cell parameters and volumes (Figure IV.10a) exhibits a clear decreasing linear trend, which is consistent with the substitution of a larger Ba by a smaller La atom, i.e. ionic radii of 1.52 Å and 1.27 Å for Ba and La respectively [15]. Even though the overall volume trend shows a decline as x values increase (Figure IV.10a), one can notice an increasing trend of the *a*/*c* ratio for both tetragonal and orthorhombic melilites (Figure IV.10b), consistent with solid solution trend. Moreover, this is even supported by the *a*/*b* ratio of the orthorhombic cell, indicating and increasing trend (Figure IV.10c), consistent with the 1D ordering of the interstitial oxides along the *a* direction.

Table IV.1. Summary of all compositions Rietveld refinements, including: reliability factors, cell parameters, weight fractions, and impurities weight fractions.

x	R_{wp}	GOF	structure	a (Å)	b (Å)	c (Å)	wt%	impurities wt%
0.3	10.91%	1.51	$P\bar{4}2_1m$	8.12688(2)	= a	5.35114(1)	99.47	0.53
0.6	8.16%	1.20	$P\bar{4}2_1m$	8.08849(1)	= a	5.29991(1)	100	-
0.65	7.12%	1.27	$P\bar{4}2_1m$	8.08170(1)	= a	5.291514(8)	100	-
0.675	7.81%	1.33	$P\bar{4}2_1m$	8.07836(2)	= a	5.28703(1)	99.84	0.16
0.7	10.41%	1.49	$P\bar{4}2_1m$	8.07489(2)	= a	5.28269(1)	100	-
0.725	11.78%	2.12	$P\bar{4}2_1m$	8.07235(2)	= a	5.27953(2)	100	-
0.75	9.11%	1.51	$P\bar{4}2_1m$	8.06891(2)	= a	5.27513(2)	76.06	-
			*Ima*2	11.43139(6)	11.39361(5)	10.55194(4)	23.94	
0.775	10.01%	1.07	$P\bar{4}2_1m$	8.06246(4)	= a	5.26941(5)	15.18	-
			*Ima*2	11.43791(8)[a]	11.36654(8)[a]	10.5397(1)[a]	84.82[b]	
0.8	8.98%	1.35	$P\bar{4}2_1m$	8.06223(7)	= a	5.2685(1)	2.32	0.09
			*Ima*2	11.45216(8)	11.35246(7)	10.53719(5)	97.59	
0.85	10.37%	1.64	$P\bar{4}2_1m$	8.0560(1)	= a	5.2614(2)	1.14	-
			*Ima*2	11.46897(5)	11.31829(4)	10.52236(3)	98.86	
0.9	13.21%	1.96	*Ima*2	11.47630(2)	11.2955(2)	10.50930(2)	99.98	0.08

[a]Cell parameter of the *Ima*2 cell with the highest wt%
[b]combined wt% of all *Ima*2 cells

Table IV.2. Cell parameters refinement strategy for the different defined orthorhombic and tetragonal cells.

parameter	Orthorhombic cell 1 (*Ima*2)	Orthorhombic cell 2 (*Ima*2)	Orthorhombic cell 3 (*Ima*2)	Orthorhombic cell 4 (*Ima*2)	Orthorhombic cell 5 (*Ima*2)	tetragonal cell ($P\bar{4}2_1m$)
a	a1: freely refined	a1+shifta	a1+2*shifta	a1+3*shifta	a1+4*shifta	a6: freely refined
b	b1: freely refined	b1+shiftb	b1+2*shiftb	b1+3*shiftb	b1+4*shiftb	a6: freely refined
c	c1: freely refined	c1+shiftc	c1+2*shiftc	c1+3*shiftc	c1+4*shiftc	c6: freely refined
wt%	20.3(2)%	21.1(2)%	19.5(2)%	11.8(2)%	12.1(2)%	15.2(1)%

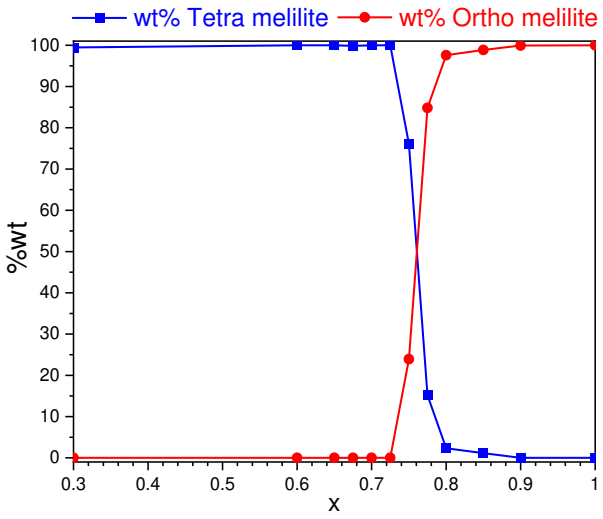

Figure IV.7. *Extracted weight% of both tetragonal and orthorhombic melilites from the performed Rietveld refinements against SPD measured* $La_{1+x}Ba_{1-x}Ga_3O_{7+x/2}$ *(*$0.3 \leq x \leq 0.9$*) compositions.*

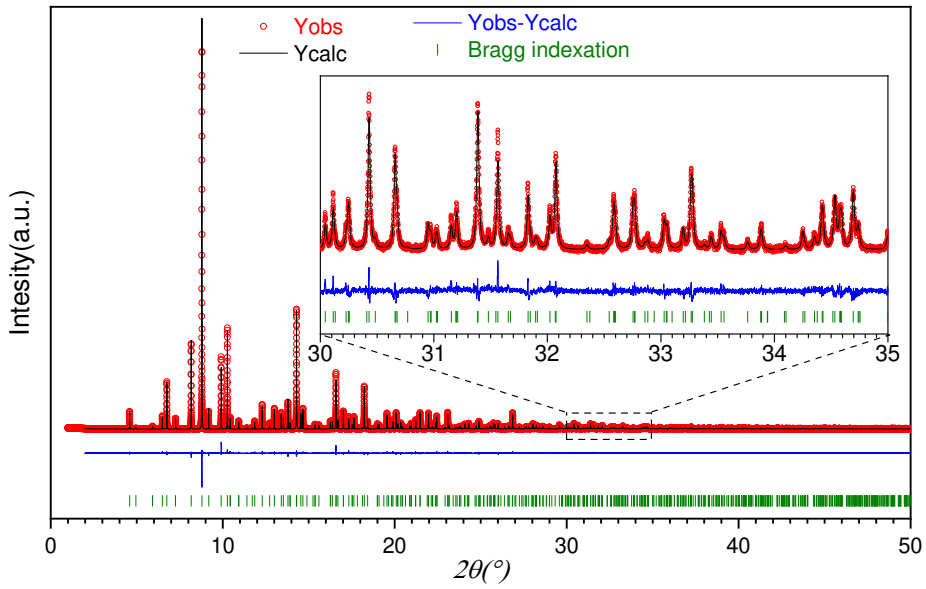

Figure IV.8. *SPD data Rietveld refinement of the* $La_{1.6}Ba_{0.4}Ga_3O_{7.3}$ *(*$x = 0.6$*) composition (*R_{wp}*= 8.16%, GOF= 1.20). Where red, black, blue and green data represents the aquired, simulated, difference and model indexation (*$P\bar{4}2_1m$*) data respectively.*

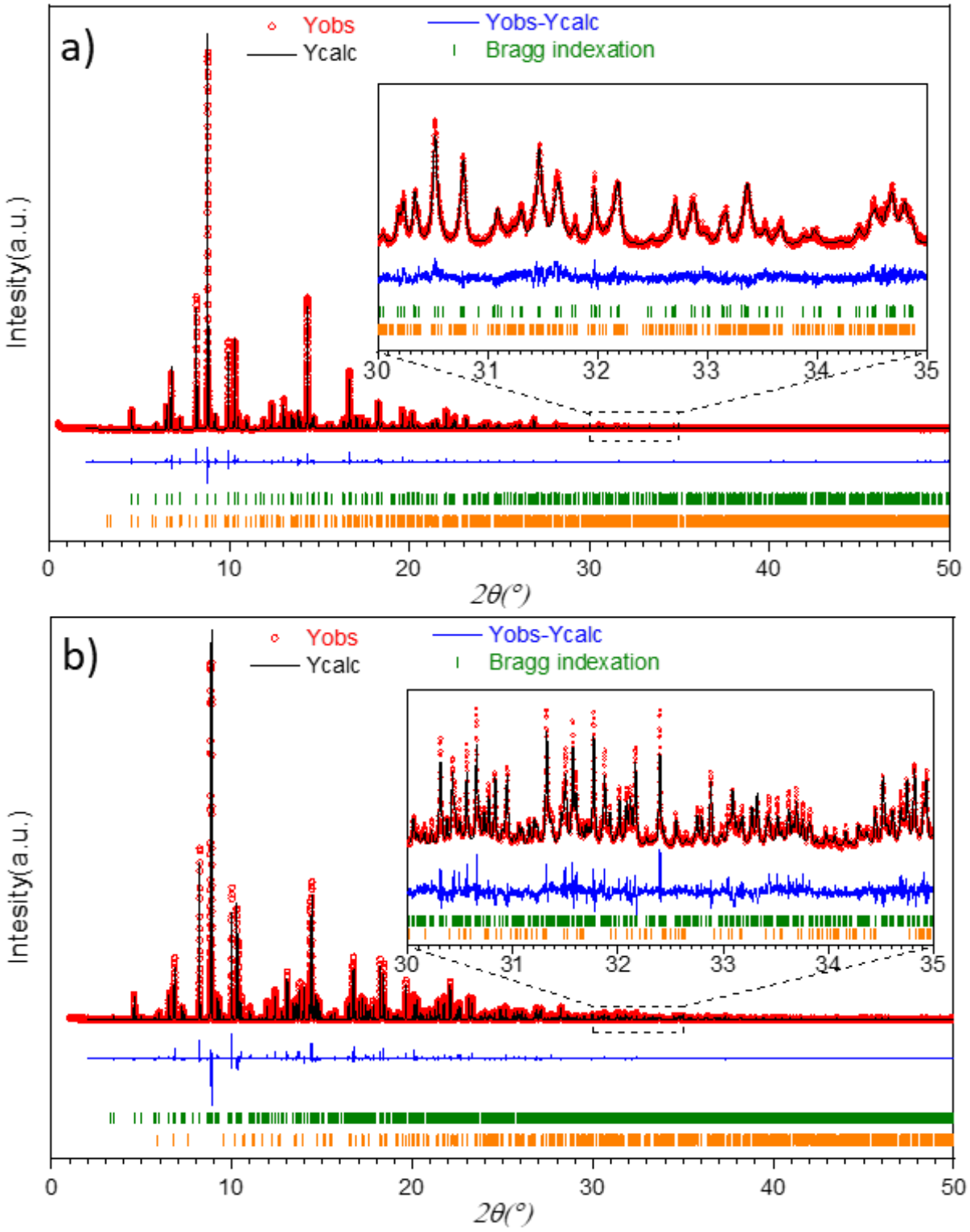

Figure IV.9. *SPD data Rietveld refinement of the a) $La_{1.75}Ba_{0.25}Ga_3O_{7.375}$(x = 0.75) composition ($R_{wp}$= 9.11%, GOF= 1.51). b) $La_{1.9}Ba_{0.1}Ga_3O_{7.45}$(x = 0.9) composition ($R_{wp}$= 13.21%, GOF= 1.96). In both panels red, black and blue data corresponds to the measured, calculated and difference curves. In the (a) panel green and orange tick marks corresponds to the $P\bar{4}2_1m$ and Ima2 melilites. Where in panel (b) green and orange tick marks corresponds to Ima2 melilite an $LaGaO_3$ perovskite.*

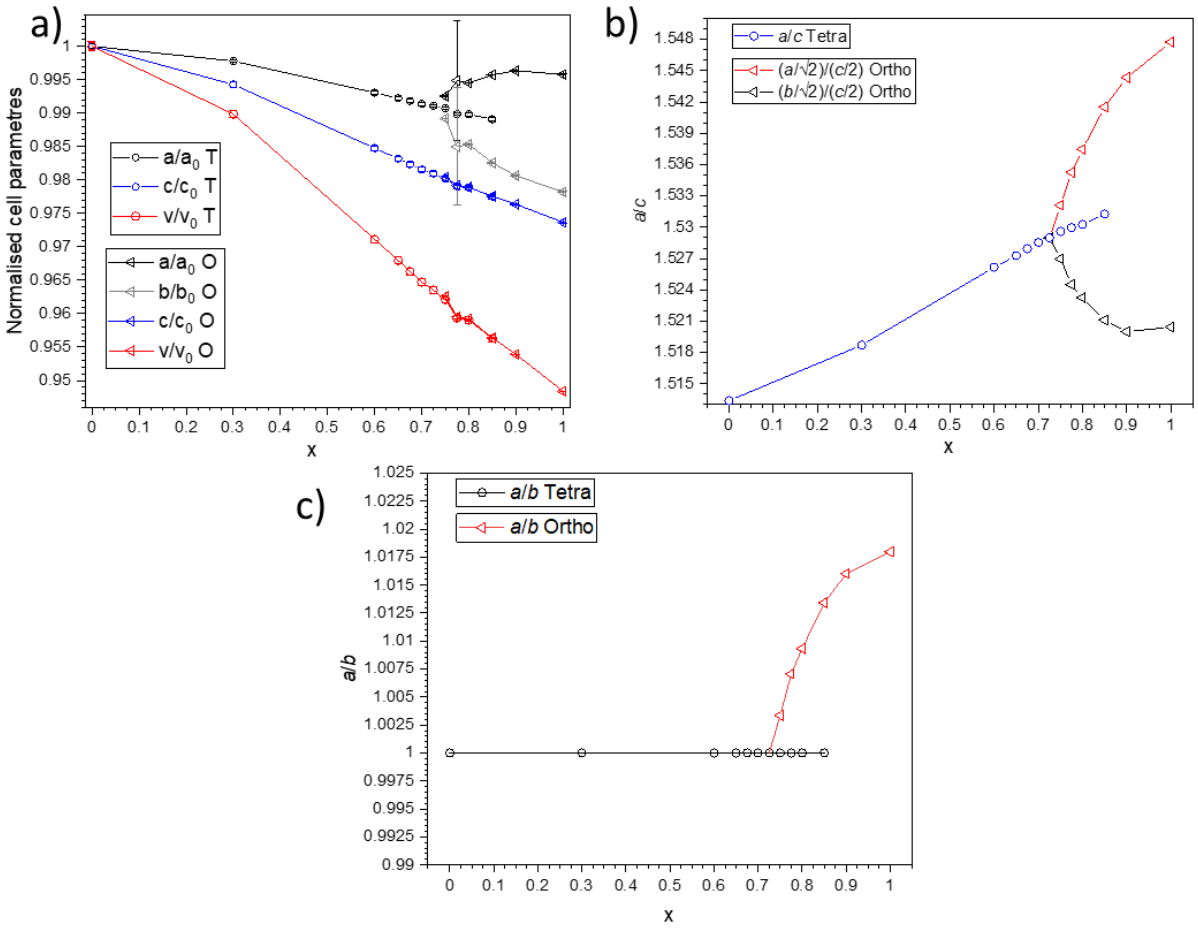

Figure IV.10. *a) Normalised cell parameters to the $LaBaGa_3O_7$ (x = 0) of both tetragonal and orthorhombic melilites extracted from Rietveld refined SPD data as a function of x (in the $La_{1+x}Ba_{1-x}Ga_3O_{7+x/2}$ solid solution). The large error bars in panel (a) for the x = 0.775 composition were drawn from the refined cell parameters distribution over the five orthorhombic melilite cells. b) and c) shows the a/c and a/b ratio of both $P\bar{4}2_1m$ and Ima2 melilites. In all three (a, b and c) panels the x = 0 and x = 1 compositions were taken from [11], [16].*

Taking a closer look at the refined structural parameters of the orthorhombic cells, one can notice in Figure IV.11a and Figure IV.11b the decreasing trend of both La1-La1 and La2-La3 distances as x values increases, consistent with the decreasing *c* parameter trend (note that the *Ima*2 structure possesses two La2-La3 distances, here we focus on the distance that contains an interstitial oxide between the La2 and La3 atoms shown Figure IV.11a). Furthermore, it is important to note the greater decrease of La2-La3 distance compared to that of La1-La1, which can be explained by the intercalation of the interstitial oxide (O_{int}) between the La3 and La2 cationic sites, increasing their local coordination from 8 to 9-coordinated lanthanums. This leads to a decrease of the (La3/La2)-O_{int} average bond distances, which gets substantially pronounced as the interstitial oxide concentration increases. This has repercussion on the averaged structure as the O_{int} concentration increases (x values increasing) the probabilities of

finding an O_{int} between a La3 and a La2 gets more significant, hence a gradient is noticed on the La3/La2-Oint bond distances. This point is further supported by the Ga5-O_{int} bond distances showing similar features (Figure IV.11c and Figure IV.11d), as they evolve in a declining trend with the increase of O_{int} concentration. The x = 0.75 composition refined *Ima*2 structure exhibits a different La2-La3 and Ga5-O_{int} distances behaviour opposing the overall trend, i.e. dLa2-La3 > dLa1-La1 and dGa5-O_{int} (x = 0.75) < dGa5-O_{int} (x = 0.775). This is most likely an artefact due to the relatively low *Ima*2 phase fraction (23.94% in wt%) in the sample.

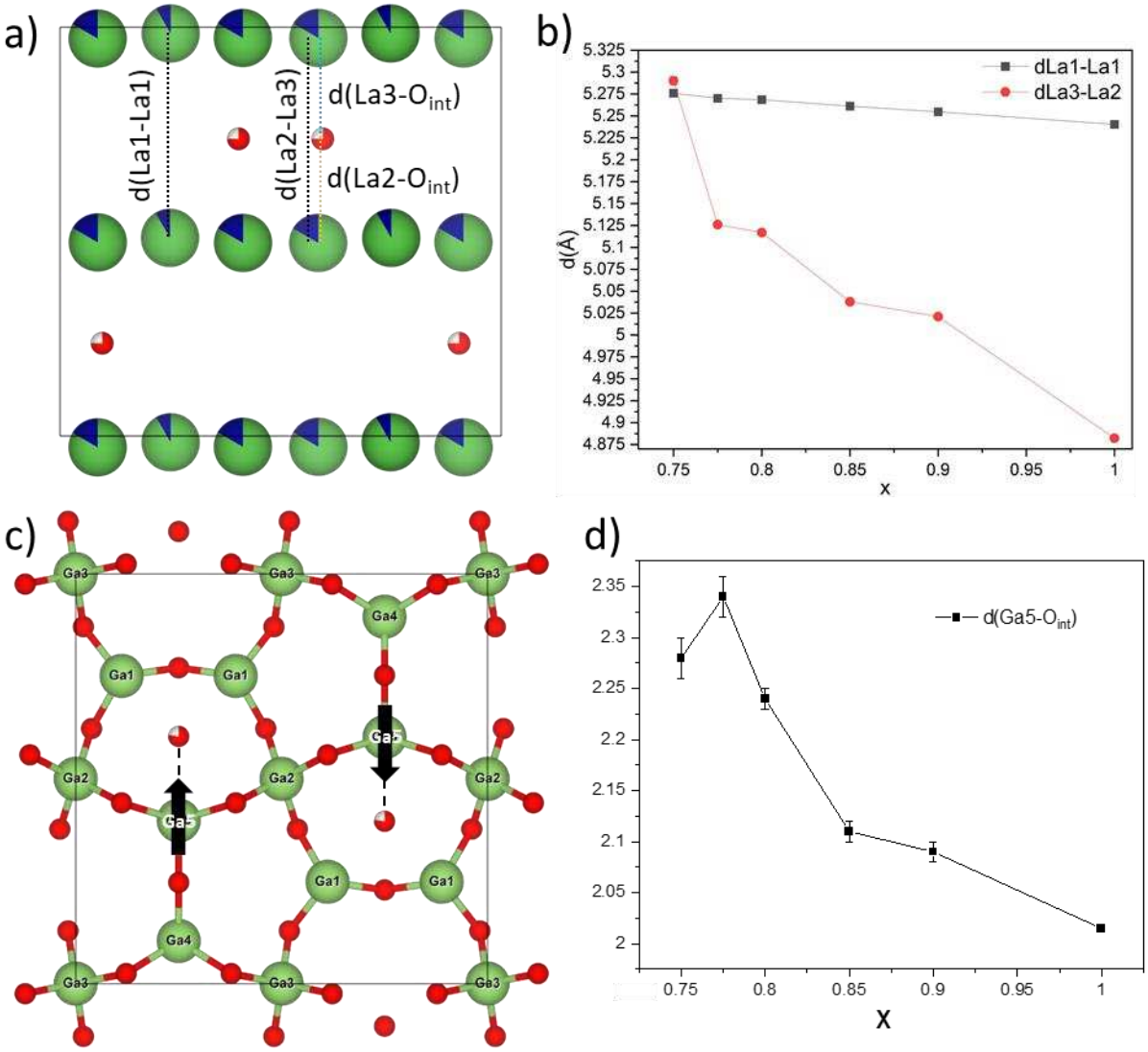

Figure IV.11. *a) Structural projection of the orthorhombic Ima*2 *melilite (x = 0.75 composition) along the* a*-axis, highlighting the La1-La1 and La3-La2 interatomic distances, which are shown in (b) as a function of x (concentration of* O_{int}*). c) Structural projection of one* $[GaO_4]_n$ *sheet from the orthorhombic Ima*2 *melilite (x = 0.75 composition) along the* c*-axis with highlighted Ga5-*O_{int} *distance, which is shown in panel (d) as a function of x (concentration of* O_{int}*). The* $La_2Ga_3O_{7.5}$ *x = 1 composition plotted in both (b) and (d) panels was taken from [11]. In (a) and (c) panels blue, dark green, light green and red spheres corresponds to Ba, La, Ga and oxygen atoms.*

IV.3.2. NPD Rietveld refinement and characterisation of the cationic/anionic disorder for $La_{1+x}Ba_{1-x}Ga_3O_{7+x/2}$ (x = 0.3, 0.6, 0.7, 0.8, 0.9) compositions.

To better illustrate the cationic and anionic distribution of La, Ba and O_{int} (interstitial oxide) over the different offered crystallographic sites by both $P\bar{4}2_1m$ and *Ima*2 melilites, and investigate possible interstitial oxide disorder over new positions as in the $La_{1+x}Ca_{1-x}Ga_3O_{7+x/2}$ ($0.55 \leq x \leq 0.64$) [5], room temperature neutron powder diffraction (NPD) measurements were acquired. Moreover, the conduction mechanism in the $La_{1+x}Ca_{1-x}Ga_3O_{7+x/2}$ ($0.55 \leq x \leq 0.64$) compounds was shown to be different at higher temperatures ($T \geq 650°C$), as indicated by the different activation energies, and was assigned to a phase transition from $P1$ to $P\bar{4}2_1m$ structure. To study this possibility and better comprehend the conductivity of the samples, variable temperature NPD data were also acquired between room temperature and 820°C for the $La_{1.9}Ba_{0.1}Ga_3O_{7.45}$ (x = 0.9) sample, which is the only composition that consists of 100% *Ima*2 melilite polymorph at room temperature. To proceed for these measurements, multiple beads of $La_{1+x}Ba_{1-x}Ga_3O_{7+x/2}$ (x = 0.3, 0.6, 0.7, 0.8 and 0.9) compositions were first synthesised, then checked for purity two beads (ground together in powder form) at a time using laboratory PXRD. This process was repeated until large phase pure batches between 2.5g and 3g were accumulated for each composition. Room and high temperature neutron powder diffraction (NPD) measurements were then conducted on the D2B line at the ILL laboratory in Grenoble, France, with a refined incident wavelength of $\lambda = 1.5936(3)$ Å over the 0°-160° (2θ) angular range.

IV.3.2.1. Room temperature NPD data analysis for $La_{1+x}Ba_{1-x}Ga_3O_{7+x/2}$ x = 0.3/ 0.6/ 0.7/ 0.8/ 0.9 compositions.

Rietveld refinement of room temperature acquired data were carried out against both high intensity (HI)* and high resolution (HR)* data sets independently for all measured compositions. These refinements conditions are described in the following:

$La_{1+x}Ba_{1-x}Ga_3O_{7+x/2}$ (x = 0.3, 0.6 and 0.7): These compositions were Rietveld refined using only the tetragonal melilite to describe the whole acquired neutron diffraction patterns. Moreover, the thermal parameters of all atoms were refined as anisotropic (except the O_{int} which B_{iso} was fixed at 1 $Å^2$). The overall composition of the oxides was subject to a penalty function which allows the O_{int} sites occupancies to refine while constraining the overall composition to near-nominal values. This strategy led to a total of 59 independently refined parameters (zero

* *See Chapter A.I section A.I.2.2.3 in the appendices for the definition of these data sets which come from the same measured 2D data.*

shift, scale factor, 11 background term, 6 profile parameters from a TCHZ profile function, axial divergence correction, 39 structural parameters) for each composition.

$La_{1.8}Ba_{0.2}Ga_3O_{7.4}$ (x = 0.8): From previously measured SPD data, this composition exhibited a mixture between both $P\bar{4}2_1m$ and *Ima*2 melilite compounds. Hence, Rietveld refinements of neutron data were carried out using both structures. First the overall composition was constrained to not move too far from the nominal using a penalty function. Moreover, unlike the previously described x = 0.3 – 0.7 compositions refinements, all the thermal parameters were refined as isotropic for both structures. After a first Rietveld run (until convergence was reached), the refined occupancies of La/Ba from the tetragonal structure yielded very high errors (i.e. occupancies of 0.8(9)La/0.1(9)Ba). This can be explained by the relatively low amount of tetragonal melilite (i.e. 14% for the HI data; 11% for the HR data, both in wt%). The A-site cations occupancies were then fixed to the nominal values for the tetragonal melilite only, while refining those from the orthorhombic polymorph. This provided the same fit to the data with unchanged reliability factors and weight fractions between the two melilite structures. Additionally, in the final Rietveld refinement, gallium atom isotropic thermal parameters were constrained to refine to a common value applied to both structures; the same restraint was applied to the oxygen atoms. By proceeding with such a refinement plan, the total amount of independently refined parameters was minimised to 98 (zero shift, 1*2 scale factor, 11 background term, 6*2 profile parameters from a TCHZ profile function, axial divergence correction, 55 + 16 structural parameters).

$La_{1.9}Ba_{0.1}Ga_3O_{7.45}$ (x = 0.9): In the SPD refinement of $La_{1.9}Ba_{0.1}Ga_3O_{7.45}$, only the orthorhombic (*Ima*2) melilite was found to be present in this composition diffraction pattern, with no strong evidence of the tetragonal ($P\bar{4}2_1m$) melilite. Consequently, Rietveld refinements of the room temperature data were carried out using only the orthorhombic model. Here again, the only constraints applied to the system were the use of the penalty function to constrain the overall composition close to the nominal value (La/Ba and O_{int} occupancies refined). Moreover, in the final Rietveld refinement, thermal parameters of all gallium atoms were constrained to refine to the same value, to avoid negative refined thermal parameters. This approach generated 87 independently refined parameter (zero shift, scale factor, 11 background term, 6 profile parameters from a TCHZ profile function, axial divergence correction, 67 structural parameters).

Reliability factors, refined plots and structural parameters of the procedures described above are shown in Table IV.4, Figure IV.12 and Table IV.3 in the main text, and Figure A. 24 to Figure A. 28 and Table A. 35 to Table A. 52 respectively, in the appendices Chapter A.IV.

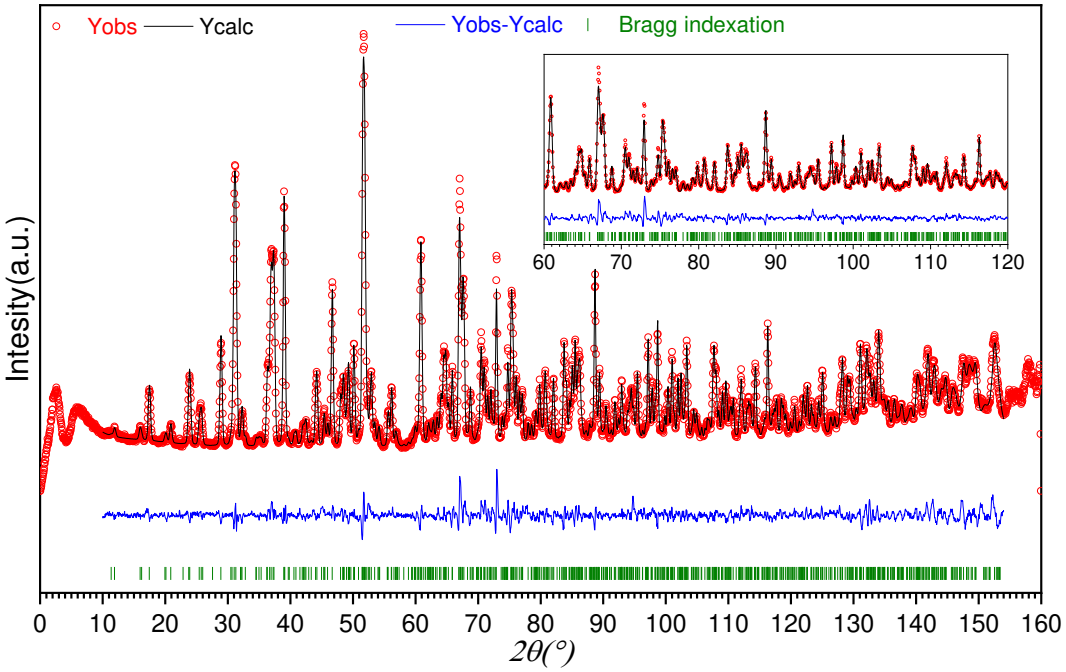

Figure IV.12. *Room temperature NPD HR data Rietveld refinement of the* $La_{1.9}Ba_{0.1}Ga_3O_{7.45}$ *(x = 0.9) composition (*R_{wp}*= 4.84%, GOF= 2.02).*

Table IV.3 Final NPD HR refinement of $La_{1.9}Ba_{0.1}Ga_3O_{7.45}$ (x = 0.9) composition structural parameters (S.G. *Ima*2, a= 11.46923(16) Å, b= 11.29077(17) Å, c= 10.50358(18) Å).

Atom	x	y	z	Occ	Biso
La1/Ba1	-0.5862(2)	0.2504(8)	0.4858(4)	0.968(6)/0.028(10)	0.38(8)
La2/Ba2	0.75	0.0870(6)	-0.0090(7)	0.894(18)/0.11(3)	0.3(2)
La3/Ba3	0.75	0.4166(7)	-0.0364(7)	0.971(18)/0.04(3)	0.6(2)
Ga1	-0.8857(3)	-0.2425(6)	0.2192(4)	1	0.43(4)[a]
Ga2	0	0	0.2373(10)	1	0.43(4)[a]
Ga3	0.5	0.5	0.2394(10)	1	0.43(4)[a]
Ga4	0.75	-0.1067(7)	-0.2467(8)	1	0.43(4)[a]
Ga5	0.25	0.0956(7)	0.2498(8)	1	0.43(4)[a]
O1	-0.8870(4)	-0.2483(9)	-0.1078(5)	1	0.57(8)
O2	-0.4760(7)	0.3659(6)	0.1444(8)	1	0.86(14)
O3	-0.5396(6)	-0.3778(6)	-0.3728(8)	1	0.61(13)
O4	-0.1258(6)	-0.0362(6)	-0.1581(8)	1	1.23(13)
O5	-0.8907(6)	0.0614(6)	0.3481(7)	1	0.87(13)
O6	0.75	0.2845(7)	0.1345(10)	1	1.47(18)
O7	0.75	-0.1223(10)	0.0758(10)	1	0.8(2)
O8	0.25	0.2487(12)	0.3279(7)	1	0.55(10)
O9	0.25	0.1080(11)	0.5833(10)	1	0.61(19)
O10	0.25	-0.0872(8)	0.2297(10)	0.878(17)	1

[a]Constrained to refine to the same value.

A first connection between SPD and NPD data refinements was made by comparing the refined cell parameters of the different structures (i.e. $P\bar{4}2_1m$ and *Ima*2), which indicated a good agreement between the two diffraction techniques (see Figure A. 23 in the appendices). Moreover, one can notice the further difference of refined weight fractions of both melilite polymorphs obtained from SPD and NPD refined data sets for the $La_{1.8}Ba_{0.2}Ga_3O_{7.4}$ (x = 0.8) composition (see Figure IV.7 and Figure IV.13). This can simply be explained by either: (i) the different synthesised sample for NPD experiments, which may have more tetragonal phase amounts due to the multiple combined beads to reach 3g of sample, compared to the SPD measured composition which needed only one bead. (ii) The broader pattern profile of neutron powder diffraction measurements making it difficult to refine accurate wt% fractions of the different present phases. Due to the low refined tetragonal melilite amount from this composition (11% and 14.1% both in wt% from HI and HR data respectively), it will not be considered for the following structural analysis.

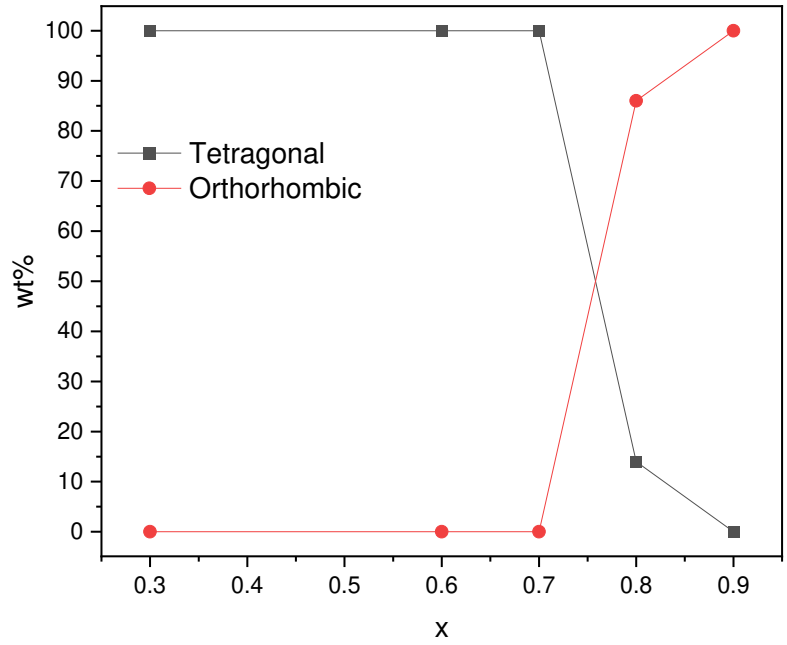

Figure IV.13. *Refined wt% of both tetragonal and orthorhombic melilite polymorphs from neutron data as a function of substituted Ba by La, noted x from the* $La_{1+x}Ba_{1-x}Ga_3O_{7+x/2}$ *solid solution.*

The cationic distribution was characterised as fully disordered for the tetragonal melilite, due to the presence of only one inequivalent A-site. The orthorhombic melilite structure which offers three possible A-sites thanks to its space group lower symmetry, allows a characterisation of the cationic distribution between La and Ba atoms over these sites. Benefiting from the constrained composition to refine close to the nominal, grants the possibility of refining the

occupancies of each of the two La and Ba atoms. For both x = 0.8 and x = 0.9 compositions, La2 and La3 sites were found to contains double the Ba content present in the La1 site (see Table IV.3 and from Table A. 47 to Table A. 52 in the appendices Chapter A.IV). However, considering the three-sigma rule of their associated errors it is not possible to discern a partial ordered from a fully disordered system, meaning that no Ba site preference can be identified within the sensitivity limits of the refinement.

It has been known from literature that the $La_{1+x}Ca_{1-x}Ga_3O_{7+x/2}$ ($0 \leq x \leq 0.64$) solid solution was reported to crystallise in a pseudo-orthorhombic melilite cell (S.G. *P*1) for $0.55 \leq x \leq 0.64$ [5] (see Figure IV.14). This compound was found to feature a partial ordering of both A-site cations and interstitial oxides (O_{int}). Out of the eight accessible A-sites, four are fully occupied by La atoms, while the remaining four are mixed between La and Ca atoms with different occupancy rates. The interstitial oxides network on the other hand was assigned to occur among four of the six five-membered $[GaO_4]_5$ melilite network forming pentagons, with partially occupied sites in a 1D ordered chains (see Figure IV.14), showing a preference for Ca bearing channels. The 1D order feature of the O_{int} network in the $La_{1+x}Ca_{1-x}Ga_3O_{7+x/2}$ $0.55 \leq x \leq 0.64$ compounds exhibit two edge sharing O_{int} chains per unit, in comparison with the *Ima*2 orthorhombic melilite which shows fully 1D ordered O_{int} chains.

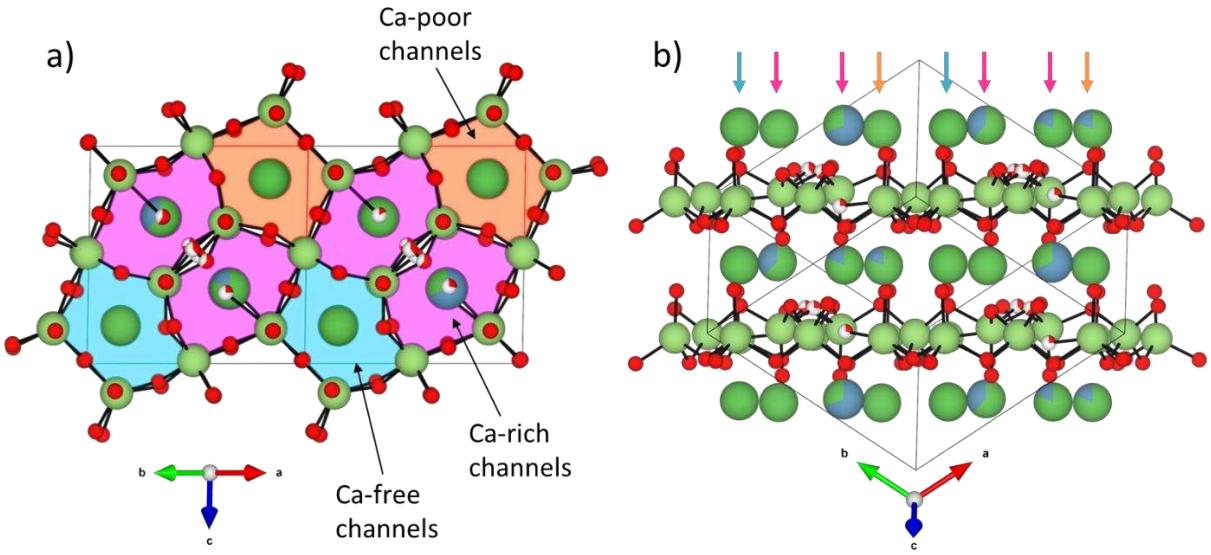

Figure IV.14. *Crystal structure of the $La_{1.64}Ca_{0.36}Ga_3O_{7.32}$ ($0 \leq x \leq 0.64$) pseudo-orthorhombic P1 melilite [5], (a) projected along its stacking direction, with light blue, pink and orange coloured surfaces indicating Ca-free, Ca-rich, and Ca-poor channels. (b) Projection along the section of stacking direction with arrows indicating the described channels using the same colour coding. Blue, dark green, light green and red spheres corresponds to Ca, La, Ga and oxygen atoms.*

To further investigate the cationic distribution of La and Ba, and a possible phase transition to a pseudo-orthorhombic *P*1 model for $La_{1+x}Ba_{1-x}Ga_3O_{7+x/2}$ ($0.6 \leq x \leq 0.9$) compositions, with a different A-sites cation ordering types (as reported for the $La_{1+x}Ca_{1-x}Ga_3O_{7+x/2}$ $0.55 \leq x \leq 0.64$ [5]). Two refinement strategies were then pursued: (i) converting the refined $P\bar{4}2_1m$ and *Ima*2 to *P*1 symmetry and using them as starting models with only La and Ba occupancies as refinable parameters; and (ii) using the reported pseudo-orthorhombic *P*1 structure of $La_{1.64}Ca_{0.36}Ga_3O_{7.32}$ as starting model with all atoms fixed B_{iso} values to 1 $Å^2$. These refinement procedures were also unsuccessful in answering the A-site cationic distribution question, as the refined occupancies associated errors were higher than the parameter itself, hence no meaningful values could be extracted. Finally, using the same strategy, La and Ba occupancies were fixed as in completely disordered system, and only the interstitial oxides positions and occupancies were let to refine. However, this procedure also had the same outcome and the related errors were higher than the parameter itself. These results mean that, even with quite different neutron scattering lengths between La and Ba (i.e. 8.24(4) fm and 5.07(3) fm respectively [17]), the amount and correlation of refined parameters is so great that the counting statistics are not sufficient to differentiate between these two elements.

It is known from the literature that intercalation of O_{int} atoms in the five-membered melilite framework forming rings centre, affects mostly the nearby oxides to satisfy its bonding conditions, hence inducing local disorder of these atoms [3], [5], [6], [11]. This is illustrated in Figure IV.15, illustrating the relaxation of the O_{int} local environment in the $La_{1.64}Ca_{0.36}Ga_3O_{7.32}$ *P*1 melilite. In this case, static disorder of the O_{int} closest oxide is so great that its split site (namely O3a and O3b in Figure IV.15) shows a distance ranging from 0.49 Å to 0.67 Å between O3a and O3b.

An examination of the refined tetragonal ($P\bar{4}2_1m$) melilite across the different measured $La_{1+x}Ba_{1-x}Ga_3O_{7+x/2}$ x = 0.3, 0.6, 0.7 compositions, reveals first an increasing anisotropy of the anisotropic thermal parameters of the different structural atoms, as displayed in Figure IV.16a, Figure IV.16b, Figure IV.16c showing an expanding atomic displacement ellipsoid (plotted in 99% probability), indicating an increased static disorder of these atoms as more Ba is substituted by La and interstitial oxide concentration augment. Moreover, in Figure IV.16d illustrating the recalculated B_{iso} values from the anisotropic thermal parameters (β_{11}, β_{22}, β_{33}, β_{12}, β_{13}, β_{23}) trend as a function of x (amount of substituted barium), it appears that for the $La_{1.3}Ba_{0.7}Ga_3O_{7.15}$ (x = 0.3) composition the thermal parameters are at their lowest values, which increase considerably to almost 3 $Å^2$ (for the O1 atom) as the tetragonal structure reaches

its stability limits (x = 0.7 composition). These results agree well with the previously observed atoms ellipsoid expansion in Figure IV.16, indicating an increasing oxide disorder due to the growing interstitial oxide (O_{int}) concentration. Additionally, the major gain of these raising variables is noticed for the O1 atom, increasing from 1.05(6) $Å^2$ to 2.88(7) $Å^2$ for x = 0.3 and 0.7 respectively, corresponding to a 174.9% inflation. For comparison, following the O1 atom, the other structural atoms can be ranked from highest to lowest increase of their calculated B_{iso} values as follow: Ga2 (135.7%), O3 (101%), La/Ba (87%), Ga1 (72.4%), O2 (4.5%). To understand this contrasting difference between the different atoms, an in-depth review of the interatomic distance is shown in Figure IV.16e. Results from this figure, showing the interatomic distances of the structural atoms with the O_{int}, further illustrate a consistent ranking with the one specified above, as the O1 being the closer atom to the interstitial oxide O_{int} followed by Ga2 and O3 atoms. In fact, due to the anionic disorder of the O_{int} atom, it induces distortions of its local structure, which is evidenced by the displacement parameters and explained by the interatomic distances. The *Ima*2 orthorhombic structure on the other hand showed similar decreasing behaviour, from neutron refinements, in terms of La1-La1 and La2-La3 distances decrease as seen from SPD refined structures (see Figure IV.17 for NPD results), which is consistent with the interstitial oxide (O_{int}) concentration increase. Comparison of the oxide displacement parameters for the orthorhombic structure is no longer valid, mainly due the high obtained errors for these parameters, but also because of the increased amount of O_{int} local environment relaxation as causing lowered symmetry of its initial space group from $P\bar{4}2_1m$ to *Ima*2.

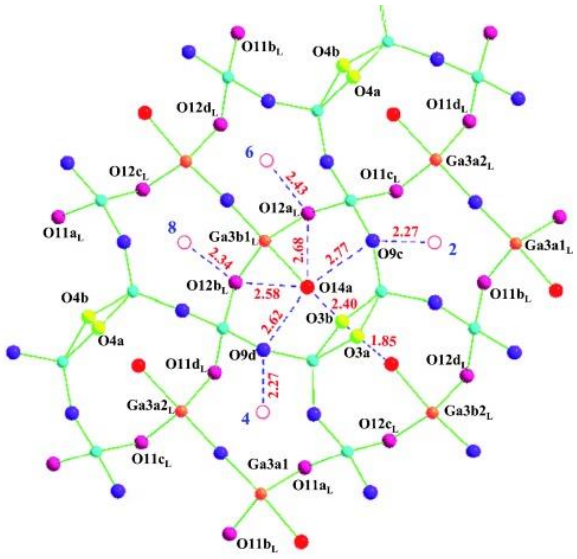

Figure IV.15. *Local distortions of the interstitial oxide (O_{int}) environment in the $La_{1.64}Ca_{0.36}Ga_3O_{7.32}$ pseudo-orthorhombic P1 compound and how it affects the neighbouring channels. The O_{int}-O_x bond distances are shown to indicate the most affected oxide atoms. Ga is represented by light blue coloured spheres while the oxides are in green, purple and blue coloured spheres arranged from the closest to the furthest channel forming oxides. This figure was taken from [5].*

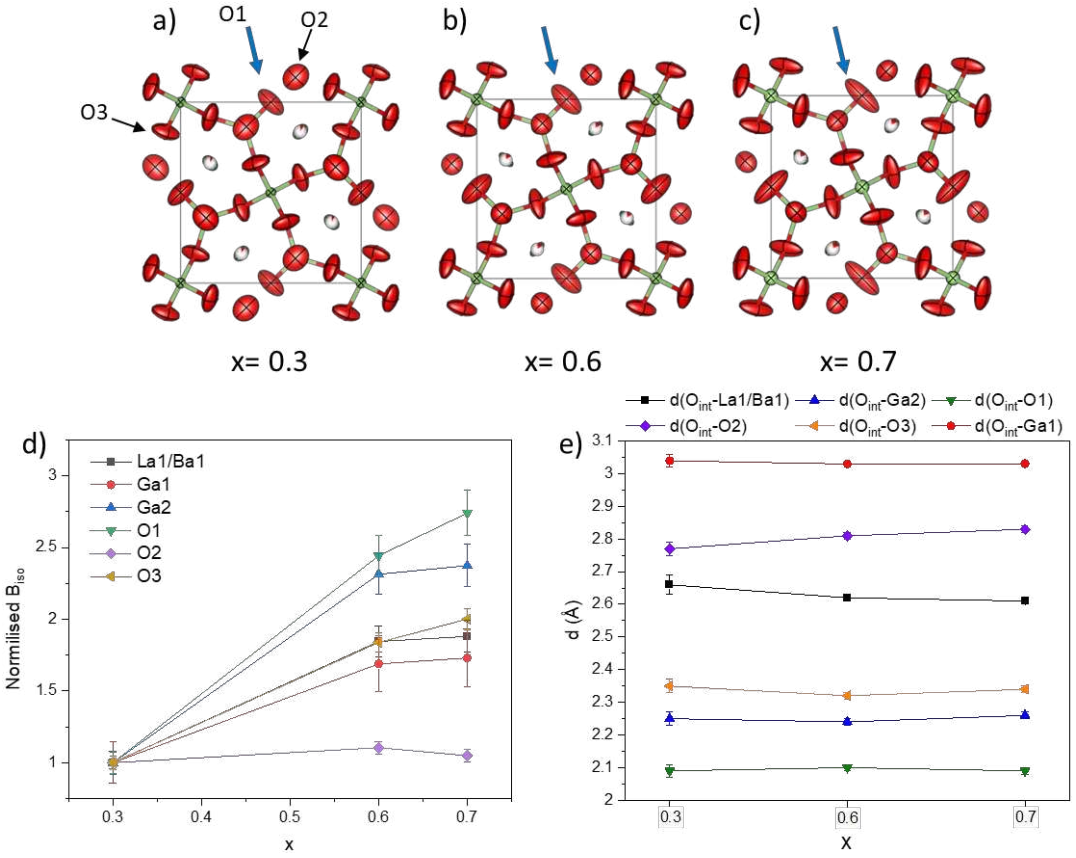

Figure IV.16. *a), b), c) Shows the refined $P\bar{4}2_1m$ structure of x = 0.3, 0.6 and 0.7 respectively projected along the c-axis and plotted in thermal ellipsoids in 99% probability. The blue arrows point the O1 atom which shows the strongest anisotropy. d) normalised plot of calculated isotropic displacement parameters for all structural atoms as a function of composition (x). e) plot of the O_{int} atom interatomic distances with the other structural atoms.*

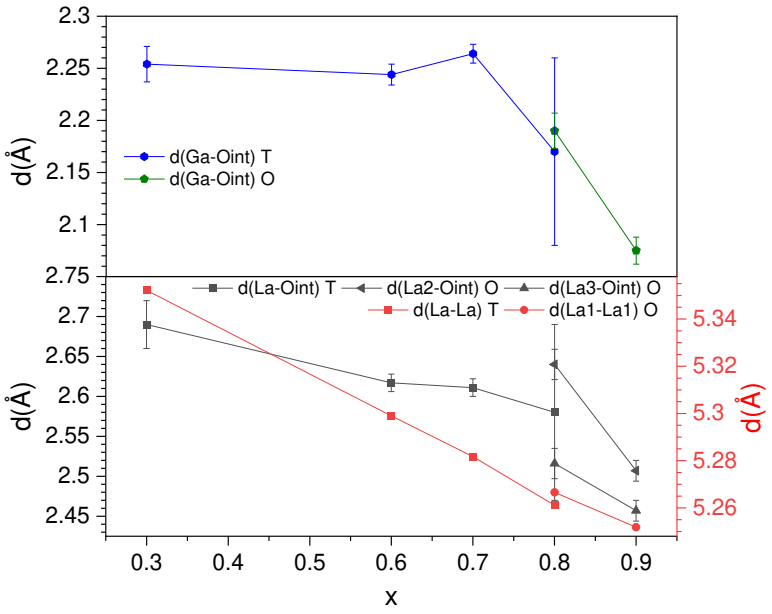

Figure IV.17. *Ga-O_{int}, La-O_{int} and La-La interatomic distances obtained from neutron refined structures across the room temperature measured composition series (x values in $La_{1+x}Ba_{1-x}Ga_3O_{7+x/2}$). With T and O referring to tetragonal $P\bar{4}2_1m$ and orthorhombic Ima2 structures.*

IV.3.2.2. Variable temperature NPD data analysis for $La_{1.9}Ba_{0.1}Ga_3O_{7.45}$ x = 0.9 composition.

Variable temperature powder X-ray diffraction (VT-PXRD) was first performed on the orthorhombic phase pure sample (i.e. $La_{1.9}Ba_{0.1}Ga_3O_{7.45}$ x = 0.9 composition), to identify its *Ima*2 to $P\bar{4}2_1m$ structure transition temperature. In Figure IV.18, the VT-PXRD measurements indicate a phase transition occurring at 755°C, with a decomposition of the $P\bar{4}2_1m$ melilite to a mixture between $LaGaO_3$ (S.G. *Pcmn*), $LaBaGa_{11}O_{20}$ (S.G. *I*2/*m*) and Ga_2O_3 (S.G. *I*2/*m*) starting at 840°C. Following these extracted temperatures, high temperature neutron powder diffraction measurements were conducted at 525°C, 720°C, 770°C and 820°C for the x = 0.9 sample. In Figure IV.19a showing the stacked NPD patterns, one can notice a disappearance of peak splitting, indicative of the phase transition toward a smaller higher symmetry cell "$P\bar{4}2_1m$" (see Figure IV.19b).

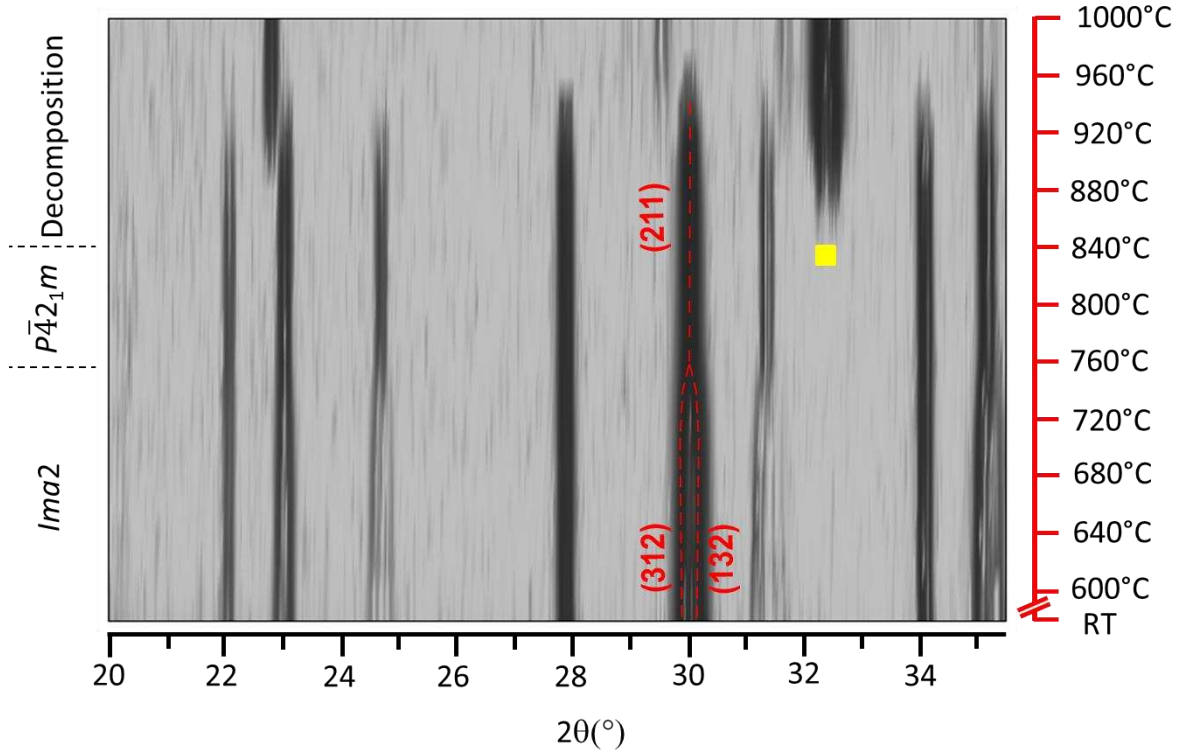

Figure IV.18. *VT-PXRD measurements (20°C step size) of $La_{1.9}Ba_{0.1}Ga_3O_{7.45}$ (x =0.9) composition, evidencing the stability of the orthorhombic Ima2 melilite vs temperature. The yellow box shows the beginning of decomposition into $LaGaO_3$ + $LaBaGa_{11}O_{20}$ + Ga_2O_3.*

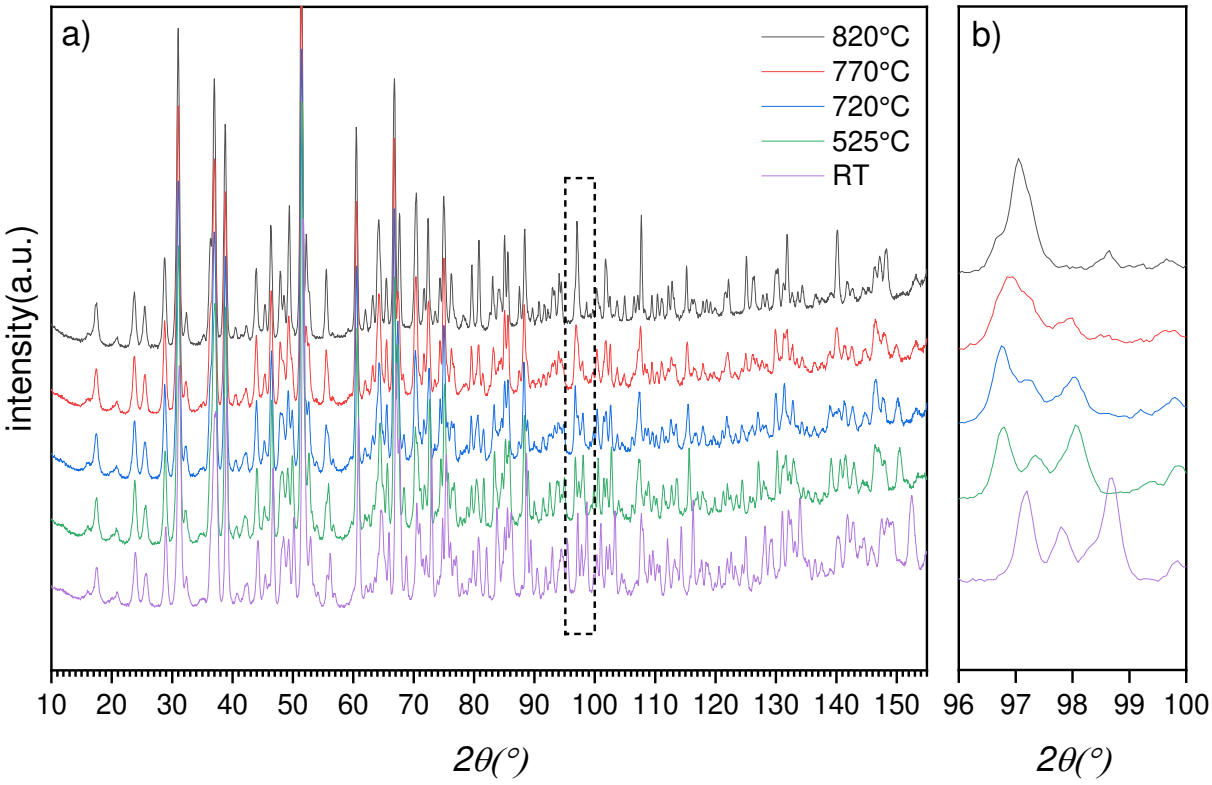

Figure IV.19. *a) Stacked high temperature neutron powder diffraction patterns of the $La_{1.9}Ba_{0.1}Ga_3O_{7.45}$ (x = 0.9) composition measurement. A zoom on the 96° - 100° (2θ) region is shown in (b) panel.*

To identify the phases present at the different measured temperatures, Rietveld refinements were also run independently against both "HI" and "HR" data, and are described as follows:

$La_{1.9}Ba_{0.1}Ga_3O_{7.45}$ (x = 0.9) at 525°C: At this temperature, Rietveld refinements were carried out using only the orthorhombic model. In analogy with previously detailed x = 0.9 composition room temperature NPD refinement in section IV.3.2.1, the overall composition was constrained to not move too far from the nominal values (La/Ba and O_{int} amounts). All gallium atoms isotropic displacement parameters were constrained to refine to the same value. This led to 87 independently refined parameters (zero shift, scale factor, 11 background term, 6 profile parameters from a TCHZ profile function, axial divergence correction, 67 structural parameters).

$La_{1.9}Ba_{0.1}Ga_3O_{7.45}$ (x = 0.9) at 720°C and 770°C: Final Rietveld refinements at these temperatures were performed using both tetragonal and orthorhombic cells to achieve the best possible description of the measured diffraction patterns. Both structures were subjected to their own individual compositional constrains. This yielded to a total of 118 refined parameters (zero shift, 1*2 scale factor, 11 background term, 6*2 profile parameters from a TCHZ profile function, axial divergence correction, 71 + 20 structural parameters).

$La_{1.9}Ba_{0.1}Ga_3O_{7.45}$ (x = 0.9) at 820°C: The final measured temperature (820°C) neutron data was refined using only the $P\bar{4}2_1m$ melilite as a starting model. The overall composition was constrained by a penalty function (La/Ba and O_{int} amounts as described before). By operating a Rietveld refinement with the described conditions, the total number of independently refined parameters was 58 (zero shift, scale factor, 11 background term, 6 profile parameters from a TCHZ profile function, axial divergence correction, 38 structural parameters).

Rietveld refinements are summarised in Table IV.4. Refined plots and structural parameters of the procedures described above are shown in Figure A. 29 to Figure A. 32 and Table A. 53 to Table A. 63 respectively, in the appendices Chapter A.IV.

Table IV.4. Summary of the obtained reliability factors and weight fractions from the performed Rietveld refinements against NPD acquired data.

x	T(°C)	Data set	R_{wp}	GOF	polymorph	wt%
0.3	RT	HI	3.15%	2,44	$P\bar{4}2_1m$	100
		HR	3.58%	1.57	$P\bar{4}2_1m$	100
0.6	RT	HI	2.73%	2.11	$P\bar{4}2_1m$	100
		HR	3.19%	1.39	$P\bar{4}2_1m$	100
0.7	RT	HI	2.88%	2.23	$P\bar{4}2_1m$	100
		HR	3.27%	1.43	$P\bar{4}2_1m$	100
0.8	RT	HI	3.67%	2.91	$P\bar{4}2_1m$	14.12
					*Ima*2	85.88
		HR	4.67%	2.08	$P\bar{4}2_1m$	11
					*Ima*2	89
0.9	RT	HI	3.77%	2.79	*Ima*2	100
		HR	4.84%	2.02	*Ima*2	100
	525	HI	3.11%	2.56	*Ima*2	100
		HR	3.89	1.81	*Ima*2	100
	720	HI	2.47%	2.04	*Ima*2	64.17
					$P\bar{4}2_1m$	35.83
		HR	3.20%	1.49	*Ima*2	65.89
					$P\bar{4}2_1m$	34.11
	770	HI	2.90%	2.37	Ima2	46.65
					$P\bar{4}2_1m$	53.35
		HR	3.50%	1.61	*Ima*2	44.25
					$P\bar{4}2_1m$	55.75
	820	HI	2.87%	2.34	$P\bar{4}2_1m$	100
		HR	3.50%	1.61	$P\bar{4}2_1m$	100

As previously discussed in section IV.3.2.1, refinement of the $La_{1.9}Ba_{0.1}Ga_3O_{7.45}$ (x = 0.9) composition room temperature neutron data, revealed no preference for Ba atoms to be hosted in a specific A-site out of the three available. The interstitial oxide distribution also did not show strong evidence of a complete disorder over the melilite $[GaO_4]_n$ framework, and good fits were secured with the orthorhombic *Ima*2 melilite structure. This was further confirmed by the 525°C refinement, which provided similar fit results and reliability factors (see Table IV.4). Moreover, from VT-PXRD measurements, it appeared that at 720°C the sample is fully orthorhombic while being fully tetragonal at 770°C, which is confirmed by the extracted cell parameters. However, from initial refinements of NPD acquired data at these temperatures, diffraction patterns could not be fully fitted using only one of the two models. Generated Fourier difference maps of the 720°C refinement with a single orthorhombic cell did not reveal any residual nuclear density which could hint at interstitial oxide disorder. Moreover, several tests

were run by filling the remaining O_{int} free channels with oxide atoms and refining the structure. Even though these refinements slightly reduced the reliability factors from (R_{wp}= 4.44% GOF= 3.64) to (R_{wp}= 4.32% GOF= 3.55), the misfits were still present, and suggest a missing structure. Thus, both tetragonal and orthorhombic melilites were added to the refinement of NPD data at both 720°C and 770°C temperatures. By doing so, a far better refinement was obtained with even lower reliability factors (see Table IV.4). Moreover, the fact that the refined weight % of tetragonal ranged from 35.8% (at 720°C) to 53.4% (at 770°C) while the orthorhombic melilite content decrease from 64.2% (at 720°C) to 46.6% (at 770°C) supports this refinement strategy. The 820°C acquired data was the easiest to refine, as the use of only the tetragonal model was sufficient to describe the whole measured diffraction pattern.

The noticed structural trend in transiting from a low symmetry (*Ima*2) to a higher symmetry ($P\bar{4}2_1m$) cells at higher temperatures, is actually consistent with the favoured greater disorder induced by the acquired thermal energy. A similar feature was noticed for the $La_{1+x}Ca_{1-x}Ga_3O_{7+x/2}$ $0.55 \leq x \leq 0.64$ solid solution, which adopts a pseudo-orthorhombic *P*1 cell at room temperature. At 700°C, this polymorph was found to be no longer stable, and transforms into the fully disordered $P\bar{4}2_1m$ melilite. The previously described Sr*RE*Ga_3O_7 *RE*= [Er-Yb] melilite compositions in Chapter II, displayed similar behaviour, when crystallised from glass precursors, are stabilised under a $P2_12_12$ polymorph due to the ordering between Sr and *RE* atoms. Eventually, at higher temperatures the fully disordered $P\bar{4}2_1m$ tetragonal melilite is stabilised at the expense of the ordered $P2_12_12$ polymorph.

IV.3.3. Stability of the tetragonal ($P\bar{4}2_1m$) small-cell vs the orthorhombic (*Ima*2) superstructure melilites.

Thermal stability of these $La_{1+x}Ba_{1-x}Ga_3O_{7+x/2}$ melilite compositions was studied by VT-PXRD measurements. Samples were heated from room temperature up to 1200°C using a 20°C step and measured over the 15° - 40° (2θ) range with a measuring step of 0.016° and a measuring time of 0.7s/step. The obtained results are coupled to the discussed results above from SPD and NPD refinement data and are plotted in a phase-diagram like plot (Figure IV.20). From this Figure, as x values increase a clear decreasing trend in the thermal stability of these melilites can be seen, this is consistent with the increasing metastability of these structures. Moreover, one can also notice the stability of the *Ima*2 structure over a wider temperature range, which is in good agreement with the previously described melilite framework inability to host the O_{int} in a fully disorder framework ($P\bar{4}2_1m$).

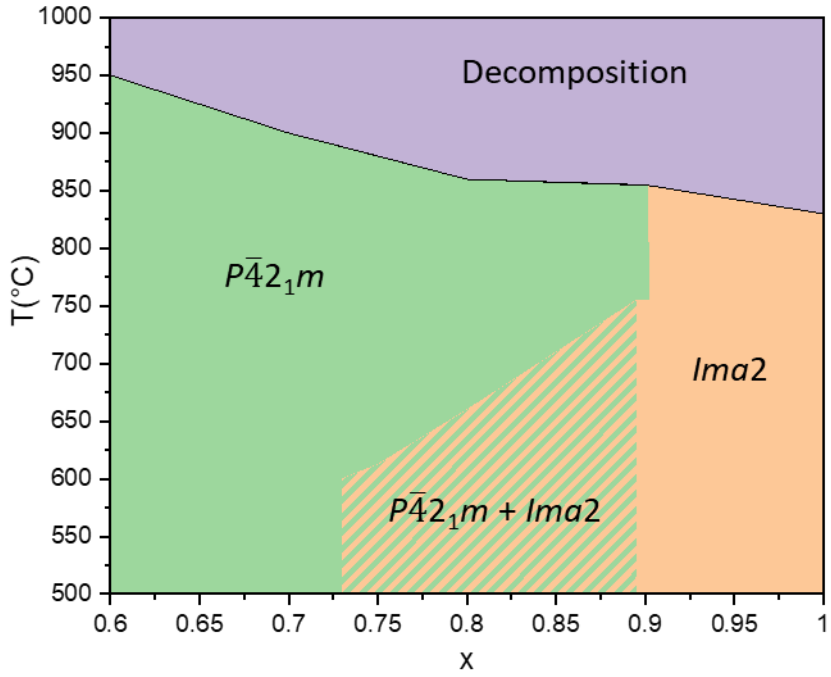

Figure IV.20. *Phase-diagram like plot of the $La_{1+x}Ba_{1-x}Ga_3O_{7+x/2}$ solid solution studied compositions, evidencing the polymorphs stability limits against x "amount of substituted barium" and temperature drown from VT-PXRD measurement. The transition temperatures from the mixed $P\bar{4}2_1m$ + Ima2 to fully $P\bar{4}2_1m$ in the 0.725 < x < 0.8 region were extrapolated from the measured x = 0.8 and 0.9 compositions. The x = 1 compound decomposition temperature was taken from [11].*

The tetragonal melilite was found to be no longer achievable phase pure by direct crystallisation from the melt starting x = 0.75 from $La_{1+x}Ba_{1-x}Ga_3O_{7+x/2}$ solid solution, as the O_{int} 1D ordered *Ima*2 melilite polymorph crystallises as a secondary phase, and forms at the expense of the $P\bar{4}2_1m$ smaller cell starting x = 0.9 composition. This means that its crystal structure is no longer stable for Ba substitution amounts higher than x = 0.9. In the melilite structures family, similar character was observed for the $La_{1+x}Ca_{1-x}Ga_3O_{7+x/2}$ solid solution, as when x values exceed 0.55 its crystal structure goes through a phase transition from $P\bar{4}2_1m$ to a pseudo-orthorhombic "trigonal" *P*1 cell, driven by the interstitial oxides ordering [5]. It is well known from the literature that the presence of interstitial oxide distorts its local environment pushing the edge-bridging oxygen atoms to the centroids of the five-neighbouring edge-sharing channels, yielding a satisfactory description of the bonding around this defect [5], [11] (i.e. BVS values around 2 for oxide). From the present $La_{1+x}Ba_{1-x}Ga_3O_{7+x/2}$ solid solution, as the La content increases, the O_{int} concentration also rises to keep charge compensation, which induces static disorder and distortions of its local environment. This is observed on the refined oxides ellipsoids directions (anisotropic displacement parameters), indicating a strong anharmonicity pointing toward adjacent $[GaO_4]_n$ pentagons centre (see Figure IV.16a, Figure

IV.16b, and Figure IV.16c). At a certain amount of Ba substitution for La (x = 0.9) the tetragonal cell is no longer capable of accommodating such amount of interstitial oxides in a disordered way while satisfying local bonding of the different O_{int}. Consequently, a structural transition occurs toward an orthorhombic melilite (S.G. *Ima*2) with ordered O_{int} network in a 1D corner sharing $[GaO_4]_5$ chains. With such ordering, the O_{int} local environment is better relaxed, hence causing less strain on the melilite $[GaO_4]_5$ infinite framework.

IV.4. AC Impedance measurements of $La_{1+x}Ba_{1-x}Ga_3O_{7+x/2}$ $0.5 \leq x \leq 09$ compositions.

The synthesised beads of $La_{1+x}Ba_{1-x}Ga_3O_{7+x/2}$ (x = 0.6, 0.7, 0.8 and 0.9) compositions were coarsely polished until a thickness of 1 mm was reached, while making sure that two parallel faces are secured. The disks were coated with gold paste and then sintered at 600°C for 30 min to eliminate the organic components present in the coating paste and ensure the formation of electrodes. Impedance spectroscopy measurements were then proceeded by Alberto José Fernández-Carrión at the university of Guilin in China, using a Solartron 1260 frequency response analyser over the 10^{-1}–10^{7} Hz frequency range and between 300°C to 800 °C temperatures each 50°C and a heating step of 6°C/min.

Figure IV.21 shows complex impedance plots of $La_{1.725}Ba_{0.275}Ga_3O_{7.3625}$ (x = 0.725) composition (i.e. the tetragonal melilite with highest amount of interstitial oxides) at different temperatures. At 300°C the complex impedance plot comprises a partial semicircle with associated capacitances of 10^{-12} F.cm^{-1}, indicative of bulk response [18], and a spike at lower frequencies with associated capacitance ranging from 10^{-11} to 10^{-8} F.cm^{-1}, gathering grain boundaries and electrode responses (Figure IV.21a and Figure IV.21b). Upon increasing temperature, the bulk semi-circle kept gradually getting smaller until it completely disappeared (at 350°C it is hardly discernible), while the electrode spike collapsed down, similar to other reported oxide conductors based on the melilite compounds [11] (Figure IV.21c). For T < 350°C the bulk resistance was extracted from the intercept of the fitted semi-circle at low frequencies. As of T ≥ 350°C, the bulk resistance was obtained from the data intercept at lower frequencies. The acquired data of $La_{1+x}Ba_{1-x}Ga_3O_{7+x/2}$ x = 0.5, 0.6, 0.7, 0.8, 0.9 compositions were analysed by the same process.

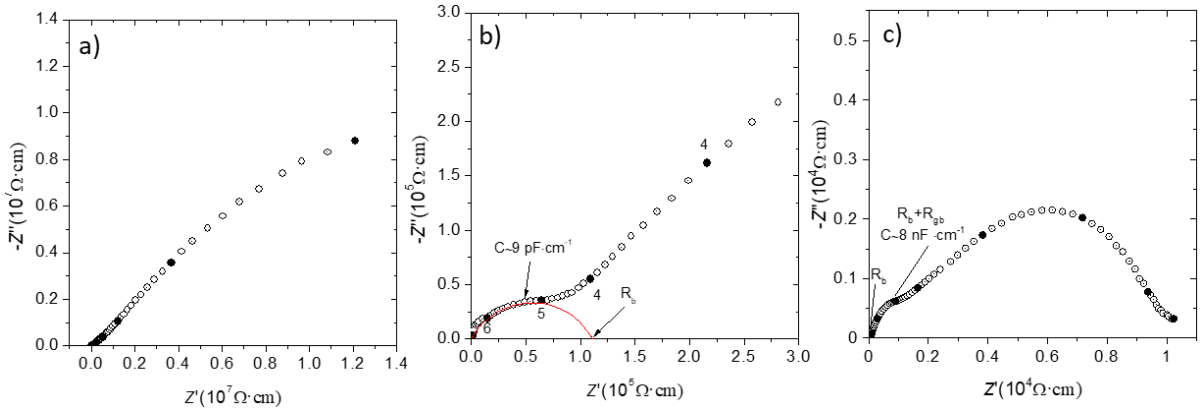

Figure IV.21. *Complex impedance plots acquired on the $La_{1.725}Ba_{0.275}Ga_3O_{7.3625}$ (x = 0.725) at 300°C in (a) and (b) panels, and 750°C in (c) panel. with (b) showing a zoom of (a) at low frequency evidencing the bulk semi-circle response.*

Arrhenius plots of the measured compositions are shown in Figure IV.22, with both $La_{1.54}Sr_{0.46}Ga_3O_{7.27}$ and $La_2Ga_3O_{7.5}$ compounds conductivity from [4], [11] overlaid for comparison. From this figure, the x = 0.6 sample exhibits the best conductivity (~ 10^{-2} S.cm^{-1}) for temperatures below 500°C, which gets slightly surpassed by the x = 0.7 composition at 500°C ≤ T, reaching 3.8×10^{-2} S.cm^{-1} at 700°C. Although these compositions exhibit high conductivity values at intermediate temperatures, they remain almost one order of magnitude lower than the best known $La_{1.54}Sr_{0.46}Ga_3O_{7.27}$ and $La_{1.64}Ca_{0.36}Ga_3O_{7.32}$ melilite ionic conductors, which display a 10^{-1} S.cm^{-1} value at 800°C. Moreover, one can notice that compounds which crystallise under the *Ima*2 structure or contain a substantial amount of the O_{int} ordered melilite polymorph (i.e. x = 0.8 and 0.9 compositions) possess lower conductivity values than the ones which crystallise under only the tetragonal $P\bar{4}2_1m$ melilite (i.e. x = 0.6 and 0.7 compounds). This is due to the interstitial oxide network difference in both polymorphs: the *Ima*2 melilite exhibits a 1D ordered O_{int} network along the *a* direction, which limits oxide diffusion to neighbouring channels in the *b* direction. In contrast with the tetragonal $P\bar{4}2_1m$ melilite, its O_{int} disordered network covers the whole 2D layered framework, which eases the charge carriers in the *ab*-plane. This argument is supplied by molecular dynamics calculations from [19], [20], which evidenced the 1D and 2D conduction mechanisms of both *Ima*2 and $P\bar{4}2_1m$ melilites, respectively. Furthermore, it appears that all measured samples feature a conductivity plateau (i.e. not evolving values) for temperatures higher than 500°C.

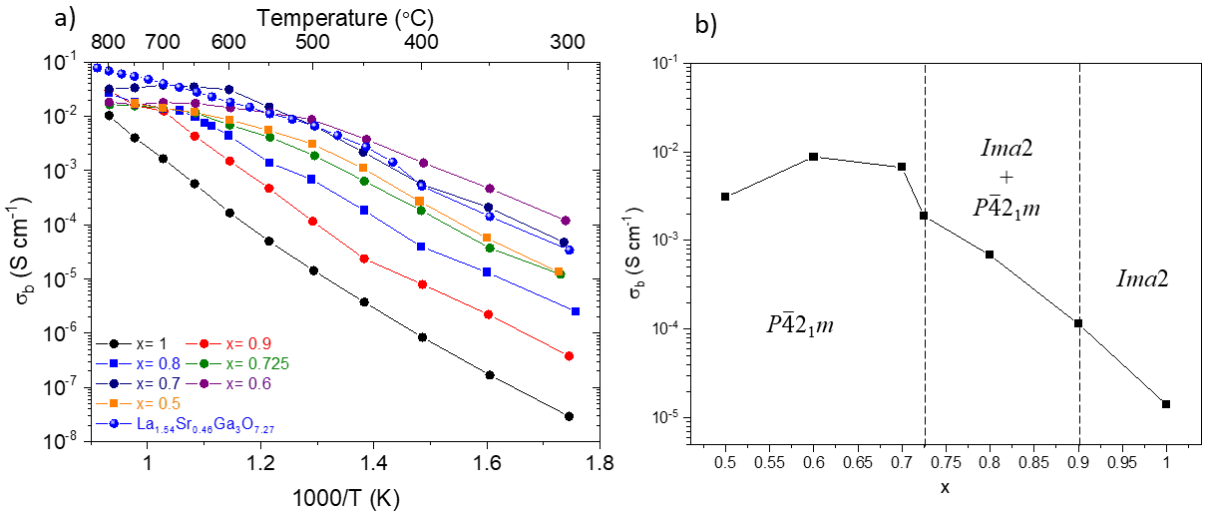

Figure IV.22. *a) Arrhenius plots of the measured $La_{1+x}Ba_{1-x}Ga_3O_{7+x/2}$ ($0.5 \leq x \leq 0.9$) compositions overlaid with $La_{1.54}Sr_{0.46}Ga_3O_{7.27}$ and $La_2Ga_3O_{7.5}$ compounds conductivity for comparison. The related activation energies are shown in Table A. 67 from Chapter A.IV in the appendices. b) Extracted conductivities of the measured solid solution compositions at 500°C as a function of x (O_{int} concentration), the vertical dashed lines represent the stability limits of each polymorph.*

This behaviour type could be related to several reasons: conduction mechanism change, phase transition, increase of the grain boundaries resistance or simply the maximum ion diffusivity was reached in these compositions as reported for several sodium ion conductors [21]–[23]. To test the phase transition hypothesis, the x = 0.6 sample was taken as a representative sample and measured by VT-PXRD with a thermal protocol replicating the AC impedance heating measuring procedure. Measurements were conducted on a freshly synthesised $La_{1.6}Ba_{0.4}Ga_3O_{7.3}$ (x = 0.6) sample, between RT and 800°C using a 50°C step/scan. In Figure IV.23 showing the measurement results, no phase transition or decomposition was observed, yet the only difference that can be noticed is the slightly broader Bragg diffraction peaks between the initial pre-heating and post-heating room temperature measurements. This could suggest a disturbed sample microstructure due the heating protocol. To investigate this, two new beads were synthesised, one was heated on a conventional open atmosphere furnace (also by replicating the AC impedance heating measuring procedure) while the other one was left as-synthesised. The two beads were optically polished and observed by scanning electron microscope (SEM). In Figure IV.24 showing both acquired images, EDX confirmed the grains composition matching the nominal; moreover, it was not possible to quantify the grain boundary compositions due to their thin domains (< 1µm). The first obvious observation from the SEM acquired images could be the slightly different contrast between the bulk and grain boundaries, as the later ones appears darker, hence possessing a lighter composition: poor in La/Ba elements. One can also notice the smaller grains (and correspondingly more grain boundaries) detected on the post heat treatment sample *vs* the as-synthesised one.

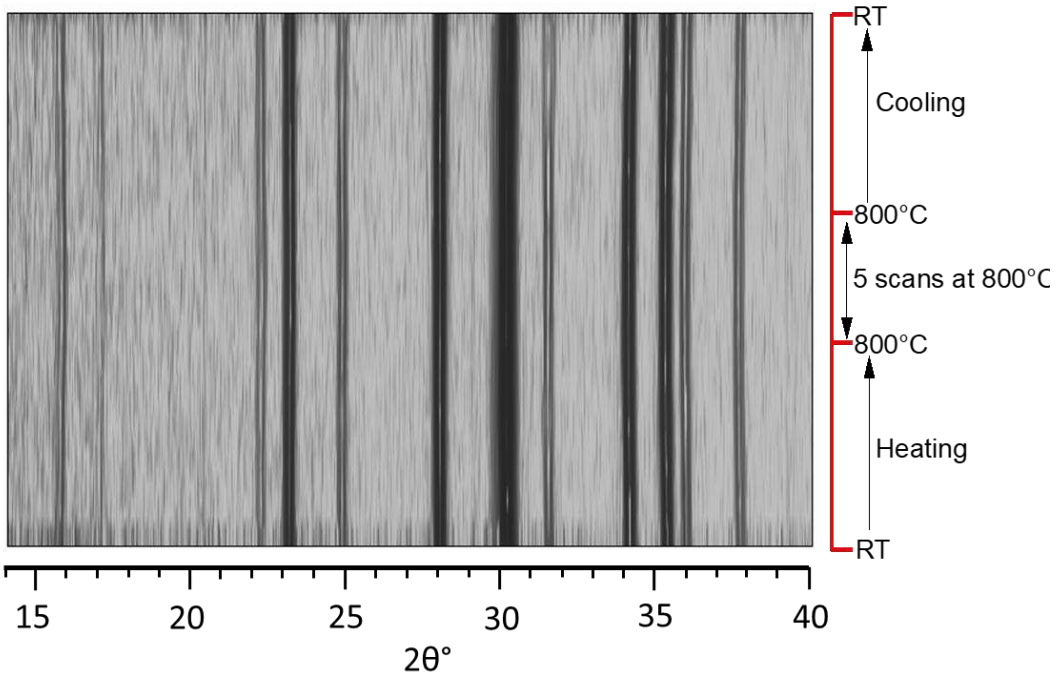

Figure IV.23. *VT-PXRD between RT and 800°C measurements of the $La_{1.6}Ba_{0.4}Ga_3O_{7.3}$ compound, using a step of 50°C/scan in the range of 14°-40°C (2θ) with a step of 0.016° and a measuring time of 1s/step. All measured diffraction patterns were indexed with the $P\bar{4}2_1m$ melilite cell.*

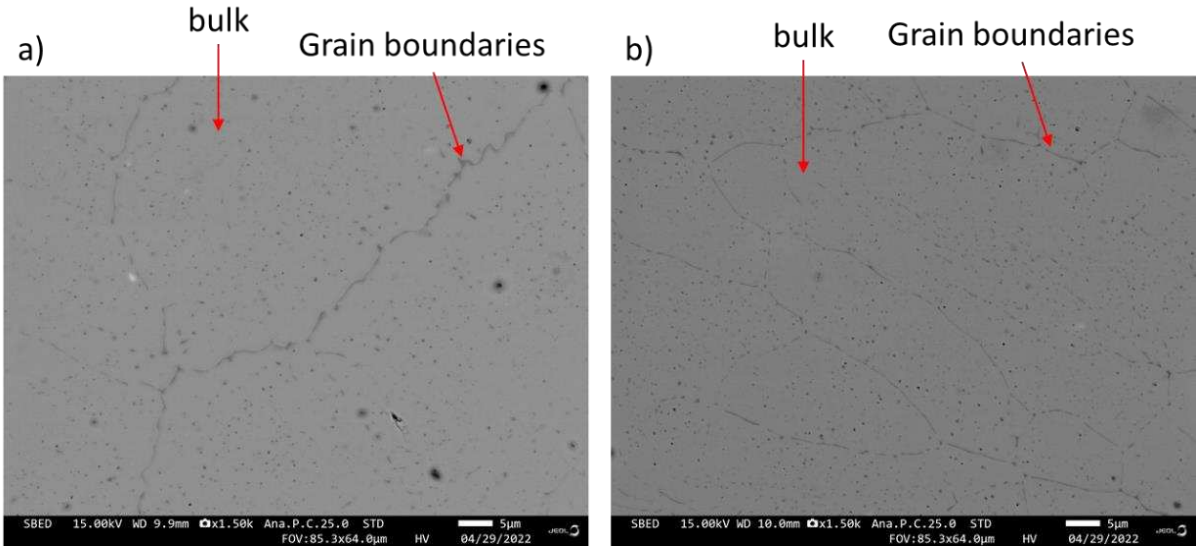

Figure IV.24. *SEM measurements on a) as-synthesised bead b) heat treated bead (replicating the AS-impedance measurement thermal protocol), in back scattered electron mode on beads of $La_{1.6}Ba_{0.4}Ga_3O_{7.3}$ composition. Both images are shown at the same enlargement scale.*

IV.5. Conclusion and perspectives.

The $La_{1+x}Ba_{1-x}Ga_3O_{7+x/2}$ solid solution synthesis was investigated in the present chapter. By using direct crystallisation of the melt as synthesis approach, the x limit previously set at x = 0.35 [6], was further extended to x = 0.9, with the x = 1 end member reported in [11]. Compositions of $La_{1+x}Ba_{1-x}Ga_3O_{7+x/2}$ ($0 \leq x \leq 0.35$) were reported to crystallise in the tetragonal $P\bar{4}2_1m$ melilite structure. In this study, from SPD data, this polymorph was shown to be further

retained until the Ba substitution amount by La reached the value of x = 0.725, hence making this composition the highest tetragonal O_{int} concentration containing melilite among the of $La_{1+x}AE_{1-x}Ga_3O_{7+x/2}$ *AE*= [Ca, Sr, Ba] melilite solid solution, and also the most interesting to characterise its conductivity. Higher substitution amounts exhibited the coexistence of two melilite types: tetragonal $P\bar{4}2_1m$ and orthorhombic *Ima*2 structures (for $0.75 \leq x \leq 0.85$). This is no longer the case for $La_{1.9}Ba_{0.1}Ga_3O_{7.45}$ (x = 0.9) composition as the orthorhombic *Ima*2 melilite was found as the only stable phase at room temperature, consistent with the previously reported $La_2Ga_3O_{7.5}$ melilite. This phase transition was linked to the inability of the small-cell tetragonal melilite to host high interstitial oxide concentration in a disordered way, while keeping satisfactory bonding conditions of all interstitial oxides, which was better seen in the anisotropic atomic displacement parameters of the O_{int} surrounding oxides. Local interstitial oxides environment relaxation was possible by the ordering of the O_{int} atoms along the *a* direction and among corner sharing five-membered $[GaO_4]_5$ network-forming pentagons. The ionic and cationic distribution was mapped by the help of NPD data collected at room temperature (for x = 0.3, 0.6, 0.7 0.8 and 0.9 compositions) and high temperature (for x =0.9 composition) among both $P\bar{4}2_1m$ and *Ima*2 melilites, which indicated a complete disorder of both A-site cations over their offered crystallographic sites, while no preference nor additional population of the interstitial oxides was found. This analysis was not possible to push further, as the refined errors of the used Ca pseudo-orthorhombic *P*1 model were very high. Finally, the bulk and total ionic conductivity of these samples was measured by AC impedance spectroscopy, and revealed a maximum value of 3×10^{-2} S.cm^{-1} for x = 0.7 at 700°C, which is within one order of magnitude of the best melilite conductor, i.e. $La_{1.54}Sr_{0.46}Ga_3O_{7.27}$ reaching a maximum value of 10^{-1} S.cm^{-1} at 800°C. The $La_{1.6}Ba_{0.4}Ga_3O_{7.2}$ (x = 0.6) compound on the other hand was found to be more conductive than the $La_{1.54}Sr_{0.46}Ga_3O_{7.27}$ melilite at lower temperatures ($300°C \leq T \leq 500°C$), however this is no longer the case for temperatures higher than 560°C as the $La_{1.54}Sr_{0.46}Ga_3O_{7.27}$ compound becomes more conductive due to the reached maximum conductivity plateau for the $La_{1.6}Ba_{0.4}Ga_3O_{7.2}$ (x = 0.6) melilite.

As perspectives for this work, the increase of doping limits in the $La_{1+x}AE_{1-x}Ga_3O_{7+x/2}$ *AE*= [Ca, Sr] melilite could be investigated by alternative synthesis approaches as shown in this Chapter (i.e. direct crystallisation from an under-cooled melt), or by other methods allowing to secure metastable phases as glass crystallisation or sol-gel synthesis, which might help extending the tetragonal phase stability to higher doping concentrations. From this study and

previously reported studies [4]–[6], [10], [11] it is clear that the melilite compounds are of interest in designing new conductive materials operating at intermediate temperatures.

IV.6. References.

[1] F.S. da Silva *et al.*, *International Journal of Hydrogen Energy*, 2017, **42**, 26020.

[2] M. Rozumek *et al.*, *Journal of the American Ceramic Society*, 2004, **87**, 1795.

[3] L. Zhou *et al.*, *The Chemical Record*, 2020, **20**, 1117.

[4] X. Kuang *et al.*, *Nature Materials*, 2008, **7**, 498.

[5] M.-R. Li *et al.*, *Angewandte Chemie International Edition*, 2010, **49**, 2362.

[6] J. Xu *et al.*, *Inorganic Chemistry*, 2017, **56**, 6897.

[7] F. Wei *et al.*, *Journal of Materials Chemistry A*, 2015, **3**, 3091.

[8] C. Tealdi *et al.*, *Advanced Functional Materials*, 2010, **20**, 3809.

[9] J. Schuett, T.K. Schultze, S. Grieshammer, *Chemistry of Materials*, 2020, **32**, 4442.

[10] C.I. Thomas *et al.*, *Chemistry of Materials*, 2010, **22**, 2510.

[11] J. Fan *et al.*, *Chemistry of Materials*, 2020, **32**, 9016.

[12] L. Zhao *et al.*, *Journal of Solid State Chemistry*, 2021, **302**, 122370.

[13] A.A. Coelho, *Journal of Applied Crystallography*, 2018, **51**, 210.

[14] P.W. Stephens, *Journal of Applied Crystallography*, 1999, **32**, 281.

[15] R.D. Shannon, *Acta crystallographica section A: crystal physics, diffraction, theoretical and general crystallography*, 1976, **32**, 751.

[16] J.M.S. Skakle *et al.*, *Powder Diffr.*, 1999, **14**, 8.

[17] V.F. Sears, *Neutron News*, 1992, **3**, 26.

[18] J.T.S. Irvine *et al.*, *Advanced Materials*, 1990, **2**, 132.

[19] C. Tealdi *et al.*, *Advanced Functional Materials*, 2010, **20**, 3874.

[20] L. Zhao *et al.*, *Journal of Solid State Chemistry*, 2021, **302**, 122370.

[21] T.J. Udovic *et al.*, *Chem. Commun.*, 2014, **50**, 3750.

[22] Y. Wang *et al.*, *Nano Materials Science*, 2019, **1**, 91.

[23] K. Yamashita, *Solid State Ionics*, 1989, **35**, 299.

Chapter V: Lanthanum Doping in the $Ca_5Ga_6O_{14}$ melilite-like Structures for New Oxide ion Conductors

V.1. Introduction.

Investigating compounds such as the melilites and melilite related structures for potential solid oxide fuel cell electrolyte materials operating at intermediate temperatures, is much of interest as stated in Chapters II and IV of this manuscript. In the CaO-Ga_2O_3 phase diagram two compositions were reported with a melilite-like framework, retaining similar $[GaO_4]_n$ framework features [1], [2]: $Ca_5Ga_6O_{14}$ and $Ca_3Ga_4O_9$. The first one is described below while the latter one is described in the appendices Chapter A.V.

The $Ca_5Ga_6O_{14}$ structure crystallises in an orthorhombic cell (S.G. *Cmc*2_1 n°36). It adopts a melilite-related structure, formed by two melilite-type $[GaO_4]_n$ sheets stacked along the *c*-axis with adjacent sheets related by a two-fold rotation about the *c*-axis (see Figure V.1). The structural calciums occupy three distinct sites accommodated between the layers,but only the Ca3 atoms are held in the melilite-like pentagonal channels centre, as due to the higher A/B cations ratio (4/5 *vs* 2/3 from the ABC_3O_7 melilite) and two-fold rotation between the framework sheets. The Ca1 and Ca2 atoms are displaced from their "ideal" melilite position to the edge of the framework-forming pentagonal channels (see Figure V.2).

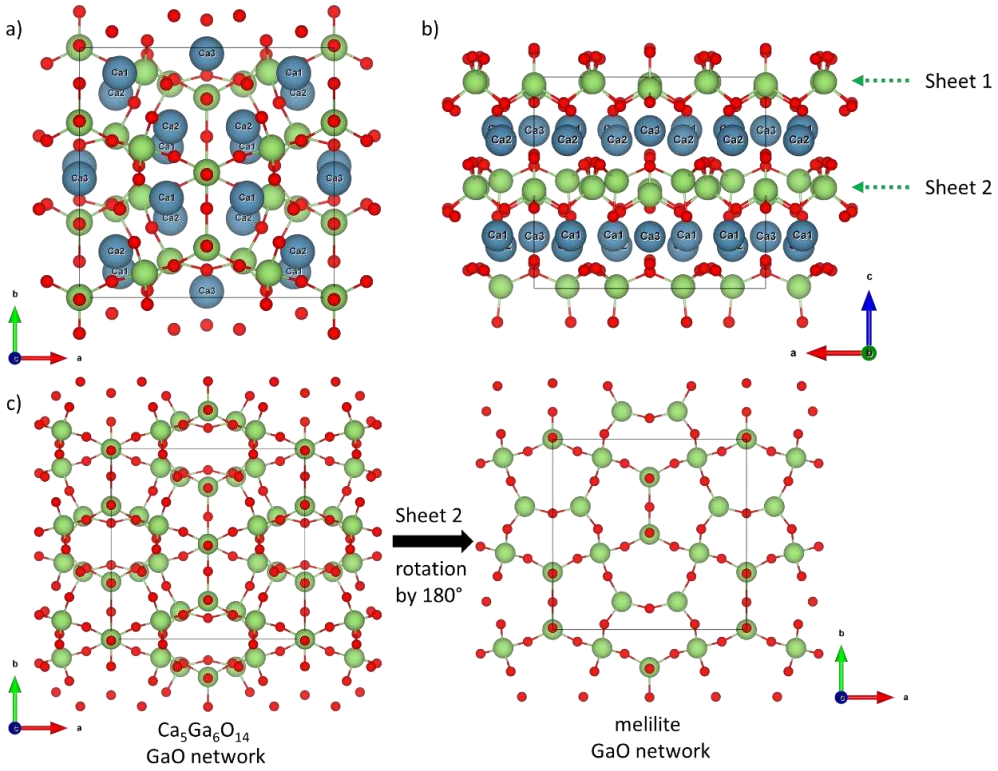

Figure V.1. *$Ca_5Ga_6O_{14}$ crystal structure projection within the c- and b-axis shown in a) and b) respectively, with blue, green and red spheres representing calcium, gallium and oxygen atoms respectively. Panel c) indicates the two-fold rotation relation between $[GaO_4]_n$ sheet 1 and 2 that leads to the melilite framework. Calciums were omitted for clarity.*

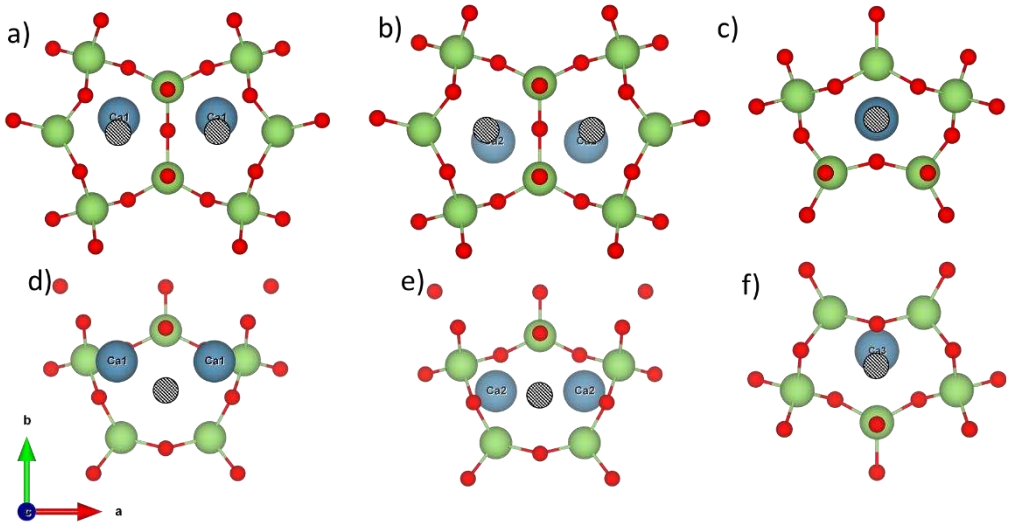

Figure V.2. *Positioning of the different A-sites in the $[GaO_4]_5$ framework pentagonal channels from sheet 1 (a, b and c panels) and sheet 2 (d, e and f panels) in the $Ca_5Ga_6O_{14}$ structure, compared to the "ideal" melilite A-site location represented by dashed black circles.*

Recent works on the two compounds described above and in the appendices chapter A.V reported these materials as potential phosphor hosts [3]–[5]. Moreover, their ionic conduction was also investigated without doping elements, which revealed promising conductivity values in the intermediate temperatures range [6], [7]. Furthermore, the oxide migration paths in both structures were explored by bond valence-based energy landscapes (BVELs) calculations [6], [7], disclosing the 2D and 3D conduction mechanisms in the $Ca_3Ga_4O_9$ and $Ca_5Ga_6O_{14}$ compounds respectively. Additionally, BVELs unveiled potential interstitial oxide positions which may improve the ionic conductivity when introduced as seen for the $La_{1+x}AE_{1-x}Ga_3O_{7+x/2}$ *AE*= [Ca, Sr, Ba] melilites [8]–[10].

This chapter will subject first identification of the energetically favourable aliovalent dopant by Ca or Ga substitution in the $Ca_5Ga_6O_{14}$ compound, synthesis and finding its dopant limits. A study of the doped and parent compounds crystal structures will be conducted by coupling synchrotron powder diffraction (SPD), neutron powder diffraction (NPD), transmission electron microscopy (TEM), density functional theory (DFT) for structural prediction, to achieve the most accurate possible description of their structures, especially to study the effect of the doping on the structure, i.e. if the charge compensation will occur by introducing cation vacancies or interstitial oxides. The $Ca_5Ga_6O_{14}$ compound was chosen instead of the $Ca_3Ga_4O_9$ due to its framework being formed by only edge sharing five-membered GaO_4 tetrahedra

(melilite-type sheet), compared to the latter one which contains a mixture of five-and four-membered GaO_4 rings, hence making the first compound the most melilite-like one.

V.2. Dopant prediction and synthesis.

V.2.1. Dopant prediction by energy calculations.

As mentioned in Chapter I, structural prediction with the help of computational methods were reported to be successful in narrowing the heavy task of synthesis exploration [11]–[13]. The following calculations were performed by Meigeng Gao and Matthew Dyer (University of Liverpool, UK). To predict the energetically favourable aliovalent dopant by Ca or Ga substitution in the $Ca_5Ga_6O_{14}$ compound, the Simdope code [14] was used to generate crystal structures according to the following substitutions:

- $Ca_{4.5}La_{0.5}Ga_6O_{14.25}$, $Ca_{4.5}Y_{0.5}Ga_6O_{14.25}$, i.e. two calcium atoms by two lanthanums or yttriums.
- $Ca_5Ga_{5.75}Nb_{0.25}O_{14.25}$, $Ca_5Ga_{5.5}Ge_{0.5}O_{14.25}$, i.e. one gallium by one niobium atom or two galliums by two germanium atoms.

The generated structures were relaxed and their related energies were calculated by DFT using the Vienna *ab*-initio Simulation Package (VASP) [15] programme. As shown in Figure V.3, Ca substitution by La or Nd atoms shows the lowest energies. However, Nd indicates a slightly higher structure energy ($\Delta E = 0.17ev$). Therefore, La was chosen as a dopant element and the investigated solid solution was then $La_xCa_{5-x}Ga_6O_{14+x/2}$ $0 \leq x \leq 5$.

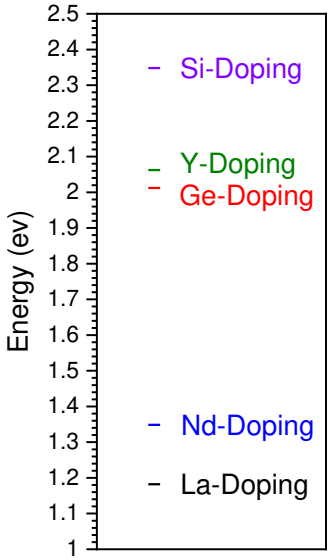

Figure V.3. *Calculated structures energies for each dopant in the $Ca_5Ga_6O_{14}$ compound.*

V.2.2. Solid-state reaction synthesis.

Stoichiometric amounts of La_2O_3 (STREM chemicals, 99.9% purity), CaO (STREM chemicals, 99.95% purity) and Ga_2O_3 (STREM chemicals, 99.998% purity), were weighted according to the nominal composition. The precursors were mixed in an agate mortar using ethanol for a better homogeneity of the mixture. The resulting powder was allowed to dry at 100°C in an open atmosphere laboratory oven for several minutes and pressed into pellets of 13 mm diameter. The pellet was placed in a platinum foil and fully covered with freshly made powder of the same composition; the covering powder acts as a "sacrificial powder", reducing Ga loss from the pellet sample during the heating process. The sample was fired at 1275°C for 48 hours in order to complete the synthesis [16]. The sacrificial powder was removed after the heating treatment by polishing the sample.

Laboratory X-ray diffraction was used to check the formed phase of the different synthesised compositions. On the stacked diffraction patterns of the different synthesised compositions (Figure V.4), compositions for which $0 \leq x \leq 0.25$ form phase pure samples that can be indexed with the $Ca_5Ga_6O_{14}$ phase. For $x > 0.25$ ($La_{0.25}Ca_{4.75}Ga_6O_{14.125}$) compositions, additional Bragg peaks were noticed in the acquired diffraction patterns, and their intensities kept rising as x values increased. These peaks were indexed as stoichiometric $LaCaGa_3O_7$ melilite (S.G. $P\bar{4}2_1m$ n°113) (see Figure V.4). To extract the cell parameters trend and approximate weight % of the crystallised impurities (for $x > 0.25$ compositions), Rietveld refinements were carried out using Topas (V6) [17]. In Figure V.5a, the cell parameters show a clear linear trend as *a* decreases while *b* and *c* increase, which leads to a small overall unit cell volume enlargement from 1361.00(4) $Å^3$ ($x = 0$) to 1362.10(4) $Å^3$ ($x = 0.25$). In the $0.25 < x < 1$ range, the cell parameters manifest a plateau, indicative of a $La_xCa_{5-x}Ga_6O_{14+x/2}$ solid solution limit at $x = 0.25$. This is supported by the growing amount of the $LaCaGa_3O_7$ secondary phase as the amount of lanthanum exceeds $x = 0.25$ (see Figure V.5b).

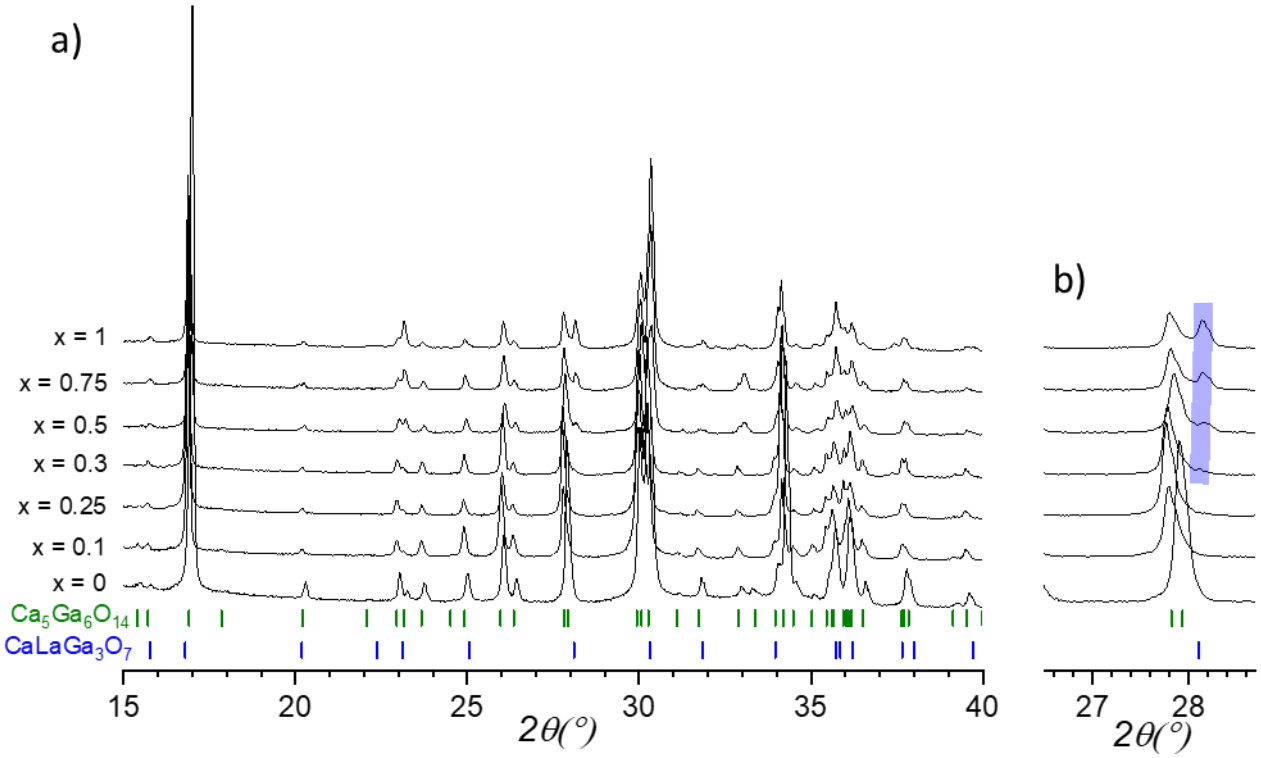

Figure V.4. *a) Stacked diffraction patterns of $La_xCa_{5-x}Ga_6O_{14+x/2}$ ($0 \leq x \leq 1$) samples synthesised by solid-state reaction, with their related indexations in green and blue representing the $Ca_5Ga_6O_{14}$ and $CaLaGa_3O_7$ respectively. b) Zoom on the 26.5°-28.7° (2θ) showing the $LaCaGa_3O_7$ melilite impurity peak arising from compositions with $x \geq 0.3$.*

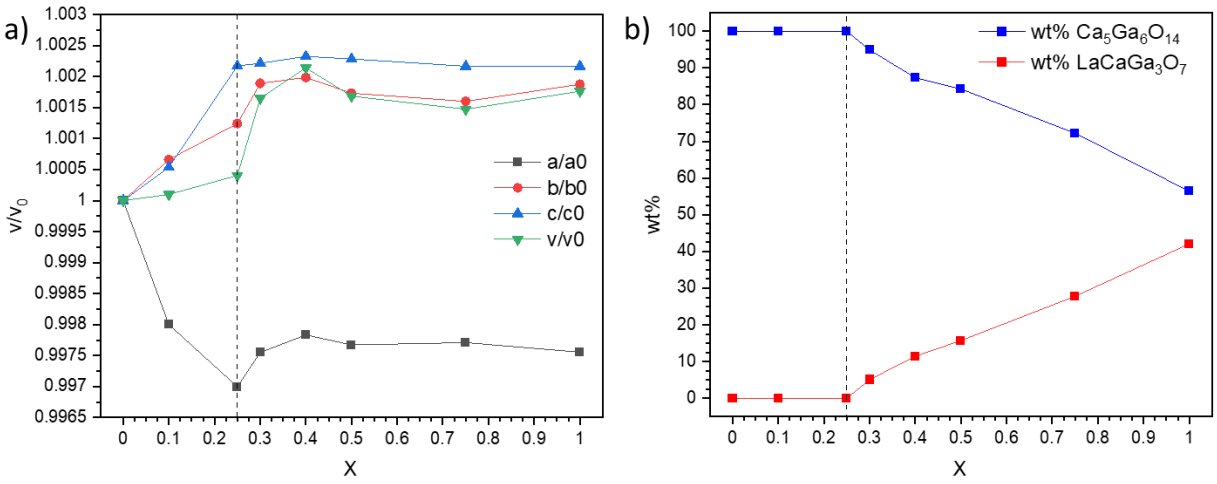

Figure V.5. *a) Normalised refined cell parameters of the $La_xCa_{5-x}Ga_6O_{14+x/2}$ ($0 \leq x \leq 1$) solid solution synthesised by solid-state reaction. b) extracted weight % of crystallised La-doped $Ca_5Ga_6O_{14}$ and $LaCaGa_3O_7$ from the $La_xCa_{5-x}Ga_6O_{14+x/2}$ ($0 \leq x \leq 1$) compositions. Vertical dashed lines in both panels indicates the x dopant limits.*

V.2.3. Attempts on extending the La-doping amounts by different synthesis routes.

To increase the dopant element concentration, i.e. to expend the x limit in the $La_xCa_{5-x}Ga_6O_{14+x/2}$ solid solution, full and congruent crystallisation from glass or undercooled melt was attempted as an alternative synthesis route, as demonstrated in previous studies [18]–[23]. To do so, the initially prepared mixture pellets were this time crushed to small chunks and melted using the ADL apparatus (described in the appendices Chapter A.I section A.I.1.1.2) [24], [25]. A pellet piece (~ 35mg) was levitated using Ar or O_2 gases, and heated using a pair of CO_2 lasers (10.6 µm) until the liquid state of the sample was reached at 1350°C. The levitating bead was either subsequently quenched by turning off the lasers to obtain glass samples, or slowly cooled to room temperature in 30 seconds by decreasing the lasers power to secure its crystallisation from the melt. A third procedure was also attempted by allowing the molten sample to touch the nozzle and turning the lasers off; the contact surface acts as a nucleation centre which leads to crystallisation of the whole bead.

Glass crystallisation attempts were unsuccessful as non-congruent crystallisation occurs from a $5CaO\text{-}3Ga_2O_3$ glass precursor, leading to mixture between $Ca_5Ga_6O_{14}$ and $Ca_3Ga_4O_9$ crystalline phases. The x = 0.3 ($La_{0.3}Ca_{4.7}Ga_6O_{14.15}$) glass material was measured first by VT-PXRD from 750°C to 1200°C using a step of 50°C/scan. In fact, Figure V.6 indicates a phase pure crystallisation of this sample at 800°C, and a decomposition starting around 900°C into $Ca_3Ga_4O_9$ + $LaCaGa_3O_7$. Nevertheless, hopes of increasing the concentration of La in the cell soon volatilised, since for the $La_{0.3}Ca_{4.7}Ga_6O_{14.15}$ (x = 0.3) ex-situ annealed glass sample at 800°C for 1 hour resulted in multi-phase crystallisation with both $LaCaGa_3O_7$ + $Ca_5Ga_6O_{14}$ phases present in the measured diffraction pattern (Figure V.7). Even by trying to optimise the conditions by decreasing the annealing temperature and time, the same two phases were present. Moreover, taking a closer and more careful look to the VT-PXRD data at 800°C, the Bragg peaks appear much broader than the solid-state synthesised samples, which can mask other phases contribution in small wt%. Direct crystallisation from the melt either by slowly cooling the sample or by contact with the nozzle were successful in achieving phase pure compounds all the way to x = 0.25. However, for x = 0.3 compounds this approach led to the crystallisation of a two phase material, with both $Ca_5Ga_6O_{14}$ and $LaCaGa_3O_7$ structures present (see Figure V.7).

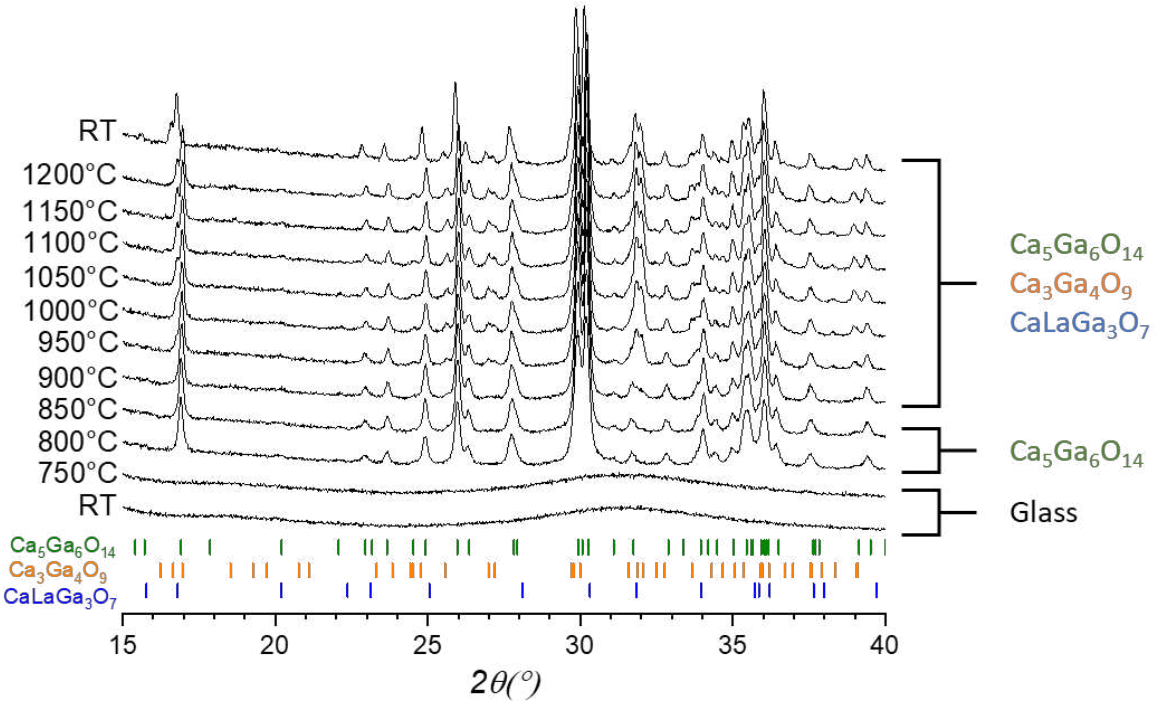

Figure V.6. *VT-PXRD measurements of $La_{0.3}Ca_{4.7}Ga_6O_{14.15}$ (x = 0.3) glass compounds between 750°C and 1200°C. The different crystallised phases are indicated by green, orange and blue tick marks, corresponding to the $Ca_5Ga_6O_{14}$, $Ca3Ga_4O_9$ and $CaLaGa_3O_7$ compounds respectively.*

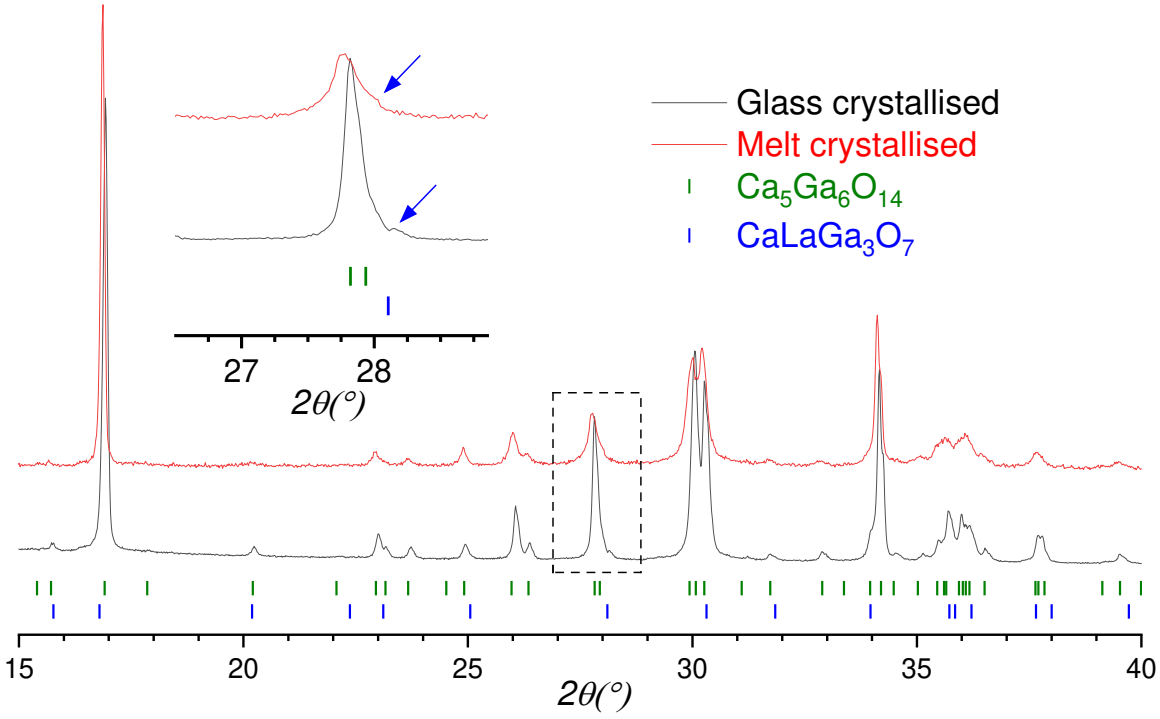

Figure V.7. *Acquired laboratory diffraction patterns of the $La_{0.3}Ca_{4.7}Ga_6O_{14.15}$ (x = 0.3) composition synthesised by glass crystallisation with an annealing treatment at 800°C for 1h (black line) and melt crystallised (red line) by slowly cooling the bead. The corresponding indexation are represented by green and blue tick marks. The insert shows an enlargement of the second $CaLaGa_3O_7$ melilite impurity peak indicated by a blue arrow.*

In a final attempt, sol-gel synthesis was considered to extend the amount of x in the $La_xCa_{5-x}Ga_6O_{14+x/2}$ solid solution. This approach was previously demonstrated to considerably extend the dopant concentration in the $La_3Ga_{5-x}Ge_{1+x}O_{14+x/2}$ langasite compounds from x = 0.3 to x = 1.5 [26]. Stoichiometric amounts of $La(NO_3)_3 \cdot 6H_2O$ (STREM chemicals, 99.99%), $Ga(NO_3)_3 \cdot 6H_2O$ (Alfa Aesar Puratronic, 99.99%) and $Ca(NO_3)_2 \cdot 4H_2O$ (STREM chemicals, 99%) were weighted according to the $La_{0.15}Ca_{4.85}Ga_6O_{14.075}$ compositions (as a test), and dissolved in deionised water. The mixture was constantly stirred and heated at 100°C while adding citric acid in a 3:1 molar ratio, ethylene glycol was added just after in 1:1 molar ratio with citric acid; the solution was kept stirred and heated for 16h until a gel was formed, the gel was then calcinated at 1000°C for 12h. The resulting powder was then heated at 1200°C for 2h to achieve crystallisation; this led to a multiphase sample as both $Ca_5Ga_6O_{14}$ and $Ca_3Ga_4O_9$ structures crystallised.

For the following characterisations, solid state reaction was chosen to synthesise both La-free and La-doped materials, as it had the sharpest Bragg diffraction peaks compared to the other crystallisation approaches.

V.3. Structural determination and analysis.

V.3.1. Purity and composition verification.

The synthesised $La_xCa_{5-x}Ga_6O_{14+x/2}$ x = 0 and x = 0.25 samples purities were checked by laboratory PXRD as they were both fully indexed with the $Ca_5Ga_6O_{14}$ structure. The samples were then subject of a composition verification by electron microprobe analysis. First, freshly synthesised samples in the form of pellets were coarsely polished to remove the covering sintered sacrificial powder. An optical quality polishing was then applied, and finally a conducting carbon layer was deposited on the freshly polished surface. As shown in Figure V.8a and Figure V.8b, imaging in backscattered electron (BSE) mode, a clear contrast between black and grey domains can be noticed. Here, the black regions represent holes / porosity in the sample and can also be induced from grain detachment during the polishing process. Moreover, the measured atomic percentage of Ca, Ga and La in both $La_xCa_{5-x}Ga_6O_{14+x/2}$ x = 0 and x = 0.25 compounds are in good agreement with the theoretical nominal values (Figure V.8c and Figure V.8d): $Ca_{5.07(4)}Ga_{5.94(3)}O_{14}$ measured *vs* $Ca_5Ga_6O_{14}$ nominal for x = 0, and $La_{0.25(1)}Ca_{4.80(3)}Ga_{6.0(3)}O_{14.125}$ measured *vs* $La_{0.25}Ca_{4.75}Ga_6O_{14.125}$ nominal for x = 0.25. Furthermore, the La-doped compound shows a nice constant La atomic % variation across the measured points. However, this is not the case for Ca and Ga cations, as the measured atomic

% varies much more than La across the different measuring points. In fact, this could be a matter of sample homogeneity at the pellet surface, i.e. residual sacrificial powder.

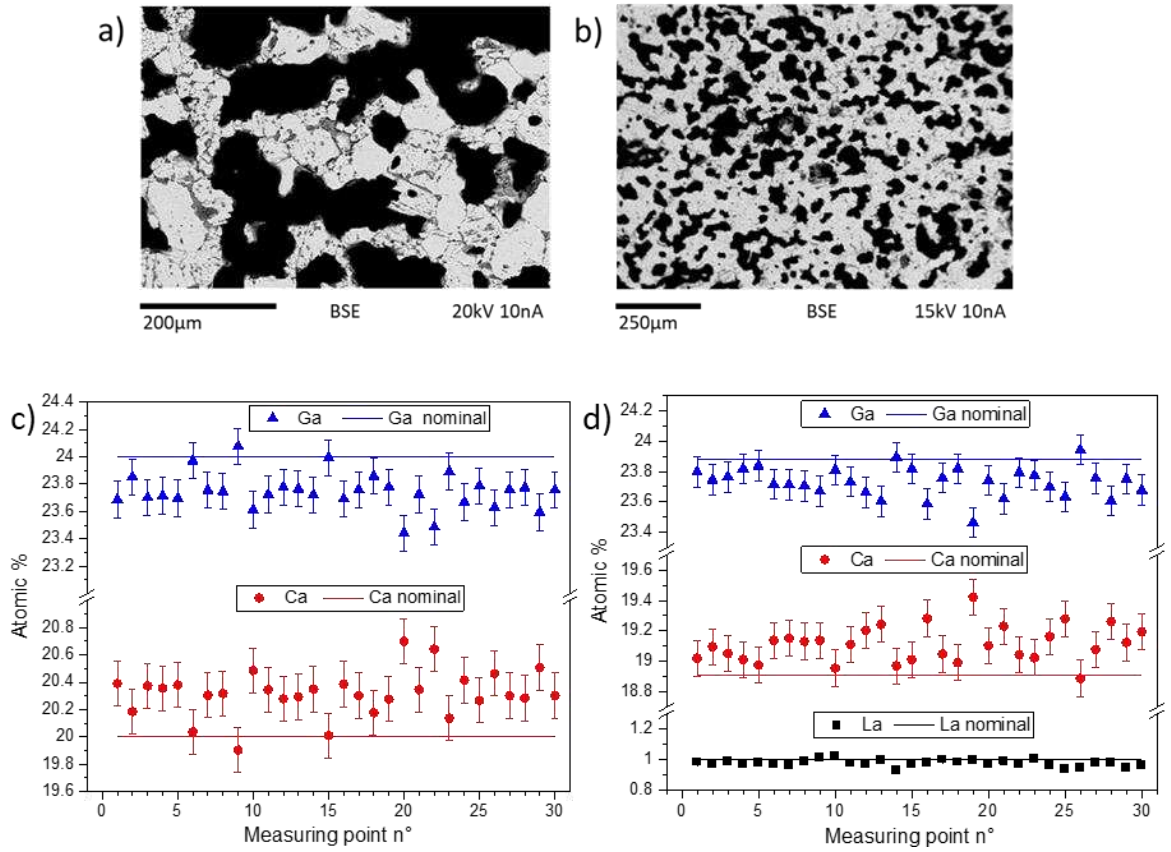

Figure V.8. *a), b) SEM imaging in backscattered electron (BSE) mode of both* $La_xCa_{5-x}Ga_6O_{14+x/2}$ *x = 0 and x = 0.25 samples respectively. c) and d) microprobe measured Ca, Ga and La content in both x = 0 and x = 0.25 compositions.*

V.3.2. SPD data analysis.

To first locate the La atom positions in the doped $Ca_5Ga_6O_{14}$ structure, synchrotron X-ray powder diffraction (SPD) measurements were conducted on both $La_xCa_{5-x}Ga_6O_{14+x/2}$ x = 0 and x = 0.25 in Soleil synchrotron at the CRISTAL beamline, with an incident wavelength of λ = 0.67153 Å. The powders were first independently diluted in amorphous SiO_2 powder according to a 1:3 wt% ratio to reduce beam absorption, filled in 0.3mm diameter quartz capillaries then measured.

A first indexation of both SPD patterns indicated that both samples are not phase pure as suggested by prior lab PXRD measurements. The x = 0 sample showed some low intensity additional Bragg peaks that could not be indexed. This impurity could originate from the sample dilution preparation, as it was not present in prior lab PXRD measurements. The x = 0.25 compound on the other hand showed the presence of CaO secondary phase, one explanation

could be the formation of CaO due to gallium evaporation during the initial synthesis process. The amount of CaO was later quantified at 0.56% (wt%).

A first constraint-free Rietveld refinement of the acquired SPD data was performed using Topas (V6) program [17]. For x = 0, with a total of 87 independently refined parameters, the refinement led to satisfactory reliability factors, with R_{wp}= 2.20%, GOF= 3.45 (see Figure V.9a for refined plot and Table V.1 for refined structural parameters). SPD data of the x = 0.25 composition was first refined with no La substitution to the $Ca_5Ga_6O_{14}$ crystal structure (87 independently refined parameter). Clear intensity misfits were observed on the refined plot, and made it obvious that something is missing from the cell. Lanthanum was then introduced in all three calcium sites with constrained occupancies of each mixed site to add up to 1, increasing the total number of refined parameters to 100. The constraint was defined in Topas as follows:

OccLa1*= 1-OccCa1 / OccLa2= 1-OccCa2 / OccLa3= 1-OccCa3

The addition of lanthanum in the cell dropped the reliability factors from R_{wp}= 2.27%, GOF= 3.58 to R_{wp}= 1.83%, GOF= 2.88. Refined La occupancies displayed its distribution over only Ca1 and Ca3 channels, as the Ca2 occupancy converged to 0.998(3). A third and final Rietveld refinement was conducted with fixed Ca2 occupancy at 1, while freely refining the La content in Ca1 and Ca3 sites (89 refined parameter). Comparing the A-sites refined occupancies [0.990(3)Ca1/0.010(3)La1 - 1Ca2/0La2 - 0.756(4)Ca3/0.244(4)La3], the disorder between Ca and La elements occurs mainly on Ca3 channels. Considering the refinement errors, Ca1 is effectively a single cation site holding only Ca atoms. See Figure V.9b for refined plot and Table V.2 for refined structural parameters. Calculating the atomic % of both La and Ca from the identified site occupancies by the Rietveld method against x = 0.25 SPD data, resulted in 1.051(5)% for La and 18.850(5)% for Ca, which is consistent with the nominal composition (0.995% La, 18.905% Ca). From these refinement results, the near-absence of CaO or other Ca-rich secondary phases and the microprobe analysis confirming the nominal composition stoichiometry, the hypothesis of charge compensation on the La-doped introduction of cation vacancies can be ruled out, which leave the second one: introduction of interstitial oxides, to be studied.

** the OccXn notation means occupation of atom X in site number n*

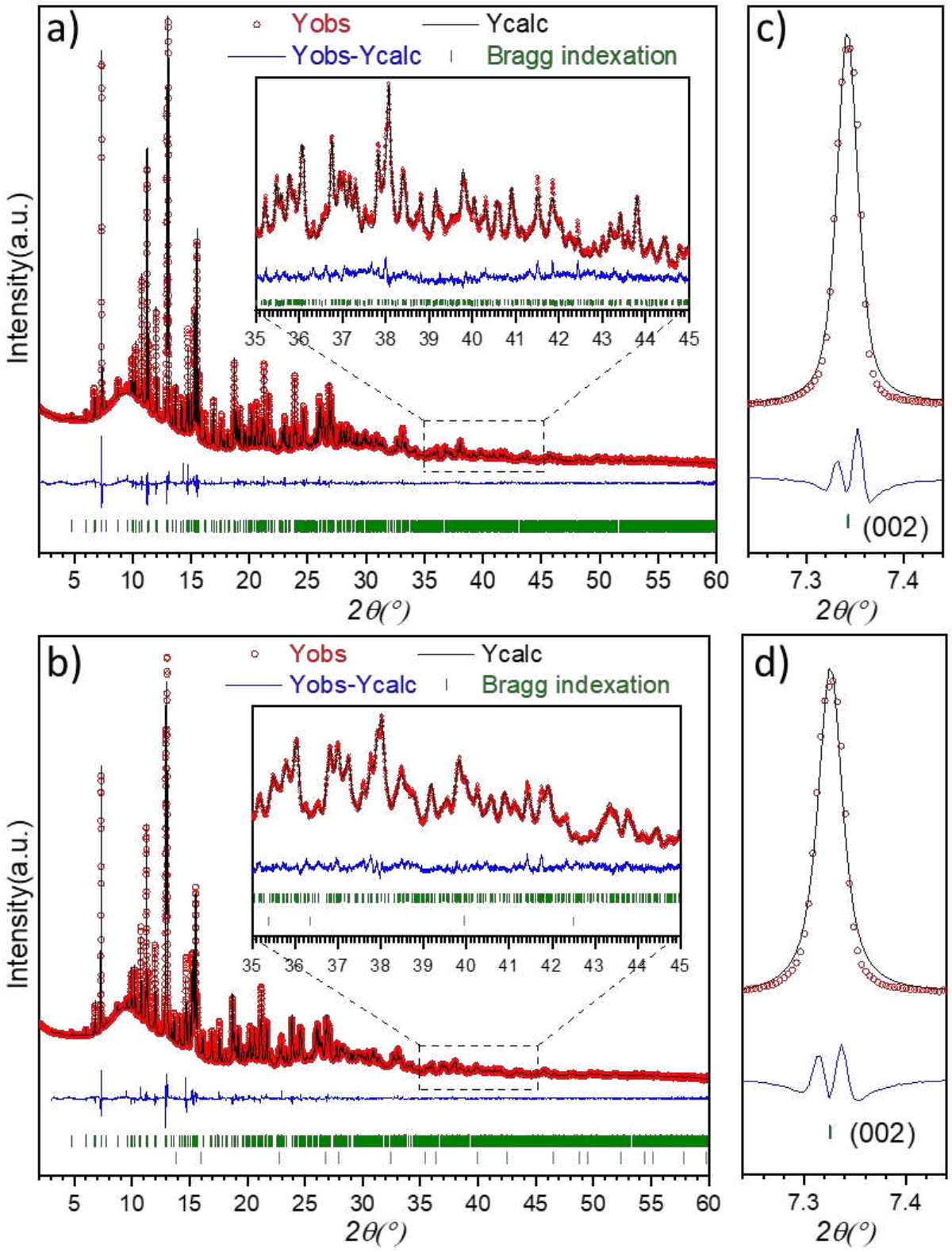

Figure V.9. *Final Rietveld refined SPD data of a) $Ca_5Ga_6O_{14}$ (x = 0) (R_{wp}= 2.06% GOF= 3.23), and b) $La_{0.25}Ca_{4.75}Ga_6O_{14.125}$ (x = 0.25) (R_{wp}= 1.67% GOF= 2.63). c) and d) shows a zoom on the (002) peak which exhibits the first biggest misfit.*

Table V.1. Refined structural parameters obtained from SPD data collected at room temperature on $Ca_5Ga_6O_{14}$. (x = 0) (*Cmc*2$_1$ space group, *a*= 11.47246(14) Å, *b*= 11.29197(14) Å and *c*= 10.50904(14) Å) sample.

Atom	Wyck	x	y	z	Occ	B_{iso}
Ca1	8b	0.1581(2)	0.1023(2)	0.25	1	0.44(5)
Ca2	8b	0.3570(2)	0.31652(19)	0.2004(3)	1	0.54(5)
Ca3	4a	0	0.5248(3)	0.2448(4)	1	0.35(8)
Ga1	8b	0.35656(9)	0.14580(12)	0.5088(3)	1	0.27(3)
Ga2	4a	0	0.30107(15)	0.4422(3)	1	0.33(4)
Ga3	4a	0	-0.00041(15)	0.4644(3)	1	0.51(4)
Ga4	8b	0.24473(12)	0.40228(10)	0.4764(3)	1	0.30(2)
O1	8b	0.2842(6)	0.2793(6)	0.5855(7)	1	0.13(5)[a]
O2	4a	0	0.6104(8)	0.5776(9)	1	0.13(5)[a]
O3	8b	0.2665(7)	0.0277(5)	0.5955(7)	1	0.13(5)[a]
O4	8b	0.3722(7)	0.4361(6)	0.3773(7)	1	0.13(5)[a]
O5	4a	0	0.1437(9)	0.3805(9)	1	0.13(5)[a]
O6	8b	0.3415(5)	0.1463(6)	0.3408(7)	1	0.13(5)[a]
O7	4a	0	0.0080(8)	0.6334(11)	1	0.13(5)[a]
O8	8b	0.1285(6)	0.3726(6)	0.3621(7)	1	0.13(5)[a]
O9	4a	0	0.2944(8)	0.6167(10)	1	0.13(5)[a]

[a]Constrained to refine to a common value

Table V.2. Refined structural parameters obtained from SPD data collected at room temperature on $La_{0.25}Ca_{4.75}Ga_6O_{14.125}$ (x = 0.25) (*Cmc*2$_1$ space group, *a*= 11.47670(8) Å, *b*= 11.29646(11) Å and *c*= 10.51206(10) Å) sample.

Atom	Wyck	x	y	z	Occ	B_{iso}
Ca1/La1	8b	0.1614(3)	0.1031(2)	0.25	0.990(3)/0.010(3)	1.52(8)
Ca2	8b	0.3559(3)	0.3218(2)	0.2001(4)	1	1.16(6)
Ca3/La3	4a	0	0.5223(2)	0.2412(3)	0.756(4)/0.244(4)	0.90(8)
Ga1	8b	0.35621(9)	0.14654(12)	0.5097(3)	1	0.38(3)
Ga2	4a	0	0.29818(16)	0.4415(3)	1	0.36(4)
Ga3	4a	0	0.00029(15)	0.4649(3)	1	0.37(4)
Ga4	8b	0.24453(12)	0.40138(10)	0.4767(3)	1	0.31(2)
O1	8b	0.2814(6)	0.2810(6)	0.5849(8)	1	0.37(5)[a]
O2	4a	0	0.6236(8)	0.5781(10)	1	0.37(5)[a]
O3	8b	0.2725(7)	0.0238(5)	0.5988(8)	1	0.37(5)[a]
O4	8b	0.3692(7)	0.4370(6)	0.3835(8)	1	0.37(5)[a]
O5	4a	0	0.1399(10)	0.3683(10)	1	0.37(5)[a]
O6	8b	0.3457(6)	0.1476(7)	0.3462(8)	1	0.37(5)
O7	4a	0	0.0091(9)	0.6331(12)	1	0.37(5)[a]
O8	8b	0.1242(6)	0.3707(7)	0.3572(7)	1	0.37(5)[a]
O9	4a	0	0.2982(8)	0.6112(11)	1	0.37(5)[a]

[a]Constrained to refine to a common value

V.3.1. STEM-HAADF imaging, EDX and EELS mapping of $La_xCa_{5-x}Ga_6O_{14+x/2}$ x = 0.25 compounds.

Powder samples of x = 0.25 composition were finely ground and dispersed in ethanol, a droplet of the mixture was deposited on a TEM copper grid layered by an amorphous holey carbon film. HRTEM (High resolution TEM) images have revealed low disorientations of nanodomains within a single crystal grain, as indicated by the perceived stretched diffracted

spots in the SAED (selected area electron diffraction) pattern shown in Figure V.10. It was therefore difficult to find a perfectly oriented large enough area to conduct the measurements on. Moreover, STEM-HAADF images were acquired along the [001] and [010] directions (see Figure V.1a and Figure V.1b for the structural projection along this two directions respectively, and Figure V.11a and Figure V.12a for the STEM-HAADF acquired images). Along these orientations, the visualised structure is a 2D projection where each observed atom actually represents a column of atoms, with heaviest ($\bar{Z}$) or denser atomic columns appearing brighter. A first observation of the STEM-HAADF images along the [001], which allows to compare the Ca1, Ca2 and Ca3 spots intensities, show more intense Ca3 spots (indicated by orange arrows in Figure V.11a) compared to the almost invisible Ca1 and Ca2 spots (indicated by red arrows in Figure V.11a). Knowing that the Ca1/Ca2 and Ca3 atom columns have the same electron density, this informs us of heavier atoms present in the Ca3 sites, consistent with the refined La occupancies on that site. The plotted Z profile from both directions indicates a higher intensity for Ca3 channels (Figure V.11b and Figure V.12b), which could be the consequence of more La introduced in the Ca3 sites as opposed to Ca1/Ca2 sites, supporting the previous analysis and results. However, this could also be the result of channelling affects arising from nearby Ca1/Ca2 sites with small Ca3-cation bond lengths. The latter explanation is more relevant for the [010] direction as the distances of Ca3-cation (first neighbours) are much more longer along the [001]: $d(Ca3\text{-}cation)_{min}$= 2.028(3) Å *vs* 1.709(5) Å in the 2D projection along the [001] and [010] respectively. To complete this analysis, Energy dispersive X-ray (EDX) mapping at the atomic scale was performed along the [001] direction to better illustrate the La dispersion over the different calcium sites. However, due to the sample degradation under the beam and poor orientation regions (disoriented nanodomains), the best maps were acquired over 20 min of tracking and changing zones (Figure V.11c). In this figure, it can be seen that the La signal is focused mainly on the Ca3 sites. Moreover, electron energy loss spectroscopy (EELS) was performed along the [010] direction, as shown in Figure V.13. It appears that La signal is more present in the Ca3 channels with no strong evidence of being also held in the Ca1/Ca2 channels. Both these results from EDX atomic mapping and EELS profiles are consistent with the refined La disorder from SPD data, as most of the La goes to the Ca3 sites.

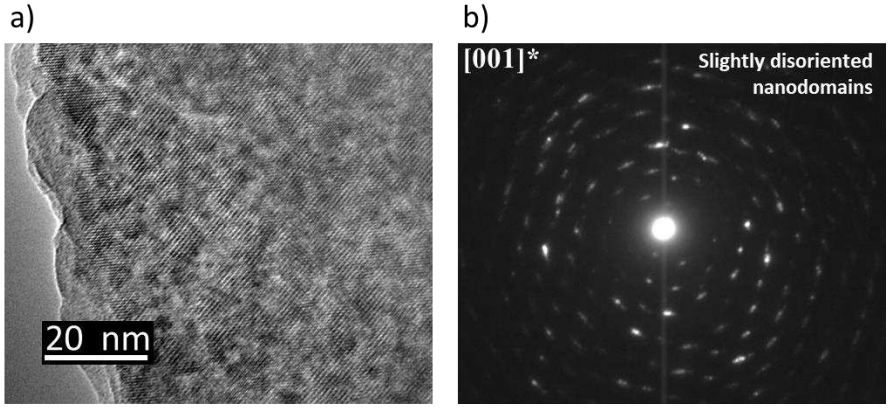

Figure V.10. *a) HRSTEM image of a $La_{0.25}Ca_{4.75}Ga_6O_{14.125}$ (x = 0.25) oriented crystal along the [001] direction, evidencing the low nanodomains disorientations. b) Selected area electron diffraction (SAED) pattern of a grain oriented along the [001] direction and showing peak streaks indicative of low disoriented nanodomains organisation.*

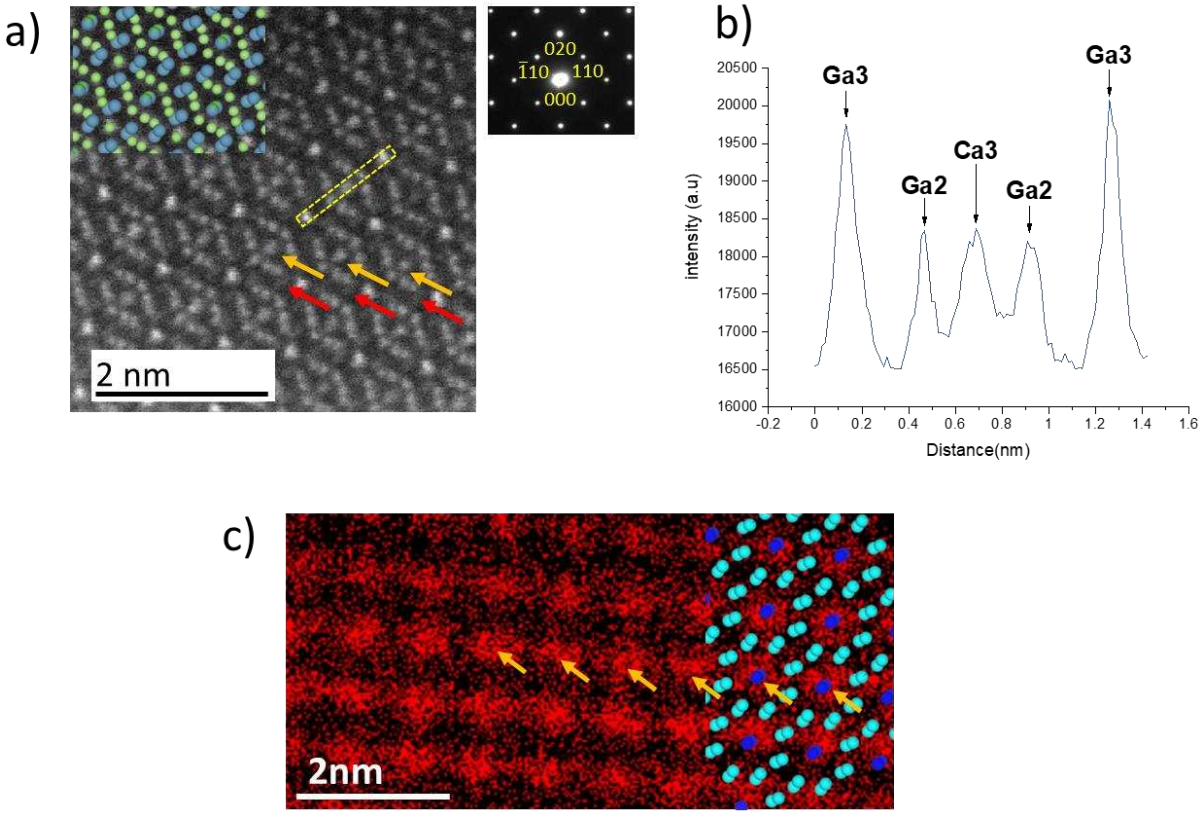

Figure V.11. *a) High resolution STEM-HAADF image of $La_{0.25}Ca_{4.75}Ga_6O_{14}$ (x = 0.25) sample oriented along the [001] (see Figure V.1a for its related crystal structure projection). The crystal related SAED is shown on the top right insert while the top left insert shows an overlay of the structure. b) the drawn Z profile from the integrated area highlighted by yellow rectangle in (a). c) STEM-EDX map of La overlaid with the calcium network, with light and dark blue spheres representing Ca/Ca2 and Ca3 atoms respectively. In panel (a) orange and red arrows indicate the Ca3 and Ca1/Ca2 sites respectively, while in panel (c) only orange arrows are shown to indicate Ca3 positions.*

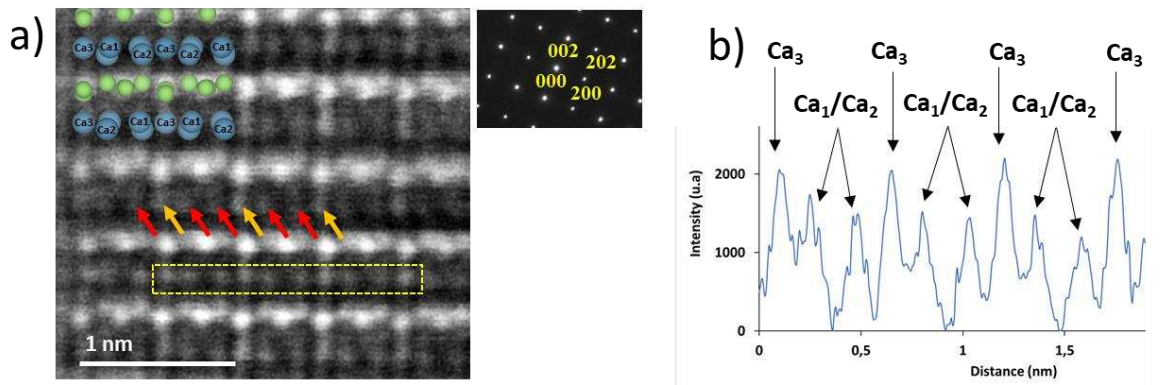

Figure V.12. *a) High resolution STEM-HAADF image of $La_{0.25}Ca_{4.75}Ga_6O_{14}$ (x = 0.25) sample oriented along the [010] (see Figure V.13b for its related crystal structure projection). The crystal related SAED is shown on the top right insert while the top left insert shows an overlay of the structure. Orange and red arrows indicate the Ca3 and Ca1/Ca2 sites. b) the drawn Z profile from the integrated area highlighted by yellow rectangle in (a).*

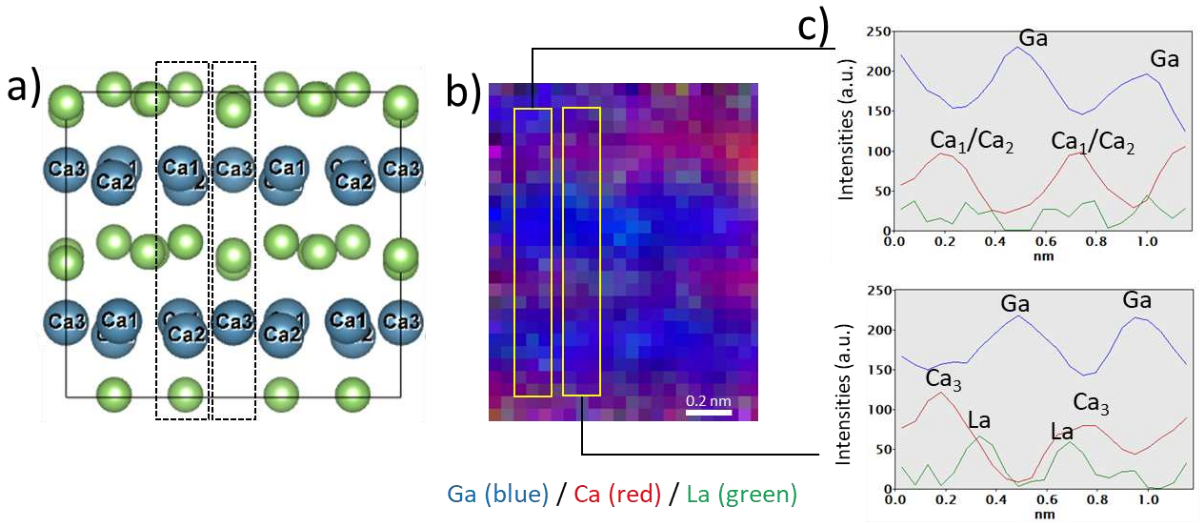

Figure V.13. *a) Structural projection of the $La_{0.25}Ca_{4.75}Ga_6O_{14.125}$ compound along the [010] direction. b) EELS map of Ca, Ga and La of a crystal oriented along the [010]. c) the extracted profiles of each element from two different regions in (b) and shown in (a).*

V.3.2. NPD data analysis.

To keep a charge balanced composition in the La-doped $Ca_5Ga_6O_{14}$, introduction of cation vacancies or O^{2-} anions are needed. The first hypothesis was quickly eliminated as no Ca- nor Ga-rich secondary phases was found and no clear evidence of vacancies was found from the cation occupancy refinements (Ca and Ga) on SPD data, in addition to the microprobe-quantified composition lying very close the nominal one. To test the second and most probable possibility, neutron powder diffraction (NPD) data were acquired against both $La_xCa_{5-x}Ga_6O_{14+x/2}$ x = 0 and 0.25 compositions. Approximately 5 g (from the same SPD measured batches) of each composition was loaded into in vanadium containers (10 mm diameter) and

sent to the ILL laboratory; NPD measurements were then conducted on the D2B beamline with an incident wavelength of λ= 1.594 Å over the 2 -160° (2θ) angular region. Both high intensity "HI" and high resolution "HR" NPD data sets were independently refined by the Rietveld method. The x = 0 compound NPD refinement plots are shown in Figure V.14a and Figure A. 34a in the appendices Chapter A.V, while the structural parameters are reported in Table V.3 and Table A. 70 in the appendices Chapter A.V. On the other extreme of the solid solution, the x = 0.25 composition, a first analysis of the refined structural parameters indicates a lower La content from both data sets (see Table A. 74). In comparison with the La content obtained from SPD data, this difference can be explained by the bigger scattering contrast between Ca and La atoms on X-ray diffraction (Z_{Ca}= 20 *vs* Z_{La}= 57) compared to neutron diffraction (Ca b_c= 4.10(2) fm *vs* La b_c= 8.24(4) fm) [27]. Refinement of NPD data were run, this time with the La content being subject of constraints, refining to values close to the nominal composition by the use of a penalty function (see Figure V.14b and Figure A. 34b in the appendices Chapter A.V for refined plot and Table V.4 and Table A. 71 in the appendices Chapter A.V for refined structural parameters) (see also Table A. 74).

Table V.3. Final Refined structural parameters obtained from NPD (HR) data collected at room temperature on $Ca_5Ga_6O_{14}$ (x = 0) (*Cmc*2$_1$ space group, *a*= 11.50417(11) Å, *b*= 11.27557(10) Å and *c*= 10.48616(10) Å) sample.

Atom	Wyck	x	y	z	Occ	Biso
Ca1	8b	0.1585(4)	0.1018(3)	0.25	1	0.55(6)
Ca2	8b	0.3576(4)	0.3159(3)	0.2033(6)	1	0.59(7)
Ca3	4a	0	0.5248(5)	0.2455(7)	1	0.77(11)
Ga1	8b	0.3557(2)	0.1466(2)	0.5102(5)	1	0.14(4)
Ga2	4a	0	0.2992(3)	0.4429(5)	1	0.15(6)
Ga3	4a	0	-0.0008(3)	0.4667(5)	1	0.32(7)
Ga4	8b	0.2449(2)	0.4023(2)	0.4789(5)	1	0.11(4)
O1	8b	0.2850(3)	0.2776(3)	0.5858(5)	1	0.47(5)
O2	4a	0	0.6163(4)	0.5752(6)	1	0.74(8)
O3	8b	0.2678(3)	0.0272(3)	0.5942(6)	1	0.56(6)
O4	8b	0.3730(3)	0.4352(3)	0.3817(6)	1	0.34(5)
O5	4a	0	0.1455(4)	0.3831(6)	1	0.45(7)
O6	8b	0.3396(2)	0.1495(3)	0.3384(5)	1	0.32(5)
O7	4a	0	0.0083(4)	0.6393(7)	1	0.67(8)
O8	8b	0.1271(3)	0.3733(3)	0.3667(6)	1	0.71(6)
O9	4a	0	0.2987(4)	0.6154(6)	1	0.51(9)

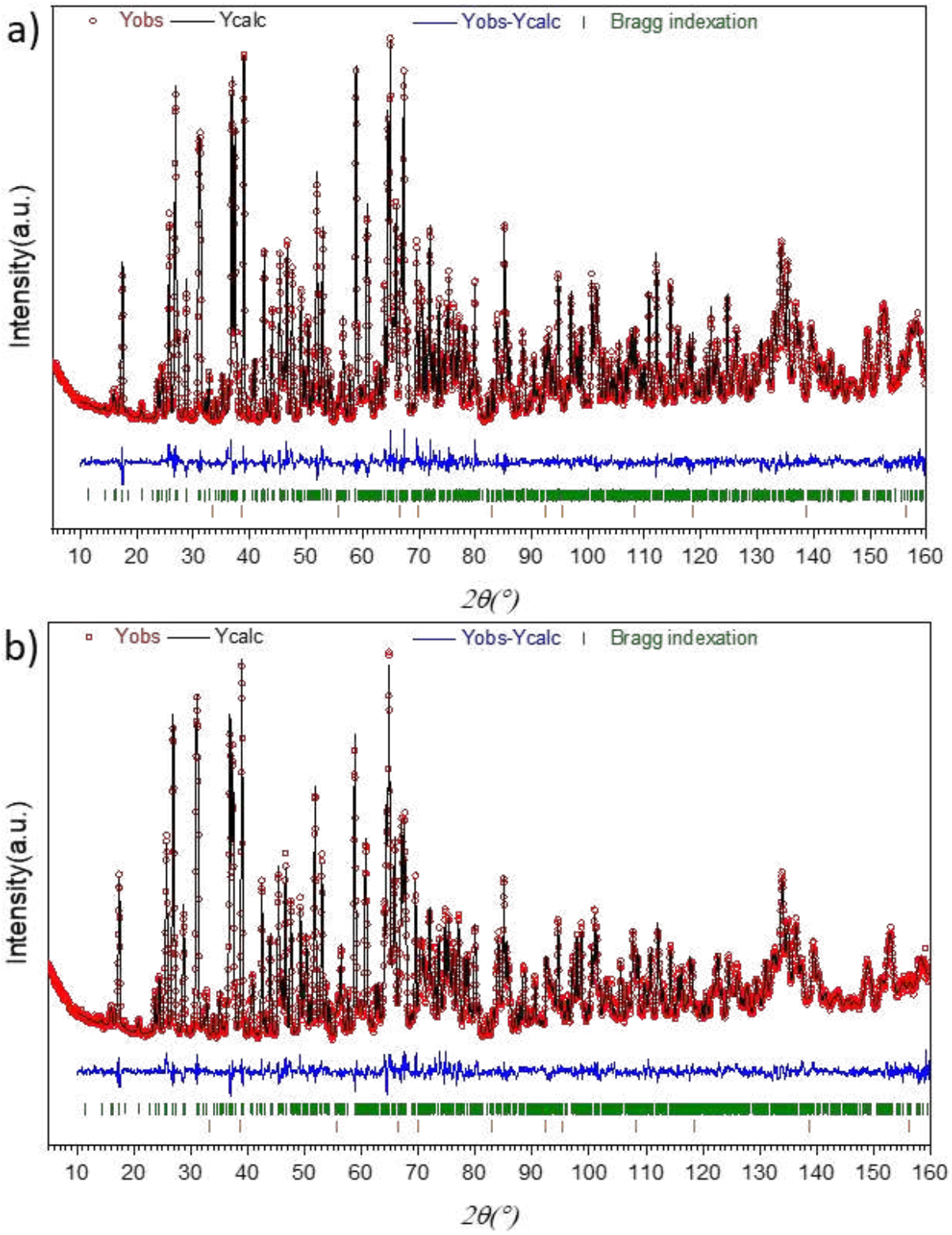

Figure V.14. *Final Rietveld refined NPD (HR) data of a) $Ca_5Ga_6O_{14}$ (x = 0) (R_{wp}= 3.58% GOF= 0.68), and b) $La_{0.25}Ca_{4.75}Ga_6O_{14.125}$ (x = 0.25) (R_{wp}= 3.21% GOF= 0.60). Green tick marks correspond to the $Ca_5Ga_6O_{14}$ and $La_{0.25}Ca_{4.75}Ga_6O_{14.125}$ structures panels (a) and (b) respectively, while the orange tick marks represent the CaO impurity quantified at ~0.08(6)% for x = 0 and ~0.71(9)% for x = 0.25 materials, both in weight%.*

Refined La occupancies on the x =0.25 phase were consistent with previous results as the cationic disorder was manifested mainly on the Ca3 sites (Table V.4). Moreover, one can perceive a big jump in the thermal parameters of the O2, O8 and O9 atoms toward higher values going from the x = 0 to the x = 0.25 material (see Figure V.15a). Furthermore, when localising these oxygen atoms in the structure, it appears that they surround the Ca3 sites (see Figure V.15b), signifying an internal disturbance caused by the cationic disorder or triggered by the residence of an interstitial oxide. Additionally, comparing the distances of this channel pentagon centroid to the nearest oxides (Figure V.16a and Figure V.16c), it reveals a small positional displacement of the O2 atom towards the outside the channel, while the others remain almost the same within the plotted 3×σ error, hence enlarging these channels to potentially accommodate an interstitial oxide. This behaviour is consistent with the one observed in the anion ordered $La_2Ga_3O_{7.5}$ and $La_{1.64}Ca_{0.36}Ga_3O_{7.32}$ melilites, where the O_{int} containing channels shows a displacement of their forming oxides toward the centroids of neighbouring $[GaO_4]_5$ pentagons to satisfy the local bonding of the interstitial oxides [8], [22], [28], as shown in Figure V.16b and Figure V.16d. Even though this displacement is weak in our $La_{0.25}Ca_{4.75}Ga_6O_{14.125}$ (x = 0.25) compared to the $La_2Ga_3O_{7.5}$ shown in the same figure, it can be linked to its much lower O_{int} content.

Table V.4. Final Refined structural parameters obtained from NPD (HR) data collected at room temperature on $La_{0.25}Ca_{4.75}Ga_6O_{14.125}$ (x = 0) (*Cmc*2$_1$ space group, *a*= 11.47246(14) Å, *b*= 11.29197(14) Å and *c*= 10.50904(14) Å) sample. La content was constrained to refine near the nominal value, which led a refined composition of: $La_{0.27(6)}Ca_{4.73(6)}Ga_6O_{14}$. Note that the composition is not charge balanced due to the interstitial oxide not added to the structure.

Atom	Wyck	x	y	z	Occ	Biso
Ca1/La1	8b	0.1576(5)	0.1014(5)	0.25	0.96(2)/0.04(2)	1.93(14)
Ca2	8b	0.3562(5)	0.3170(5)	0.2042(8)	1	1.78(10)
Ca3/La3	4a	0	0.5220(6)	0.2426(8)	0.81(3)/0.19(3)	0.88(15)
Ga1	8b	0.3562(2)	0.1470(3)	0.5112(6)	1	0.23(5)
Ga2	4a	0	0.2975(4)	0.4437(7)	1	0.59(8)
Ga3	4a	0	0.0003(4)	0.4685(7)	1	0.39(8)
Ga4	8b	0.2432(3)	0.4020(3)	0.4799(6)	1	0.33(5)
O1	8b	0.2839(3)	0.2778(3)	0.5848(7)	1	0.68(6)
O2	4a	0	0.6239(6)	0.5750(8)	1	1.99(12)
O3	8b	0.2725(3)	0.0247(3)	0.5955(7)	1	0.76(7)
O4	8b	0.3726(4)	0.4350(3)	0.3824(7)	1	0.79(8)
O5	4a	0	0.1461(5)	0.3820(7)	1	0.48(9)
O6	8b	0.3405(3)	0.1482(4)	0.3397(7)	1	0.54(7)
O7	4a	0	0.0095(6)	0.6393(8)	1	0.98(11)
O8	8b	0.1267(4)	0.3718(4)	0.3658(7)	1	1.30(9)
O9	4a	0	0.3015(5)	0.6135(9)	1	1.16(12)

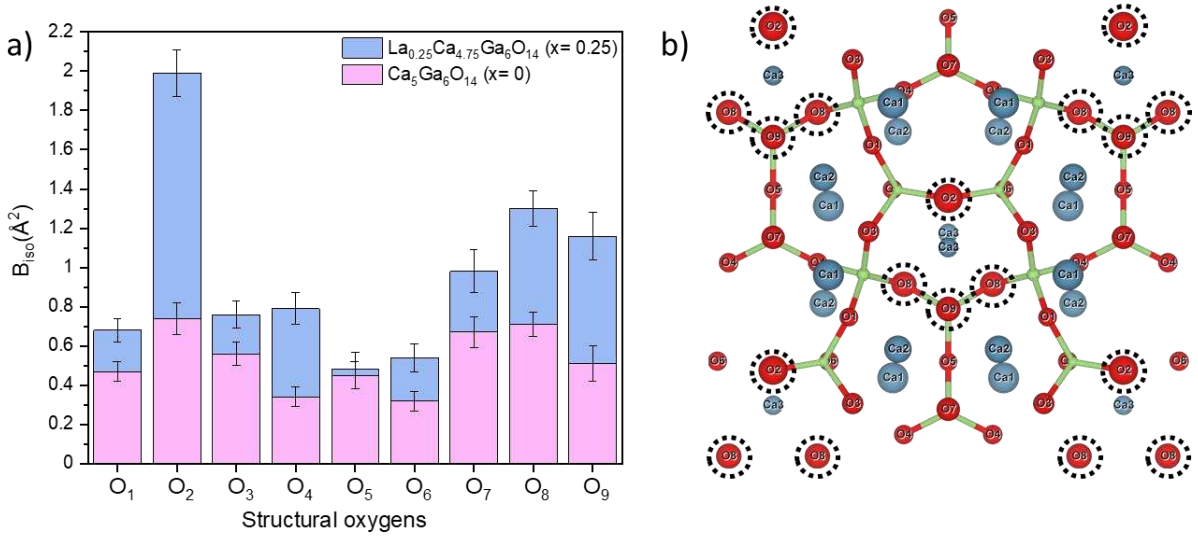

Figure V.15. *a) Comparison between NPD (HR) refined oxygens displacement parameters against both x = 0 and x = 0.25 materials. b) highlighted O2, O8 and O9 positions inside the $Ca_5Ga_6O_{14}$ cell.*

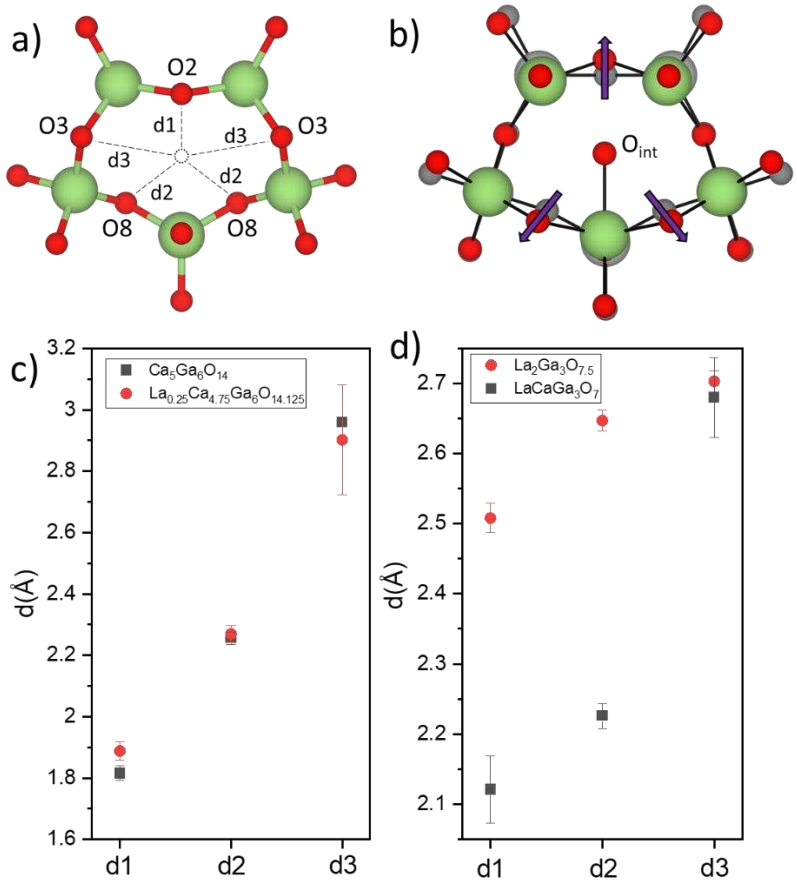

Figure V.16. *a) Structural projection of the Ca3 channels pentagons along the c-axis in the $Ca_5Ga_6O_{14}$ compound. b) Overlay between of one $[GaO_4]_5$ framework pentagonal channels from the $LaCaGa_3O_7$ melilite (grey atoms) and the O_{int} containing channel from the $La_2Ga_3O_{7.5}$ melilite (coloured atoms), with purple arrows indicating the displacement direction of the channels forming oxides. In both panels green and red spheres represent gallium and oxygen atoms. c) and d) panels shows the determined distances from the channels centroids to the labelled oxides from (a) and (b) respectively, with errors plotted in 3 ×σ.*

V.3.3. Interstitial oxide position determination by Fourier difference map and maximum entropy method (MEM) calculations from NPD data.

Fourier difference maps of the x = 0.25 compound were generated using Topas (V6) [17] from its refined NPD data, and visualised using Vesta [29]. In Figure V.17a, from the NPD (HR) refined data, almost no Fourier peak can be distinguished as the maximum positive nuclear density is at the same level as the maximum negative density (see also Figure A. 35a and Figure A. 35c in the appendices Chapter A.V). In contrast with the NPD (HI) refined data, from their Fourier difference map (Figure V.17b) a very small intensity Fourier peak can be identified in the Ca3 channels by the GaO sheets level at the (x = 1/2, y= 0.025, z=0.51) position, typical of an interstitial oxide "O_{int}" as positioned in the melilite structures[8]–[10], [22] (see also Figure A. 35b and Figure A. 35d in the appendices Chapter A.V). An oxygen atom was placed at this position and freely refined its y, z coordinates and site occupancy while fixing its x coordinate to 1/2 (mirror plane) and defining its B_{iso} as a mean value of the structural oxygens B_{iso} values. Refinements with this additional oxide did not improve the overall fit and the same reliability factors were retained. Even though a stable refinement was obtained, the barely distinguishable weak intensity of the Fourier peak from the noise (see positive to negative nuclear density intensity in Figure A. 35c and Figure A. 35d) implies further investigations in confirming the interstitial oxide existence in that position.

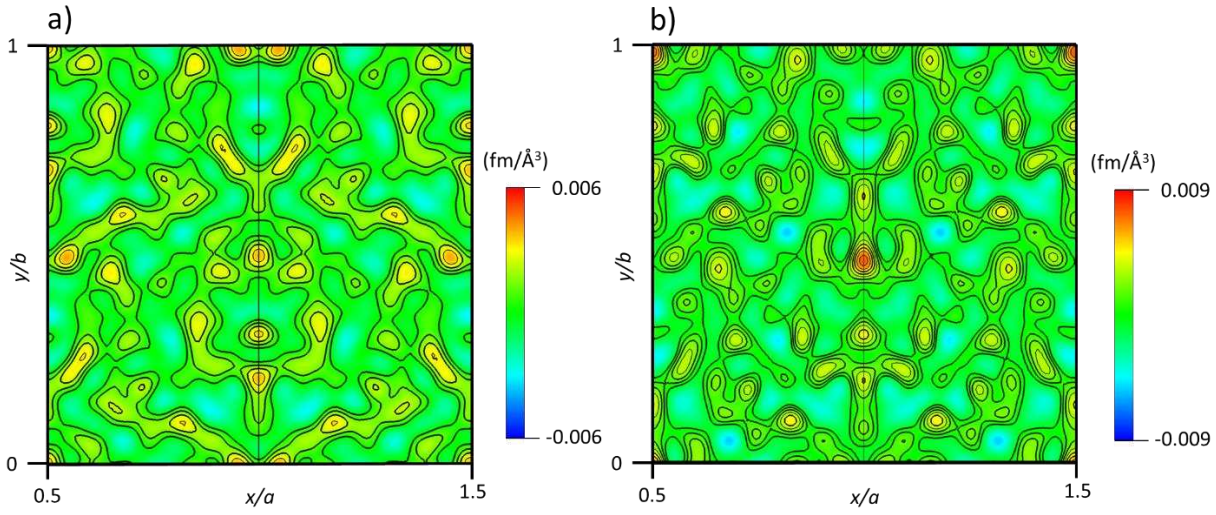

Figure V.17. *a), b) Fourier difference map section at z= 0.51 centred at the Ca3 channels from $La_{0.25}Ca_{4.75}Ga_6O_{14.125}$ NPD (HR) and NPD (HI) refined data respectively.*

Extracting as much information as possible from an incomplete and noisy data set can be challenging in particular in the case of disorder. The maximum entropy method (MEM) was

introduced as an alternative strategy to the inverse Fourier transform for constructing the most probable electron/neutron density maps using as constraints a given X-ray/neutron diffraction data set when refinements or Fourier syntheses fail to describe accurately the whole system (i.e. noisy data, light elements density covered by heavier elements, low elements concentration, static or dynamic disorder…). The use of the maximum entropy method has been demonstrated in many crystallographic works as a powerful calculation process in solving the problems stated above [30]–[35].

After the unsuccessful attempt at low temperature NPD data analysis in confirming or denying the interstitial oxide position at the one defined by RT-NPD analysis, as described in section V.3.2, MEM calculations were carried out by Olivier Hernandez (ISCR laboratory, Rennes) against the room temperature collected NPD (HR) data set using the Dysnomia program [36]. First, a new Rietveld refinement was performed against the NPD HR data using the Rietan-FP program [37] (Howard asymmetry correction, peak-shift correction, scale factor, 11 background polynomial parameters, 10 profile parameters from a split pseudo-Voigt profile function and 59 structural parameters for x = 0 composition [2 for x = 0.25 composition, which corresponds to the La occupancies in Ca1 and Ca3 sites], resulting in a total of 82 independently refined parameter for x = 0 compound [84 for x = 0.25 compound]). The refinement led to reliability factors in the same range as observed previously (R_{wp}= 3.60% GOF= 1.45) and (R_{wp}= 3.12% GOF= 1.34) for both $Ca_5Ga_6O_{14}$ and $La_{0.25}Ca_{4.75}Ga_6O_{14.125}$ compounds respectively, with their respective refined structural parameters presented in Table A. 72 and Table A. 73. The extracted F_{obs} from 671 and 652 independent reflections for both x = 0 and x = 0.25 compounds respectively using Rietan-FP, were used in Dysnomia as F_{obs} constraints to reconstruct their related nuclear density by MEM calculations in the real space. A flat prior density was used as well as traditional *F*-constraints of second order.

From the MEM calculated nuclear density maps, it appears that the observed weak Fourier peak on $La_{0.25}Ca_{4.75}Ga_6O_{14.125}$ x = 0.25 NPD (HI) Fourier difference map (described in section V.3.2) is no longer existent (see Figure V.18), which puts in serious doubts its interpretation as an actual Fourier peak and suggests that it is only noise amplified due to its symmetry position. Moreover, comparing the nuclear density of both x = 0 and x = 0.25 compounds, most oxide atoms appears to maintain a regularly shaped nuclear density. However, for the La-doped compound a clear anharmonicity can be observed on the O2 atom nuclear density, which is completely absent in the La-free material (see Figure V.18). These results are consistent with the isotropic refined oxygens displacement parameters noted in section V.3.2, and indicating

the biggest B_{iso} value for the O2 atom. This O2 behaviour can be related to a high positional disorder of this atom, distorting the local environment of the Ca3 site. Similar features can be discerned in the melilite compounds when an interstitial oxide is located in the $[GaO_4]_5$ pentagons centre, causing distortions of the Ga-O-Ga angles, which pushes the equivalent oxide to our O2 atom in those systems far from its initial position enlarging the A-sites channels (shown in Figure V.16b) [8], [9], [22]. Further MEM calculation using the NPD (HI) data and an advanced MEM calculation (derived constraints MEM) are under investigations

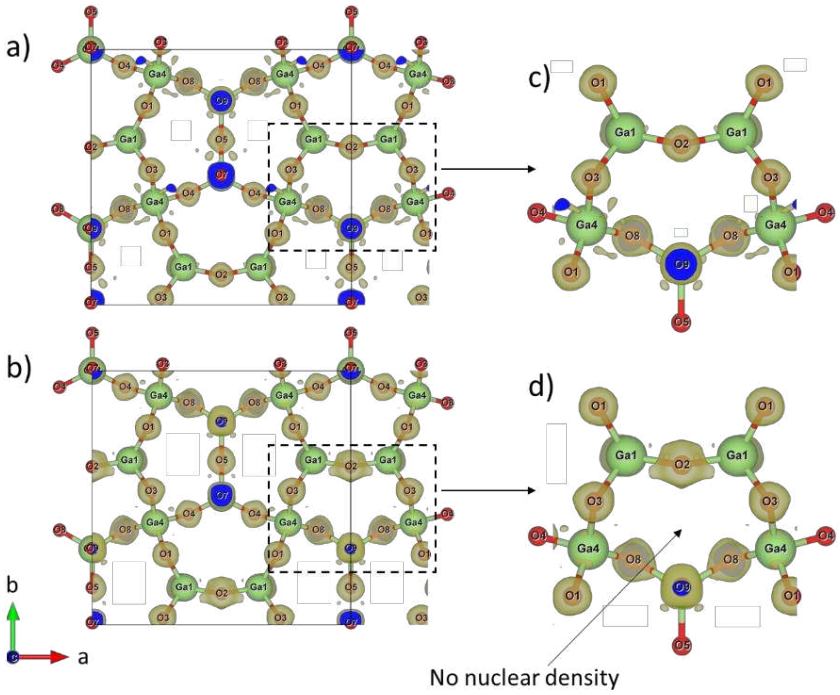

Figure V.18. *a), b) Crystal structure projection of an $[GaO_4]_n$ infinite sheet from the NPD refined $Ca_5Ga_6O_{14}$ and $La_{0.25}Ca_{4.75}Ga_6O_{14.125}$ compounds respectively within the c-axis. The reconstructed nuclear density from MEM calculation of x = 0 and x = 0.25 compound is overlayed in panels (a) and (b) respectively, both at isosurface level of 0.0325. c), d) Shows a zoom on the Ca3 channels.*

V.3.4. Density functional theory (DFT) calculations and determination of the most energetically stable structure.

Computational prediction of crystal structures can be useful in the accelerated discovery of novel compounds with new crystal structures and optimised properties [11]–[13], [38], [39]. Regarding this aspect, Meigeng Gao (University of Liverpool, UK) has showed in her thesis the potential of probing/predicting the crystal structure of new oxide ion conductor materials by DFT calculations [40]. This approach is described in this section to define the most energetically stable configuration of the La-doped $Ca_5Ga_6O_{14}$ structure with an interstitial oxide.

In this section, the structural calculations were performed by Matthew Dyer from the University of Liverpool (UK). As initially described in section V.2 for the dopant prediction, the Simdope code [14] was used to generate initial crystal structures in *P*1 with two substituted calciums by two lanthanum atoms with the introduction of one interstitial oxide held in the centre of one $[GaO_4]_5$ pentagon to keep the $Ca_{4.5}La_{0.5}Ga_6O_{14.25}$ composition charge balanced. Note that each of the initially generated structures had an interstitial oxide positioned in a different $[GaO_4]_5$ pentagon. DFT calculations were performed using the Vienna *ab*-initio Simulation Package (VASP) [15], using the PBE [41] functional and PAW [42] potentials. Both the unit cell and atomic positions were relaxed until the forces were minimised, leading to the most energetically favourable configurations.

Out of 500+ calculated structures, the two lowest-energy configurations were selected for comparison (Figure V.19a). Both relaxed cells were pseudo-orthorhombic with a slightly different β angle, 90.59° and 90.22° for configuration538 and configuration542 respectively. Interestingly, both structures held the O_{int} in the Ca3 channels, at the $[GaO_4]_n$ sheet level (see Figure V.20a and Figure V.20b). This observation is consistent with the detected trend on the relaxed structures containing the O_{int} in the Ca3 channels, indicating lower structure energies *vs* the Ca1/Ca2 O_{int} containing channels structures (see Figure V.19b). In contrast with previously reported melilites containing interstitial oxides, Config542 manifests an O_{int} positioning in the Ca3 $[GaO_4]_5$ pentagons centre, directly between two lanthanum atoms (see Figure V.20c). Config538 on the other hand manifests a slight shift of the O_{int} from the La-La axis centre in the mirror plane (see Figure V.20d). Calculated bond valence sum (BVS) of the interstitial oxide in both configurations revealed to be 1.66 in config542 and 1.78 in config538, these results indicate that the O_{int} is better suited in config538 as this its calculated charge is closer to the theoretical value of 2. However, it is not completely impossible for an oxide to sit in an under-bonded site if the overall structure energy is lower than other where the oxide atom is occupying a less under-bonded site, which the case for confige542 exhibiting the lowest structure energy. Moreover, comparing our maximum La-doped (x = 0.25) RT-NPD refined model to both predicted configurations by DFT, one can notice a huge increase of the O3-Ga1-O2 angle, varying from 100.0(4)° (our $L_{0.25}Ca_{4.75}Ga_6O_{14.125}$ RT-NPD refined structure) to 140.24° and 113.20° for config538 and config542 respectively (Figure V.21a and Figure V.21b), pushing the O2 atom from its initial position (Figure V.22). This actually indicates the caused local distortion of the Ca3 channels when an interstitial oxide in present on that site, similar to the reported $La_2Ga_3O_{7.5}$ with a notable increase of the equivalent angles in

comparison to the undoped La*AE*Ga$_3$O$_7$ *AE*= [Ca, Sr, Ba], proportional to config542 (see Figure V.21c).

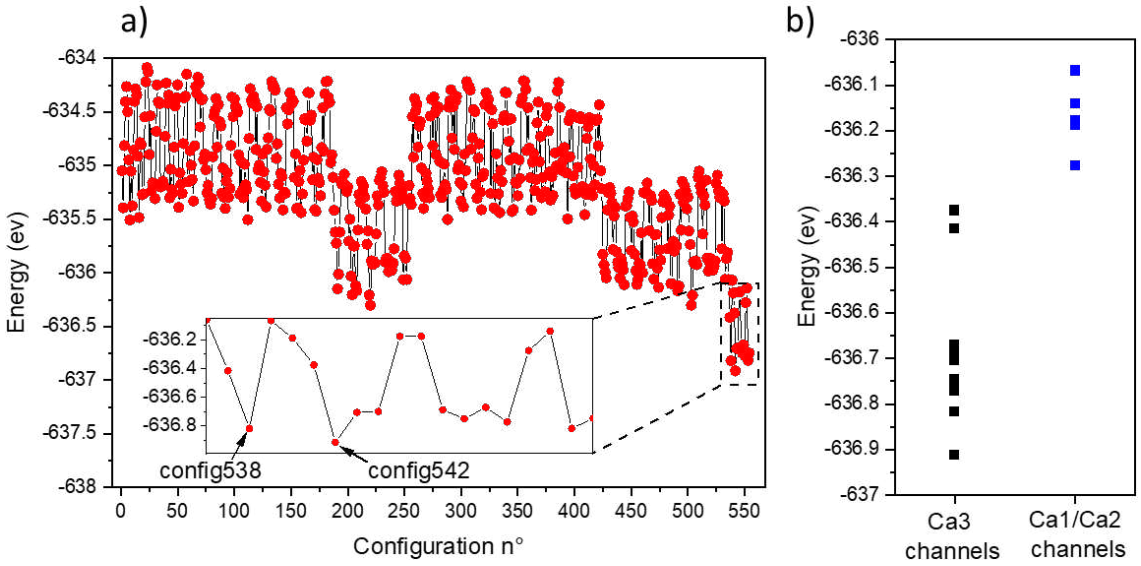

Figure V.19. *a) Calculated energies for the 554 DFT relaxed structures, with the insert indicating the lowest energy structures. b) Energies of the relaxed structures highlighted by a dashed rectangle in (a) plotted in O_{int} containing channels.*

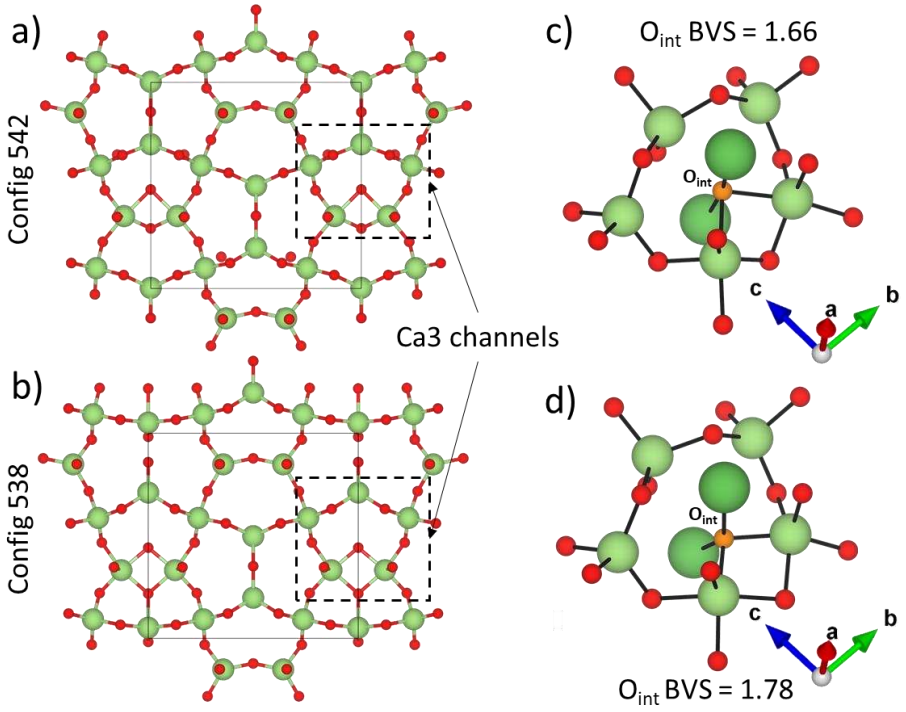

Figure V.20. *Crystal structure projection of an $[GaO_4]_n$ infinite sheet from the two energetically favourable predicted structures of La-doped $Ca_5Ga_6O_{14}$ compound, with a) and b) corresponding to configuration538 and configuration542 respectively. c) and d) zoomed view of the Ca3 channel showing the local environments of the O_{int} and its shift between the two predicted configurations. Green and red spheres represent gallium and oxygen atoms, while the interstitial oxides are highlighted in orange in both c) and d) panels.*

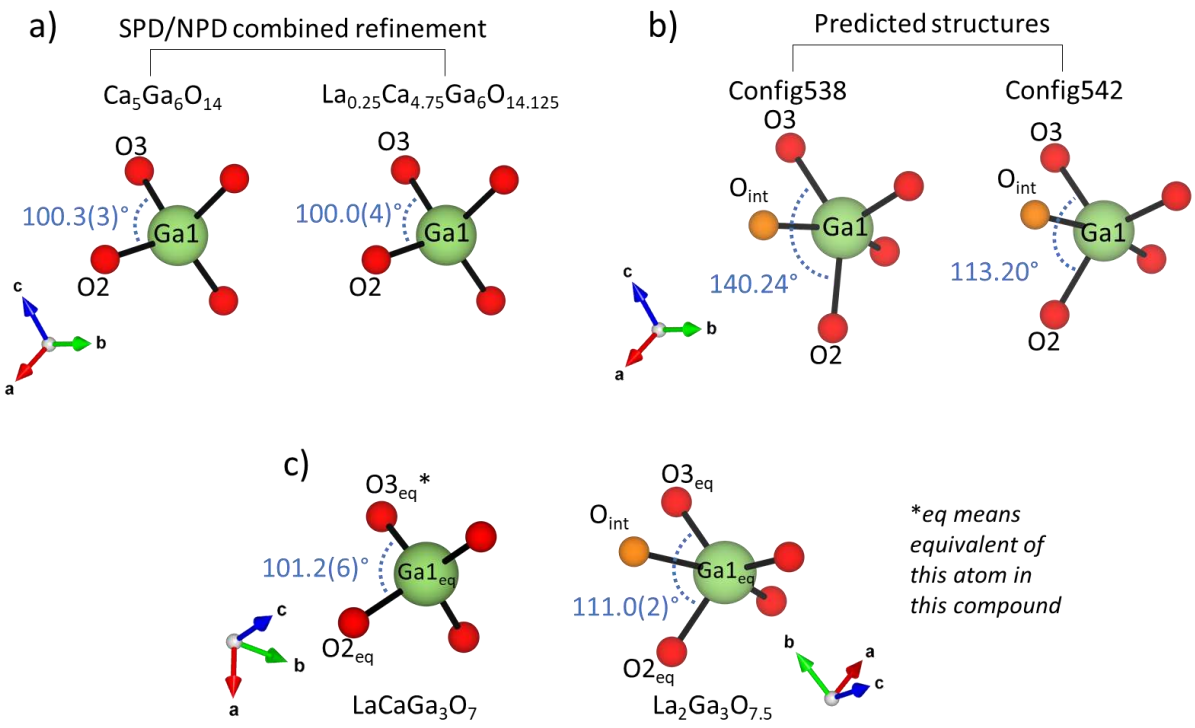

Figure V.21. *Local distortion of the O3-Ga1-O2 angle of: a) $La_xCa_{5-x}Ga_6O_{14+x/2}$ x = 0, 0.25, b) both predicted config538 and config542 structures, c) $LaCaGa_3O_7$ [43] and $La_2Ga_3O_{7.5}$ [22] for comparison.*

Furthermore, overlaying both predicted structures with our refined NPD model (Figure V.22), it is clear that the O2 atom is the most displaced one. This local distortion of the O2 atom is manifested when an interstitial oxide is present on the Ca3 channels, meaning that on the average structure this atom (O2) should possess higher displacement parameters than the other structural oxides which are less affected/constrained by the existence of the O_{int}. These observations are consistent with the maximum entropy method calculations, which indicated a strong nuclear density anharmonicity of the O2 atom compared to the other structural oxides as explicated in section V.3.3, Figure V.18c and Figure V.18d.

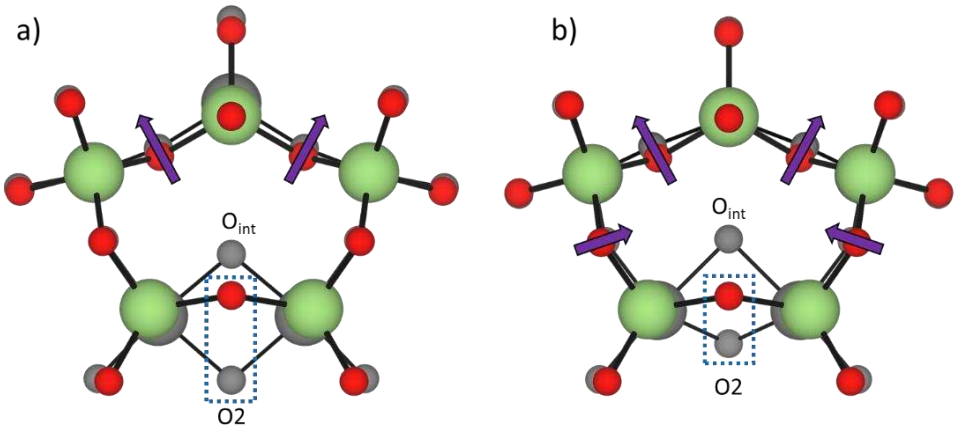

Figure V.22. *Overlay of the $La_{0.25}Ca_{4.75}Ga_6O_{14.125}$ NPD refined structure (coloured atoms) with both predicted config538 (grey atoms) and config542 (grey atoms) in a) and b) panels respectively. The purple arrows indicate the oxides displacement directions.*

V.4. Sample preparation and ionic conductivity properties.

V.4.1. Pellet densifying attempts.

In order to proceed to AC impedance measurements, a dense sample (ideal density >95%) is needed to ensure an optimised charge transport within the sample. The initially sintered pellets of $La_xCa_{5-x}Ga_6O_{14+x/2}$ x = 0 and 0.25 compositions were polished to get rid of the sacrificial powder first. The pellets were then subject to a density measurement by Archimedes law (as described in the appendices Chapter A.I section A.I.6.1). The pellets were found to be 67% dense. In fact, this low density is not surprising considering the observed amount of porosity in the acquired SEM (BSE mode) images (shown in section V.3.1 Figure V.8). Attempts to sinter the powder at higher temperatures could not be possible as the sample melts between 1300°C-1350°C. To attain materials with higher density, spark plasma sintering (SPS) operating at high temperature and high pressure was considered as a sintering route to achieve this goal. After several of attempts by Sebastien Chenu at the IRCER laboratory in Limoges, the SPS synthesis protocol for achieving 99% dense pellets was found to be as follows: the initially synthesised $La_xCa_{5-x}Ga_6O_{14+x/2}$ x = 0 and 0.25 compositions were ground to powder and then ball milled using a planetary mill for 10 min independently. The resulting powders were filled in graphite dies of 10 mm diameter each. The powder samples were then sintered by spark plasma sintering process, at 800°C under a 100MPa pressure for 2 minutes and then at 1150°C under a 100MPa pressure for 5 minutes (100°C/min for both heating steps). The synthesised pellets had a dark black colour due to the carbon diffusion from the graphite die (Figure V.23). Laboratory X-ray diffraction measurements were performed on freshly SPS

synthesised pellets to check for possible phase degradation. The diffraction patterns were Pawley refined and indicated the presence of the main $Ca_5Ga_6O_{14}$ and a small amount (0.62%wt quantified by a Rietveld refinement) of CaO phases.

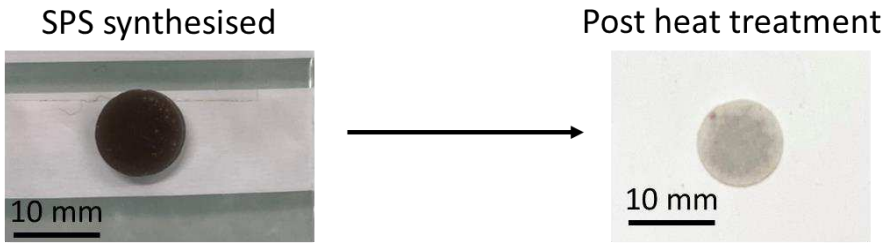

Figure V.23. *Image of the SPS synthesised pellet pre and post heat treatment.*

The pellets were polished until a thickness of 0.7 mm was reached, then annealed at 900°C for 6h under O_2 gas flow to remove as much carbon as possible from the pellets; at the end of this heat treatment the samples retained a light grey colour (Figure V.23). Previous trials with a longer annealing process and temperatures higher than 900°C revealed unsuccessful, as the colour remained the same for the 6h treatment, or the sample decomposed.

V.4.2. Impedance measurements.

The final prepared samples described above (section V.4.1) were coarsely polished to obtain two parallel faces. Silver paste was coated on both opposite faces of the pellets and fired at 600°C for 30min to evaporate the organic components from the paste and form electrodes. Impedance measurements were then carried out using the Solartron SI 1260 apparatus by Leire Del Campo at the CEMHTI laboratory. Data were acquired in the 0.1Hz - 32MHz frequency range from room temperature to 800°C using a step of 4°C/min. In Figure V.24a and Figure V.24b showing the evolution of complex impedance plots for both $La_xCa_{5-x}Ga_6O_{14+x/2}$ x = 0 and x = 0.25 compounds, it is clear that no signal is recorded for the La-free sample for temperatures below 600°C. This reflects the very low electrical conductivity of this material below 600°C. Moreover, no clear separation between two semi-circles can be discerned on the Nyquist plots, making it hard to distinguish the bulk from grain boundaries responses. Therefore, only the total conductivity was deducted from the semi-circle interception with the x-axis.

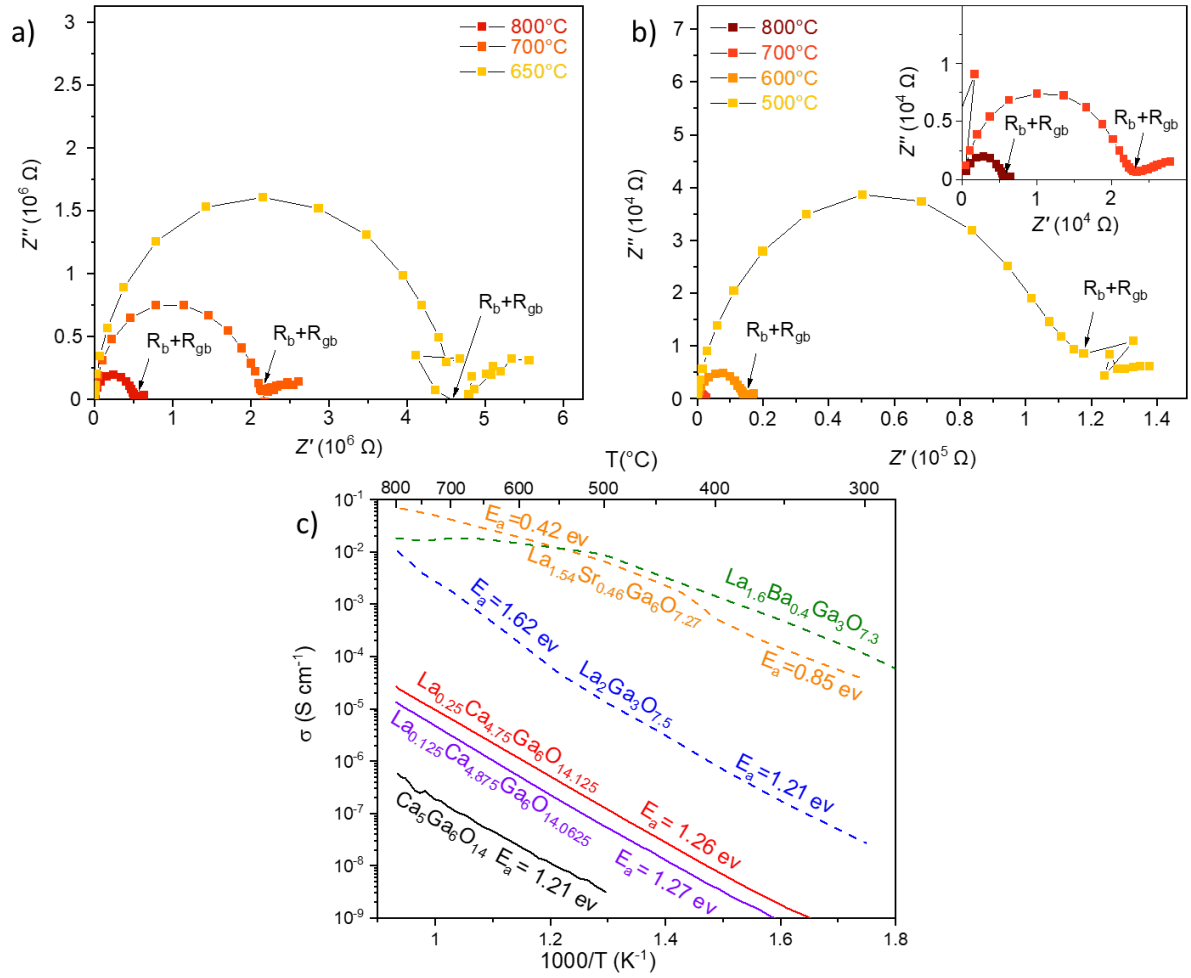

Figure V.24. *a), b) Complex impedance plots at different temperatures for $Ca_5Ga_6O_{14}$ (x = 0) and $La_{0.25}Ca_{4.75}Ga_6O_{14.125}$ (x = 0.25) compounds respectively. c) Arrhenius plots of the total conductivity (dashed lines) of compounds from this work, compared to the other melilite compounds from [9], [22] and Chapter IV of this thesis.*

From the Arrhenius plots presented in Figure V.24c, they indicate an increase in the ionic conductivity of the $La_xCa_{5-x}Ga_6O_{14+x/2}$ samples in the following order: x = 0, x =0.125, x = 0.25; these results are consistent with the increase of the interstitial oxide concentration. At 800°C a maximum value of $\sigma = 2*10^{-5}$ S.cm^{-1} is reached for $La_{0.25}Ca_{4.75}Ga_6O_{14.125}$, which is two orders of magnitude higher than $Ca_5Ga_6O_{14}$, which reaches a conductivity of $\sigma = 5*10^{-7}$ S.cm^{-1} at 800°C. Even though such an increase is observed between La-free and La-doped samples, the x = 0.25 compound still exhibits a much lower conductivity capacity than the previously described $La_{1.7}Ba_{0.3}Ga_3O_{7.35}$ melilite in Chapter IV and the best known $La_{1.54}Sr_{0.46}Ga_3O_{7.27}$ melilite conductor [9] displaying 0.1 S.cm^{-1} at 800°C. This difference can be explained by the much higher concentration and positional disorder of the interstitial oxides in the orthorhombic and tetragonal melilites in which, the first one sees its O_{int} forming one-dimensionally (1D) ordered chains over the *a* direction (in $La_2Ga_3O_{7.5}$), while the latter one with lower O_{int} concentrations adopts a two-dimensional (2D) O_{int} network covering their whole underlying

framework over the *ab*-plane (see Figure V.25). These types O_{int} distribution facilitate the oxides mobility as the charge carrier can hop between neighbouring channels in the structure. This was previously explained in Chapter IV. In contrast with our final model of the $La_{0.25}Ca_{4.75}Ga_6O_{14.125}$ compound, defined by combining SPD, NPD, MEM and DFT prediction, the underlying O_{int} distribution can be described as 0D confined network (Figure V.25c) in which the O_{int} is hosted in isolated Ca3 channels, inhibiting charge transport within the *ab*-plane due to the need for these oxides to migrate via energetically unfavourable neighbouring Ca1/Ca2 channels. Moreover, for similar O_{int} concentration per formula unit in the Sr-based melilites, i.e. $La_{1.12}Sr_{0.88}Ga_3O_{7.06}$, this sample exhibit a conductivity value 1.5×10^{-4} $S.cm^{-1}$ at 800°C which is one order of magnitude higher than the $La_{0.25}Ca_{4.75}Ga_6O_{14.125}$ (x = 0.25) studied material at the same temperature. This could indicate that with higher O_{int} concentration (i.e. higher doping amount) the conductivity of this material might increase as in the Sr-based malilites.

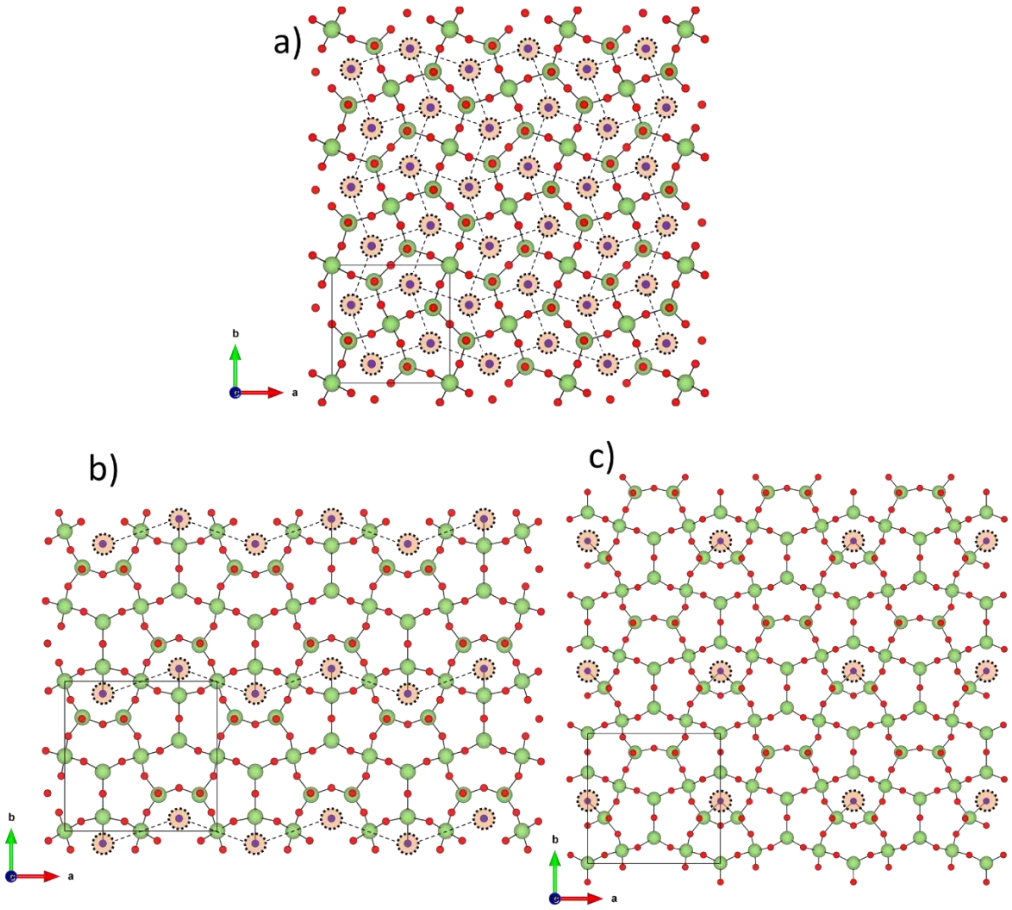

Figure V.25. *Different interstitial oxide ordering in the mellite family, with a) fully disordered forming a 2D network from [10], b) 1D ordered in a chain-like dispersion from [22], c) 0D confined O_{int} dispersion from the DFT predicted config542 (this work).With green and red spheres representing gallium and oxygene atoms. The interstitial oxide are coloured in blue and highlited by an orange transparent circle.*

The $Ca_{12}Al_{14-x}Ga_xO_{33}$ mayenite solid-solution was found to crystallise in the $Ca_5Ga_6O_{14}$ structure for $8 \leq x$ by a glass crystallisation synthesis approach [7]. Conductivity of the x = 14 compound from this mayenite solution (i.e. $Ca_5Ga_{5.82}O_{14-\delta}$) was found to reach 10^{-3} S.cm^{-1} at 800°C, which is two order of magnitudes higher than our $La_{0.25}Ca_{4.75}Ga_6O_{14.125}$ compound. Moreover, EDS quantification of the Ca content at surface of the negative electrode and cross section of the sample poste impedance measurement, evidenced a high Ca concentration at the surface of the negative electrode, totally absent in the cross section of the sample [7]. The authors explained this inhomogeneity by possible Ca conduction mechanisms operating. This could suggest possible cationic conduction in our synthesised $La_xCa_{5-x}Ga_6O_{14+x/2}$ (x = 0) and (x = 0.25) samples on top of the oxide ion one. Even though the authors showed that for the fully Al substituted in $Ca_{12}Al_{14-x}Ga_xO_{33}$ solid solution (x = 14) crystalline phase sees all its Ca sites are fully occupied, with Ga sites are partially occupied by Rietveld refinements against lab acquired PXRD data, to satisfy the nominal composition. The left amorphous amount was not quantified, as the samples were synthesised by crystallisation from glass precursors. Hence, another explanation could be diffusion of amorphous Ca left on the residual glass. Therefore, it is hard to compare our sample properties the one reported by the authors in [7] as of the different synthesis approached in the two studies, i.e. solid-state reaction in this work *vs* glass crystallisation in [7].

V.5. Conclusion and perspectives.

In this chapter, DFT calculations helped to target the synthesis exploration work, and suggested that lanthanum is the most favoured element for doping the $Ca_5Ga_6O_{14}$ compound and making new oxide ion conductor materials. The synthesis of the doped compound by different methods revealed that experimentally only a low amount could be introduced into the crystal structure (i.e. $La_xCa_{5-x}Ga_6O_{14+x/2}$ $x_{max} = 0.25$). The crystal structure of both the La-free and maximum La-doped compounds were studied by a combination of SPD, TEM, NPD, MEM and DFT. From SPD data, the La positioning was defined to occur among both Ca1 and Ca3 sites. However, the amount of La in the Ca3 sites was far superior to that in Ca1 sites. This was confirmed by DFT, STEM-HAADF imaging showing brighter Ca3 spots, but also confirmed by STEM-EDS and EELS mapping of the La. The successful substitution of Ca^{2+} by La^{3+} cations in the $Ca_5Ga_6O_{14}$ structure implies a charge balancing by either cationic vacancies or interstitial oxides. From SPD refinements and composition verification by microprobe, no strong evidence of cationic vacancies could be found nor the presence of secondary Ca- or Ga-rich phases, which ruled out this possibility. The hypothesis of O_{int} introduction was

investigated by neutron diffraction data analysis. However, these investigations did not achieve direct identification of the interstitial oxide position: even by applying maximum entropy method calculations, the interstitial oxide was still not apparent. Nevertheless, by MEM a clear disturbance of the Ca3 channel local environment was observed in the constructed nuclear density. These obtained results were in qualitative agreement with the predicted structures by DFT with the most energetically suitable positions for the interstitial oxide to be held in, as the calculations indicated a significant distortion of the Ca3 channel environments. Finally, the AC impedance measurements indicated an increase of nearly two orders of magnitude from the La-free $Ca_5Ga_6O_{14}$ to the maximum La-doped $Ca_5Ga_6O_{14}$ compounds, which is consistent with the introduction of interstitial oxides.

As perspectives for this work, many exploring paths can be followed. For instance, Nd can be investigated in doping the $Ca_5Ga_6O_{14}$ structure as its energy lay close to the lanthanum. The synthesis of *RE*-doped $Ca_3Ga_4O_9$ phase could also be investigated for new oxide ion conductor materials, as the non-doped material exhibits a conductivity of almost 3×10^{-3} S.cm^{-1} at 1000°C. Therefore, finding the right aliovalent dopant element and benefiting from a melilite related framework (described in Chapter A.V) could allow the increase of this conductivity value by few factors.

V.6. References.

[1] A.-R. Schulze *et al.*, *Monatshefte für Chemie / Chemical Monthly*, 1981, **112**, 149.

[2] A.I. Bilyj *et al.*, *Kristallografiâ*, 1986, **31**, 1217.

[3] D. Liu *et al.*, *Advanced Optical Materials*, 2020, **8**, 2001037.

[4] N. Li *et al.*, *Journal of Alloys and Compounds*, 2021, **858**, 157719.

[5] Z. Liu *et al.*, *Journal of the American Ceramic Society*, 2019, **102**, 3823.

[6] Y. Yasui *et al.*, *Inorganic Chemistry*, 2019, **58**, 9460.

[7] Y. Lv *et al.*, *Inorganic Chemistry*, 2021, **60**, 2446.

[8] M.-R. Li *et al.*, *Angewandte Chemie International Edition*, 2010, **49**, 2362.

[9] X. Kuang *et al.*, *Nature Materials*, 2008, **7**, 498.

[10] J. Xu *et al.*, *Inorganic Chemistry*, 2017, **56**, 6897.

[11] C.M. Collins *et al.*, *Angewandte Chemie International Edition*, 2021, **60**, 16457.

[12] J. Gamon *et al.*, *Chemistry of Materials*, 2019, **31**, 9699.

[13] M.S. Dyer *et al.*, *Science*, 2013, **340**, 847.

[14] L. Enciso-Maldonado *et al.*, *Chemistry of Materials*, 2015, **27**, 2074.

[15] G. Kresse *et al.*, *Physical Review B*, 1996, **54**, 11169.

[16] A.S. Tolkacheva *et al.*, *Russian Journal of Physical Chemistry A*, 2018, **92**, 1243.

[17] A.A. Coelho, *Journal of Applied Crystallography*, 2018, **51**, 210.

[18] M. Boyer *et al.*, *CrystEngComm*, 2015, **17**, 6127.

[19] C. Genevois *et al.*, *Inorganic Chemistry*, 2021, **60**, 12339.

[20] M. Boyer *et al.*, *Journal of Materials Chemistry A*, 2018, **6**, 5276.

[21] A.J. Fernandez-Carrion *et al.*, *Inorganic Chemistry*, 2017, **56**, 14446.

[22] J. Fan *et al.*, *Chemistry of Materials*, 2020, **32**, 9016.

[23] H. Bazzaoui *et al.*, *Inorganic Chemistry*, 2022, **61**, 9339.

[24] C.J. Benmore *et al.*, *Advances in Physics: X*, 2017, **2**, 717.

[25] D.A. Winborne *et al.*, *Metallurgical Transactions B*, 1976, **7**, 711.

[26] M. Diaz-Lopez *et al.*, *Chemistry of Materials*, 2019, **31**, 5742.

[27] V.F. Sears, *Neutron News*, 1992, **3**, 26.

[28] L. Zhou *et al.*, *The Chemical Record*, 2020, **20**, 1117.

[29] K. Momma *et al.*, *Journal of Applied Crystallography*, 2011, **44**, 1272.

[30] M. Sakata *et al.*, *Acta Crystallographica Section A: Foundations of Crystallography*, 1990, **46**, 263.

[31] L. Le Dréau *et al.*, *Inorganic Chemistry*, 2012, **51**, 9789.

[32] Y. Idemoto *et al.*, *Inorganic Chemistry*, 2019, **58**, 5664.

[33] A. Gilane *et al.*, *Inorganic Chemistry*, 2022, **61**, 1597.

[34] C.J. Gilmore, *Acta Crystallographica Section A: Foundations of Crystallography*, 1996, **52**, 561.

[35] Y. Hu *et al.*, *Journal of Materials Chemistry*, 2012, **22**, 18744.

[36] K. Momma *et al.*, *Powder Diffraction*, 2013, **28**, 184.

[37] F. Izumi *et al.*, *Solid State Phenomena*, 2007, **130**, 15.

[38] C. Collins *et al.*, *Nature*, 2017, **546**, 280.

[39] J.K. Gupta, Computational Investigations of New Functional Metal Oxide Materials to Assist Synthesis, PhD thesis, 2017.

[40] M. Gao, Exploring the Chromium Poisoning Mechanisms and Development of New Ionic Electrolyte Materials in Solid Oxide Fuel Cell, PhD thesis, Liverpool, 2022.

[41] J.P. Perdew *et al.*, *Physical Review Letters*, 1996, **77**, 3865.

[42] G. Kresse *et al.*, *Physical Review B*, 1999, **59**, 1758.

[43] J.M.S. Skakle *et al.*, *Powder Diffr.*, 1999, **14**, 8.

General conclusion

The purpose of the presented work in this thesis is to develop new materials with high performing properties for different application types, and is motivated by the increasing demand for new materials from different parties. These solid-state chemistry studies group the melilites and melilite-related materials with potential interest for their optical and ionic conduction properties. The use of aerodynamic levitation coupled to two CO_2 lasers (ADL) allowed the synthesis of glass precursors of these materials in the form of spherical beads by melting the composition first and quenching them with high cooling rates (~ 300°C/s) while levitating the sample. Crystallisation of the glass then took place using the adequate heat treatment (studied by DSC and VT-PXRD) to secure phase pure fully-dense ceramics. Using the ADL also enables direct crystallisation from the under-cooled liquid as a new synthesis approach to reach for new metastable materials unreachable by conventional solid-state reactions. The studied compositions and structures were characterised by coupling multiple diffraction techniques i.e. powder X-ray diffraction (laboratory and synchrotron), neutron diffraction, selected area electron diffraction, scanning electronic microscopy, transmission electronic microscopy; and solid-state nuclear magnetic resonance spectroscopy. The macroscopic properties on the other hand were investigated by luminescence spectroscopy and AC-impedance spectroscopy.

The new $P2_12_12$ fully ordered superstructured Sr*RE*Ga_3O_7 *RE*= [Ho – Yb] melilite family [1] was first investigated to extend its stability limits to other rare earths. The Dy and Lu analogues were successfully synthesised by crystallisation of glass precursor samples. However, it was not possible to synthesise the Tb compound in this new polymorph as this was attributed to the Tb^{3+} inability to be held in a [6+1] coordination-type due to its bigger size. Different hypothetical ordering-types of the A-site cations are discussed why they are disfavoured. Investigation on the thermal stability of this new melilite polymorph revealed the occurrence of a phase transition at high temperature into the parent fully disordered $P\bar{4}2_1m$ melilite, which suggested the possibility of stabilising this structure by rapid cooling to room temperature. The synthesis of this disordered polymorph was well achieved for the whole series *RE*= [Dy – Yb], previously unreported for Tm and Yb compounds. Moreover, the luminescence properties were investigated for the $SrErGa_3O_7$ $P2_12_12$, $P\bar{4}2_1m$ and glass compounds. The results have showed the A-site cation ordering effect on their optical properties, as its Er emission band showed double the intensity of its $P\bar{4}2_1m$ and glass analogues. The main

challenge of this study was to adapt the glass crystallisation process for the $SrLuGa_3O_7$ $P2_12_12$ and $SrYbGa_3O_7$ $P\bar{4}2_1m$ compounds as secondary phases were easily induced.

In continuity of ordered/disordered systems, the $Ca_3Ga_{2-2x}Zn_xGe_{4+x}O_{14}$ ($0 \leq x \leq 1$) solid-solution crystallising in the langasite structural family, which is related to the melilite structure, synthesis was investigated by both full and congruent crystallisation from glass or the molten liquid. The *P*321 trigonal langasite was retained for the whole solid solution, hence achieving the first *P*321 $Ca_3ZnGe_5O_{14}$ previously reported to crystallise under a monoclinic *C*2 polymorph [2]. This solid solution present three isoelectronic elements i.e. Ga^{3+}, Zn^{2+} and Ge^{4+}, which makes its related cationic disorder characterisation challenging and not feasible by X-ray diffraction due to the absence of scattering contrast. To overcome this difficulty, neutron diffraction was used for the x = 0 and 1 end members which showed the occurrence of the cationic disorder between Ga/Ge (x = 0) and Zn/Ge (x = 1) among the B- and C-sites (i.e. 1a and 3f positions). Moreover, for the x = 0.5 compound a starting structural model was built by first quantifying the disorder from a unique 2D fitting of STEM-EDS images of each cation among the same sites. By proceeding in this way, justified chemical constraints were applied to the Rietveld refinement against this sample neutron data and divulged the same disorder trend seen in the end members. The main difficulties encountered in this project, apart from the highly challenging synthesis of phase pure sample, were the different neutron refinements strategies as of the low neutron scattering contrast between Ga and Ge for the $Ca_3Ga_2Ge_4O_{14}$ compound. Also, the development of a whole new analytical protocol of the atomic-scale STEM-EDS maps.

The second part of this thesis was focussed on ionic conducting materials. By adopting direct crystallisation from the molten liquid, the highest interstitial oxide containing $P\bar{4}2_1m$ tetragonal melilite was successfully synthesised in the $La_{1+x}Ba_{1-x}Ga_3O_{7+x/2}$ solid solution with x = 0.725. Moreover, the solid solution was further synthesised to x = 0.9, with x = 1 studied previously at CEMHTI [3], which crystallises under the *Ima*2 orthorhombic melilite polymorph. Furthermore, the structural trend was studied by X-ray and neutron diffraction, revealing the complete La/Ba disorder over the possible A-sites, while the interstitial oxides remained disordered in the $P\bar{4}2_1m$ polymorph and are chain like ordered in the *Iam*2 melilite structure. The study of these compounds by AC-impedance spectroscopy displayed the highest conductivities for $La_{1.6}Ba_{0.4}Ga_3O_{7.3}$ at 500°C (~10^{-2} S.cm^{-1}), equalling the best known melilite conductors: $La_{1.54}Sr_{0.44}Ga_3O_{7.27}$ (~10^{-2} S.cm^{-1}) $La_{1.64}Ca_{0.36}Ga_3O_{7.35}$ (~6.5×10^{-3} S.cm^{-1}) [4], [5] at the same temperature. However, at higher temperatures Arrhenius plots exhibited a plateau

with the highest value of ~7×10^{-1} S.cm^{-1} secured by the $La_{1.7}Ba_{0.3}Ga_3O_{7.35}$ compound at 800°C, which is less than an order of magnitude lower than $La_{1.54}Sr_{0.44}Ga_3O_{7.27}$ and $La_{1.64}Ca_{0.36}Ga_3O_{7.35}$ both reaching ~10^{-1} S.cm^{-1} [4], [5].

Following these results, we were interested in developing new ionic conductor materials with a melilite-like structure. The $Ca_5Ga_6O_{14}$ structure matched our demands as it has the same melilite layered network stacked antiparallelly with different positioning of the A-sites. Lanthanum was found to be the most energetically favourable dopant element among the studied ones by DFT. The synthesis of the $La_xCa_{5-x}Ga_3O_{14+x/2}$ solid solution was successfully achieved by solid-state reaction with a maximum dopant amount of x = 0.25. Further synthesis investigations to extend the doping limits were conducted by glass crystallisation, direct crystallisation of the melt, and sol-gels; however, all these attempts were unsuccessful as $LaCaGa_3O_7$ or $Ca_3Ga_4O_9$ impurities were part of the samples. Characterisation by X-ray synchrotron diffraction of the cationic disorder between La and Ca atoms was found to occur only among the Ca3 sites, which are the most open melilite-resembling channels. Moreover, from Rietveld analysis against SPD data no cationic vacancies were found to take place in the refined structure, which eliminates the possibility of charge balancing by cations vacancies. The interstitial oxide position was not possible to determine by neutron diffraction data analysis. Even though a Fourier peak can be observed on Fourier difference maps from NPD Rietveld analysis, the maximum entropy method has showed its none presence in the reconstructed neutron density from the same set of NPD data. The most energetically favourable configuration for the interstitial oxide and lanthanum positioning in the structure were computed by DFT calculations, and revealed their arrangement among the Ca3 channels where the O_{int} is stabilised directly between two lanthanum atoms at the $[GaO_4]_n$ sheets level, consistent with the observed Fourier peak from NPD data analysis and previous reported melilite conductors. Ionic conductivity of the doped sample exhibited an increase of two order of magnitudes over the La-free compound: 2×10^{-5} S.cm^{-1} (x = 0.25) *vs* $5*10^{-7}$ S.cm^{-1} (x = 0) at 800°C. Moreover, due to the 0D arrangement aspect of the interstitial oxides, the conductivity of these materials is far below the one of those melilites crystallising under the small cell tetragonal polymorph.

Tthe use of aerodynamic levitation coupled to two CO_2 lasers was shown to help achieve vitrification of different compositions unreachable by conventional melt quench process, which can then be used as metastable precursors to crystallise in new out of equilibrium structures. Moreover, the ADL was also shown to facilitate direct crystallisation from an under-cooled melt for some compositions. Regarding these aspects, many reported unvitrifiable systems by

conventional melt quench process, or even unexplored compositions are of interest to investigate their glass synthesis using the ADL. For instance, and as mentioned in Chapter II the Ba-based melilites especially the Ba*RE*Ga_3O_7 *RE*= [Yb, Lu] compositions, where the size mismatch between the alkali and rare earth metals is maximised, can be interesting to investigated how the melilite framework distort to accommodate such a size difference. The synthesised $Ca_3Ga_{2-2x}Zn_xGe_{4+x}O_{14}$ ($0 \leq x \leq 1$) solid solution compositions exhibiting a highly disordered layered framework, are much of interest in complementing their study by functionalising these materials (e.g. by Cr^{3+}) and investigate their related optical properties, as shown in nearby compositions $Zn_{1+x}Ga_{2-2x}(Ge,Sn)_xO_4:Cr^{3+}$ crystallising in the spinel structures [6]. Additionally, the adopted 2D atomic scale STEM-EDS maps refinement approach of different cations from the same compound, was the key in elucidating the disorder between three isoelectronic elements in the $Ca_3ZnGe_5O_{14}$ (x = 1) compound. Therefore, this new characterisation technique can be used in many different materials where their related disorder characterisation remains a challenge, as in high entropy oxides (HEO). Finally, knowing that an alkali free melilite was reported, i.e. $La_2Ga_3O_{7.5}$, but also from Chapter IV reporting the $La_{1.725}Ba_{0.275}Ga_3O_{7.3625}$ as the tetragonal $P\bar{4}2_1m$ melilite with the highest interstitial oxide content, both achieved by proceeding direct crystallisation from an under-cooled melt. This procedure could be extrapolated to the Ca-based and Sr-based La*AE*Ga_3O_7 melilites to extend their relative doping amounts, which may improve their already high conductivity values.

The ABC_3O_7 melilites, AB_2O_4 spinels, ABO_3 perovskites and $A_3B_5O_{12}$ garnets are well studied structures in the literature due to their crystalline structures ability to accommodate a variety of different nature, size and oxidation state elements in different coordination types [7–10], which leads to a multiple of interesting properties [11–14]. In this context, the occurrence of previously described langsite structures in chapter III are of interest materials. These structures family are mainly known for their piezoelectric properties [15,16]. Nevertheless, these compounds family, especially the $La_3Ga_5(Ge/Si)O_{14}$ compound, are readily synthesised as large-scale transparent single-crystals [17]. Several studies have developed new optically active langasite compounds, for example the rare earth doped $La_3SbZn_3Si_2O_{14}$ composition which showed white light emission [18], or the cationic framework ordered $La_3Ga_5MO_{14}:Eu3^+$ (*M* = Zr, Hf, Sn) as red-emitting LED phosphors [19]. However, langasite materials with high small rare earth (Ho - Lu) concentration fully occupying the A-sites positions were never reported due to their challenging synthesis. By proceeding crystallisation from a glass precursor or an under-cooled melt it could be interesting to investigate the synthesis of these langasite

compositions, i.e. $RE_3Ga_5GeO_{14}$ *RE* = (Ho – Lu), in the hunt of new optically active materials. Additionally, investigating the possible synthesis of $RE_{3-x}AE_xGa_{5-x}Ge_{1+x}O_{14}$ with possible different ordering-types between the rare earth and the alkali earth metals when the size mismatch between these two is maximised, as seen in chapter II and reported in [20] for the melilite structures, knowing the structural similarities between these two structures.

References:

[1] C. Genevois *et al.*, *Inorg. Chem.*, 2021, **60**, 12339.

[2] G. J. Redhammer, *Acta Crystallogr. Sect. C Struct. Chem.*, 2015, **71**, 80.

[3] J. Fan *et al.*, *Chem. Mater.*, 2020, **32**, 9016.

[4] M.-R. Li *et al.*, *Angew. Chem. Int. Ed.*, 2010, **49**, 2362.

[5] X. Kuang *et al.*, *Nat. Mater.*, 2008, **7**, 498.

[6] M. Allix *et al.*, *Chem. Mater.*, 2013, **25**, 1600.

[7] Z. Xia *et al.*, *Accounts of Chemical Research*, 2017, **50**, 1222.

[8] J.P. Smit *et al.*, *Chemistry - A European Journal*, 2006, **12**, 5944.

[9] M.G. Kanatzidis, *Accounts of Chemical Research*, 2005, **38**, 359.

[10] R.E. Schaak *et al.*, *Chemistry of Materials*, 2002, **14**, 1455.

[11] K.M. Ok *et al.*, *Chemical Society Reviews*, 2006, **35**, 710.

[12] Z. Xia *et al.*, *Chemical Society Reviews*, 2017, **46**, 275.

[13] Z. Xia *et al.*, *Progress in Materials Science*, 2016, **84**, 59.

[14] Q. Zhao *et al.*, *Chemical Reviews*, 2017, **117**, 10121.

[15] A. Pavlovska *et al.*, *Acta Crystallographica Section B Structural Science*, 2002, **58**, 939.

[16] S. Zhang *et al.*, *Journal of the American Ceramic Society*, 2011, **94**, 3153.

[17] T. Taishi *et al.*, *Journal of Crystal Growth*, 2007, **304**, 4.

[18] A. Bhim *et al.*, *Dalton Transactions*, 2020, **49**, 17649.

[19] A. Reinhardt *et al.*, *Journal of Luminescence*, 2020, **218**, 116833.

[20] C. Genevois *et al.*, *Inorganic Chemistry*, 2021, **60**, 12339.

Appendices

Chapter A.I: Experimental methods.

A.I.1. Synthesis.

A.I.1.1. Through glass or melt crystallisation.

Before operating glass synthesis, a homogeneous composition was prepared by mixing stoichiometric amounts of the starting precursors in an agate mortar using ethanol. The composition was dried in a conventional oven at 100°C or over the bench for few minutes. The resulting powder mixture was either melted in an open atmosphere furnace or using the aerodynamic levitation coupled to two CO_2 lasers.

A.I.1.1.1. Using conventional furnace (T≤1750°C).

The mixture is placed in a Pt crucible and introduced in an open atmosphere furnace at 20°C higher than the melting temperature determined from the phase diagram of the studied system in order to melt the sample. After 1 hour, the Pt crucible was taken out from the furnace and either air or water quenched, which allowed to achieve a glass material. This method is easy to operates and allows to synthesis large batches of glass in one go. Despite its simplicity and wide usage, this routine has few down points which can be challenging to overcome: (i) the cooling rates are not always sufficient to obtain glass for systems that energetically favours crystallisation. (ii) This approach implies the sample to be in contact with the crucible, which can be a source of impurities; moreover, the contact surface between the sample and the crucible acts as a nucleation centre which can trigger the samples crystallisation, highly disfavoured in glass synthesis.

A.I.1.1.2. Using aerodynamic levitation (ADL) coupled to two CO2 lasers (max T ≈ 3100°C).

In the CEHMTI laboratory, to overcome the downsides of conventional melt quench synthesis of glass, listed earlier in section A.I.1.1.1, aerodynamic levitation (ADL) coupled to two CO_2 lasers was opted as an alternative synthesis approach (see Figure A. 1).

In order to operates the material synthesis using the ADL apparatus, the starting sample need to be compacted, typically in pellet form. The pellet is broken into small pieces and a fragment is then placed into the nozzle. A gas flow is turned on to help the sample levitate in its liquid form. A pair of CO_2 lasers (10.6 μm) are used to heat the sample from above and below to ensure its homogeneity. A set of pyrometers are used to read the samples temperatures from its emissivity, which allows a complete control of the heating and the cooling processes. The levitating molten bead can be either quenched by shutting off the lasers attaining glass samples,

or slowly cooled down to room temperature to crystallises it from the melt. The use of CO2 lasers makes it possible to reach very high temperatures estimated around 3000°C. Moreover, this contactless synthesis approach between the sample and the nozzle allows to avoid the contamination and nucleation problems cited above. Furthermore, the synthesised beads have usually a diameter between 1 and 5mm, which make them very small in size, hence reaching high cooling rates (between 1000°C - 300°C / s depending on the levitating gas).

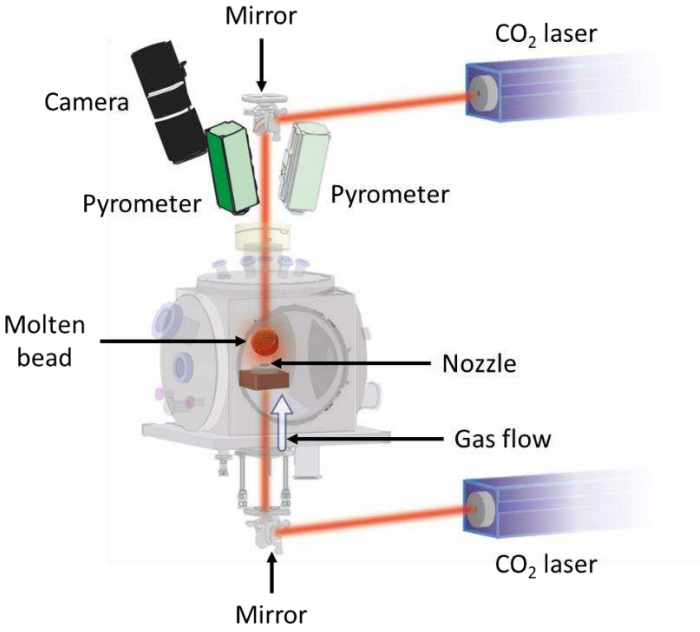

Figure A. 1. ***Aerodynamic levitation coupled to two CO_2 lasers montage.***

A.I.2. Characterisation techniques of the synthesised samples.

A.I.2.1. Differential scanning calorimetry (DSC) thermal analysis.

Differential scanning calorimetry (DSC) measurements for the present work were conducted on a Setaram MULTI HTC 1600 apparatus, which contains two chambers dedicated to a sample and a reference, operating at high temperatures all the way to 1600°C under argon gas flow. The sample and reference chambers are heated simultaneously with a dedicated heating source for each. DSC records the heat flow difference between the sample and reference as they are both heated at once. When the sample goes through a structural or matter state evolution (i.e. crystallisation, phase transition, fusion…), it requires a different energy than the reference to keep both at the same temperature, which is manifested by either an exothermal or endothermal peak.

Differential scanning calorimetry (DSC) is one off the first characterisation techniques to be run after the glass synthesis, as it permits to determine the most important physical quantities

(i.e. glass transition T_g and crystallisation T_c temperatures), for a controlled glass crystallisation process.

A.I.2.2. Average and local structure characterisation.

A.I.2.2.1. Room and variable temperatures laboratory powder X-ray diffraction. RT-PXRD and VT-PXRD.

Room temperature laboratory X-ray diffraction measurements were conducted on powder samples using a Bruker D8 Advance (Cu Kα radiation) equipped with a LynxEye XE detector operating in a Bragg Brentano (θ°-θ°) configuration (Figure A. 2a), meaning that both X-ray source and detector moves at the same time with the same angles in opposite direction, while the sample's position is fixed. X-ray diffraction is a powerful tool in characterisation of the averaged structure of the measured sample, as peak positions, width and intensities supply information about the unit cell parameters, microstructure and atomic parameters respectively. Moreover, it can also provide insight information about the sample purity (phase indexation) to a certain precision degree.

The principle of X-ray diffraction is fairly simple; the X-rays are generated by application of a potential difference between the cathode and anode, these rays are directed toward the sample. The interaction between the sample and incident radiation involves three distinct phenomena: (i) diffracted rays, (ii) transmitted rays and (iii) absorbed rays. The detector collects the diffracted rays and plots them in a diffraction pattern (Figure A. 2b), with the x-axis in diffraction angle (2θ°) and y-axis in collected counts. The sample is a very crucial step, as if it is not well executed (big grains, preferred orientation…), extracting valuable information reflecting the reality of the sample from the diffraction patterns might be a hard task to complete.

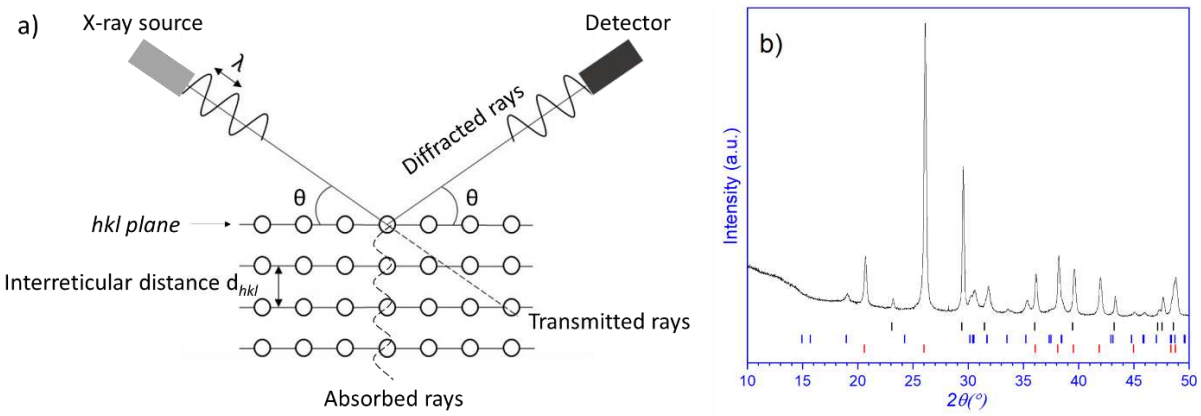

Figure A. 2. *X-ray diffraction principle is shown in a) while b) indicates an example of a measured diffraction pattern of a multiphased sample.*

In-situ variable temperatures powder X-ray diffraction (VT-PXRD) was performed using a Bruker D8 Advance laboratory diffractometer (also Cu Kα radiation, Bragg–Brentano geometry) equipped with a Vantec detector and an Anton Paar HTK1200N furnace for measurements up 1200°C, or with an Anton Paar HTK1600N for measurements up to 1600°C.

A.I.2.2.2. Synchrotron X-ray diffraction.

To reach high resolution diffraction with very low instrumental contribution in the diffracted peak shapes with low background noise, useful in evidencing low intensity peaks band crucial for accurate structural factors, synchrotron powder X-ray diffraction (SPXRD or SPD) is often the best option to go for (Figure A. 3a). Synchrotron facilities rely on the principle of accelerating electrons to very high energies and make them change direction, emitting an intense beam of synchrotron radiation which is sent down the beamline. These rays get filtered using a monochromator, depending of the beamline application (see Figure A. 3b). In this PhD work, SPD measurements related to the projects discussed in Chapter II, III, IV were collected on the 11BM beamline at the Advanced Photon Source (APS) of the Argonne National Laboratory in the United States. The 11BM beamline collects X-ray diffraction data in ~1 hour with an incident wavelength of λ= 0.458084 Å over an angular range of 1°-50° (2θ) with a very high resolution ($\frac{\Delta Q}{Q} \approx 1.4 \times 10^{-4}$, step size = 0.0001°) thanks to its high flux (5×10^{11} photons/second at 30 keV). Moreover, its short wavelength (λ= 0.458084 Å) allows to explore a longer Q ($Å^{-1}$) range, which provides more information about the atomic occupancies and thermal parameters. SPD data illustrated in Chapter V were measured on the CRISTAL beamline at soleil synchrotron in France with an incident wavelength of λ= 0.67153 Å over the angular range of 1°-60° (2θ) and a step size of 0.004°.

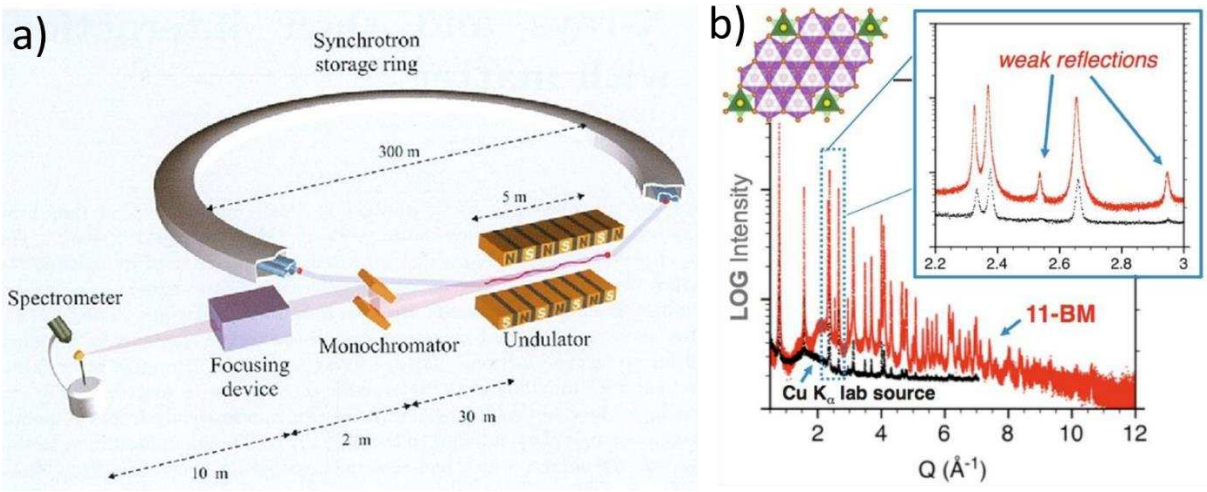

Figure A. 3. *a) Synchrotron accelerator scheme. b) comparison between laboratory and synchrotron X-ray sources.*

A.I.2.2.3. Neutron diffraction.

Elements with a small number of electrons are usually hard to distinguish from X-ray diffraction, especially if the material contain both heavy and light elements, as X-ray diffraction is based on the interaction with the electronic density of the atoms. Usually the suitable solution to extract valuable information about these atoms is to proceed neutron diffraction as their scattering is not the same (e.g. oxygen is much more visible in neutron diffraction than X-ray diffraction). Moreover, this technique can also be used when two elements have close atomic number but different neutron scattering lengths, which make it possible to characterize their respective occupancies on the same site. Furthermore, neutron diffraction doesn't show strong peak intensity extinction at high angle as seen in XRD; this advantage can be linked to the independent relation between the scattering lengths and diffraction angle. It is worth noting that large amounts of sample (~5g) are used in order to keep reasonable acquisition time.

Neutron powder diffraction (NPD) data presented in Chapter III were acquired on the instrument MEREDIT at the Nuclear Physics Institute, Czech Republic, which provides an incident wave length of λ= 1.46 Å and a measuring range between 4°-144° (2θ) and a step size of 0.08° with a measuring time of 970s/step. As for NPD data displayed in Chapters IV and V, measurements were conducted on the D2B line in the ILL laboratory, France. The incident wavelength of this neutron line is λ= 1.60 Å, with a measuring range of 4°-160° (2θ), a step of 0.05°, and a total measuring a time of 14400 seconds.

The measured data at the D2B line were provided in the form of two data sets: high intensity "HI" and high resolution "HR". HI data are the integration of the whole 2D pattern, whereas

the HR data are the integration over a centred region of the 2D pattern which provide better signal to noise ration with lower peaks intensity (Figure A. 4).

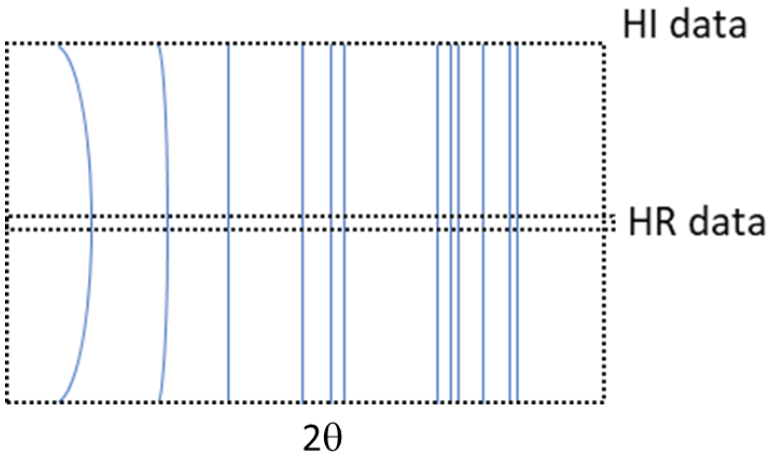

Figure A. 4. *Illustration of an acquired neutron powder diffraction pattern showing the integrated regions for HI and HR data sets.*

A.I.2.2.4. Electron diffraction.

Electron diffraction is a technique for probing crystals at the nanometric scale, where each crystallite can be diffracted individually; this is a great advantage in multiphase samples, as each phase can be studied independently. Electron diffraction allows each hkl peak to be diffracted individually, as seen in single crystals X-ray diffraction, which is highly valued for accurately determining cell parameters and space group symmetry of the crystalline phase. In our case, the observed samples were either under powder or thin foil form: (i) for powder specimens, a small amount of sample was ground in an agate mortar and dispersed in ethanol; a droplet of this suspension was then deposited onto a copper grid layered by a holey amorphous carbon film. (ii) for thn foil specimens, the starting sample was first mechanically polished using a tripod and inlaid diamond discs until a thickness of 50µm was reached; The thin foil was then obtained by argon ion milling (PIPS GATAN).

Electron diffraction was performed using a CM20 transmission electronic microscope (TEM) operating at 200kV or a JEOL ARM200F (JEOL Ltd.) Cold FEG TEM. Both are equipped with a double-tilt holder that allows orienting the crystals in all specific directions.

A.I.2.2.5. Maximum entropy method (MEM).

The maximum entropy method is a model-free calculation process, able to reconstruct the whole electron or nuclear density within the unit cell using X-ray or neutron phased structure factors. This method was introduced as an alternative to the inverse Fourier transform calculation process due to the limits and artefacts associated to the calculation of $\rho(r)$ from the

observed structure factors (issues due to incomplete and noisy data) [1]. The principal of MEM calculations relies on the probability's theory (Bayesian statistics).

"Deduction = Hypothesises & measurements"

$$pr(\text{Sc}|\text{DI}) = pr(\text{Sc}|\text{I}) \times pr(\text{D}|\text{ScI})$$

$$\downarrow \qquad \downarrow \qquad \downarrow$$

$$Posterior = Prior \times Likelihood$$

$$pr(\text{Sc}|\text{I}) \propto e^{\alpha S} \qquad pr(\text{D}|\text{ScI}) \propto e^{-\frac{1}{2}\chi^2} \qquad \log(pr(\text{Sc}|\text{DI})) \propto \alpha S - \frac{1}{2}\chi^2$$

- pr(X1|X2): probability that X1 is true under the condition that X2 is true.
- Sc: Hypothesis or Scene to validate (the density in the unit cell).
- D: New data of a certain observation (the diffraction data).
- I: the prior information (about Sc before getting D), the prior density (either flat or corresponding to any "relevant" structural model).

The deduction $\{pr(\text{Sc}|\text{DI})\}$ is hence maximised by the maximisation of the Shannon entropy term S and the minimization of the likelihood term (χ term or F-constraints), which depends on the agreement between the experimentally observed F_{obs} and the MEM calculated F_{MEM} obtained by Fourier transform of the MEM trial density at the considered iteration cycle of the calculations. The entropy S measures the total amount of uncertainty represented by this distribution, after all relevant information has been taken into account: $S = -k \sum_{n=1}^{N} \rho_n \ln(\rho_n)$ with k a positive constant and ρ_n set of probabilities associated to these statements.

A.I.2.2.6. Nuclear magnetic resonance (NMR).

Solid state nuclear magnetic resonance (NMR) spectroscopy, is a powerful characterisation technique in probing the local structure/environment of a chosen nuclei. Moreover, this technique is based on the Zeeman Effect. NMR studies of a nuclei requires a nuclear spin $I \neq 0$ of the probe atom. The spinning nature of an atom nucleus generates a moment I consequently a magnetic moment μ. In the absence of an external magnetic field, the nuclear spins are degenerate, meaning that they are disoriented and possess the same energy. When an external magnetic field B_0 is applied, it provokes a splitting into 2I+1 possible orientations separated by Larmor frequency (ν_0).

$$\nu_0 = \frac{\gamma B_0}{2\pi} \qquad \textbf{(Equation A.1)}$$

In solids the magnetic field around each nucleus is affected by the electronic cloud of the neighbouring nuclei, causing different interactions types (i.e. chemical shift interaction, direct dipole-dipole interaction, J-coupling interaction, quadripolar interaction) interfering with the Zeeman Effect.

A.I.3. Structural solution and refinements.

A.I.3.1. The Rietveld method.

The acquired laboratory, synchrotron or neutron diffraction data were subject of analysis by the Rietveld method, which simulates a diffraction pattern from a theoretical model (structure) and compare it to the measured diffraction pattern. The simulated intensities at a certain 2θ value (here we call it *i*) are calculated using the following mathematical formula:

$$Y_{calc\,i} = \sum_{\phi}^{N} S_{\phi} \sum_{k=k1}^{k2} J_{\phi k} \,.\, Lp_{\phi k} . O_{\phi k} . M . \left|F_{\phi k}\right|^2 . \Omega_{i\phi k} + Y_{back\,i} \qquad \textbf{(Equation A.2)}$$

- $Y_{calc\,i}$: Calculated intensity at position (in 2θ).
- $Y_{back\,i}$: Background calculated intensity at the i^{th} position (in 2θ).
- S_{ϕ}: Scale factor proportional to the number of unit cells contributing to the scattering divided by the unit cell volume.
- $J_{\phi k}$: Multiplicity factor of the k^{th} reflection.
- $Lp_{\phi k}$: Lorentz-polarisation factor.
- $O_{\phi k}$: Preferred orientation correction factor.
- M: Beam absorption correction function.
- $\left|F_{\phi k}\right|$: Structural factor.
- $\Omega_{i\phi k}$: Profile function.

The background is usually defined either manually, or by a polynomial function type (Chebyshev, Legendre). In powder diffraction problems, a Pseudo-Voigt profile function is commonly used to describe the patterns intensity distribution around a peak *k*, as it combines both Gaussian (from the instrument, i.e. *U V W*) and Lorentzian (from the sample, i.e. microstructure and crystallite size *X Y*) contributions. In this work a TCHZ profile function was used as it considers the diffraction angle dependent Gaussian and Lorentzian broadening variations.

To judge the quality of a Rietveld refinement and how the theoretical model compares to the experimental data, a first look at the difference curve ($Y_{obs\,i} - Y_{calc\,i}$) can help identifying the poorly fitted regions; the flatter this difference curve is the better it is. Moreover, after each

refinement cycle, reliability factors (R_p, R_{wp}, R_{Bragg}, χ^2) are calculated which also provides information about the fit quality; the lower these values are the better it is. These factors are calculated using the following formulas:

- R-profile: $R_p = 100.\frac{\sum_i |Y_{obs\,i} - Y_{calc\,i}|}{\sum_i Y_{obs\,i}}$ (**Equation A.3**)
- R-weighted profile: $R_{wp} = 100.\sqrt{\frac{\sum_i W_i (Y_{obs\,i} - Y_{calc\,i})^2}{\sum_i W_i Y_{obs\,i}^2}}$ (**Equation A.4**)
- Bragg residue: $R_{Bragg} = 100.\frac{\sum_k |I_{obs\,k} - I_{calc\,k}|}{\sum_k I_{obs\,k}}$ (**Equation A.5**)

  with $I_{obs\,k}$ and $I_{clac\,k}$ being the observed and calculated intensities of the k^{th} Bragg reflexion.
- Experimental statistic factor: $R_{exp} = \sqrt{\frac{(N-P+C)}{\sum_i W_i Y_{obs\,i}^2}}$ (**Equation A.6**)

  with N, P and C represent the number of used measured points, number of refined parameters and used constraints respectively.
- Goodness of fit (GOF): $\chi^2 = \left(\frac{R_{wp}}{R_{exp}}\right)^2$ (**Equation A.7**)

In this PhD work Topas academic (V6) [2] was used as main refinement program.

A.I.3.2. *ab-initio* structure solution.

To understand a compound macroscopic property a better understanding of its crystal structure is indeed needed. First, the acquired powder X-ray diffraction pattern is indexed against the ICDD data base, comparing the existing structures cell parameters to the measured peak position. If the pattern is fully indexed, Rietveld refinements can be proceeded to refine the crystal structure. However, if the indexation part fails, meaning that no structure from the used data base can be associated to the experimental diffraction pattern, structural solution take place to elucidate the crystal structure of this new compound.

In solving a new material crystal structure, three major steps must be followed:

- First step is finding the cell parameters, also called indexation, this step can be fulfilled using Dicvol [3] programme implemented in WinPlotR [4] from the FullProf [5] programme. The resulting solutions are associated with merit figures defined by Wolff and Smith [6], [7], which allows to choose the best solution with the highest merit. A Lebail [8] or Pawley [9] refinement is carried out at the end of this step to extract the (zero shift, precise cell parameters and the profile parameters). Most importantly it allows to refine, with the most accuracy possible, the peaks intensities which indicates the *hkl* extinction conditions; hence, narrowing

the number of possible space groups to one or few of them. In this thesis the Space group Test implemented in JANA2006 [10] program was used. As easy as it may sounds to use a programme for the finding the right space group, from powder samples diffraction data, this task can be very challenging due to peak overlapping, in which case depending on the sample a different technique can be employed to elucidate the *hkl* extinction conditions.

- Second step after finding the right cell parameters and space group, is to locate the positions of the different atoms inside the structure. This type of information is provided by the diffracted peak intensities, and can be exploited by different methods (direct, Patterson, maximum entropy…) using different approaches (charge flipping, simulated annealing…) implemented in a variety of programs, JANA2006 [10], Topas [2], FOX [11]…etc. Usually the heaviest atoms are placed first as they have the strongest scattering contribution. The lightest atoms are latter localised by Fourier difference maps analysis and added to the structure.
- The third and final step is to use the Rietveld method to refine the different remaining atomic parameters (atomic positions, occupation rates in case of disordered materials, related thermal parameters. This step is of a big importance to give the best averaged structural description of the measured sample.

A.I.4. Microstructure and atomic scale observations.

A.I.4.1. Scanning electron microscopy (SEM).

To check the samples surface morphology, chemical composition and homogeneity; scanning electronic microscopy (SEM) coupled to energy dispersive X-ray spectrometer, measurements were conducted on a Field Emission Gun-SEM MERLIN (ZEISS). As shown in **Figure A. 5**, the generated homogeneous electrons beam is focused on a spot of the sample allowing the scanning of its surface. Arising signals can be analysed in three different modes:

- Secondary electrons (SE): When the incident beam hits the sample, the latter valence electrons are ejected (called secondary electrons). In this mode the only information provided are the sample's morphology and topology.
- Backscattered electrons (BSE): The elastic interaction between the incident beam and the sample's nucleus, results in a bounce back of the beam's electrons (called backscattered electrons). In this mode the chemical homogeneity can be observed as the quantity of backscattered electrons is dependent of the Z atomic number, this means that in imaging, brighter regions have a correspond to a higher atomic number.

- X-ray elemental analysis: the chemical composition of the measured sample can be determined in this mode. This is possible from the generated X-rays from the inelastic interaction between the electron beam and sample's core electrons.

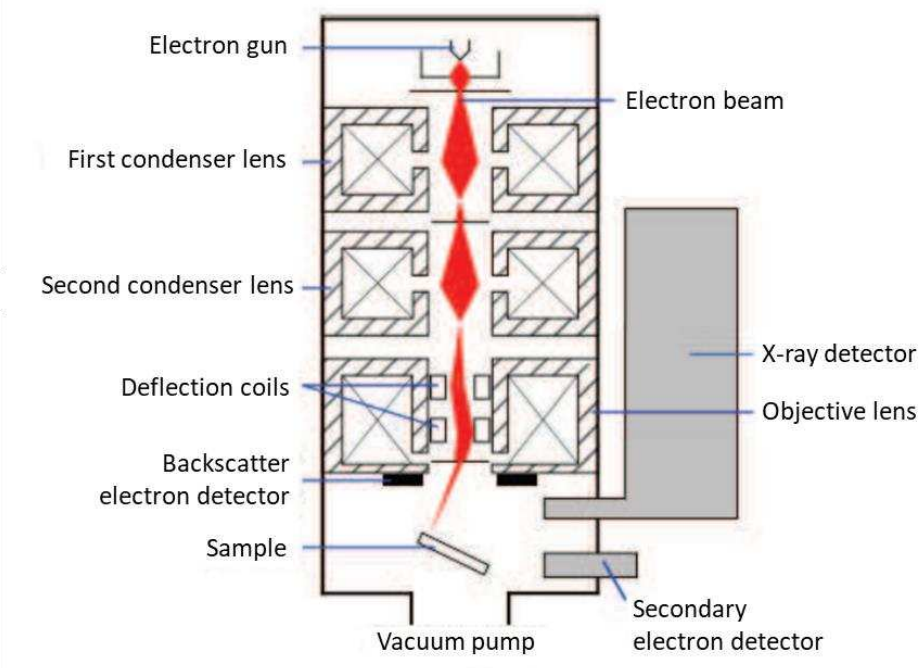

Figure A. 5. *Scheme of an SEM components.*

A.I.4.2. Transmission electron microscopy (TEM).

To observe samples from the nanometre to the atomic scale, TEM is a powerful technique that can help in achieving this task, however the sample thickness needs to be thin enough, a few tens of nanometres, in order for the beam to go through. The samples preparation methods have been described in the electron diffraction part. Two imaging modes have been proceeded in this thesis, TEM and STEM-HAADF (see Figure A. 6a and Figure A. 6b. In TEM mode, the bright field imaging is obtained by selecting only the transmitted beam, the generated image of the crystals in Bragg diffraction conditions show a dark contrast, while the brighter contrast indicates crystals in non-diffraction conditions or none-crystalline sample. The bright field mode mostly provides key information about the sample microstructure (morphology, crystallinity, crystallite size and dispersion). Dark field mode on the other hand, is operated by selecting one or multiple diffracted beams, which allow a selective imaging of a chosen phase in a multiphased sample. Moreover, the crystals at the origin of the selected diffracted beams will appear brighter in the acquired image.

Atomic scale imaging was performed in the high-resolution Scanning Transmission Electron Microscopy-High Angle Annular Dark Field (STEM-HAADF) mode, on a double corrected

JEOL ARM200F (JEOL Ltd.) Cold FEG Transmission Electron Microscope (TEM). Before proceeding to the atomic scale imaging, the sample must to be oriented in the desired direction with the help of the electron diffraction. STEM-HAADF imaging is constructed by the collection of wide-angle scattered electrons (angles > 50 mrad) using an annular detector (Figure A. 6b). The images obtained are in chemical contrast, i.e. the heaviest elements or phases will appear brighter. In order to obtain more information on the sample cationic distribution, elemental maps at the atomic scale were performed by EDS (Energy Dispersive X-ray Spectroscopy) or EELS (Electron Energy Loss Spectroscopy).

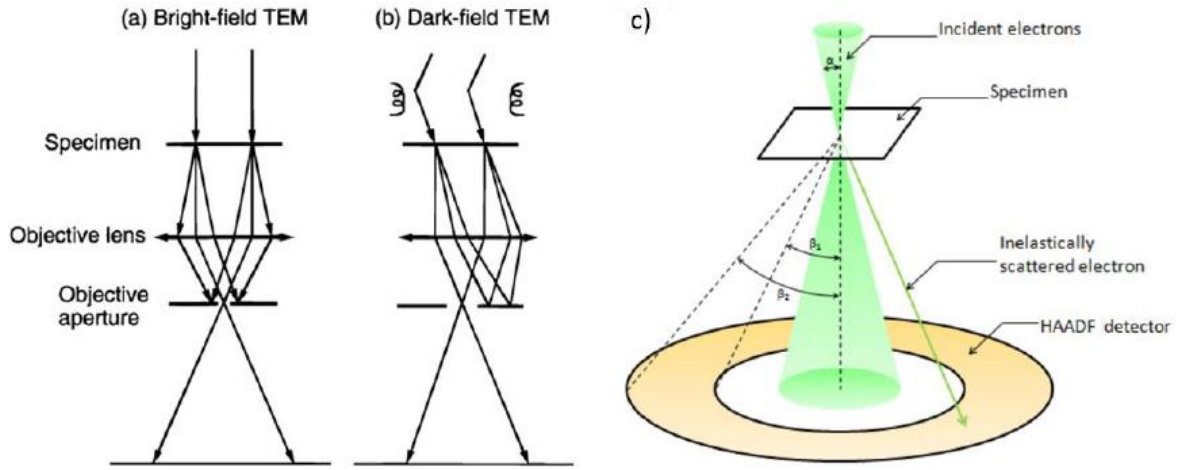

Figure A. 6. *Schemes of TEM imaging concept in bright (a), dark field (b) modes and STEM-HAADF mode (c). Figures were takesn from [12] and [13].*

A.I.5. Properties measurements.

A.I.5.1. Photoluminescence measurements.

Photoluminescence is the occurrence light emission under photon absorption. While an emission measurement on a certain spectral range, the source radiation wavelength is fixed. Photoluminescence spectra were recorded at room temperature using a Horiba-Jobin-Yvon Nanolog spectrofluorimeter, equipped with a 450 W Xe lamp source coupled to a double monochromator for excitation, and an iHR320 spectrometer coupled to an infrared PMT detector sensitive from 950 to 1650 nm (Hamamatsu).

A.I.5.2. AC Impedance measurements.

Ionic conductivity of the samples was characterised by AC-impedance spectroscopy. Two different setups were used depending on the sample size. For small polished beads measurements were conducted on a Solartron 1260 (Chapter IV) in University of Guilin, China,

by Alberto J. Ferná ndez-Carrión as part of international collaborations. Samples in the form of dense pellets were measured in house on a Solartron SI 1260 by Leire del Campo (Chapter V).

The sample subject of this characterisation is first polished from both sides, these surfaces are coated by platinum or silver paste (both surfaces needs to have the same paste nature). The samples go under an annealing treatment to evaporates the organic compounds from the coating; hence, forming electrodes. AC-impedance experiments consists on applying an alternating voltage $E(\omega)$ ($\omega = 2\pi f$) of low amplitude and variable frequency. As a consequence, a current $I(\omega)$ is generated and measured. The recorded data are usually plotted in Nyquist diagrams, involving Z' and -Z'' which represents the real and imaginary parts of the impedance $Z(\omega)$ respectively.

$$Z(\omega) = \frac{E(\omega)}{I(\omega)} = \frac{U_0 e^{(j\omega)}}{I_0 e^{j(\omega t+\varphi)}} = Z' + jZ'' \qquad \textbf{(Equation A.8)}$$

In the ideal scenario, Nyquist plots of a measured ceramic should divulge two clear semi-circles, which corresponds to the bulk (usually at higher frequencies) and grain boundaries (usually at lower frequencies) responses (see Figure A. 7). However, it's not always the case and overlapping of the semi-circles is often observed. The intersection point between the semi-circles and the x axis is defined as the resistance of either the bulk (R_b) or bulk+grain boundaries ($R_b + R_{gb}$) (depending on which semi-circle it is). The defined R_b can be used in the following formula to calculate its related conductivity σ at this temperature.

$$\sigma_b = \frac{1}{R_b} \times \frac{l}{S} \qquad \textbf{(Equation A.9)}$$

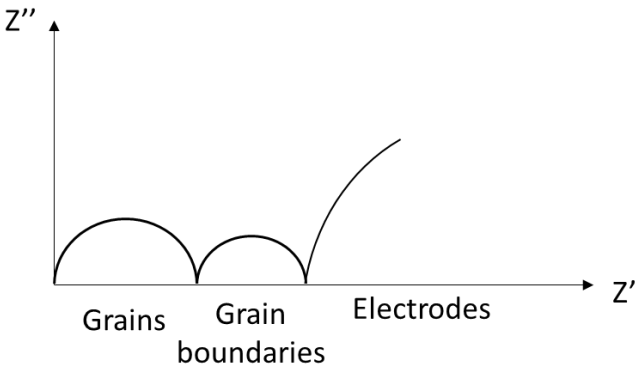

Figure A. 7. ***Complex impedance curves of a polycrystalline sample in the ideal case.***

A.I.6.Other characterisation techniques.

A.I.6.1. Density measurements by Archimedes law.

To characterise the pellets density post SPS process, Archimedes method was pursued using the montage illustrated in **Figure A. 8**. The sample is weighted in air atmosphere (m_a) and when immerged in a solvent (m_s). The samples density can thus be estimated using the following formula: $\rho_{sample} = \frac{m_a}{m_a - m_s} \times \rho_{solv}$. In this work absolute ethanol was used as a solvent.

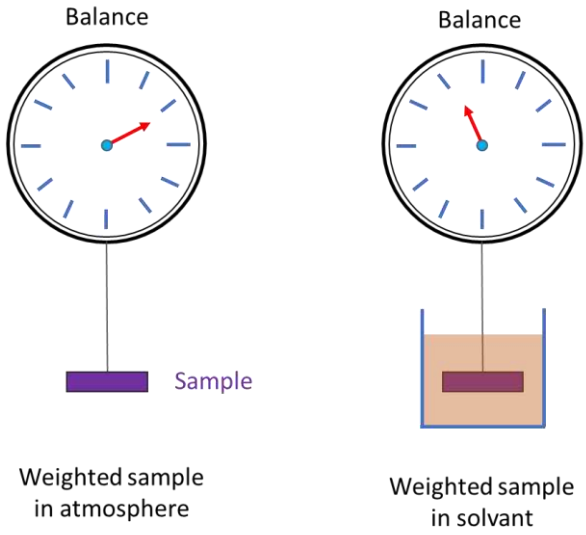

Figure A. 8. *Density measurement using Archimedes method.*

A.I.7. References.

[1] A.K. Livesey *et al.*, *Acta Crystallographica Section A: Foundations of Crystallography*, 1985, **41**, 113.

[2] A.A. Coelho, *Journal of Applied Crystallography*, 2018, **51**, 210.

[3] A. Boultif *et al.*, *Journal of Applied Crystallography*, 1991, **24**, 987.

[4] T. Roisnel *et al.*, *In Materials Science Forum. Proceedings of the European Powder Diffraction Conf. (EPDIC 7)*, 2001.

[5] J. Rodríguez-Carvajal, *Physica B: Condensed Matter*, 1993, **192**, 55.

[6] P.M. de Wolff, *Journal of Applied Crystallography*, 1972, **5**, 243.

[7] G.S. Smith *et al.*, *Journal of Applied Crystallography*, 1979, **12**, 60.

[8] A. Le Bail *et al.*, *Materials Research Bulletin*, 1988, **23**, 447.

[9] G.S. Pawley, *Journal of Applied Crystallography*, 1981, **14**, 357.

[10] V. Petricek *et al.*, *Institute of Physics, Academy of Sciences of the Czech Republic*, 2006, **162**, 53.

[11] V. Favre-Nicolin *et al.*, *Journal of Applied Crystallography*, 2002, **35**, 734.

[12] Z.L. Wang, *The Journal of Physical Chemistry B*, 2000, **104**, 1153.

[13] https://www.jeol.co.jp/en/words/emterms/search_result.html?keyword=HAADF-STEM. [Accessed: 30-Jul-2022].

Chapter A.II: Supplementary information for Chapter II.

A.II.1.Comparison with other superstructured melilites.

The reported commensurate structure of $Ca_2CoSi_2O_7$ ackermanites (part of the melilite family), possess a fully ordered B-site $(Co,Si)O_4$ tetrahedral framework, with Co and Si being held on the 4- and 3-corner shared tetrahedra respectively, with an A-sites network formed by only Ca atoms. The B-sites cations ordering over the layered framework drives a distortion of the A-sites pentagonal channels in order to satisfy the local Si-O and Co-O first coordination sphere bonding (1.647(1) Å 1.952(2) Å respectively), varying the Ca's coordination from 6 to 8. This distortion is manifested by a tripling of both *a* and *b* cell parameters, resulting in a 3×3×1 supercell (S.G. $P2_12_12$; a = 23.510 (4) Å, b = 23.510 (4) Å, c = 5.025 (1) Å)[40], [41] (see **Figure VI.1**). In **Figure VI.2**a showing its structural projection within the *c*-axis expanded to four cells along *a* and *b* directions, the different distorted A-site channels can be spotted in a confined parent-melilite cells clusters, separated by step-like of undistorted $[(Co,Si)O_4]_5$ pentagons.

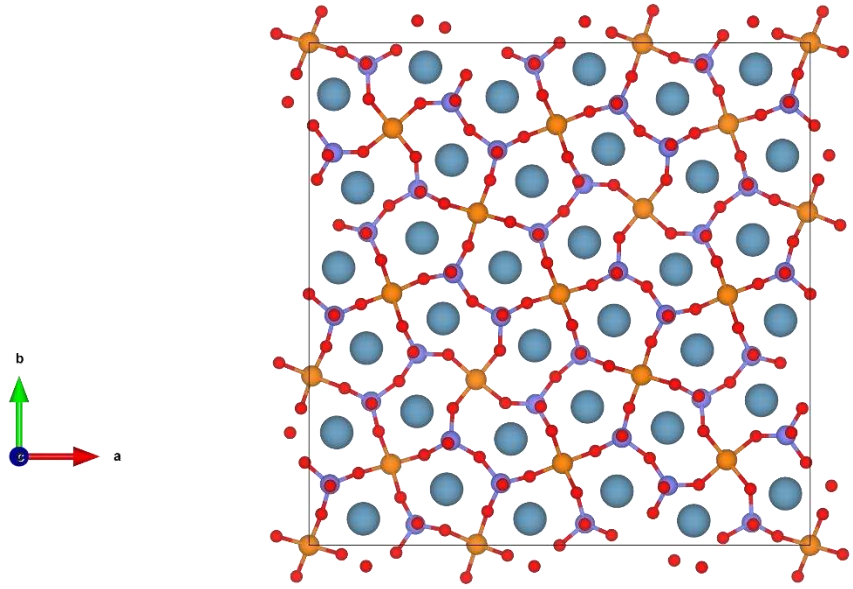

Figure VI.1. *$Ca_2CoSi_2O_7$ structure projection within the c-axis showing the B-site ordering, with Ca in blue, Co in orange and Si in light purple and oxides in red.*

To enable comparison between $SrREGa_3O_7$ *RE*= [Dy – Lu] ordered melilites and commensurate $Ca_2CoSi_2O_7$ ackermanites, a description of the underlaying $[Co(Si)_2]O_7$ framework tiling is needed. In Figure VI.2b and Figure VI.2c two tiling types can be

differentiated: **X** and **Y**; however, to construct the whole $[Co(Si)_2]O_7$ tetrahedra arrangement, combination of **X**, **X**', **X***, **X***' and **Y** (* and ' refers to a in plane or perpendicular 180° rotation of the tile respectively) tiling is required. In this case the tiling arrangement is proceeded in regard to satisfy the condition of spreading the distorted parent melilite sub-cells while keeping a fully ordered B-sites nest, which imposes an expansion of the parent tetragonal melilite. This induces the tripling of both *a* and *b* parameters; different from the observed cell amplification in the Sr*RE*Ga_3O_7 *RE*= [Dy – Lu] ordered melilites, occurring only along the *a*-axis.

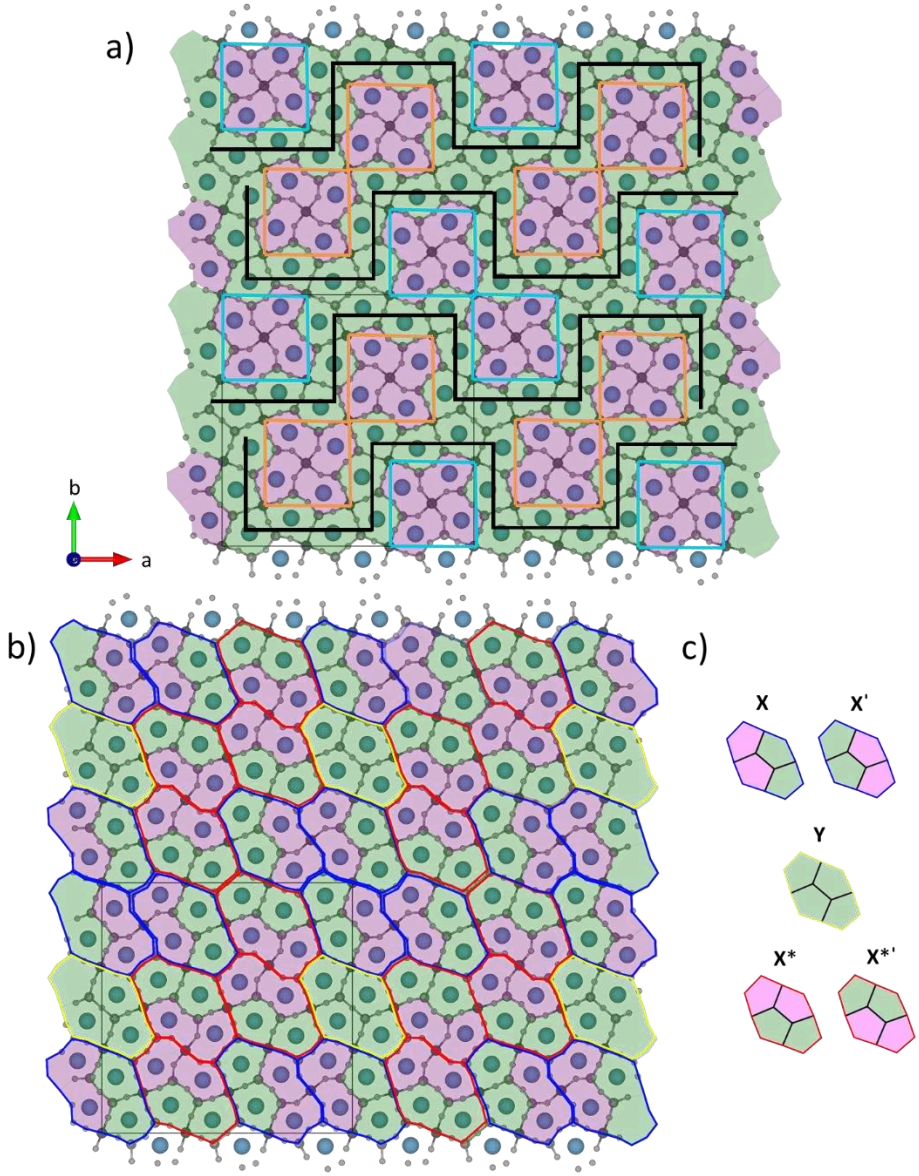

Figure VI.2. *Four $Ca_2CoSi_2O_7$ cells projection within the c-axis showing the $[Co(Si)_2]O_7$ framework distortion described in two ways: a) combination of framework distorted parent melilite cells (blue and orange squares) isolated by a 2D step-like framework (black lines) of undistorted A-sites pentagonal channels, b) two-dimensional stack (along the b-axis) of 1D sequences of : (i)XX*X' (y= 0.25), (ii)Y X*'X* (y= 0.5), (iii) X'XX*' (y= 0.75), with X, X', Y, X*, X*' tilling described in c). In all panels the green and purple shading highlight both undistorted and distorted $[(Co/Si)O_4]_5$ pentagonal channels respectively.*

A.II.2. Complementary Figures and Tables.

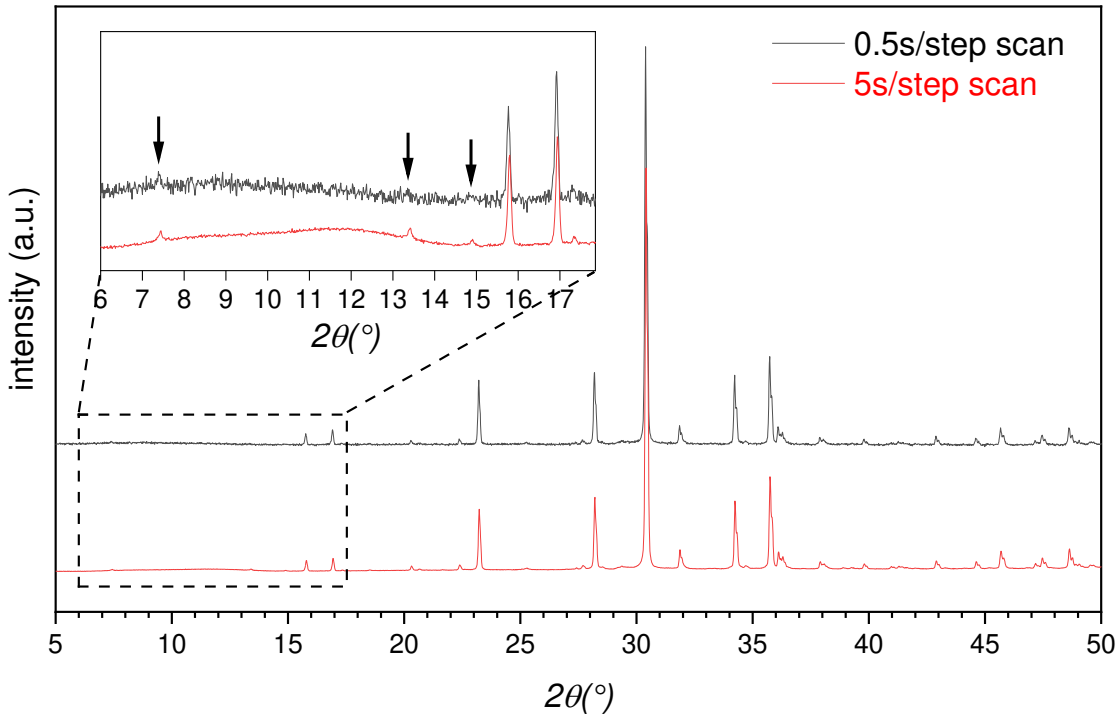

Figure A. 9. *Comparison between two scans acquired in the 5°-50° (2θ) range using a 0.015° step and 0.5s/step (black pattern), 5s/step (red pattern) as measuring times of the $SrYGa_3O_7$ melilite, evidencing the superstructure peaks after longer counting indicated by black arrows in the insert.*

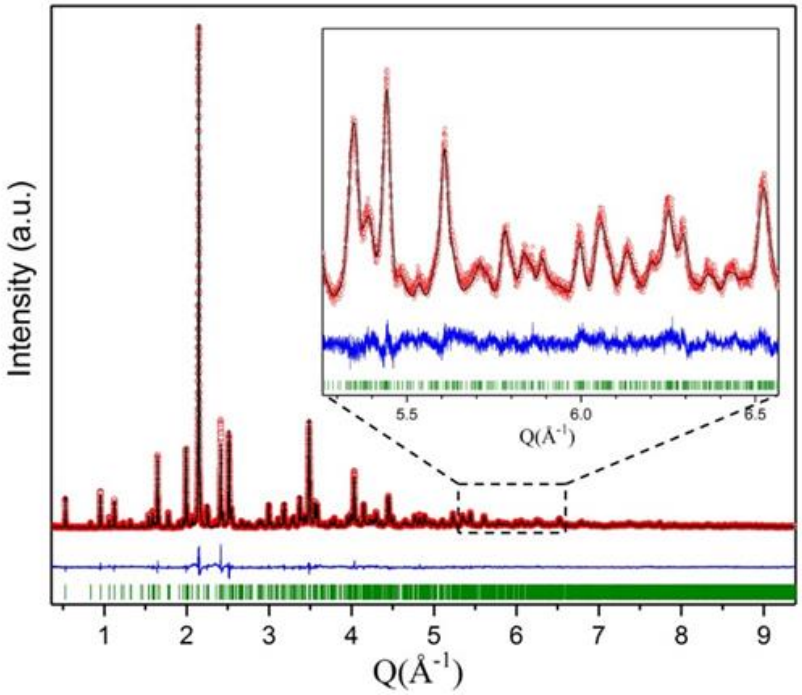

Figure A. 10. *Rietveld refinement of $SrLuGa_3O_7$ ordered melilite (R_p= 6.87% R_{wp}= 9.18%) (SPD data). Observed (black dot), calculated (red line), and difference (blue line) profiles are shown. The set of green vertical lines corresponds to reflection positions.*

Table A. 1 Final refined structural parameters obtained from SPD data collected at room temperature on the $SrLuGa_3O_7$ superstructure melilite ($P2_12_12$ space group, a = 23.6710(2) Å, b = 7.91556(8) Å and c = 5.20516(4) Å). Note that the oxide x, y, z coordinates were subjected to soft restraints to keep them close to the corresponding values from $SrYbGa_3O_7$ (see Chapter II section II.4.1).

Atom	Site	x	y	z	Occ	B_{iso}
Lu1/Sr1	4c	0.22070(6)	0.14247(18)	0.4963(3)	0.520(4)/0.480(4)	0.94(3)
Lu2/Sr2	4c	0.38160(5)	0.31180(14)	0.4570(2)	0.891(3)/0.109(3)	0.87(3)
Sr3/Lu3	4c	0.0496(2)	0.3225(7)	0.5062(14)	0.455(2)/0.045(2)	1.00(7)[a]
Sr3/Lu3’	4c	0.0640(2)	0.3547(6)	0.5045(15)	0.455(2)/0.045(2)	1.00(7)[a]
Ga1	4c	0.44881(10)	0.1435(3)	0.0138(6)	1	0.53(2)[b]
Ga2	2a	0	0	0.9723(9)	1	0.53(2)[a]
Ga3	4c	0.17413(12)	0.4805(3)	0.9982(8)	1	0.53(2)[a]
Ga4	4c	0.28907(10)	0.3346(3)	0.9555(5)	1	0.53(2)[a]
Ga5	4c	0.11930(12)	0.1239(3)	0.0287(5)	1	0.53(2)[a]
O1	4c	0.4540(7)	0.341(2)	0.201(3)	1	2.3(1)[c]
O2	4c	0.3857(7)	0.070(2)	0.182(3)	1	2.3(1)[c]
O3	4c	0.2947(6)	0.337(2)	0.305(3)	1	2.3(1)[c]
O4	4c	0.4404(7)	0.148(2)	0.690(3)	1	2.3(1)[c]
O5	4c	0.1266(8)	0.114(2)	0.701(2)	1	2.3(1)[c]
O6	2b	0.5	0	0.149(4)	1	2.3(1)[c]
O7	4c	0.2271(8)	0.435(2)	0.776(4)	1	2.3(1)[c]
O8	4c	0.0490(6)	0.140(2)	0.160(3)	1	2.3(1)[c]
O9	4c	0.2953(7)	0.131(2)	0.774(4)	1	2.3(1)[c]
O10	4c	0.1519(7)	0.296(2)	0.199(3)	1	2.3(1)[c]
O11	4c	0.3483(7)	0.446(2)	0.790(2)	1	2.3(1)[c]

[a,b,c] Constrained to refine the same value

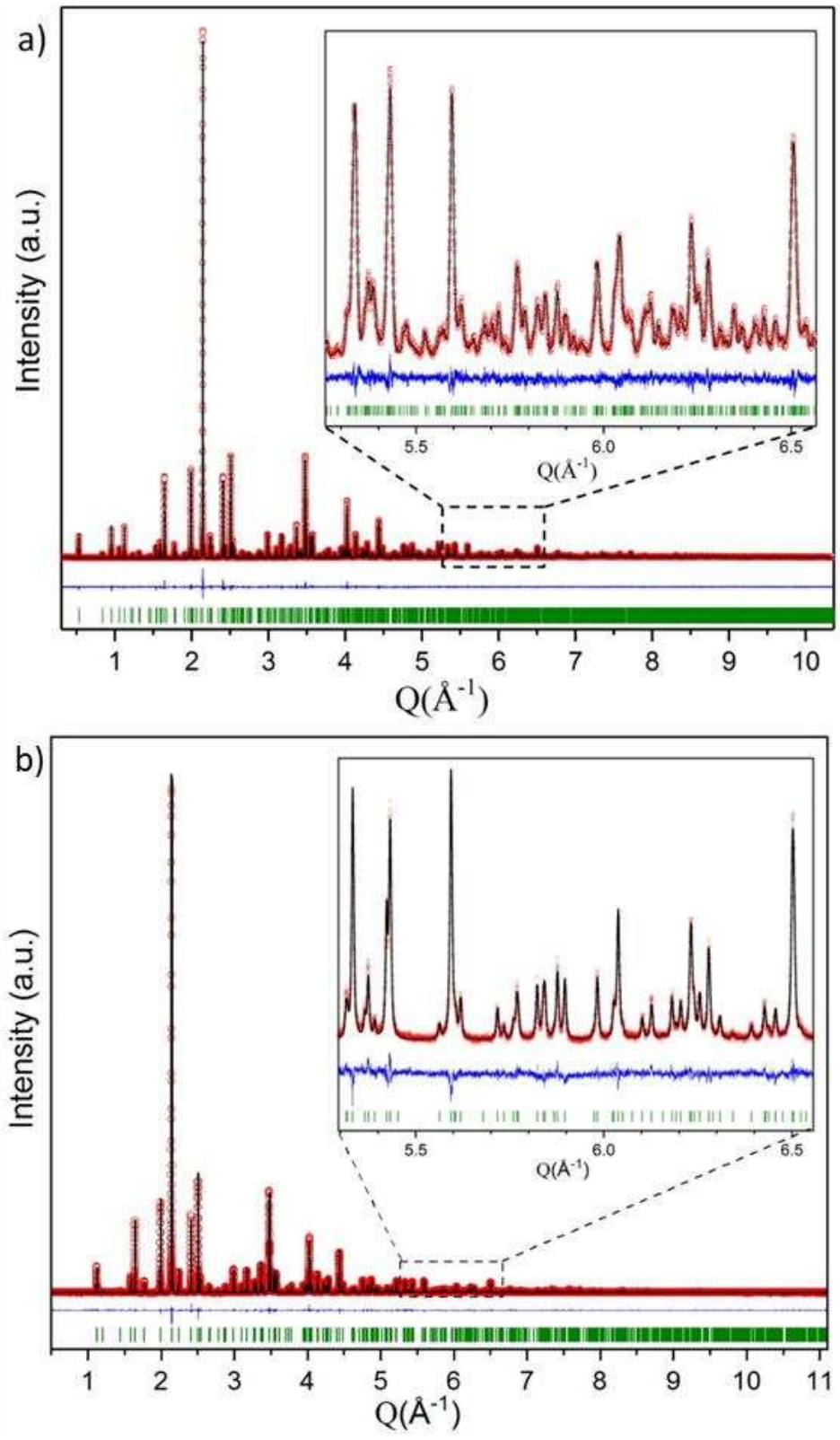

Figure A. 11. *Rietveld refinement of a) $SrTmGa_3O_7$ ordered melilite (R_p= 5.28% R_{wp}= 7.06%) (SPD data) and b) $SrTmGa_3O_7$ disordered melilite (SPD data, R_p= 6.36% R_{wp}= 8.32%). Observed (black dot), calculated (red line), and difference (blue line) profiles are shown. The set of green vertical lines corresponds to reflection positions.*

Table A. 2. Final refined structural parameters obtained from SPD data collected at room temperature on the $SrTmGa_3O_7$ superstructure melilite ($P2_12_12$ space group, a = 23.74405(8) Å, b = 7.92635(3) Å and c = 5.21619(2) Å).

Atom	Site	x	y	z	Occ	B_{iso}
Tm1/ Sr1	4c	0.21996(3)	0.14458(8)	0.49507(13)	0.5/0.5	0.472(12)
Tm2	4c	0.38119(2)	0.31222(6)	0.45491(10)	1	0.545(10)
Sr3	4c	0.05781(4)	0.33948(13)	0.5090(2)	1	0.68(2)
Ga1	4c	0.44927(5)	0.14431(16)	0.0101(3)	1	0.40(2)
Ga2	2a	0	0	0.9800(4)	1	0.38(3)
Ga3	4c	0.17290(6)	0.48152(15)	0.9992(3)	1	0.28(2)
Ga4	4c	0.28920(5)	0.33617(15)	0.9518(2)	1	0.23(2)
Ga5	4c	0.11827(6)	0.12410(14)	0.0312(2)	1	0.34(2)
O1	4c	0.4575(3)	0.3414(10)	0.2031(14)	1	1.02(4)[a]
O2	4c	0.3860(3)	0.0699(9)	0.1978(14)	1	1.02(4)[a]
O3	4c	0.2907(3)	0.3382(10)	0.3003(12)	1	1.02(4)[a]
O4	4c	0.4439(3)	0.1450(10)	0.6755(13)	1	1.02(4)[a]
O5	4c	0.1282(3)	0.1206(9)	0.6855(11)	1	1.02(4)[a]
O6	2b	0.5	0	0.1570(18)	1	1.02(4)[a]
O7	4c	0.2258(3)	0.4230(10)	0.7708(17)	1	1.02(4)[a]
O8	4c	0.0482(3)	0.1424(10)	0.1656(14)	1	1.02(4)[a]
O9	4c	0.2982(3)	0.1308(10)	0.7806(17)	1	1.02(4)[a]
O10	4c	0.1519(3)	0.3020(10)	0.1986(14)	1	1.02(4)[a]
O11	4c	0.3467(3)	0.4558(10)	0.7984(12)	1	1.02(4)[a]

[a] Constrained to refine to the same value

Table A. 3. Final refined structural parameters of the $SrTmGa_3O_7$ disordered melilite ($P\bar{4}2_1m$ space group, $a = b$ = 7.92455(3) Å, and c = 5.21558(2) Å).

Atom	Site	x	y	z	Occ	B_{iso}
Tm1/Sr1	4e	0.33812(3)	0.16188(3)	0.51362(10)	0.5/0.5	1.783(8)
Ga1	2a	0	0	0	1	1.08(2)
Ga2	4e	0.14401(4)	0.35599(4)	0.96889(14)	1	1.07(1)
O1	2c	0.5	0	0.1854(11)	1	3.31(5)[a]
O2	4e	0.1418(3)	0.3582(3)	0.3109(6)	1	3.31(5)[a]
O3	8f	0.0956(3)	0.1603(3)	0.7952(6)	1	3.31(5)[a]

[a] Constrained to refine to the same value

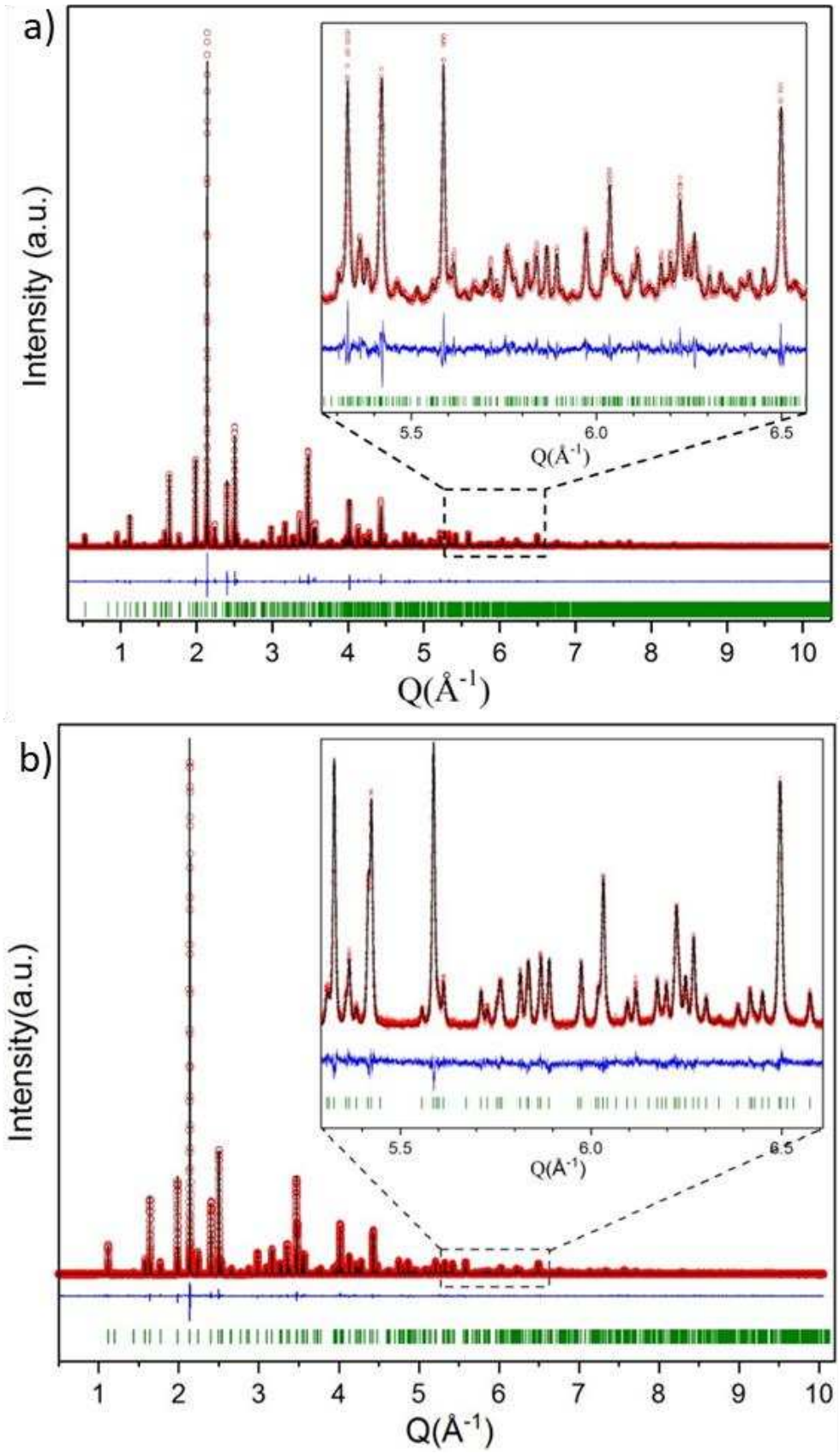

Figure A. 12. *Rietveld refinement of a) $SrErGa_3O_7$ ordered melilite (R_p= 6.70% R_{wp}= 8.60%) (SPD data) and b) $SrErGa_3O_7$ disordered melilite (SPD data, R_p= 6.78% R_{wp}= 8.75 %). Observed (black dot), calculated (red line), and difference (blue line) profiles are shown. The set of green vertical lines corresponds to reflection positions.*

Table A. 4. Final refined structural parameters obtained from SPD data collected at room temperature on the $SrErGa_3O_7$ superstructure melilite ($P2_12_12$ space group, a = 23.7790(1) Å, b = 7.93013(4) Å and c = 5.22786(2) *Å).*

Atom	Site	x	y	z	Occ	B_{iso}
Er1/ Sr1	4c	2.400(12)	2.400(12)	2.400(12)	0.504(3)/0.496(3)	0.64(2)
Er2/ Sr2	4c	2.431(12)	2.431(12)	2.431(12)	0.863(3)/0.137(3)	0.449(17)
Sr3/Er3	4c	0.05550(6)	0.33884(18)	0.5025(3)	0.868(4)/0.132(4)	0.90(3)
Ga1	4c	0.44958(8)	0.1445(2)	0.0139(3)	1	0.32(3)
Ga2	2a	0	0	0.9854(7)	1	0.35(4)
Ga3	4c	0.17125(8)	0.4862(2)	0.0016(6)	1	0.27(3)
Ga4	4c	0.28803(7)	0.3416(2)	0.9573(3)	1	0.26(3)
Ga5	4c	0.11858(9)	0.1279(2)	0.0331(3)	1	0.29(3)
O1	4c	0.4580(5)	0.3503(15)	0.195(2)	1	0.88(6)[a]
O2	4c	0.3834(5)	0.0776(13)	0.206(2)	1	0.88(6)[a]
O3	4c	0.2903(4)	0.3408(14)	0.3119(17)	1	0.88(6)[a]
O4	4c	0.4425(5)	0.1491(15)	0.6797(18)	1	0.88(6)[a]
O5	4c	0.1279(6)	0.1195(13)	0.6936(15)	1	0.88(6)[a]
O6	2b	0.5	0	0.152(2)	1	0.88(6)[a]
O7	4c	0.2276(5)	0.4305(14)	0.768(2)	1	0.88(6)[a]
O8	4c	0.0489(5)	0.1335(14)	0.170(2)	1	0.88(6)[a]
O9	4c	0.2989(5)	0.1465(15)	0.785(2)	1	0.88(6)[a]
O10	4c	0.1491(5)	0.3086(14)	0.195(2)	1	0.88(6)[a]
O11	4c	0.3441(5)	0.4570(13)	0.7905(16)	1	0.88(6)[a]

[a] Constrained to refine to the same value

Table A. 5. Final refined structural parameters of the $SrErGa_3O_7$ disordered melilite ($P\bar{4}2_1m$ space group, $a = b$ = 7.93227(2) Å, and c = 5.22367(2) Å).

Atom	Site	x	y	z	Occ	B_{iso}
Er1/Sr1	4e	0.33837(2)	0.16163(2)	0.51404(8)	0.5/0.5	1.670(6)
Ga1	2a	0	0	0	1	1.09(1)
Ga2	4e	0.14408(4)	0.35592(4)	0.96875(12)	1	1.06(1)
O1	2c	0.5	0	0.1852(9)	1	3.18(5)[a]
O2	4e	0.1414(3)	0.3586(3)	0.3095(5)	1	3.18(5)[a]
O3	8f	0.0944(3)	0.1603(3)	0.7932(5)	1	3.18(5)[a]

[a] Constrained to refine to the same value

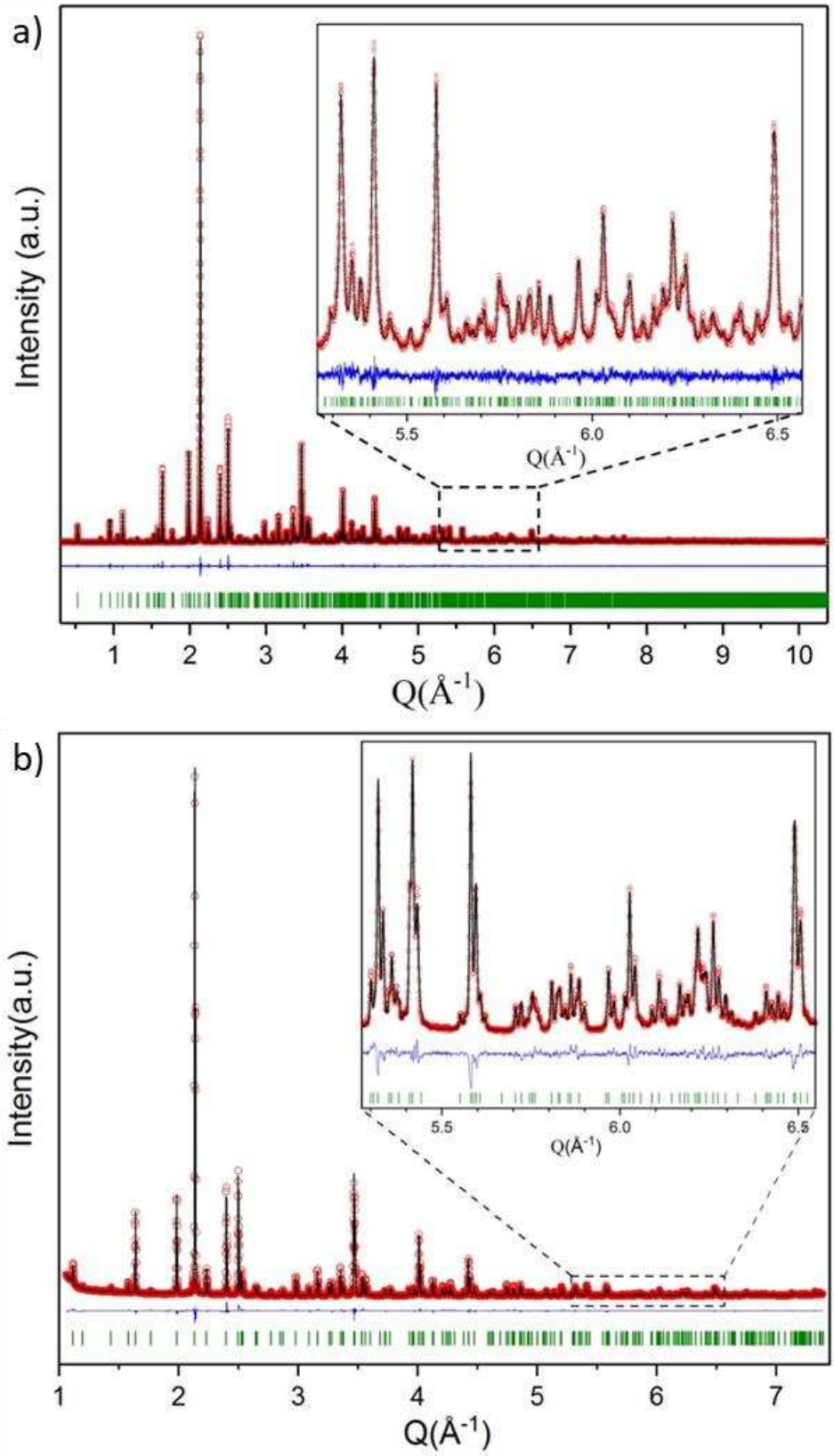

Figure A. 13. *Rietveld refinement of a) $SrHoGa_3O_7$ ordered melilite (SPD data, R_p= 4.85% R_{wp}= 6.30%) and b) $SrHoGa_3O_7$ disordered melilite (lab data, R_p= 1.41% R_{wp}= 2.08%). Observed (black dot), calculated (red line), and difference (blue line) profiles are shown. The set of green vertical lines corresponds to reflection positions.*

Table A. 6. Final refined structural parameters obtained from SPD data collected at room temperature on the $SrHoGa_3O_7$ superstructure melilite ($P2_12_12$ space group, a = 23.8034(1) Å, b = 7.93800(4) Å and c = 5.23828(2) Å).

Atom	Site	x	y	z	Occ	B_{iso}
Ho1/ Sr1	4c	0.21976(4)	0.14841(10)	0.49652(14)	0.499(2)/0.501(2)	0.63(2)
Ho2/Sr2	4c	0.38174(3)	0.31544(8)	0.45774(11)	0.924(2)/0.076(2)	0.57(1)
Sr3/ Ho3	4c	0.05660(5)	0.33980(16)	0.5059(2)	0.924(3)/0.076(3)	1.15(3)
Ga1	4c	0.44942(6)	0.14477(19)	0.0122(3)	1	0.57(3)
Ga2	2a	0	0	0.9842(5)	1	0.61(4)
Ga3	4c	0.17200(6)	0.48408(18)	0.0028(4)	1	0.46(2)
Ga4	4c	0.28820(6)	0.33958(18)	0.9549(3)	1	0.41(3)
Ga5	4c	0.11873(7)	0.12693(18)	0.0329(2)	1	0.40(2)
O1	4c	0.4568(4)	0.3471(12)	0.2000(17)	1	1.05(4)[a]
O2	4c	0.3862(4)	0.0749(11)	0.1940(17)	1	1.05(4)[a]
O3	4c	0.2893(4)	0.3454(12)	0.3003(12)	1	1.05(4)[a]
O4	4c	0.4412(4)	0.1512(12)	0.6774(13)	1	1.05(4)[a]
O5	4c	0.1263(5)	0.1161(11)	0.6915(11)	1	1.05(4)[a]
O6	2b	0.5	0	0.1534(19)	1	1.05(4)[a]
O7	4c	0.2258(4)	0.4286(11)	0.7706(18)	1	1.05(4)[a]
O8	4c	0.0489(4)	0.1336(11)	0.1682(16)	1	1.05(4)[a]
O9	4c	0.2975(4)	0.1355(12)	0.7869(19)	1	1.05(4)[a]
O10	4c	0.1509(4)	0.3098(12)	0.2047(16)	1	1.05(4)[a]
O11	4c	0.3455(4)	0.4564(10)	0.7999(12)	1	1.05(4)[a]

[a] Constrained to refine to the same value

Table A. 7. Final refined structural parameters of the $SrHoGa_3O_7$ disordered melilite ($P\bar{4}2_1m$ space group, $a = b$ = 7.93999(2) Å, and c = 5.23060(2) Å).

Atom	Site	x	y	Z	Occ	B_{iso}
Ho1/Sr1	4e	0.33867(5)	0.16133(5)	0.51151(14)	0.5/0.5	1.06(2)
Ga1	2a	0	0	0	1	0.61(3)
Ga2	4e	0.14444(7)	0.35556(7)	0.96831(17)	1	0.77(2)
O1	2c	0.5	0	0.1757(10)	1	2.27(6)[a]
O2	4e	0.1422(4)	0.3578(4)	0.3186(6)	1	2.27(6)[a]
O3	8f	0.0940(4)	0.1626(4)	0.7916(6)	1	2.27(6)[a]

[a] Constrained to refine to the same value

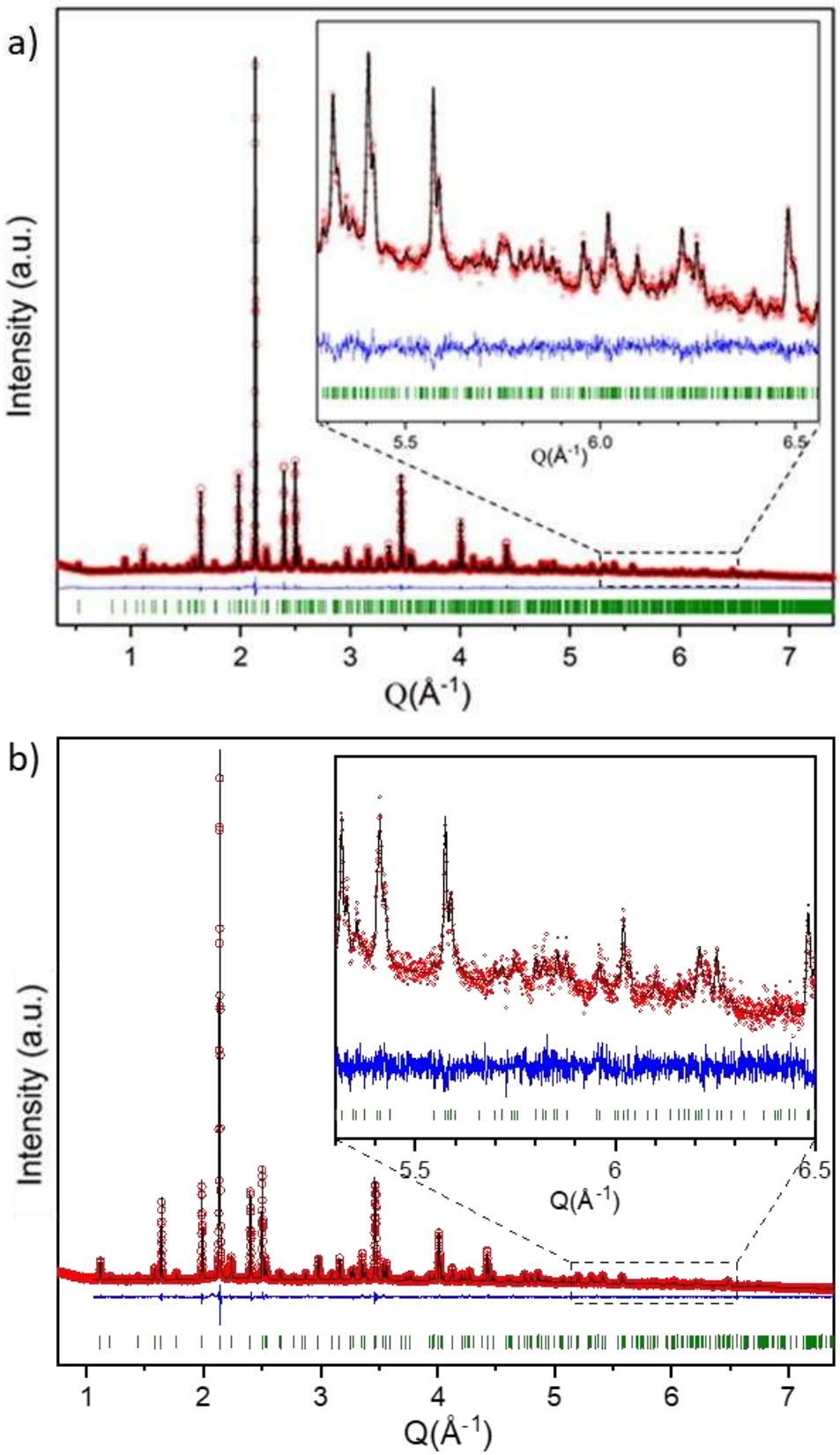

Figure A. 14. *Rietveld refinement of a) $SrDyGa_3O_7$ ordered melilite (lab data, R_p= 1.66% R_{wp}= 2.21%) and b) $SrDyGa_3O_7$ disordered melilite (lab data, R_p= 2.62% R_{wp}= 3.35%). Observed (black dot), calculated (red line), and difference (blue line) profiles are shown. The set of green vertical lines corresponds to reflection positions.*

Table A. 8. Final refined structural parameters obtained from lab XRPD data collected at room temperature on the $SrDyGa_3O_7$ superstructure melilite ($P2_12_12$ space group, a = 23.8404(3) Å, b = 7.9510(1) Å and c = 5.24314(2) Å).

Atom	Site	x	y	z	Occ	B_{iso}
Dy1/Sr1	4c	0.2210(2)	0.1475(5)	0.4976(6)	0.50(1)/0.50(1)	1.3(1)
Dy2/Sr2	4c	0.38229(17)	0.3203(4)	0.4609(5)	0.90(1)/0.10(1)	0.92(9)
Sr3/Dy3	4c	0.0558(2)	0.3372(7)	0.5076(7)	0.90(1)/0.10(1)	1.4(1)
Ga1	4c	0.0558(2)	0.3372(7)	0.5076(7)	1	0.8(2)
Ga2	2a	0.4501(3)	0.1441(9)	0.0111(10)	1	1.6(2)
Ga3	4c	0	0	0.998(2)	1	0.2(1)
Ga4	4c	0.1710(3)	0.4826(8)	0.9962(18)	1	0.8(2)
Ga5	4c	0.2873(3)	0.3374(9)	0.9535(11)	1	0.7(2)
O1	4c	0.1182(3)	0.1274(9)	0.0322(8)	1	0.3(2)[a]
O2	4c	0.4541(12)	0.330(4)	0.226(5)	1	0.3(2)[a]
O3	4c	0.3927(12)	0.077(3)	0.175(5)	1	0.3(2)[a]
O4	4c	0.2888(14)	0.360(4)	0.295(3)	1	0.3(2)[a]
O5	4c	0.4417(11)	0.150(4)	0.650(4)	1	0.3(2)[a]
O6	2b	0.1217(15)	0.120(4)	0.672(4)	1	0.3(2)[a]
O7	4c	0.5	0	0.146(5)	1	0.3(2)[a]
O8	4c	0.2226(14)	0.433(4)	0.805(6)	1	0.3(2)[a]
O9	4c	0.0510(10)	0.126(4)	0.149(4)	1	0.3(2)[a]
O10	4c	0.3051(12)	0.116(3)	0.730(5)	1	0.3(2)[a]
O11	4c	0.1451(12)	0.312(3)	0.261(4)	1	0.3(2)[a]

[a] Constrained to refine to the same value

Table A. 9. Final refined structural parameters of the $SrDyGa_3O_7$ disordered melilite ($P\bar{4}2_1m$ space group, $a = b$ = 7.95008(6) Å, and c = 5.23788(4) Å).

Atom	Site	x	y	Z	Occ	B_{iso}
Ho1/Sr1	4e	0.33874(10)	0.16126(10)	0.5121(3)	0.5/0.5	1.82(4)
Ga1	2a	0	0	0	1	1.36(7)
Ga2	4e	0.14504(15)	0.35496(15)	0.9688(4)	1	1.45(6)
O1	2c	0.5	0	0.187(2)	1	2.25(1)[a]
O2	4e	0.1433(8)	0.3567(8)	0.3153(13)	1	2.25(1)[a]
O3	8f	0.0893(7)	0.1610(8)	0.7873(15)	1	2.25(1)[a]

[a] Constrained to refine to the same value

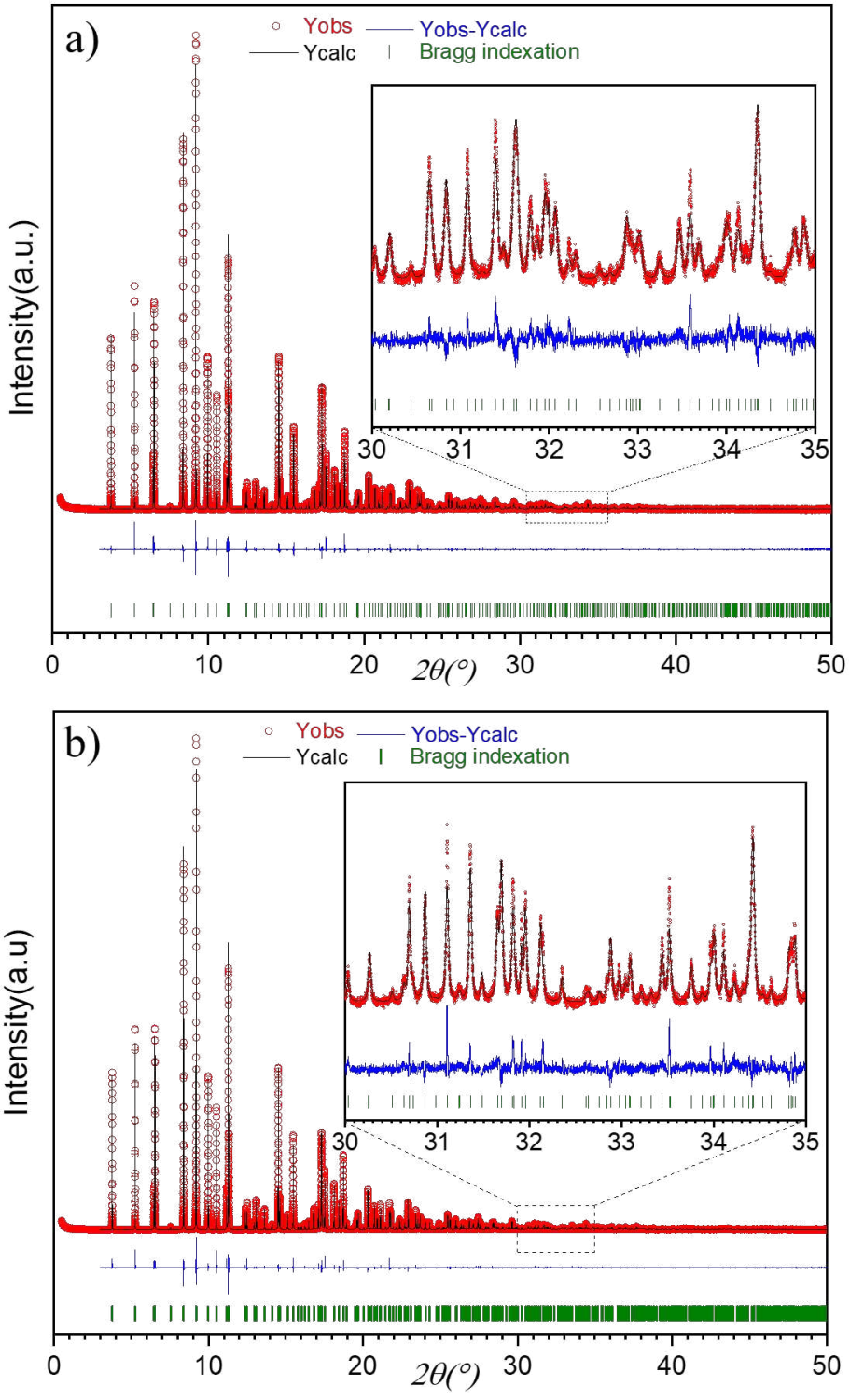

Figure A. 15. *Rietveld refinement of a) $Ca_3Ga_{1.5}Zn_{0.25}Ge_{4.25}O_{14}$ (x = 0.25) (SPD data, R_p= 8.465% R_{wp}= 10.907%) and b) $Ca_3GaZn_{0.5}Ge_{4.5}O_{14}$ (x = 0.5) (SPD data, R_p= 7.617% R_{wp}= 9.506%). Observed (red dot), calculated (black line), and difference (blue line) profiles are shown. The set of green vertical lines corresponds to reflection positions.*

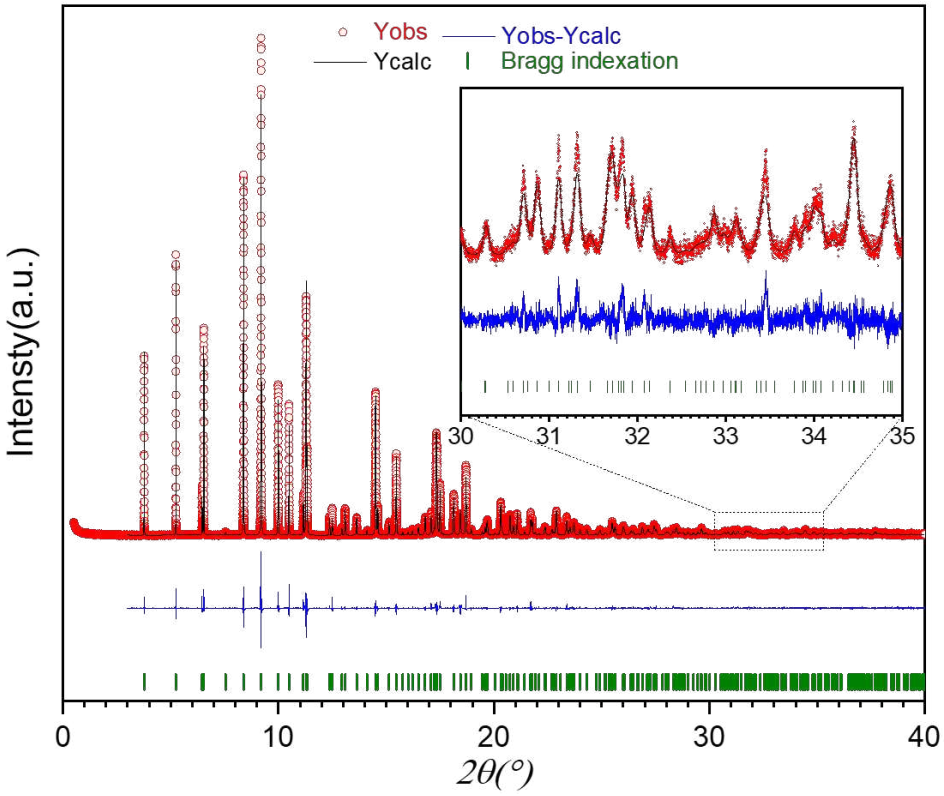

Figure A. 16. *Rietveld refinement of $Ca_3Ga_{0.5}Zn_{0.75}Ge_{4.75}O_{14}$ (x = 0.75) (SPD data, R_p= 8.465% R_{wp}= 10.907%). Observed (red dot), calculated (black line), and difference (blue line) profiles are shown. The set of green vertical lines corresponds to reflection positions.*

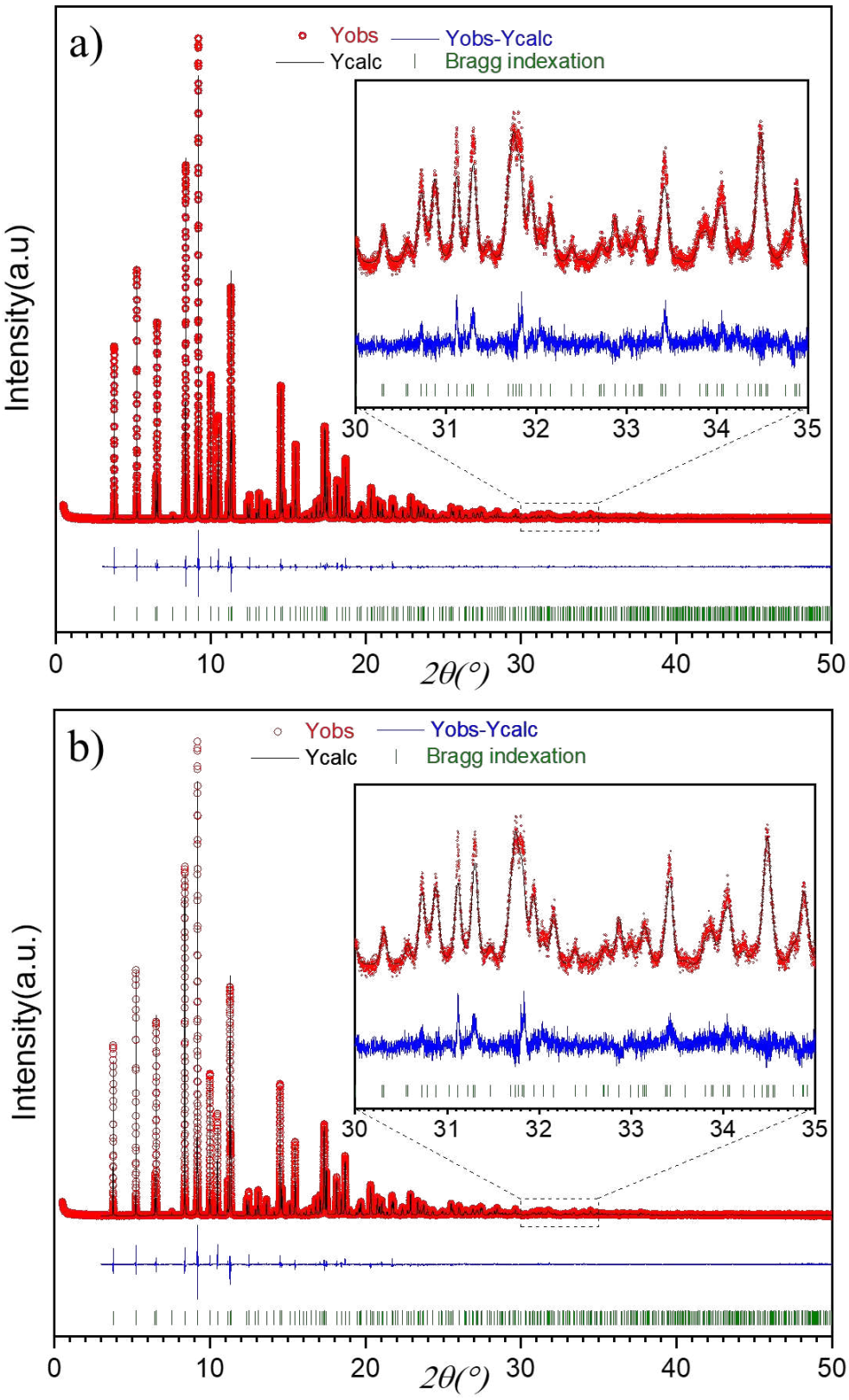

Figure A. 17. *Rietveld refinement of $Ca_3ZnGe_5O_{14}$(x = 1) SPD data against the hexagonal P321 cell, a) without strain (R_p= 7.18% R_{wp}= 8.93%), b) modelled strain (R_p= 7.02% R_{wp}= 8.75%). Observed (red dot), calculated (black line), and difference (blue line) profiles are shown. The set of green vertical lines corresponds to reflection positions.*

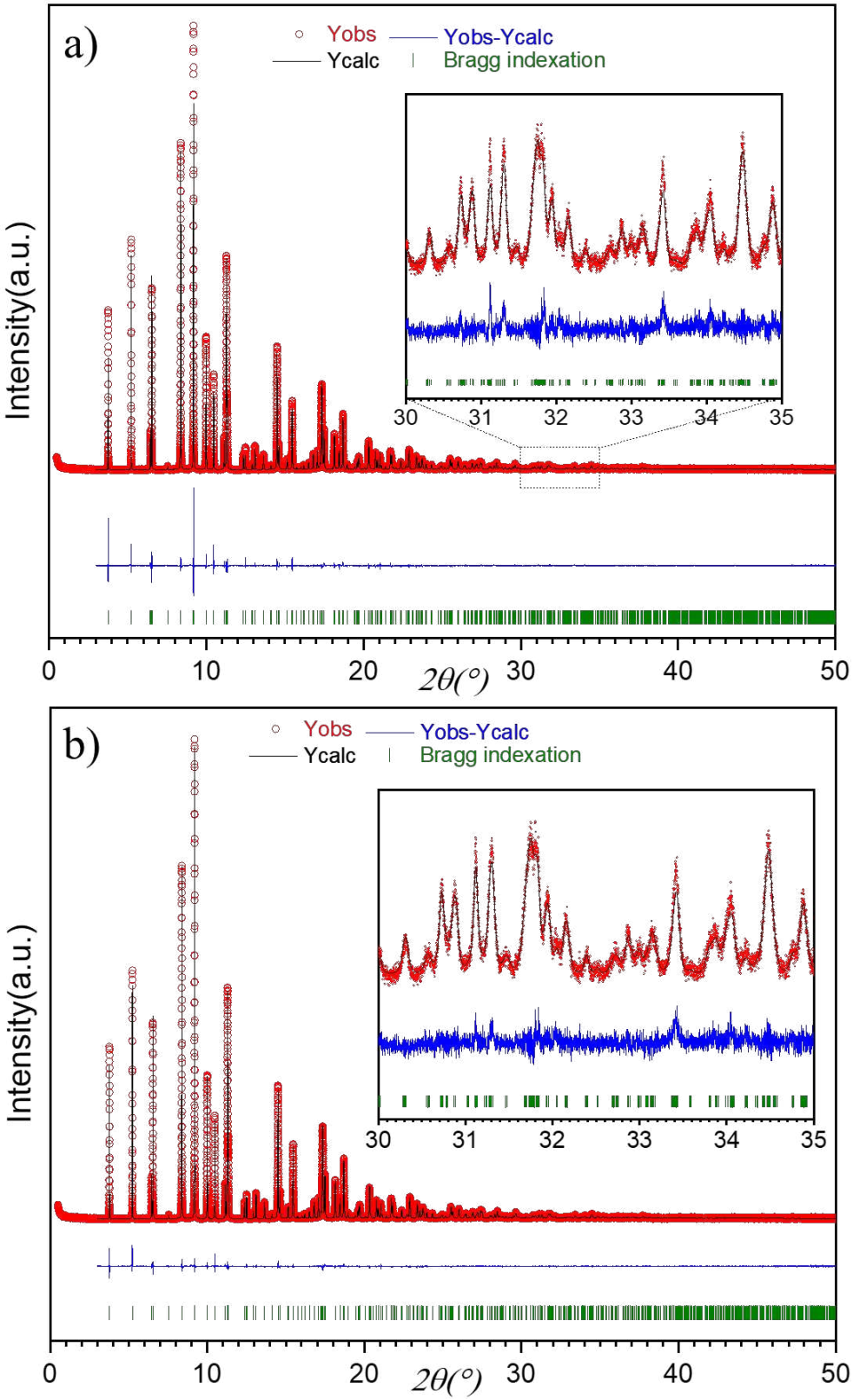

Figure A. 18. *Rietveld refinement of $Ca_3ZnGe_5O_{14}$ (x = 1) SPD data against the monoclinic C2 structure, a) without strain (R_p= 7.20% R_{wp}= 8.93%), b) modelled strain (R_p= 5.14% R_{wp}= 6.68%). Observed (red dot), calculated (black line), and difference (blue line) profiles are shown. The set of green vertical lines corresponds to reflection positions.*

Table A. 10. Refined structural parameters obtained from SPD data collected at room temperature on $Ca_3Ga_{1.5}Zn_{0.25}Ge_{4.25}O_{14}$ (x = 0.25) (*P*321 space group, *a*= 8.05847(2) Å and *c*= 4.986577(14) Å) sample.

Atom	Position	x	y	z	Occ	Biso
Ca	3e	0.41970(8)	0	0	1	1.02(1)
Ga1/Ge1/Zn1	1a	0	0	0	1*	1.04(1)
Ga2/Ge2/Zn2	3f	0.76349(4)	0	0.5	1*	0.90(1)
Ge3	2d	1/3	2/3	0.53149(10)	1	0.76(1)
O1	2d	1/3	2/3	0.1913(5)	1	1.40(3)[a]
O2	6g	0.4649(2)	0.3170(2)	0.3183(3)	1	1.40(3)[a]
O3	6g	0.2165(2)	0.0759(2)	0.7588(3)	1	1.40(3)[a]

*Site was put to be fully occupied without refining each atom occupancy
[a]: constrained to refine to the same Biso values.

Table A. 11. Refined structural parameters obtained from SPD data collected at room temperature on $Ca_3GaZn_{0.5}Ge_{4.5}O_{14}$ (x = 0.5) (*P*321 space group, *a*= 8.041920(12) Å and *c*= 4.999015(8) Å) sample.

Atom	Position	x	y	z	Occ	Biso
Ca	3e	0.41956(8)	0	0	1	1.00(1)
Ga1/Ge1/Zn1	1a	0	0	0	1*	1.15(1)
Ga2/Ge2/Zn2	3f	0.76427(4)	0	0.5	1*	1.006(6)
Ge3	2d	1/3	2/3	0.52968(9)	1	0.844(7)
O1	2d	1/3	2/3	0.1867(5)	1	1.72(2)[a]
O2	6g	0.4650(2)	0.3164(2)	0.3208(3)	1	1.72(2)[a]
O3	6g	0.21624(19)	0.0756(2)	0.7547(3)	1	1.72(2)[a]

*Site was put to be fully occupied without refining each atom occupancy
[a]: constrained to refine to the same Biso values.

Table A. 12. Refined structural parameters obtained from SPD data collected at room temperature on $Ca_3Ga_{0.5}Zn_{0.75}Ge_{4.75}O_{14}$ (x = 0.75) (*P*321 space group, *a*= 8.03574(2) Å and *c*= 5.009068(17) Å) sample.

Atom	Position	x	y	z	Occ	Biso
Ca	3e	0.41827(11)	0	0	1	0.92(2)
Ga1/Ge1/Zn1	1a	0	0	0	1*	1.26(2)
Ga2/Ge2/Zn2	3f	0.76488(6)	0	0.5	1*	0.971(1)
Ge3	2d	1/3	2/3	0.52939(14)	1	0.79(1)
O1	2d	1/3	2/3	0.1880(7)	1	1.26(4)[a]
O2	6g	0.4676(3)	0.3187(3)	0.3224(4)	1	1.26(4)[a]
O3	6g	0.2203(2)	0.0763(3)	0.7527(4)	1	1.26(4)[a]

*Site was put to be fully occupied without refining each atom occupancy
[a]: constrained to refine to the same Biso values.

Table A. 13. Refined structural parameters obtained from SPD data collected at room temperature on $Ca_3ZnGe_5O_{14}$ (*P*321 space group, *a*= 8.02916(2) Å and *c*= 5.014362(17) Å) sample. No strain modelled.

Atom	Position	x	y	z	Occ	Biso
Ca	3e	0.41846(8)	0	0	1	1.15(1)
Zn1/Ge1	1a	0	0	0	1*	1.47 (1)
Zn2/Ge2	3f	0.76506(4)	0	0.5	1*	1.126(7)
Ge3	2d	1/3	2/3	0.52816(11)	1	0.999(8)
O1	2d	1/3	2/3	0.1926(5)	1	1.91(3)[a]
O2	6g	0.4676(2)	0.3195(2)	0.3230(3)	1	1.91(3)[a]
O3	6g	0.22065(19)	0.0772(2)	0.7502(3)	1	1.91(3)[a]

*Site was put to be fully occupied without refining each atom occupancy

[a]: constrained to refine to the same Biso values.

Table A. 14. Refined structural parameters obtained from SPD data collected at room temperature on $Ca_3ZnGe_5O_{14}$ (*C*2 space group, *a*= 13.91669(9) Å, *b*= 8.02315(5) Å, *c*= 5.01415(2) Å and *β*= 90.0759(4) °) sample. No strain modelled.

Atom	Position	x	y	z	Occ	Biso
Ca1	2a	0.5	0.7623(5)	0	1	1.44(8)
Ca2	4c	0.2917(2)	0.3948(4)	0.0006(7)	1	1.02(4)
Zn1	1a	0.11841(10)	0.56943(16)	0.4969(4)	1	1.39(3)
Ge1	4c	0.33313(10)	0.6860(2)	0.47222(13)	1	0.96(1)
Ge2	2b	0.5	0.41986(18)	0.5	1	0.92(4)
Ge3	4c	0.5	0.1858(3)	0	1	1.00(1)
O1	4c	0.1177(4)	0.6953(9)	0.7829(10)	1	1.21(4)[a]
O2	4c	0.1611(6)	0.3732(11)	0.680(2)	1	1.21(4)[a]
O3	4c	0.4249(5)	0.5748(11)	0.3031(15)	1	1.21(4)[a]
O4	4c	0.4317(5)	0.3296(9)	0.7441(13)	1	1.21(4)[a]
O5	4c	0.3341(6)	0.6729(11)	0.8088(6)	1	1.21(4)[a]
O6	4c	0.0234(4)	0.4947(8)	0.2834(13)	1	1.21(4)[a]
O7	4c	0.2304(5)	0.5907(10)	0.3407(17)	1	1.21(4)[a]

[a]: constrained to refine to the same Biso values.

Table A. 15. Refined structural parameters obtained from SPD data collected at room temperature on $Ca_3ZnGe_5O_{14}$ (*C*2 space group, *a*= 13.90286(11) Å, *b*= 8.03170(7) Å, *c*= 5.014276(16) Å and *β*= 89.9544(10) °) sample. Modelled strain.

Atom	Position	x	y	z	Occ	Biso
Ca1	2a	0.5	0.7601(4)	0	1	0.45(6)
Ca2	4c	0.2903(2)	0.3895(5)	0.0005(8)	1	1.55(4)
Zn1	1a	0.11569(10)	0.55532(16)	0.5034(4)	1	1.25(3)
Ge1	4c	0.33367(13)	0.6757(3)	0.47220(10)	1	0.980(7)
Ge2	2b	0.5	0.4145(2)	0.5	1	1.07(5)
Ge3	4c	0.5	0.1800(4)	0	1	0.97(1)
O1	4c	0.1017(4)	0.7363(7)	0.7201(10)	1	1.46(3)[a]
O2	4c	0.1562(6)	0.3734(13)	0.674(2)	1	1.46(3)[a]
O3	4c	0.4298(6)	0.5696(13)	0.3262(18)	1	1.46(3)[a]
O4	4c	0.4377(4)	0.3391(9)	0.7873(9)	1	1.46(3)[a]
O5	4c	0.3344(7)	0.679(2)	0.8071(4)	1	1.46(3)[a]
O6	4c	0.0451(5)	0.4900(9)	0.2636(13)	1	1.46(3)[a]
O7	4c	0.2364(6)	0.5876(13)	0.3066(17)	1	1.46(3)[a]

[a]: constrained to refine to the same Biso values.

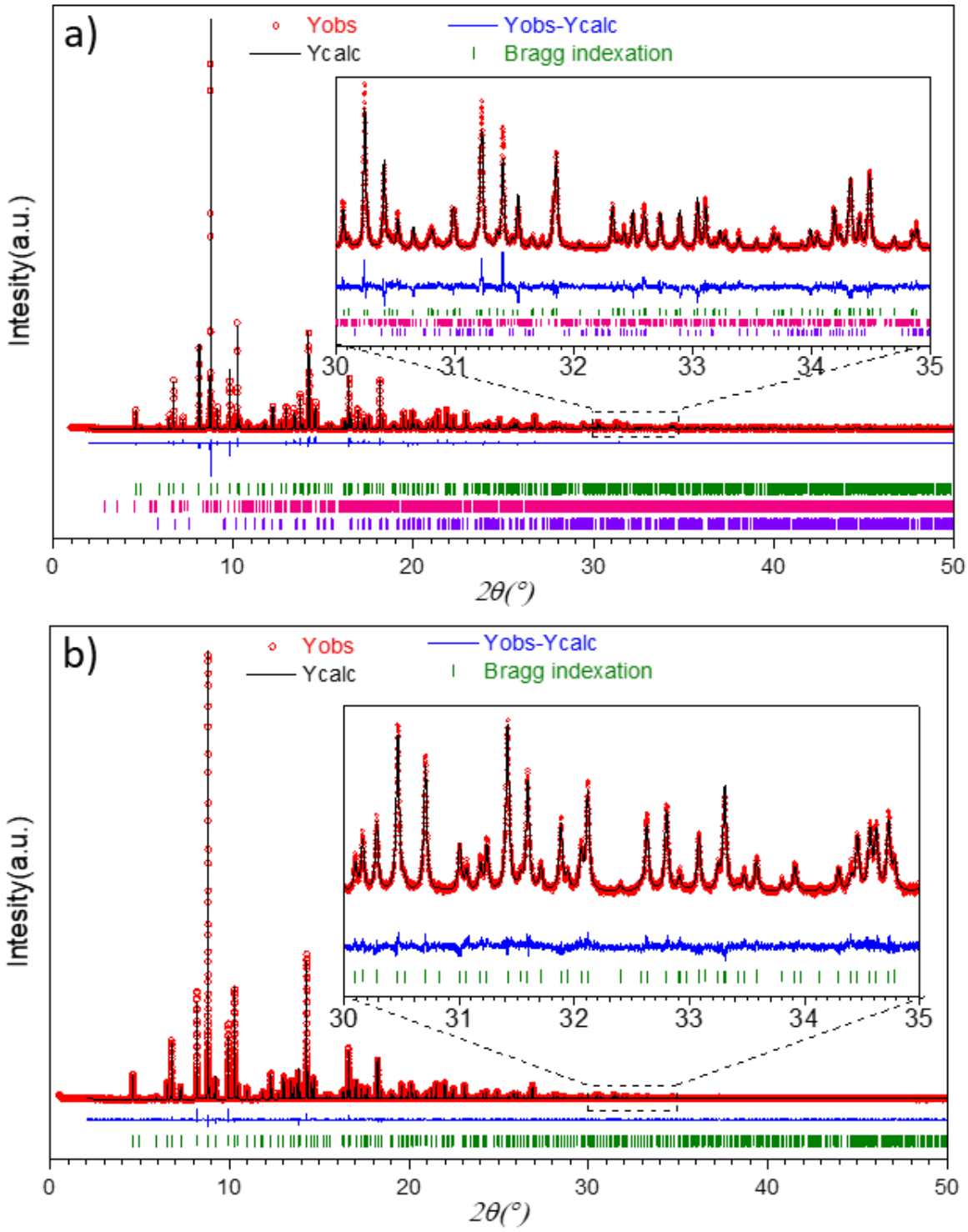

Figure A. 19. *SPD data Rietveld refinement of the a) $La_{1.3}Ba_{0.7}Ga_3O_{7.15}$(x = 0.3) composition ($R_{wp}$= 10.91%, GOF= 1.51). b) $La_{1.65}Ba_{0.35}Ga_3O_{7.325}$ (x = 0.65) composition (R_{wp}= 7.12%, GOF= 1.27). In both panels red, black and blue data corresponds to the measured, calculated and difference curves, with green tick marks corresponding to the $P\bar{4}2_1m$ tetragonal melilite. In the (a) panel pink and purple tick marks corresponds to $LaGaO_3$ perovskite and $LaBa_2Ga_{11}O_{20}$ phase.*

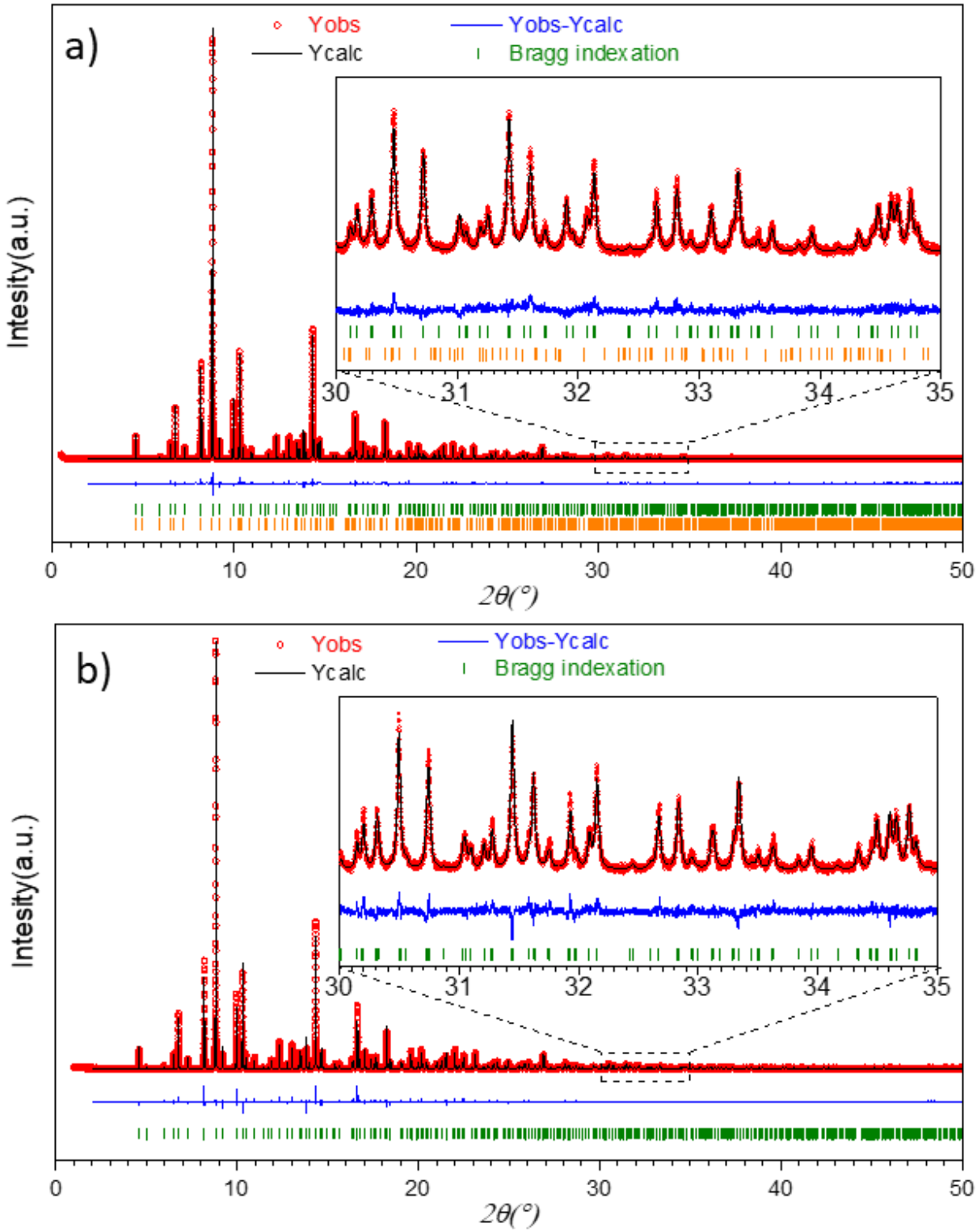

Figure A. 20. *SPD data Rietveld refinement of the a) $La_{1.675}Ba_{0.3375}Ga_3O_{7.3625}$ (x = 0.675) composition (R_{wp}= 7.81%, GOF= 1.33). b) $La_{1.7}Ba_{0.3}Ga_3O_{7.35}$ (x = 0.7) composition (R_{wp}= 10.41%, GOF= 1.49). In both panels red, black and blue data corresponds to the measured, calculated and difference curves, with green tick marks corresponding to the $P\bar{4}2_1m$ tetragonal melilite. Orange tick marks in panel (a) represents the $La_{1.3}Ba_{0.7}Ga_3O_{7.15}$ (x = 0.3) impurity indexation.*

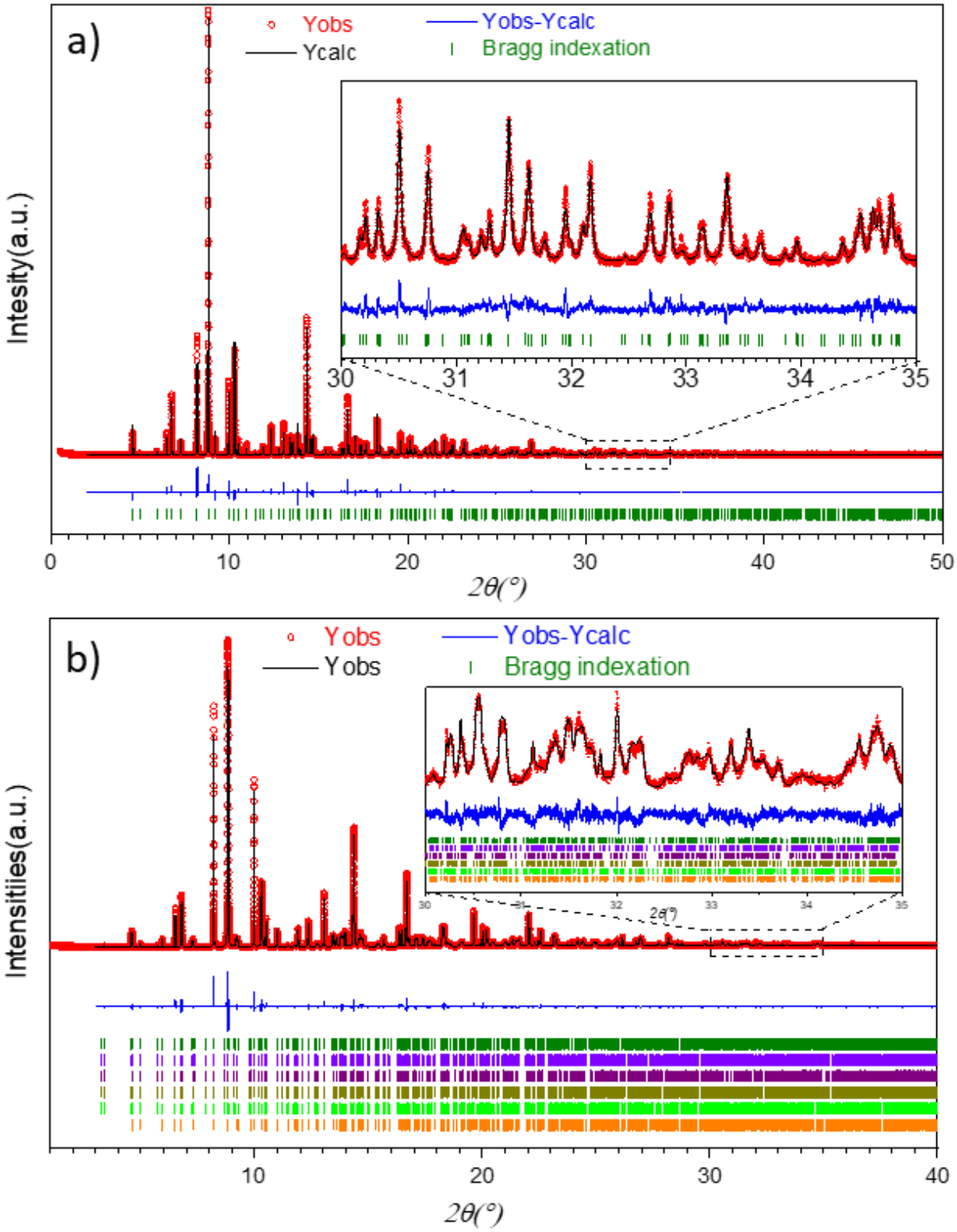

Figure A. 21. *SPD data Rietveld refinement of the a) $La_{1.725}Ba_{0.275}Ga_3O_{7.3625}$ (x = 0.725) composition (R_{wp}= 11.78%, GOF= 2.12). b) $La_{1.775}Ba_{0.227}Ga_3O_{7.3875}$ (x = 0.775) composition (R_{wp}= 10.01%, GOF= 1.07). In both panels red, black and blue data corresponds to the measured, calculated and difference curves. In panel (a) green tick marks corresponds to the $P\bar{4}2_1m$ tetragonal melilite. In panel (b) orange tick marks represent the $P\bar{4}2_1m$ tetragonal melilite, while the remaining corresponds to the five Ima2 cells used in the multi-cell approach.*

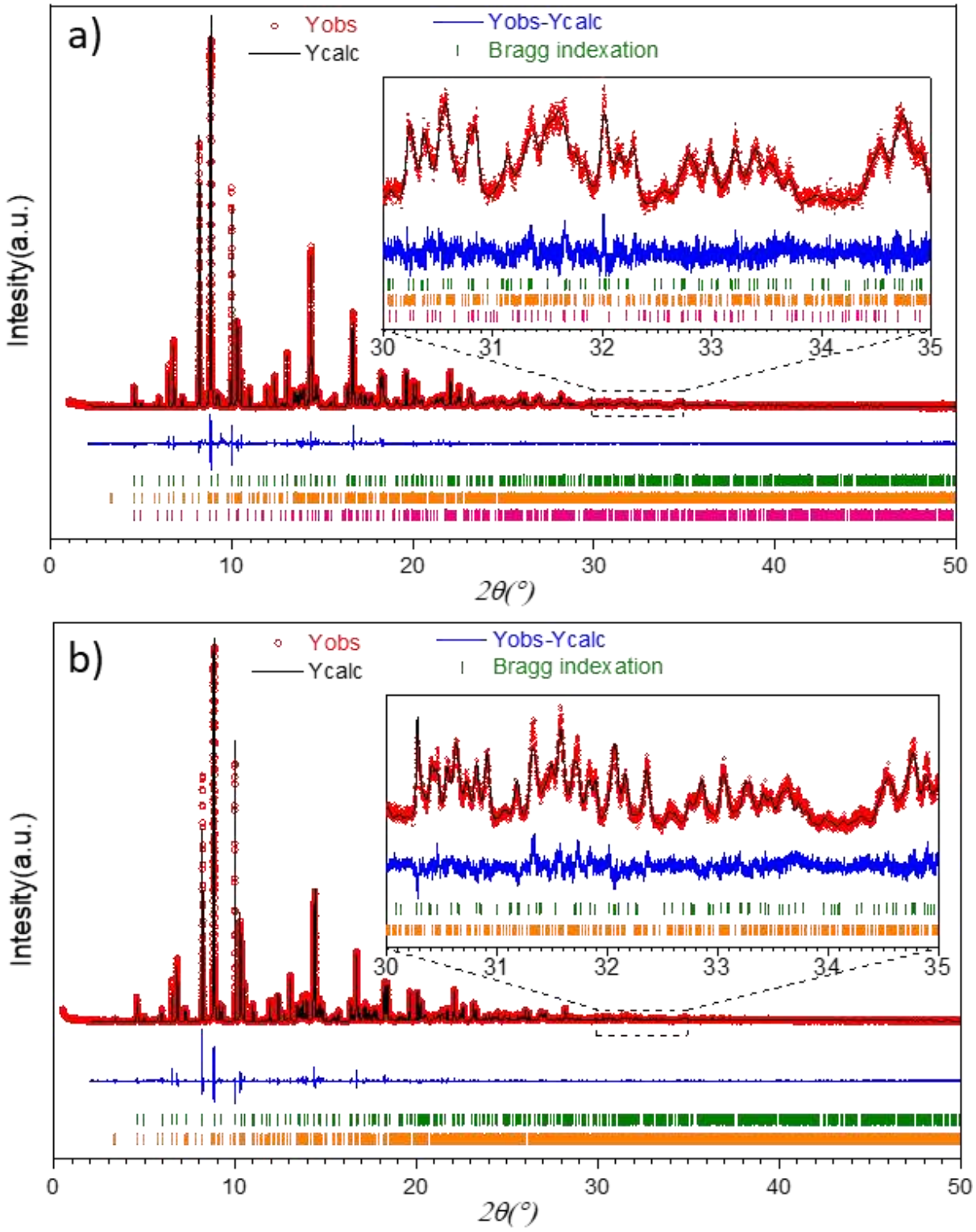

Figure A. 22. *SPD data Rietveld refinement of the a) $La_{1.8}Ba_{0.2}Ga_3O_{7.4}$ (x = 0.8) composition (R_{wp}= 8.98%, GOF= 1.35). b) $La_{1.85}Ba_{0.15}Ga_3O_{7.425}$ (x = 0.85) composition (R_{wp}= 10.37%, GOF= 1.64). In both panels red, black and blue data corresponds to the measured, calculated and difference curves, with green and orange tick marks corresponding to the $P\bar{4}2_1m$ and Ima2 melilites. Pink tick marks in panel (a) represents the $La_{1.3}Ba_{0.7}Ga_3O_{7.15}$ (x = 0.3) impurity indexation.*

Table A. 16. Final refined $La_{1.3}Ba_{0.7}Ga_3O_{7.15}$ (x = 0.3) composition structural parameters (S.G. $P\bar{4}2_1m$, a= b= 8.12688(2) Å, c= 5.35114(1) Å).

Atom	x	y	z	Occ	B_{iso}
La1/Ba1	0.33616(2)	0.16384(2)	0.50816(7)	0.65/0.35	0.402(4)
Ga1	0	0	0	1	0.204(10)
Ga2	0.14217(4)	0.35783(4)	-0.03032(11)	1	0.542(9)
O1	0.5	0	0.1901(8)	1	0.77(3)
O2	0.1388(3)	0.3612(3)	0.3131(5)	1	0.77(3)
O3	0.0847(3)	0.1636(3)	0.7935(4)	1	0.77(3)
O4	0.358(3)	0.142(3)	0.056(7)	0.075	0.77(3)

Table A. 17. Final refined $La_{1.6}Ba_{0.4}Ga_3O_{7.3}$ (x = 0.6) composition structural parameters (S.G. $P\bar{4}2_1$m, a= b= 8.08170(1) Å, c= 5.291514(8) Å).

Atom	x	y	z	Occ	B_{iso}
La1/Ba1	0.335860(18)	0.164140(18)	0.50785(7)	0.8/0.2	0.761(4)
Ga1	0	0	0	1	0.492(9)
Ga2	0.14197(3)	0.35803(3)	-0.03021(10)	1	0.982(9)
O1	0.5	0	0.1871(7)	1	1.43(3)
O2	0.1387(2)	0.3613(2)	0.3127(4)	1	1.43(3)
O3	0.0825(2)	0.1624(2)	0.7924(3)	1	1.43(3)
O4	0.3436(12)	0.1564(12)	0.018(4)	0.15	1.43(3)

Table A. 18. Final refined $La_{1.65}Ba_{0.35}Ga_3O_{7.325}$ (x = 0.65) composition structural parameters (S.G. $P\bar{4}2_1$m, a= b= 8.08849(1) Å, c= 5.29991(1) Å).

Atom	x	y	z	Occ	B_{iso}
La1/Ba1	0.335690(17)	0.164310(17)	0.50756(6)	0.825/0.175	1.007(4)
Ga1	0	0	0	1	0.678(9)
Ga2	0.14199(3)	0.35801(3)	-0.03164(10)	1	1.261(8)
O1	0.5	0	0.1941(6)	1	1.54(3)
O2	0.13590(19)	0.36410(19)	0.3137(4)	1	1.54(3)
O3	0.08324(18)	0.1644(2)	0.7920(3)	1	1.54(3)
O4	0.3442(10)	0.1558(10)	-0.003(3)	0.1625	1.54(3)

Table A. 19. Final refined $La_{1.675}Ba_{0.325}Ga_3O_{7.3375}$ (x = 0.675) composition structural parameters (S.G. $P\bar{4}2_1m$, $a = b = 8.07836(2)$ Å, $c = 5.28703(1)$ Å).

Atom	x	y	z	Occ	B_{iso}
La1/Ba1	0.335820(19)	0.164180(19)	0.50797(7)	0.8375/0.1675	1.213(4)
Ga1	0	0	0	1	0.872(10)
Ga2	0.14215(3)	0.35785(3)	-0.03170(11)	1	1.393(10)
O1	0.5	0	0.1914(7)	1	2.06(3)
O2	0.1372(2)	0.3628(2)	0.3055(4)	1	2.06(3)
O3	0.0837(2)	0.1639(2)	0.7928(3)	1	2.06(3)
O4	0.3501(11)	0.1499(11)	0.032(3)	0.16875	2.06(3)

Table A. 20. Final refined $La_{1.7}Ba_{0.3}Ga_3O_{7.35}$ (x = 0.7) composition structural parameters (S.G. $P\bar{4}2_1m$, $a = b = 8.07489(2)$ Å, $c = 5.28269(1)$ Å).

Atom	x	y	z	Occ	B_{iso}
La1/Ba1	0.33549(2)	0.16451(2)	0.50774(10)	0.85/0.15	0.737(5)
Ga1	0	0	0	1	0.413(12)
Ga2	0.14219(4)	0.35781(4)	-0.03048(14)	1	0.934(12)
O1	0.5	0	0.1840(10)	1	1.48(4)
O2	0.1346(3)	0.3654(3)	0.3130(6)	1	1.48(4)
O3	0.0834(3)	0.1635(3)	0.7883(5)	1	1.48(4)
O4	0.33549(2)	0.16451(2)	0.003(5)	0.175	1.48(4)

Table A. 21. Final refined $La_{1.725}Ba_{0.275}Ga_3O_{7.3625}$ (x = 0.725) composition structural parameters (S.G. $P\bar{4}2_1m$, $a = b = 8.07235(2)$ Å, $c = 5.27953(2)$ Å).

Atom	x	y	z	Occ	B_{iso}
La1/Ba1	0.33569(3)	0.16431(3)	0.50894(10)	0.8675/0.1375	1.107(6)
Ga1	0	0	0	1	0.766(15)
Ga2	0.14221(5)	0.35779(5)	-0.03121(16)	1	1.363(14)
O1	0.5	0	0.1950(11)	1	2.29(5)
O2	0.1345(3)	0.3655(3)	0.3009(7)	1	2.29(5)
O3	0.0855(3)	0.1641(3)	0.7894(6)	1	2.29(5)
O4	0.3481(8)	0.1519(8)	0.0582(18)	0.3625	2.29(5)

Table A. 22. Final refined $La_{1.75}Ba_{0.25}Ga_3O_{7.375}$ (x = 0.75) composition structural parameters (S.G. $P\bar{4}2_1m$, a= b= 8.06891(2) Å, c= 5.27513(2) Å).

Atom	x	y	z	Occ	B_{iso}
La1/Ba1	0.33515(8)	0.16485(8)	0.4990(3)	0.875/0.125	1.38(3)
Ga1	0	0	0	1	0.90(5)
Ga2	0.14206(13)	0.35794(13)	-0.0270(6)	1	1.63(4)
O1	0.5	0	0.185(3)	1	0.77(11)
O2	0.1368(8)	0.3632(8)	0.3262(18)	1	0.77(11)
O3	0.0836(7)	0.1640(9)	0.7983(16)	1	0.77(11)
O4	0.33515(8)	0.16485(8)	-0.000(11)	0.25	0.77(11)

Table A. 23. Final refined $La_{1.75}Ba_{0.25}Ga_3O_{7.375}$ (x = 0.75) composition structural parameters (S.G. *Ima*2, a= 11.43139(6) Å, b= 11.39361(5) Å, c= 10.55194(4) Å).

Atom	x	y	z	Occ	Biso
La1/Ba1	-0.58610(6)	0.2493(2)	0.48475(13)	0.9167/0.0833[a]	0.714(18)
La2/Ba2	0.75	0.0852(2)	-0.0276(3)	0.8334/0.1667[a]	0.98(7)
La3/Ba3	0.75	0.4144(3)	-0.0263(3)	0.8333/0.1667	1.28(8)
Ga1	-0.88855(11)	-0.2494(5)	0.2123(3)	1	1.08(4)
Ga2	0	0	0.2218(5)	1	0.11(11)
Ga3	0.5	0.5	0.2340(6)	1	1.17(14)
Ga4	0.75	-0.1053(8)	-0.2572(6)	1	1.59(16)
Ga5	0.25	0.1038(7)	0.2475(5)	1	0.54(13)
O1	-0.8893(8)	-0.244(2)	-0.1230(11)	1	1.57(8)
O2	-0.4777(11)	0.3618(12)	0.1243(15)	1	1.57(8)
O3	-0.5508(11)	-0.3804(12)	-0.3788(17)	1	1.57(8)
O4	-0.1306(12)	-0.0368(13)	-0.1710(17)	1	1.57(8)
O5	-0.8936(12)	0.0530(13)	0.3445(15)	1	1.57(8)
O6	0.75	0.2768(13)	0.1348(17)	1	1.57(8)
O7	0.75	-0.122(3)	0.074(3)	1	1.57(8)
O8	0.25	0.251(4)	0.3308(15)	1	1.57(8)
O9	0.25	0.120(3)	0.577(3)	1	1.57(8)
O10	0.25	-0.0955(13)	0.227(3)	0.75[a]	1.57(8)

[a]Fixed to the nominal composition

Table A. 24. Final refined $La_{1.775}Ba_{0.225}Ga_3O_{7.3875}$ (x = 0.775) composition cell 1 structural parameters (S.G. *Ima*2, *a*= 11.45837(7) Å, *b*= 11.34648(7) Å, *c*= 10.53977(9) Å).

Atom	x	y	z	Occ	Biso
La1/Ba1	-0.58686(8)	0.24858(19)	0.4817(6)	0.8875/0.075[a]	0.38443[b]
La2/Ba2	0.75	0.0849(3)	-0.0264(7)	0.8875/0.15[a]	0.45365[b]
La3/Ba3	0.75	0.4158(3)	-0.0344(7)	0.8875/0.15[a]	0.77528[b]
Ga1	-0.88671(15)	-0.2535(3)	0.2113(7)	1	0.89918[b]
Ga2	0	0	0.2299(8)	1	0.31456[b]
Ga3	0.5	0.5	0.2358(7)	1	0.01001[b]
Ga4	0.75	-0.1045(4)	-0.2569(8)	1	1.07162[b]
Ga5	0.25	0.0998(4)	0.2391(8)	1	0.33539[b]
O1	-0.88723[b]	-0.26809[b]	-0.11788[b]	1	0.3209[b]
O2	-0.48405[b]	0.36824[b]	0.12209[b]	1	0.3209[b]
O3	-0.55204[b]	-0.36768[b]	-0.37826[b]	1	0.3209[b]
O4	-0.13731[b]	-0.03781[b]	-0.17337[b]	1	0.3209[b]
O5	-0.89494[b]	0.05828[b]	0.34768[b]	1	0.3209[b]
O6	0.75	0.27628[b]	0.13621[b]	1	0.3209[b]
O7	0.75	-0.13585[b]	0.07166[b]	1	0.3209[b]
O8	0.25	0.2346[b]	0.33203[b]	1	0.3209[b]
O9	0.25	0.1051[b]	0.57471[b]	1	0.3209[b]
O10	0.25	-0.10097[b]	0.228[b]	0.775[a]	0.3209[b]

[a]Fixed to the nominal composition

[b]Fixed from the Stephens refinement approach

Table A. 25. Final refined $La_{1.775}Ba_{0.225}Ga_3O_{7.3875}$ (x = 0.775) composition cell 2 structural parameters (S.G. *Ima*2, *a*= 11.43792(8) Å, *b*= 11.36654(8) Å, *c*= 10.5397(1) Å).

Atom	x	y	z	Occ	Biso
La1/Ba1	-0.58686(8)	0.24858(19)	0.4817(6)	0.8875/0.075[a]	0.38443[b]
La2/Ba2	0.75	0.0849(3)	-0.0264(7)	0.8875/0.15[a]	0.45365[b]
La3/Ba3	0.75	0.4158(3)	-0.0344(7)	0.8875/0.15[a]	0.77528[b]
Ga1	-0.88671(15)	-0.2535(3)	0.2113(7)	1	0.89918[b]
Ga2	0	0	0.2299(8)	1	0.31456[b]
Ga3	0.5	0.5	0.2358(7)	1	0.01001[b]
Ga4	0.75	-0.1045(4)	-0.2569(8)	1	1.07162[b]
Ga5	0.25	0.0998(4)	0.2391(8)	1	0.33539[b]
O1	-0.88723[b]	-0.26809[b]	-0.11788[b]	1	0.3209[b]
O2	-0.48405[b]	0.36824[b]	0.12209[b]	1	0.3209[b]
O3	-0.55204[b]	-0.36768[b]	-0.37826[b]	1	0.3209[b]
O4	-0.13731[b]	-0.03781[b]	-0.17337[b]	1	0.3209[b]
O5	-0.89494[b]	0.05828[b]	0.34768[b]	1	0.3209[b]
O6	0.75	0.27628[b]	0.13621[b]	1	0.3209[b]
O7	0.75	-0.13585[b]	0.07166[b]	1	0.3209[b]
O8	0.25	0.2346[b]	0.33203[b]	1	0.3209[b]
O9	0.25	0.1051[b]	0.57471[b]	1	0.3209[b]
O10	0.25	-0.10097[b]	0.228[b]	0.775[a]	0.3209[b]

[a]Fixed to the nominal composition

[b]Fixed from the Stephens refinement approach

Table A. 26. Final refined $La_{1.775}Ba_{0.225}Ga_3O_{7.3875}$ (x = 0.775) composition cell 3 structural parameters (S.G. *Ima*2, *a*= 11.41747(9) Å, *b*= 11.3866(1) Å, *c*= 10.5396(1) Å).

Atom	x	y	z	Occ	Biso
La1/Ba1	-0.58686(8)	0.24858(19)	0.4817(6)	0.8875/0.075[a]	0.38443[b]
La2/Ba2	0.75	0.0849(3)	-0.0264(7)	0.8875/0.15[a]	0.45365[b]
La3/Ba3	0.75	0.4158(3)	-0.0344(7)	0.8875/0.15[a]	0.77528[b]
Ga1	-0.88671(15)	-0.2535(3)	0.2113(7)	1	0.89918[b]
Ga2	0	0	0.2299(8)	1	0.31456[b]
Ga3	0.5	0.5	0.2358(7)	1	0.01001[b]
Ga4	0.75	-0.1045(4)	-0.2569(8)	1	1.07162[b]
Ga5	0.25	0.0998(4)	0.2391(8)	1	0.33539[b]
O1	-0.88723[b]	-0.26809[b]	-0.11788[b]	1	0.3209[b]
O2	-0.48405[b]	0.36824[b]	0.12209[b]	1	0.3209[b]
O3	-0.55204[b]	-0.36768[b]	-0.37826[b]	1	0.3209[b]
O4	-0.13731[b]	-0.03781[b]	-0.17337[b]	1	0.3209[b]
O5	-0.89494[b]	0.05828[b]	0.34768[b]	1	0.3209[b]
O6	0.75	0.27628[b]	0.13621[b]	1	0.3209[b]
O7	0.75	-0.13585[b]	0.07166[b]	1	0.3209[b]
O8	0.25	0.2346[b]	0.33203[b]	1	0.3209[b]
O9	0.25	0.1051[b]	0.57471[b]	1	0.3209[b]
O10	0.25	-0.10097[b]	0.228[b]	0.775[a]	0.3209[b]

[a]Fixed to the nominal composition

[b]Fixed from the Stephens refinement approach

Table A. 27. Final refined $La_{1.775}Ba_{0.225}Ga_3O_{7.3875}$ (x = 0.775) composition cell 4 structural parameters (S.G. *Ima*2, *a*= 11.3970(1) Å, *b*= 11.4064(1) Å, *c*= 10.5396(2) Å).

Atom	x	y	z	Occ	Biso
La1/Ba1	-0.58686(8)	0.24858(19)	0.4817(6)	0.8875/0.075[a]	0.38443[b]
La2/Ba2	0.75	0.0849(3)	-0.0264(7)	0.8875/0.15[a]	0.45365[b]
La3/Ba3	0.75	0.4158(3)	-0.0344(7)	0.8875/0.15[a]	0.77528[b]
Ga1	-0.88671(15)	-0.2535(3)	0.2113(7)	1	0.89918[b]
Ga2	0	0	0.2299(8)	1	0.31456[b]
Ga3	0.5	0.5	0.2358(7)	1	0.01001[b]
Ga4	0.75	-0.1045(4)	-0.2569(8)	1	1.07162[b]
Ga5	0.25	0.0998(4)	0.2391(8)	1	0.33539[b]
O1	-0.88723[b]	-0.26809[b]	-0.11788[b]	1	0.3209[b]
O2	-0.48405[b]	0.36824[b]	0.12209[b]	1	0.3209[b]
O3	-0.55204[b]	-0.36768[b]	-0.37826[b]	1	0.3209[b]
O4	-0.13731[b]	-0.03781[b]	-0.17337[b]	1	0.3209[b]
O5	-0.89494[b]	0.05828[b]	0.34768[b]	1	0.3209[b]
O6	0.75	0.27628[b]	0.13621[b]	1	0.3209[b]
O7	0.75	-0.13585[b]	0.07166[b]	1	0.3209[b]
O8	0.25	0.2346[b]	0.33203[b]	1	0.3209[b]
O9	0.25	0.1051[b]	0.57471[b]	1	0.3209[b]
O10	0.25	-0.10097[b]	0.228[b]	0.775[a]	0.3209[b]

[a]Fixed to the nominal composition

[b]Fixed from the Stephens refinement approach

Table A. 28. Final refined $La_{1.775}Ba_{0.225}Ga_3O_{7.3875}$ (x = 0.775) composition cell 5 structural parameters (S.G. *Ima*2, *a*= 11.3561(2) Å, *b*= 11.4468(2) Å, *c*= 10.5394(2) Å).

Atom	x	y	z	Occ	Biso
La1/Ba1	-0.58686(8)	0.24858(19)	0.4817(6)	0.8875/0.075[a]	0.38443[b]
La2/Ba2	0.75	0.0849(3)	-0.0264(7)	0.8875/0.15[a]	0.45365[b]
La3/Ba3	0.75	0.4158(3)	-0.0344(7)	0.8875/0.15[a]	0.77528[b]
Ga1	-0.88671(15)	-0.2535(3)	0.2113(7)	1	0.89918[b]
Ga2	0	0	0.2299(8)	1	0.31456[b]
Ga3	0.5	0.5	0.2358(7)	1	0.01001[b]
Ga4	0.75	-0.1045(4)	-0.2569(8)	1	1.07162[b]
Ga5	0.25	0.0998(4)	0.2391(8)	1	0.33539[b]
O1	-0.88723[b]	-0.26809[b]	-0.11788[b]	1	0.3209[b]
O2	-0.48405[b]	0.36824[b]	0.12209[b]	1	0.3209[b]
O3	-0.55204[b]	-0.36768[b]	-0.37826[b]	1	0.3209[b]
O4	-0.13731[b]	-0.03781[b]	-0.17337[b]	1	0.3209[b]
O5	-0.89494[b]	0.05828[b]	0.34768[b]	1	0.3209[b]
O6	0.75	0.27628[b]	0.13621[b]	1	0.3209[b]
O7	0.75	-0.13585[b]	0.07166[b]	1	0.3209[b]
O8	0.25	0.2346[b]	0.33203[b]	1	0.3209[b]
O9	0.25	0.1051[b]	0.57471[b]	1	0.3209[b]
O10	0.25	-0.10097[b]	0.228[b]	0.775[a]	0.3209[b]

[a]Fixed to the nominal composition

[b]Fixed from the Stephens refinement approach

Table A. 29. Final refined $La_{1.775}Ba0_{.225}Ga_3O_{7.3875}$ (x = 0.775) composition cell 6 structural parameters (S.G. $P\bar{4}2_1m$, *a*= *b*= 8.06246(4) Å, *c*= 5.26941(5) Å).

Atom	x	Y	z	Occ	B_{iso}
La1/Ba1	0.33499(17)	0.16501(17)	0.4851(5)	0.8875/0.1125[a]	1.38348[b]
Ga1	0	0	0	1	0.9019[b]
Ga2	0.1410(3)	0.3590(3)	-0.0298(11)	1	1.62865[b]
O1	0.5	0	0.18535[b]	1	0.76567[b]
O2	0.13683[b]	0.36317[b]	0.32623[b]	1	0.76567[b]
O3	0.08361[b]	0.16396[b]	0.79828[b]	1	0.76567[b]
O4	0.33499[b]	0.16501[b]	-0.00039[b]	0.19375[a]	0.76567[b]

[a]Fixed to the nominal composition

[b]Fixed from the Stephens refinement approach

Table A. 30. Final refined $La_{1.8}Ba_{0.2}Ga_3O_{7.4}$ (x = 0.8) composition structural parameters (S.G. *Ima*2, *a*= 11.45216(8) Å, *b*= 11.35246(7) Å, *c*= 10.53719(5) Å).

Atom	x	y	z	Occ	Biso
La1/Ba1	-0.58647(5)	0.2493(3)	0.48233(11)	0.933/0.066[a]	0.290(14)
La2/Ba2	0.75	0.0850(3)	-0.01863(18)	0.866/0.133[a]	0.94(8)
La3/Ba3	0.75	0.4153(3)	-0.03299(18)	0.866/0.133[a]	0.29(6)
Ga1	-0.88777(10)	-0.2517(3)	0.2135(2)	1	0.66(3)
Ga2	0	0	0.2317(7)	1	-0.15(6)
Ga3	0.5	0.5	0.2330(8)	1	0.74(8)
Ga4	0.75	-0.1068(4)	-0.2549(5)	1	0.77(11)
Ga5	0.25	0.0998(4)	0.2433(5)	1	0.27(9)
O1	-0.8866(6)	-0.2613(12)	-0.1143(8)	1	0.25(7)[b]
O2	-0.4814(9)	0.3655(9)	0.1335(11)	1	0.25(7)[b]
O3	-0.5488(9)	-0.3777(10)	-0.3752(13)	1	0.25(7)[b]
O4	-0.1306(9)	-0.0281(8)	-0.1579(11)	1	0.25(7)[b]
O5	-0.8920(9)	0.0603(8)	0.3509(10)	1	0.25(7)[b]
O6	0.75	0.2792(11)	0.1387(13)	1	0.25(7)[b]
O7	0.75	-0.1248(15)	0.0674(17)	1	0.25(7)[b]
O8	0.25	0.246(3)	0.3174(12)	1	0.25(7)[b]
O9	0.25	0.1029(14)	0.5740(17)	1	0.25(7)[b]
O10	0.25	-0.0964(11)	0.220(2)	0.8[a]	0.25(7)[b]

[a]Fixed to the nominal composition.

[b]Constrained to refine to the same value.

Table A. 31. Final refined $La_{1.8}Ba_{0.2}Ga_3O_{7.4}$ (x = 0.8) composition structural parameters (S.G. $P\bar{4}2_1m$, *a*= *b*= 8.06223(7) Å, *c*= 5.26848(12) Å).

Atom	x	Y	z	Occ	B_{iso}
La1/Ba1	0.3359(2)	0.1641(2)	0.5021(10)	0.9/0.1[a]	4.18(13)
Ga1	0	0	0	1	1.94(17)
Ga2	0.1462(4)	0.3539(4)	-0.0411(16)	1	3.72(16)
O1	0.5	0	0.192(8)	1	1.4(3)[b]
O2	0.1118(19)	0.3882(19)	0.303(5)	1	1.4(3)[b]
O3	0.0882(16)	0.1649(18)	0.797(5)	1	1.4(3)[b]
O4	0.3359(2)	0.1641(2)	-0.01(3)	0.2[a]	1.4(3)[b]

[a]Fixed to the nominal composition

[b]Constrained to refine to the same value

Table A. 32. Final refined $La_{1.85}Ba_{0.15}Ga_3O_{7.425}$ (x = 0.85) composition structural parameters (S.G. *Ima*2, *a*= 11.45216(8) Å, *b*= 11.35246(7) Å, *c*= 10.53719(5) Å).

Atom	x	y	z	Occ	Biso
La1/Ba1	-0.58709(4)	0.2505(3)	0.48323(7)	0.95/0.05[a]	0.597(11)
La2/Ba2	0.75	0.0860(3)	-0.01311(13)	0.9/0.1[a]	1.38(6)
La3/Ba3	0.75	0.4168(3)	-0.03437(12)	0.9/0.1[a]	0.66(5)
Ga1	-0.88662(8)	-0.2465(2)	0.21383(14)	1	0.88(2)
Ga2	0	0	0.2318(5)	1	0.20(5)
Ga3	0.5	0.5	0.2385(4)	1	0.59(6)
Ga4	0.75	-0.1035(3)	-0.2536(4)	1	1.15(8)
Ga5	0.25	0.0996(3)	0.2448(3)	1	0.46(7)
O1	-0.8864(5)	-0.2573(13)	-0.1119(6)	1	0.70(5)[b]
O2	-0.4713(9)	0.3722(9)	0.1365(8)	1	0.70(5)[b]
O3	-0.5436(9)	-0.3751(9)	-0.3789(9)	1	0.70(5)[b]
O4	-0.1192(8)	-0.0391(8)	-0.1597(8)	1	0.70(5)[b]
O5	-0.8885(7)	0.0622(7)	0.3414(8)	1	0.70(5)[b]
O6	0.75	0.2888(9)	0.1369(10)	1	0.70(5)[b]
O7	0.75	-0.1276(11)	0.0693(12)	1	0.70(5)[b]
O8	0.25	0.2579(17)	0.3202(8)	1	0.70(5)[b]
O9	0.25	0.1069(12)	0.5737(12)	1	0.70(5)[b]
O10	0.25	-0.0855(10)	0.2182(14)	0.85[a]	0.70(5)[b]

[a]Fixed to the nominal composition.

[b]Constrained to refine to the same value.

Table A. 33. Final refined $La_{1.85}Ba_{0.15}Ga_3O_{7.425}$ (x = 0.85) composition structural parameters (S.G. $P\bar{4}2_1m$, *a*= *b*= 8.05604(13) Å, *c*= 5.26135(15) Å).

Atom	x	Y	z	Occ	B_{iso}
La1/Ba1	0.33729	0.16271	0.50966	0.925/0.075[a]	1[b]
Ga1	0	0	0	1	1[b]
Ga2	0.14537	0.35463	-0.03938	1	1[b]
O1	0.5	0	0.22063	1	1[b]
O2	0.10528	0.39472	0.28488	1	1[b]
O3	0.08388	0.17379	0.78697	1	1[b]
O4	0.33729	0.16271	-0.02503	0.2125[a]	1[b]

[a]Fixed to the nominal composition

[b]Fixed to 1 due to the negative refined vlues

Table A. 34. Final refined $La_{1.9}Ba_{0.1}Ga_3O_{7.45}$ (x = 0.9) composition structural parameters (S.G. *Ima*2, *a*= 11.476307(15) Å, *b*= 11.295461(18) Å, *c*= 10.509301(17) Å).

Atom	x	y	z	Occ	Biso
La1/Ba1	-0.58736(4)	0.24971(16)	0.48395(6)	0,977/0.033[a]	0.201(9)
La2/Ba2	0.75	0.08735(15)	-0.01300(11)	0.944/0.066[a]	0.44(3)
La3/Ba3	0.75	0.41916(16)	-0.03541(10)	0.944/0.066[a]	0.70(4)
Ga1	-0.88576(7)	-0.24753(18)	0.21307(11)	1	0.114(9)
Ga2	0	0	0.2354(3)	1	0.114(9)
Ga3	0.5	0.5	0.2390(3)	1	0.114(9)
Ga4	0.75	-0.1034(2)	-0.25127(18)	1	0.114(9)
Ga5	0.25	0.0982(2)	0.24736(19)	1	0.114(9)
O1	-0.8883(5)	-0.2527(12)	-0.1116(7)	1	0.69(5)[b]
O2	-0.4722(9)	0.3741(8)	0.1368(9)	1	0.69(5)[b]
O3	-0.5368(9)	-0.3702(9)	-0.3764(9)	1	0.69(5)[b]
O4	-0.1240(7)	-0.0369(8)	-0.1550(8)	1	0.69(5)[b]
O5	-0.8874(7)	0.0623(8)	0.3467(8)	1	0.69(5)[b]
O6	0.75	0.2841(10)	0.1338(11)	1	0.69(5)[b]
O7	0.75	-0.1273(12)	0.0755(12)	1	0.69(5)[b]
O8	0.25	0.2535(16)	0.3237(9)	1	0.69(5)[b]
O9	0.25	0.1143(12)	0.5804(12)	1	0.69(5)[b]
O10	0.25	-0.0863(9)	0.2436(13)	0.9[a]	0.69(5)[b]

[a]Fixed to the nominal composition.

[b]Constrained to refine to the same value.

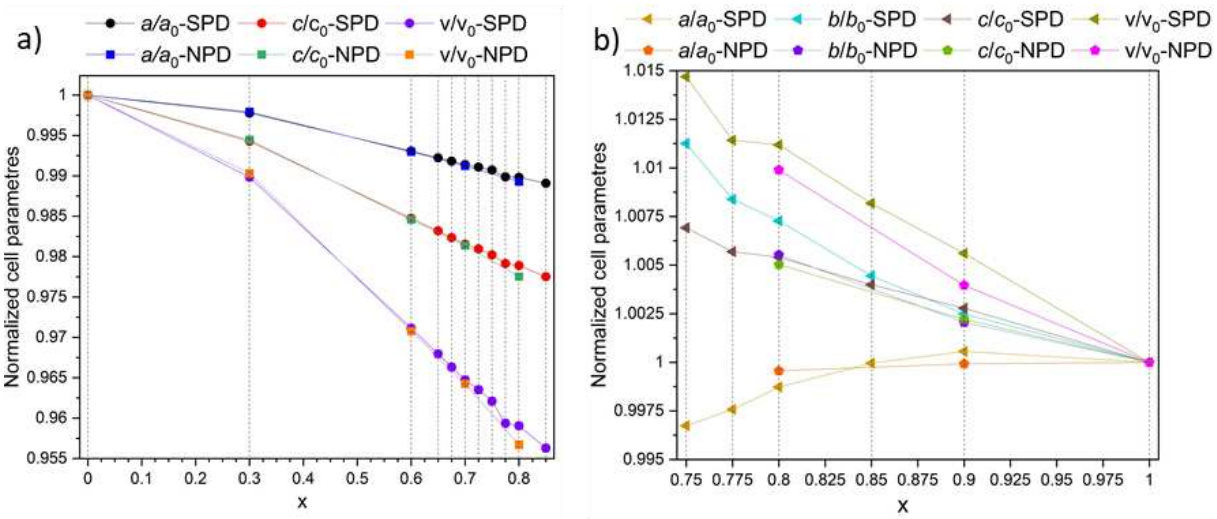

Figure A. 23. *Normalised refined cell parameter of the $La_{1+x}Ba_{1-x}Ga_3O_{7+x/2}$ solid solution measured compositions from both SPD and NPD data.*

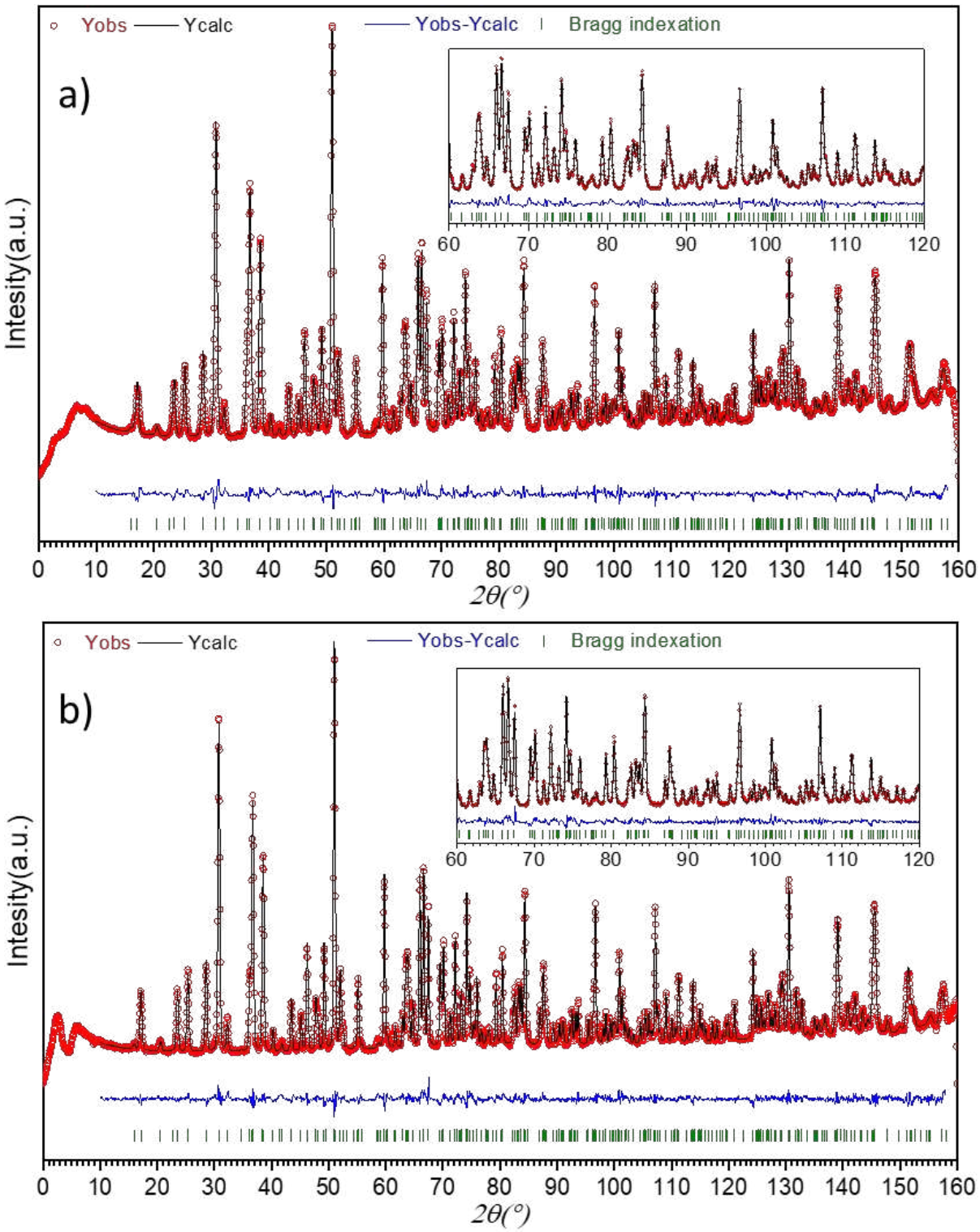

Figure A. 24. *Room temperature NPD (a) HI, (b) HR data Rietveld refinement of the* $La_{1.3}Ba_{0.7}Ga_3O_{7.15}$ *(x = 0.3) composition.*

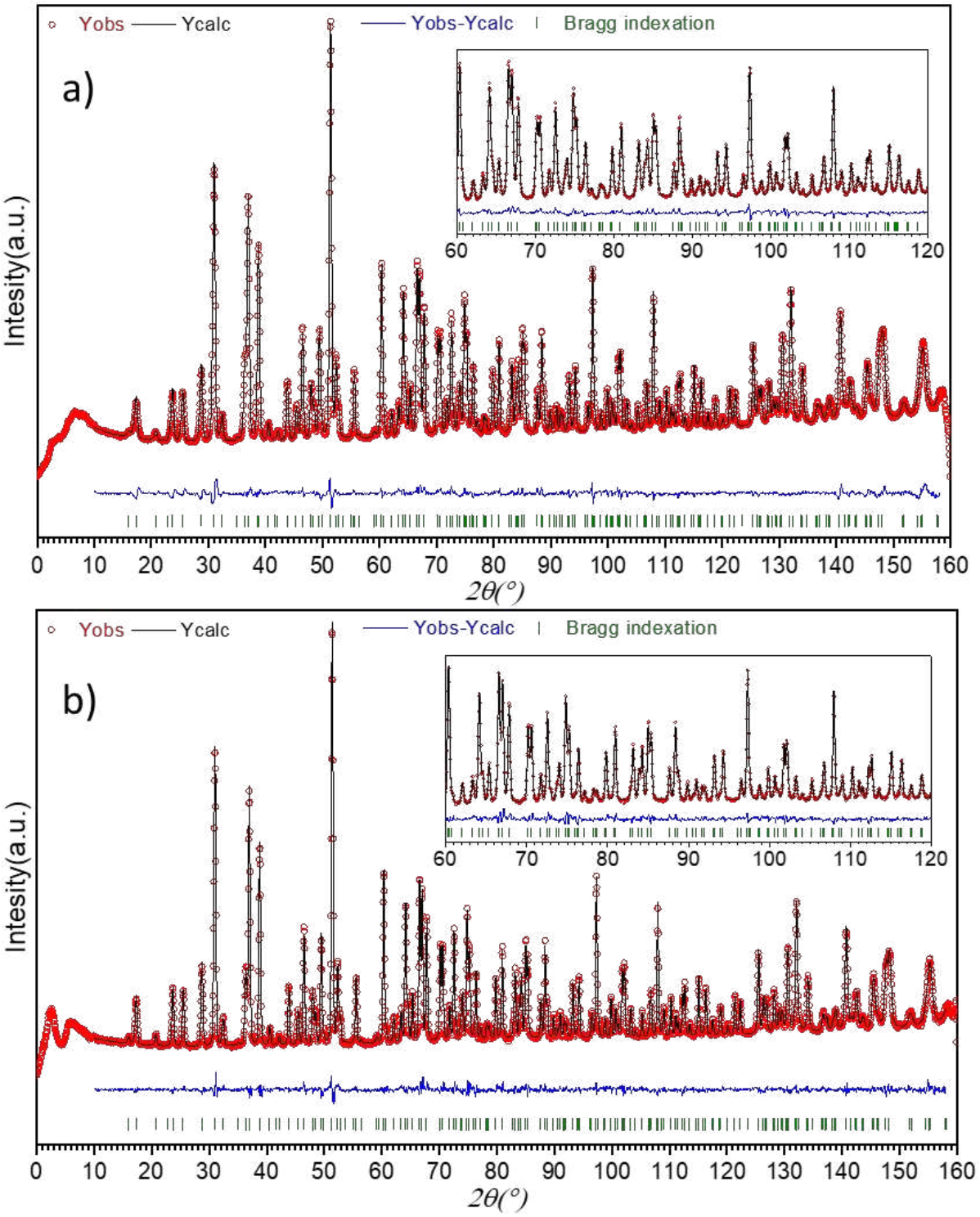

Figure A. 25. *Room temperature NPD (a) HI, (b) HR data Rietveld refinement of the* $La_{1.6}Ba_{0.4}Ga_3O_{7.3}$ *(x = 0.6) composition.*

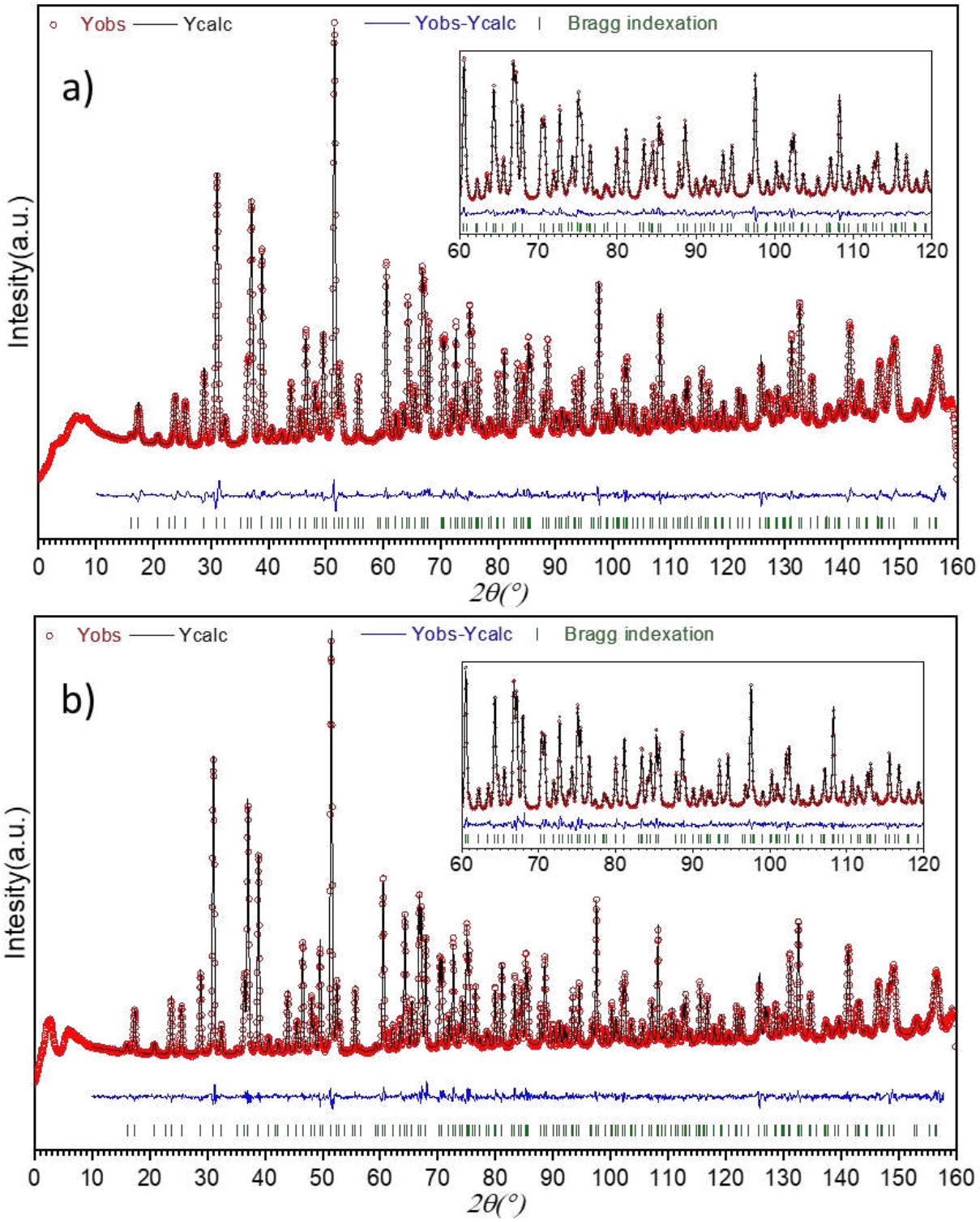

Figure A. 26. *Room temperature NPD (a) HI, (b) HR data Rietveld refinement of the* $La_{1.7}Ba_{0.3}Ga_3O_{7.35}$ *(x = 0.7) composition.*

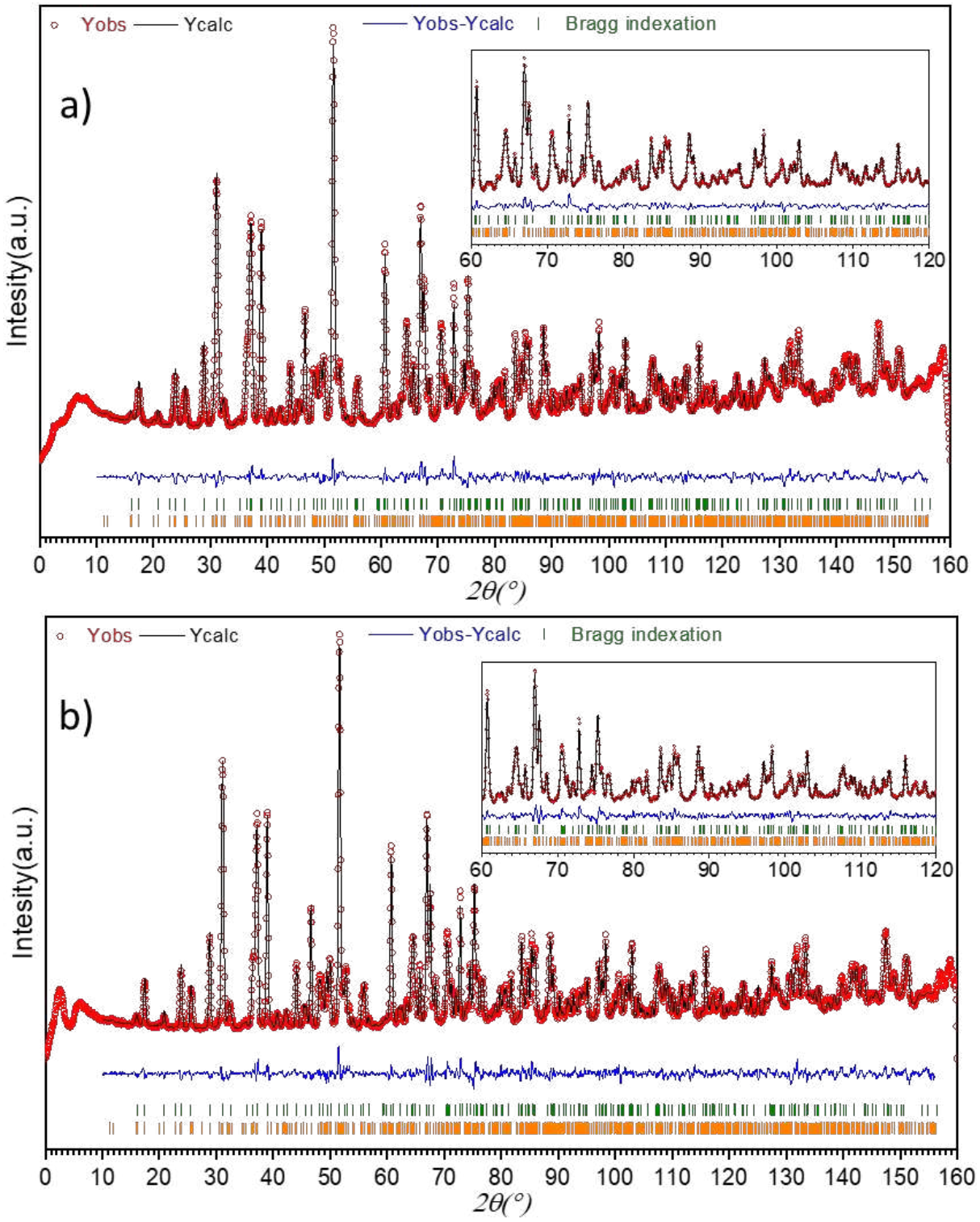

Figure A. 27. *Room temperature NPD (a) HI, (b) HR data Rietveld refinement of the* $La_{1.8}Ba_{0.2}Ga_3O_{7.4}$ *(x = 0.8) composition.*

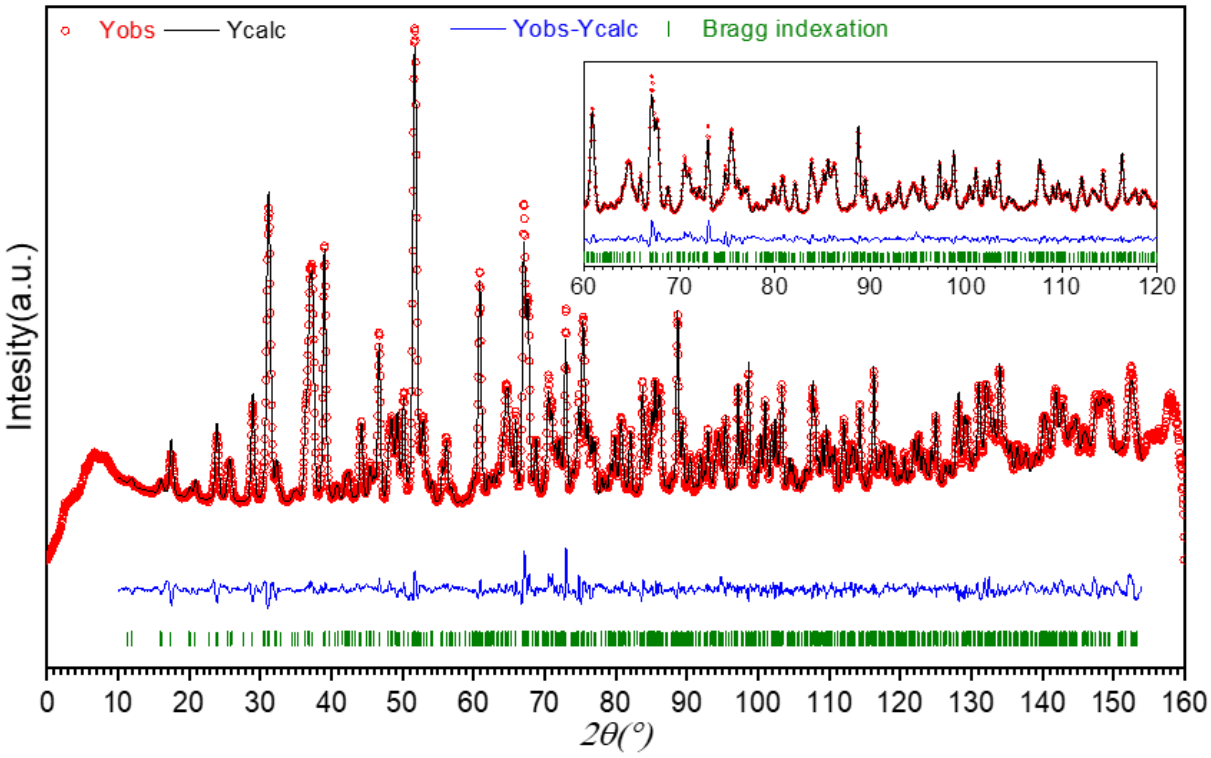

Figure A. 28. *Room temperature NPD HI data Rietveld refinement of the* $La_{1.9}Ba_{0.1}Ga_3O_{7.45}$ *(x = 0.9) composition.*

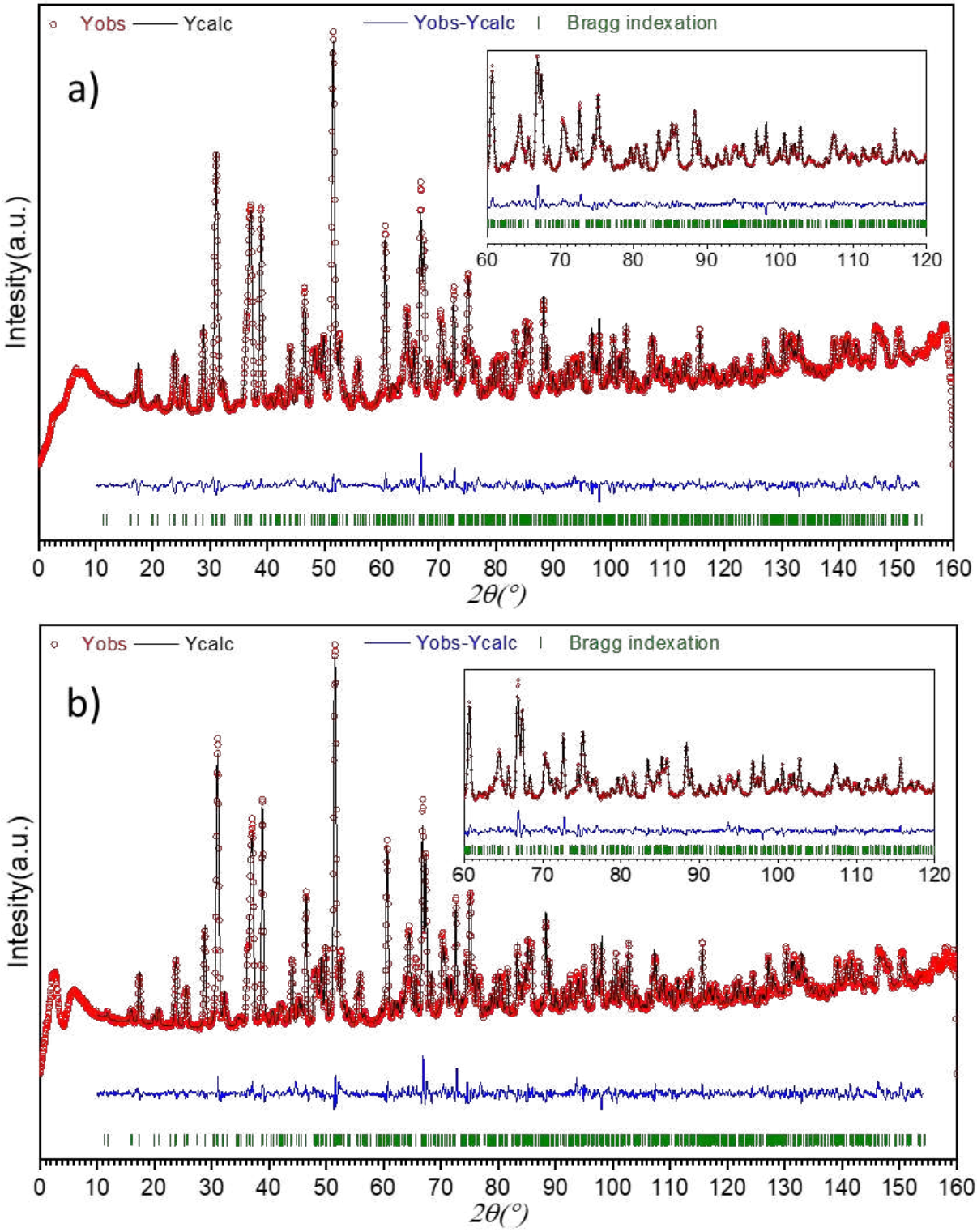

Figure A. 29. *525°C NPD (a) HI, (b) HR data Rietveld refinement of the* $La_{1.9}Ba_{0.1}Ga_3O_{7.45}$ *(x = 0.9) composition.*

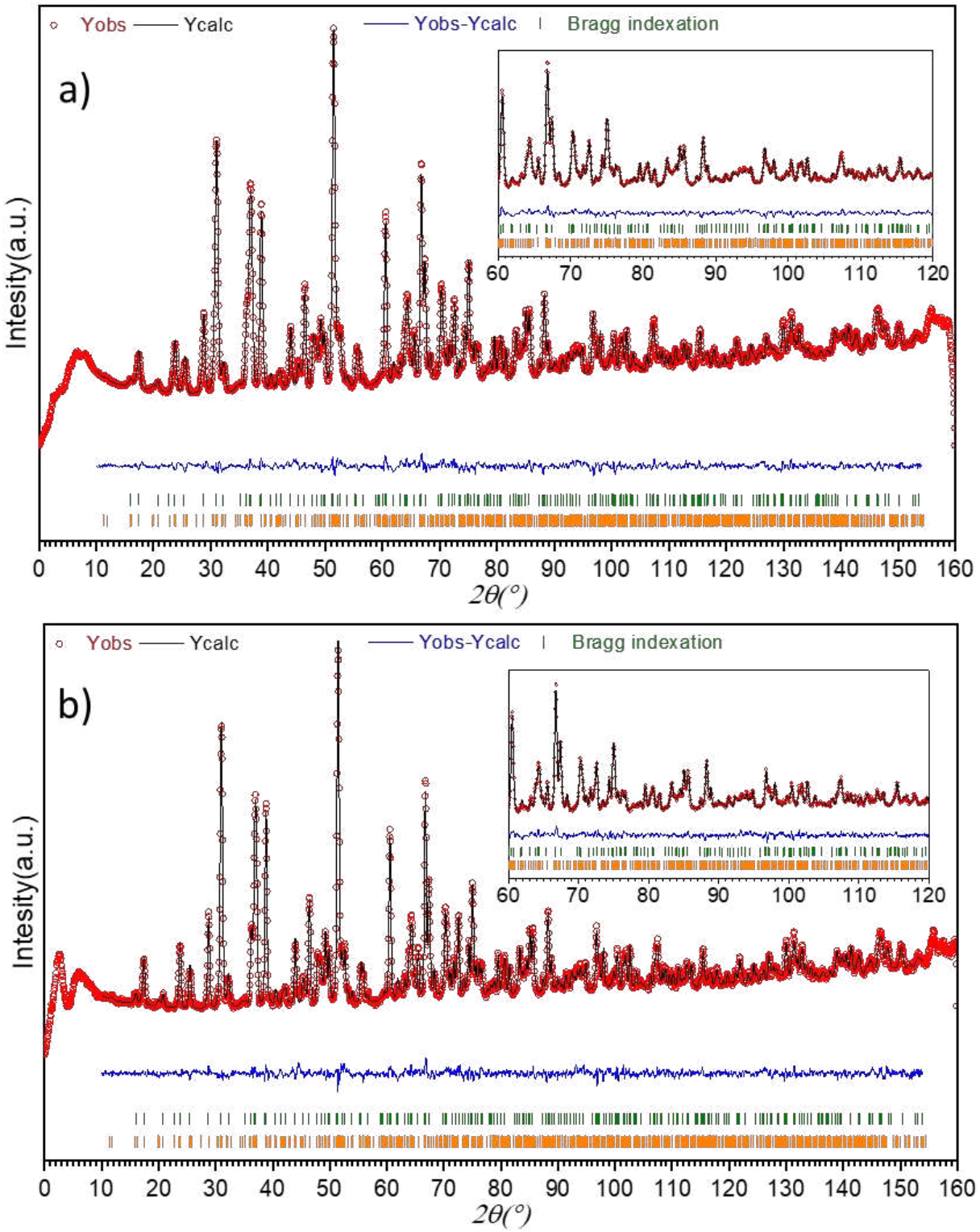

Figure A. 30. *720°C NPD (a) HI, (b) HR data Rietveld refinement of the* $La_{1.9}Ba_{0.1}Ga_3O_{7.45}$ *(x = 0.9) composition.*

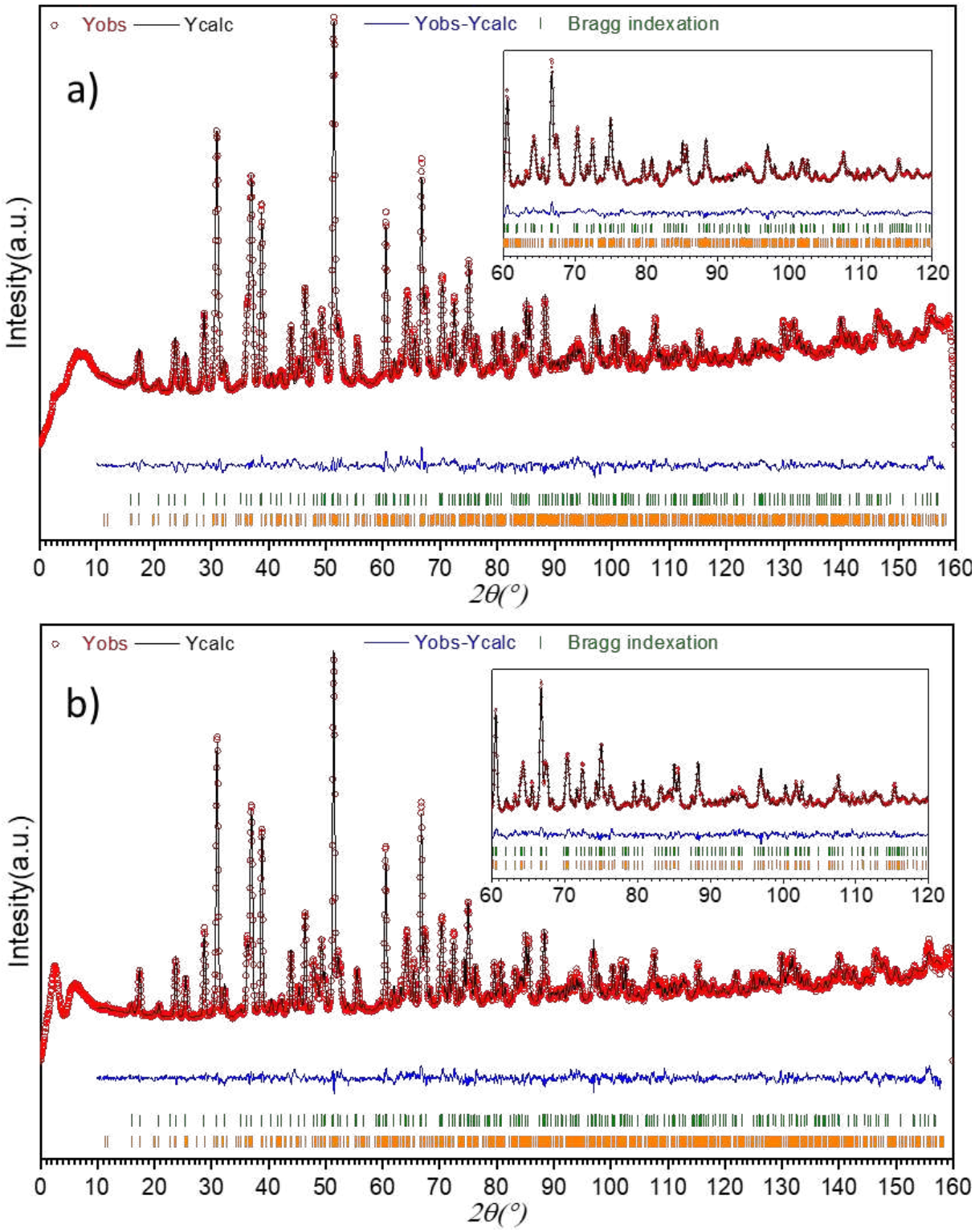

Figure A. 31. *770°C NPD (a) HI, (b) HR data Rietveld refinement of the* $La_{1.9}Ba_{0.1}Ga_3O_{7.45}$ *(x = 0.9) composition.*

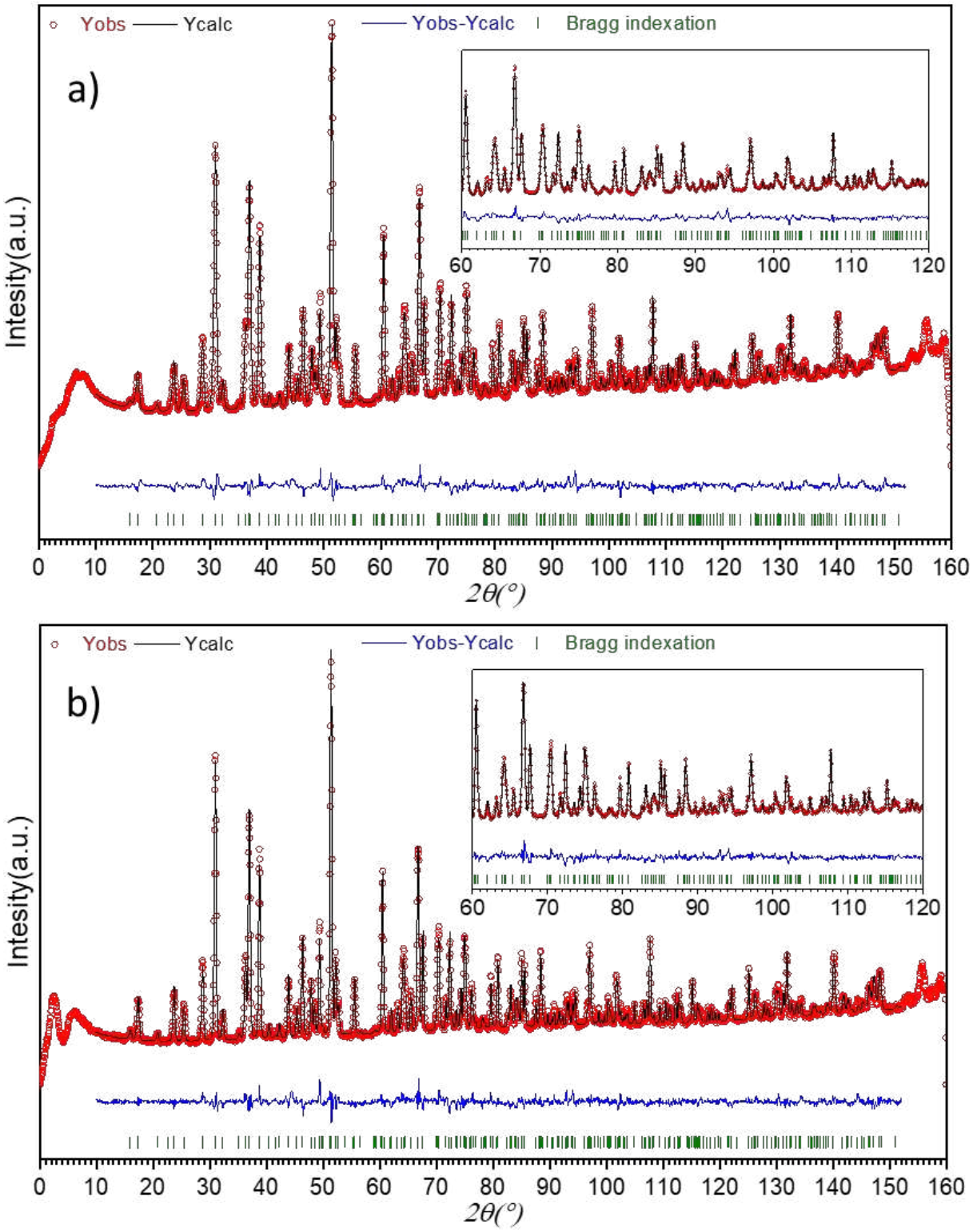

Figure A. 32. *820°C NPD (a) HI, (b) HR data Rietveld refinement of the $La_{1.9}Ba_{0.1}Ga_3O_{7.45}$ (x = 0.9) composition.*

Table A. 35. Final NPD HI refined data of $La_{1.3}Ba_{0.7}Ga_3O_{7.15}$ (x = 0.3) composition structural parameters (S.G. $P\bar{4}2_1m$, $a = b = 8.13053(4)$ Å, $c = 5.35381(6)$ Å).

Atom	x	y	z	Occ	B_{iso}
La1/Ba1	0.33682(10)	0.16318(10)	0.5091(3)	0.676(8)/0.324(8)	0.76(4)
Ga1	0	0	0	1	0.46(5)
Ga2	0.14189(12)	0.35811(12)	-0.0308(2)	1	0.72(4)
O1	0.5	0	0.1843(5)	1	1.81(10)
O2	0.13865(19)	0.36135(19)	0.3054(3)	1	1.76(6)
O3	0.08327(16)	0.16343(18)	0.8016(3)	1	1.66(6)
O4	0.333(2)	0.167(2)	0.008(5)	0.075(3)	1

Table A. 36. Refined anisotropic thermal parameters of $La_{1.3}Ba_{0.7}Ga_3O_{7.15}$ (x = 0.3) composition from NPD HI data.

Atom	B_{11}	B_{22}	B_{33}	B_{12}	B_{13}	B_{23}
La1/Ba1	0.60(2)	0.60(3)	1.10(6)	0.31(4)	0.02(4)	-0.02(4)
Ga1	0.32(4)	0.32(4)	0.76(6)	0	0	0
Ga2	0.73(3)	0.73(3)	0.70(6)	-0.07(4)	0.14(3)	-0.14(3)
O1	1.94(8)	1.94(8)	1.54(13)	-1.25(10)	0	0
O2	2.33(6)	2.33(6)	0.62(6)	-0.47(7)	-0.14(5)	0.14(5)
O3	2.65(7)	0.95(6)	1.38(6)	-0.45(6)	0.77(5)	0.10(6)

Table A. 37. Final NPD HR refined data of $La_{1.3}Ba_{0.7}Ga_3O_{7.15}$ (x = 0.3) composition structural parameters (S.G. $P\bar{4}2_1m$, $a = b = 8.1280(12)$ Å, $c = 5.3522(8)$ Å).

Atom	x	y	z	Occ	B_{iso}
La1/Ba1	0.33670(11)	0.16330(11)	0.5086(3)	0.662(8)/0.338(8)	0.81(4)
Ga1	0	0	0	1	0.53(5)
Ga2	0.14198(11)	0.35802(11)	-0.0316(3)	1	0.79(4)
O1	0.5	0	0.1833(5)	1	1.98(10)
O2	0.13843(19)	0.36157(19)	0.3055(3)	1	1.76(6)
O3	0.08330(17)	0.16336(19)	0.8027(3)	1	1.72(6)
O4	0.337(2)	0.163(2)	0.012(5)	0.075(3)	1

Table A. 38. Refined anisotropic thermal parameters of $La_{1.3}Ba_{0.7}Ga_3O_{7.15}$ (x = 0.3) composition from NPD HR data.

Atom	B_{11}	B_{22}	B_{33}	B_{12}	B_{13}	B_{23}
La1/Ba1	0.72(2)	0.71(3)	1.00(6)	0.25(4)	0.02(4)	-0.02(4)
Ga1	0.32(4)	0.32(4)	0.96(7)	0	0	0
Ga2	0.75(3)	0.75(3)	0.87(6)	-0.13(5)	0.15(3)	-0.15(3)
O1	2.20(8)	2.20(8)	1.54(13)	-1.30(11)	0	0
O2	2.26(6)	2.25(6)	0.77(6)	-0.40(8)	-0.13(5)	0.13(5)
O3	2.61(7)	1.06(6)	1.50(6)	-0.62(6)	0.71(5)	0.09(5)

Table A. 39. Final NPD HI refined data of $La_{1.6}Ba_{0.4}Ga_3O_{7.3}$ (x = 0.6) composition structural parameters (S.G. $P\bar{4}2_1m$, $a = b = 8.09083(4)$ Å, $c = 5.30112(6)$ Å).

Atom	x	y	z	Occ	B_{iso}
La1/Ba1	0.33657(9)	0.16343(9)	0.5075(3)	0.799(7)/0.201(7)	0.85(4)
Ga1	0	0	0	1	0.50(5)
Ga2	0.14198(11)	0.35802(11)	-0.0313(3)	1	0.96(4)
O1	0.5	0	0.1875(5)	1	2.57(10)
O2	0.13771(15)	0.36229(15)	0.3091(3)	1	1.23(5)
O3	0.08307(15)	0.16396(18)	0.7970(2)	1	1.92(6)
O4	0.3363(10)	0.1637(10)	-0.001(2)	0.152(3)	1

Table A. 40. Refined anisotropic thermal parameters of $La_{1.6}Ba_{0.4}Ga_3O_{7.3}$ (x = 0.6) composition from NPD HI data.

Atom	B_{11}	B_{22}	B_{33}	B_{12}	B_{13}	B_{23}
La1/Ba1	0.58(3)	0.58(3)	1.39(6)	0.37(3)	-0.02(3)	0.02(3)
Ga1	0.35(4)	0.35(4)	0.77(6)	0	0	0
Ga2	1.12(3)	1.12(3)	0.64(6)	-0.10(5)	0.01(3)	-0.01(3)
O1	3.09(9)	3.09(7)	1.52(13)	-2.14(11)	0	0
O2	1.56(5)	1.56(5)	0.58(6)	-0.14(6)	-0.06(3)	0.06(3)
O3	3.37(7)	0.83(5)	1.56(6)	-0.68(5)	1.34(4)	-0.09(5)

Table A. 41. Final NPD HR refined data of $La_{1.6}Ba_{0.4}Ga_3O_{7.3}$ (x = 0.6) composition structural parameters (S.G. $P\bar{4}2_1m$, $a = b = 8.08771(3)$ Å, $c = 5.29899(5)$ Å).

Atom	x	y	z	Occ	B_{iso}
La1/Ba1	0.33671(10)	0.16329(10)	0.5071(3)	0.804(8)/0.196(8)	0.90(4)
Ga1	0	0	0	1	0.53(5)
Ga2	0.14209(12)	0.35791(12)	-0.0314(3)	1	1.02(5)
O1	0.5	0	0.1877(5)	1	2.52(11)
O2	0.13770(16)	0.36230(16)	0.3095(3)	1	1.22(5)
O3	0.08321(16)	0.16384(19)	0.7977(3)	1	1.88(7)
O4	0.3377(11)	0.1623(11)	0.001(2)	0.143(3)	1

Table A. 42. Refined anisotropic thermal parameters of $La_{1.6}Ba_{0.4}Ga_3O_{7.3}$ (x = 0.6) composition from NPD HR data.

Atom	B_{11}	B_{22}	B_{33}	B_{12}	B_{13}	B_{23}
La1/Ba1	0.63(3)	0.63(3)	1.44(6)	0.41(4)	-0.03(3)	0.03(4)
Ga1	0.43(4)	0.43(4)	0.75(6)	0,00	0,00	0
Ga2	1.18(4)	1.18(4)	0.68(6)	-0.21(5)	-0.02(3)	0.02(3)
O1	3.00(10)	3.00(10)	1.57(13)	-1.85(12)	0,00	0
O2	1.52(5)	1.52(5)	0.62(6)	0.05(6)	-0.10(4)	0.10(4)
O3	3.13(8)	1.02(5)	1.48(6)	-0.65(6)	1.16(4)	-0.10(5)

Table A. 43. Final NPD HI refined data of $La_{1.7}Ba_{0.3}Ga_3O_{7.35}$ (x = 0.7) composition structural parameters (S.G. $P\bar{4}2_1m$, $a = b = 8.07722(4)$ Å, $c = 5.28401(6)$ Å).

Atom	x	y	z	Occ	B_{iso}
La1/Ba1	0.33604(10)	0.16396(10)	0.5079(3)	0.853(8)/0.147(8)	0.86(4)
Ga1	0	0	0	1	0.50(5)
Ga2	0.14179(11)	0.35821(11)	-0.0318(3)	1	0.98(5)
O1	0.5	0	0.1889(5)	1	2.89(11)
O2	0.13695(16)	0.36305(16)	0.3102(3)	1	1.17(5)
O3	0.08251(16)	0.1636(2)	0.7951(3)	1	2.09(7)
O4	0.3384(9)	0.1616(9)	0.0024(18)	0.180(3)	1

Table A. 44. Refined anisotropic thermal parameters of $La_{1.7}Ba_{0.3}Ga_3O_{7.35}$ (x = 0.7) composition from NPD HI data.

Atom	B_{11}	B_{22}	B_{33}	B_{12}	B_{13}	B_{23}
La1/Ba1	0.63(3)	0.63(3)	1.33(6)	0.28(4)	-0.14(4)	0.14(4)
Ga1	0.50(4)	0.50(4)	0.51(6)	0	0	0
Ga2	1.22(4)	1.22(4)	0.52(6)	-0.01(5)	0.15(3)	-0.15(3)
O1	3.74(10)	3.74(10)	1.17(12)	-2.73(12)	0	0
O2	1.50(5)	1.50(5)	0.51(6)	-0.29(6)	-0.13(3)	0.13(3)
O3	3.80(8)	1.00(5)	1.46(6)	-0.60(6)	1.56(5)	0.03(5)

Table A. 45. Final NPD HR refined data of $La_{1.7}Ba_{0.3}Ga_3O_{7.35}$ (x = 0.7) composition structural parameters (S.G. $P\bar{4}2_1m$, $a = b = 8.07364(4)$ Å, $c = 5.28175(6)$ Å).

Atom	x	y	z	Occ	B_{iso}
La1/Ba1	0.33591(10)	0.16409(10)	0.5078(3)	0.868(8)/0.132(8)	0.87(4)
Ga1	0	0	0	1	0.54(5)
Ga2	0.14168(12)	0.35832(12)	-0.0324(3)	1	1.00(5)
O1	0.5	0	0.1893(5)	1	2.80(12)
O2	0.13701(17)	0.36299(17)	0.3101(3)	1	1.19(6)
O3	0.08251(17)	0.1634(2)	0.7955(3)	1	2.10(7)
O4	0.3393(10)	0.1607(10)	0.002(2)	0.168(3)	1

Table A. 46. Refined anisotropic thermal parameters of $La_{1.7}Ba_{0.3}Ga_3O_{7.35}$ (x = 0.7) composition from NPD HR data.

Atom	B_{11}	B_{22}	B_{33}	B_{12}	B_{13}	B_{23}
La1/Ba1	0.68(3)	0.68(3)	1.26(6)	0.21(4)	-0.17(4)	0.17(4)
Ga1	0.60(4)	0.60(4)	0.43(6)	0	0	0
Ga2	1.18(4)	1.18(4)	0.64(6)	-0.02(5)	0.15(3)	-0.16(3)
O1	3.71(11)	3.71(11)	0.97(12)	-2.78(14)	0	0
O2	1.45(6)	1.45(6)	0.66(6)	-0.21(6)	-0.18(4)	0.18(4)
O3	3.77(9)	1.01(6)	1.52(6)	-0.62(6)	1.45(5)	0.05(6)

Table A. 47. Final NPD HI refined data of $La_{1.8}Ba_{0.2}Ga_3O_{7.4}$ (x = 0.8) composition structural parameters (S.G. $P\bar{4}2_1m$, a= b= 8.0575(6) Å, c= 5.2605(9) Å).

Atom	x	y	z	Occ	B_{iso}
La1/Ba1	0.3355(15)	0.1645(15)	0.478(4)	0.9/0.1	2.4(6)
Ga1	0	0	0	1	1.7(6)[a]
Ga2	0.1479(16)	0.3521(16)	-0.027(4)	1	1.7(6)[a]
O1	0.5	0	0.191(7)	1	2.0(6)[b]
O2	0.1405(19)	0.3595(19)	0.314(4)	1	2.0(6)[b]
O3	0.0859(16)	0.161(2)	0.792(4)	1	2.0(6)[b]
O4	0.342(7)	0.158(7)	0.016(18)	0.20(4)	1

[a,b]Constrained to refine to the same value.

Table A. 48. Final NPD HI refined data of $La_{1.8}Ba_{0.2}Ga_3O_{7.4}$ (x = 0.8) composition structural parameters (S.G. *Ima*2, a= 11.46696(19) Å, b= 11.33164(19) Å, c= 10.5347(2) Å).

Atom	x	y	z	Occ	Biso
La1/Ba1	-0.5864(2)	0.2497(7)	0.4769(4)	0.929(7)/0.076(11)	0.21(10)
La2/Ba2	0.75	0.0865(9)	-0.0253(10)	0.85(2)/0.16(3)	1.2(3)
La3/Ba3	0.75	0.4154(8)	-0.0371(8)	0.92(2)/0.09(3)	0.8(3)
Ga1	-0.8872(3)	-0.2468(7)	0.2095(4)	1	0.49(7)[a]
Ga2	0	0	0.2288(10)	1	0.49(7)[a]
Ga3	0.5	0.5	0.2269(10)	1	0.49(7)[a]
Ga4	0.75	-0.1051(8)	-0.2546(10)	1	0.49(7)[a]
Ga5	0.25	0.1000(8)	0.2402(10)	1	0.49(7)[a]
O1	-0.8869(4)	-0.2503(11)	-0.1174(5)	1	0.87(7)[b]
O2	-0.4746(5)	0.3684(6)	0.1364(7)	1	0.87(7)[b]
O3	-0.5447(6)	-0.3805(6)	-0.3854(7)	1	0.87(7)[b]
O4	-0.1270(6)	-0.0368(6)	-0.1705(8)	1	0.87(7)[b]
O5	-0.8883(6)	0.0589(6)	0.3388(8)	1	0.87(7)[b]
O6	0.75	0.2789(6)	0.1291(9)	1	0.87(7)[b]
O7	0.75	-0.1195(11)	0.0671(11)	1	0.87(7)[b]
O8	0.25	0.2490(13)	0.3164(7)	1	0.87(7)[b]
O9	0.25	0.1114(12)	0.5716(12)	1	0.87(7)[b]
O10	0.25	-0.0892(10)	0.2254(13)	0.77(2)	1

[a,b]Constrained to refine to the same value.

Table A. 49. Final NPD HR refined data of $La_{1.8}Ba_{0.2}Ga_3O_{7.4}$ (x = 0.8) composition structural parameters (S.G. $P\bar{4}2_1m$, $a = b = 8.0578(6)$ Å, $c = 5.2611(9)$ Å).

Atom	x	y	z	Occ	B_{iso}
La1/Ba1	0.3361(17)	0.1639(17)	0.471(4)	0.9/0.1	1.4(6)
Ga1	0	0	0	1	0.8(6)[a]
Ga2	0.1505(17)	0.3496(17)	-0.023(4)	1	0.8(6)[a]
O1	0.5	0	0.184(7)	1	1.1(6)[b]
O2	0.139(2)	0.361(2)	0.313(5)	1	1.1(6)[b]
O3	0.0820(17)	0.158(2)	0.784(4)	1	1.1(6)[b]
O4	0.341(10)	0.159(10)	-0.02(2)	0.20(5)	1

[a,b]Constrained to refine to the same value.

Table A. 50. Final NPD HR refined data of $La_{1.8}Ba_{0.2}Ga_3O_{7.4}$ (x = 0.8) composition structural parameters (S.G. *Ima*2, $a = 11.46505(19)$ Å, $b = 11.32986(19)$ Å, $c = 10.5331(2)$ Å).

Atom	x	y	z	Occ	Biso
La1/Ba1	-0.5859(3)	0.2492(8)	0.4775(4)	0.928(7)/0.076(11)	0.28(11)
La2/Ba2	0.75	0.0853(9)	-0.0266(10)	0.85(2)/0.16(3)	1.2(3)
La3/Ba3	0.75	0.4167(10)	-0.0374(10)	0.92(2)/0.09(3)	1.4(3)
Ga1	-0.8869(4)	-0.2467(8)	0.2095(4)	1	0.67(7)[a]
Ga2	0	0	0.2273(12)	1	0.67(7)[a]
Ga3	0.5	0.5	0.2263(12)	1	0.67(7)[a]
Ga4	0.75	-0.1041(9)	-0.2563(12)	1	0.67(7)[a]
Ga5	0.25	0.1010(9)	0.2416(12)	1	0.67(7)[a]
O1	-0.8870(5)	-0.2501(12)	-0.1176(6)	1	0.96(7)[b]
O2	-0.4744(6)	0.3690(7)	0.1363(8)	1	0.96(7)[b]
O3	-0.5445(7)	-0.3787(7)	-0.3822(8)	1	0.96(7)[b]
O4	-0.1295(6)	-0.0360(6)	-0.1709(8)	1	0.96(7)[b]
O5	-0.8882(7)	0.0585(6)	0.3384(8)	1	0.96(7)[b]
O6	0.75	0.2798(7)	0.1275(10)	1	0.96(7)[b]
O7	0.75	-0.1196(13)	0.0680(14)	1	0.96(7)[b]
O8	0.25	0.2495(15)	0.3162(8)	1	0.96(7)[b]
O9	0.25	0.1130(14)	0.5712(15)	1	0.96(7)[b]
O10	0.25	-0.0916(11)	0.2239(14)	0.76(2)	1

[a,b]Constrained to refine to the same value.

Table A. 51. Final NPD HI refined data of $La_{1.9}Ba_{0.1}Ga_3O_{7.45}$ (x = 0.9) composition structural parameters (S.G. *Ima*2, *a*= 11.47152(16) Å, *b*= 11.29287(17) Å, *c*= 10.50526(18) Å).

Atom	x	y	z	Occ	Biso
La1/Ba1	-0.5868(2)	0.2502(7)	0.4861(3)	0.966(6)/0.028(10)	0.27(7)
La2/Ba2	0.75	0.0870(6)	-0.0081(6)	0.892(17)/0.11(3)	0.4(2)
La3/Ba3	0.75	0.4165(6)	-0.0346(6)	0.969(17)/0.04(3)	0.49(18)
Ga1	-0.8858(3)	-0.2422(5)	0.2191(3)	1	0.33(3)[a]
Ga2	0	0	0.2388(9)	1	0.33(3)[a]
Ga3	0.5	0.5	0.2391(8)	1	0.33(3)[a]
Ga4	0.75	-0.1056(6)	-0.2466(7)	1	0.33(3)[a]
Ga5	0.25	0.0966(6)	0.2485(8)	1	0.33(3)[a]
O1	-0.8859(3)	-0.2488(8)	-0.1079(4)	1	0.42(7)
O2	-0.4761(6)	0.3658(6)	0.1456(7)	1	0.80(12)
O3	-0.5395(5)	-0.3775(5)	-0.3750(7)	1	0.32(10)
O4	-0.1248(5)	-0.0357(5)	-0.1591(7)	1	0.87(11)
O5	-0.8909(5)	0.0617(5)	0.3485(6)	1	0.59(11)
O6	0.75	0.2835(6)	0.1341(9)	1	1.13(14)
O7	0.75	-0.1227(9)	0.0752(9)	1	0.74(19)
O8	0.25	0.2501(10)	0.3267(6)	1	0.58(9)
O9	0.25	0.1082(10)	0.5845(9)	1	0.60(17)
O10	0.25	-0.0858(7)	0.2296(9)	0.892(15)	1

[a]Constrained to refine to the same value.

Table A. 52. Final NPD HR refined data of $La_{1.9}Ba_{0.1}Ga_3O_{7.45}$ (x = 0.9) composition structural parameters (S.G. *Ima*2, *a*= 11.46923(16) Å, *b*= 11.29077(17) Å, *c*= 10.50358(18) Å).

Atom	x	y	z	Occ	Biso
La1/Ba1	-0.5862(2)	0.2504(8)	0.4858(4)	0.968(6)/0.028(10)	0.38(8)
La2/Ba2	0.75	0.0870(6)	-0.0090(7)	0.894(18)/0.11(3)	0.3(2)
La3/Ba3	0.75	0.4166(7)	-0.0364(7)	0.971(18)/0.04(3)	0.6(2)
Ga1	-0.8857(3)	-0.2425(6)	0.2192(4)	1	0.43(4)[a]
Ga2	0	0	0.2373(10)	1	0.43(4)[a]
Ga3	0.5	0.5	0.2394(10)	1	0.43(4)[a]
Ga4	0.75	-0.1067(7)	-0.2467(8)	1	0.43(4)[a]
Ga5	0.25	0.0956(7)	0.2498(8)	1	0.43(4)[a]
O1	-0.8870(4)	-0.2483(9)	-0.1078(5)	1	0.57(8)
O2	-0.4760(7)	0.3659(6)	0.1444(8)	1	0.86(14)
O3	-0.5396(6)	-0.3778(6)	-0.3728(8)	1	0.61(13)
O4	-0.1258(6)	-0.0362(6)	-0.1581(8)	1	1.23(13)
O5	-0.8907(6)	0.0614(6)	0.3481(7)	1	0.87(13)
O6	0.75	0.2845(7)	0.1345(10)	1	1.47(18)
O7	0.75	-0.1223(10)	0.0758(10)	1	0.8(2)
O8	0.25	0.2487(12)	0.3279(7)	1	0.55(10)
O9	0.25	0.1080(11)	0.5833(10)	1	0.61(19)
O10	0.25	-0.0872(8)	0.2297(10)	0.878(17)	1

[a]Constrained to refine to the same value.

Table A. 53. Final 525°C NPD HI refined data of $La_{1.9}Ba_{0.1}Ga_3O_{7.45}$ (x = 0.9) composition structural parameters (S.G. *Ima*2, *a*= 11.5006(2) Å, *b*= 11.3487(2) Å, *c*= 10.5398(2) Å).

Atom	x	y	z	Occ	Biso
La1/Ba1	-0.5867(3)	0.2508(7)	0.4877(4)	0.967(6)/0.045(10)	1.19(9)
La2/Ba2	0.75	0.0871(8)	-0.0079(8)	0.945(18)/0.06(3)	1.7(3)
La3/Ba3	0.75	0.4169(8)	-0.0298(8)	0.945(18)/0.05(3)	1.6(2)
Ga1	-0.8852(3)	-0.2411(5)	0.2228(4)	1	1.06(4)[a]
Ga2	0	0	0.2382(11)	1	1.06(4)[a]
Ga3	0.5	0.5	0.2368(11)	1	1.06(4)[a]
Ga4	0.75	-0.1049(7)	-0.2427(9)	1	1.06(4)[a]
Ga5	0.25	0.0984(7)	0.2494(10)	1	1.06(4)[a]
O1	-0.8857(4)	-0.2481(8)	-0.1069(5)	1	1.00(8)
O2	-0.4771(6)	0.3663(6)	0.1461(8)	1	1.75(14)
O3	-0.5402(6)	-0.3770(5)	-0.3737(7)	1	0.83(12)
O4	-0.1242(6)	-0.0338(6)	-0.1591(8)	1	1.68(14)
O5	-0.8895(6)	0.0626(6)	0.3522(7)	1	1.28(12)
O6	0.75	0.2792(7)	0.1382(9)	1	1.60(16)
O7	0.75	-0.1246(9)	0.0759(10)	1	1.08(19)
O8	0.25	0.2519(13)	0.3271(8)	1	1.72(12)
O9	0.25	0.1065(11)	0.5844(12)	1	1.9(2)
O10	0.25	-0.0836(9)	0.2318(10)	0.871(19)	1.8(2)

[a]Constrained to refine to the same value.

Table A. 54. Final 525°C NPD HR refined data of $La_{1.9}Ba_{0.1}Ga_3O_{7.45}$ (x = 0.9) composition structural parameters (S.G. *Ima*2, *a*= 11.5005(2) Å, *b*= 11.3482(2) Å, *c*= 10.5396(2) Å).

Atom	x	y	z	Occ	Biso
La1/Ba1	-0.5862(3)	0.2502(9)	0.4885(5)	0.988(6)/0.002(10)	1.08(10)
La2/Ba2	0.75	0.0866(8)	-0.0082(9)	0.902(19)/0.10(3)	1.4(3)
La3/Ba3	0.75	0.4173(9)	-0.0305(9)	0.902(19)/0.10(3)	1.6(3)
Ga1	-0.8855(4)	-0.2413(6)	0.2219(5)	1	1.10(4)[a]
Ga2	0	0	0.2380(13)	1	1.10(4)[a]
Ga3	0.5	0.5	0.2393(12)	1	1.10(4)[a]
Ga4	0.75	-0.1048(8)	-0.2435(10)	1	1.10(4)[a]
Ga5	0.25	0.0987(8)	0.2492(11)	1	1.10(4)[a]
O1	-0.8866(4)	-0.2489(10)	-0.1072(5)	1	1.02(9)
O2	-0.4777(8)	0.3672(8)	0.1464(10)	1	2.12(19)
O3	-0.5402(6)	-0.3766(6)	-0.3707(9)	1	0.86(14)
O4	-0.1250(7)	-0.0351(7)	-0.1576(9)	1	1.82(17)
O5	-0.8889(7)	0.0622(7)	0.3519(9)	1	1.52(16)
O6	0.75	0.2801(8)	0.1385(10)	1	1.68(19)
O7	0.75	-0.1252(10)	0.0769(12)	1	1.4(2)
O8	0.25	0.2513(15)	0.3273(8)	1	1.53(14)
O9	0.25	0.1068(12)	0.5830(13)	1	1.5(2)
O10	0.25	-0.0844(10)	0.2316(12)	0.85(2)	1.7(3)

[a]Constrained to refine to the same value.

Table A. 55. Final 720°C NPD HI refined data of $La_{1.9}Ba_{0.1}Ga_3O_{7.45}$ (x = 0.9) composition structural parameters (S.G. $P\bar{4}2_1m$, a= b= 8.1201(3) Å, c= 5.2791(4)) Å).

Atom	x	y	z	Occ	B_{iso}
La1/Ba1	0.3362(6)	0.1638(6)	0.514(2)	0.95(2)/0.05(2)	2.2(2)
Ga1	0	0	0	1	1.82(17)
Ga2	0.1398(7)	0.3602(7)	-0.028(2)	1	1.82(17)
O1	0.5	0	0.206(3)	1	2.0(3)
O2	0.1382(9)	0.3618(9)	0.308(2)	1	2.4(2)
O3	0.0873	0.1645(10)	0.7959(17)	1	2.7(2)
O4	0.326(2)	0.174(2)	0.006(8)	0.234(17)	1

Table A. 56. Final 720°C NPD HI refined data of $La_{1.9}Ba_{0.1}Ga_3O_{7.45}$ (x = 0.9) composition structural parameters (S.G. *Ima*2, a= 11.5122(3) Å, b= 11.3611(3) Å, c= 10.5622(4) Å).

Atom	x	y	z	Occ	Biso
La1/Ba1	-0.5870(4)	0.2502(9)	0.4862(7)	0.954(11)/0.036(18)	1.37(15)
La2/Ba2	0.75	0.0842(10)	-0.0112(11)	0.95(2)/0.06(4)	2.0(4)
La3/Ba3	0.75	0.4154(10)	-0.0291(12)	0.94(2)/0.07(4)	1.9(3)
Ga1	-0.8859(5)	-0.2409(8)	0.2231(8)	1	1.77(13)
Ga2	0	0	0.2456(11)	1	1.2(2)
Ga3	0.5	0.5	0.2340(11)	1	0.79(18)
Ga4	0.75	-0.1067(9)	-0.2443(11)	1	1.1(2)
Ga5	0.25	0.0948(9)	0.2513(12)	1	1.3(2)
O1	-0.8870(7)	-0.2457(9)	-0.1079(7)	1	1.18(14)
O2	-0.4829(9)	0.3647(8)	0.1536(10)	1	1.86(18)
O3	-0.5434(7)	-0.3797(7)	-0.3790(10)	1	1.41(17)
O4	-0.1205(9)	-0.0346(8)	-0.1577(11)	1	1.9(2)
O5	-0.8912(8)	0.0646(7)	0.3520(9)	1	1.33(17)
O6	0.75	0.2794(9)	0.1477(15)	1	2.2(3)
O7	0.75	-0.1251(12)	0.0775(15)	1	1.9(3)
O8	0.25	0.2490(19)	0.3271(13)	1	2.6(2)
O9	0.25	0.1088(13)	0.5823(14)	1	1.4(3)
O10	0.25	-0.0824(13)	0.227(2)	0.79(3)	1

Table A. 57. Final 720°C NPD HR refined data of $La_{1.9}Ba_{0.1}Ga_3O_{7.45}$ (x = 0.9) composition structural parameters (S.G. $P\bar{4}2_1m$, a= b= 8.1177(3) Å, c= 5.2782(4) Å).

Atom	x	y	z	Occ	B_{iso}
La1/Ba1	0.3362(6)	0.1638(6)	0.518(2)	0.95(1)/0.05(2)	2.2(2)
Ga1	0	0	0	1	2.1(2)
Ga2	0.1399(7)	0.3601(7)	-0.026(2)	1	2.1(2)
O1	0.5	0	0.194(4)	1	2.4(3)
O2	0.1360(10)	0.3640(10)	0.308(3)	1	2.6(3)
O3	0.0873	0.1639(12)	0.795(2)	1	3.6(3)
O4	0.322(3)	0.178(3)	-0.003(12)	0.182(17)	1

Table A. 58. Final 720°C NPD HR refined data of $La_{1.9}Ba_{0.1}Ga_3O_{7.45}$ (x = 0.9) composition structural parameters (S.G. *Ima*2, a= 11.5103(3) Å, b= 11.3588(3) Å, c= 10.5592(3) Å).

Atom	x	y	z	Occ	Biso
La1/Ba1	-0.5867(5)	0.2495(10)	0.4869(7)	0.954(12)/0.046(19)	1.26(16)
La2/Ba2	0.75	0.0853(10)	-0.0093(12)	0.95(2)/0.05(4)	1.5(4)
La3/Ba3	0.75	0.4165(12)	-0.0302(13)	0.93(2)/0.07(4)	2.0(4)
Ga1	-0.8860(6)	-0.2412(9)	0.2220(8)	1	1.54(13)
Ga2	0	0	0.2438(13)	1	1.1(2)
Ga3	0.5	0.5	0.2352(13)	1	0.74(19)
Ga4	0.75	-0.1063(10)	-0.2440(12)	1	0.9(2)
Ga5	0.25	0.0938(10)	0.2508(14)	1	1.3(3)
O1	-0.8889(7)	-0.2463(11)	-0.1086(8)	1	1.04(14)
O2	-0.4802(10)	0.3663(10)	0.1514(12)	1	1.9(2)
O3	-0.5418(9)	-0.3779(8)	-0.3768(11)	1	1.29(19)
O4	-0.1224(10)	-0.0328(9)	-0.1569(12)	1	1.7(2)
O5	-0.8894(10)	0.0644(8)	0.3514(10)	1	1.34(19)
O6	0.75	0.2782(10)	0.1439(15)	1	1.6(3)
O7	0.75	-0.1238(14)	0.0776(17)	1	1.7(3)
O8	0.25	0.247(2)	0.3299(16)	1	2.7(3)
O9	0.25	0.1080(15)	0.5814(16)	1	1.4(3)
O10	0.25	-0.0827(13)	0.227(2)	0.89(3)	1

Table A. 59. Final 770°C NPD HI refined data of $La_{1.9}Ba_{0.1}Ga_3O_{7.45}$ (x = 0.9) composition structural parameters (S.G. $P\bar{4}2_1m$, a= b= 8.11246(16) Å, c= 5.2807(3) Å).

Atom	x	y	z	Occ	B_{iso}
La1/Ba1	0.3357(4)	0.1643(4)	0.5097(16)	0.955(10)/0.051(17)	2.11(15)
Ga1	0	0	0	1	1.34(14)
Ga2	0.1417(5)	0.3583(5)	-0.0260(15)	1	2.22(13)
O1	0.5	0	0.200(2)	1	2.11(18)
O2	0.1356(6)	0.3644(6)	0.3125(16)	1	2.29(16)
O3	0.0873	0.1621(7)	0.7917(12)	1	2.66(13)
O4	0.326(2)	0.174(2)	-0.011(6)	0.218(13)	1

Table A. 60. Final 770°C NPD HI refined data of $La_{1.9}Ba_{0.1}Ga_3O_{7.45}$ (x = 0.9) composition structural parameters (S.G. *Ima*2, a= 11.5107(4) Å, b= 11.3705(4) Å, c= 10.5663(5) Å).

Atom	x	y	z	Occ	Biso
La1/Ba1	-0.5861(8)	0.2501(13)	0.4812(11)	0.963(18/0.03(3)	1.9(2)
La2/Ba2	0.75	0.0829(17)	-0.0175(19)	0.95(3)/0.07(6)	2.5(6)
La3/Ba3	0.75	0.4114(16)	-0.0288(18)	0.93(3)/0.07(5)	1.8(5)
Ga1	-0.8855(8)	-0.2436(12)	0.2216(11)	1	1.19(18)
Ga2	0	0	0.2477(15)	1	1.2(3)
Ga3	0.5	0.5	0.2325(17)	1	0.9(3)
Ga4	0.75	-0.1112(15)	-0.2443(17)	1	1.3(3)
Ga5	0.25	0.0919(13)	0.2503(15)	1	0.5(3)
O1	-0.8917(11)	-0.2449(14)	-0.1105(11)	1	0.9(2)
O2	-0.4881(13)	0.3615(11)	0.1568(15)	1	1.7(3)
O3	-0.5465(10)	-0.3805(10)	-0.3789(13)	1	0.6(2)
O4	-0.1191(14)	-0.0379(14)	-0.1608(17)	1	1.9(3)
O5	-0.8923(14)	0.0670(12)	0.3532(14)	1	1.6(3)
O6	0.75	0.2832(18)	0.154(3)	1	3.1(5)
O7	0.75	-0.1243(17)	0.077(2)	1	1.0(4)
O8	0.25	0.257(3)	0.327(2)	1	2.7(4)
O9	0.25	0.1053(19)	0.584(2)	1	1.7(4)
O10	0.25	-0.088(2)	0.221(3)	0.89(5)	1

Table A. 61. Final 770°C NPD HR refined data of $La_{1.9}Ba_{0.1}Ga_3O_{7.45}$ (x = 0.9) composition structural parameters (S.G. $P\bar{4}2_1m$, a= b= 8.11146(14) Å, c= 5.2804(3) Å).

Atom	x	y	z	Occ	B_{iso}
La1/Ba1	0.3361(4)	0.1639(4)	0.5107(15)	0.956(12)/0.05(2)	2.08(17)
Ga1	0	0	0	1	1.00(14)
Ga2	0.1417(5)	0.3583(5)	-0.0259(15)	1	2.17(13)
O1	0.5	0	0.196(2)	1	1.99(19)
O2	0.1366(6)	0.3634(6)	0.3114(16)	1	2.16(16)
O3	0.0873	0.1629(8)	0.7916(14)	1	3.05(15)
O4	0.3156(18)	0.1845(18)	-0.033(5)	0.256(13)	1

Table A. 62. Final 770°C NPD HR refined data of $La_{1.9}Ba_{0.1}Ga_3O_{7.45}$ (x = 0.9) composition structural parameters (S.G. *Ima*2, a= 11.5095(4) Å, b= 11.3697(4) Å, c= 10.5639(5) Å).

Atom	x	y	z	Occ	Biso
La1/Ba1	-0.5852(7)	0.2543(14)	0.4621(12)	0.97(2)/0.03(3)	1.5(3)
La2/Ba2	0.75	0.083(2)	-0.032(2)	0.94(4)/0.07(6)	3.0(7)
La3/Ba3	0.75	0.4134(15)	-0.0508(17)	0.93(3)/0.07(5)	1.3(5)
Ga1	-0.8852(8)	-0.2398(12)	0.2007(11)	1	1.0(2)
Ga2	0	0	0.2242(19)	1	1.3(4)
Ga3	0.5	0.5	0.212(2)	1	0.9(3)
Ga4	0.75	-0.1031(15)	-0.2646(18)	1	0.9(3)
Ga5	0.25	0.0943(14)	0.2269(19)	1	0.7(3)
O1	-0.8920(12)	-0.2477(17)	-0.1321(13)	1	1.3(2)
O2	-0.4817(16)	0.3662(14)	0.1334(19)	1	2.1(3)
O3	-0.5453(12)	-0.3787(12)	-0.3997(16)	1	0.9(3)
O4	-0.1222(17)	-0.0329(15)	-0.183(2)	1	2.3(4)
O5	-0.8904(14)	0.0644(12)	0.3324(15)	1	1.2(3)
O6	0.75	0.2826(17)	0.125(3)	1	2.1(5)
O7	0.75	-0.125(2)	0.057(3)	1	1.7(5)
O8	0.25	0.250(3)	0.306(2)	1	2.8(4)
O9	0.25	0.106(2)	0.563(2)	1	1.2(4)
O10	0.25	-0.0827(13)	0.227(2)	0.89(3)	1

Table A. 63. Final 820°C NPD HI refined data of $La_{1.9}Ba_{0.1}Ga_3O_{7.45}$ (x = 0.9) composition structural parameters (S.G. $P\bar{4}2_1m$, a= b= 8.11195(7) Å, c= 5.28584(10) Å).

Atom	x	y	z	Occ	B_{iso}
La1/Ba1	0.33517(14)	0.16483(14)	0.5069(4)	0.951(2)/0.050(3)	2.10(6)
Ga1	0	0	0	1	1.48(8)
Ga2	0.14122(18)	0.35878(18)	-0.0297(4)	1	1.85(6)
O1	0.5	0	0.1911(9)	1	4.13(18)
O2	0.1367(2)	0.3633(2)	0.3104(4)	1	2.07(8)
O3	0.0873	0.1637(3)	0.7955(4)	1	3.86(12)
O4	0.3259(7)	0.1741(7)	0.0009(19)	0.225(4)	1

Table A. 64. Refined anisotropic thermal parameters of $La_{1.9}Ba_{0.1}Ga_3O_{7.45}$ (x = 0.9) composition from 820°C NPD HI data.

Atom	B_{11}	B_{22}	B_{33}	B_{12}	B_{13}	B_{23}
La1/Ba1	1.96(5)	1.96(5)	2.37(8)	0.74(6)	0.13(6)	-0.13(6)
Ga1	0.94(6)	0.94(6)	2.57(12)	0	0	0
Ga2	2.16(6)	2.16(6)	1.21(8)	-0.32(8)	0.01(6)	-0.01(6)
O1	4.82(16)	4.82(16)	2.76(24)	-3.32(24)	0	0
O2	2.80(8)	2.80(8)	0.62(9)	-0.02(10)	0.10(6)	-0.10(6)
O3	6.25(14)	1.88(8)	3.44(11)	-1.22(10)	2.72(9)	0.31(10)

Table A. 65. Final 820°C NPD HR refined data of $La_{1.9}Ba_{0.1}Ga_3O_{7.45}$ (x = 0.9) composition structural parameters (S.G. $P\bar{4}2_1m$, a= b= 8.10865(6) Å, c= 5.28369(9) Å).

Atom	x	y	z	Occ	B_{iso}
La1/Ba1	0.33538(16)	0.16462(16)	0.5083(5)	0.950(2)/0.050(4)	2.12(7)
Ga1	0	0	0	1	1.45(9)
Ga2	0.14099(19)	0.35901(19)	-0.0302(4)	1	1.86(7)
O1	0.5	0	0.1915(9)	1	3.92(18)
O2	0.1370(3)	0.3630(3)	0.3100(4)	1	2.22(10)
O3	0.0873	0.1640(3)	0.7957(5)	1	4.05(13)
O4	0.3262(8)	0.1738(8)	0.002(2)	0.225(4)	1

Table A. 66. Refined anisotropic thermal parameters of $La_{1.9}Ba_{0.1}Ga_3O_{7.45}$ (x = 0.9) composition from 820°C NPD HR data.

Atom	B_{11}	B_{22}	B_{33}	B_{12}	B_{13}	B_{23}
La1/Ba1	1.93(6)	1.93(6)	2.50(10)	0.67(6)	0.14(7)	-0.14(7)
Ga1	0.98(7)	0.98(7)	2.39(12)	0	0	0
Ga2	2.22(6)	2.22(6)	1.15(9)	0.27(8)	0.13(6)	-0.13(6)
O1	4.66(16)	4.66(16)	2.45(24)	-3.40(24)	0	0
O2	2.87(10)	2.87(10)	0.92(10)	0.05(12)	0.09(6)	-0.09(6)
O3	6.32(15)	2.23(10)	3.59(13)	-1.13(10)	2.57(10)	-0.29(11)

Table A. 67. Extracted activation energies from Arrhenius plots of the $La_{1+x}Ba_{1-x}Ga_3O_{7+x/2}$ solid solution compositions.

x value	Ea (eV)
1	1.21(3) (300 - 600 °C) / 1.62(2) (600 - 800 °C)
0.9	1.25(2) (300-800 °C)
0.8	1.08(2) (300 - 650 °C) / 0.50(6) (650 - 800 °C)
0.725	0.95(3) (300 - 650 °C)
0.7	0.96(3) (300 - 600 °C)
0.6	0.92(3) (300 - 500 °C)
0.5	0.96(4) (300 - 500 °C) / 0.48(2)(500 - 650 C)

Chapter A.V: Supplementary information for Chapter V.

The $Ca_3Ga_4O_9$ compound was reported to crystallise in an orthorhombic cell (S.G. *Cmm*2 n°35), and is composed of a singular $[GaO_4]_n$ infinite sheet and four distinct calcium sites; these A-sites are sandwiched between two framework sheets along the stacking direction and sits in the centre of the $[GaO_4]_x$ (x = 4 or 5) rings on the *ab*-plane (Figure A. 33). In Figure A. 33b, showing its crystal structure projection along the *c*-axis evidencing the different Ca coordinations, it is clear that only Ca2 and Ca4 channels manifest the melilite-like pentagonal features. Moreover, Ca1 and Ca3 channels create a two-dimensional honeycomb-like framework which isolates the melilites hexagonal tiles formed by Ca2/Ca4 sites.

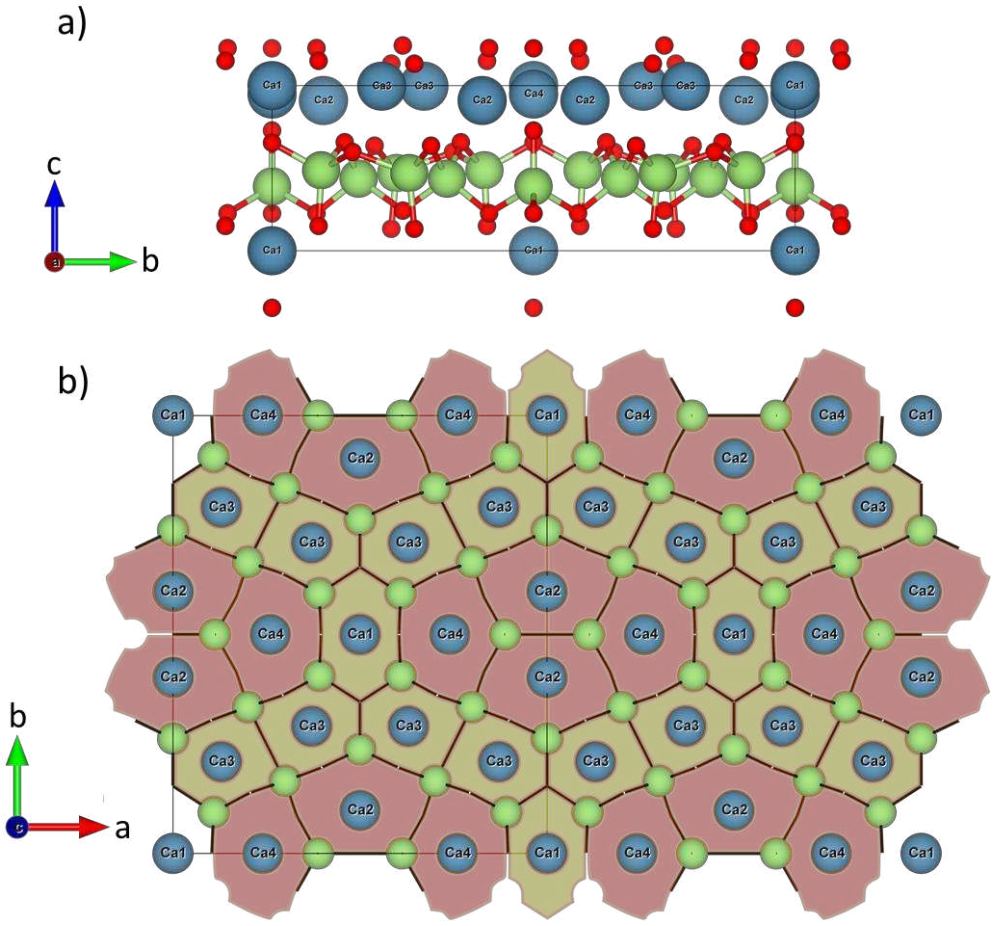

Figure A. 33. *$Ca_3Ga_4O_9$ crystal structure projection within the a-axis in a) and the stacking direction (c-axis) in b), with blue, green and red spheres representing calcium, gallium and oxygen atoms respectively. In b) panel, the isolated melilite-type hexagonal tiles formed by Ca2 and Ca4 channels are highlighted in red, while the 2D honeycomb-like network formed by the $[GaO_4]_4$ Ca1, Ca3 channels are in yellow. Oxygen atoms were omitted in panel b) for better clarity.*

Table A. 68. Refined structural parameters obtained from SPD data collected at room temperature on $Ca_5Ga_6O_{14}$ (x = 0) (*Cmc*2 space group, *a*= 11.50564(7) Å, *b*= 11.27722(8) Å and *c*= 10.48698(8) Å) sample.

Atom	Wyck	x	y	z	Occ	Biso
Ca1	8b	0.1581(2)	0.1023(2)	0.25	1	0.44(5)
Ca2	8b	0.3570(2)	0.31652(19)	0.2004(3)	1	0.54(5)
Ca3	4a	0	0.5248(3)	0.2448(4)	1	0.35(8)
Ga1	8b	0.35656(9)	0.14580(12)	0.5088(3)	1	0.27(3)
Ga2	4a	0	0.30107(15)	0.4422(3)	1	0.33(4)
Ga3	4a	0	-0.00041(15)	0.4644(3)	1	0.51(4)
Ga4	8b	0.24473(12)	0.40228(10)	0.4764(3)	1	0.30(2)
O1	8b	0.2842(6)	0.2793(6)	0.5855(7)	1	0.13(5)
O2	4a	0	0.6104(8)	0.5776(9)	1	0.13(5)
O3	8b	0.2665(7)	0.0277(5)	0.5955(7)	1	0.13(5)
O4	8b	0.3722(7)	0.4361(6)	0.3773(7)	1	0.13(5)
O5	4a	0	0.1437(9)	0.3805(9)	1	0.13(5)
O6	8b	0.3415(5)	0.1463(6)	0.3408(7)	1	0.13(5)
O7	4a	0	0.0080(8)	0.6334(11)	1	0.13(5)
O8	8b	0.1285(6)	0.3726(6)	0.3621(7)	1	0.13(5)
O9	4a	0	0.2944(8)	0.6167(10)	1	0.13(5)

Table A. 69. Refined structural parameters obtained from SPD data collected at room temperature on $La_{0.25}Ca_{4.75}Ga_6O_{14.125}$ (x = 0) (*Cmc*2 space group, *a*= 11.47670(8) Å, *b*= 11.29646(11) Å and *c*= 10.51206(10) Å) sample.

Atom	Wyck	x	y	z	Occ	Biso
Ca1/La1	8b	0.1614(3)	0.1031(2)	0.25	0.990(3)/0.010(3)	1.52(8)
Ca2	8b	0.3559(3)	0.3218(2)	0.2001(4)	1	1.16(6)
Ca3/La3	4a	0	0.5223(2)	0.2412(3)	0.756(4)/0.244(4)	0.90(8)
Ga1	8b	0.35621(9)	0.14654(12)	0.5097(3)	1	0.38(3)
Ga2	4a	0	0.29818(16)	0.4415(3)	1	0.36(4)
Ga3	4a	0	0.00029(15)	0.4649(3)	1	0.37(4)
Ga4	8b	0.24453(12)	0.40138(10)	0.4767(3)	1	0.31(2)
O1	8b	0.2814(6)	0.2810(6)	0.5849(8)	1	0.37(5)
O2	4a	0	0.6236(8)	0.5781(10)	1	0.37(5)
O3	8b	0.2725(7)	0.0238(5)	0.5988(8)	1	0.37(5)
O4	8b	0.3692(7)	0.4370(6)	0.3835(8)	1	0.37(5)
O5	4a	0	0.1399(10)	0.3683(10)	1	0.37(5)
O6	8b	0.3457(6)	0.1476(7)	0.3462(8)	1	0.37(5)
O7	4a	0	0.0091(9)	0.6331(12)	1	0.37(5)
O8	8b	0.1242(6)	0.3707(7)	0.3572(7)	1	0.37(5)
O9	4a	0	0.2982(8)	0.6112(11)	1	0.37(5)

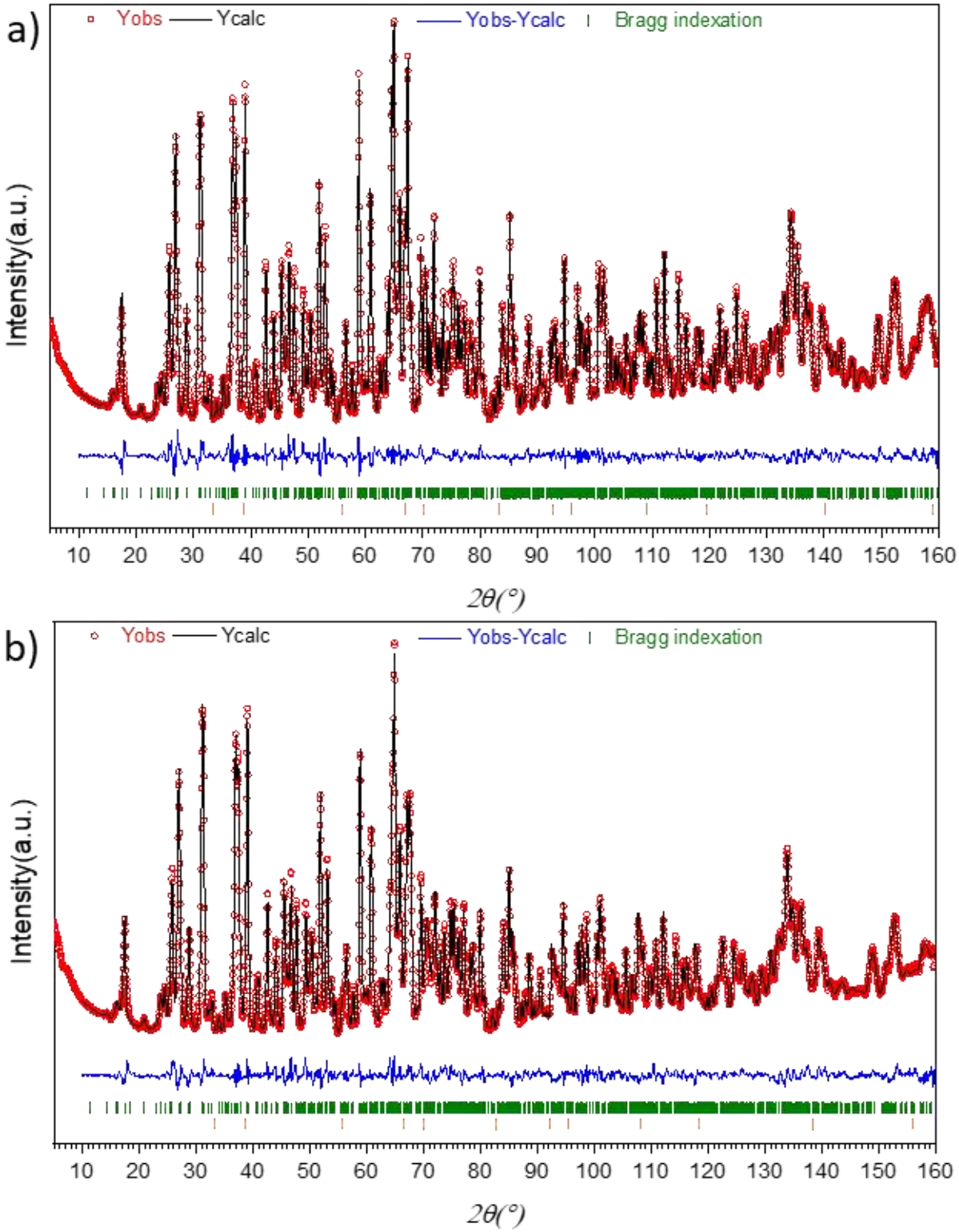

Figure A. 34. *Final Rietveld refined NPD (HR) data of a) $Ca_5Ga_6O_{14}$ (x = 0) (R_{wp}= 3.03% GOF= 1.00), and b) $La_{0.25}Ca_{4.75}Ga_6O_{14.125}$ (x = 0.25) (R_{wp}= 2.76% GOF= 0.90). Green tick marks correspond to the Ca5Ga6O14 and La0.25Ca4.75Ga6O14.125 structures panels (a) and (b) respectively, while the orange tick marks represent the CaO impurity quantified at ~0.19(6)% for x = 0 and ~0.69(9)% for x = 0.25 materials, both in weight%.*

Table A. 70. Refined structural parameters obtained from NPD (HI) data collected at room temperature on $Ca_5Ga_6O_{14}$ (x = 0) (*Cmc*2$_1$ space group, *a*= 11.51140(13) Å, *b*= 11.28267(12) Å and *c*= 10.49288(12) Å) sample.

Atom	Wyck	x	y	z	Occ	Biso
Ca1/La1	8b	0.1584(3)	0.1013(3)	0.25	1	0.87(6)
Ca2	8b	0.3582(4)	0.3164(3)	0.2028(6)	1	0.79(7)
Ca3/La3	4a	0	0.5251(5)	0.2453(6)	1	0.73(10)
Ga1	8b	0.35648(19)	0.1462(2)	0.5103(5)	1	0.21(4)
Ga2	4a	0	0.2993(3)	0.4446(5)	1	0.45(6)
Ga3	4a	0	-0.0009(3)	0.4660(5)	1	0.30(6)
Ga4	8b	0.2454(2)	0.4018(2)	0.4793(5)	1	0.13(4)
O1	8b	0.2850(2)	0.2781(3)	0.5863(5)	1	0.51(5)
O2	4a	0	0.6162(4)	0.5744(6)	1	0.83(8)
O3	8b	0.2674(3)	0.0271(3)	0.5958(6)	1	0.75(6)
O4	8b	0.3727(3)	0.4350(3)	0.3816(6)	1	0.47(5)
O5	4a	0	0.1467(4)	0.3831(6)	1	0.54(7)
O6	8b	0.3394(2)	0.1497(3)	0.3382(5)	1	0.44(5)
O7	4a	0	0.0087(4)	0.6392(7)	1	0.93(8)
O8	8b	0.1261(3)	0.3732(3)	0.3668(6)	1	0.95(6)
O9	4a	0	0.2991(4)	0.6145(6)	1	0.44(9)

Table A. 71. Refined structural parameters obtained from NPD (HI) data collected at room temperature on $La_{0.25}Ca_{4.75}Ga_6O_{14.125}$ (x = 0.25) (*Cmc*2$_1$ space group, *a*= 11.48245(16) Å, *b*= 11.30189(16) Å and *c*= 10.51841(17) Å) sample. La content was constrained to refine near the nominal value (penalty function used), which led a refined composition of: $La_{0.27(7)}Ca_{4.73(7)}Ga_6O_{14}$. Note that the composition is not charge balanced due to the interstitial oxide not added to the structure.

Atom	Wyck	x	y	z	Occ	Biso
Ca1/La1	8b	0.1580(5)	0.1012(5)	0.25	0.97(2)/0.03(2)	1.77(13)
Ca2	8b	0.3557(5)	0.3165(4)	0.2038(7)	1	1.41(9)
Ca3/La3	4a	0	0.5212(5)	0.2429(7)	0.79(3)/0.21(3)	0.85(14)
Ga1	8b	0.3560(2)	0.1469(3)	0.5121(6)	1	0.25(4)
Ga2	4a	0	0.2979(4)	0.4444(7)	1	1.00(9)
Ga3	4a	0	0.0003(4)	0.4682(6)	1	0.50(8)
Ga4	8b	0.2437(3)	0.4012(3)	0.4805(6)	1	0.44(5)
O1	8b	0.2832(3)	0.2771(3)	0.5867(7)	1	0.68(6)
O2	4a	0	0.6220(5)	0.5754(7)	1	1.59(11)
O3	8b	0.2730(3)	0.0251(3)	0.5971(7)	1	1.05(7)
O4	8b	0.3732(4)	0.4350(3)	0.3838(7)	1	0.73(7)
O5	4a	0	0.1469(5)	0.3822(7)	1	0.76(9)
O6	8b	0.3407(3)	0.1493(4)	0.3401(6)	1	0.85(7)
O7	4a	0	0.0089(6)	0.6409(8)	1	1.18(10)
O8	8b	0.1270(4)	0.3722(4)	0.3660(7)	1	1.43(8)
O9	4a	0	0.3002(5)	0.6140(8)	1	1.24(12)

Table A. 72. Refined structural parameters obtained from NPD (HR) data collected at room temperature on $Ca_5Ga_6O_{14}$ (x = 0) (*Cmc*2$_1$ space group, *a*= 11.5019(2) Å, *b*= 11.2734(2) Å and *c*= 10.4840(2) Å) sample using the Rietan program.

Atom	Wyck	x	y	z	Occ	Biso
Ca1/La1	8b	0.1586(4)	0.1019(4)	0.25	1.0	0.79(6)
Ca2	8b	0.3578(4)	0.3161(3)	0.2036(6)	1.0	0.69(7)
Ca3/La3	4a	0	0.5253(5)	0.2439(7)	1.0	0.85(11)
Ga1	8b	0.3552(2)	0.1464(2)	0.5104(5)	1.0	0.31(4)
Ga2	4a	0	0.2995(3)	0.4433(5)	1.0	0.32(6)
Ga3	4a	0	-0.0005(3)	0.4667(5)	1.0	0.61(7)
Ga4	8b	0.2450(2)	0.4021(2)	0.4795(5)	1.0	0.36(4)
O1	8b	0.2848(3)	0.2779(3)	0.5873(5)	1.0	0.58(5)
O2	4a	0	0.6169(4)	0.5763(6)	1.0	0.58(8)
O3	8b	0.2681(3)	0.0269(3)	0.5938(6)	1.0	0.58(6)
O4	8b	0.3734(3)	0.4341(3)	0.3823(6)	1.0	0.45(6)
O5	4a	0	0.1467(4)	0.3829(6)	1.0	0.61(7)
O6	8b	0.3391(3)	0.1496(3)	0.3382(5)	1.0	0.57(2)
O7	4a	0	0.0087(4)	0.6387(7)	1.0	0.75(8)
O8	8b	0.1273(3)	0.3731(3)	0.3666(6)	1.0	0.83(6)
O9	4a	0	0.2985(4)	0.6157(6)	1.0	0.75(9)

Table A. 73. Refined structural parameters obtained from NPD (HR) data collected at room temperature on $La_{0.25}Ca_{4.75}Ga_6O_{14.125}$ (x = 0.25) (*Cmc*2$_1$ space group, *a*= 11.4716(3) Å, *b*= 11.2913(2) Å and *c*= 10.5082(2) Å) sample using the Rietan program.

Atom	Wyck	x	y	z	Occ	Biso
Ca1/La1	8b	0.1573(5)	0.0993(5)	0.25	0.93(2)/0.07(2)	2.10(13)
Ca2	8b	0.3580(5)	0.3171(4)	0.2044(8)	1.0	1.77(10)
Ca3/La3	4a	0.0	0.5217(5)	0.2414(7)	0.87(3)/0.13(3)	0.89(14)
Ga1	8b	0.3565(2)	0.1469(3)	0.5112(6)	1.0	0.32(5)
Ga2	4a	0.0	0.2982(4)	0.4444(7)	1.0	0.78(8)
Ga3	4a	0.0	-0.0002(4)	0.4689(7)	1.0	0.50(8)
Ga4	8b	0.2429(3)	0.4020(3)	0.4805(6)	1.0	0.46(5)
O1	8b	0.2840(3)	0.2773(3)	0.5855(7)	1.0	0.72(6)
O2	4a	0.0	0.6243(5)	0.5777(7)	1.0	1.90(11)
O3	8b	0.2724(3)	0.0246(3)	0.5950(7)	1.0	0.89(6)
O4	8b	0.3724(4)	0.4345(3)	0.3830(7)	1.0	0.87(8)
O5	4a	0.0	0.1480(5)	0.3825(7)	1.0	0.71(8)
O6	8b	0.3408(3)	0.1477(4)	0.3407(6)	1.0	0.77(7)
O7	4a	0.0	0.0110(5)	0.6407(8)	1.0	0.91(10)
O8	8b	0.1240(4)	0.3712(4)	0.3661(7)	1.0	1.20(8)
O9	4a	0.0	0.3018(5)	0.6153(8)	1.0	1.02(11)

Table A. 74. Comparison of the different refined Ca/La content and the reliability factors on both high intensity (HI) and high resolution (HR) NPD data refinements, with and without constraints.

Data set	NPD HI			
Refinement type	No constraints		Constrained La content	
Atom site	Ca1/La1	Ca3/La3	Ca1/La1	Ca3/La3
Refined occupancy	0.99(2)Ca1 0.01(2)La1	0.83(3)Ca3 0.17(3)La3	0.97(2)Ca1 0.03(2)La1	0.79(3)Ca3 0.21(3)La3
Reliability factors	R_{wp}= 2.72% GOF= 0.89		R_{wp}= 2.76% GOF= 0.90	
Data set	NPD HR			
Refinement type	No constraints		Constrained La content	
Site	Ca1/La1	Ca3/La3	Ca1/La1	Ca3/La3
Refined occupancy	0.99(2)Ca1 0.01(2)La1	0.91(3)Ca3 0.09(3)La3	0.96(2)Ca1 0.04(2)La1	0.81(3)Ca3 0.18(3)La3
Reliability factors	R_{wp}= 3.20% GOF= 0.59		R_{wp}= 3.21% GOF= 0.60	

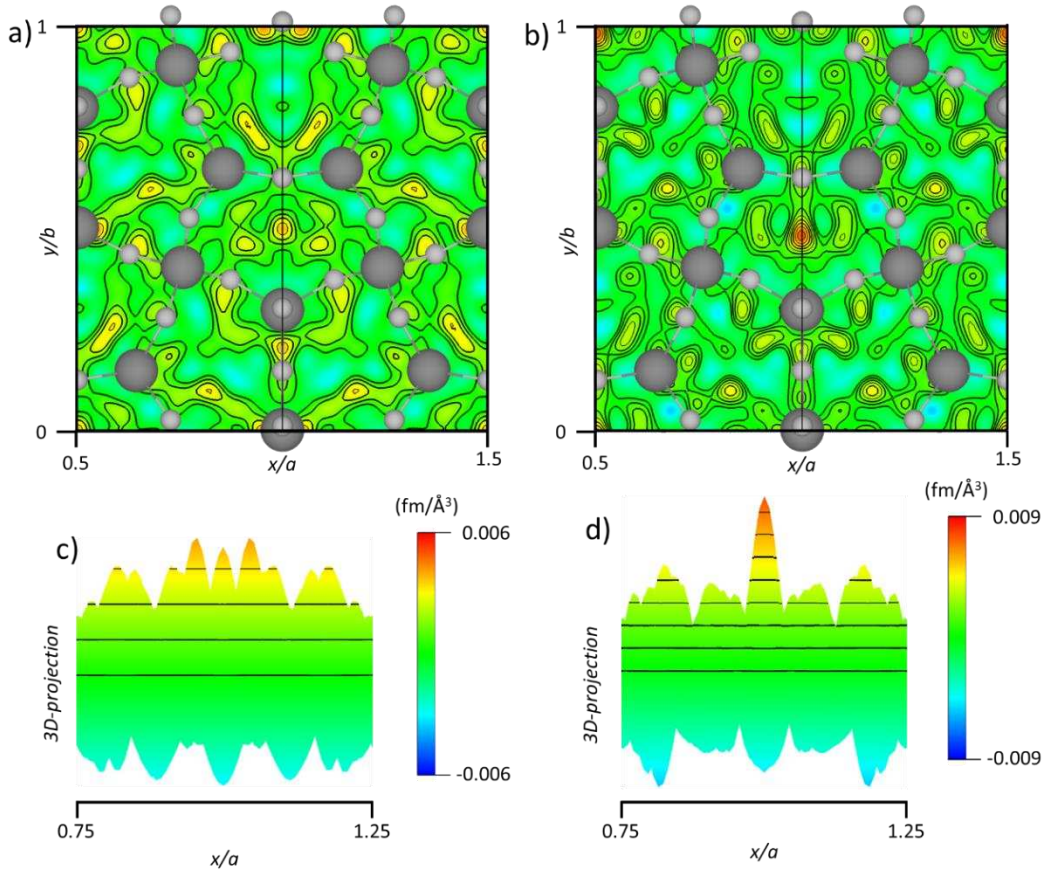

Figure A. 35. *a) and b) Fourier difference map section at z= 0.51 centered at the Ca3 channels from $La_{0.25}Ca_{4.75}Ga_6O_{14.125}$ NPD (HR) and NPD (HI) refined data respectively. One $[GaO_4]_n$ sheet is overlayed in both a) and b) panels with dark grey and light grey spheres corresponding to Ga and O atoms. c) and d), 3D-projection of the Fourier difference maps shown in a) and b) respectively.*

« Last but not least, I wanna thank me. I wanna thank me for believing in me. I wanna thank me for doing all this hard work. I wanna thank me for having no days off. I wanna thank me for, for never quitting. »

Snoop Dogg

Résumé en Français

Résumé de l'Introduction générale

La conception et le développement de nouveaux matériaux sont nécessaires dans la société d'aujourd'hui pour différents types d'applications : médicales [1–6], stockage et conversion de l'énergie [7–10], industrielle [11], [12] …etc. Le défi principal à relever pour répondre à la demande continuelle de nouveaux matériaux est de trouver une méthode de synthèse qui permette d'atteindre l'état hors-équilibre des matériaux pour accéder à de nouvelles phases cristallines. Au laboratoire CHEMTI, une méthode originale et unique a été développée : la cristallisation complète et congruente à partir d'un verre massif ou d'un liquide surfondu. L'utilisation de la lévitation aérodynamique couplée à un chauffage par deux lasers CO_2 permet de fondre des échantillons avec des températures de fusions supérieures à 2000°C. Ce dispositif permet également d'atteindre des vitesses de refroidissements atteignant 1000°C/s, permettant de figer l'état désordonné de la matière jusqu'à solidification de cette dernière. Par ailleurs, la vitesse de refroidissement peut aussi être contrôlée pour maitriser la cristallisation des échantillons à partir du liquide fondu à haute température.

Cette technique originale de synthèse a été utilisé au cours de cette thèse qui est divisée en cinq chapitres, avec une répartition par thématiques de matériaux :

- Matériaux pour l'optique.
- Matériaux pour l'énergie.

Le premier chapitre de ce manuscrit consiste en un état de l'art des différentes méthodes de synthèses employées pour l'obtention de nouveaux matériaux. Un intérêt particulier est donné aux méthodes de synthèse par cristallisation du verre ou du liquide fondu, avec différents exemples de matériaux clés réalisés.

Le chapitre II traite de la synthèse, caractérisation structurale et stabilité thermique de nouvelles phases cristallines de type Sr*RE*Ga_3O_7 RE = [Dy-Lu / Y] apparentées à la structure des mélilites.

Le troisième chapitre de ce manuscrit concerne la synthèse et la caractérisation du désordre chimique dans la nouvelle solution solide $Ca_3Ga_{2-2x}Zn_xGe_{4+x}O_{14}$ ($0 \leq x \leq 1$). L'un des points forts de ce chapitre est la quantification du désordre chimique entre trois cations isoélectroniques (Ga, Zn, Ge) dans le composé $Ca_3GaZn_{0.5}Ge_{4.5}O_{14}$ ($x = 0.5$) par affinement 2D de cartographies STEM-EDS des différents cations, acquises à l'échelle atomique.

Les chapitres IV et V traitent du développement de nouveaux matériaux de structure mélilite ($La_{1+x}Ba_{1-x}Ga_3O_{7+x/2}$) ou dérivés de cette structure ($La_xCa_{5-x}Ga_6O_{14+x/2}$), avec des propriétés de conductivité anionique pour des applications de type pile à combustible à oxyde solide. Ici aussi une panoplie de techniques (DRX synchrotron, neutron, MET, MEB…etc) a été employée pour caractériser le plus finement possible les matériaux.

Références:

[1] C. Greskovich, S. Duclos, *Annual Review of Materials Science*, 1997, **27**, 69.

[2] S.J. Duclos *et al.*, *Nuclear Instruments and Methods in Physics Research Section A: Accelerators, Spectrometers, Detectors and Associated Equipment*, 2003, **505**, 68.

[3] L.S. Bass, *et al.*, *Lasers in Surgery and Medicine*, 1995, **17**, 315.

[4] S. Balasubramanian, *et al.*, *International Journal of Pharmaceutical Sciences and Research*, 2017, **8**, 4950-4959.

[5] M. Vallet-Regí, *Dalton Transactions*, 2006, 5211.

[6] E. Meechoowas *et al.*, *Materials Today: Proceedings*, 2022, **65**, 2407.

[7] J.L. Black, *Glassy Metals I*, 1981, 167.

[8] J.H. Campbell, *et al.*, *Journal of Non-Crystalline Solids*, 2000, **263**, 318-341.

[9] S. Supriya, *Journal of Inorganic and Organometallic Polymers and Materials*, 2022, 1-18.

[10] J. Lin *et al.*, *Chemical Engineering Journal*, 2022, **444**, 136538.

[11] C.B. Carter, *et al.*, Ceramic Materials. Springer New York, 2013, 766.

[12] Y. Lakhdar *et al.*, *Progress in Materials Science*, 2021, **116**, 100736.

Résumé du Chapitre I : État de l'art

La science des matériaux est un vaste champ de recherche qui lie à la fois des aspects chimiques (synthèses, structures…) et physiques (caractérisation des propriétés macroscopiques). La compréhension des liens entre ces deux aspects est importante pour le développement de nouveaux matériaux aux performances accrues. De récents travaux de recherche ont démontré la possibilité de prédire la structure cristalline ainsi que les propriétés physiques d'une composition chimique donnée par calculs DFT [1-4]. L'obstacle majeur rencontré après la prédiction du matériau (structure et/ou propriétés) est la synthèse de ce dernier, parfois impossible par des voies de synthèses classiques.

En chimie du solide, la méthode de synthèse des matériaux inorganiques la plus répondue et la réaction à l'état solide. Cette voie de synthèse est simple à opérer, elle nécessite un fin broyage et un mélange homogène des réactifs. Pour mettre en œuvre la réaction de ces derniers, des températures élevées ($900°C \leq T \leq 1700°C$) et de longs temps de chauffage sont requis. Dans certains cas, plusieurs traitements thermiques consécutifs avec broyages intermédiaires sont nécessaires pour une réaction complète. Ceci s'explique par l'énergie et le temps demandés par la migration des atomes au sein d'un grain d'un des précurseurs vers les joints de grains pour former de nouvelles liaisons et créer le nouveau composé. Par ailleurs, les hautes températures utilisées lors de la réaction amènent aux produits les plus stables thermodynamiquement [5], il est donc difficile d'atteindre des phases intermédiaires hors-équilibre.

La Figure I.1 du chapitre I montre un comparatif de plusieurs voies de synthèse permettant de stabiliser des phases hors-équilibre et indiquant les avantages et les inconvénients de chacune d'entre elles. Au cours de cette thèse, les voies de synthèses assistées par fusion ont été utilisées, notamment une approche unique déployée au laboratoire CEMHTI : la lévitation aérodynamique couplée au chauffage laser (CO_2). Cette technique consiste à préparer un mélange homogène par broyage manuel des poudres de précurseurs, puis à presser la poudre sous forme de pastille. La pastille est ensuite cassée en petits morceaux de 30 mg qui sont déposés sur une buse conique. Deux lasers CO_2 dirigés par un jeu de miroirs (depuis le haut et le bas) chauffent l'échantillon qui lévite à l'aide d'un jet de gaz. La puissance des lasers est augmentée progressivement jusqu'à ce que l'échantillon atteigne l'état fondu, il est alors maintenu pendant quelques secondes dans cet état puis les lasers sont coupés, ce qui permet de

refroidir très rapidement l'échantillon et possiblement de figer l'état désordonné du liquide fondu à l'état solide, formant ainsi un verre.

Le verre étant un état métastable, la cristallisation peut être induite par un traitement thermique adéquat à des températures relativement basses ($T \leq 900°C$), ce qui permet de stabiliser des phases cristallines intermédiaires hors-équilibre (Figure I.2 et Figure I.4 du chapitre I). Le suivi d'une telle procédure de synthèse a par exemple permis la découverte de la nouvelle phase cristalline $BaAl_4O_7$ avec une cristallisation contrôlée de deux nouveaux polymorphes α ou β [6]. Il est important de noter que cette nouvelle phase cristalline n'est pas accessible par réaction en phase solide. De plus, ce composé cristallisé en « bulk » a été répertorié comme la première céramique transparente synthétisée par cristallisation complète d'un verre massif [6]. Ces travaux ont motivé de nombreuses recherches sur les nouveaux matériaux transparents obtenus par cristallisation complète et congruente du verre pour des applications optiques, photoniques, énergétiques, etc (plusieurs exemples sont cités dans le chapitre I de ce manuscrit).

L'utilisation de la lévitation aérodynamique permet aussi la cristallisation de phases cristallines hors-équilibre à partir du liquide surfondu par contrôle de la vitesse de refroidissement (diminution de la puissance des lasers de façon progressive). Cette procédure a été utilisée lors de la synthèse du composé cristallin $La_2Ga_3O_{7.5}$ [7], non accessible par réaction à l'état solide. Ce composé a la particularité de représenter la limite x = 1 de la solution solide $La_{1+x}AE_{1-x}Ga_3O_7$ apparentée a la famille des structures mélilites, cristallisant dans une surstructure orthorhombique de la maille parent tétragonale, avec la plus haute teneur d'oxygènes interstitiels répertoriée pour cette famille de structure. Par ailleurs, ce matériau représente des valeurs de conductivité anionique intéressantes (0.01 $S.cm^{-1}$ à 800°C), seulement un ordre de grandeur inférieure aux meilleurs conducteurs anioniques de la famille des mélilites (i.e. $La_{1.54}Sr_{0.46}Ga_3O_{7.27}$ et $La_{1.64}Ca_{0.36}Ga_3O_{7.32}$ atteignant des valeurs de 0.1 $S.cm^{-1}$ à 800°C).

Les différents types de conducteurs anioniques sont décrits plus en détails dans le chapitre I, avec une attention particulière portée à la famille des mélilites.

Références :

[1] C. Collins *et al.*, *Nature*, 2017, **546**, 280.

[2] M.S. Dyer *et al.*, *Science*, 2013, **340**, 847.

[3] A.R. Oganov *et al.*, *Nature Reviews Materials*, 2019, **4**, 331.

[4] J. Gamon *et al.*, *Chemistry of Materials*, 2019, **31**, 9699.

[5] I.P. Parkin, *Encyclopedia of Materials: Science and Technology*, 2001, 8675-8679.

[6] M. Allix *et al.*, *Advanced Materials*, 2012, **24**, 5570.

[7] J. Fan *et al.*, *Chemistry of Materials*, 2020, **32**, 9016.

Résumé du Chapitre II : Mise en ordre cationique et stabilité thermique des mélilites Sr*RE*Ga_3O_7 *RE* = [Dy-Lu / Y]

Le sujet des travaux abordés dans ce chapitre s'inscrit dans la suite de la thèse de Marina Boyer (soutenu le 22 septembre 2016, université d'Orléans) menée au sein du laboratoire CEMHTI. Pendant sa thèse, Marina Boyer a réussi la synthèse d'une nouvelle phase mélilite Sr*RE*Ga_3O_7 *RE* = [Ho-Yb] cristallisant dans une surstructure (groupe d'espace $P2_12_12$) de la maille parent tétragonale (groupe d'espace $P\bar{4}2_1m$) avec un triplement du paramètre *a* de la maille (3**a*, *b*, *c*). Ce triplement a été attribué à la mise en ordre des cations Sr^{2+} et RE^{3+} présents dans les sites A de la structure induisant 1 site totalement occupé par la terre rare, 1 site totalement occupé par le strontium et un dernier site mixte 50%/50% entre la terre rare et le strontium (chapitre II, Figure II.1). Cette mise en ordre est possible grâce à une certaine flexibilité du sous-réseau en couche de la mélilite formé par des tétraèdres d'oxyde de gallium (GaO_4), où chaque GaO_4 est lié par trois ou quatre de ses sommets. Dans ce travail de thèse, la synthèse de cette nouvelle phase a été réalisée avec succès pour deux autres terres rares *RE* = [Dy, Lu] par cristallisation à partir d'un précurseur vitreux de même composition, préalablement synthétisé par lévitation aérodynamique.

L'étude thermique de ces composés par calorimétrie différentielle à balayage a permis de mettre en évidence les températures de transition vitreuses (T_g), cristallisation (T_c) mais aussi de transition de phase ($P\bar{4}2_1m \rightarrow P2_12_12$). Grâce à cette étude, un traitement thermique différent du premier a été appliqué à de nouveaux échantillons vitreux et a permis de stabiliser la phase parent $P\bar{4}2_1m$ de la mélilite pour la série *RE* = [Dy-Yb / Y], non répertoriée précédemment pour l'ytterbium.

La structure parent et la surstructure ordonnée de ces matériaux ont été finement étudiées par affinement Rietveld sur des données de diffraction des rayons x par rayonnement synchrotron et par microscopie électronique en transmission (STEM-HAADF et STEM-EDX). L'affinement Rietveld a mis en évidence la complexité de la mise en ordre des composés à l'Ho et à l'Er, pour lesquels les trois sites sont mixtes entre la terre rare et le strontium. Cependant, l'observation par MET du $SrYGa_3O_7$ à l'échelle atomique a montré la coexistence des deux polymorphes de la mélilite ($P\bar{4}2_1m + P2_12_12$) au sein du même grain (chapitre II, Figure II.11), ce qui expliquerait les occupations mixtes affinées par la méthode Rietveld. Un diagramme de stabilité entre les deux polymorphes de la mélilite a été tracé en combinant les résultats de la

DSC et des mesures diffraction des rayons X réalisées *in situ* à des températures variables en fonction du ratio de la taille des deux cations occupant le site A.

Finalement, des mesures de photoluminescence sur les composés $SrErGa_3O_7$ montrent une intensité supérieure (×2) de la bande d'émission du Er^{3+} pour la mélilite $P2_12_12$ comparée à la phase parent et l'analogue vitreux, confirmant ainsi la mise en ordre observée sur le site A.

Résumé du Chapitre III : Synthèse et caractérisation de l'ordre/désordre entre trois cations isoélectronique dans le composé $Ca_3Ga_{2-2x}Zn_xGe_{4+x}O_{14}$ ($0 \leq x \leq 1$) par une approche multi-techniques

L'étude de la synthèse et de la caractérisation structurale de la solution solide de formule $Ca_3Ga_{2-2x}Zn_xGe_{4+x}O_{14}$ fait l'objet de ce troisième chapitre. La synthèse des composés de cette solution solide a été réalisée avec succès par cristallisation à partir d'un précurseur vitreux de même composition obtenu à l'aide de la lévitation aérodynamique. Cependant, pour le composé $Ca_3Ga_2Ge_4O_{14}$ (x = 0), des taux de cristallinité bien meilleurs ont été obtenus par cristallisation directe du liquide surfondu. La diffraction des rayons X par rayonnement synchrotron a montré la rétention d'une structure de type langasite (groupe d'espace *P*321) sur l'ensemble des composés de cette solution solide. Le composé $Ca_3ZnGe_5O_{14}$ (x = 1) dans ce travail a été indexé dans une maille de symétrie *P*321. Ceci dit, dans la littérature ce composé a été répertorié sous une forme de monocristal avec une maille monoclinique *C*2. Ceci est un exemple concret de la synthèse par cristallisation à partir du verre qui permet d'obtenir de nouvelles phases hors-équilibre.

L'étude du désordre chimique entre les éléments Ga/Ge pour le composé (x = 0) et Zn/Ge pour le composé (x = 1) étant impossible par diffraction des rayons X puisque les cations possèdent un même nombre d'électrons, nous avons utilisé la résonance magnétique nucléaire du ^{71}Ga et du ^{67}Zn, et la diffraction des neutrons. Le couplage entre ces deux techniques nous a permis de montrer que sur les trois sites de position de Wykoff 1a (coordinance six), 3f et 2d (les deux en coordinance quatre), le désordre chimique existe seulement sur les sites 1a et 3f avec des occupations quasiment égales 50%/50% pour le composé (x = 0). Dans le composé (x = 1), Zn montre une très faible population du site 3f 16(1)% contre 52(4)% dans le site 1a, ce qui s'explique par sa préférence à être en coordinance six. Les sites 2d quant à eux restent totalement occupés par des atomes de Ge. Ces résultats sont appuyés par les calculs de BVS pour chaque cation dans les trois différents sites cristallographiques.

Pour la composition $Ca_3GaZn_{0.5}Ge_{4.5}O_{14}$ (x = 0.5) contenant trois cations isoélectroniques (Ga^{3+}, Ge^{4+}, Zn^{2+}), la caractérisation du désordre entre ces trois éléments devient impossible par diffractions des neutrons seule. Pour résoudre ce problème, une technique originale a été mise en œuvre : l'affinement 2D des cartographies STEM-EDS acquises à l'échèle atomique

pour les différents cations. L'intensité affiné des cations est normalisée a 1 pour les trois cations dans chaque type de site, ce qui nous permet de déduire des taux d'occupations du Ga, Ge at Zn dans les sites 1a, 3f et 2d. Les résultats obtenus sont ensuite confrontés à des donnés de diffraction neutrons par affinement Rietveld et montrent des facteurs d'accord satisfaisants.

Résumé du Chapitre IV : Nouveaux conducteurs anioniques oxydes par extension de la gamme de dopage dans les mélilites $La_{1+x}Ba_{1-x}Ga_3O_{7+x/2}$ ($0.3 \leq x \leq 0.9$)

La limite de la solution solide $La_{1+x}Ba_{1-x}Ga_3O_{7+x/2}$ a été répertorié dans la littérature pour une valeur de x = 0.35 suite à des synthèses par réaction à l'état solide. De nouveaux travaux menés au laboratoire CEMHTI ont montré la possibilité de synthétiser la phase $La_2Ga_3O_{7.5}$ (x = 1) par cristallisation à partir du liquide surfondu. La découverte de cette nouvelle phase nous a permis de nous intéresser et de réaliser avec succès la synthèse des compositions intermédiaires de la solution solide $La_{1+x}Ba_{1-x}Ga_3O_{7+x/2}$ ($0.3 \leq x < 1$) par cristallisation directe du liquide surfondu. Le composé x = 1 cristallise dans une surstructure orthorhombique (groupe d'espace *Ima*2) avec un réseau anionique d'oxygènes interstitiels ordonné selon l'axe *a* en forme de chaine, contrairement à celui de la mélilite parent tétragonal $P\bar{4}2_1m$ qui présente un désordre complet sur le plan *ab* (Figure I.11, Chapitre I).

Une analyse par diffraction des rayons X par rayonnement synchrotron nous a permis de classer les domaines de composition cristallisant dans la structure $P\bar{4}2_1m$ ($0 \leq x \leq 0.725$), *Ima*2 ($0.9 \leq x \leq 1$) ainsi que les domaines mixtes ($0.725 < x < 0.9$). Le défi de cette étude par DRX synchrotron, a été l'affinement Rietveld du diffractogramme de la composition (x = 0.775) qui représentait une asymétrie de pic très large. Pour attaquer ce problème, plusieurs méthodes ont été déployées : description d'asymétrie de pic par le modèle de Stephens, harmoniques sphériques et l'approche multi-mailles. Le désordre chimique entre La/Ba et les oxygènes interstitiels dans les matériaux synthétisés a été confirmé par des affinements Rietveld effectués sur des diffractogrammes neutrons à température ambiante, mais aussi à hautes températures pour le composé (x = 0.9).

La caractérisation des propriétés de conductivité anionique effectuée par spectroscopie d'impédance a indiqué une valeur maximum de 3×10^{-2} $S.cm^{-1}$ atteinte pour la composition $La_{1.7}Ba_{0.7}Ga_3O_{7.35}$ (x = 0.7) à 700°C, légèrement inférieure à celle des meilleurs mélilites (i.e. $La_{1.54}Sr_{0.46}Ga_3O_{7.27}$ atteignant une valeur de 10^{-1} $S.cm^{-1}$ à 800°C). Ceci dit, les tracés d'Arrhenius des compositions ($0.5 \leq x < 0.9$) témoignent d'un plateau de la conduction, où les valeurs de cette dernière n'évoluent quasiment plus à hautes températures. Ce phénomène a été étudié plus en détails par diffraction des rayons X *in situ* à température variable et par microscopie électronique à balayage, confirmant une évolution de la microstructure avec la

température, ce qui pourrait expliquer la stagnation du comportement de conductivité mesuré à haute température.

Résumé du Chapitre V : Dopage au lanthane dans la structure $Ca_5Ga_6O_{14}$ de type mélilite pour de nouveaux conducteurs anioniques

L'intérêt porté au composé $Ca_5Ga_6O_{14}$ est dû à sa structure cristalline de type mélilite. Ce composé cristallise dans une maille orthorhombique (groupe d'espace $Cmc2_1$) avec une structure en couche formée par deux feuillets $[GaO_4]_n$ de type mélilite empilés de façon antiparallèle selon l'axe *c*. Cette différence d'empilement induit des contraints de liaisons sur les cations calcium des sites A ; par conséquent ces derniers sont décalés de leurs position ''idéale'' dans la maille vers les bords des pentagones $[GaO_4]_5$ sur la projection selon l'axe *c* (Figure V.1 et V.2, Chapitre V). La substitution du Ca ou du Ga par un cation aliovalent a été d'abord sondée par calculs DFT. Ces calculs ont déterminé que le lanthane est l'élément le plus favorable énergétiquement pour la stabilisation de la structure dopée. La synthèse de la solution solide $La_xCa_{5-x}Ga_6O_{14+x/2}$ a ainsi été étudiée par différents procédés : réaction à l'état solide, cristallisation à partir d'un verre ou du liquide surfondu et par méthode sol-gel. Parmi cette panoplie de méthodes, la synthèse par réaction solide s'est avérée la plus appropriée avec une substitution maximum de x = 0.25 et des taux de cristallinité améliorés.

Une première analyse par DRX synchrotron a démontré que le désordre chimique entre La et Ca ne se localise que sur le site Ca3. Ce résultat s'explique par la structure locale du site Ca3 qui représente le plus de similarités avec la structure mélilite parent (canaux ouverts avec positionnement du Ca au centre). D'autres analyses par cartographie STEM-EDX du lanthane ainsi que l'analyse par méthode Rietveld de diffractogrammes neutrons ont confirmé ce résultat sur le désordre chimique entre La et Ca.

Pour conserver la neutralité de charge de la composition après dopage, l'introduction de lacunes cationiques ou d'ions oxydes interstitiels est impérative. Des analyses par microsonde de Castaing et affinement des taux d'occupation des cations Ca et Ga sur les diffractogrammes rayons X synchrotron et neutron de la phase dopé (x = 0.25) n'ont pas indiqué un déficit en Ca ou en Ga, ce qui nous permet d'écarter la première hypothèse.

L'hypothèse de l'introduction d'oxygènes interstitiels a été étudiée par carte de Fourier différence et par méthode de maximum entropie sur les diffractogrammes neutrons. Une perturbation de la structure locale du site Ca3 peut être clairement visualisée à travers les paramètres thermiques affinés des oxydes, mais aussi à travers la densité nucléaire reconstruite

par calculs MEM. Par ailleurs, étant donné le faible taux de dopage, une augmentation de seulement 0.89% de la quantité d'oxygène est attendue, ce qui rend la localisation de ces derniers très difficile. La structure du composé dopé a finalement été prédite par calculs DFT indiquant la structure la plus énergétiquement stable. Ces calculs ont mis en évidence la présence d'oxydes interstitiels dans les canaux des sites Ca3 au niveau des feuillets $[GaO_4]_n$, totalement en accord avec les résultats obtenus sur la perturbation de la structure locale du site Ca3.

Les propriétés de conduction anionique montrent une augmentation de deux ordres de grandeur de la conductivité de la phase non dopée vers la phase dopée. Cependant, les valeurs de conductivité de ces composés restent relativement faibles avec une valeur maximum atteinte de 2×10^{-5} S.cm^{-1} à 800°C pour la phase $La_{0.25}Ca_{4.75}Ga_6O_{14.125}$ (x = 0.25).

Résumé de la Conclusion générale

Les travaux présentés dans cette thèse ont pour but le développement de nouveaux matériaux hautement performants pour diverses applications. Ces études de chimie du solide portent sur les structures de type mélilites, mais aussi des matériaux avec des structures apparentées aux mélilites présentant un intérêt potentiel pour leurs propriétés optiques et de conduction ionique. L'utilisation de la lévitation aérodynamique couplée au chauffage par laser CO_2 a permis de synthétiser des précurseurs vitreux de ces matériaux sous forme de billes sphériques en fondant d'abord la composition puis en effectuant une trempe avec des vitesses de refroidissement élevées (~ 300°C/s) tout en faisant léviter l'échantillon. Cette lévitation d'échantillons permet d'éviter la présence d'impuretés mais aussi de centres de nucléation qui induiraient une cristallisation hétérogène lors du refroidissement. Le verre obtenu est ensuite cristallisé par un traitement thermique adéquat (préalablement étudié par DSC et diffraction des rayons X *in situ* à des températures variables). L'utilisation de la lévitation aérodynamique comme outil de synthèse a permis aussi d'opérer la cristallisation des échantillons directement à partir du liquide surfondu, atteignant ainsi des nouvelles phases hors-équilibre.

La cristallisation du verre a permis d'élargir la famille des mélilites ($P\bar{4}2_1m$) avec des petites terres rares RE = Yb, mais aussi la famille des mélilites ($P2_12_12$) a d'autres terres rares RE = Dy, Lu. La structure cristalline de ces deux polymorphes ainsi que leur stabilité thermique ont été étudiés, permettant le tracé d'un ''diagramme de phase'' indiquant le domaine de stabilité de chacun d'eux (chapitre II). Cette méthode de synthèse originale a permis aussi la synthèse de la nouvelle solution solide $Ca_3Ga_{2-2x}Zn_xGe_{4+x}O_{14}$ ($0 \leq x \leq 1$) cristallisant sous une symétrie $P321$ de la structure langasite (chapitre III). Le composé $Ca_3Ga_2Ge_4O_{14}$ ($x = 0$) a été aussi synthétisé par cristallisation directe du liquide surfondu avec des taux de cristallinité largement supérieur a ceux obtenues par cristallisation du verre. Cette deuxième technique de synthèse s'est révélé être le seul moyen de repousser les limites des dopants dans la solution solide $La_{1+x}Ba_{1-x}Ga_3O_{7+x/2}$ ($0.35 \leq x < 1$), établie a $x = 0.35$ dans la littérature. Cette famille de compositions cristallise dans la famille des mélilites sous différent polymorphes : $P\bar{4}2_1m$ pour $0 \leq x \leq 0.725$ et $Ima2$ pour $0.9 \leq x$. De ce fait, nous avons réussi à stabiliser à température ambiante la mélilite tétragonale $P\bar{4}2_1m$ avec la plus haute concentration en oxygènes interstitiels (i.e. $La_{1.725}Ba_{0.275}Ga_3O_{7.3625}$ $x = 0.725$).

Les compositions et les structures étudiées dans ce document de thèse ont été caractérisées en couplant plusieurs techniques de diffraction : la diffraction des rayons X sur poudre (en laboratoire et au synchrotron), la diffraction des neutrons, la diffraction des électrons, la microscopie électronique à balayage, la microscopie électronique à transmission et la spectroscopie de résonance magnétique nucléaire du solide. Les propriétés physiques ont été étudiées par spectroscopie de luminescence et spectroscopie d'impédance AC.

Inorganic Chemistry

pubs.acs.org/IC Article

Emergence of A-Site Cation Order in the Small Rare-Earth Melilites $SrREGa_3O_7$ (*RE* = Dy−Lu, Y)

Cécile Genevois, Haytem Bazzaoui, Marina Boyer, Sandra Ory, Yannick Ledemi, Younès Messaddeq, Michael J. Pitcher,* and Mathieu Allix*

Cite This: *Inorg. Chem.* 2021, 60, 12339−12354 Read Online

ACCESS | Metrics & More | Article Recommendations | Supporting Information

ABSTRACT: $SrREGa_3O_7$ melilite ceramics with large rare-earth elements (*RE* = La to Y) are famous materials especially known for their luminescence properties. Using an innovative approach, the full and congruent crystallization from glass process, $SrREGa_3O_7$ transparent polycrystalline ceramics with small rare earth elements (*RE* = Dy−Lu and Y) have been successfully synthesized and characterized. Interestingly, compared to the classic tetragonal ($P\bar{4}2_1m$) melilite structure composed of mixed Sr/*RE* cationic sites, these compositions can crystallize in a 3 × 1 × 1 orthorhombic ($P2_12_12$) superstructure. A detailed study of the superstructure, investigated using different techniques (synchrotron and neutron powder diffraction, STEM-HAADF imaging, and EDS mapping), highlights the existence of a Sr/*RE* cation ordering favored by a large Sr/*RE* size mismatch and a sufficiently small *RE* cation. An appropriate control of the synthesis conditions through glass crystallization enables the formation of the desired polymorphs, either ordered or disordered. The influence of this tailored cationic ordering/disordering on the *RE* luminescent spectroscopic properties have been investigated. A stronger structuration of the *RE* emission band is observed in the ordered ceramic compared to the disordered ceramic and the glass, whose band shapes are very similar, indicating that the *RE* environments in the glass and disordered ceramic are close.

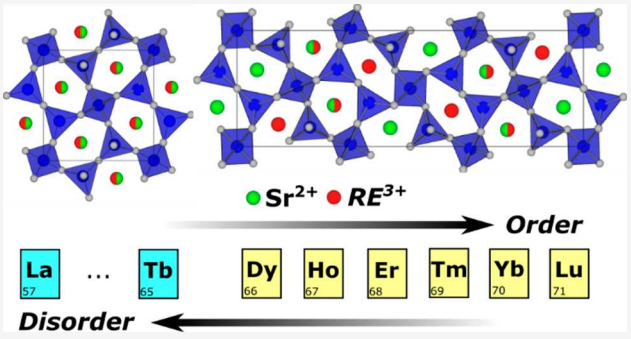

1. INTRODUCTION

The melilite gallates $SrREGa_3O_7$ with the largest *RE* cations, i.e., *RE* = La to Y, are well-known for their luminescence properties observed on single crystal or powder materials.[1−5] These compounds are readily synthesized by conventional ceramic methods and adopt the tetragonal melilite structure with a uniform $[Ga_3O_7]$ framework layer and fully disordered Sr/*RE* ("A-site") cations. In contrast, the compositions with *RE* smaller than Tm have not been widely studied, because they are challenging to synthesize, and they appear to have more complex structures that have not been fully characterized.[6,7] The introduction of small A-site cations (or more precisely, the imposition of a low A/B ionic radius ratio[8]) is known to induce distortions of the melilite framework, for example in the åckermanites $Ca_2MSi_2O_7$ ($M = Mg^{2+}$, Co^{2+})[9−11] and the gallates $CaREGa_3O_7$ (*RE* = La, Nd),[8,12] which both have high concentrations of Ca^{2+} on the A sites. These melilites undergo complex incommensurate structural distortions due to the size mismatch between the Ca/*RE* sublattice and the tetrahedral framework layer, producing a modulated distribution of A-site environments ranging from six- to eight-coordinate in $CaNdGa_3O_7$, which are better adapted for the local coordination of Ca^{2+} than the single eight-coordinate A site exhibited in the undistorted parent phase.

An initial study of $SrREGa_3O_7$ in the small-*RE* range (*RE* = Eu−Yb, Y) was motivated by the search for new luminescent transparent ceramics.[7] Transparent ceramics showing luminescence properties are key materials in the development of numerous applications such as laser gain media and scintillating inorganic materials.[13−18] Indeed, they combine the advantages of transparent media, such as volume excitation/emission, with ceramic optical emission properties, i.e., narrow and intense emission bands. Transparent ceramics are usually synthesized through complex powder sintering processes, requiring high temperature and high pressure to remove residual porosities acting like light scattering centers and consequently limiting the transparency of the resulting material.[16,19,20] An alternative synthesis approach, full crystallization from glass, was recently proposed to achieve

Received: May 25, 2021
Published: August 4, 2021

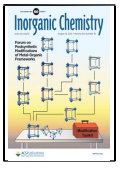

https://doi.org/10.1021/acs.inorgchem.1c01565
Inorg. Chem. 2021, 60, 12339−12354

transparent ceramics.[21−27] This process can lead to fully dense ceramics, i.e., ceramics without porosity, if the density difference between the glass and the crystalline phases remains limited, thus preventing the appearance of cracks during crystallization. The full and congruent crystallization process also leads to very thin grain boundaries.[22] Therefore, the possibility to achieve fully dense ceramics with thin grain boundaries, two of the main requirements for transparent ceramics synthesis, has enabled the use of full glass crystallization to access new transparent ceramic compositions. This was particularly demonstrated for innovative materials showing noncubic symmetry, as long as the birefringence effect remained limited.[7,21,22,28,29]

Moreover, crystallization from glass is a process operating at relatively low temperatures compared to conventional powder sintering and solid state processes, thus offering the possibility to access new metastable crystalline phases as demonstrated for $BaAl_4O_7$,[21,30] $Sr_{1+x/2}Al_{2+x}Si_{2-x}O_8$,[22] $Sr_{1-x/2}Al_{2-x}Si_xO_4$,[28,31] and $Bi_{0.8}Nb_{0.8}Te_{2.4}O_8$ transparent ceramics.[32] Using this method, we were successful in synthesizing new transparent to $SrRECa_3O_7$ ceramics with both small *RE* cations (*RE* = Eu, Gd, Tb, Dy, Ho, Y, Er, Tm, and Yb) and substantial nonstoichiometries ($Sr_{1-x}RE_{1+x}Ga_3O_{7+x/2}$ with *RE* = Eu, Gd, and Tb).[7,26] Some members of the transparent ceramic $SrRECa_3O_7$ family were found to have additional features in their PXRD patterns, implying additional complexity in their crystal structures, but this was not investigated in detail.[7]

Here, we investigate the structure and the phase stability of the $SrRECa_3O_7$ (*RE* = Y, Dy, Ho, Er, Tm, Yb, and Lu) melilites. In contrast to the modulated $CaRECa_3O_7$ melilites, we find that these materials can crystallize in a new cation-ordered 3 × 1 × 1 melilite superstructure, which produces three distinct A-site environments and enables the large size difference between Sr and the small RE^{3+} cations to be accommodated by the tetrahedral framework. Furthermore, by tuning the synthesis conditions, it is possible to isolate disordered polymorphs for the *RE* = Dy, Ho, Er, Tm, and Yb members. The superstructure description is detailed by means of synchrotron and neutron powder diffraction Rietveld refinements, which are coupled to observations from scanning transmission electron microscopy−high angle annular dark field (STEM-HAADF) imaging and X-ray energy dispersive spectroscopy (EDS) elemental mapping. Moreover, atomic-resolution STEM-HAADF imaging and EDS elemental mapping enable direct observation of Sr^{2+} and RE^{3+} cation ordering in the melilite structure. Last, the broad optical transmission range (from the UV up to the mid-infrared) and photoluminescence properties of these new $SrRECa_3O_7$ melilites are measured. A significant influence of the Sr/*RE* ordering/disordering is reported on the *RE* emission band features in the glasses and ordered and disordered ceramics.

2. EXPERIMENTAL SECTION

2.1. Synthesis Procedure. The small rare-earth compounds $SrRECa_3O_7$ (*RE* = Dy−Lu, Y) and the known tetragonal melilite $SrTbCa_3O_7$ were synthesized by a full crystallization from glass process. First, high purity $SrCO_3$, RE_2O_3, and Ga_2O_3 powders (Strem Chemicals, purity >99.9%) were weighed in stoichiometric amounts and ground together in an agate mortar using ethanol to homogenize the mixture. The resulting powder was then dried, pressed into pellets, and broken into fragments of ∼50 mg. The fragments were then levitated individually in an argon gas jet and melted at approximately 1650 °C (determined by optical pyrometry) using a pair of CO_2 lasers (10.6 μm),[33] held for several seconds to allow homogenization, and then quenched radiatively to room temperature by shutting off the lasers (an estimated cooling rate of 300 °C s^{-1}) to produce the precursor glasses as spherical beads. Full crystallization of the glass precursors was then achieved by a single heat treatment performed under air in a conventional muffle furnace at temperatures between 805 and 815 °C. Crystallization protocols for each specific composition are detailed in section 3.1.

2.2. Thermal Analysis. Differential scanning calorimetry (DSC) was performed on a Setaram MULTI HTC 1600 instrument. Powder samples of ∼200 mg, obtained by crushing several beads of the same composition, were contained in platinum crucibles and scanned at a rate of 10 K min^{-1} in flowing argon.

2.3. Powder Diffraction. Laboratory X-ray powder diffraction (PXRD) analyses were performed in Bragg−Brentano geometry using a D8 Advance Bruker laboratory diffractometer (Cu Kα radiation) equipped with a LynxEye XE detector. *In situ* high-temperature diffraction data were collected under air using two different setups depending on the maximum temperature required. For measurements up to 1200 °C, variable temperature VT-PXRD data were recorded using an HTK1200N Anton Paar furnace. The powder sample was placed in a platinum-lined corundum sample holder. Data were collected from 10 to 40° (2θ) with a 0.024° step size and an acquisition time of 1 s/step. Phase transitions were tracked while heating from 740 to 900 °C for *RE* = Ho−Lu, from 740 to 1000 °C for Dy, and from 740 to 1100 °C for Tb, using 5 °C steps. Data were also acquired during cooling from the maximum temperature down to 400 °C (300 °C for *RE* = Ho). For measurements up to 1600 °C, VT-PXRD data were recorded every 50 °C from room temperature up to 1500 °C using an Anton Paar oven chamber (HTK1600N model) from 19 to 38° (2θ) with a 0.016° step size and an acquisition time of 1 s per step. Synchrotron powder diffraction (SPD) was carried out on the 11-BM beamline at the Advanced Photon Source (APS, Argonne National Laboratory, U.S.) for compositions *RE* = Ho, Er, Tm, Yb, and Lu. Data were acquired at room temperature from powder loaded in a 0.8 mm diameter Kapton tube with an incident wavelength of λ = 0.41423 or 0.45787 Å over an angular range of 1−50° (2θ) with a step size of 0.001°. Note that the precursor glass powders were scaled up to ∼1 g for these experiments by combining several crushed beads. Neutron powder diffraction (NPD) data were obtained at the Laboratoire Léon Brillouin (LLB, Saclay, France) on the 3T2 diffractometer at room temperature for *RE* = Yb using an 8-mm-diameter vanadium tube. Data were collected with wavelength of λ = 1.229 Å over the 10−120° 2θ range with a 0.05° step size, for a total of 22 h acquisition time. A large (∼5 g) powder sample was produced for this experiment by crushing a large number of individual beads. Structure refinements were performed from powder diffraction data using TOPAS Academic version 6.[34]

2.4. Electron Diffraction and Imaging. Selected area electron diffraction (SAED) experiments were carried out on a Philips CM20 transmission electron microscope (TEM) to determine the cell parameters and space group of the transparent polycrystalline ceramics. Atomic-resolution STEM-HAADF micrographs and EDS elemental mapping were performed on a JEOL ARM200F (JEOL Ltd.) Cold FEG TEM operating at 200 kV, equipped with a double spherical aberration corrector and fitted with a JEOL SDD CENTURIO EDS system. The cationic ordering in $SrYbGa_3O_7$ was imaged on the atomic scale using STEM-EDS elemental mapping and STEM-HAADF imaging mode with a 68−174.5 mrad inner-outer collection angle. The probe size used is 0.13 and 0.1 nm, respectively. The samples were first prepared by mechanical polishing with a tripod and inlaid diamond discs until a 50 μm thickness. The thin foils were then obtained by argon ion milling (PIPS GATAN).

2.5. Optical Transmission and Photoluminescence Spectroscopies. Optical transmission spectra were recorded on polished samples in the UV−visible−near-infrared (NIR) and infrared ranges using an Agilent Cary 5000 UV−vis−NIR double beam spectrophotometer and a PerkinElmer Frontier FTIR spectrometer, respectively. Photoluminescence spectra were recorded at room temperature on bulk and powder samples using a Horiba-Jobin-Yvon Nanolog spectrofluorimeter, equipped with a 450 W Xe lamp source coupled

https://doi.org/10.1021/acs.inorgchem.1c01565
Inorg. Chem. 2021, 60, 12339−12354

to a double monochromator for excitation, and an iHR320 spectrometer coupled to an infrared PMT detector sensitive from 950 to 1650 nm (Hamamatsu). Special attention was paid to collect the emission spectra under the same experimental conditions to allow their accurate comparison.

3. RESULTS

3.1. Glass-Crystallization Synthesis of Ceramic Powders. The precursor glasses prepared by the aerodynamic levitation laser-melting procedure (see section 2.1) were confirmed to be amorphous by PXRD prior to a provisional thermal analysis by DSC conducted on heating up to 920 °C. Fully amorphous samples were obtained for all of the compositions attempted, with the exception of the end member *RE* = Lu, which contained weak Bragg peaks consistent with the presence of a small amount of crystalline melilite (Figure S1). The glass crystallization temperatures, signified by a strong exothermic peak in the DSC, were found to occur in the range 804−860 °C (see section 3.4); the decrease of the rare-earth size from Tb−Lu induces a systematic increase of the glass transition and crystallization temperatures (associated with increased rigidity of the glass network).[35] Glass powders were finally heat treated for 2 h at 815 °C and cooled down in the furnace (for *RE* = Tb−Yb, Y) or heat treated for 2 h at 805 °C and quenched by placing the Pt crucible in water (for *RE* = Lu) to produce polycrystalline samples.

Laboratory PXRD of these samples showed that two distinct crystal structures had formed, according to the identity of the rare earth ion. For the larger rare earths (*RE* = Tb, Dy, Ho and Y), the PXRDs were readily indexed to the familiar tetragonal melilite structure ($P\bar{4}2_1m$ with $a \approx 7.9$ and $c \approx 5.2$ Å). However, the smaller rare earths (*RE* = Er, Tm, Yb, Lu) exhibited a more complex PXRD pattern which contained the main reflections of the melilite structure, and an additional set of weak reflections. These patterns were indexed using Dicvol,[36] revealing a 3-fold expansion of the melilite unit cell along the *a* axis to produce a new orthorhombic supercell of dimensions ($a \approx 23.70$ Å, $b \approx 7.92$ Å, and $c \approx 5.21$ Å). The detailed determination of the 3 × 1 × 1 melilite structure by powder crystallography and electron microscopy is described first in sections 3.2 and 3.3. The compositional and thermal stability of this superstructure, as determined by variable temperature PXRD and DSC measurements, is then described in section 3.4.

Attempts to synthesize the small-rare earth compositions (*RE* = Ho−Lu) directly by classic solid-state reaction were not successful. For example, a variable-temperature PXRD experiment showed that a reaction mixture of $SrCO_3$−Yb_2O_3−Ga_2O_3 produces $SrGa_2O_4$ and $Yb_3Ga_5O_{12}$ as the only ternary phases before melting at 1500 °C (Figure S2). As reported by Boyer et al.,[7] it is possible to synthesize Sr*RE*Ga_3O_7 transparent ceramics of these compositions by full crystallization from glass (Figure S3a), starting from Sr*RE*Ga_3O_7 glass beads produced as described in section 2.1 and annealing them in a second step: the transparent ceramics thus produced exhibit the same PXRD patterns as for the powder samples described above.

3.2. Solution and Refinement of the 3 × 1 × 1 Superstructure. Sr*RE*Ga_3O_7 synchrotron X-ray diffraction (SPD) and selected area electron diffraction (SAED) patterns were consistent with laboratory PXRD, confirming the presence of a superstructure with a supercell corresponding to a tripling of the *a* axis in a 3 × 1 × 1 expansion (Figure 1) of the tetragonal melilite parent cell (Figure S4). The only observed reflection conditions were *h*00, *h* = 2*n*, and 0*k*0, *k* = 2*n*, consistent with space group $P2_12_12$. Note that we did not see any evidence of satellite peaks in the SrTmGa_3O_7 SAED

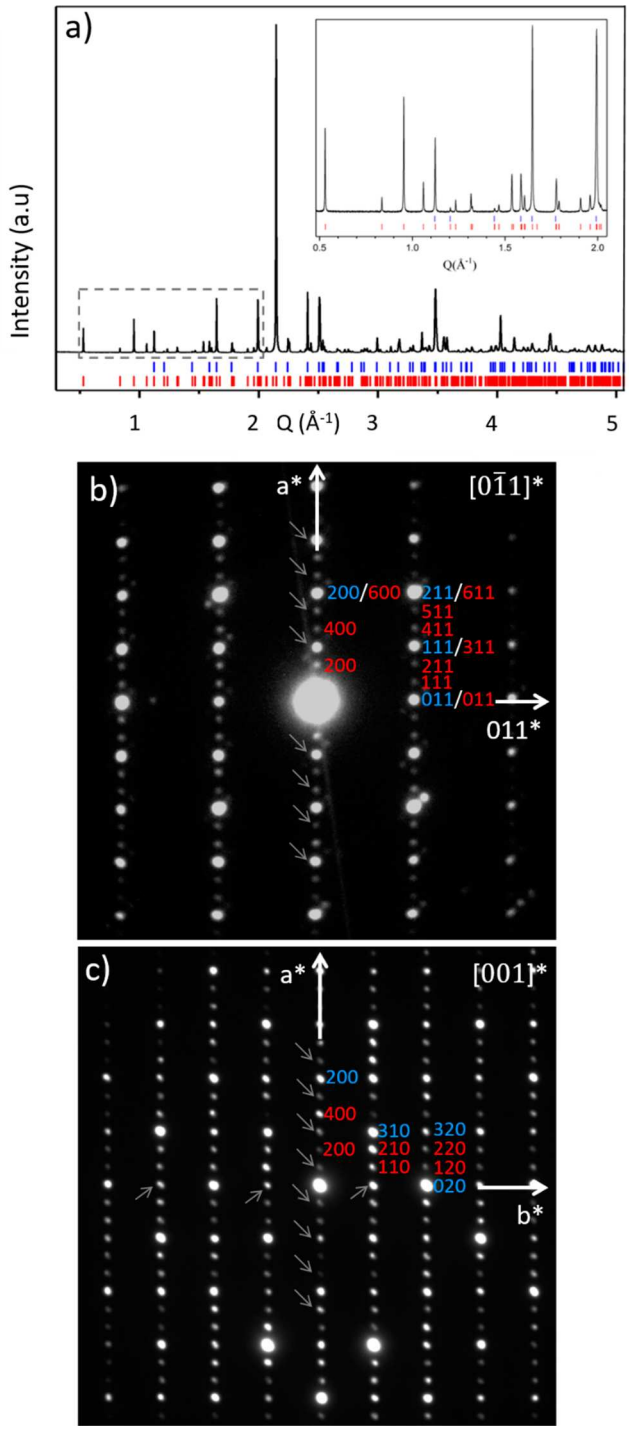

Figure 1. (a) Synchrotron powder diffraction data of the $SrYbGa_3O_7$ melilite phase indexed with the $P\bar{4}2_1m$ melilite substructure (blue marks) and in the 3 × 1 × 1 $P2_12_12$ superstructure (red marks). (b) [0−11]* and [001]* Selected Area Electron Diffraction patterns of the $SrTmGa_3O_7$ melilite phase synthesized by full crystallization from glass. The indexations of the tetragonal melilite substructure (a = 7.9 Å × c = 5.2 Å, $P\bar{4}2_1m$) and the 3 × 1 × 1 superstructure (a = 23.7 Å × b = 7.9 Å × c = 5.2 Å, $P2_12_12$) are shown in blue and red, respectively. The arrows point to the reflections assigned to double diffraction.

https://doi.org/10.1021/acs.inorgchem.1c01565
Inorg. Chem. 2021, 60, 12339−12354

patterns, which implies that the crystal structure is commensurate (in contrast to small-alkaline-earth melilites such as $CaLaGa_3O_7$ and $CaNdGa_3O_7$, which exhibit incommensurate structural distortions).[8,12]

We selected $SrYbGa_3O_7$ as a representative sample for detailed structural analysis due to the high stability of the 3 × 1 × 1 superstructure at this composition (see section 3.4), and its favorable neutron diffraction characteristics (relatively low neutron absorption by Yb and good scattering contrast between Yb/Sr). The structure was solved by charge-flipping[37,38] (implemented in JANA2006[39] through the Superflip software[40,41]) followed by Fourier difference mapping, as described in the Supporting Information. The final Rietveld analysis was performed against SPD and NPD data simultaneously. Initial refinement of the Sr/Yb occupancies of the A sites produced three distinct A sites with equal multiplicity: a mixed Yb/Sr site ("Yb1/Sr1," refined occupancy 0.498(1)/0.501(1)), a Yb-dominated site ("Yb2" (0.977(1)/0.023(1)), and a Sr-dominated site ("Sr3" (0.025(2)/0.975(2)). The amount of site inversion being very limited, these values were then fixed to ideal occupancies (0.5/0.5, 1/0, and 0/1, respectively), which did not affect the goodness of fit. All atomic coordinates were then refined in addition to anisotropic thermal parameters (Sr/Yb positions only) or isotropic thermal parameters (Ga and oxide positions) to give reliability factors R_{wp} = 4.427%, R_p = 3.772%, and χ^2 = 1.035. The Rietveld refinement is presented in Figure 2, Table 1, and Table S1, with the principal interatomic distances presented in Table 2 and Table S2.

The refined $SrYbGa_3O_7$ melilite superstructure is presented in Figure 3. Its crystal structure retains the topology of the parent melilite structure, where corner-sharing GaO_4 tetrahedra form two-dimensional Ga_3O_7 sheets with the A cations accommodated in pentagonal channels that align parallel to the stacking axis. In the tetragonal parent structure (e.g., the structure of $SrLaGa_3O_7$, shown in Figure 3b), the Sr/La site cations are fully disordered, and the channels are symmetrically equivalent with the eight nearest-neighbor A−O distances in the range 2.51−2.94 Å.[6,42] In contrast, in $SrYbGa_3O_7$, the ordering of large/small A site cations (eight-coordinate ionic radii of 1.25 and 0.985 Å for Sr^{2+} and Yb^{3+}, respectively) over three different sites causes the Ga_3O_7 framework to distort (Figure 3a). This produces three distinct channel types which have equal multiplicity.

The A sites in the Sr-containing channels Yb1/Sr1 (half-occupied by Sr^{2+}) and Sr3 (fully occupied by Sr^{2+}) can be considered as distorted versions of the eight-coordinate square-antiprismatic A-sites found in the parent melilite $SrLaGa_3O_7$ (Figure 3d and e). In the Sr3 channels, the bond valence sum (BVS) for Sr^{2+} is 1.76, which is comparable to that found in the undistorted $SrLaGa_3O_7$ (BVS = 2.04), despite its broad distribution of Sr−O distances in the range 2.430(4)−3.195(4) Å (Figure 3e). It is clear that Yb^{3+} would be severely under-bonded at this site (BVS for Yb^{3+} = 1.23). The Yb1/Sr1 sites have A−O distances clustered neatly in the range 2.342(4)−2.702(4) Å (Figure 3d). These sites retain a formal coordination number of 8 but are smaller than the Sr3 sites and smaller than the A-sites of $SrLaGa_3O_7$. Here, the calculated BVS values indicate a compromise between the bonding preferences of Sr^{2+} (which is formally overbonded, with BVS = 2.68) and Yb^{3+} (formally under-bonded, with BVS = 1.87). Such values are comparable with those found in the previously published structure of disordered $SrYGa_3O_7$ (where BVS for Sr^{2+} = 2.37; Y^{3+} = 1.81).[6] In contrast to the Sr3 and Yb1/Sr1 sites, the Yb2 sites (fully occupied by Yb^{3+}) are substantially different from those found in $SrLaGa_3O_7$ and can be considered to have [6 + 1] coordination defined by six short Yb−O distances in the range 2.228(4)−2.517(4) Å that form a triangular-prismatic first coordination sphere, and one long Yb−O distance of 2.967(4). Note that the next-shortest Yb2−O distance is 3.711(3) Å (Yb2−O11), which is beyond the range usually considered for bonding. This site is small enough to accommodate Yb^{3+} with a BVS of 2.68, whereas coordination of Sr^{2+} would be disfavored (BVS for Sr^{2+} = 3.84). The six short Yb−O distances cause a severe narrowing of the pentagonal channel, as shown by the deviation of its geometry from the ideal case of $SrLaGa_3O_7$ (Figure 3c). The refined A−O distances for all three sites are shown in Table 2. The relationship between the arrangement of the A sites in two dimensions and the corresponding framework distortion is discussed in more detail in section 4.1.

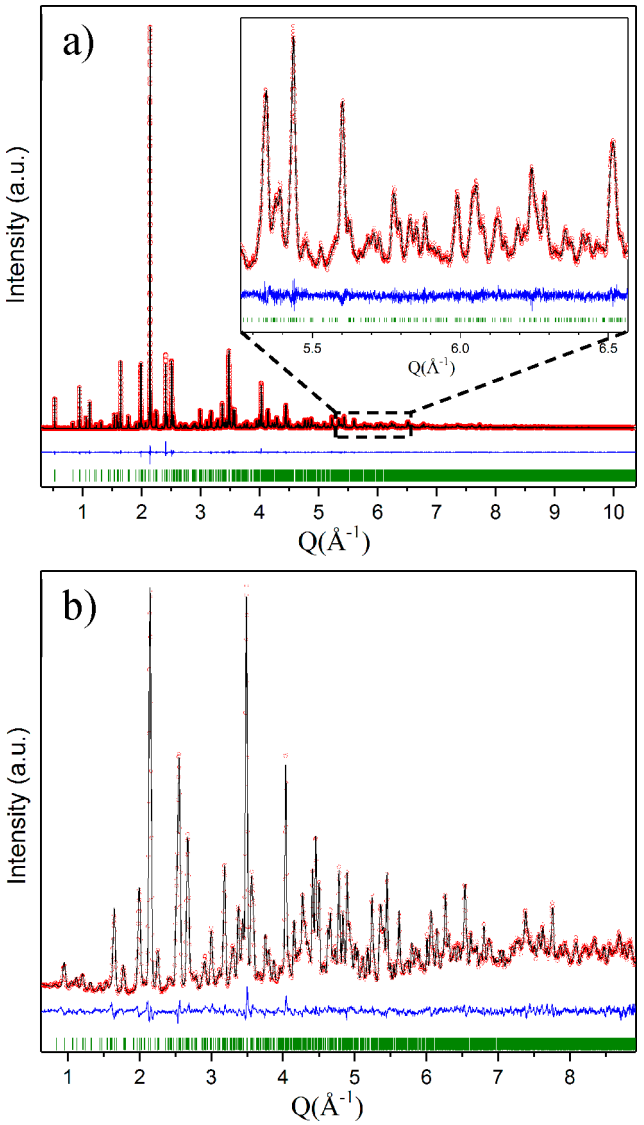

Figure 2. Combined Rietveld refinement of SPD (a) and NPD (b) data on cation-ordered $SrYbGa_3O_7$ melilite at room temperature (R_p = 3.772%, R_{wp} = 4.427%). Observed (red points), calculated (black line), and difference (blue line) profiles are shown. The green tick marks correspond to allowed reflection positions.

https://doi.org/10.1021/acs.inorgchem.1c01565
Inorg. Chem. 2021, 60, 12339−12354

Table 1. Structural Parameters of Cation-Ordered $SrYbGa_3O_7$ Obtained by Rietveld Refinement against SPD and NPD Data (Combined) at Room Temperature ($P2_12_12$ Space Group, a = 23.70167(7) Å, b = 7.92110(3) Å, and c = 5.21162(2) Å)

atom	site	x	y	z	occ	U(eq)
Yb1/Sr1	4c	0.21967(3)	0.14373(8)	0.49426(12)	0.5/0.5	0.0077(2)[a]
Yb2	4c	0.38103(2)	0.30934(6)	0.45529(9)	1	0.0101(1)[a]
Sr3	4c	0.05795(4)	0.33953(11)	0.50839(18)	1	0.0098(2)[a]
Ga1	4c	0.44940(4)	0.14505(14)	0.0131(2)	1	0.0054(3)
Ga2	2a	0	0	0.9759(4)	1	0.0066(4)
Ga3	4c	0.17317(5)	0.48007(13)	0.0014(3)	1	0.0047(2)
Ga4	4c	0.28948(4)	0.33540(13)	0.9535(2)	1	0.0056(3)
Ga5	4c	0.11858(5)	0.12314(12)	0.03036(19)	1	0.0065(3)
O1	4c	0.45607(14)	0.3444(5)	0.2033(7)	1	0.0089(7)
O2	4c	0.38457(14)	0.0730(4)	0.1899(6)	1	0.0043(7)
O3	4c	0.29223(14)	0.3327(5)	0.3001(7)	1	0.0190(10)
O4	4c	0.44114(14)	0.1434(5)	0.6766(6)	1	0.0095(7)
O5	4c	0.12726(17)	0.1121(5)	0.6862(6)	1	0.0150(8)
O6	2b	0.5	0	0.1551(9)	1	0.0082(10)
O7	4c	0.22859(17)	0.4269(5)	0.7736(8)	1	0.0156(8)
O8	4c	0.04632(15)	0.1439(5)	0.1532(7)	1	0.0167(9)
O9	4c	0.29646(16)	0.1315(6)	0.7764(8)	1	0.0173(9)
O10	4c	0.15349(17)	0.2993(5)	0.2025(7)	1	0.0170(9)
O11	4c	0.34815(14)	0.4525(4)	0.7940(6)	1	0.0079(7)

[a]The thermal parameters of Yb1/Sr1, Yb2, and Sr3 were refined as anisotropic (see details in Table S1).

Table 2. A−O Interatomic Distances and Bond Valence Sums Calculated for the Three Crystallographic A Sites of Cation-Ordered $SrYbGa_3O_7$

bond	length (Å)	bond	length (Å)	bond	length (Å)
(Sr/Yb)1-O9	2.342(4)	Yb2−O1	2.228(3)	Sr3−O8	2.430(4)
(Sr/Yb)1-O5	2.421(4)	Yb2−O11	2.238(3)	Sr3−O6	2.565(3)
(Sr/Yb)1-O3	2.494(4)	Yb2−O4	2.256(4)	Sr3−O4	2.593(4)
(Sr/Yb)1-O10	2.508(4)	Yb2−O3	2.262(3)	Sr3−O5	2.608(4)
(Sr/Yb)1-O7	2.531(4)	Yb2−O2	2.329(3)	Sr3−O2	2.783(3)
(Sr/Yb)1-O11	2.671(3)	Yb2−O5	2.517(4)	Sr3−O10	2.788(4)
(Sr/Yb)1-O7	2.682(4)	Yb2−O9	2.967(4)	Sr3−O4	2.935(3)
(Sr/Yb)1-O3	2.702(4)	Yb2−O11	3.711(3)	Sr3−O1	3.195(4)
BVS (Sr)	2.68	BVS (Sr)	3.84	BVS (Sr)	1.76
BVS (Yb)	1.87	BVS (Yb)	2.68	BVS (Yb)	1.23

3.3. Atomic-Scale Imaging of the 3 × 1 × 1 Superstructure (*RE* = Yb). The Rietveld refinements of $SrYbGa_3O_7$ provide an average structural model describing the superstructure with three distinct crystallographic A sites (one fully occupied by Yb, one fully occupied by Sr, and one shared equally by Sr and Yb), but it may not provide an accurate picture of the local Yb/Sr distribution on the nanometer scale. To investigate the possibility of local deviation in the Yb/Sr distribution (e.g., the presence of areas enriched in Yb or Sr), EDS mapping and STEM-HAADF imaging were performed on the atomic scale, on the $SrYbGa_3O_7$ sample oriented along the [001] direction (Figure 4a and Figure 5). Along this direction, the columns of atoms are composed of the same crystallographic A site (Yb1/Sr1 with a 50/50 occupancy or Yb2 as fully occupied by Yb or Sr3 as fully occupied by Sr; Figure 3a).

STEM-EDS elemental mapping of the three cations, Ga, Sr, and Yb, on the atomic scale (where each point corresponds to a column of atoms with the same chemical nature) shows GaO sites (blue), pure Yb2 sites (red), pure Sr3 sites (green), and mixed Yb1/Sr1 sites highlighted by yellow arrows (Figure 5). This result confirms and allows the cationic organization proposed by powder diffraction to be visualized.

Scanning transmission electron microscopy−high angle annular dark field (STEM-HAADF) is a Z-contrast imaging mode whose signal is essentially dominated by Rutherford scattering, with a cross-section proportional to Z^2 (Z being the atomic number).[43−45] For thin objects (several tens of nanometers), an analytical expression of the Z dependence of the image intensity can be approximated by an exponential function of the form $I \propto Z^n$ with n in the range between 1.6 and 2, depending on the annular dark field (ADF) detector geometry (collection angle). On the atomic scale, for a column composed of several elements (i) with a ratio m_i and Z_i being the atomic number of the element i, this formula becomes $I \propto \sum_i (m_i Z_i^n)$. Consequently, one of the advantages of this imaging mode is the possibility to distinguish between chemically different atomic column sites. However, the intensities are highly sensitive to the number of atoms in the atomic column. Considering this point, atomic resolution STEM-HAADF images have been acquired with a $SrYbGa_3O_7$ crystal oriented along the [001] direction in order to stack the same number of atoms along all the atomic columns, whatever their chemical nature (Figure 4a). The cation ordering was then determined by indexing the atomic columns from the brightest to the darkest contrasts in relation with the heaviest sites to the lightest atoms: Yb2 (Z = 70) > Yb1/Sr1 50:50 mixed ($\overline{Z} \approx 56$) > GaO ($\overline{Z}$ = 39) ≈ Sr3 (Z = 38). Only the Sr and GaO atomic columns are difficult to distinguish accurately due to their very close atomic numbers. However, by comparison with the EDS elemental maps (Figure 5) and the embedded simulated STEM-HAADF image (top right corner of Figure 4a), all the crystalline sites are identified. The simulated STEM-HAADF image of the $SrYbGa_3O_7$ superstructure, oriented along the

https://doi.org/10.1021/acs.inorgchem.1c01565
Inorg. Chem. 2021, 60, 12339−12354

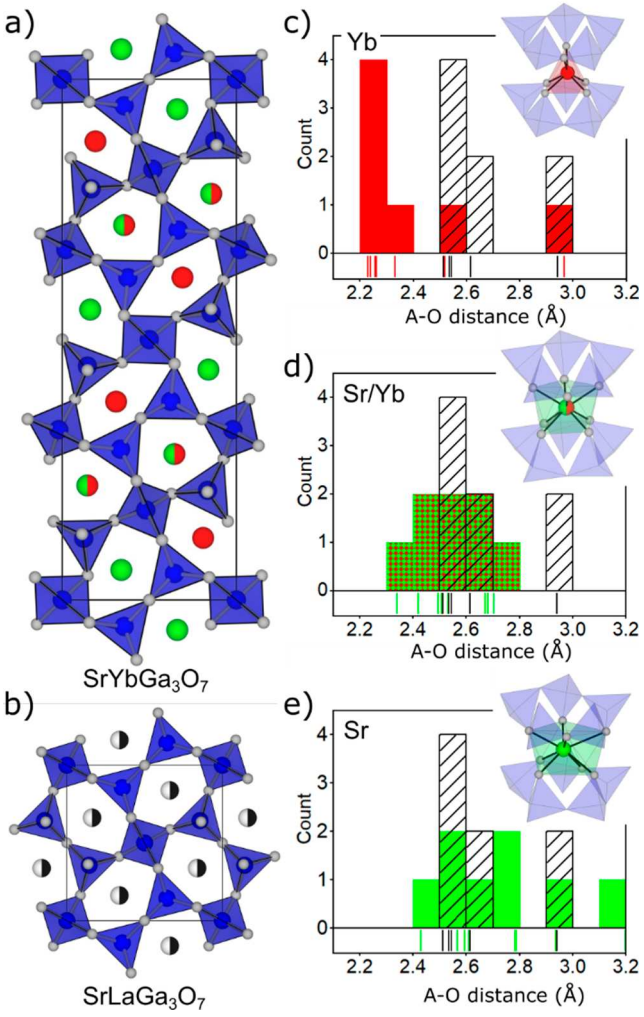

Figure 3. [001] projections of (a) the cation-ordered 3 × 1 × 1 melilite superstructure of $SrYbGa_3O_7$, with GaO_4 tetrahedra in blue, Sr in green, and Yb in red. (b) The parent melilite structure of $SrLaGa_3O_7$, with the disordered Sr/La site in black/white. (c–e) Histograms showing the distribution of refined A–O distances in $SrYbGa_3O_7$ for Yb (red), Sr/Yb (patterned green/red), and Sr (green) sites. Each histogram is overlaid with the published A–O distances of the undistorted $SrLaGa_3O_7$ parent phase (patterned black/white bars).

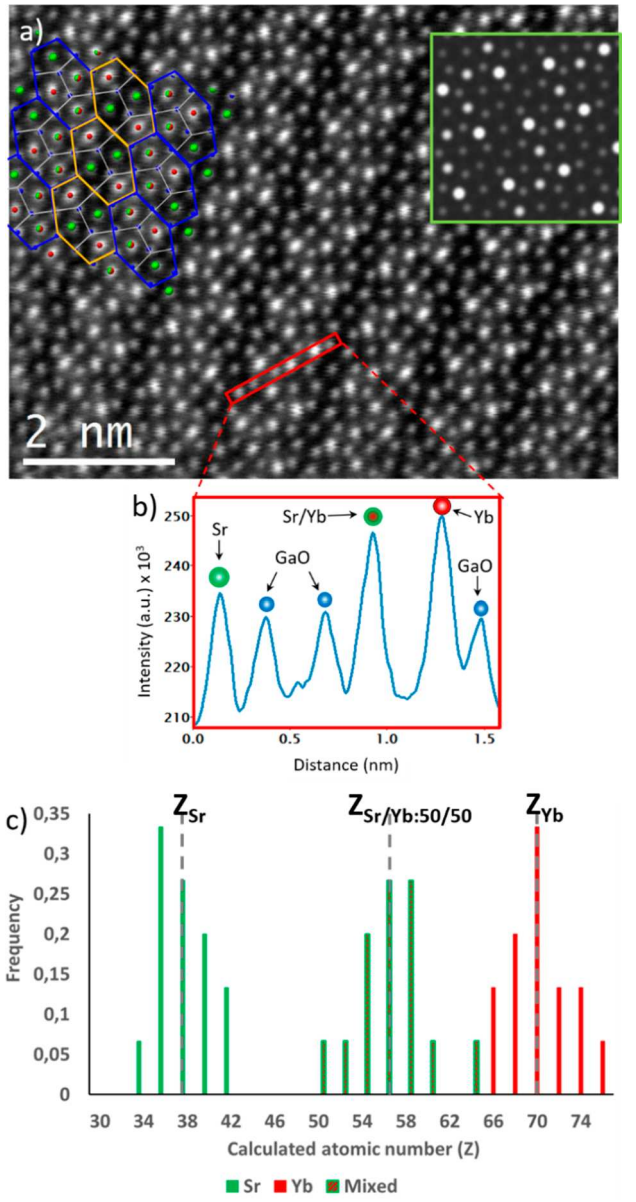

Figure 4. (a) Atomic scale STEM-HAADF micrograph of the $SrYbGa_3O_7$ superstructure sample oriented along the [001] zone axis. The hexagonal ABA′ tiling, from the discussion in section 4.1, is overlaid to highlight the superstructure (Ga, Yb1/Sr1, Yb2, and Sr3 atoms are respectively represented in blue, red, green/red, and green). The green framed inset corresponds to a STEM-HAADF simulated image by JEMS software. (b) Experimental profile corresponding to the red framed box area. (c) Distribution of the calculated atomic number (Z) from the measured peak volumes for each crystallographic site (Yb1/Sr1, Yb2, and Sr3).

[001] zone axis, was obtained using the JEMS software[46] from the cif file of the superstructure. It is a simple projection of the structure convolved with the electron probe intensity of the microscope. The channeling effects have not been simulated. A perfect match in terms of distances and positions between the experimental STEM-HAADF images and the melilite structure resolved from synchrotron and neutron powder diffraction experiments was found with no sign of modulation or default in the crystallographic site organization.

Recent works[47,48] have demonstrated that a quantification of the total intensity of the scattered electrons (V) for individual atomic columns can enable the nature of unknown columns to be assigned via the formula $V \approx \sum_i (m_i Z_i^n)$ with $n \approx 2$ and m_i being the weighting of the different elements i composing the atomic column. This formula has been employed to determine the local Yb1/Sr1 distribution over the mixed site, i.e., the deviation around the ideal average 50/50 value determined from powder diffraction. Multiple factors such as thickness variation, the level of noise, and channeling can affect the signal. To limit these artifacts, the intensity profiles were extracted for each projected position from the same STEM-HAADF image, assuming the thickness of the sample to be almost constant through the image (8 nm × 6 nm), as well as the different factors affecting the signal. The signal obtained for each atomic column was fitted with a background signal and a Gaussian function determined for each type of crystallographic site (Sr3, Yb2, Yb1/Sr1; Figure 4b).[49] The chemical composition of atomic columns of the same crystallographic site (Sr3, Yb2, Yb1/Sr1) can be compared to each other by

https://doi.org/10.1021/acs.inorgchem.1c01565
Inorg. Chem. 2021, 60, 12339–12354

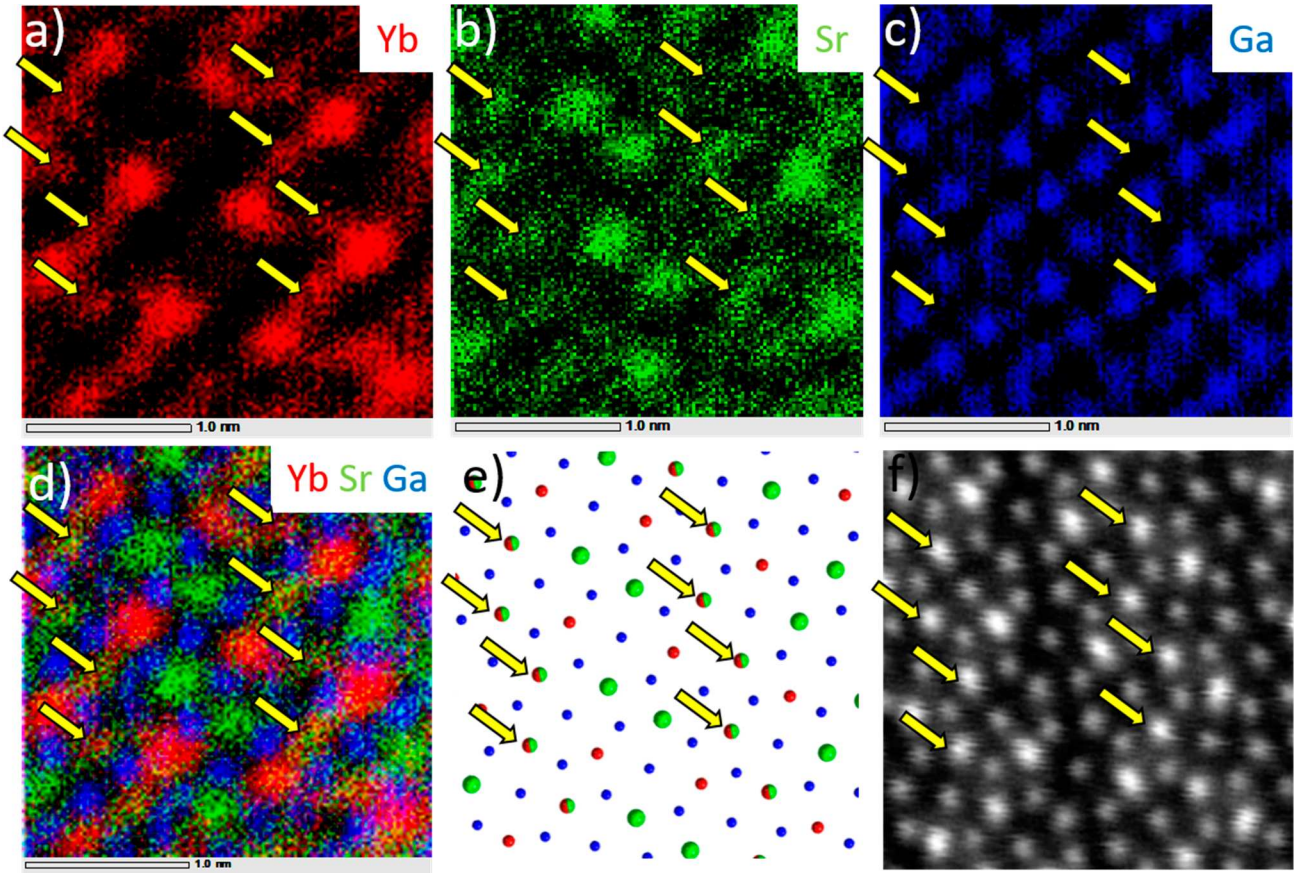

Figure 5. Atomic-scale STEM-EDS elemental maps of the cations (a) Yb (red), (b) Sr (green), (c) Ga (blue), and (d) the overlaid EDS maps showing the mixed sites (50:50 Yb1/Sr1) in red/green highlighted by yellow arrows. (e) $SrYbGa_3O_7$ superstructure projection of the cationic sites along the [001] axis. Ga atoms are drawn in blue, Sr3 sites in green, Yb2 sites in red, and the mixed sites (50/50 Yb1/Sr1) in red/green. (f) STEM-HAADF image of the $SrYbGa_3O_7$ superstructure along the [001] zone axis. On all the images, the yellow arrows highlight the mixed Yb1/Sr1 sites (50/50 average occupancy).

looking at the corresponding volumes under the peaks which are proportional to the total intensity of electrons scattered toward the ADF detector. According to the formula $V \approx \sum_i (m_i Z_i^n)$ with V being the volume under the peak and Z being the atomic number of the site, the factor n has been determined for each crystallographic site considering the mixed Yb1/Sr1 site with an average 50/50 occupancy. The n values obtained for the sites Sr3, Yb1/Sr1, and Yb2 were 2.1, 1.99, and 1.94, respectively, in agreement with the literature that predicts an n factor close to 2. Considering these n values, a Z atomic number has been calculated for each measured atomic column, and its distribution is presented on the Figure 4c. The three different crystallographic A sites are well distinguished, and their average Z values agree with the occupancies Yb/Sr: 1/0 (Z_{Yb} = 70), 0/1 (Z_{Sr} = 38), and 0.5/0.5 ($\overline{Z_{Yb/Sr}} \approx 56$), respectively. The pure Sr3 and Yb2 crystallographic sites show a small Z distribution (±13% and ±7%, respectively) which can be linked to deviation due to the different factors previously described which affect the signal. In comparison, the variation of the Z value to the Yb1/Sr1 mixed atomic columns (±14%) is similar to the pure Sr crystallographic site, corresponding to a low variability of the chemical composition between each mixed Yb1/Sr1 atomic column, which represent between 40 and 100 cells along the c axis (i.e., 20 to 50 nm in thickness).

3.4. Thermal Stability and Structural Phase Diagram Across the Series *RE* = Tb−Lu, Y. The occurrence of the 3 × 1 × 1 superstructure as a function of composition (*RE* = Tb−Lu, Y) and temperature were mapped by a combination of *in situ* high-temperature PXRD and thermal analysis by DSC. The PXRD experiments started from precursor glasses, which were heated in 5 °C steps from 740 °C, until the point where thermal decomposition of the melilite into binary (RE_2O_3) and ternary (garnet-type) oxides was observed. This was then followed by measurements on cooling to room temperature, as shown in Figure 6. A measurement time of 30 min step^{-1} was used to ensure the reliable detection of low-intensity superstructure peaks, resulting in an average heating rate of approximately 0.17 °C min^{-1}. The *RE* = Lu member was found to have the lowest thermal stability with decomposition products appearing at 830 °C, which is only ∼50 °C higher than its glass crystallization temperature, and this was the only sample to decompose substantially during the measurement. The *RE* = Ho, Er, Tm, and Yb members were found to have higher decomposition temperatures in the range 850−870 °C. This, together with their lower glass-crystallization temperatures, means that a wider temperature window is available for their synthesis. Members with rare earths larger than Ho were found to be the most stable with respect to decomposition: *RE* = Y, Dy, and Tb were found to decompose at 890, 965, and 1010 °C, respectively. For comparison, *RE* = Gd is not susceptible to thermal decomposition, as demonstrated by successful melt-growths of single crystals.[50] This indicates that

https://doi.org/10.1021/acs.inorgchem.1c01565
Inorg. Chem. 2021, 60, 12339−12354

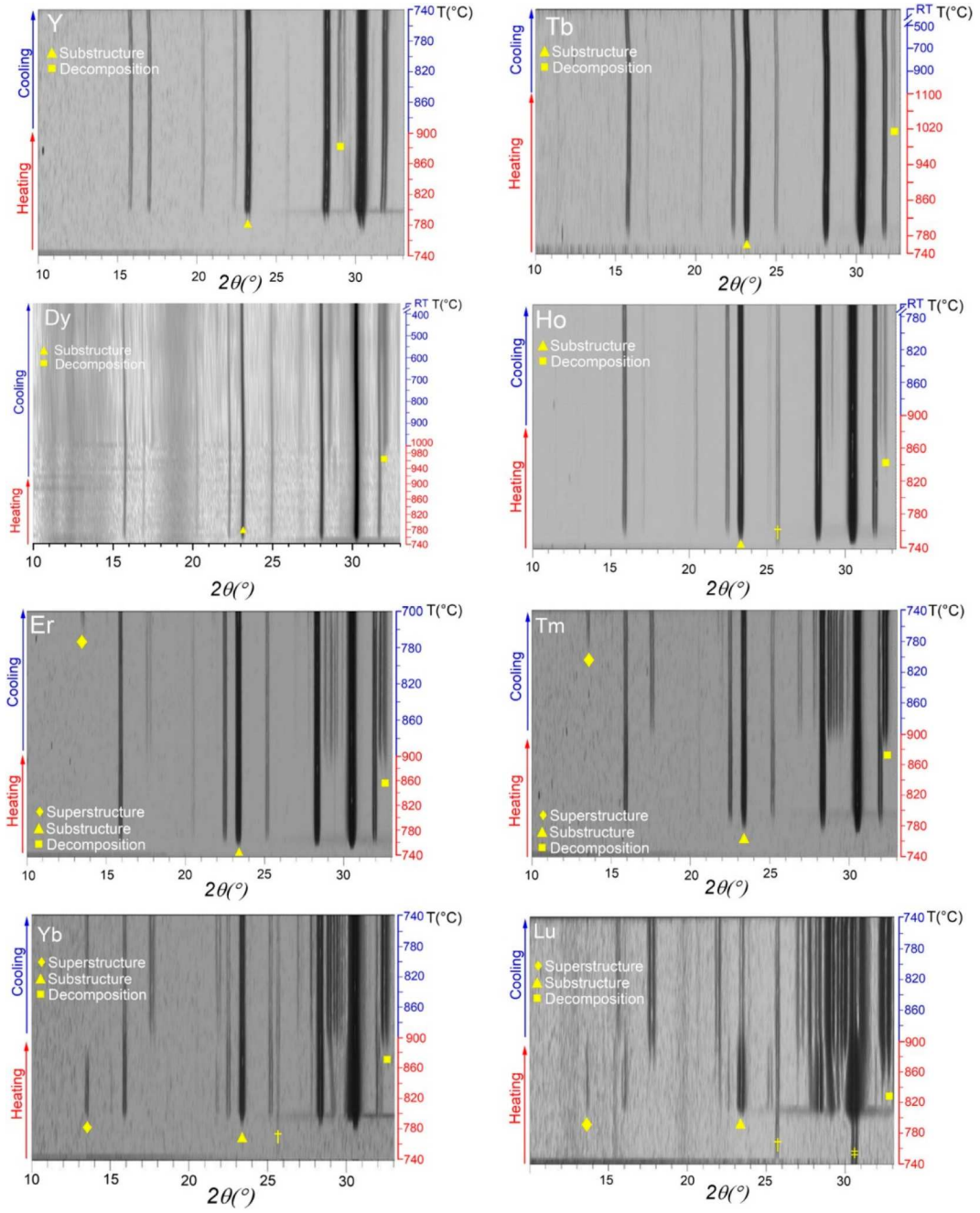

Figure 6. Variable temperature powder X-ray diffraction (VT-PXRD) on Sr*RE*Ga_3O_7 (RE = Tb−Lu, Y) on heating and cooling, starting from the precursor glasses. Peaks representing the initial melilite (substructure) crystallization, the 3 × 1 × 1 structural ordering (superstructure), and the onset of decomposition are indicated, respectively, by triangle, diamond, and square symbols. Note that the maximum intensities of the decomposition peaks are between 1 and 3% (Tb, Dy, Ho, Er, Y) or 5 and 8% (Tm, Yb) of the most-intense melilite peak, while Lu decomposed substantially (∼50%). Peaks labeled † arise from the alumina sample holder. The precursor glass for *RE* = Lu contained a small amount of crystallized melilite, indicated by ‡.

the boundary of the metastable small-rare-earth melilites lies between *RE* = Gd and Tb (see Figure 8).

The onset temperatures of the parent (A-site disordered) tetragonal melilite and 3 × 1 × 1 superstructure peaks revealed three categories of behavior that depend on the size of the rare earth cation. (i) The smallest *RE* members (*RE* = Yb and Lu) were found to crystallize directly into the 3 × 1 × 1 melilite superstructure upon heating. In these compounds, the superstructure was retained throughout the experiment on cooling to room temperature. (ii) The intermediate-*RE* members (*RE* = Er and Tm) crystallized first into the parent melilite structure, which was then retained up to high temperature. However, on cooling below 720 and 790 °C, respectively, they transformed into the 3 × 1 × 1 superstructure, which was then retained all the way to room temperature. (iii) The largest *RE* members (*RE* = Tb, Dy, Y and Ho) crystallized into the parent melilite structure and retained this structure throughout the experiment. Note that, in all cases, the products obtained at room temperature were

https://doi.org/10.1021/acs.inorgchem.1c01565
Inorg. Chem. 2021, 60, 12339−12354

consistent with the results of *ex situ* crystallization described in section 3.1.

The DSC scans, measured in parallel with the *in situ* PXRD over the range 25−925 °C, used a constant temperature scan rate of 10 °C min^{-1} on heating and cooling (Figure 7),

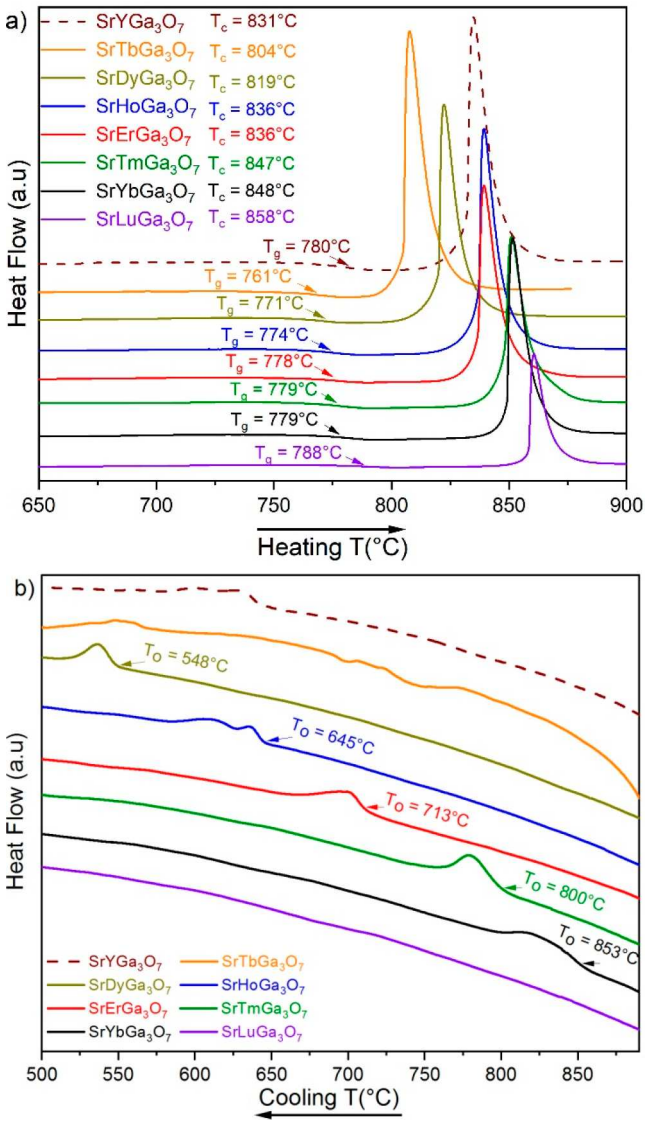

Figure 7. Differential scanning calorimetry (DSC) measurements of Sr*RE*Ga_3O_7 (*RE* = Tb−Lu, Y) glass composition, where T_g, T_c, and T_o are glass transition, crystallization, and ordering temperatures, respectively. (a) Heating plots using a 10 °C/min heating rate from room temperature to 925 °C. (b) Cooling plots using a 10 °C/min cooling rate from 925 °C to room temperature.

substantially faster that the average rate of the *in situ* PXRD experiments. The DSC data collected on heating are dominated by the strong exothermic peaks from glass crystallization in the range 804 °C (*RE* = Tb) to 858 °C (*RE* = Lu), as shown in Figure 7a. However, with the exception of the end members (*RE* = Tb and Lu), the cooling curves were found to exhibit a small exothermic peak whose position varied systematically with composition, as shown in Figure 7b. The onset temperatures of these peaks are strongly correlated with the identity of the *RE* cation: a maximum of 853 °C was observed for *RE* = Yb, with a near-monotonic decrease to 548 °C for *RE* = Dy. For Er and Tm, their peaks at 713 and 800 °C, respectively, agree closely with the superstructure ordering temperatures observed on cooling *in situ* by PXRD. Postmeasurement *ex situ* PXRD scans showed that all of these samples, with the exception of *RE* = Tb (which showed no exothermic peak on cooling), had crystallized in the 3 × 1 × 1 superstructure (Figure S5). The exothermic event observed on cooling thus corresponds to a structural phase transition from the tetragonal parent melilite structure to the orthorhombic 3 × 1 × 1 melilite superstructure.

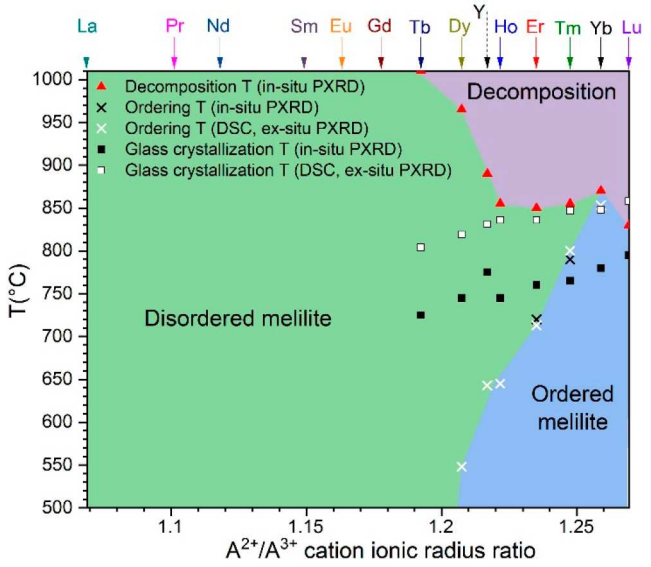

Figure 8. Sr*RE*Ga_3O_7 phase diagram showing the maximum extent of the 3 × 1 × 1 superstructure domain, as a function of temperature and A-site ionic radius ratio. The points for *RE* = Tb−Lu, Y are drawn from DSC and VT-PXRD results (this work), while the region *RE* = La−Gd is drawn from the literature.[6]

These thermal analysis results demonstrate that the 3 × 1 × 1 superstructure can be formed for the larger rare-earth members *RE* = Dy, Y, and Ho if they are crystallized with appropriate heating and cooling rates (Figure S6). Furthermore, they suggest that it should be possible to recover the parent tetragonal polymorphs of the intermediate- and small-*RE* members (Er−Yb) at room temperature by rapid cooling from the disordered domain (Figure S6). To test this, we used a conventional muffle furnace to heat powdered precursor glasses of each composition (*RE* = Er, Tm, and Yb) in a platinum crucible at 10 °C min^{-1} to ∼50 °C above their transition temperatures T_o (defined by the exothermic peak in the DSC cooling scan) and then immediately quenched them to room temperature by removing them from the furnace. PXRD confirmed that the tetragonal parent melilite structure had been isolated for each of these compositions (Figures S7, S8). Attempts to quench $SrLuGa_3O_7$ in this way, from ∼10 °C below its decomposition temperature, only produced the 3 × 1 × 1 superstructure. This is consistent with the absence of a phase transition peak in the DSC cooling scan of this compound: our results indicate that this structure is cation-ordered through its entire stability range.

3.5. Structural Trends Across the Series *RE* = Dy−Lu, Y. The structural model derived for $SrYbGa_3O_7$ was used as a template for Rietveld refinement of the 3 × 1 × 1 superstructure polymorphs of *RE* = Ho, Er, Tm, and Lu

https://doi.org/10.1021/acs.inorgchem.1c01565
Inorg. Chem. 2021, 60, 12339−12354

(using SPD data) and *RE* = Dy (using laboratory PXRD; Figures S9–S12). For *RE* = Ho, Er, and Tm, the lattice parameters, atomic positions, and isotropic thermal parameters were refined (with all oxygen atoms assigned the same thermal parameter; Tables S3–S12), and the fractional occupancies of Sr and *RE* on the three A sites were refined with a global compositional constraint to match the nominal stoichiometry. This produced good fits to the data for all compositions (for structural parameters and agreement factors, see Tables S3–S8 and Figures S10, S11). These refinements all revealed a partitioning of Sr and *RE* over the three A sites that is consistent with the structure of $SrYbGa_3O_7$. Like $SrYbGa_3O_7$, the next-smallest member, $SrTmGa_3O_7$, was found to exhibit complete cation ordering on the A sites, while refinements of the larger *RE* = Dy–Er members revealed a small amount of disorder between the *RE*2 and Sr3 sites. This can be seen most clearly for $SrErGa_3O_7$, where Er occupancy refined to 0.50 for RE1/Sr1, 0.866(3) for RE2, and 0.130(4) for Sr3. These structures are still strongly cation-ordered, but these small deviations from the $SrYbGa_3O_7$ model are consistent with the weakening stability of the 3 × 1 × 1 superstructure as the *RE* radius increases (sections 3.4 and 4.2). It is possible that this apparent partial Sr/*RE* site inversion, indicated by the Rietveld refinements, actually corresponds to the presence of fully disordered microstructural domains in these samples: this appears to be the case for *RE* = Y, where HRTEM imaging and associated FFTs show clearly, in a single grain, the coexistence of ordered and disordered nanodomains of size 20–30 nm with the same [001]* orientation (Figure S13), suggesting that disorder is introduced on the nanometer scale, rather than on the unit cell scale. The possible existence of such ordered/disordered domains in the *RE* = Dy–Er members provides an alternative explanation for the partial disorder over the *RE*2 and Sr3 sites, which is apparent in their refined (average) structures.

The SPD data revealed $SrLuGa_3O_7$ to have a lower crystallinity than the other members with significantly broader Bragg peaks, consistent with its high glass-crystallization temperature and small thermal stability window. For this composition only, deviations of the Ga–O distances from their corresponding values in $SrYbGa_3O_7$ were restrained by a penalty function in order to obtain a physically plausible model. Additionally, it was necessary to split the Lu3 site to avoid an unphysically large thermal parameter at this site. Although this produced a satisfactory fit to the SPD data (R_{wp} = 9.18%, R_p = 6.87%, see Table S9), these factors render the *RE* = Lu model less precise than those of the other highly crystalline *RE* members and may indicate complex local disorder in this sample.

The disordered polymorphs, which were synthesized for *RE* = Dy–Yb by quenching from high temperatures (see section 3.4), have ionic radius ratios of the A (Sr/*RE*) and B (Ga) cations that lie close to the incommensurately ordered structural domain proposed by Wei et al.[8,12] for the small alkaline-earth melilites $CaREGa_3O_7$. To test this possibility, we conducted SAED measurements on disordered $SrTmGa_3O_7$ (Figure S4), which confirmed the tetragonal $P\bar{4}2_1m$ indexation and contained no evidence of incommensurate satellite reflections. We then proceeded with Rietveld analysis using laboratory PXRD data with the tetragonal $P\bar{4}2_1m$ model of the parent melilite $SrLaGa_3O_7$ as a structural template (Figures S10, S11). Unit cell parameters and atomic coordinates were refined with no additional constraints. Across the series, the trend in lattice parameters follows the expected lanthanide contraction and is consistent with the trend observed in the superstructured polymorphs (see normalized lattice parameters, Figure S14 and Table S13, S15, S17, S19). The mean Sr/*RE*–O distances were found to lie in the range 2.590(8)–2.600(5) Å, which is consistent with the parent $SrLaGa_3O_7$ melilite (mean Sr/La–O 2.655 Å; Tables S14, S16, S18, and S20).

3.6. Optical Properties. The optical transmission spectra in the UV–vis–NIR range (200 to 2700 nm) of the $SrREGa_3O_7$ glasses and ceramics have already been reported in anterior works.[7] Optical transparency of both glasses and ceramics actually spans from ∼300 nm up to ∼7 μm (at an arbitrary transmittance value of 10% for 1 mm thick samples), as can be seen in and confirmed by the transmission windows presented in Figure S15. Optical scattering losses can be observed on all of the ceramics in the short-wavelength region of their transmission spectra, as expected. Maximum transmission also drops from 80% for the glasses down to 40–60% for the ceramics, except for the $SrYbGa_3O_7$ ceramic, which maintains above 70% of transmission in the mid-infrared range. Moreover, a clear structuration (narrower bandwidth and sharper peak intensity) of the absorption bands characteristic to the *RE* cations is also noticed: around 1480–1530 nm for the Er^{3+} ion, 1900–2000 nm for the Ho^{3+} ion, 1600–1800 nm for the Tm^{3+} ion, and 975 nm for the Yb^{3+} ion, for instance (Figure S16). This confirms the structural environment ordering around the *RE* cation induced during the full crystallization from the glass. To better evidence this influence, emission photoluminescence spectroscopic measurements were focused on the $SrErGa_3O_7$ melilites. The fluorescence spectroscopy of the Er^{3+} ion is indeed well-known and exploited in numerous applications (e.g., in optical fiber amplifier for telecommunications). The emission spectra recorded in the 1400–1650 nm region under excitation at 520 nm on glass and ceramic melilite bulks reveal a strong enhancement of the emission intensity in the ceramic material (Figure S17). In addition, one can observe a raising of several structured peaks along the Er^{3+} broad emission band in the ceramic, resulting from the more defined structural ordering around the Er^{3+} ions.

Photoluminescence emission spectra have been also recorded on the $SrErGa_3O_7$ glass and ordered and disordered ceramic powdered samples, as presented in Figure 9. Strictly the same experimental conditions and amounts of finely crushed powders were employed to enable accurate comparison of their emission spectrum. In comparison with the emission spectra recorded on bulk polished samples (Figure S17), no significant difference of emission intensity is noticed here between the glass and ceramics emission band. Then, one can also notice a stronger structuration of the band in the ordered ceramic vs the disordered ceramic, whose band shape is very similar to that recorded in the glass.

DISCUSSION

4.1. Origin of the 3 × 1 × 1 Superstructure. While the preference of the large (Sr) and small (*RE*) cations for different coordination sites explains the occurrence and relative stabilities of the ordered and disordered structures in this series (see section 4.2), it does not explain why the 3 × 1 × 1 superstructure retains a substantial degree of disorder, i.e., why Sr and *RE* are ordered over three different sites (Sr-only, *RE*-only and mixed), instead of segregating completely over two

https://doi.org/10.1021/acs.inorgchem.1c01565
Inorg. Chem. 2021, 60, 12339–12354

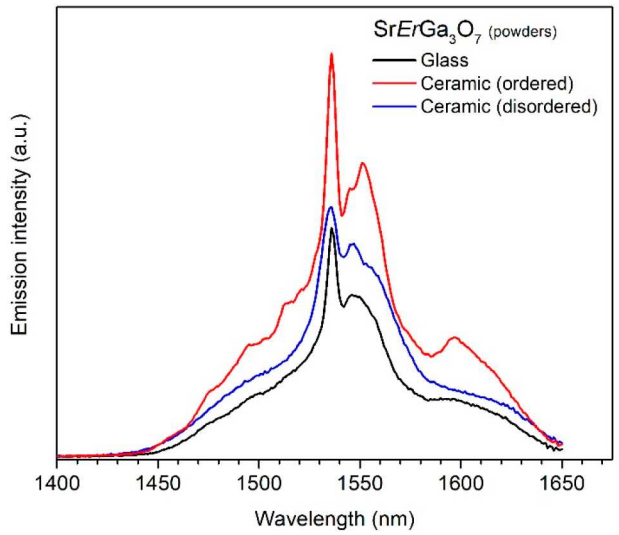

Figure 9. Near infrared emission band of the $SrErGa_3O_7$ glass and ordered and disordered ceramics powdered samples, under excitation at 520 nm (Xe lamp source). Data were collected under strictly the same conditions.

sites (Sr-only and *RE*-only), which would give a fully ordered structure. This can be considered by expanding the view of the 3 × 1 × 1 superstructure (Figure 10) to reveal the full complexity of the cation ordering. The most striking feature is that the small highly distorted *RE*2 sites, populated exclusively by *RE*, are arranged in two dimensions on a pseudohexagonal sublattice which maximizes their separation (Figure 10a). This arrangement means that the highly distorted pentagonal channels that host them are not required to share edges with each other. In contrast, the larger Sr and Sr/*RE*1 sites are not arranged pseudohexagonally and instead form one-dimensional stripe-like sublattices parallel to the *b* axis.

The underlying melilite structure can be described as a hexagonal tiling ("MacMahon's net" or "Cairo pentagonal tiling" corresponding to a pair of orthogonal interpenetrating hexagonal nets),[51,52] as illustrated in Figure 10b. Here, it can be seen that two tile types **A** and **B** are required to describe the structure fully, and these tessellate in stripes along the *b* axis (Figure 10b) in sequence **ABA′** (where **A′** = 180° rotation of **A**) to produce the observed 3-fold unit cell expansion. Tile **A** is a half-ordered structural fragment containing 1 × Sr site, 1 × *RE* site, and 2 × mixed sites. Tile **B** is a fully ordered structural fragment containing 2 × Sr sites and 2 × *RE* sites. **ABA′** is, therefore, 2/3-ordered. For the purpose of discussion, a fully disordered structural fragment (tile **C**) is also illustrated in Figure 10c.

The stability of **ABA′** tiling can be explained by comparison with the simpler hypothetical structures produced by its individual components **A** and **B**. It can be seen that **AA′** (= **BC**) tiling supports a wide separation of the small highly distorted *RE*2 sites with no requirement for edge-sharing between the highly distorted *RE*2 pentagonal channels, but it produces a low overall population of these sites (1/4), with half of the cations accommodated on mixed sites. This hypothetical half-ordered structure is disfavored, because it does not maximize the number of small *RE*2 sites available for the [6 + 1] coordination of RE^{3+}. In contrast, the hypothetical fully ordered structure afforded by **BB** tiling yields the highest possible population of *RE*2 sites (1/2), but it is disfavored because it requires each of these highly distorted channels to share edges (as indicated by the black outline in Figure 10c). It follows that the **ABA′** tiling is a compromise between the local bonding preferences of the small *RE* cation (which demands a high population of [6 + 1] *RE*2 sites) and the limited flexibility of the host framework, which cannot distort to support two such sites in close proximity locally. The 3 × 1 × 1 superstructure thus retains 1/3 of its A sites as mixed sites, which are larger and less distorted than *RE*2, as a buffer between the fully ordered fragments. This maximizes the *RE*2 [6 + 1] population, while keeping the Ga_3O_7 framework strain to within acceptable limits.

4.2. Competition between Ordered and Disordered Polymorphs. The trends in thermodynamic and structural stability in the $SrREGa_3O_7$ series depend strongly on the ionic radius of the *RE* cation (Figure 8). The 3 × 1 × 1 superstructure is most stable when the cation mismatch is largest: the Lu member is ordered over its entire stability range, and the Yb member has a very strong tendency toward ordering with only a narrow window between its cation-disordering and decomposition temperatures. As the *RE* ionic radius increases, the stability of the superstructure decreases until the disordered polymorph becomes dominant when *RE* is larger than Er. This trend can also be seen in the fact that $SrErGa_3O_7$ and $SrTmGa_3O_7$ are readily synthesized in their ordered polymorphs by ex situ crystallization in a muffle furnace, while in $SrDyGa_3O_7$ and $SrHoGa_3O_7$ the 3 × 1 × 1 superstructure can only be obtained by precise control of the annealing protocol (see section 3.4). $SrYGa_3O_7$ presents an intermediate case, with isolated fully ordered nanodomains forming on ex-situ crystallization. Eventually, when the *RE* radius becomes sufficiently large (*RE* = Tb), cation ordering is no longer observed. This trend is consistent with the nature of the superstructure itself: the distortion of the Ga_3O_7 framework to generate a set of highly distorted pentagonal channels that accommodate *RE* in [6 + 1] coordination requires A site cations that are small enough to occupy such a site. This implies that the formation of the 3 × 1 × 1 superstructure not only is dependent upon Sr/*RE* size mismatch but is also conditional upon the absolute size of the *RE* cation. For example, this may explain why the Ba-based melilites $BaNdGa_3O_7$ (A-site ionic radius radio r_{Ba}/r_{Nd} = 1.28, assuming 8-fold coordination) and $BaSmGa_3O_7$ (r_{Ba}/r_{Sm} = 1.32)[6] adopt the tetragonal $P\bar{4}2_1m$ structure despite having Ba/*RE* radius ratios that are similar to that of $SrYbGa_3O_7$ (r_{Sr}/r_{Yb} = 1.28), as Nd^{3+} and Sm^{3+} are too large to tolerate [6 + 1] coordination. The opposite case is presented by $CaErGa_3O_7$:[6] this compound is reported to adopt the tetragonal parent structure despite the presence of the small Er^{3+} cation, which may be because the relatively weak size contrast between Ca^{2+} and Er^{3+} (r_{Ca}/r_{Er} = 1.12) is insufficient to drive long-range ordering. These examples suggest that both a large A-cation size contrast (e.g., $AE^{2+}/RE^{3+} \approx 1.28$) and a sufficiently small *RE* cation (Dy^{3+} or smaller) must be present together to stabilize the 3 × 1 × 1 superstructure.

Alternative framework distortions that are available to small-cation melilite gallates are the 5D modulated structures of $CaLaGa_3O_7$ and $CaNdGa_3O_7$. In these compounds, a pair of modulation vectors parallel to the basal axes of the tetragonal melilite parent cell generate a set of six-, seven- and eight-coordinate A sites (versus eight-coordinate-only in the tetragonal parent phase). The population of these sites by Ca and *RE* is nonrandom, with Ca showing a preference for the

https://doi.org/10.1021/acs.inorgchem.1c01565
Inorg. Chem. 2021, 60, 12339−12354

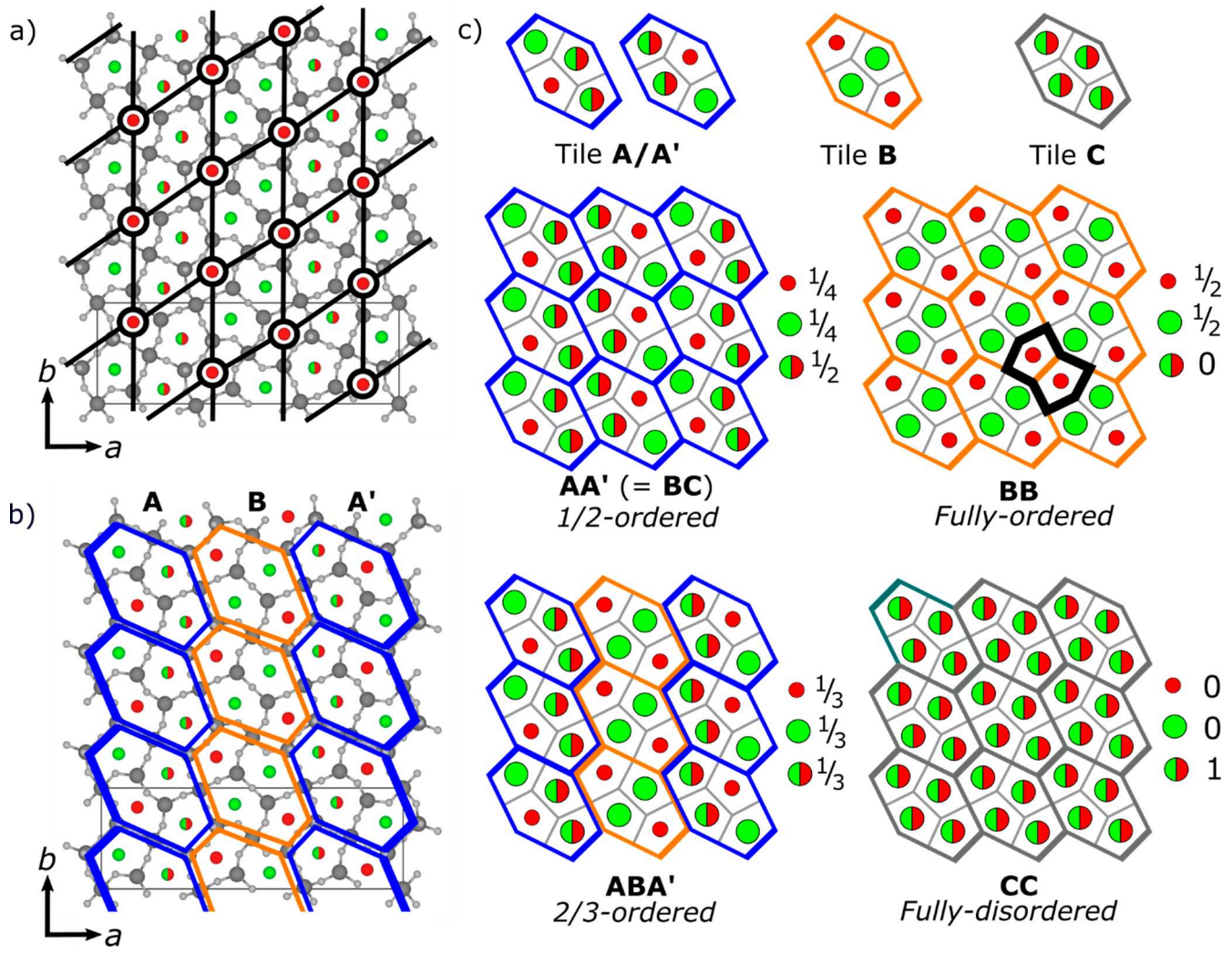

Figure 10. Long-range structural ordering in $SrYbGa_3O_7$. (a) The experimentally observed arrangement of *RE*2 sites on a pseudohexagonal sublattice which maximizes their separation. (b) The experimentally observed structure viewed as a hexagonal tiling with two tile types in a striped **ABA′** arrangement. (c) The tiles **A**, **B**, and **C** can be combined to produce the hypothetical half-ordered **AA′** (=**BC**) structure, the hypothetical fully ordered **BB** structure, and the disordered **CC** structure (parent melilite). The fractional population of each site is shown next to each structure. Note that **BB** contains pairs of edge-sharing *RE*2 sites (black outline), while **AA′** contains a low population of *RE*2 sites (1/4). The intergrowth of **AA′** and **BB** fragments to form **ABA′** eliminates *RE*2−*RE*2 edge-sharing by reducing the population of *RE*2 sites to an intermediate value (1/3).

six-coordinate sites (e.g., these sites are approximately 60% occupied by Ca and 40% by Nd in $CaNdGa_3O_7$). In these compounds, the average A-site cation radius (e.g., 1.115 Å for $CaNdGa_3O_7$) is comparable to that found in $SrYbGa_3O_7$ (1.123 Å), and this drives the distortion of the framework to reduce the average size of the channels, although the six-coordinate channels exhibited by $CaNdGa_3O_7$ (six A−O distances of 2.4−2.7 Å and two of 2.9−3.1 Å) are not as small or distorted as those found in the 3 × 1 × 1 superstructure of $SrYbGa_3O_7$(six distances of 2.22−2.52 Å and one of 2.97 Å). The relatively low contrast in ionic radii between Ca/Nd (= 1.01) may not provide a sufficient driving force for full cation ordering such as that found in the 3 × 1 × 1 superstructure (Sr/Yb = 1.28). Note that the absence of satellite peaks in the SAED patterns of quenched $SrTmGa_3O_7$ (which adopts tetragonal parent structure, as described in section 3.2; Figure S4) is consistent with the conclusions of Wei et al.,[8] who describe the relationship between structural modulation and A/B cation radius ratio: while it is close to the proposed boundary, the average A site cation radius in $SrTmGa_3O_7$ is not sufficiently small to induce modulation.

In summary, the interplay between the tetragonal parent structure, the 5D modulated structures, and the 3 × 1 × 1 superstructure is governed by the average size of the A-site cations (a small average radius is required for the modulated structures and 3 × 1 × 1 superstructures); the contrast between the A site radii (high contrast favors the 3 × 1 × 1 superstructure over the modulated structures); and the absolute ionic radius of the *RE* cation (3 × 1 × 1 superstructure is only stable if *RE* < Tb^{3+}), as shown schematically in Figure 11.

4.3. Effect of Structural Ordering on Optical Properties. The structural ordering of the $SrREGa_3O_7$ melilites leads to a decrease of their optical transmission in the bulk form (Figure S15), resulting from light scattering losses at the grain boundaries, as well-known and described in the literature.[15,53] This effect is particularly pronounced in the short wavelength region and can also affect the maximum transmission of the bulk ceramic.

https://doi.org/10.1021/acs.inorgchem.1c01565
Inorg. Chem. 2021, 60, 12339−12354

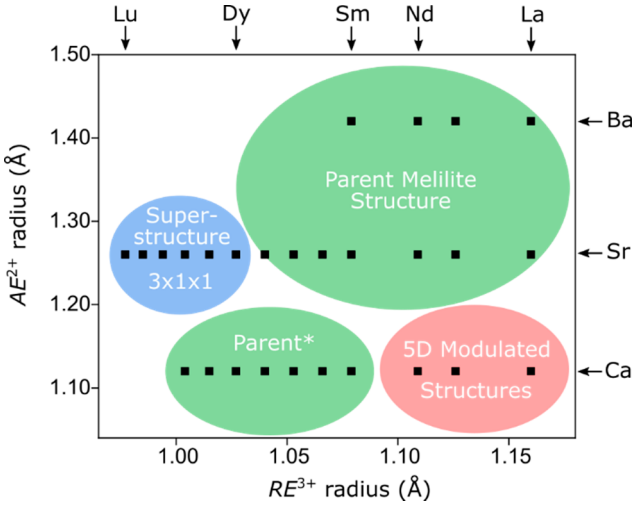

Figure 11. Phase diagram indicating the different structural orderings reported for the (*AE*,*RE*)Ga_3O_7 melilite family, according to the ionic radii of their A site cations. The parent structure and 5D-modulated structure regions have been compiled from the literature.[6,8,12] Note that the parent structure region for *AE* = Ca, marked with an asterisk, was reported prior to the discovery of structural modulation in $CaLaGa_3O_7$ and $CaNdGa_3O_7$.

The photoluminescence spectroscopic properties of *RE* doped glass ceramics have been intensively studied in the past 20 years.[54−57] It is commonly accepted that structural ordering around the *RE* ions resulting from controlled crystallization of their parent glasses can significantly modify their emission features by increasing their emission intensities, for instance. Such enhancement can be particularly strong (over 100×) when energy levels of the *RE* ions are more efficiently excited through energy transfers between the *RE* ions after their incorporation into the crystalline phase. Their migration within the material can also lead to an optimized *RE* interionic distance favorable to these energy transfers. The absorption and emission band shapes of *RE* ions in a structured environment are expected to be affected, by showing a narrower line width and more intense absorption/emission peaks, similarly to that observed in single crystals.[54−57]

Here, a clear structuration of the absorption bands of the Sr*RE*Ga_3O_7 ceramic melilites is observed (Figure S16), thus illustrating this structural ordering around the *RE* ions. Then, the increase of intensity observed in the emission spectra recorded on the $SrErGa_3O_7$ bulk ceramic (Figure S17) can be mostly attributed to the light scattering induced by grain boundaries and the experimental technique used to excite and collect emitted light. Both excitation and emission light pathways are indeed expanded in the transparent bulk ceramic in comparison with the glass. This assumption is clearly supported by the emission spectra presented in Figure 9, where the glass and ceramic melilites were finely crushed to obtain comparable grain size, minimizing therefore the scattering related to the sample textures/morphologies. The observed increase of Er^{3+} emission intensity in the ceramic vs the glass powdered melilites is then not as high as that observed in the bulk's measurement (Figure S17).

Nevertheless, as one can observe in Figure 9, there is a notable difference of spectral emission line shapes between the disordered and ordered ceramics. The strong structuration of the emission band observed in the ordered melilite ceramic can be compared, to some extent, to the sharp spectral bands of Er^{3+} in YAG single crystals and transparent ceramics,[58] indicating a long-range ordering. The structural environment of the *RE* ions is well-defined and identical across the material, resulting in these sharper band features. On the other hand, the emission line shape of the disordered ceramic is continuously broadened and very similar to that of the glass, indicating that the *RE* environment in the glass and disordered are close.

The near- and mid-infrared emission bands of the Sr*RE*Ga_3O_7 melilites make them potential candidates for the development of infrared solid state lasers and compact sources for dentistry, surgery, remote sensing, environment, and security and defense,[59−64] which should motivate further spectroscopic study of these materials in the 2−5 μm range, for example using low temperature conditions and/or time-resolved spectroscopy.

5. CONCLUSION

We have shown that the glass crystallization method can be used to synthesize a series of small rare-earth melilites Sr*RE*Ga_3O_7 (*RE* = Dy−Lu, Y) with control of their crystal structures and luminescence properties. These compounds are found to be metastable, with thermal decomposition temperatures in the range 800−850 °C for the smallest rare-earths Ho−Lu, which makes them challenging to access by conventional high-temperature ceramic methods. By tuning the crystallization conditions, we have shown that it is possible to isolate two different crystal structures for each composition. The first is a conventional tetragonal melilite structure with fully disordered A site cations, which forms readily for the larger rare-earth members *RE* = Dy−Er but can also be obtained for the smaller rare-earth members (all except *RE* = Lu) by rapid quenching from a high temperature. The second accessible crystal structure is a 3 × 1 × 1 melilite superstructure with Sr and *RE* ordered over three distinct A sites of equal multiplicity (Sr-only, *RE*-only, and mixed Sr/*RE*), which is strongly favored for the smallest rare-earth members *RE* = Tm, Yb, and Lu, but can also be isolated for the larger members Dy−Er and Y by appropriate control of heating and cooling rates during crystallization. In this structure, cation ordering is driven by the bonding requirements of the small *RE* cation, which adopts a highly distorted [6 + 1] coordination. The host Ga_3O_7 framework accommodates these [6 + 1] sites in a pseudohexagonal arrangement which maximizes their separation but limits their population to 1/3 of the A sites. This competition between the bonding demands of RE^{3+} and the flexibility of the host framework favors the retention of the mixed Sr/*RE* site (population 1/3) which acts as a buffer between fully ordered structural fragments. The 3 × 1 × 1 superstructure offers an alternative way to order small A cations in the melilite structure, which contrasts with the previously reported modulated distortions in Ca-based analogues $CaLaGa_3O_7$ and $CaNdGa_3O_7$, which are partially cation-ordered. We propose that the particular combination of average A-site size (ionic radius), A-site size contrast, and absolute size of the *RE* cation are the key parameters that control the ordering type in these structures and note that the 3 × 1 × 1 structures and modulated structures occupy two distinct regions of this parameter space. Finally, we show that the control of cationic ordering around Er^{3+} ions in $SrErGa_3O_7$ ceramics influences the luminescence properties, revealing a comparable structural environment in both disordered ceramics and glasses, while samples that adopt long-range ordering of Sr/Er in the 3 × 1 × 1 superstructure produce

https://doi.org/10.1021/acs.inorgchem.1c01565
Inorg. Chem. 2021, 60, 12339−12354

sharper spectral bands that are reminiscent of YAG single crystals or transparent ceramics. With their broad optical transmission range (extending up to 6−7 μm wavelengths) and ease of fabrication, the Sr*RE*Ga$_3$O$_7$ glass and ceramic melilites appear to be promising *RE* host materials for active photonic applications.

■ ASSOCIATED CONTENT

Supporting Information

The Supporting Information is available free of charge at https://pubs.acs.org/doi/10.1021/acs.inorgchem.1c01565.

Structure solution description; photograph of samples, in situ X-ray powder diffraction data, Rietveld refinement plots, transmission electron microscopy, stability domains and optical properties (Figures S1−S7); Refined structural parameters and interatomic distances (Tables S1−S20) (PDF)

Accession Codes

CCDC 2081671−2081676 and 2081688−2081692 contain the supplementary crystallographic data for this paper. These data can be obtained free of charge via www.ccdc.cam.ac.uk/data_request/cif, or by emailing data_request@ccdc.cam.ac.uk, or by contacting The Cambridge Crystallographic Data Centre, 12 Union Road, Cambridge CB2 1EZ, UK; fax: +44 1223 336033.

■ AUTHOR INFORMATION

Corresponding Authors

Mathieu Allix − *CNRS, CEMHTI UPR 3079, Université Orléans, F-45071 Orléans, France;* orcid.org/0000-0001-9317-1316; Email: mathieu.allix@cnrs-orleans.fr

Michael J. Pitcher − *CNRS, CEMHTI UPR 3079, Université Orléans, F-45071 Orléans, France;* orcid.org/0000-0003-2044-6774; Email: michael.pitcher@cnrs-orleans.fr

Authors

Cécile Genevois − *CNRS, CEMHTI UPR 3079, Université Orléans, F-45071 Orléans, France*

Haytem Bazzaoui − *CNRS, CEMHTI UPR 3079, Université Orléans, F-45071 Orléans, France*

Marina Boyer − *CNRS, CEMHTI UPR 3079, Université Orléans, F-45071 Orléans, France*

Sandra Ory − *CNRS, CEMHTI UPR 3079, Université Orléans, F-45071 Orléans, France*

Yannick Ledemi − *Center for Optics, Photonics and Laser, Université Laval, Quebec City, Canada*

Younès Messaddeq − *Center for Optics, Photonics and Laser, Université Laval, Quebec City, Canada;* orcid.org/0000-0002-0868-2726

Complete contact information is available at: https://pubs.acs.org/10.1021/acs.inorgchem.1c01565

Notes

The authors declare no competing financial interest.

■ ACKNOWLEDGMENTS

Use of the Advanced Photon Source at Argonne National Laboratory was supported by the U.S. Department of Energy, Office of Science, Office of Basic Energy Sciences, under Contract No. DE-AC02-06CH11357. The authors acknowledge Dr. F. Porcher for neutron experiments which were performed at the Laboratoire Léon Brillouin in Saclay (France). The authors thank the ICMN and CME laboratories (Orléans, France) for CM20 TEM and PIPS access, respectively. This project has benefited from the facilities of the Platform MACLE-CVL. This project is cofunded by the European Union, the Région - Centre Val de Loire, and the French minister of research (MESRI - DRRT). Europe is committed to the Centre-Val de Loire region with the European regional development fund (ERDF). M.P. acknowledges funding from the Agence Nationale de la Recherche (project CAPRE). The authors also acknowledge the Canadian Excellence Research Chair program (CERC) in Photonics Innovations, the Fonds de Recherche Québécois sur la Nature et les Technologies (FRQNT), and the Canadian Foundation for Innovation (CFI).

■ REFERENCES

(1) Zhang, Y.; Yin, X.; Yu, H.; Cong, H.; Zhang, H.; Wang, J.; Boughton, R. I. Growth and Piezoelectric Properties of Melilite ABC3O7 Crystals. *Cryst. Growth Des.* **2012**, *12* (2), 622−628.

(2) Karbowiak, M.; Gnutek, P.; Rudowicz, C.; Ryba-Romanowski, W. Crystal-Field Analysis for RE3+ Ions in Laser Materials: II. Absorption Spectra and Energy Levels Calculations for Nd3+ Ions Doped into SrLaGa3O7 and BaLaGa3O7 Crystals and Tm3+ Ions in SrGdGa3O7. *Chem. Phys.* **2011**, *387* (1), 69−78.

(3) Xia, H.; Feng, J.; Wang, Y.; Li, J.; Jia, Z.; Tu, C. Evaluation of Spectroscopic Properties of Er3+/Yb3+/Pr3+: SrGdGa3O7 Crystal for Use in Mid-Infrared Lasers. *Sci. Rep.* **2015**, *5* (1), 13988.

(4) Kaminskii, A. A.; Yu, H. H.; Wang, J. Y.; Zhang, Y. Y.; Zhang, H. J.; Lux, O.; Rhee, H.; Eichler, H. J.; Hanuza, J.; Yoneda, H.; Shirakawa, A. Tetragonal SrGdGa3O7and SrLaGa3O7—Novel SRS-Active Crystals. *Laser Phys.* **2014**, *24* (8), 085803.

(5) Zhang, X.; Zhang, J.; Liang, L.; Su, Q. Luminescence of SrGdGa3O7:RE3+(RE = Eu, Tb) Phosphors and Energy Transfer from Gd3+ to RE3+. *Mater. Res. Bull.* **2005**, *40* (2), 281−288.

(6) Skakle, J. M. S.; Herd, R. Crystal Chemistry of (RE, A)2M3O7 Compounds (RE = Y, Lanthanide; A = Ba, Sr, Ca; M = Al, Ga). *Powder Diffr.* **1999**, *14* (3), 195−202.

(7) Boyer, M.; Carrion, A. J. F.; Ory, S.; Becerro, A. I.; Villette, S.; Eliseeva, S. V.; Petoud, S.; Aballea, P.; Matzen, G.; Allix, M. Transparent Polycrystalline SrREGa$_3$O$_7$ Melilite Ceramics: Potential Phosphors for Tuneable Solid State Lighting. *J. Mater. Chem. C* **2016**, *4* (15), 3238−3247.

(8) Wei, F.; Baikie, T.; An, T.; Kloc, C.; Wei, J.; White, T. Crystal Chemistry of Melilite [CaLa]2[Ga]2[Ga2O7]2: A Five Dimensional Solid Electrolyte. *Inorg. Chem.* **2012**, *51* (10), 5941−5949.

(9) Seifert, F.; Czank, M.; Simons, B.; Schmahl, W. A Commensurate-Incommensurate Phase Transition in Iron-Bearing Åkermanites. *Phys. Chem. Miner.* **1987**, *14* (1), 26−35.

(10) Hemingway, B. S.; Evans, H. T.; Nord, G. L.; Haselton, H. T. Akermanite: Phase Transitions in Heat Capacity and Thermal Expansion and Revised Thermodynamic Data. 10. *Canadian Mineralogist* **1986**, *24* (3), 425.

(11) Hagiya, K.; Ohmasa, M.; Iishi, K. The Modulated Structure of Synthetic Co-Åkermanite, Ca2CoSi2O7. *Acta Crystallogr., Sect. B: Struct. Sci.* **1993**, *49* (2), 172−179.

(12) Wei, F.; Baikie, T.; An, T.; Schreyer, M.; Kloc, C.; White, T. J. Five-Dimensional Incommensurate Structure of the Melilite Electrolyte [CaNd]2[Ga]2[Ga2O7]2. *J. Am. Chem. Soc.* **2011**, *133* (38), 15200−15211.

(13) Xiao, Z.; Yu, S.; Li, Y.; Ruan, S.; Kong, L. B.; Huang, Q.; Huang, Z.; Zhou, K.; Su, H.; Yao, Z.; Que, W.; Liu, Y.; Zhang, T.; Wang, J.; Liu, P.; Shen, D.; Allix, M.; Zhang, J.; Tang, D. Materials Development and Potential Applications of Transparent Ceramics: A Review. *Mater. Sci. Eng., R* **2020**, *139*, 100518.

(14) Won, R. Ceramic Future. *Nat. Photonics* **2008**, *2* (4), 216−217.

(15) Ikesue, A.; Aung, Y. L. Ceramic Laser Materials. *Nat. Photonics* **2008**, *2* (12), 721−727.

(16) Krell, A.; Klimke, J.; Hutzler, T. Transparent Compact Ceramics: Inherent Physical Issues. *Opt. Mater.* **2009**, *31* (8), 1144−1150.
(17) Chen, S.; Wu, Y. New Opportunities for Transparent Ceramics. *Am. Ceram. Soc. Bull.* **2013**, *92* (2), 32−37.
(18) Goldstein, A.; Krell, A. Transparent Ceramics at 50: Progress Made and Further Prospects. *J. Am. Ceram. Soc.* **2016**, *99* (10), 3173−3197.
(19) Apetz, R.; van Bruggen, M. P. B. Transparent Alumina: A Light-Scattering Model. *J. Am. Ceram. Soc.* **2003**, *86* (3), 480−486.
(20) Messing, G. L.; Stevenson, A. J. Toward Pore-Free Ceramics. *Science* **2008**, *322* (5900), 383−384.
(21) Allix, M.; Alahrache, S.; Fayon, F.; Suchomel, M.; Porcher, F.; Cardinal, T.; Matzen, G. Highly Transparent $BaAl_4O7$ Polycrystalline Ceramic Obtained by Full Crystallization from Glass. *Adv. Mater.* **2012**, *24* (41), 5570−5575.
(22) Al Saghir, K.; Chenu, S.; Veron, E.; Fayon, F.; Suchomel, M.; Genevois, C.; Porcher, F.; Matzen, G.; Massiot, D.; Allix, M. Transparency through Structural Disorder: A New Concept for Innovative Transparent Ceramics. *Chem. Mater.* **2015**, *27* (2), 508−514.
(23) Bertrand, A.; Carreaud, J.; Chenu, S.; Allix, M.; Véron, E.; Duclère, J.-R.; Launay, Y.; Hayakawa, T.; Genevois, C.; Brisset, F.; Célarié, F.; Thomas, P.; Delaizir, G. Scalable and Formable Tellurite-Based Transparent Ceramics for Near Infrared Applications. *Adv. Opt. Mater.* **2016**, *4* (10), 1482−1486.
(24) Irifune, T.; Kawakami, K.; Arimoto, T.; Ohfuji, H.; Kunimoto, T.; Shinmei, T. Pressure-Induced Nano-Crystallization of Silicate Garnets from Glass. *Nat. Commun.* **2016**, *7* (1), 13753.
(25) Ma, X.; Li, X.; Li, J.; Genevois, C.; Ma, B.; Etienne, A.; Wan, C.; Véron, E.; Peng, Z.; Allix, M. Pressureless Glass Crystallization of Transparent Yttrium Aluminum Garnet-Based Nanoceramics. *Nat. Commun.* **2018**, *9* (1), 1−9.
(26) Boyer, M.; Yang, X.; Fernandez Carrion, A. J.; Wang, Q.; Veron, E.; Genevois, C.; Hennet, L.; Matzen, G.; Suard, E.; Thiaudiere, D.; Castro, C.; Pelloquin, D.; Kong, L. B.; Kuang, X.; Allix, M. First Transparent Oxide Ion Conducting Ceramics Synthesized by Full Crystallization from Glass. *J. Mater. Chem. A* **2018**, *6* (13), 5276−5289.
(27) Alahraché, S.; Al Saghir, K.; Chenu, S.; Véron, E.; De Sousa Meneses, D.; Becerro, A. I.; Ocaña, M.; Moretti, F.; Patton, G.; Dujardin, C.; Cussó, F.; Guin, J.-P.; Nivard, M.; Sangleboeuf, J.-C.; Matzen, G.; Allix, M. Perfectly Transparent $Sr_3Al_2O_6$ Polycrystalline Ceramic Elaborated from Glass Crystallization. *Chem. Mater.* **2013**, *25* (20), 4017−4024.
(28) Wisniewski, W.; Fernández-Carrión, A. J.; Schöppe, P.; Rüssel, C.; Allix, M. Oriented Nucleation and Crystal Growth in SrO-Al_2O_3-SiO_2 Tectosilicate Glasses. *CrystEngComm* **2018**, *20* (25), 3455−3466.
(29) Boyer, M.; Alahraché, S.; Genevois, C.; Licheron, M.; Lefevre, F.-X.; Castro, C.; Bonnefont, G.; Patton, G.; Moretti, F.; Dujardin, C.; Matzen, G.; Allix, M. Enhanced Transparency through Second Phase Crystallization in BaAl4O7 Scintillating Ceramics. *Cryst. Growth Des.* **2016**, *16* (1), 386−395.
(30) Alahraché, S.; Allix, M.; Matzen, G.; Millot, F.; Licheron, M.; Cardinal, T.; Garcia, A.; Saghir, K. A. Verres, Vitroceramiques et Ceramiques d'aluminates Transparents. WO2013079707 A1, 2013.
(31) Fernandez-Carrion, A. J.; Al Saghir, K.; Veron, E.; Becerro, A. I.; Porcher, F.; Wisniewski, W.; Matzen, G.; Fayon, F.; Allix, M. Local Disorder and Tunable Luminescence in Sr1-x/2Al2-XSixO4 ($0.2 \leq x \leq 0.5$) Transparent Ceramics. *Inorg. Chem.* **2017**, *56* (23), 14446−14458.
(32) Rousse, G.; Baptiste, B.; Lelong, G. Crystal Structures of $Li_6B_4O_9$ and $Li_3B_{11}O_{18}$ and Application of the Dimensional Reduction Formalism to Lithium Borates. *Inorg. Chem.* **2014**, *53* (12), 6034−6041.
(33) Weber, J. K. R. The Containerless Synthesis of Glass. *Int. J. Appl. Glass Sci.* **2010**, *1* (3), 248−256.
(34) Coelho, A. A. TOPAS and TOPAS-Academic: An Optimization Program Integrating Computer Algebra and Crystallographic Objects Written in C++. *J. Appl. Crystallogr.* **2018**, *51* (1), 210−218.
(35) Rosenflanz, A.; Frey, M.; Endres, B.; Anderson, T.; Richards, E.; Schardt, C. Bulk Glasses and Ultrahard Nanoceramics Based on Alumina and Rare-Earth Oxides. *Nature* **2004**, *430* (7001), 761−764.
(36) Boultif, A.; Louër, D. Indexing of Powder Diffraction Patterns for Low-Symmetry Lattices by the Successive Dichotomy Method. *J. Appl. Crystallogr.* **1991**, *24* (6), 987−993.
(37) Oszlányi, G.; Sütö, A. Ab Initio Structure Solution by Charge Flipping. *Acta Crystallogr., Sect. A: Found. Crystallogr.* **2004**, *60* (2), 134−141.
(38) Oszlányi, G.; Sütö, A. Ab Initio Structure Solution by Charge Flipping. II. Use of Weak Reflections. *Acta Crystallogr., Sect. A: Found. Crystallogr.* **2005**, *61* (1), 147−152.
(39) Petříček, V.; Dušek, M.; Palatinus, L. Crystallographic Computing System JANA2006: General Features. *Z. Kristallogr. - Cryst. Mater.* **2014**, *229* (5), 345−352.
(40) Palatinus, L.; Chapuis, G. SUPERFLIP - a Computer Program for the Solution of Crystal Structures by Charge Flipping in Arbitrary Dimensions. *J. Appl. Crystallogr.* **2007**, *40* (4), 786−790.
(41) Baerlocher, C.; McCusker, L. B.; Palatinus, L. Charge Flipping Combined with Histogram Matching to Solve Complex Crystal Structures from Powder Diffraction Data. *Z. Kristallogr.* **2007**, *222*, 47−53.
(42) Steins, M.; Schmitz, W.; Uecker, R.; Doerschel, J. Crystal Structure of Strontium Lanthanum Trigallium Heptoxide, (Sr0.5La0.5)2Ga3O7. *Z. Kristallogr. - New Cryst. Struct.* **1997**, *212* (1), 76−76.
(43) Pennycook, S. J.; Boatner, L. A. Chemically Sensitive Structure-Imaging with a Scanning Transmission Electron Microscope. *Nature* **1988**, *336* (6199), 565−567.
(44) Hartel, P.; Rose, H.; Dinges, C. Conditions and Reasons for Incoherent Imaging in STEM. *Ultramicroscopy* **1996**, *63* (2), 93−114.
(45) Pennycook, S. J.; Jesson, D. E. High-Resolution Z-Contrast Imaging of Crystals. *Ultramicroscopy* **1991**, *37* (1), 14−38.
(46) Stadelmann, P. JEMS. https://www.jems-swiss.ch/ (accessed May 4, 2020).
(47) Van Aert, S.; Verbeeck, J.; Erni, R.; Bals, S.; Luysberg, M.; Dyck, D. V.; Tendeloo, G. V. Quantitative Atomic Resolution Mapping Using High-Angle Annular Dark Field Scanning Transmission Electron Microscopy. *Ultramicroscopy* **2009**, *109* (10), 1236−1244.
(48) Martinez, G. T.; Rosenauer, A.; De Backer, A.; Verbeeck, J.; Van Aert, S. Quantitative Composition Determination at the Atomic Level Using Model-Based High-Angle Annular Dark Field Scanning Transmission Electron Microscopy. *Ultramicroscopy* **2014**, *137*, 12−19.
(49) De Sousa Meneses, D. Focus - Curve fitting software. https://www.cemhti.cnrs-orleans.fr/pot/software/focus.html (accessed Apr 7, 2020).
(50) Scott, M. A.; Russell, D. L.; Henderson, B.; Han, T. P. J.; Gallagher, H. G. Crystal growth and optical characterisation of novel $3d^2$ ion laser hosts. *J. Cryst. Growth* **1998**, *183* (3), 366−376.
(51) O'Keefe, M.; Hyde, B. G.; Anderson, J. S. Plane Nets in Crystal Chemistry. *Philos. Trans. R. Soc. London Ser. Math. Phys. Sci.* **1980**, *295* (1417), 553−618.
(52) Fan, J.; Sarou-Kanian, V.; Yang, X.; Diaz-Lopez, M.; Fayon, F.; Kuang, X.; Pitcher, M. J.; Allix, M. $La_2Ga_3O_{7.5}$: A Metastable Ternary Melilite with a Super-Excess of Interstitial Oxide Ions Synthesized by Direct Crystallization of the Melt. *Chem. Mater.* **2020**, *32* (20), 9016−9025.
(53) Hendy, S. Light Scattering in Transparent Glass Ceramics. *Appl. Phys. Lett.* **2002**, *81* (7), 1171−1173.
(54) Fedorov, P. P.; Luginina, A. A.; Popov, A. I. Transparent Oxyfluoride Glass Ceramics. *J. Fluorine Chem.* **2015**, *172*, 22−50.
(55) Neuville, D. R.; Cormier, L.; Caurant, D.; Montagne, L. *From Glass to Crystal*; EDP Sciences, 2021.

(56) Liu, X.; Zhou, J.; Zhou, S.; Yue, Y.; Qiu, J. Transparent Glass-Ceramics Functionalized by Dispersed Crystals. *Prog. Mater. Sci.* **2018**, *97*, 38−96.
(57) de Pablos-Martín, A.; Durán, A.; Pascual, M. J. Nanocrystallisation in Oxyfluoride Systems: Mechanisms of Crystallisation and Photonic Properties. *Int. Mater. Rev.* **2012**, *57* (3), 165−186.
(58) Yang, H.; Zhang, J.; Luo, D.; Lin, H.; Shen, D.; Tang, D. Novel Transparent Ceramics for Solid-State Lasers. *High Power Laser Sci. Eng.* **2013**, *1* (3−4), 138−147.
(59) Verma, S. K.; Maheshwari, S.; Singh, R. K.; Chaudhari, P. K. Laser in Dentistry: An Innovative Tool in Modern Dental Practice. *Natl. J. Maxillofac. Surg.* **2012**, *3* (2), 124−132.
(60) Jean, B.; Bende, T. Mid-IR Laser Applications in Medicine. In *Solid-State Mid-Infrared Laser Sources*; Sorokina, I. T., Vodopyanov, K. L., Eds.; Topics in Applied Physics; Springer: Berlin, 2003; pp 530−565. DOI: 10.1007/3-540-36491-9_12.
(61) Waynant, R. W.; Ilev, I. K.; Gannot, I. Mid-Infrared Laser Applications in Medicine and Biology. *Philos. Trans. R. Soc., A* **2001**, *359* (1780), 635−644.
(62) Walsh, B. M.; Lee, H. R.; Barnes, N. P. Mid Infrared Lasers for Remote Sensing Applications. *J. Lumin.* **2016**, *169*, 400−405.
(63) Werle, P.; Slemr, F.; Maurer, K.; Kormann, R.; Mücke, R.; Jänker, B. Near- and Mid-Infrared Laser-Optical Sensors for Gas Analysis. *Opt. Lasers Eng.* **2002**, *37* (2), 101−114.
(64) Affan Ahmed, S.; Mohsin, M.; Zubair Ali, S. M. Survey and Technological Analysis of Laser and Its Defense Applications. *Def. Technol.* **2021**, *17* (2), 583−592.

https://doi.org/10.1021/acs.inorgchem.1c01565
Inorg. Chem. 2021, 60, 12339−12354

Supporting Information for "Emergence of A-site Cation Order in the Small Rare-Earth Melilites Sr*RE*Ga$_3$O$_7$ (*RE* = Dy-Lu, Y)"

Cécile Genevois[a], Haytem Bazzaoui[a], Marina Boyer[a], Sandra Ory[a], Yannick Ledemi[b], Younès Messaddeq[b], Michael J. Pitcher[a*] and Mathieu Allix[a*]

[a] CNRS, CEMHTI UPR 3079, Univ. Orléans, F-45071 Orléans, France. E-mail: mathieu.allix@cnrs-orleans.fr, michael.pitcher@cnrs-orleans.fr

[b] Center for Optics, Photonics and Laser, Université Laval, Quebec City, Canada

Contents:

Structure solution of $SrYbGa_3O_7$ from powder diffraction data

Using the unit cell and space group derived by powder indexing and SAED (a = 23.7 Å x b = 7.9 Å x c = 5.2 Å, $P2_12_12$; see Figure 1 of main manuscript), a Le Bail refinement was performed on SPD data, followed by charge flipping (implemented in Jana2006 through the Superflip software) to obtain the cation coordinates of a starting structural model. Convergence was rapidly achieved and eight chemically-plausible cation positions were identified, consistent with the melilite structure (7x 4c positions corresponding to three Yb/Sr sites and four Ga sites, and 1x 2a position corresponding to a Ga site). At this stage, A sites were considered to be occupied 50/50 by Yb/Sr. Using this cation-only model, a combined Rietveld refinement was performed on both SPD and NPD data by refining the occupancies of the three Yb/Sr cationic sites (subject to a compositional constraint to an overall stoichiometry of $SrYbGa_3$, and individual constraints to keep each site fully occupied by cations). Fourier difference maps were then calculated to determine the oxygen positions by an iterative process: eleven oxygen sites were thus localized on residual density peaks situated at 1.8-1.9 Å of Ga and 2.2-2.7 Å of Yb/Sr cations, completing the structural model. Rietveld refinement then proceeded as described in the main manuscript (section 3.2).

Table S1. Refined anisotropic thermal parameters obtained from SPD and NPD data collected at room temperature on cation-ordered $SrYbGa_3O_7$ ($P2_12_12$ space group, a = 23.70164(7) Å, b = 7.92109(3) Å and c = 5.21162(2) Å). This materials supplements Table 1 of the main manuscript.

	U11	U22	U33	U12	U13	U23
Yb1/Sr1	0.0086(3)	0.0089(3)	0.0049(4)	-0.0022(3)	-0.0019(3)	-0.0007(3)
Yb2	0.0118(3)	0.0179(3)	0.0044(2)	0.0010(2)	-0.0028(3)	-0.0057(2)
Sr3	0.0170(6)	0.0065(5)	0.0055(6)	0.0065(4)	-0.0017(5)	-0.0002(6)

Table S2. Refined Ga-O interatomic distances obtained from cation-ordered $SrYbGa_3O_7$ from SPD and NPD data. This material supplements Table 2 of the main manuscript.

Bond	Length(Å)	Bond	Length(Å)	Bond	Length(Å)
Ga1-O4	1.765(3)	Ga3-O9	1.816(4)	Ga5-O5	1.807(3)
Ga1-O6	1.818(2)	Ga3-O7	1.820(4)	Ga5-O11	1.813(3)
Ga1-O1	1.871(4)	Ga3-O10	1.835(4)	Ga5-O8	1.836(4)
Ga1-O2	1.880(3)	Ga3-O2	1.846(3)	Ga5-O10	1.854(4)
Ga2-O8	1.833(4)	Ga4-O3	1.808(4)		
Ga2-O8	1.833(4)	Ga4-O11	1.867(3)		
Ga2-O1	1.864(4)	Ga4-O7	1.867(3)		
Ga2-O1	1.864(4)	Ga4-O9	1.868(4)		

Table S3. Refined structural parameters obtained from SPD data collected at room temperature on cation-ordered $SrTmGa_3O_7$ ($P2_12_12$ space group, a = 23.74405(8) Å, b = 7.92635(3) Å and c = 5.21619(2) Å).

Atom	Site	x	Y	z	Occ	U_{iso}
Tm1/ Sr1	4c	0.21996(3)	0.14458(8)	0.49507(13)	0.5/0.5	0.0060(2)
Tm2	4c	0.38119(2)	0.31222(6)	0.45491(10)	1	0.0069(1)
Sr3	4c	0.05781(4)	0.33948(13)	0.5090(2)	1	0.0086(3)
Ga1	4c	0.44927(5)	0.14431(16)	0.0101(3)	1	0.0051(3)
Ga2	2a	0	0	0.9800(4)	1	0.0048(4)
Ga3	4c	0.17290(6)	0.48152(15)	0.9992(3)	1	0.0036(3)
Ga4	4c	0.28920(5)	0.33617(15)	0.9518(2)	1	0.0029(3)
Ga5	4c	0.11827(6)	0.12410(14)	0.0312(2)	1	0.0043(3)
O1	4c	0.4575(3)	0.3414(10)	0.2031(14)	1	0.0129(6)[a]
O2	4c	0.3860(3)	0.0699(9)	0.1978(14)	1	0.0129(6)[a]
O3	4c	0.2907(3)	0.3382(10)	0.3003(12)	1	0.0129(6)[a]
O4	4c	0.4439(3)	0.1450(10)	0.6755(13)	1	0.0129(6)[a]
O5	4c	0.1282(3)	0.1206(9)	0.6855(11)	1	0.0129(6)[a]
O6	2b	0.5	0	0.1570(18)	1	0.0129(6)[a]
O7	4c	0.2258(3)	0.4230(10)	0.7708(17)	1	0.0129(6)[a]
O8	4c	0.0482(3)	0.1424(10)	0.1656(14)	1	0.0129(6)[a]
O9	4c	0.2982(3)	0.1308(10)	0.7806(17)	1	0.0129(6)[a]
O10	4c	0.1519(3)	0.3020(10)	0.1986(14)	1	0.0129(6)[a]
O11	4c	0.3467(3)	0.4558(10)	0.7984(12)	1	0.0129(6)[a]

[a]: constrained to refine to the same U_{iso} values

Table S4. Refined interatomic distances ($d_{A\text{-}O}$ up to 3 Å) obtained from cation-ordered $SrTmGa_3O_7$ from SPD data.

Bond	Length(Å)	Bond	Length(Å)	Bond	Length(Å)
(Sr/Tm)1-O9	2.384(8)	Tm2-O1	2.249(7)	Sr3-O8	2.387(7)
(Sr/Tm)1-O5	2.402(8)	Tm2-O11	2.276(7)	Sr3-O6	2.557(6)
(Sr/Tm)1-O3	2.493(7)	Tm2-O4	2.302(8)	Sr3-O5	2.579(8)
(Sr/Tm)1-O10	2.562(7)	Tm2-O3	2.303(7)	Sr3-O4	2.606(8)
(Sr/Tm)1-O7	2.582(8)	Tm2-O2	2.345(7)	Sr3-O2	2.731(7)
(Sr/Tm)1-O7	2.638(8)	Tm2-O5	2.561(7)	Sr3-O10	2.774(7)
(Sr/Tm)1-O11	2.662(7)	Tm2-O9	2.973(8)	Sr3-O4	2.874(8)
(Sr/Tm)1-O3	2.665(8)				
Ga1-O4	1.750(7)	Ga3-O9	1.786(8)	Ga5-O11	1.806(7)
Ga1-O6	1.829(4)	Ga3-O7	1.792(8)	Ga5-O8	1.811(7)
Ga1-O1	1.869(8)	Ga3-O10	1.832(8)	Ga5-O5	1.819(6)
Ga1-O2	1.888(8)	Ga3-O2	1.871(8)	Ga5-O10	1.840(8)
Ga2-O1	1.874(8)	Ga4-O3	1.818(6)		
Ga2-O1	1.874(8)	Ga4-O11	1.844(8)		
Ga2-O8	1.877(8)	Ga4-O9	1.869(8)		
Ga2-O8	1.877(8)	Ga4-O7	1.906(8)		

Tables S5. Refined structural parameters obtained from SPD data collected at room temperature on cation-ordered $SrErGa_3O_7$ ($P2_12_12$ space group, a = 23.7790(1) Å, b = 7.93013(4) Å and c = 5.22786(2) Å).

Atom	Site	x	y	z	Occ	U_{iso}
Er1/ Sr1	4c	2.400(12)	2.400(12)	2.400(12)	0.504(3)/0.496(3)	0.0081(3)
Er2/ Sr2	4c	2.431(12)	2.431(12)	2.431(12)	0.863(3)/0.137(3)	0.0057(2)
Sr3/Er3	4c	0.05550(6)	0.33884(18)	0.5025(3)	0.868(4)/0.132(4)	0.0114(4)
Ga1	4c	0.44958(8)	0.1445(2)	0.0139(3)	1	0.0041(4)
Ga2	2a	0	0	0.9854(7)	1	0.0045(6)
Ga3	4c	0.17125(8)	0.4862(2)	0.0016(6)	1	0.0035(3)
Ga4	4c	0.28803(7)	0.3416(2)	0.9573(3)	1	0.0033(4)
Ga5	4c	0.11858(9)	0.1279(2)	0.0331(3)	1	0.0036(4)
O1	4c	0.4580(5)	0.3503(15)	0.195(2)	1	0.0112(7)[a]
O2	4c	0.3834(5)	0.0776(13)	0.206(2)	1	0.0112(7)[a]
O3	4c	0.2903(4)	0.3408(14)	0.3119(17)	1	0.0112(7)[a]
O4	4c	0.4425(5)	0.1491(15)	0.6797(18)	1	0.0112(7)[a]
O5	4c	0.1279(6)	0.1195(13)	0.6936(15)	1	0.0112(7)[a]
O6	2b	0.5	0	0.152(2)	1	0.0112(7)[a]
O7	4c	0.2276(5)	0.4305(14)	0.768(2)	1	0.0112(7)[a]
O8	4c	0.0489(5)	0.1335(14)	0.170(2)	1	0.0112(7)[a]
O9	4c	0.2989(5)	0.1465(15)	0.785(2)	1	0.0112(7)[a]
O10	4c	0.1491(5)	0.3086(14)	0.195(2)	1	0.0112(7)[a]
O11	4c	0.3441(5)	0.4570(13)	0.7905(16)	1	0.0112(7)[a]

[a]: constrained to refine to the same U_{iso} values

Table S6. Refined interatomic distances ($d_{A\text{-}O}$ up to 3 Å) obtained from cation-ordered $SrErGa_3O_7$ from SPD data.

Bond	Length(Å)	Bond	Length(Å)	Bond	Length(Å)
(Sr/Er)1-O9	2.400(12)	Er2-O11	2.245(9)	Sr3-O8	2.387(11)
(Sr/Er)1-O5	2.431(12)	Er2-O4	2.272(11)	Sr3-O6	2.576(9)
(Sr/Er)1-O3	2.454(11)	Er2-O1	2.298(11)	Sr3-O4	2.639(12)
(Sr/Er)1-O7	2.553(12)	Er2-O2	2.310(11)	Sr3-O5	2.643(12)
(Sr/Er)1-O10	2.634(11)	Er2-O3	2.316(10)	Sr3-O10	2.756(11)
(Sr/Er)1-O11	2.637(10)	Er2-O5	2.548(11)	Sr3-O2	2.832(11)
(Sr/Er)1-O7	2.639(12)	Er2-O9	2.929(12)	Sr3-O4	2.852(12)
(Sr/Er)1-O3	2.658(11)				
Ga1-O4	1.756(10)	Ga3-O10	1.812(11)	Ga5-O5	1.790(8)
Ga1-O6	1.809(6)	Ga3-O9	1.834(12)	Ga5-O8	1.805(11)
Ga1-O1	1.897(12)	Ga3-O2	1.842(12)	Ga5-O10	1.816(11)
Ga1-O2	1.941(11)	Ga3-O7	1.866(12)	Ga5-O11	1.864(10)
Ga2-O1	1.816(12)	Ga4-O9	1.809(12)		
Ga2-O1	1.816(12)	Ga4-O11	1.837(10)		
Ga2-O8	1.845(12)	Ga4-O3	1.855(9)		
Ga2-O8	1.845(12)	Ga4-O7	1.882(12)		

Tables S7. Refined structural parameters obtained from SPD data collected at room temperature on cation-ordered $SrHoGa_3O_7$ from SPD data ($P2_12_12$ space group, a = 23.8034(1) Å, b = 7.93800(4) Å and c = 5.23828(2) Å).

Atom	Site	x	y	z	Occ	U_{iso}
Ho1/ Sr1	4c	0.21976(4)	0.14841(10)	0.49652(14)	0.499(2)/0.501(2)	0.0080(2)
Ho2/Sr2	4c	0.38174(3)	0.31544(8)	0.45774(11)	0.924(2)/0.076(2)	0.0072(2)
Sr3/ Ho3	4c	0.05660(5)	0.33980(16)	0.5059(2)	0.924(3)/0.076(3)	0.0146(3)
Ga1	4c	0.44942(6)	0.14477(19)	0.0122(3)	1	0.0072(4)
Ga2	2a	0	0	0.9842(5)	1	0.0078(4)
Ga3	4c	0.17200(6)	0.48408(18)	0.0028(4)	1	0.0058(3)
Ga4	4c	0.28820(6)	0.33958(18)	0.9549(3)	1	0.0052(3)
Ga5	4c	0.11873(7)	0.12693(18)	0.0329(2)	1	0.0051(3)
O1	4c	0.4568(4)	0.3471(12)	0.2000(17)	1	0.0133(6)[a]
O2	4c	0.3862(4)	0.0749(11)	0.1940(17)	1	0.0133(6)[a]
O3	4c	0.2893(4)	0.3454(12)	0.3003(12)	1	0.0133(6)[a]
O4	4c	0.4412(4)	0.1512(12)	0.6774(13)	1	0.0133(6)[a]
O5	4c	0.1263(5)	0.1161(11)	0.6915(11)	1	0.0133(6)[a]
O6	2b	0.5	0	0.1534(19)	1	0.0133(6)[a]
O7	4c	0.2258(4)	0.4286(11)	0.7706(18)	1	0.0133(6)[a]
O8	4c	0.0489(4)	0.1336(11)	0.1682(16)	1	0.0133(6)[a]
O9	4c	0.2975(4)	0.1355(12)	0.7869(19)	1	0.0133(6)[a]
O10	4c	0.1509(4)	0.3098(12)	0.2047(16)	1	0.0133(6)[a]
O11	4c	0.3455(4)	0.4564(10)	0.7999(12)	1	0.0133(6)[a]

[a]: constrained to refine to the same U_{iso} values

Table S8. Refined interatomic distances ($d_{A\text{-}O}$ up to 3 Å) obtained in cation-ordered $SrHoGa_3O_7$ from SPD data.

Bond	Length(Å)	Bond	Length(Å)	Bond	Length(Å)
(Sr/Ho)1-O9	2.398(9)	Ho2-O4	2.242(9)	Sr3-O8	2.417(9)
(Sr/Ho)1-O5	2.461(10)	Ho2-O1	2.253(9)	Sr3-O6	2.572(7)
(Sr/Ho)1-O3	2.498(9)	Ho2-O11	2.282(7)	Sr3-O5	2.617(9)
(Sr/Ho)1-O10	2.582(9)	Ho2-O2	2.359(8)	Sr3-O4	2.652(10
(Sr/Ho)1-O7	2.585(9)	Ho2-O3	2.362(9)	Sr3-O10	2.754(8)
(Sr/Ho)1-O3	2.639(9)	Ho2-O5	2.519(8)	Sr3-O2	2.794(9)
(Sr/Ho)1-O7	2.651(9)	Ho2-O9	3.006(9)	Sr3-O4	2.911(9)
(Sr/Ho)1-O11	2.673(8)				
Ga1-O4	1.765(7)	Ga3-O9	1.785(9)	Ga5-O5	1.799(6)
Ga1-O6	1.821(5)	Ga3-O10	1.812(9)	Ga5-O8	1.808(9)
Ga1-O2	1.865(9)	Ga3-O7	1.820(10)	Ga5-O11	1.823(8)
Ga1-O1	1.892(10)	Ga3-O2	1.871(9)	Ga5-O10	1.872(9)
Ga2-O8	1.846(9)	Ga4-O3	1.810(7)		
Ga2-O8	1.846(9)	Ga4-O11	1.838(8)		
Ga2-O1	1.861(9)	Ga4-O9	1.857(9)		
Ga2-O1	1.861(9)	Ga4-O7	1.907(9)		

Tables S9. Refined structural parameters obtained from SPD data collected at room temperature on cation-ordered $SrLuGa_3O_7$ ($P2_12_12$ space group, a = 23.6710(2) Å, b = 7.91556(8) Å and c = 5.20516(4) Å). Note that the oxide x, y, z coordinates and U values were subjected to soft restraints to keep them close to the corresponding values from $SrYbGa_3O_7$ (see main text).

[a], [b], [c]: constrained to refine to the same U_{iso} values

Atom	Site	x	y	z	Occ	U_{iso}
Lu1/Sr1	4c	0.22070(6)	0.14247(18)	0.4963(3)	0.520(4)/0.480(4)	0.0119(4)
Lu2/Sr2	4c	0.38160(5)	0.31180(14)	0.4570(2)	0.891(3)/0.109(3)	0.0111(4)
Sr3/Lu3	4c	0.0496(2)	0.3225(7)	0.5062(14)	0.455(2)/0.045(2)	0.0126(9)[a]
Sr3/Lu3'	4c	0.0640(2)	0.3547(6)	0.5045(15)	0.455(2)/0.045(2)	0.0126(9)[a]
Ga1	4c	0.44881(10)	0.1435(3)	0.0138(6)	1	0.0067(2)[b]
Ga2	2a	0	0	0.9723(9)	1	0.0067(2)[b]
Ga3	4c	0.17413(12)	0.4805(3)	0.9982(8)	1	0.0067(2)[b]
Ga4	4c	0.28907(10)	0.3346(3)	0.9555(5)	1	0.0067(2)[b]
Ga5	4c	0.11930(12)	0.1239(3)	0.0287(5)	1	0.0067(2)[b]
O1	4c	0.4540(7)	0.341(2)	0.201(3)	1	0.0285(13)[c]
O2	4c	0.3857(7)	0.070(2)	0.182(3)	1	0.0285(13)[c]
O3	4c	0.2947(6)	0.337(2)	0.305(3)	1	0.0285(13)[c]
O4	4c	0.4404(7)	0.148(2)	0.690(3)	1	0.0285(13)[c]
O5	4c	0.1266(8)	0.114(2)	0.701(2)	1	0.0285(13)[c]
O6	2b	0.5	0	0.149(4)	1	0.0285(13)[c]
O7	4c	0.2271(8)	0.435(2)	0.776(4)	1	0.0285(13)[c]
O8	4c	0.0490(6)	0.140(2)	0.160(3)	1	0.0285(13)[c]
O9	4c	0.2953(7)	0.131(2)	0.774(4)	1	0.0285(13)[c]
O10	4c	0.1519(7)	0.296(2)	0.199(3)	1	0.0285(13)[c]
O11	4c	0.3483(7)	0.446(2)	0.790(2)	1	0.0285(13)[c]

Table S10. Interatomic distances ($d_{A\text{-}O}$ up to 3 Å) obtained in cation-ordered $SrLuGa_3O_7$ from SPD data.

Bond	Length(Å)	Bond	Length(Å)	Bond	Length(Å)
(Lu1/Sr1)-O9	2.284(19)	(Lu2/Sr2)-O11	2.179(14)	(Sr3/Lu3)-O8	2.311(17)
(Lu1/Sr1)-O5	2.479(18)	(Lu2/Sr2)-O1	2.184(17)	(Sr3/Lu3)-O6	2.564(16)
(Lu1/Sr1)-O7	2.494(18)	(Lu2/Sr2)-O3	2.212(15)	(Sr3/Lu3)-O5	2.659(18)
(Lu1/Sr1)-O3	2.535(17)	(Lu2/Sr2)-O4	2.258(17)	(Sr3/Lu3)-O4	2.780(18)
(Lu1/Sr1)-O10	2.554(17)	(Lu2/Sr2)-O2	2.389(16)	(Sr3/Lu3)-O4	2.791(17)
(Lu1/Sr1)-O3	2.659(18)	(Lu2/Sr2)-O5	2.537(16)	(Sr3/Lu3)-O10	2.908(18)
(Lu1/Sr1)-O11	2.702(15)	(Lu2/Sr2)-O9	2.991(18)	(Sr3/Lu3)-O2	2.970(17)
(Lu1/Sr1)-O7	2.742(18)				
(Sr3/Lu3')-O8	2.498(17)				
(Sr3/Lu3')-O4	2.533(18)				
(Sr3/Lu3')-O5	2.621(17)				
(Sr3/Lu3')-O6	2.621(15)				
(Sr3/Lu3')-O2	2.643(17)				
(Sr3/Lu3')-O10	2.659(18)				
Ga1-O4	1.696(17)	Ga3-O7	1.743(19)	Ga5-O5	1.718(13)
Ga1-O6	1.803(9)	Ga3-O9	1.830(19)	Ga5-O10	1.802(18)
Ga1-O2	1.827(16)	Ga3-O2	1.842(17)	Ga5-O8	1.802(16)
Ga1-O1	1.848(18)	Ga3-O10	1.872(17)	Ga5-O11	1.862(15)
Ga2-O8	1.877(17)	Ga4-O3	1.823(15)		
Ga2-O8	1.877(17)	Ga4-O11	1.868(16)		
Ga2-O1	1.891(17)	Ga4-O7	1.874(19)		
Ga2-O1	1.891(17)	Ga4-O9	1.913(18)		

Tables S11. Refined structural parameters obtained from laboratory PXRD data collected at room temperature on cation-ordered $SrDyGa_3O_7$ from laboratory PXRD data ($P2_12_12$ space group, a = 23.8404(3) Å, b = 7.9510(1) Å and c = 5.24314(2) Å).

a: constrained to refine to the same U_{iso} values

Atom	Site	x	y	z	Occ	U_{iso}
Dy1/Sr1	4c	0.2210(2)	0.1475(5)	0.4976(6)	0.50(1)/0.50(1)	0.017(2)
Dy2/Sr2	4c	0.38229(17)	0.3203(4)	0.4609(5)	0.90(9)/0.100(9)	0.012(1)
Sr3/Dy3	4c	0.0558(2)	0.3372(7)	0.5076(7)	0.90(1)/0.10(1)	0.018(2)
Ga1	4c	0.0558(2)	0.3372(7)	0.5076(7)	1	0.010(2)
Ga2	2a	0.4501(3)	0.1441(9)	0.0111(10)	1	0.020(3)
Ga3	4c	0	0	0.998(2)	1	0.003(1)
Ga4	4c	0.1710(3)	0.4826(8)	0.9962(18)	1	0.012(2)
Ga5	4c	0.2873(3)	0.3374(9)	0.9535(11)	1	0.009(2)
O1	4c	0.1182(3)	0.1274(9)	0.0322(8)	1	0.004(2)[a]
O2	4c	0.4541(12)	0.330(4)	0.226(5)	1	0.004(2)[a]
O3	4c	0.3927(12)	0.077(3)	0.175(5)	1	0.004(2)[a]
O4	4c	0.2888(14)	0.360(4)	0.295(3)	1	0.004(2)[a]
O5	4c	0.4417(11)	0.150(4)	0.650(4)	1	0.004(2)[a]
O6	2b	0.1217(15)	0.120(4)	0.672(4)	1	0.004(2)[a]
O7	4c	0.5	0	0.146(5)	1	0.004(2)[a]
O8	4c	0.2226(14)	0.433(4)	0.805(6)	1	0.004(2)[a]
O9	4c	0.0510(10)	0.126(4)	0.149(4)	1	0.004(2)[a]
O10	4c	0.3051(12)	0.116(3)	0.730(5)	1	0.004(2)[a]
O11	4c	0.1451(12)	0.312(3)	0.261(4)	1	0.004(2)[a]

Table S12. Refined interatomic distances ($d_{A\text{-}O}$ up to 3 Å) obtained from cation-ordered $SrDyGa_3O_7$ from laboratory PXRD data.

Bond	Length(Å)	Bond	Length(Å)	Bond	Length(Å)
(Dy1/Sr1)-O9	2.36(3)	(Dy 2/Sr2)-O1	2.11(3)	(Sr3/ Dy3)-O5	2.49(3)
(Dy 1/Sr1)-O3	2.54(3)	(Dy 2/Sr2)-O4	2.20(3)	(Sr3/ Dy3)-O10	2.50(3)
(Dy 1/Sr1)-O5	2.55(3)	(Dy 2/Sr2)-O11	2.27(2)	(Sr3/ Dy3)-O8	2.52(3)
(Dy 1/Sr1)-O10	2.55(3)	(Dy 2/Sr2)-O3	2.41(3)	(Sr3/ Dy3)-O6	2.60(2)
(Dy 1/Sr1)-O3	2.57(3)	(Dy 2/Sr2)-O2	2.46(3)	(Sr3/ Dy3)-O4	2.62(3)
(Dy 1/Sr1)-O7	2.69(3)	(Dy 2/Sr2)-O5	2.49(3)	(Sr3/ Dy3)-O2	2.81(3)
(Dy 1/Sr1)-O11	2.71(3)	(Dy 2/Sr2)-O9	2.83(3)	(Sr3/ Dy3)-O4	2.84(3)
(Dy 1/Sr1)-O7	2.79(3)				
Ga1-O2	1.70(3)	Ga3-O7	1.63(3)	Ga5-O8	1.72(2)
Ga1-O6	1.80(1)	Ga3-O9	1.87(3)	Ga5-O11	1.81(3)
Ga1-O1	1.86(3)	Ga3-O2	1.92(3)	Ga5-O5	1.89(2)
Ga1-O4	1.90(2)	Ga3-O10	2.04(3)	Ga5-O10	2.00(3)
Ga2-O8	1.76(3)	Ga4-O3	1.80(1)		
Ga2-O8	1.76(3)	Ga4-O11	1.87(3)		
Ga2-O1	2.10(3)	Ga4-O7	1.89(3)		
Ga2-O1	2.10(3)	Ga4-O9	2.16(3)		

Table S13. Refined structural parameters of disordered $SrYbGa_3O_7$ from laboratory PXRD data (P-42_1m space group, $a = b = 7.91985(9)$ Å and $c = 5.21070(7)$ Å).

Atom	Site	x	y	z	Occ	U_{iso}
Yb1/Sr1	4e	0.33863(9)	0.16137(9)	0.5123(4)	0.5/0.5	0.0353(5)
Ga1	2a	0	0	0	1	0.0254(8)
Ga2	4e	0.14503(15)	0.35497(15)	0.9698(5)	1	0.0289(7)
O1	2c	0.5	0	0.179(2)	1	0.050(2)
O2	4e	0.1438(9)	0.3562(9)	0.2990(14)	1	0.050(2)
O3	8f	0.0932(7)	0.1615(8)	0.7782(15)	1	0.050(2)

[a]: constrained to refine to the same U_{iso} values

Table S14. Refined interatomic distances of disordered $SrYbGa_3O_7$ from laboratory PXRD data.

Bond	Length(Å)	Bond	Length(Å)	Bond	Length(Å)
(Yb1/Sr1)-O3	2.387(7)	Ga1-O3	1.875(7)	Ga2-O2	1.716(8)
(Yb1/Sr1)-O3	2.387(7)	Ga1-O3	1.875(7)	Ga2-O1	1.800(6)
(Yb1/Sr1)-O2	2.449(9)	Ga1-O3	1.875(7)	Ga2-O3	1.875(7)
(Yb1/Sr1)-O1	2.507(9)	Ga1-O3	1.875(7)	Ga2-O3	1.875(7)
(Yb1/Sr1)-O2	2.613(7)				
(Yb1/Sr1)-O2	2.613(7)				
(Yb1/Sr1)-O3	2.885(7)				
(Yb1/Sr1)-O3	2.885(7)				

Table S15. Refined structural parameters of disordered $SrTmGa_3O_7$ from SPD data (P-42_1m space group, $a = b = 7.92455(3)$ Å, and $c = 5.21558(2)$ Å).

Atom	Site	x	y	z	Occ	U_{iso}
Tm1/Sr1	4e	0.33812(3)	0.16188(3)	0.51362(10)	0.5/0.5	0.0226(1)
Ga1	2a	0	0	0	1	0.0136(2)
Ga2	4e	0.14401(4)	0.35599(4)	0.96889(14)	1	0.0135(2)
O1	2c	0.5	0	0.1854(11)	1	0.0420(7)[a]
O2	4e	0.1418(3)	0.3582(3)	0.3109(6)	1	0.0420(7)[a]
O3	8f	0.0956(3)	0.1603(3)	0.7952(6)	1	0.0420(7)[a]

[a]: constrained to refine to the same U_{iso} values

Table S16. Refined interatomic distances of disordered from SPD data $SrTmGa_3O_7$.

Bond	Length(Å)	Bond	Length(Å)	Bond	Length(Å)
(Tm1/Sr1)-O3	2.420(3)	Ga1-O3	1.824(3)	Ga2-O2	1.784(3)
(Tm1/Sr1)-O3	2.420(3)	Ga1-O3	1.824(3)	Ga2-O1	1.804(3)
(Tm1/Sr1)-O2	2.441(3)	Ga1-O3	1.824(3)	Ga2-O3	1.836(3)
(Tm1/Sr1)-O1	2.494(4)	Ga1-O3	1.824(3)	Ga2-O3	1.837(3)
(Tm1/Sr1)-O2	2.579(3)				
(Tm1/Sr1)-O2	2.580(3)				
(Tm1/Sr1)-O3	2.957(3)				
(Tm1/Sr1)-O3	2.957(3)				

Table S17. Refined structural parameters of disordered $SrErGa_3O_7$ from SPD data (*P*-42_1m space group, $a = b = 7.93227(2)$ Å, and $c = 5.22367(2)$ Å).

Atom	Site	x	y	z	Occ	U_{iso}
Er1/Sr1	4e	0.33837(2)	0.16163(2)	0.51404(8)	0.5	0.02116(8)
Ga1	2a	0	0	0	1	0.0138(2)
Ga2	4e	0.14408(4)	0.35592(4)	0.96875(12)	1	0.0134(1)
O1	2c	0.5	0	0.1852(9)	1	0.0403(6)[a]
O2	4e	0.1414(3)	0.3586(3)	0.3095(5)	1	0.0403(6)[a]
O3	8f	0.0944(3)	0.1603(3)	0.7932(5)	1	0.0403(6)[a]

[a]: constrained to refine to the same U_{iso} values

Table S18. Refined interatomic distances of disordered $SrErGa_3O_7$ from SPD data.

Bond	Length(Å)	Bond	Length(Å)	Bond	Length(Å)
(Er1/Sr1)-O3	2.423(3)	Ga1-O3	1.829(2)	Ga2-O2	1.780(3)
(Er1/Sr1)-O3	2.423(3)	Ga1-O3	1.829(2)	Ga2-O1	1.805(2)
(Er1/Sr1)-O2	2.455(3)	Ga1-O3	1.829(2)	Ga2-O3	1.845(2)
(Er1/Sr1)-O1	2.497(3)	Ga1-O3	1.829(2)	Ga2-O3	1.845(2)
(Er1/Sr1)-O2	2.579(2)				
(Er1/Sr1)-O2	2.579(2)				
(Er1/Sr1)-O3	2.949(2)				
(Er1/Sr1)-O3	2.949(2)				

Table S19. Refined structural parameters of disordered $SrHoGa_3O_7$ from laboratory PXRD data (P-42_1m space group, $a = b = 7.93999(2)$ Å, and $c = 5.23060(2)$ Å, $R_p = 1.413\%$ $R_{wp} = 2.081\%$).

Atom	Site	x	y	z	Occ	U_{iso}
Ho1/Sr1	4e	0.33867(5)	0.16133(5)	0.51151(14)	0.5/0.5	0.0134(2)
Ga1	2a	0	0	0	1	0.0077(3)
Ga2	4e	0.14444(7)	0.35556(7)	0.96831(17)	1	0.0097(3)
O1	2c	0.5	0	0.1757(10)	1	0.0287(8)[a]
O2	4e	0.1422(4)	0.3578(4)	0.3186(6)	1	0.0287(8)[a]
O3	8f	0.0940(4)	0.1626(4)	0.7916(6)	1	0.0287(8)[a]

[a]: constrained to refine to the same U_{iso} values

Table S20. Refined interatomic distances of disordered $SrHoGa_3O_7$ from laboratory PXRD data.

Bond	Length(Å)	Bond	Length(Å)	Bond	Length(Å)
(Ho1/Sr1)-O2	2.456(3)	Ga1-O3	1.847(3)	Ga2-O1	1.788(2)
(Ho1/Sr1)-O3	2.433(3)	Ga1-O3	1.847(3)	Ga2-O2	1.832(3)
(Ho1/Sr1)-O3	2.434(3)	Ga1-O3	1.847(3)	Ga2-O3	1.834(3)
(Ho1/Sr1)-O1	2.523(4)	Ga1-O3	1.847(3)	Ga2-O3	1.834(3)
(Ho1/Sr1)-O2	2.573(3)				
(Ho1/Sr1)-O2	2.573(3)				
(Ho1/Sr1)-O3	2.929(3)				
(Ho1/Sr1)-O3	2.929(3)				

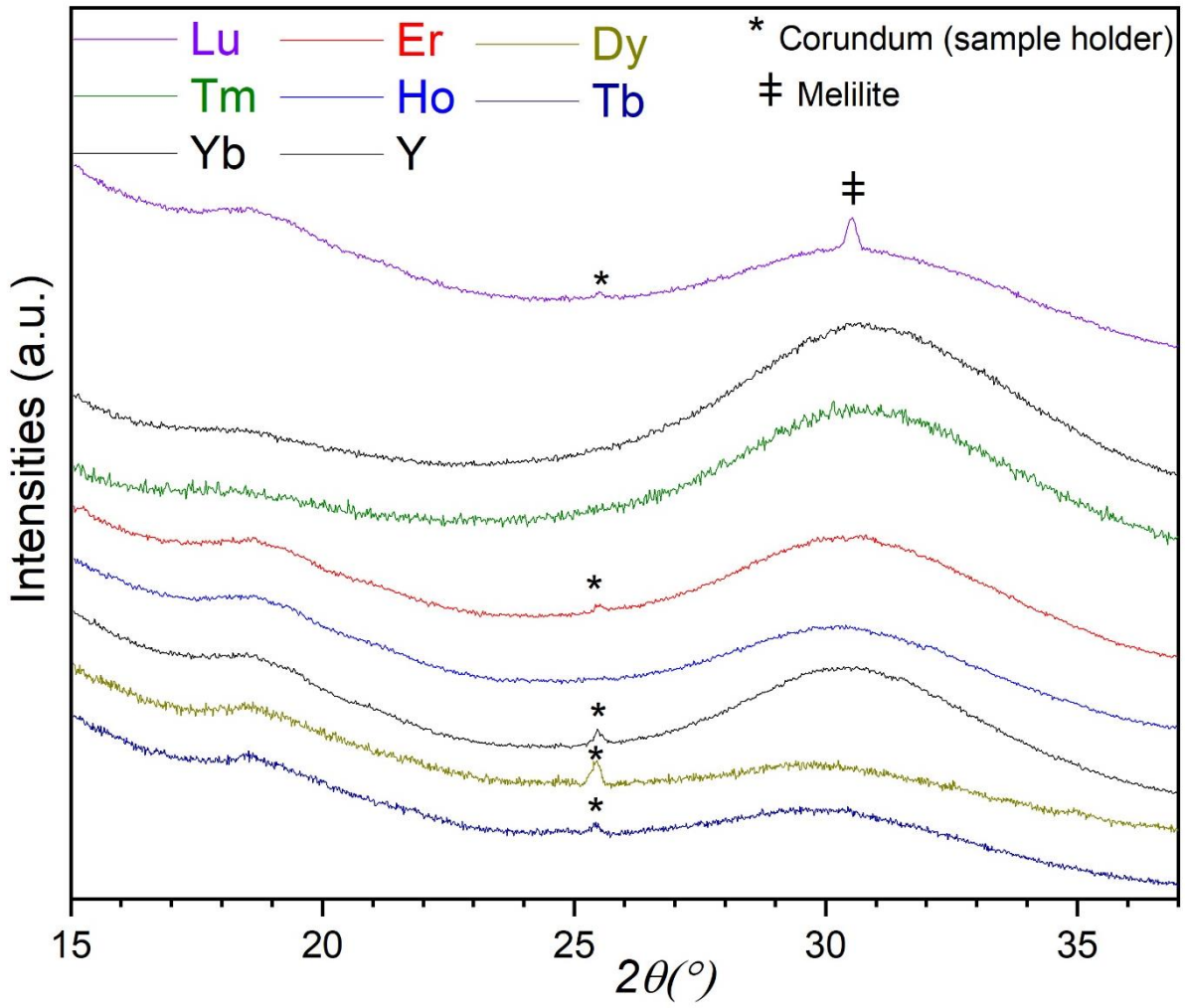

Figure S1. Laboratory X-ray powder diffraction data of Sr*RE*Ga$_3$O$_7$ (*RE* = Tb-Lu, Y) glass samples synthesized by aerodynamic levitation coupled to laser heating (ADL).

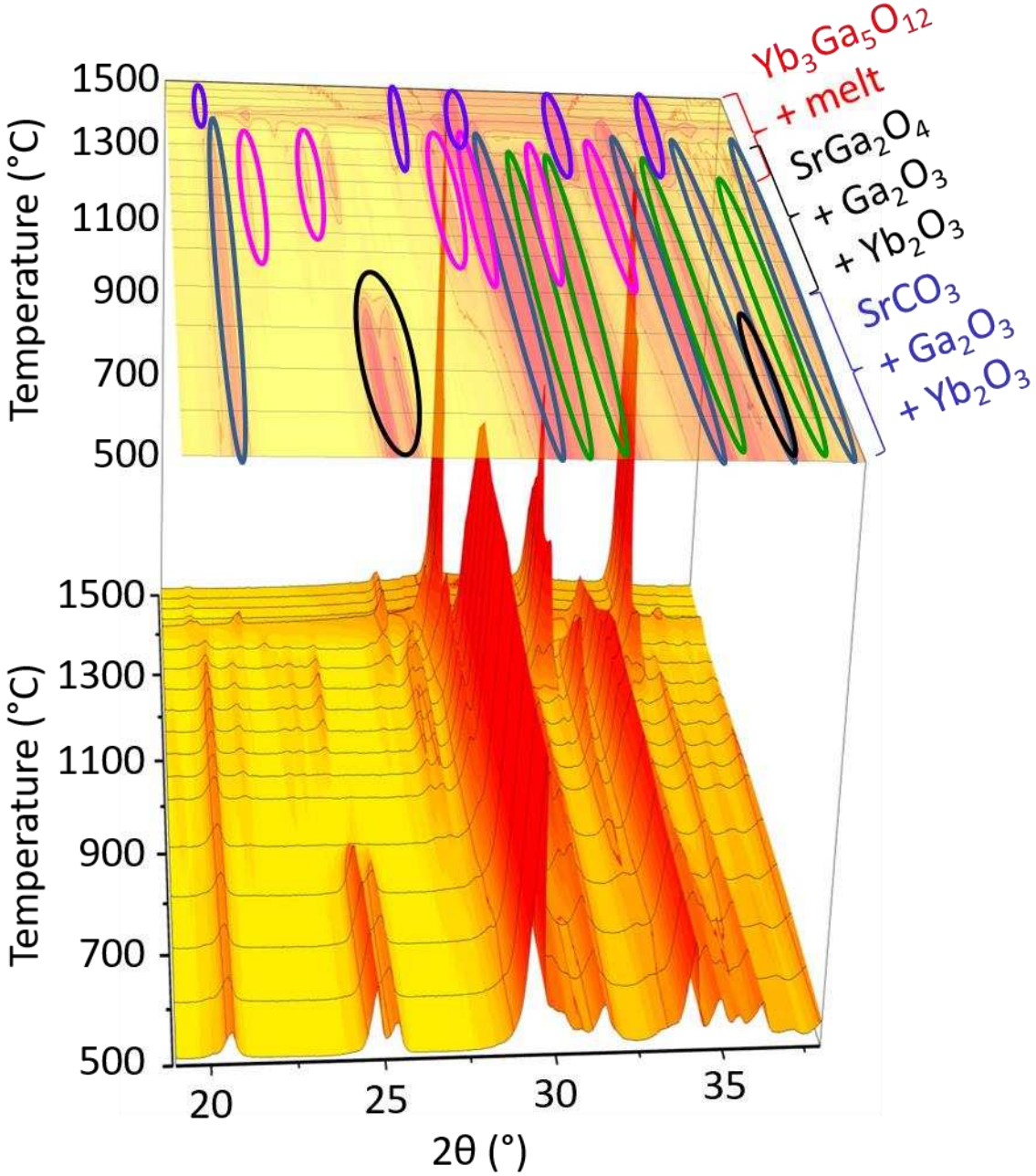

Figure S2. In situ X-ray powder diffraction data of the nominal $SrYbGa_3O_7$ composition recorded from 500°C up to 1500 °C (no phase modification occurs between room temperature and 500°C). The different colors correspond to the indexation of $SrCO_3$ (black), Yb_2O_3 (blue), Ga_2O_3 (green), $SrGa_2O_4$ (pink) and $Yb_3Ga_5O_{12}$ (purple). From room temperature to 900°C only the $SrCO_3$, Yb_2O_3 and Ga_2O_3 precursors are present. At 900°C $SrCO_3$ reacts with Ga_2O_3 to form $SrGa_2O_4$. At 1250°C Yb_2O_3 and residual Ga_2O_3 react to form the $Yb_3Ga_5O_{12}$ garnet and the other crystalline phases melt from 1350°C.

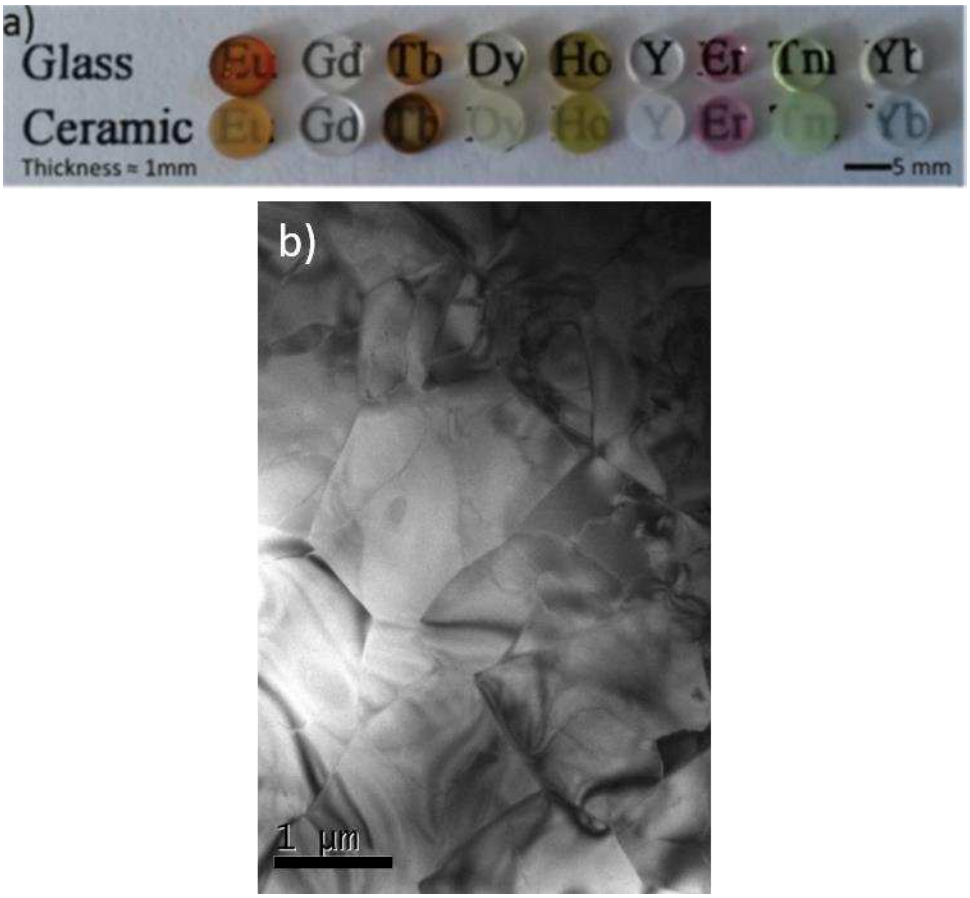

Figure S3. (a) Photograph of the $SrREGa_3O_7$ polished glass and ceramic materials (from Boyer et al., J. Mater. Chem. C, 2016, 4, 3238). (b) Bright field TEM micrograph of the $SrYbGa_3O_7$ transparent ceramic showing a wide grain size distribution and the absence of residual glass, porosity or secondary phase.

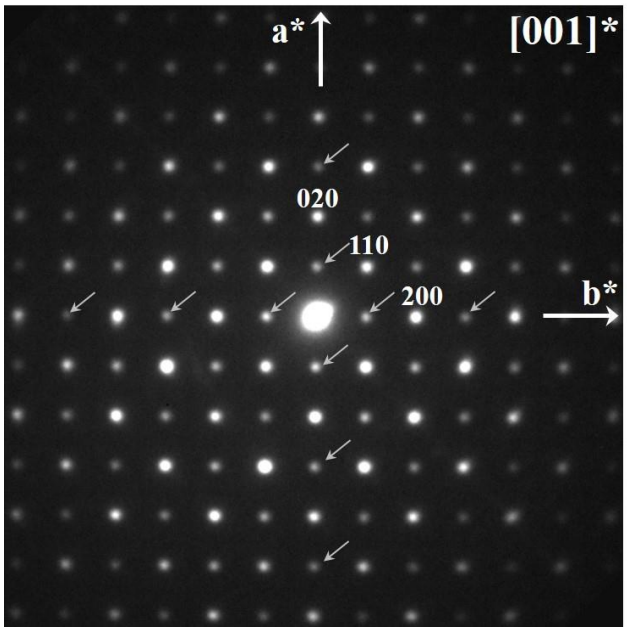

Figure S4. [001]* Selected Area Electron Diffraction pattern of disordered $SrTmGa_3O_7$ melilite parent synthesized by rapid quenching from the high-temperature disordered domain. The indexation of the classic tetragonal melilite structure (a=7.9 Å x c = 5.2 Å, $P\text{-}42_1m$) is reported and the arrows point the reflections assigned to double diffraction.

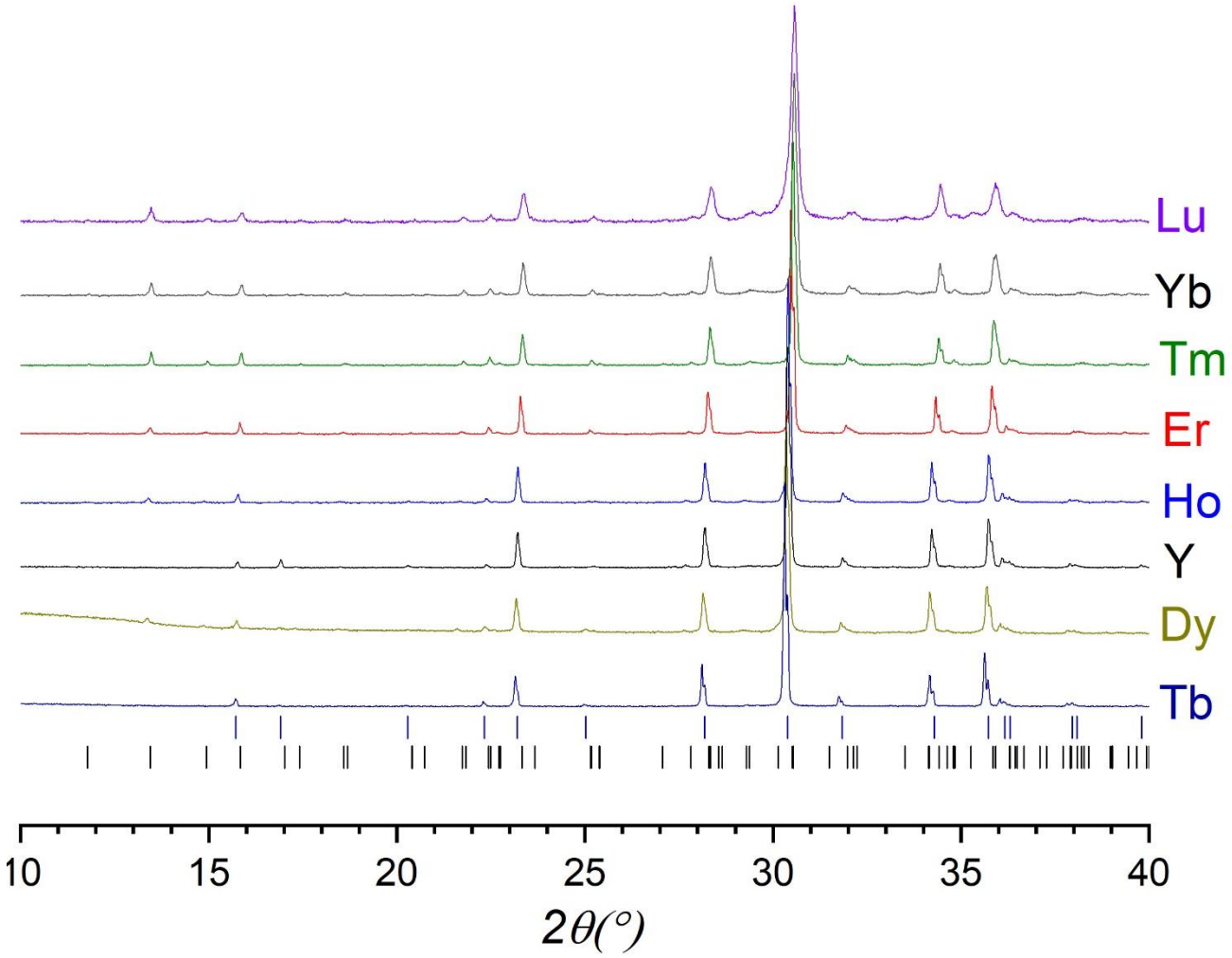

Figure S5. Post-DSC PXRD data of Sr*RE*Ga_3O_7, where black and dark blue tick marks correspond to the $P2_12_12$ 3x1x1 ordered superstructure (exhibited by *RE* = Dy – Lu, Y) and the $P\text{-}42_1m$ disordered structure (exhibited by $SrTbGa_3O_7$ only) respectively.

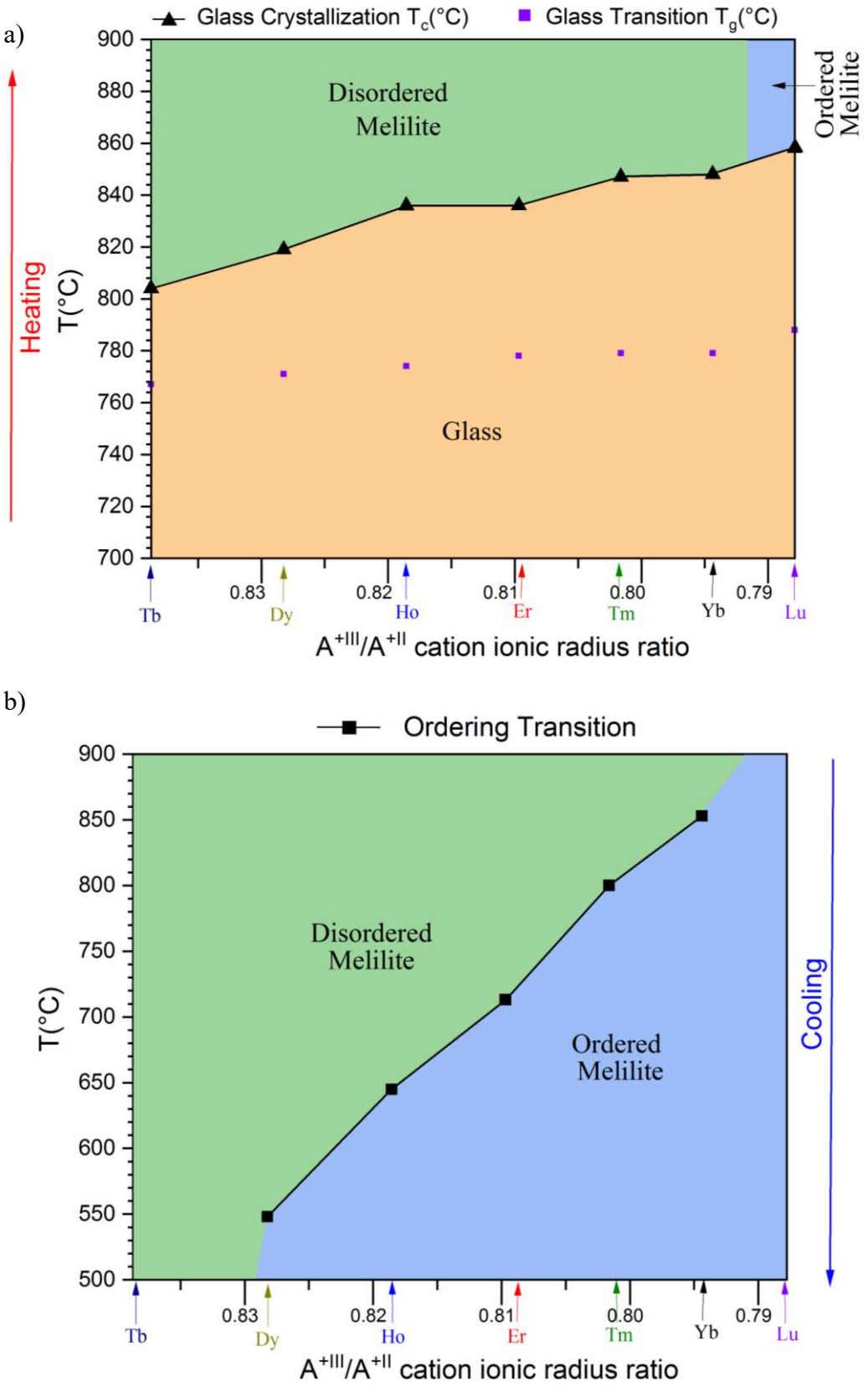

Figure S6. Glass, ordered and disordered melilite Sr*RE*Ga_3O_7 (*RE* =Tb – Lu, Y) domains of stability on (a) heating and (b) cooling at rates of 10°C min^{-1}, drawn from DSC results (Figure 7, main manuscript) and PXRD measurements performed post-DSC (Figure S5).

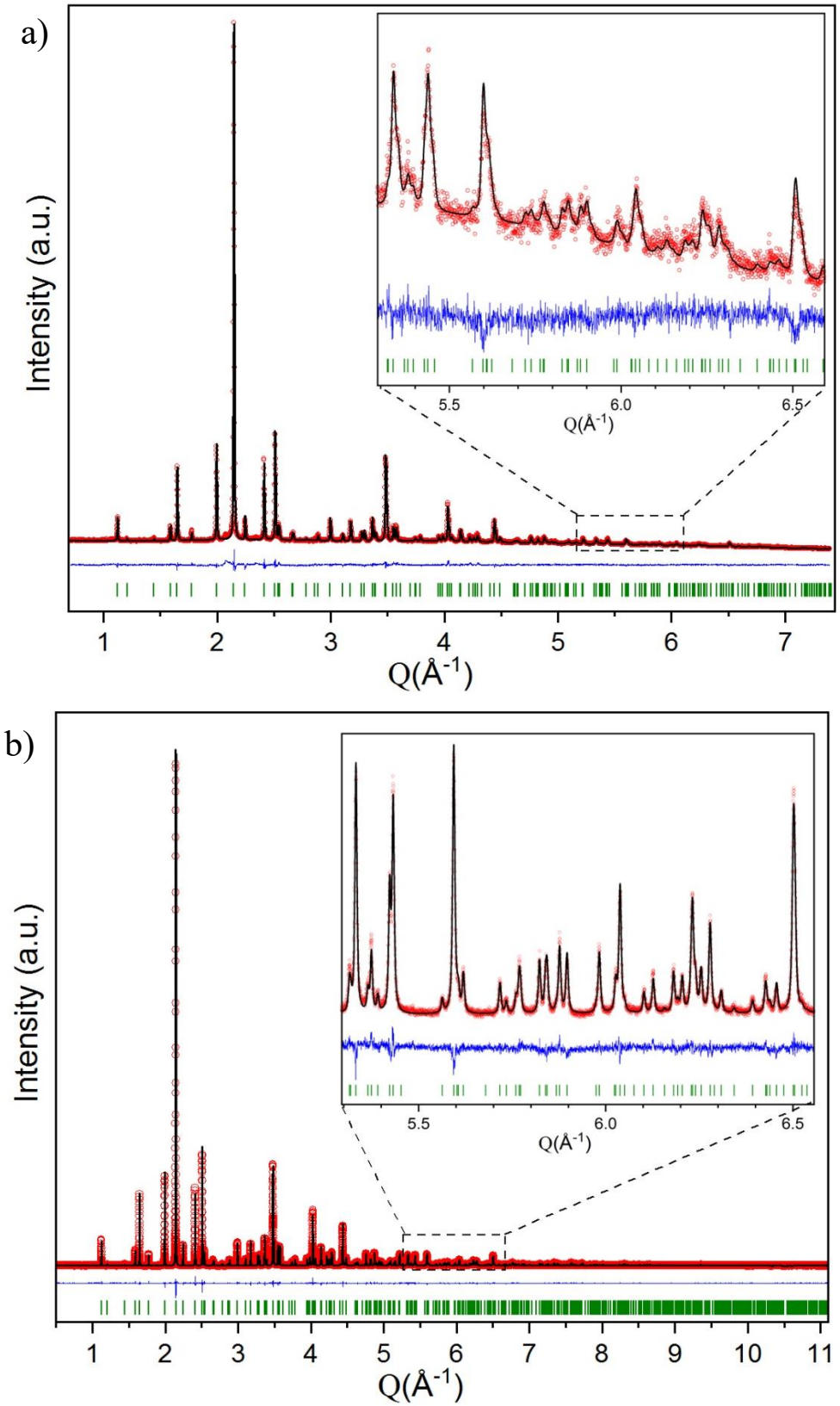

Figure S7. Rietveld refinement of a) disordered $SrYbGa_3O_7$ (laboratory PXRD data, R_p = 2.87% R_{wp} = 3.83%) and b) disordered $SrTmGa_3O_7$ (SPD data, R_p = 6.36% R_{wp} = 8.32%). Observed (black dot), calculated (red line), and difference (blue line) profiles are shown. The set of green vertical lines corresponds to reflection positions.

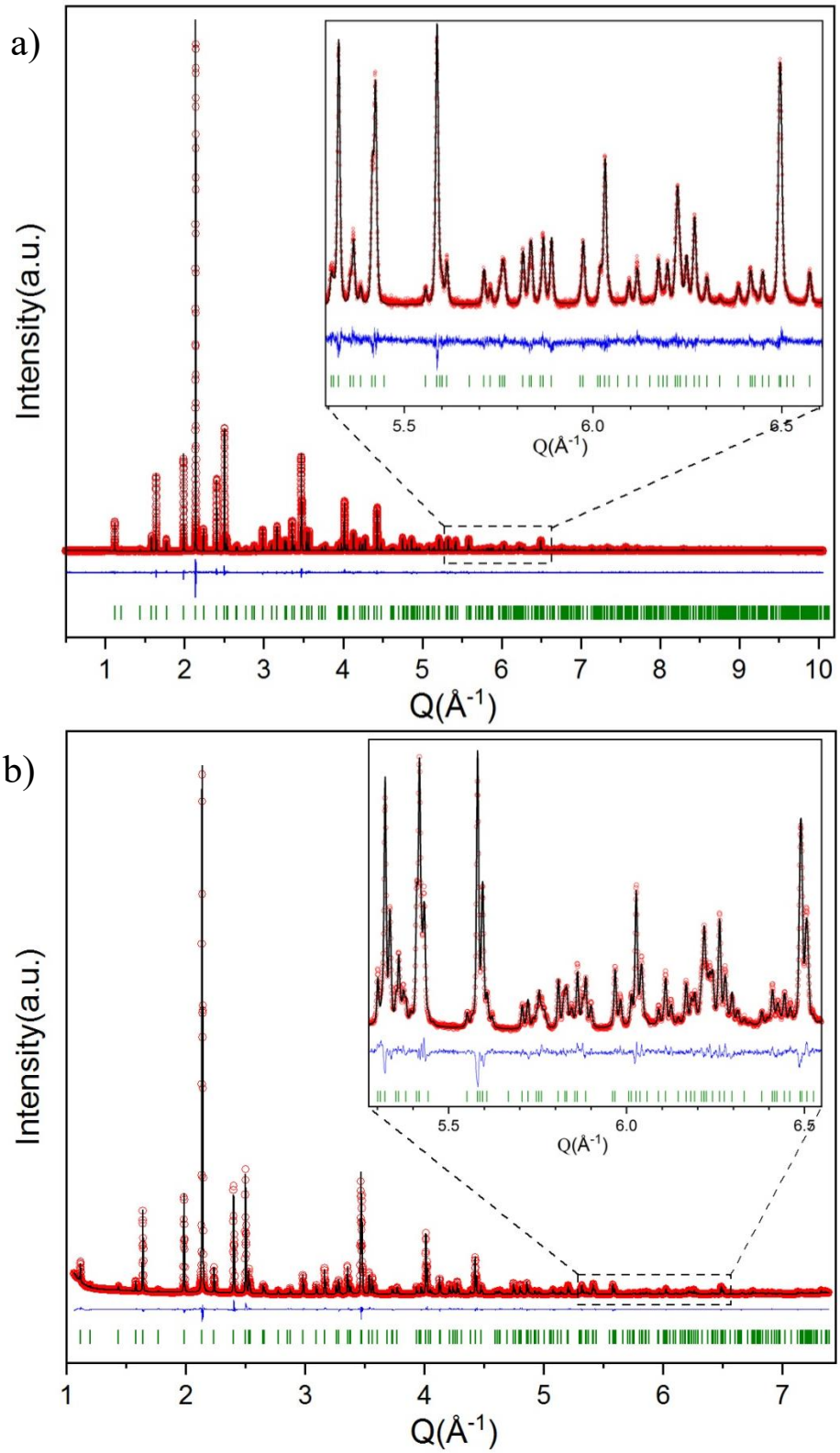

Figure S8. Rietveld refinement of a) disordered $SrErGa_3O_7$ (SPD data, R_p = 6.78% R_{wp} = 8.75 %) and b) $SrHoGa_3O_7$ disordered melilite (laboratory PXRD data, R_p = 1.41% R_{wp} = 2.08%). Observed (black dot), calculated (red line), and difference (blue line) profiles are shown. The set of green vertical lines corresponds to reflection positions.

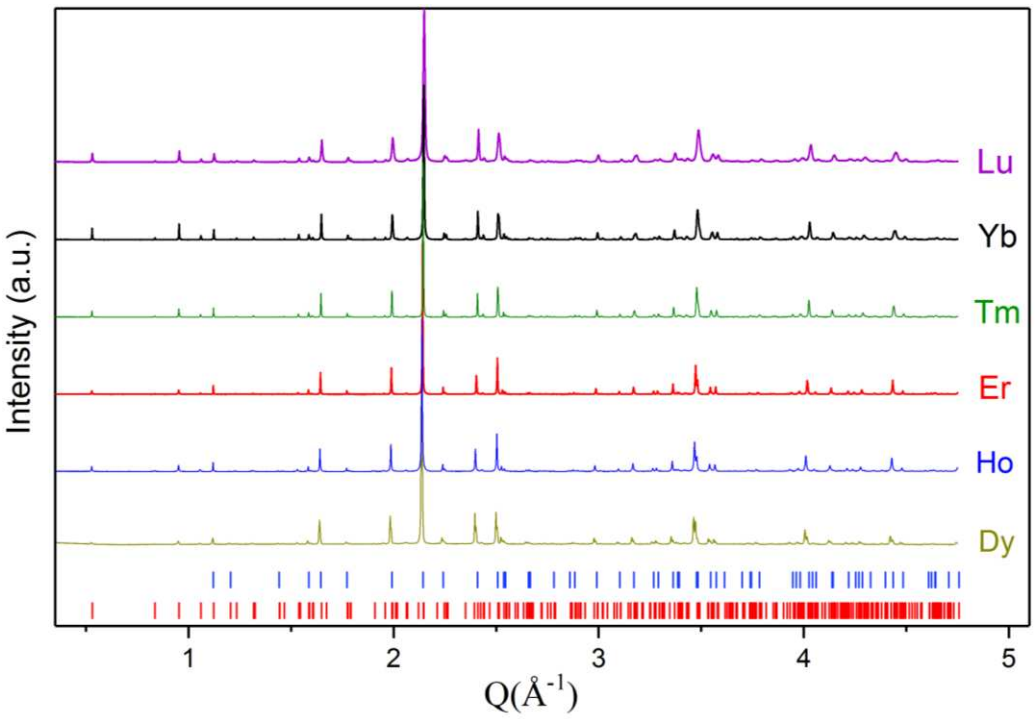

Figure S9. Normalized **s**ynchrotron powder diffraction (SPD) data of Sr*RE*Ga$_3$O$_7$ (*RE* = Ho, Er, Tm, Yb and Lu) and laboratory powder diffraction data collected on SrDyGa$_3$O$_7$. Red marks correspond to the 3x1x1 melilite supercell (orthorhombic, $P2_12_12$, $a \approx 23.7$ Å, $b \approx 7.9$ Å and $c \approx 5.2$ Å), and blue marks to the classic melilite cell (tetragonal, $P\text{-}42_1m$, $a = 7.9$ Å x $c = 5.2$ Å).

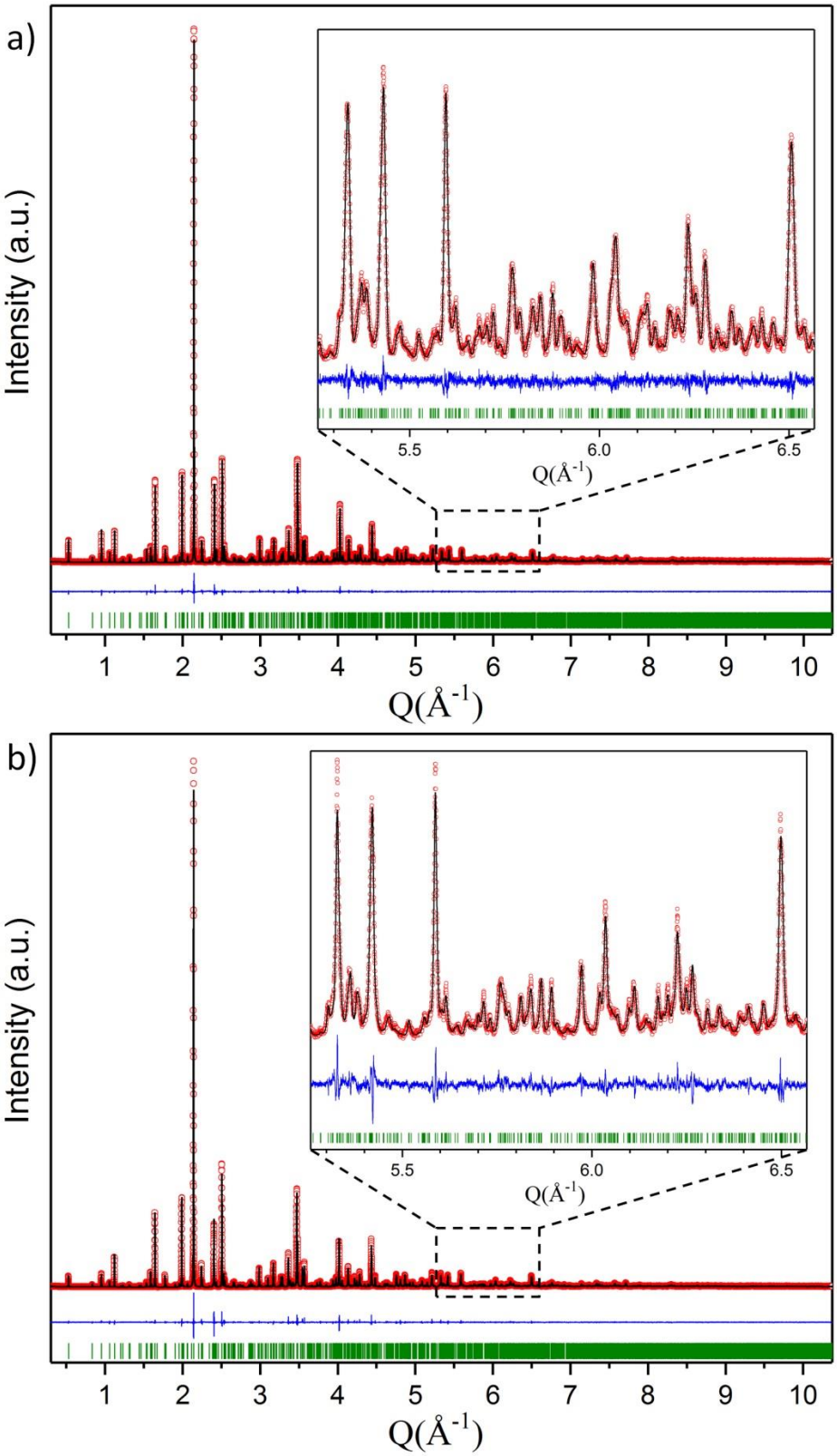

Figure S10. Rietveld refinement of a) $SrTmGa_3O_7$ ($R_p = 5.28\%$ $R_{wp} = 7.06\%$) and b) $SrErGa_3O_7$ ($R_p = 6.70\%$ $R_{wp} = 8.60\%$) ordered melilites (SPD data). Observed (black dot), calculated (red line), and difference (blue line) profiles are shown. The set of green vertical lines corresponds to reflection positions.

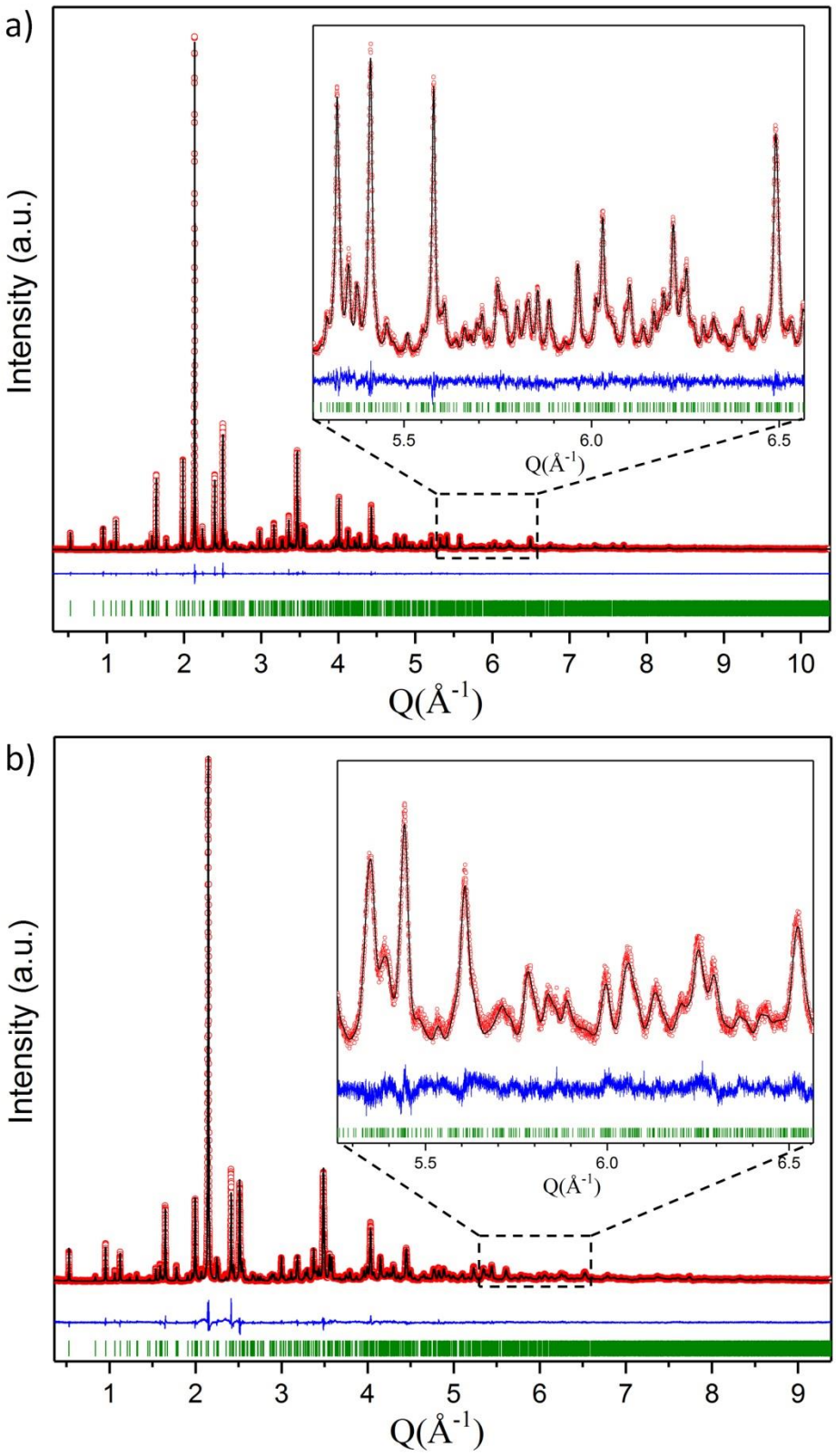

Figure S11. Rietveld refinement of a) $SrHoGa_3O_7$ (R_p = 4.85% R_{wp} = 6.30%) and b) $SrLuGa_3O_7$ (R_p = 6.87% R_{wp} = 9.18%) ordered melilites (SPD data). Observed (black dot), calculated (red line), and difference (blue line) profiles are shown. The set of green vertical lines corresponds to reflection positions.

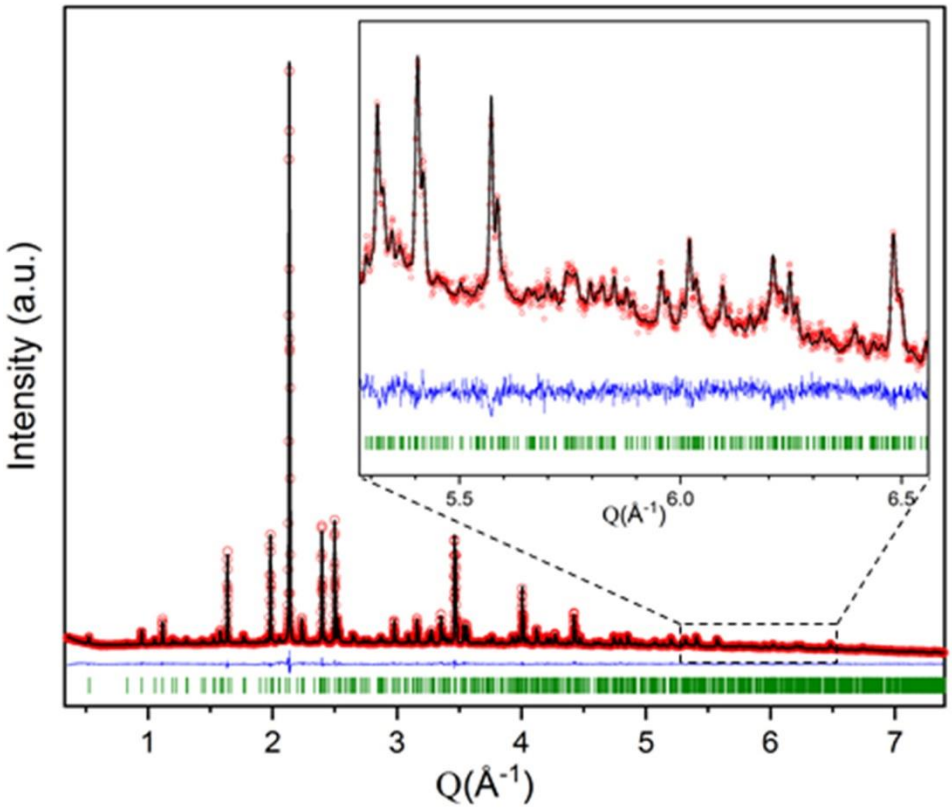

Figure S12. Rietveld refinement of $SrDyGa_3O_7$ ordered melilite (laboratory data, $R_p = 1.66\%$ $R_{wp} = 2.21\%$). Observed (black dot), calculated (red line), and difference (blue line) profiles are shown. The set of green vertical lines corresponds to reflection positions.

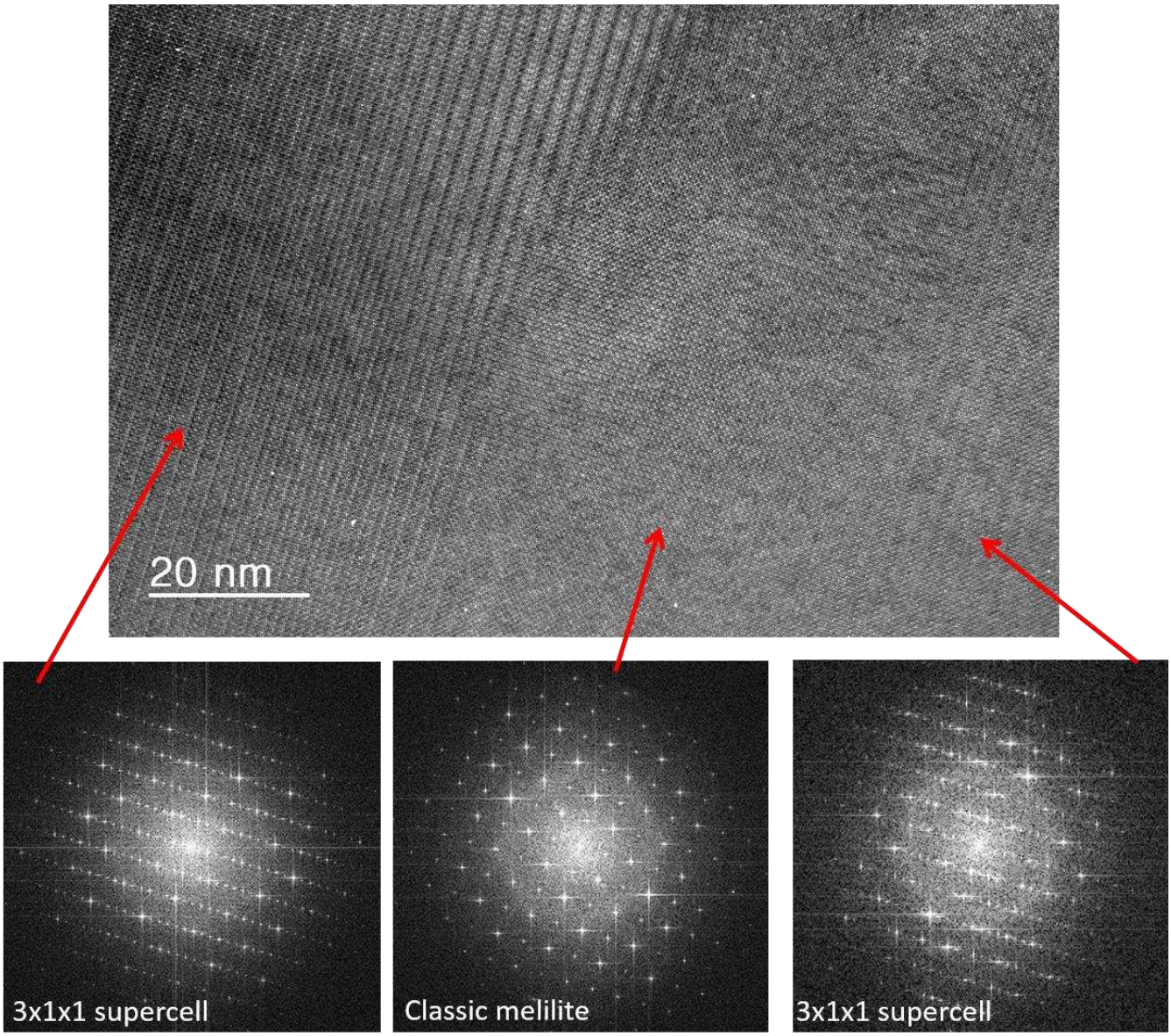

Figure S13. [001]* HRTEM image and associated FFTs of the $SrYGa_3O_7$ melilite parent synthesized by full crystallization from glass. Disordered classic tetragonal *P*-42_1m melilite structure and ordered 3x1x1 *P*2_12_12 melilite supercell coexist like close neighboring nanodomains.

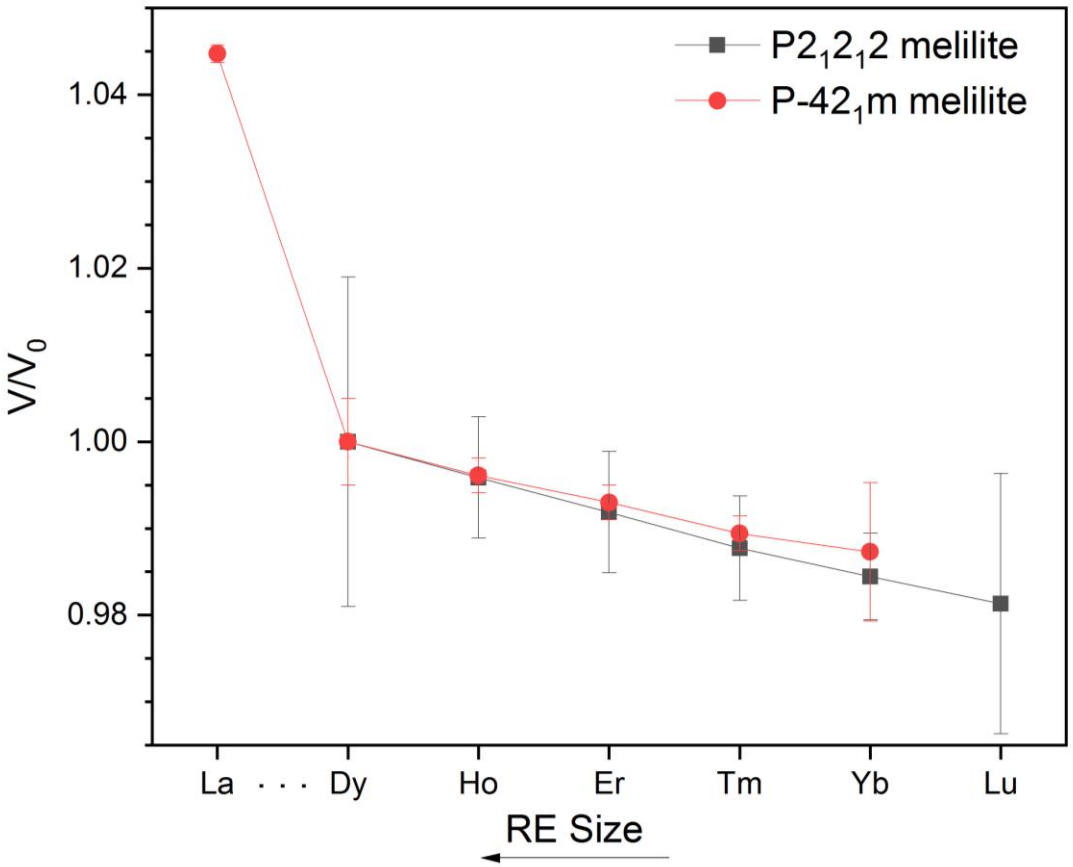

Figure S14. Evolution of the unit cell volume across the $SrREGa_3O_7$ (*RE* = Dy – Lu) series. *RE* = Dy was chosen as V_0. The cell volume for $SrLaGa_3O_7$ is added for comparison.

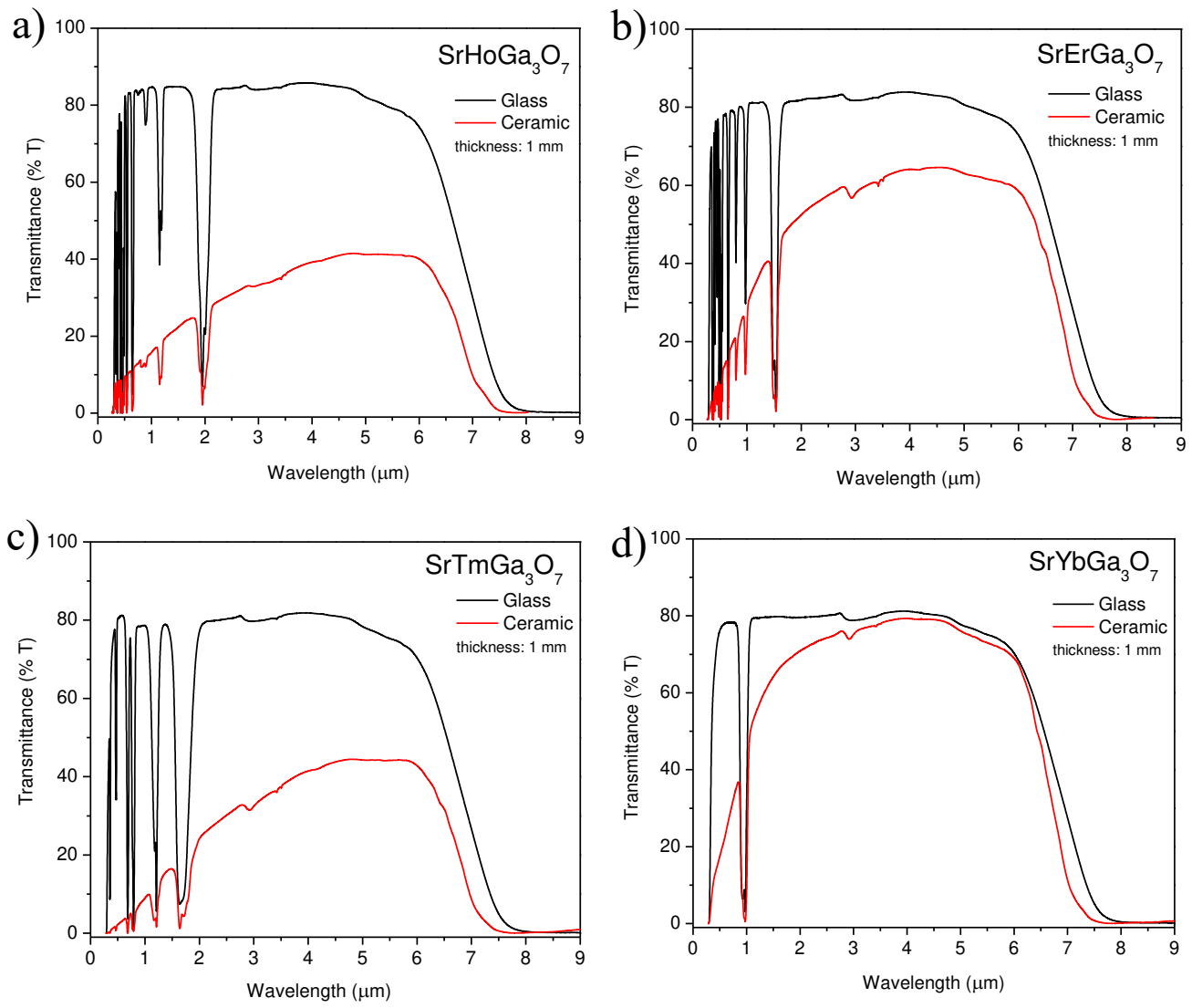

Figure S15. Optical transmission windows of the $SrHoGa_3O_7$ (a), $SrErGa_3O_7$ (b), $SrTmGa_3O_7$ (c), and $SrYbGa_3O_7$ (d) glass and ceramic melilites, recorded by UV-visible-NIR and FTIR transmission spectroscopies and normalized for 1 mm thickness[27].

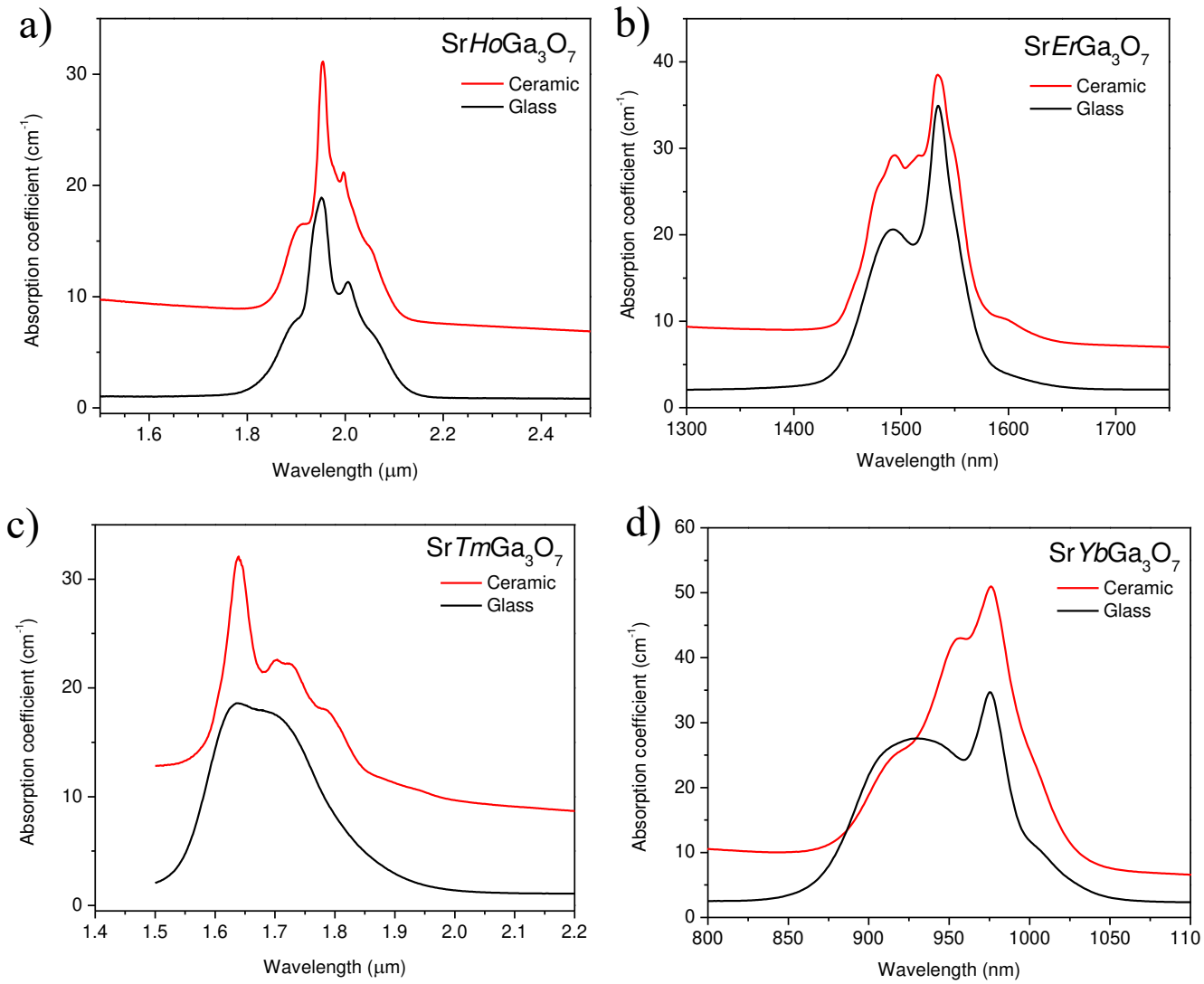

Figure S16. Absorption coefficient spectra of the $SrHoGa_3O_7$ (a), $SrErGa_3O_7$ (b), $SrTmGa_3O_7$ (c), and $SrYbGa_3O_7$ (d) glass and ceramic melilites. Data were not corrected with respect to Fresnel optical losses; the increase of background absorption observed in the ceramics' spectra is due to scattering losses (see Figure S15).

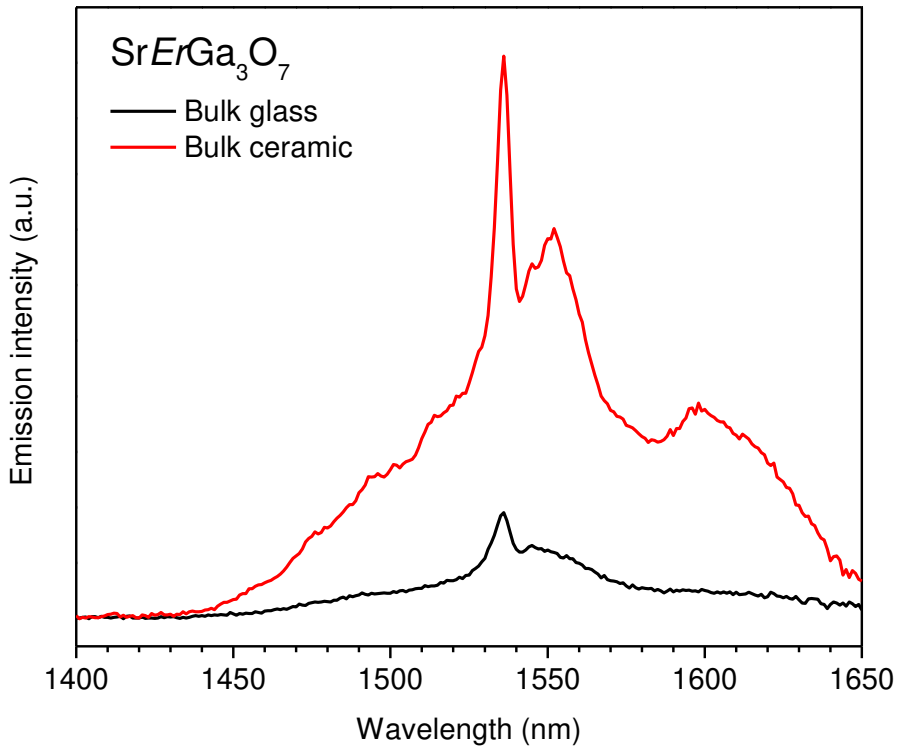

Figure S17. Emission photoluminescence spectra recorded on polished bulk Sr*Er*Ga$_3$O$_7$ glass and ceramic melilites, under 520 nm excitation wavelength (from Xe lamp). Data were collected in the strictly same conditions.

Inorganic Chemistry

pubs.acs.org/IC

Article

Stabilization of the Trigonal Langasite Structure in $Ca_3Ga_{2-2x}Zn_xGe_{4+x}O_{14}$ ($0 \leq x \leq 1$) with Partial Ordering of Three Isoelectronic Cations Characterized by a Multitechnique Approach

Haytem Bazzaoui, Cécile Genevois, Dominique Massiot, Vincent Sarou-Kanian, Emmanuel Veron, Sébastien Chenu, Přemysl Beran, Michael J. Pitcher,* and Mathieu Allix*

Cite This: *Inorg. Chem.* 2022, 61, 9339−9351

Read Online

ACCESS | Metrics & More | Article Recommendations | Supporting Information

ABSTRACT: Crystallization of oxide glasses rich in Zn^{2+}, Ga^{3+}, and Ge^{4+} is of interest for the synthesis of new transparent ceramics. In this context, we report the identification and detailed structural characterization of a new solid solution $Ca_3Ga_{2-2x}Zn_xGe_{4+x}O_{14}$ ($0 \leq x \leq 1$). These compounds adopt the trigonal langasite structure type, offering three possible crystallographic sites for the coordination of isoelectronic Zn^{2+}, Ga^{3+}, and Ge^{4+}. We used neutron diffraction to determine distributions of Ga^{3+}/Ge^{4+} and Zn^{2+}/Ge^{4+} in the simpler end members $Ca_3Ga_2Ge_4O_{14}$ and $Ca_3ZnGe_5O_{14}$, while for the complex intermediate member $Ca_3GaZn_{0.5}Ge_{4.5}O_{14}$, we used an original approach combining quantitative 2D analysis of atomic-resolution STEM-EDS maps with neutron diffraction. This revealed that, across the solid solution, the tetrahedral D sites remain fully occupied by Ge^{4+}, while Zn^{2+}, Ga^{3+}, and the remaining Ge^{4+} are shared between octahedral B- and tetrahedral C sites in proportions that depend upon their relative ionic radii. The adoption of the trigonal langasite structure by glass-crystallized $Ca_3ZnGe_5O_{14}$, a compound that was previously observed only in a distorted monoclinic langasite polymorph, is attributed to substantial disorder between Zn^{2+} and Ge^{4+} over the B and C sites. The quantitative 2D refinement of atomic-resolution STEM-EDS maps is applicable to a wide range of materials where multiple cations with poor scattering contrast are distributed over different crystallographic sites in a crystal structure.

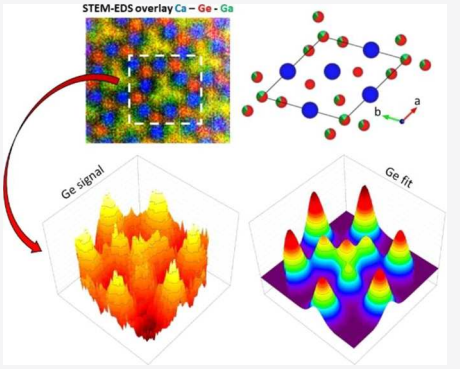

1. INTRODUCTION

Controlled crystallization of glass precursors in ternary or quaternary phase fields is a demonstrated route to technologically useful transparent ceramics by offering suitable control of the microstructure to minimize light scattering.[1−8] We previously reported long-lasting red luminescence in the spinel $Zn_{1+x}Ga_{2-2x}Ge_xO_4:Cr^{3+}$,[9] followed by the synthesis of transparent glass ceramics at similar compositions by controlled crystallization of $Na_2O−ZnO−Ga_2O_3−GeO_2$ glass precursors. In these materials, Zn^{2+}, Ga^{3+}, and Ge^{4+} undergo a nanoscale phase segregation to leave a dispersion of $ZnGa_2O_4$ nanocrystals embedded in a GeO_2-rich glassy matrix,[10] producing bulk glass ceramics with high transparency in the visible and infrared spectral regions. Such materials can be functionalized by the addition of Cr^{3+} to induce long-lasting red luminescence in the full volume of the ceramic.[11] Other multinary oxide phase fields containing Zn, Ga, and Ge are therefore of interest for their potential to host controllable phase separation phenomena and hence optically transparent functionalizable glass ceramics. The existence in the phase diagram of a stable high-symmetry crystal structure able to host multiple cations, thus fulfilling the role of $ZnGa_2O_4$, which may be an advantage in this respect. Solid solutions of the langasite-type compounds $Ca_3Ga_2Ge_4O_{14}$ and $Ca_3ZnGe_5O_{14}$ are therefore of interest as potential nano-crystallization products from $CaO−ZnO−Ga_2O_3−GeO_2$ precursor glasses.

The langasite structure, of general formula $A_3BC_3D_2O_{14}$, is a layered framework structure type constructed from corner-sharing $(C,D)O_4$ tetrahedra and BO_6 octahedra; the BO_6 octahedra also bridge adjacent layers, forming 8-coordinate interlayer sites for A cations, which are arranged in channels along the stacking axis (Figure 1). The structure type, which is of interest for properties arising from its polarity,[5,6,12] optical transparency,[3,4] or ability to host interstitial oxide ions,[13] can accommodate multiple cations with different coordination preferences: the A sites tend to host alkaline- and rare-earth cations, while transition metal and *p*-block cations tend to be distributed across the corner-linked B, C, and D sites. $Ca_3Ga_2Ge_4O_{14}$ is readily synthesized in bulk and adopts the common trigonal langasite structure (space group *P*321). In

Received: April 7, 2022
Published: June 3, 2022

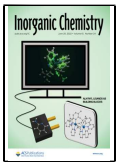

https://doi.org/10.1021/acs.inorgchem.2c01173
Inorg. Chem. 2022, 61, 9339−9351

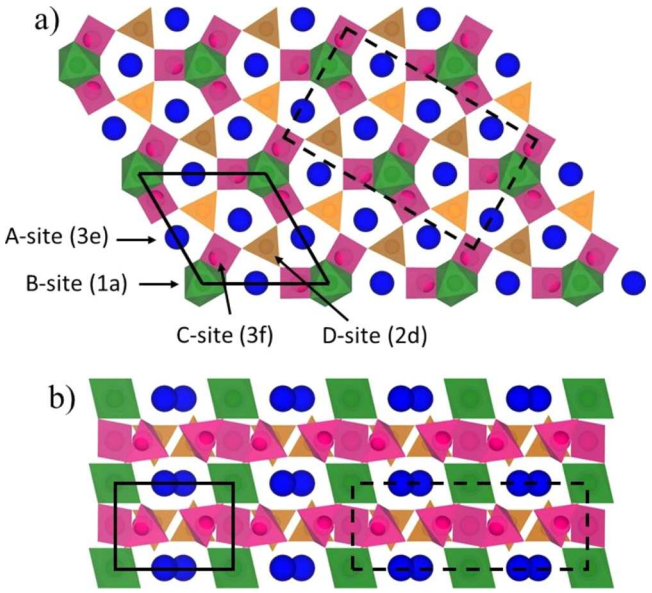

Figure 1. Crystal structure projection of the $A_3BC_3D_2O_{14}$ langasite structure family along the (a) *c*-axis and (b) *b*-axis, showing both the *P*321 cell (straight black lines) and *C*2 cell (dashed black lines).

contrast, $Ca_3ZnGe_5O_{14}$ appears to be difficult to synthesize in bulk, and has only been isolated in the form of small single crystals as a byproduct from the synthesis of $Ca_3Cu_{0.95}Zn_{0.05}Ge_2O_6$;[14] it adopts a distorted langasite framework, corresponding to a twofold expansion of the parent unit cell and reducing the symmetry from *P*321 to its monoclinic subgroup *C*2 (a distortion that is also observed in certain temperature and pressure regimes for other langasites such as $La_3Nb_{0.5}Ga_{5.5}O_{14}$).[15,16] The trigonal and monoclinic unit cells are projected together onto the same underlying langasite structure in Figure 1.

In both compounds, the absence of X-ray scattering contrast between $Ga^{3+}/Ge^{4+}$and Zn^{2+}/Ge^{4+} means that the distribution of these cations over the three framework sites (B, C, and D) cannot be obtained directly by conventional (non-anomalous) X-ray diffraction methods, and instead indirect routes (e.g., analysis based on refined bond distances) have been used to deduce the nature and extent of cation ordering.[17] Such isoelectronic pairs can be distinguished directly by neutron diffraction (NPD), as demonstrated for $La_3Ga_{5-x}Ge_{1+x}O_{14+x/2}$,[13] but NPD alone cannot be used for direct analysis of more complex systems with three or more isoelectronic cations distributed over the framework sites B, C, and D. Atomic-resolution STEM-EDS mapping offers a solution to this problem by detecting each element type directly with a spatial resolution of around 2−3 Å. While this technique is most often used qualitatively, intensities of atomic columns can be extracted by Gaussian curve fitting which is most often applied to 1D line profiles to provide quantitative information about atomic site occupancies.[18] Furthermore, Gaussian fitting of entire 2D map sections has been demonstrated for $SrTiO_3$ thin films[19] and then applied to distinguish multiple elements with close atomic number in FeCoNi alloys.[20] The 2D fitting approach has the advantage of considering the actual nature of the two-dimensional data set: it reduces errors associated with the subjective selection of the location and boundaries of a line profile (which is problematic where the atomic columns of interest do not lie on a perfectly straight line, or where adjacent columns overlap to contribute unwanted intensity to the profile) and produces contour maps that are more intuitive for crystallographic problems.

It can be challenging to characterize cation ordering in crystalline systems where the scatterers have a similar atomic number or where there are more than two cation species involved in the ordering, especially when the ordering is incomplete. The ability to resolve such problems is important in many contexts, for example, where cation ordering controls structural polarity,[21] suppresses thermal conductivity,[22] or influences lithium battery cyclability.[23] Here, we report the synthesis of a complete solid solution $(1-x)Ca_3Ga_2Ge_4O_{14}-(x)Ca_3ZnGe_5O_{14}$ $(0 \le x \le 1)$ by full crystallization from glass, with full structural characterization by synchrotron powder X-ray diffraction (PXRD) and neutron diffraction, and quantitative use of atomic-resolution STEM-EDS on powder specimens based on the development of a 2D fitting procedure to extract quantitative information on the distribution of Zn^{2+}, Ga^{3+}, and Ge^{4+} over the available framework sites in the $x = 0.5$ member $Ca_3Zn_{0.5}GaGe_{4.5}O_{14}$.

2. EXPERIMENTAL SECTION

2.1. Synthesis Procedure. Samples of composition $Ca_3Ga_{2-2x}Zn_xGe_{4+x}O_{14}$ were synthesized either by direct crystallization of the melt (for $x = 0$), or by full and congruent crystallization from glass (for $0.25 \le x \le 1$). First, stoichiometric amounts from high-purity precursors $CaCO_3$ 99.95%, Ga_2O_3 99.998%, ZnO 99.999%, and GeO_2 99.9% (all from Strem Chemicals) were weighed according to the nominal composition for $0 < x \le 1$. For $x = 0$, an excess of 2% (wt %) of GeO_2 was added to the initial mixture to compensate for partial volatilization (see Figure S1). The precursors were then ground together for several minutes in an agate mortar using ethanol to improve the homogeneity of the mixture. The resulting powder was dried and pressed into pellets, then divided into fragments of ∼35 mg each. Pellet chunks were melted individually by aerodynamic levitation (ADL) in an argon gas jet coupled to two CO_2 lasers (10.6 μm). These samples melted between 1250 and 1350 °C (depending on the composition), and were further heated up to 1500 °C to ensure their homogeneity, then subsequently quenched by turning the lasers off, reaching high cooling rates (estimated around 300 °C/s) in order to achieve vitrification, and leading to glass precursors in the form of spherical beads for $Ca_3Ga_{2-2x}Zn_xGe_{4+x}O_{14}$ with compositions $0.25 \le x \le 1$. For $Ca_3Ga_2Ge_4O_{14}$ $(x = 0)$, the argon gas flow was adjusted so that the levitating molten bead touches the nozzle. The contact surface thus acts as a nucleation center for crystallization of the entire bead when the lasers are turned off. This process produced a higher crystallinity of the sample compared to glass-crystallized samples of the composition, as confirmed by laboratory PXRD, showing narrower diffraction peaks for the molten liquid crystallized sample compared to the glass-crystallized sample (see Figure S3). The amorphous $(0.25 \le x \le 1)$/crystalline $(x = 0)$ state of resulting beads was further confirmed by laboratory PXRD (see Figures S2 and S3). The glass precursor samples were then crystallized in air at temperatures between 800 and 815 °C (characteristic crystallization temperatures obtained by DSC, as shown in Figure 2a), for 2−3 h (see Section 3.1).

2.2. Thermal Analysis. Differential scanning calorimetry (DSC) was performed on a Setaram MULTI HTC 1600 instrument to determine the glass transition and crystallization temperatures of each composition. A ∼300 mg powder sample was used, contained within a platinum crucible, with argon as the purging gas and a heating and cooling rate of 10 °C/min, samples were heated up to 900 °C. The measured temperatures have an incertitude of ±2 °C.

2.3. Powder Diffraction. Room temperature laboratory PXRD was performed using a Bruker D8 Advance laboratory diffractometer (Cu K_α radiation) equipped with a LynxEye XE detector in Bragg−Brentano geometry, with powders dispersed on a low-background

https://doi.org/10.1021/acs.inorgchem.2c01173
Inorg. Chem. 2022, 61, 9339−9351

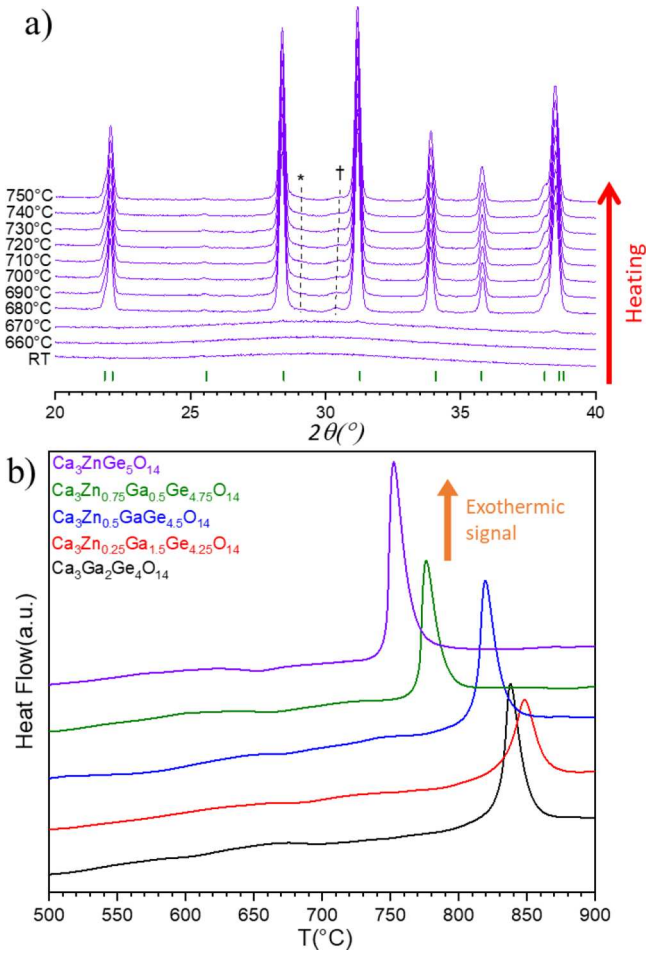

Figure 2. (a) Variable temperature PXRD measurements on the $Ca_3ZnGe_5O_{14}$ $x = 1$ glass composition showing its crystallization upon heating (0.5 °C/min heating rates), where * and † represent the $CaZnGe_2O_6$ and $Ca_2ZnGe_2O_7$ impurities, respectively. Green tick marks represent the *P*321 $Ca_3ZnGe_5O_{14}$ indexation. (b) DSC measurements of $Ca_3Ga_{2-2x}Zn_xGe_{4+x}O_{14}$ $x = 0$ (black), 0.25 (red), 0.5 (blue), 0.75 (green), and 1 (purple) samples, using a 10 °C/min rates upon heating.

silicon wafer. In situ variable temperature PXRD was performed using a Bruker D8 Advance laboratory diffractometer (also Cu K_α radiation, Bragg−Brentano geometry) equipped with a Vantec detector and an Anton Paar HTK1200N furnace. Powders obtained from crushed glass beads were placed in a platinum-lined corundum sample holder and heated under air. Data were collected from 30 to 600 °C in one heating step, and then to 1200 °C using a 10 °C step size, an angular range of 20−39° (2θ) with a 0.016° step size and counting time of 0.7 s/step. Synchrotron powder diffraction (SPD) measurements were collected on the 11BM beamline (Argonne National Laboratory) in the United States, for samples of composition $Ca_3Ga_{2-2x}Zn_xGe_{4+x}O_{14}$, where $x = 0$, 0.25, 0.5, 0.75, and 1. Crystallized beads were crushed to powder (one bead per composition) and filled into 0.8 mm diameter Kapton capillaries. Data were acquired with an incident wavelength of $\lambda = 0.458084$ Å from 1 to 50° (2θ) with a step size of 0.001° and a 0.1 s measuring time per step. Neutron powder diffraction (NPD) data were acquired for samples of composition $Ca_3Ga_{2-2x}Zn_xGe_{4+x}O_{14}$ $x = 0$, 0.5 and 1, on the instrument MEREDIT at the Nuclear Physics Institute, Czech Republic, with $\lambda = 1.46$ Å in the range 4−144° (2θ), using a step size of 0.08° and a measuring time of 970 s per step. Samples were scaled up to ∼5 g for $x = 0$, 0.5 and ∼4 g for $x = 1$, by crushing and combining ∼100 individually crystallized beads for neutron diffraction experiments. Structural analysis and Rietveld refinements[24] were performed using TOPAS Academic (v.6).[25] Bond valence sums (BVS) were calculated by the method of Brown and Altermatt.[26]

2.4. Transmission Electron Microscopy. The cation distributions were investigated at the atomic scale via high-resolution scanning transmission electron microscopy-high angle annular dark field (STEM-HAADF) imaging and energy dispersive X-ray spectroscopy (EDS) elemental mapping. These experiments were performed on a JEOL ARM200F (JEOL Ltd.) Cold FEG transmission electron microscope (TEM) operating at 200 kV, equipped with a double spherical aberration corrector and fitted with a JEOL SDD CENTURIO EDS system. In STEM-HAADF imaging mode, a 68−174.5 mrad inner-outer collection angle and a 0.1 nm probe size were used while in STEM-EDS mapping a probe size of 0.13 nm was chosen. Fine sample powder was first homogeneously dispersed in ethanol, and then one droplet of this suspension was deposited on a TEM amorphous holey carbon-coated copper grid and left to dry.

3. RESULTS

3.1. Synthesis by Crystallization from Glass and Molten Liquid. Classic solid-state reaction routes were first investigated in the synthesis of $Ca_3Ga_2Ge_4O_{14}$ ($x = 0$); however, we were not able to prepare single-phase powders by this route (see Supporting Information Section I for more details). Crystallization from glass was then considered as an alternative synthesis route, as this approach was shown to help accessing new metastable crystalline phases.[2−4,27] Initial attempts to make precursor glass of composition $Ca_3Ga_2Ge_4O_{14}$ ($x = 0$) used a conventional melt-quenching technique, by melting the reaction mixture in a platinum crucible at 1300 °C for 1 h, then quenching by placing the bottom of the crucible in a bath of water without any sample-water contact. After thermal treatment, these glasses showed a heterogeneous crystallization, leading to a mixture of gallate and germanate phases. In contrast, glass beads produced using the faster cooling rates offered by the ADL apparatus were found to crystallize into single-phase langasite materials after heat treatment at 815 °C. By further tuning of the ADL experimental conditions, we found that direct crystallization of the molten bead (see Section 2.1) produced single-phase langasite materials with sharper diffraction peaks (see Figure S3). We used the directly crystallized materials for all structural characterizations of the composition $x = 0$.

Single-phase langasite materials were obtained for $0.25 \leq x \leq 1$ by crystallization of precursor glasses obtained by ADL. The highest quality samples were obtained by crystallizing the beads in bulk form rather than crushed (powder) form due to surface crystallization of the secondary phases $CaZnGe_2O_6$ and $Ca_2ZnGe_2O_7$ (see Figure S4): in situ PXRD of $Ca_3ZnGe_5O_{14}$ ($x = 1$) glass powder shows the crystallization of the langasite phase above 670 °C, which occurs simultaneously with crystallization of these minor impurities (Figure 2a). In Figure S5, we show a comparison between DSC heating curves of $Ca_3ZnGe_5O_{14}$ ($x = 1$) glass, measured under powder and bulk form. The powder sample exhibits a lower T_c, consistent with a more facile surface crystallization mechanism. As shown in Figure 2b, DSC measurements were conducted on a single glass bead for each composition to determine their glass transition (T_g) and glass crystallization (T_c) temperatures (see Table S1). To achieve full and congruent crystallization from glass, the resulting glass beads for $0 < x \leq 1$ were heated at 815 °C for 2 h ($0 < x < 1$) and at 800 °C for 3 h ($x = 1$), under bulk form to prevent surface crystallization of impurities. Beads prepared in this way contained langasite-type $Ca_3Ga_{2-2x}Zn_xGe_{4+x}O_{14}$ as the only crystalline phase.

https://doi.org/10.1021/acs.inorgchem.2c01173
Inorg. Chem. 2022, 61, 9339−9351

3.2. Structure Evolution from $0 \leq x \leq 1$ by Synchrotron XRD. The reported $Ca_3ZnGe_5O_{14}$ monoclinic langasite structure (SG. *C*2, a = 13.938(5) Å, b = 7.941(3) Å, c = 5.0560(17) Å, and β = 90.817(4)°),[14] was described as a fully ordered structure where Zn^{2+} cations are accommodated on the octahedral (B) sites, while Ge^{4+} cations occupy the remaining tetrahedral (C- and D-) sites. To further investigate the possibility of a monoclinic distortion for glass-crystallized samples close to this composition (x = 1), SPD measurements were conducted on samples of composition x = 0, 0.25, 0.5, 0.75, and 1.

Across the solid solution, all SPD patterns (Figure S6) could be indexed with the parent hexagonal langasite cell with a systematic peak shift (Figure 3a), and no extra peaks became apparent as the composition approaches x = 1, indicating that the *P*321 structure is retained for all compositions. Figure 3b shows a direct comparison between the acquired SPD pattern of $Ca_3ZnGe_5O_{14}$ (x = 1), and a simulated SPD pattern of $Ca_3ZnGe_5O_{14}$ (reported *C*2 structure)[14] under the same measuring conditions. The simulated *C*2 diffraction pattern contains many additional Bragg peaks that are not present in the acquired pattern, which is fully indexed to the hexagonal *P*321 $Ca_3Ga_2Ge_4O_{14}$ cell.

Rietveld refinements were carried out using the $Ca_3Ga_2Ge_4O_{14}$ structure reported by Mill et al.[17] (SG *P*321, a = 8.076 Å, c = 4.974 Å) as a starting model for all compositions, keeping the same number of total refined parameters for each sample (15 background terms, zero shift, scale factor, 6 profile parameters (TCHZ profile function), axial divergence and 17 atomic parameters, resulting in 41 refined independent parameters). The B-, C-, and D sites were fixed to be fully occupied by cations with no refinement of the Ga^{3+}, Ge^{4+}, or Zn^{2+} partial occupancies. The refined cell parameters (from SPD data) show opposing trends in the a and c parameters, giving a very weak decrease in unit cell volume but a marked increase in c/a ratio with increasing x (Figure 3c). Such behavior is consistent with the substitution of Ga^{3+} (ionic radius of 0.62 and 0.47 Å in 6- and 4-coordination, respectively) by a mixture of smaller Ge^{4+} (0.53 and 0.39 Å) and larger Zn^{2+} (0.74 and 0.60 Å),[28] and is also seen in other langasite-type solid solutions such as $La_3Ga_{5-x}Ge_{1+x}O_{14+x/2}$.[13] The refinements led to satisfactory reliability factors for the entire measured series (see Figures S8–S10 for SPD Rietveld refinement plots and Tables S2–S6 for refined structural parameters).

As shown in Figure 3b, the $Ca_3ZnGe_5O_{14}$ (x = 1) sample synthesized by glass crystallization produces far fewer Bragg reflections than the previously reported monoclinic (*C*2) structure, and can be indexed fully to the trigonal (*P*321) structure. We also compared the Rietveld fits obtained from both structural models. Provisional refinement of both models produced misfits due to an *hkl*-dependent peak broadening in the measured pattern. This was modeled using the Stephens description[29] for trigonal and monoclinic symmetries, respectively, thus reducing the R_{wp} and χ^2 values from [8.98%, 2.01] to [7.36%, 1.35] for the *P*321 model and from [8.93%, 1.99] to [6.68%, 1.10] for the *C*2 model (see Figures S10 and S12 for SPD refinements and Tables S6–S9 for refined structural parameters). The unit cell of the *C*2 model, refined to an essentially orthorhombic symmetry corresponding to a decrease of β from 90.817(4)° (published starting model)[14] to 89.955(1)°. Even though the *C*2 model provides a marginally better fit to the whole pattern when the Stephens broadening functions are applied, the lower symmetry of this structure allows more refinable parameters (68 + 10 parameters from Stephens description) than the *P*321 space

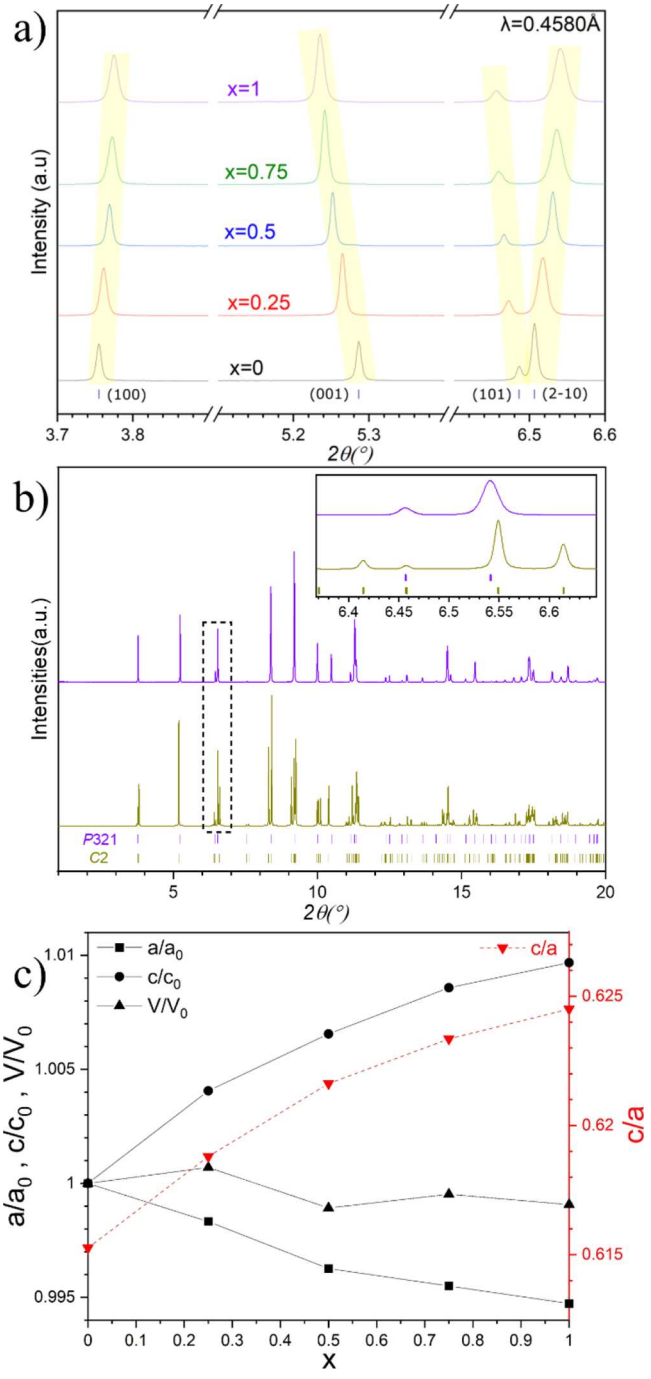

Figure 3. (a) Synchrotron powder diffraction data from $Ca_3Ga_{2-2x}Zn_xGe_{4+x}O_{14}$ x = 0 (black), 0.25 (red), 0.5 (blue), 0.75 (green), and 1 (purple), highlighting the systematic shift of the (100), (001), and (101)/(2$\bar{1}$0) peaks due to the Ga^{3+} substitution by Zn^{2+} and Ge^{4+}. Dark blue tick marks correspond to $Ca_3Ga_2Ge_4O_{14}$ (space group *P*321). (b) SPD pattern of glass-crystallized $Ca_3ZnGe_5O_{14}$ (purple) compared with a simulated pattern of the previously reported monoclinic *C*2 structure[14] (dark yellow), with their respective cell indexations (dark yellow and purple tick marks). (c) Normalized refined cell parameters (from Rietveld analysis) of the *P*321 langasite structure across the solid solution series to the parent $Ca_3Ga_2Ge_4O_{14}$ cell parameters.

https://doi.org/10.1021/acs.inorgchem.2c01173
Inorg. Chem. 2022, 61, 9339−9351

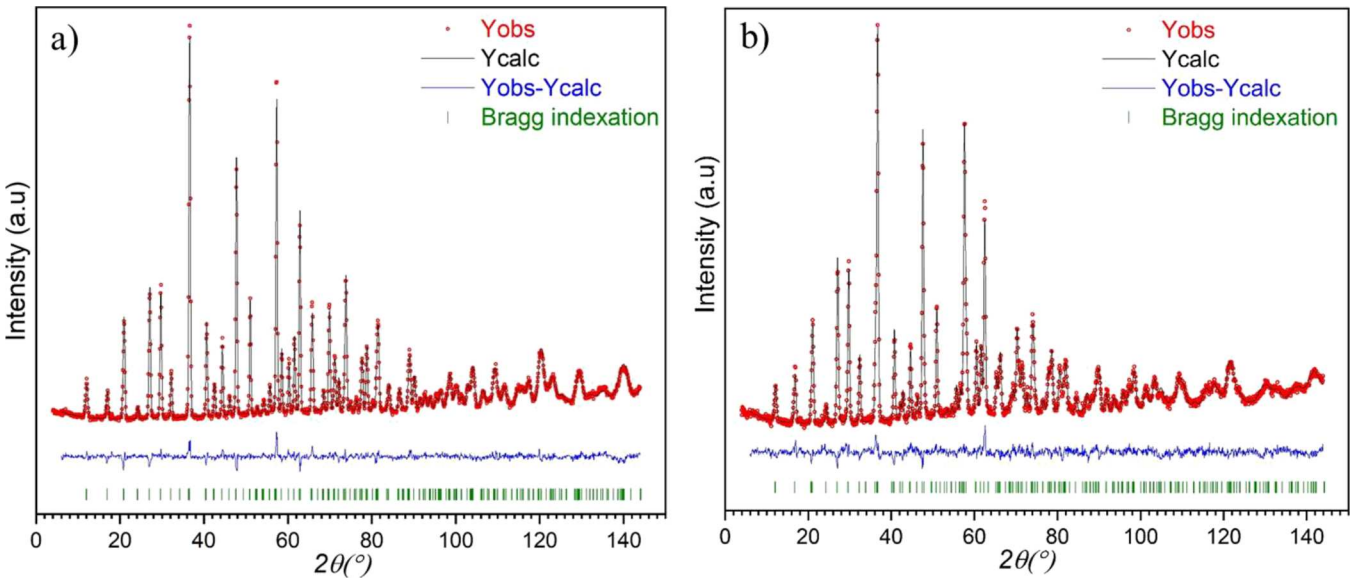

Figure 4. NPD Rietveld refinements plots of (a) $Ca_3Ga_2Ge_4O_{14}$ (x = 0), R_p = 3.04%, R_{wp} = 3.83%; (b) $Ca_3ZnGe_5O_{14}$ (x = 1), R_p = 3.43%, R_{wp} = 4.35%. Observed (red dot), calculated (black line), and difference (blue line) profiles are shown. The green tick marks correspond to allowed reflection positions.

Table 1. Refined Structural Parameters Obtained from NPD Data Collected at Room Temperature on $Ca_3Ga_2Ge_4O_{14}$ ($P321$ Space Group, a = 8.0712(2) Å and c = 4.9680(2) Å)

atom	position	x	y	z	Occ	B_{iso}
Ca	3e	0.4183(7)	0	0	1	0.91(10)
Ga1/Ge1	1a	0	0	0	0.51(8)/0.49(8)	0.92(5)[a]
Ga2/Ge2	3f	0.7635(4)	0	1/2	0.50(3)/0.50(3)	0.92(5)[a]
Ge3	2d	1/3	2/3	0.5273(9)	1[b]	0.92(5)[a]
O1	2d	1/3	2/3	0.1843(11)	1	1.18(4)[a]
O2	6g	0.4616(5)	0.3144(4)	0.3113(6)	1	1.18(4)[a]
O3	6g	0.2174(4)	0.0793(4)	0.7667(6)	1	1.18(4)[a]

[a]Constrained to refine to the same B_{iso} values. [b]Fixed at 1 after its initial refined value converged to almost 1.

Table 2. Refined Structural Parameters Obtained from NPD Data Collected at Room Temperature on $Ca_3ZnGe_5O_{14}$ ($P321$ Space Group, a = 8.0308(3) Å and c = 5.0164(4) Å)

atom	position	x	y	z	Occ	B_{iso}
Ca	3e	0.4198(8)	0	0	1	1.18(13)
Zn1/Ge1	1a	0	0	0	0.52(4)/0.48(4)	1.09(8)[a]
Zn2/Ge2	3f	0.7674(5)	0	1/2	0.16(1)/0.84(1)	1.09(8)[a]
Ge3	2d	1/3	2/3	0.5295(12)	1[b]	1.09(8)[a]
O1	2d	1/3	2/3	0.1854(17)	1	2.17(7)[a]
O2	6g	0.4617(7)	0.3173(5)	0.3139(10)	1	2.17(7)[a]
O3	6g	0.2227(6)	0.0785(6)	0.7585(10)	1	2.17(7)[a]

[a]Constrained to refine to the same B_{iso} values. [b]Fixed at 1 after its initial refined value converged to almost 1.

group (41 + 5 parameters from Stephens description), and the refined model is almost indistinguishable from its trigonal counterpart, as shown in Figure S7 an overlay of both refined structures against the same acquired SPD data. We therefore consider the trigonal $P321$ structure to be the simplest and most appropriate description of glass-crystallized $Ca_3ZnGe_5O_{14}$ (x = 1).

To test the stability of the $Ca_3ZnGe_5O_{14}$ (x = 1) $P321$ structure against T(°C) and a possible phase transition ($P321$ → $C2$), variable temperature PXRD (VT-PXRD) measurements were carried out on a glass-crystallized $Ca_3ZnGe_5O_{14}$ (x = 1) sample, from room temperature to 700 °C in steps of 100 °C. As shown on Figure S12, the cell parameters display a linear increasing trend and no discontinuous changes were noticed (as demonstrated in[16] for some langasite compositions under pressure, where their cell parameters trend shows a discontinuity due to a phase transition from $P321$ to $C2$), suggesting that the hexagonal polymorph is retained until its decomposition.

3.3. Distribution of Two Cations in x = 0, 1 End Members by Neutron Diffraction. The end-member compositions (x = 0, 1) host only two cation species on the framework (B, C, D) sites, with different neutron scattering lengths (8.185(20) fm, 7.288(2) fm, and 5.680(5) fm for Ge, Ga, and Zn, respectively),[30] allowing the use of NPD to refine the Ga/Ge and Zn/Ge ratios directly. Rietveld refinements

https://doi.org/10.1021/acs.inorgchem.2c01173
Inorg. Chem. 2022, 61, 9339−9351

Table 3. Cation Oxide Interatomic Distances and Bond Valence Sums Calculated for all Ga and Ge Sites of $Ca_3Ga_2Ge_4O_{14}$

site	bond	length (Å)	site	bond	length (Å)	site	bond	length (Å)
B(1a)	*M*−O3 x6	1.926(3)	C(3f)	*M*−O3 x2	1.787(4)	D(2d)	*M*−O1 x1	1.704(7)
				M−O2 x2	1.853(5)		*M*−O2 x3	1.776(4)
	BVS (Ga)[a]	3.53(2)		BVS (Ga)[a]	3.37(2)		BVS (Ga)[a]	3.72(3)
	BVS (Ge)[a]	3.71(2)		BVS (Ge)[a]	3.49(2)		BVS (Ge)[a]	3.91(3)

[a]Calculated with a distance cut off at 3 Å.

Table 4. Cation Oxide Interatomic Distances and Bond Valence Sums Calculated for All Zn and Ge Sites of $Ca_3ZnGe_5O_{14}$

site	bond	length (Å)	site	bond	length (Å)	site	bond	length (Å)
B(1a)	*M*−O3 x6	1.984(6)	C(3f)	*M*−O3 x2	1.767(6)	D(2d)	*M*−O1 x1	1.73(1)
				M−O2 x2	1.862(6)		*M*−O2 x3	1.770(6)
	BVS (Zn)[a]	2.74(2)		BVS (Zn)[a]	3.06(2)		BVS (Zn)[a]	3.29(3)
	BVS (Ge)[a]	3.17(2)		BVS (Ge)[a]	3.58(2)		BVS (Ge)[a]	3.89(4)

[a]Calculated with a distance cut off at 3 Å

against NPD data were constrained to keep each mixed site fully occupied and an overall composition matching the nominal; see Figure 4a,b for refined plots, and Tables 1 and 2 for refined structural parameters. The refinements of neutron data for the $x = 0$ sample showed that the cationic disorder is distributed over the octahedral 1a and tetrahedral 3f sites (as previously reported in refs 17, 31), while the tetrahedral 2d site remains fully occupied by Ge. Refined occupancies led to 0.51(8)Ga/0.49(8)Ge on the 1a site and 0.50(3)Ga/0.50(3) Ge on the 3f site, which displays a complete disorder over these two crystallographic sites (see Tables 1 and 2). This is consistent with a non-quantitative ^{71}Ga QPASS NMR spectrum collected from the $Ca_3Ga_2Ge_4O_{14}$ sample, which showed resonances from 6- and 4-coordinate gallium (as described in Supporting Information Section II).

Rietveld refined NPD data for the $x = 1$ fully substituted end member also confirmed that the cationic disorder occurs between the 1a and 3f sites, while the 2d site remains fully occupied by Ge atoms. The refined occupancies over the mixed sites, 0.52(4)Zn/0.48(4)Ge on the 1a and 0.16(1)Zn/0.84(1)Ge on the 3f, show that only Zn atoms are randomly dispersed over the two coordination types, 52(4)% on the 1a 6-coordinated site and 16(1)% on the 3f 4-coordinated site. The B- and C-site cation oxide distances show notable differences going from the $Ca_3Ga_2Ge_4O_{14}$ langasite to the fully Zn/Ge-substituted compound $Ca_3ZnGe_5O_{14}$ (Tables 3 and 4).

The B-site *M*−O3 bond length increases from 1.926(3) Å (Ga1/Ge1-O3) to 1.984(6) Å (Zn1/Ge1-O3), which allows an 8.7% increase of the polyhedral volume, while both C-site *M*−O3 and *M*−O2 bonds lengths decrease from 1.787(4) Å (Ga2/Ge2-O3) and 1.853(5) Å (Ga2/Ge2-O2), to 1.767(6) Å (Zn2/Ge2-O3) and 1.862(6) Å (Zn2/Ge2-O2), respectively, leading to the 3f site tetrahedron a volume decrease of 2.1%. These results are consistent with the refined occupancies of each site for both end members, where Ga^{3+} is fully exchanged by the larger Zn^{2+} cation on the 1a site and only one-third by the same larger cation on the 3f site, while the other two-thirds are substituted by a smaller Ge^{4+} cation. The hypothesis of a fully ordered hexagonal langasite structure for both end members was considered by Rietveld refinement with different fixed Ga/Ge and Zn/Ge occupancies on both 1a and 3f sites against NPD data. In Figure S13a,b, a shallow χ^2 minimum can be detected when the amount of Ga^{3+} and Zn^{2+} approaches 50% occupancy of the 1a site for $x = 0$ and 1, respectively. Moreover, subtle peak intensity misfits at low angle can be spotted when Ga^{3+} or Zn^{2+} scattering density is focused on one of the two cationic disordered sites, inducing over- or undercalculated peak intensities (Figure S13c,d). The intensity misfits are more visible for the Zn^{2+} compound $x = 1$, compared to the Ga^{3+} compound $x = 0$ due to their close neutron scattering lengths.[30] Furthermore, BVS calculations (Tables 3 and 4), indicate that only the 2d site is suitable for Ge^{4+}, BVS = 3.91(3) and 3.89(4) with a mean Ge3−O distance of 1.758(4) and 1.759(3) Å for both $x = 0$ and $x = 1$ compounds, respectively. For the 1a and 3f sites, the BVS values indicate that all three cations are either under- or overbonded in the two different coordination types, which is consistent with the partial cation disorder observed by Rietveld refinement. The trend in bond distances and atomic site occupancies from NPD is discussed together with the bond distance trend from SPD across the full series ($x = 0$, 0.5, 1) in Section 4.

3.4. Distribution of Three Cations in $x = 0.5$ by STEM-EDS and Neutron Diffraction. To analyze the distribution of three isoelectronic cations over multiple crystallographic sites, as required for the intermediate composition $Ca_3GaZn_{0.5}Ge_{4.5}O_{14}$ ($x = 0.5$), neutron diffraction must be combined with another complementary technique. Here, our approach is to extract direct quantitative information about the cation distributions by atomic-resolution STEM-EDS, and use this to construct a Rietveld model with appropriate (chemically justified) constraints on the refined cation occupancies.

In order to visualize the 2D structural projection of the $Ca_3GaZn_{0.5}Ge_{4.5}O_{14}$, the sample was oriented along the [001]* direction (Figure 5a) and imaged in STEM-HAADF mode at the atomic scale (Figure 5b,c). Along the [001]* direction, each column of atoms is composed of only one type of crystallographic site with the same density (see Figure 1).

In STEM-HAADF mode, the intensity of the acquired images is proportional to the thickness of the sample (e), the density (ρ) and the average atomic number (Z): $I \propto e\rho Z^n$, where n is in the range 1.6−2. The thickness of the sample was measured at 60 nm by electron energy loss spectroscopy (EELS), which represents close to 120 superimposed unit cells (120 atoms per column). It was estimated to remain unchanged across the entire imaged area (≈5 nm × 5 nm). In these conditions, the intensity in the STEM-HAADF images is essentially due to the average atomic number (Z) of the crystallographic site. The 3e sites, being composed of the lightest cations ($Z_{Ca} = 20$), appear the darkest while the 1a, 3f,

https://doi.org/10.1021/acs.inorgchem.2c01173
Inorg. Chem. 2022, 61, 9339−9351

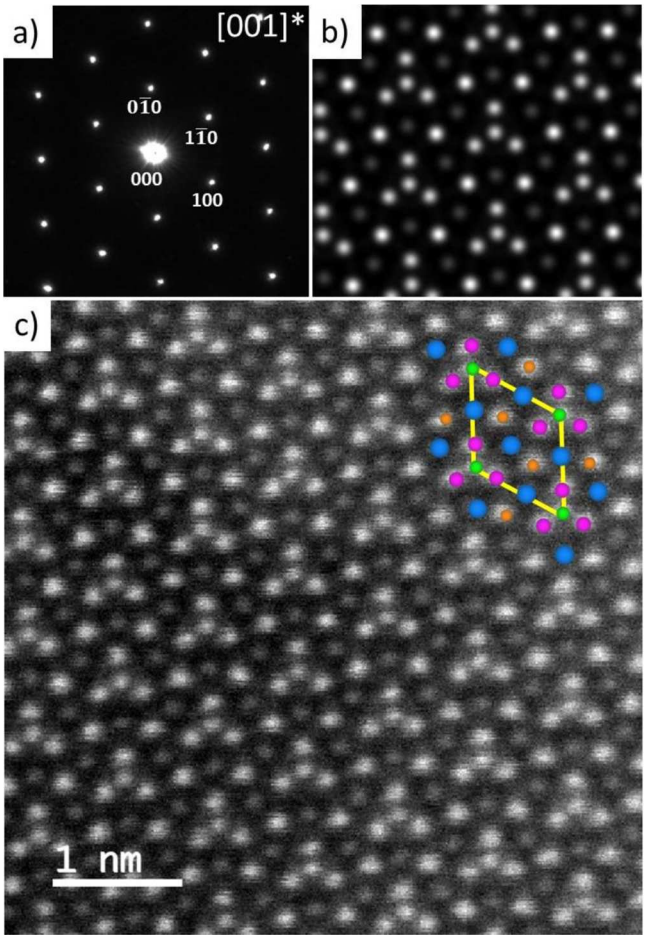

Figure 5. (a) Selected area electron diffraction (SAED) pattern of the $Ca_3GaZn_{0.5}Ge_{4.5}O_{14}$ (x = 0.5) sample oriented along the [001]* direction, with (b) and (c) showing simulated (using JEMS software)[32] and measured STEM-HAADF images, respectively. The corresponding crystal structure projection is overlaid on the top-right corner of the image, where blue, green, pink and orange points represent the 3e, 1a, 3f, and 2d crystallographic sites, respectively.

and 2d sites appear brighter due to the presence of heavier cations (Z_{Ge} = 32, Z_{Ga} = 31, and Z_{Zn} = 30). However, as Ge, Ga, and Zn are of similar atomic number ($Z_{Ge} \approx Z_{Ga} \approx Z_{Zn}$), it is not possible to determine the distribution of these three cations on the 1a, 3f, and 2d crystallographic sites using only the intensities of the STEM-HAADF images. Consequently, EDS mapping at the atomic scale was carried out (Figure 6). The maps acquired on several zones of the same grain were aggregated in order to improve the signal-to-noise ratio and to tend toward an average model. A Wiener filter was then applied to highlight the atomic positions. The 3e site is clearly visible and composed only of Ca as expected, while the 2d site contains only Ge, and the 3f and 1a sites are mixed, which is consistent with the refined structures of $Ca_3Ga_{2-2x}Zn_xGe_{4+x}O_{14}$ both end members x = 0 and x = 1.

The Ga and Ge signals appear clearly on both the 1a and 3f sites, while the Zn signal seems to be focused on the 1a sites; visually, it is difficult to confirm its presence on the 3f site. In order to gain more information and determine the Ga, Ge, and Zn cation ratio on the 1a and 3f sites, a 1D analysis was performed by extracting an intensity profile through the sites from the EDS maps. The width of the profile (the orange rectangle overlaid on Figure 6b) was optimized in order to integrate as much signal as possible without introducing interference from the neighboring 1a and 3f column signals. In such a configuration, with a small distance between the cation sites 1a−3f (≈1.9 Å), it is not possible to integrate the full signal for each crystallographic site (Figure 6b).

Using a Gaussian decomposition and assuming that the area under the curve is proportional to the element content, the ratios of the elements Ge, Ga, and Zn between sites 1a and 3f were determined (Figure 7). The Gaussian coordinates were defined for the 1a and 3f sites from the Ge profile, which is best defined thanks to its high concentration, and then fixed for all the other element profiles (Ga and Zn) in order to integrate the signal in the same positions. As the Zn content is low, its profile was first refined using only one Gaussian contribution at the 1a coordinates (see Figure S14). However, a single Gaussian could not describe the entire profile, and a second Gaussian was added at the 3f position, indicating a small amount of Zn also present on this site. The calculated ratios between the 1a and 3f sites for the three cations were: (Ge_{1a}/Ge_{3f} = 0.9) (Ga_{1a}/Ga_{3f} = 1.17) (Zn_{1a}/Zn_{3f} = 2.6). Considering the nominal composition $Ca_3GaZn_{0.5}Ge_{4.5}O_{14}$, which has been checked by EDS analyses, and a 2d pure Ge site, the compositions of the mixed 1a and 3f sites have been determined and reported in Table 6: 0.23(10)Zn/0.54(5)Ge/0.28(8)Ga and 0.09(4)Zn/0.67(2)Ge/0.24(3)Ga, respectively. These results show a very good agreement with refined occupancies from NPD data. Nevertheless, this 1D approach has certain limitations such as the application of a Wiener filter on the elementary maps, which can induce a bias, as well as the inability to integrate the signal through the entire sites due to the small distance between the neighboring 1a and 3f sites. Such problems can be reduced by a two-dimensional fitting approach such as that demonstrated by Lu et al.,[19,20] so that a wider region of the map is used for quantitative analysis.

We chose to analyze two regions from the central part of the 2D elemental images to minimize possible errors or deformation at the borders. These two regions are centered on 1a sites and extending to their first 3f and 2d neighbors, defining polygonal regions with minimal contributions of other sites (see Figure S15). We then performed a refinement for each cation (Zn, Ga, and Ge) using the simplest possible model of a background offset and a sum of two-dimensional Gaussian lines for each site. Each 2D Gaussian is characterized by its x and y positions, width at half maximum, and amplitude.

The Ge data (with the best signal-to-noise ratio due to the high concentration of Ge in the cell) were refined first to extract the peak positions, width and amplitude for each of the 1a and 3f sites (note that the three 3f sites surrounding the 1a sites were constrained to keep the same peak width, for each of the two selected zones independently). The Zn and Ga data were then refined with constrained peak position and peak width from the Ge ones, hence extracting only the amplitude as refined value for these two cations on the 1a and 3f sites. Refinements of the STEM-EDS maps from zone 1 are shown in Figure 8. The equivalent zone 2 refinements are shown in Figure S16. The compositions of each column were extracted using the same calculation logic as the one used for the 1D refinements and normalizing the occupancies to 1.

Following the quantitative analysis by STEM-EDS, we constructed a Rietveld model for refinement against NPD data. Using the observation that the 2d site is dominated by Ge (Figure 6d and Figure 8), and by analogy with the x = 0 and 1 members (Tables 1 and 2), we fixed the 2d site in x = 0.5 to be

https://doi.org/10.1021/acs.inorgchem.2c01173
Inorg. Chem. 2022, 61, 9339−9351

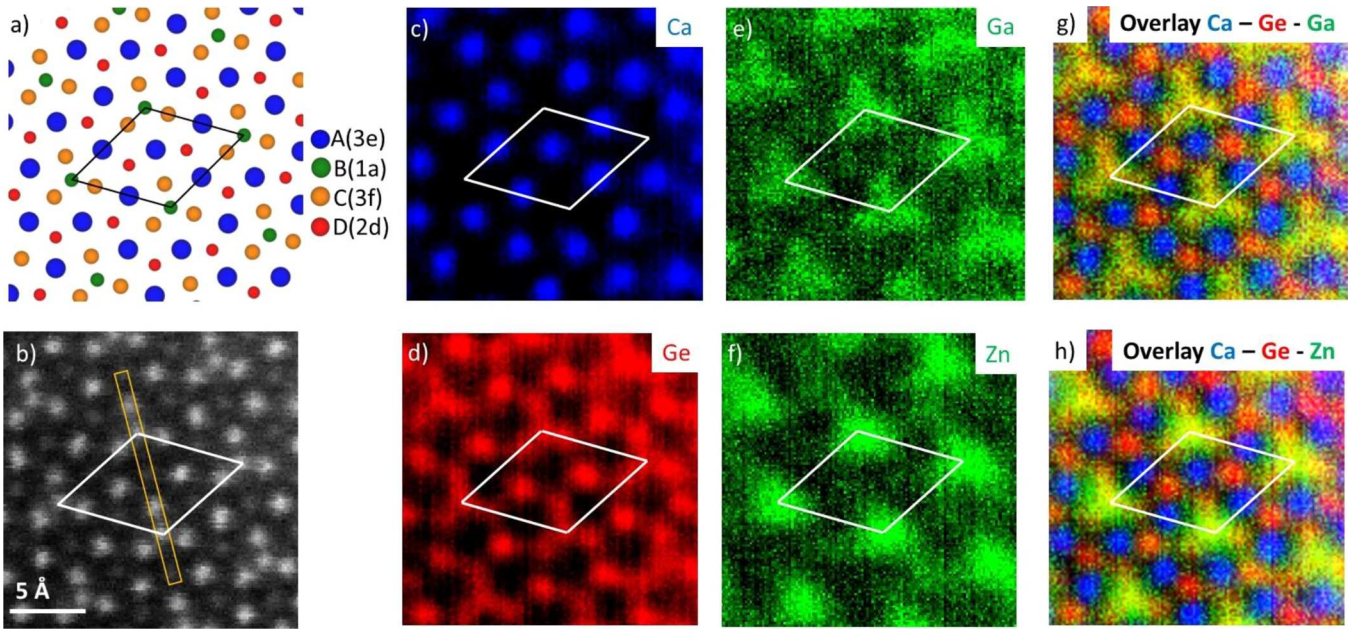

Figure 6. (a) Scheme of the trigonal *P*321 structure projected along [001] and (b) its corresponding atomic-resolution STEM-HAADF image for the $Ca_3GaZn_{0.5}Ge_{4.5}O_{14}$ (x = 0.5) composition. Atomic-scale STEM-EDS maps of the cations (c) Ca in blue, (d) Ge in red, (e) Ga in green (Wiener filtered image), and (f) Zn in green (Wiener strong filtered image). The overlaid EDS maps of "Ca, Ga, Ge" and "Ca, Zn, Ge" are shown in (g) and (h), respectively. The crystallographic unit cell is outlined in white in panels (b–h). The orange rectangle overlaid on (b) is the region used for 1D profile fitting presented in Figure 7.

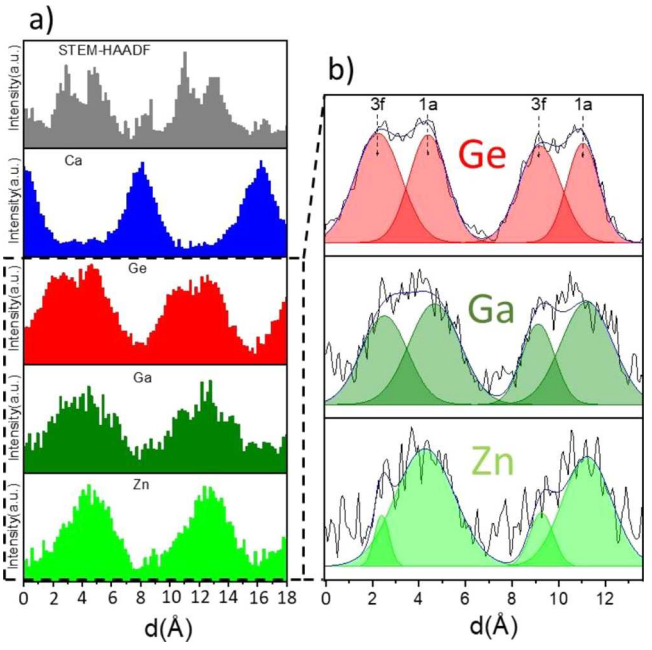

Figure 7. (a) STEM-HAADF intensity profile in gray and EDS profiles of Ca, Ge, Ga, and Zn (in blue, red, dark green, and light green, respectively). The signal was integrated from the drawn orange rectangle in Figure 6b. (b) In black, EDS profiles of Ge, Ga, and Zn extracted from the STEM-EDS raw maps. The signals are integrated through the orange strip on two neighboring 1a and 3f sites (Figure 6b). The calculated signals decomposed in Gaussian curves (blue), and the integrated areas (red for Ge and dark and light green for Ga and Zn) under the calculated curves have been overlaid.

occupied exclusively by Ge. We then populated the 1a and 3f sites with the remaining Zn, Ga, and Ge atoms, weighted according to their apparent site preferences from STEM-EDS and end-member Rietveld refinements (0.25Ga/0.251Zn/0.5Ge and 0.25Ga/0.083Zn/0.667Ge for 1a and 3f, respectively). Constraints were then applied to (i) keep each site fully occupied by cations (Zn + Ga + Ge = 1) and (ii) fix the global composition to the nominal value $Ca_3GaGe_{4.5}Zn_{0.5}O_{14}$. The Zn, Ga, and Ge occupancies of 1a and 3f were then refined subject to these constraints.

The refined Zn and Ge occupancies on both sites led to a Zn distribution close to the one in the $Ca_3ZnGe_5O_{14}$, x = 1 compound, where Zn and Ga are disposed in a 43(6)%/57(6)% and 25(2)%/75(2)% ratios between the two 1a and 3f sites, respectively, while Ge is disposed between the 1a, 3f, and 2d sites in a 0.12(1)%/0.44(1)%/0.44% ratio; see Figure 9 and Table 5 for refined plot and parameters. The results show good agreement between the Rietveld refinement and the STEM-EDS results, as shown in Table 6.

4. DISCUSSION

High-resolution SPD shows that the crystal structures of $Ca_3Ga_{2-2x}Ge_{4+x}Zn_xO_{14}$ ($0 \le x \le 1$) can all be indexed to a trigonal unit cell (*P*321) when crystallized from precursor glasses or directly from their melts. This is consistent with the reported crystal structure of $Ca_3Ga_2Ge_4O_{14}$, which is also trigonal when synthesized by single-crystal growth methods, but it contrasts with a previous study on $Ca_3ZnGe_5O_{14}$ single crystals which are metrically monoclinic. As described in Section 3.2, the refinement of trigonal and monoclinic models against the acquired SPD pattern of $Ca_3ZnGe_5O_{14}$ (x = 1) produced very similar fits and near-identical structures, and we thus retained the simpler trigonal model as the most appropriate structural description. The underlying difference between trigonal glass-crystallized $Ca_3ZnGe_5O_{14}$ and monoclinic single-crystal $Ca_3ZnGe_5O_{14}$[14] lies in the distribution of Zn^{2+} and Ge^{4+} between the octahedral (1a) and tetrahedral (3f) sites. In single-crystal $Ca_3ZnGe_5O_{14}$,[14] these cations are

https://doi.org/10.1021/acs.inorgchem.2c01173
Inorg. Chem. 2022, 61, 9339–9351

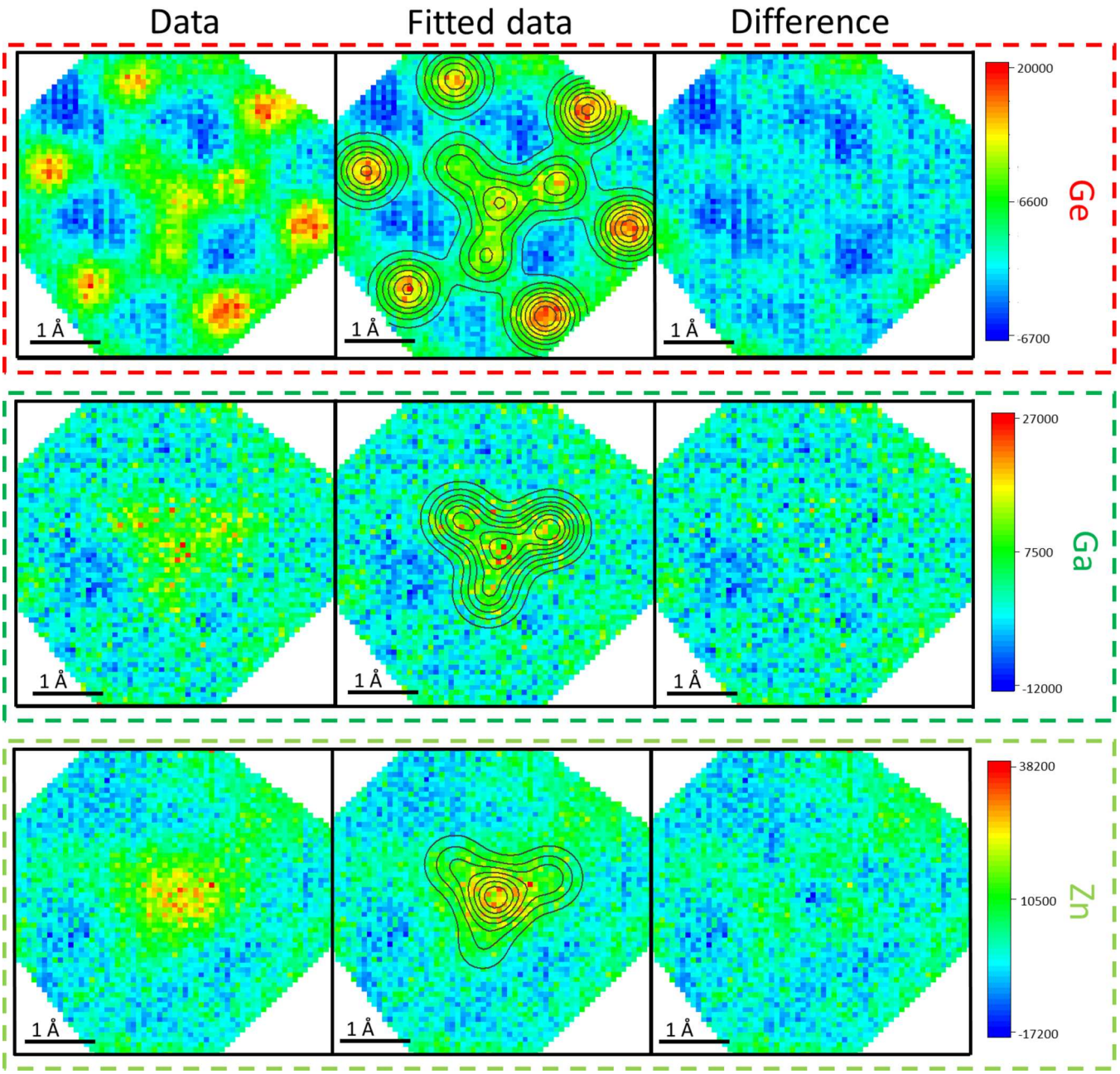

Figure 8. STEM-EDS 2D refinement plots of Ge, Ga, and Zn from zone1, where the left column represents the data (after processing), the middle column fitted data (fit in black contours) and the difference plots in the right column.

fully ordered with Zn^{2+} exclusively in octahedral coordination. In contrast, glass-crystallized $Ca_3ZnGe_5O_{14}$ contains a significant amount of site inversion with Zn^{2+} partially occupying the tetrahedral 3f sites. This can also be seen by comparison of the B-, C-, and D-site polyhedral volumes of the two structures. In Table 7, we show a comparison between the octahedral (1a), tetrahedral (3f and 2d) Zn−O distances in glass-crystallized (trigonal) and single-crystal (monoclinic) $Ca_3ZnGe_5O_{14}$: in the trigonal structure, these distances are significantly shorter for the 1a site, and slightly longer for the 3f, while they show similar values for the 2d site, consistent with refined partial occupancies of only the 1a and 3f by smaller Ge^{4+} and bigger Zn^{2+}. We note that the symmetry-reducing monoclinic distortion is not a prerequisite for this type of Zn^{2+}/Ge^{4+} ordering, which implies that the monoclinic distortion of the lattice is induced by the cation ordering and its associated changes in the average size of the framework polyhedra.

At the other extreme of the solid solution, $Ca_3Ga_2Ge_4O_{14}$ (x = 0), there are some minor differences in the extent of Ga^{3+}/Ge^{4+} ordering between the melt-crystallized materials that we report here, and single-crystal materials described in the literature,[33] despite the retention of trigonal $P321$ symmetry (see Table 8). In melt-crystallized $Ca_3Ga_2Ge_4O_{14}$, Ga^{3+} ions are distributed over the octahedral 1a and tetrahedral 3f sites, while the tetrahedral 2d sites are occupied exclusively by Ge^{4+}; only 25(4)% of the total Ga content is in octahedral coordination, whereas the remaining 75(4)% is tetrahedrally coordinated. This is consistent with the reported Ga/Ge coordination environments in $Ca_3Ga_2Ge_4O_{14}$ glass determined

https://doi.org/10.1021/acs.inorgchem.2c01173
Inorg. Chem. 2022, 61, 9339−9351

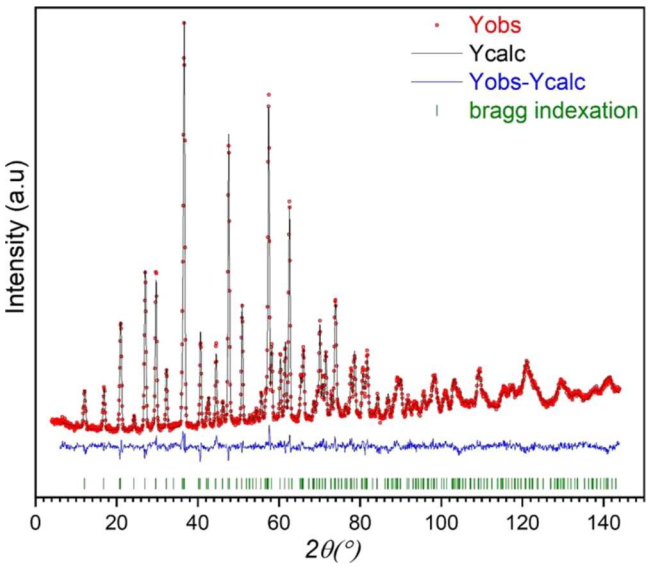

Figure 9. NPD Rietveld refinements plot of $Ca_3GaZn_{0.5}Ge_{4.5}O_{14}$ (x = 0.5) R_p = 2.97% R_{wp} = 3.80%. Observed (red dot), calculated (black line), and difference (blue line) profiles are shown. The green tick marks correspond to allowed reflection positions.

by EXAFS.[34] In single-crystal $Ca_3Ga_2Ge_4O_{14}$,[33] anomalous X-ray scattering methods have shown that only ~10% of the Ga^{3+} cations are present in octahedral coordination (1a), with the remainder present at the tetrahedral (3f) site. In both materials, the tetrahedral 2d site is occupied exclusively by Ge^{4+}, which may help to maximize separation of the most highly charged cations, and hence minimize electrostatic repulsion between them. This confirms that the synthesis route can influence the extent of Ga^{3+}/Ge^{4+} ordering in these structures, with melt-crystallization favoring a higher degree of disorder in this case, compared to the single crystals synthesized by a Czochralski method.[33]

In complex glass-crystallized compositions with three isoelectronic cations ($Zn^{2+}/Ga^{3+}/Ge^{4+}$) distributed over the three possible octahedral and tetrahedral framework sites, exemplified by $Ca_3GaZn_{0.5}Ge_{4.5}O_{14}$ (x = 0.5), which is reported here for the first time, a combined approach between NPD refinements and quantitative 2D fitting to atomic-resolution STEM-EDS maps was applied. The analysis of $Ca_3GaZn_{0.5}Ge_{4.5}O_{14}$ shows that the structure evolves progressively as the solid solution is traversed. This is seen in the unit cell parameters (Figure 3c) and the Rietveld refined M−O distances at the 1a (octahedral), 3f (tetrahedral), and 2d (tetrahedral) framework sites (Figure 10): as Zn^{2+} is substituted into the structure, there is a marked increase in the volume of the MO_6 octahedra which goes against the overall decreasing trend in unit cell volume, indicating that the 1a site is becoming preferentially populated by larger cations. It was possible to quantify directly the cation distribution in $Ca_3GaZn_{0.5}Ge_{4.5}O_{14}$ (x = 0.5) by 2D fitting to atomic-

Table 6. Refined Occupancies for Zn, Ga, and Ge on the 1a, 3f, and 2d Sites, Extracted from NPD Data and STEM-EDS Maps

	site atom	1a	3f	2d
NPD refinement	Zn	0.22(3)	0.09(1)	0
	Ga	0.25(2)	0.25(1)	0
	Ge	0.53(2)	0.66(1)	1
1D refinement	Zn	0.23(10)[a]	0.09(4)[a]	0
	Ga	0.28(8)[a]	0.24(3)[a]	0
	Ge	0.54(5)[a]	0.67(2)[a]	1
2D refinement	Zn	0.18(3)[b]	0.11(3)[b]	0
	Ga	0.24(2)[b]	0.26(2)[b]	0
	Ge	0.59(2)[b]	0.64(2)[b]	1

[a]Errors were estimated by calculating standard deviation from the fitted areas of the 1D EDS profiles over the averaged 4 (1a, 3f sites) on the cell corners, shown in Figure 6d−f. [b]Mean values from zone 1 and zone 2 refinements. See Table S11 for zone1 and zone2 individual refined occupancies.

Table 7. Comparison between the Reported *C*2[14] and NPD Refined *P*321 M−O Bond of the $Ca_3ZnGe_5O_{14}$ (x = 1) Composition

		reported *C*2	refined *P*321
bond lengths (Å)	*M*1−O1[a] x2	2.10(1)	1.985(2)
	*M*1−O4[a] x2	2.008(9)	1.985(2)
	*M*1−O6[a] x2	1.992(8)	1.985(2)
V (Å^3)	*M*1[a] octa site	10.77(2)	10.08(2)
bond lengths (Å)	*M*1−O6[a] x1	1.731(8)	1.740(1)
	*M*1−O2[a] x1	1.830(7)	1.862(6)
	*M*1−O1[a] x1	1.718(10)	1.740(1)
	*M*1−O7[a] x1	1.830(7)	1.862(6)
V (Å^3)	*M*1[a] tetra site	2.74(2)	2.86(2)
bond lengths (Å)	*M*3−O4[a] x2	1.749(9)	1.862(6)
	*M*3−O3[a] x2	1.852(7)	1.767(6)
V (Å^3)	*M*3[a] tetra site	2.77(2)	2.86(2)
bond lengths (Å)	*M*2−O7[a] x1	1.768(6)	1.770(7)
	*M*2−O5[a] x1	1.714(8)	1.727(11)
	*M*2−O3[a] x1	1.767(7)	1.770(7)
	*M*2−O2[a] x1	1.769(7)	1.770(7)
V (Å^3)	*M*2[a] tetra site	2.71(2)	2.74(2)

[a]M−O atoms notation taken from *C*2 model; see Table S10 for the *P*321 analogue atoms.

Table 5. Refined Structural Parameters Obtained from NPD Data Collected at Room Temperature on $Ca_3GaZn_{0.5}Ge_{4.5}O_{14}$ (x = 0.5) (*P*321 Space Group, a = 8.0460(2) Å and c = 4.9994(2) Å) Sample

atom	position	x	y	z	occupancy	B_{iso}
Ca	3e	0.4198(7)	0	0	1	1.12(11)
Ga1/Ge1/Zn1	1a	0	0	0	0.25(2)/0.531(15)/0.22(3)	0.98(6)[a]
Ga2/Ge2/Zn2	3f	0.7648(4)	0	1/2	0.250(8)/0.656(5)/0.094(10)	0.98(6)[a]
Ge3	2d	1/3	2/3	0.5283(9)	1	0.98(6)[a]
O1	2d	1/3	2/3	0.1874(13)	1	1.66(5)[a]
O2	6g	0.4629(5)	0.3175(4)	0.3120(7)	1	1.66(5)[a]
O3	6g	0.2208(5)	0.0788(4)	0.7631(7)	1	1.66(5)[a]

[a]Constrained to refine to the same B_{iso} values.

https://doi.org/10.1021/acs.inorgchem.2c01173
Inorg. Chem. 2022, 61, 9339−9351

Table 8. Comparison between the Refined Occupancies of Ga and Ge in the 1a, 3f, and 2d Sites from Melt-Crystallized (This Work) and Single Crystal[33] on the $Ca_3Ga_2Ge_4O_{14}$ (x = 0) Compound

	melt-crystallized			single crystal[33]		
site atom	1a	3f	2d	1a	3f	2d
Ga	0.51(8)	0.50(3)	0	0.2	0.6	0
Ge	0.49(8)	0.50(3)	1	0.8	0.4	1

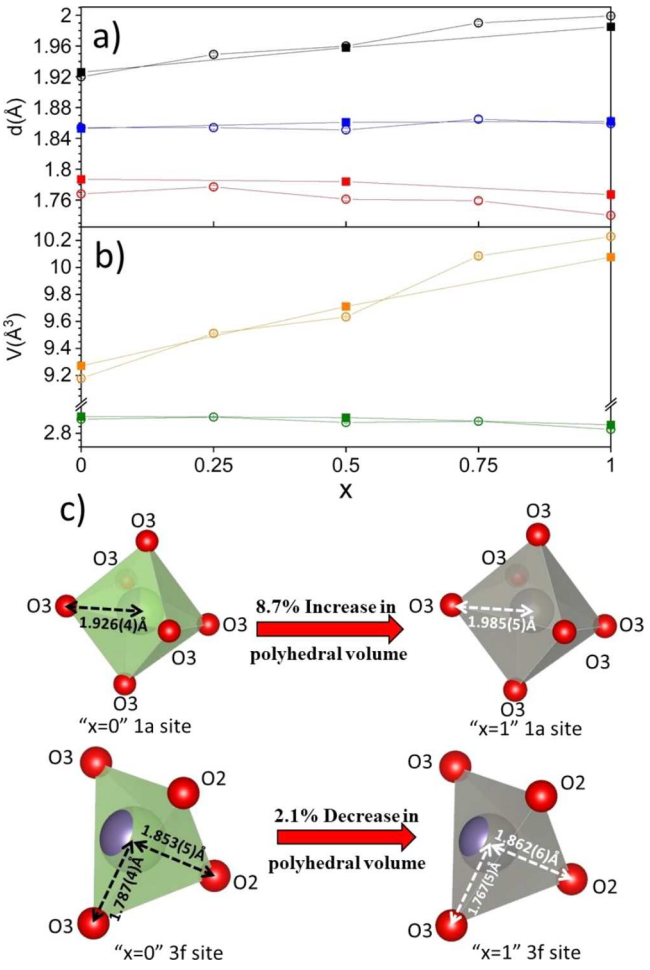

Figure 10. Refined M−O distances from SPD and NPD (hollow circles and filled squares, respectively) for compositions $0 \leq x \leq 1$. (a) B−O3 (black), C−O2 (blue), and C−O3 (red) distances and (b) their corresponding polyhedral volumes BO_6 (1a, orange) and CO_4 (3f, green). (c) Cationic 1a and 3f site coordination and their nearby interatomic distances for both x = 0 and x = 1 compounds from NPD refinements.

resolution STEM-EDS images followed by NPD refinements: this confirmed directly that Zn^{2+} shows the strongest preference for octahedral coordination, while Ga^{3+} and Ge^{4+} have similar proportions in octahedral and tetrahedral coordination (and that, in common with the end-member compositions, the 2d tetrahedral site is occupied exclusively by Ge^{4+}). This distribution is essentially consistent with the relative ionic radii of these cations. Across the solid solution, there is also a notable increase of the refined oxygen thermal parameter values, from B_{iso} = 1.18(4) Å^2 (x = 0) and 1.66(5) Å^2 (x = 0.5) to 2.17(7) Å^2 (x = 1), consistent with the observed cationic disorder and the increase of the size mismatch at the B and C sites due to the Ga^{3+} substitution by Zn^{2+} and Ge^{4+}.

Characterization of the cation distributions in complex bulk materials containing several cations with close atomic and neutron scattering factors is a nontrivial problem that is usually approached by coupling different characterization techniques. For example, a recent study of the high entropy spinel $(Cr_{0.2}Mn_{0.2}Fe_{0.2}Co_{0.2}Ni_{0.2})_3O_4$ with five different first-row transition metal cations distributed over two crystallographic sites, combines multiple complementary diffraction and spectroscopic techniques to fully characterize the material.[35] Our analysis of the $Zn^{2+}/Ga^{3+}/Ge^{4+}$ distribution over three crystallographic sites in $Ca_3GaZn_{0.5}Ge_{4.5}O_{14}$ demonstrates that the quantitative use of atomic-resolution STEM-EDS mapping, using a 2D fitting program to directly extract the occupancies of each element, has the potential to be very useful for such problems that can simplify crystallographic analysis and can be applied in many different contexts if sufficiently high-quality data can be obtained from a suitable crystallite orientation. Here, we have shown that it is possible to fit the different elemental contributions from atomic columns with extremely small spatial separations (e.g., atomic columns spaced by approximately 2 Å are clearly resolved in the case of Ge^{4+}, as shown in Figure 6) and with relatively low cation concentrations (e.g., a Zn^{2+} 3f site occupancy of 0.1). For Zn^{2+} and Ga^{3+}, which have weaker STEM-EDS signals due to their low populations in $Ca_3GaZn_{0.5}Ge_{4.5}O_{14}$, 2D fitting makes it possible to extract independent occupancies from the adjacent 1a and 3f sites. Such high spatial resolution and sensitivity should make it possible to study many different structure types in this way.

5. CONCLUSIONS

We have synthesized a new solid solution $Ca_3Ga_{2-2x}Zn_xGe_{4+x}O_{14}$ ($0 \leq x \leq 1$) by direct crystallization from an under-cooled melt (x = 0) and glass crystallization ($0.25 \leq x \leq 1$), and characterized the evolution of structure and cation distribution across the solid solution by coupling SPD and NPD to atomic-resolution STEM-EDS. We showed that the trigonal langasite structure (space group $P321$) can be retained across the whole solid solution, even for the composition $Ca_3ZnGe_5O_{14}$ (x = 1), which was previously reported in a distorted monoclinic langasite structure (space group $C2$). Using NPD, we found that the simpler end-member compounds $Ca_3Ga_2Ge_4O_{14}$ (x = 0) and $Ca_3ZnGe_5O_{14}$ (x = 1) have isoelectronic cations (Ga^{3+}/Ge^{4+} and Zn^{2+}/Ge^{4+}, respectively) distributed over the tetrahedral 3f and octahedral 1a sites, while the tetrahedral 2d sites are occupied exclusively by Ge^{4+}. This partial disordering of Zn^{2+} and Ge^{4+} over two crystallographic sites in glass-crystallized $Ca_3ZnGe_5O_{14}$ marks a major difference from its previously reported monoclinic structure, which is fully ordered with Zn^{2+} in purely octahedral coordination (1a) and Ge^{4+} purely tetrahedral (3f). The partial disordering of Zn^{2+}/Ge^{4+}, introduced by the crystallization from glass synthesis technique, presumably accounts for the suppression of the monoclinic distortion and stabilization of the trigonal structure in this material.

In the more complex case of $Ca_3GaZn_{0.5}Ge_{4.5}O_{14}$ (x = 0.5), where three isoelectronic cations (Zn^{2+}, Ga^{3+} and Ge^{4+}) can be distributed over three possible sites, we used atomic-resolution STEM-EDS to image their distributions directly, and then extracted their site occupancy values quantitatively via 2D fitting by adapting the Fit2D program (developed originally for

https://doi.org/10.1021/acs.inorgchem.2c01173
Inorg. Chem. 2022, 61, 9339−9351

fitting 2D NMR spectra). This allowed us to construct a suitable Rietveld model for refinement against NPD data using chemically justified site occupancy constraints. These results confirmed that the tetrahedral 2d site is occupied exclusively by Ge^{4+} at $x = 0.5$ (in common with the simpler $x = 0$, 1 end members), while Zn^{2+}, Ga^{3+} and the remaining Ge^{4+} are distributed over the octahedral (1a) and tetrahedral (3f) sites in proportions that correlate to their ionic radii: the Zn^{2+} ions show the greatest tendency toward octahedral coordination, while a higher proportion of Ga^{3+} and Ge^{4+} are present at the 3f sites. To our knowledge, this is the first time that quantitative 2D fitting of atomic-resolution STEM-EDS maps has been applied to this type of problem in a bulk oxide material. In principle, this approach can be applied to other materials classes where it is important to understand the distributions of cations with similar scattering factors (e.g., adjacent transition metals, lanthanides or *p*-block elements) over multiple crystallographic sites within a structure.

■ ASSOCIATED CONTENT

Supporting Information

The Supporting Information is available free of charge at https://pubs.acs.org/doi/10.1021/acs.inorgchem.2c01173.

Solid-state synthesis description, ^{71}Ga NMR, VT-PXRD, Rietveld refined SDP data plots, STEM-EDS refined zones, Rietveld refined structural parameters (PDF)

Accession Codes

CCDC 2163439−2163441 contain the supplementary crystallographic data for this paper. These data can be obtained free of charge via www.ccdc.cam.ac.uk/data_request/cif, or by emailing data_request@ccdc.cam.ac.uk, or by contacting The Cambridge Crystallographic Data Centre, 12 Union Road, Cambridge CB2 1EZ, UK; fax: +44 1223 336033.

■ AUTHOR INFORMATION

Corresponding Authors

Michael J. Pitcher − *CEMHTI, CNRS UPR 3079, Orléans 45071, France;* orcid.org/0000-0003-2044-6774; Email: michael.pitcher@cnrs-orleans.fr

Mathieu Allix − *CEMHTI, CNRS UPR 3079, Orléans 45071, France;* orcid.org/0000-0001-9317-1316; Email: mathieu.allix@cnrs-orleans.fr

Authors

Haytem Bazzaoui − *CEMHTI, CNRS UPR 3079, Orléans 45071, France*

Cécile Genevois − *CEMHTI, CNRS UPR 3079, Orléans 45071, France*

Dominique Massiot − *CEMHTI, CNRS UPR 3079, Orléans 45071, France;* orcid.org/0000-0003-1207-7040

Vincent Sarou-Kanian − *CEMHTI, CNRS UPR 3079, Orléans 45071, France;* orcid.org/0000-0001-9611-8377

Emmanuel Veron − *CEMHTI, CNRS UPR 3079, Orléans 45071, France*

Sébastien Chenu − *UMR CNRS 6226, Rennes Institute of Chemical Sciences, Rennes 35042, France*

Přemysl Beran − *Nuclear Physics Institute of the CAS, Řež 250 68, Czech Republic; European Spallation Source, ESS ERIC, Lund SE-22100, Sweden*

Complete contact information is available at: https://pubs.acs.org/10.1021/acs.inorgchem.2c01173

Notes

The authors declare no competing financial interest.

The used code for 2D refinements of STEM-EDS maps and refined data are available at: https://github.com/DoMassiot/Fit2DLangasiteData

■ ACKNOWLEDGMENTS

This work was supported by the Agence Nationale de la Recherche (France), under the project PERSIST (ANR-18-CE08-0012), and has also benefited from the electron microscopy facilities of the Platform MACLE-CVL, which was cofunded by the European Union and Centre-Val de Loire Region (FEDER). We thank Sandra Ory (CEMHTI, Orléans, France) for assistance with DSC measurements. Neutron diffraction experiments were carried out by Charles Hervoches at the CANAM infrastructure of the Nuclear Physics Institute (Řež, Czech Republic) and infrastructure of reactors LVR-15 and LR-0, supported through the Ministry of Education, Youth and Sports project LM2015056 and LM2018120, respectively. Use of the Advanced Photon Source at Argonne National Laboratory was supported by the U. S. Department of Energy, Office of Science, Office of Basic Energy Sciences, under Contract No. DE-AC02-06CH11357.

■ REFERENCES

(1) Boyer, M.; Carrion, A. J. F.; Ory, S.; Becerro, A. I.; Villette, S.; Eliseeva, S. V.; Petoud, S.; Aballea, P.; Matzen, G.; Allix, M. Transparent Polycrystalline $SrREGa_3O_7$ Melilite Ceramics: Potential Phosphors for Tuneable Solid State Lighting. *J. Mater. Chem. C* **2016**, *4*, 3238−3247.

(2) Boyer, M.; Alahraché, S.; Genevois, C.; Licheron, M.; Lefevre, F.-X.; Castro, C.; Bonnefont, G.; Patton, G.; Moretti, F.; Dujardin, C.; Matzen, G.; Allix, M. Enhanced Transparency through Second Phase Crystallization in $BaAl_4O_7$ Scintillating Ceramics. *Cryst. Growth Des.* **2016**, *16*, 386−395.

(3) Allix, M.; Alahrache, S.; Fayon, F.; Suchomel, M.; Porcher, F.; Cardinal, T.; Matzen, G. Highly Transparent BaAl4O7 Polycrystalline Ceramic Obtained by Full Crystallization from Glass. *Adv. Mater.* **2012**, *24*, 5570−5575.

(4) Fernandez-Carrion, A. J.; Al Saghir, K.; Veron, E.; Becerro, A. I.; Porcher, F.; Wisniewski, W.; Matzen, G.; Fayon, F.; Allix, M. Local Disorder and Tunable Luminescence in $Sr_{1-x}/_2Al_{2-x}Si_xO_4$ ($0.2 \leq x \leq 0.5$) Transparent Ceramics. *Inorg. Chem.* **2017**, *56*, 14446−14458.

(5) Irifune, T.; Kawakami, K.; Arimoto, T.; Ohfuji, H.; Kunimoto, T.; Shinmei, T. Pressure-Induced Nano-Crystallization of Silicate Garnets from Glass. *Nat. Commun.* **2016**, *7*, 13753.

(6) Ma, X.; Li, X.; Li, J.; Genevois, C.; Ma, B.; Etienne, A.; Wan, C.; Véron, E.; Peng, Z.; Allix, M. Pressureless Glass Crystallization of Transparent Yttrium Aluminum Garnet-Based Nanoceramics. *Nat. Commun.* **2018**, *9*, 1175.

(7) Bertrand, A.; Carreaud, J.; Chenu, S.; Allix, M.; Véron, E.; Duclère, J.; Launay, Y.; Hayakawa, T.; Genevois, C.; Brisset, F.; Célarié, F.; Thomas, P.; Delaizir, G. Scalable and Formable Tellurite-Based Transparent Ceramics for Near Infrared Applications. *Adv. Opt. Mater.* **2016**, *4*, 1482−1486.

(8) Al Saghir, K.; Chenu, S.; Veron, E.; Fayon, F.; Suchomel, M.; Genevois, C.; Porcher, F.; Matzen, G.; Massiot, D.; Allix, M. Transparency through Structural Disorder: A New Concept for Innovative Transparent Ceramics. *Chem. Mater.* **2015**, *27*, 508−514.

(9) Allix, M.; Chenu, S.; Véron, E.; Poumeyrol, T.; Kouadri-Boudjelthia, E. A.; Alahraché, S.; Porcher, F.; Massiot, D.; Fayon, F. Considerable Improvement of Long-Persistent Luminescence in Germanium and Tin Substituted $ZnGa_2O_4$. *Chem. Mater.* **2013**, *25*, 1600−1606.

(10) Chenu, S.; Véron, E.; Genevois, C.; Matzen, G.; Cardinal, T.; Etienne, A.; Massiot, D.; Allix, M. Tuneable Nanostructuring of

Highly Transparent Zinc Gallogermanate Glasses and Glass-Ceramics. *Adv. Opt. Mater.* **2014**, *2*, 364−372.
(11) Chenu, S.; Véron, E.; Genevois, C.; Garcia, A.; Matzen, G.; Allix, M. Long-Lasting Luminescent $ZnGa_2O_4$:Cr^{3+} Transparent Glass-Ceramics. *J. Mater. Chem. C* **2014**, *2*, 10002−10010.
(12) Zhang, S.; Yu, F. Piezoelectric Materials for High Temperature Sensors. *J. Am. Ceram. Soc.* **2011**, *94*, 3153−3170.
(13) Diaz-Lopez, M.; Shin, J. F.; Li, M.; Dyer, M. S.; Pitcher, M. J.; Claridge, J. B.; Blanc, F.; Rosseinsky, M. J. Interstitial Oxide Ion Conductivity in the Langasite Structure: Carrier Trapping by Formation of $(Ga,Ge)_2O_8$ Units in $La_{28}Ga_{5-x}Ge_{1+x}O_{14+x/2}$ ($0 < x \leq 1.5$). *Chem. Mater.* **2019**, *31*, 5742−5758.
(14) Redhammer, G. J. $Ca_3ZnGeO_2[Ge_4O_{12}]$: A Ca−Zn Germanate Related to the Mineral Taikanite. *Acta Crystallogr. Sect. C Struct. Chem.* **2015**, *71*, 80−83.
(15) Pavlovska, A.; Werner, S.; Maximov, B.; Mill, B. Pressure-Induced Phase Transitions of Piezoelectric Single Crystals from the Langasite Family: $La_3Nb_{0.5}Ga_{5.5}O_{14}$ and $La_3Ta_{0.5}Ga_{5.5}O_{14}$. *Acta Crystallogr. B* **2002**, *58*, 939−947.
(16) Mill, B. V.; Maksimov, B. A.; Pisarevskii, Y. V.; Danilova, N. P.; Pavlovska, A.; Werner, S.; Schneider, J. Phase Transitions in Compounds with the $Ca_3Ga_2Ge_4O_{14}$ Structure. *Crystallogr. Rep.* **2004**, *49*, 60−69.
(17) Mill, B. V.; Klimenkova, A. A.; Maximov, B. A.; Molchanov, V. N.; Pushcharovsky, D. Y. Enantiomorphism of the $Ca_3Ga_2Ge_4O_{14}$ Compound and Comparison of the $Ca_3Ga_2Ge_4O_{14}$ and $Sr_3Ga_2Ge_4O_{14}$ Structures. *Crystallogr. Rep.* **2007**, *52*, 785−794.
(18) Lu, P.; Xiong, J.; Van Benthem, M.; Jia, Q. Atomic-Scale Chemical Quantification of Oxide Interfaces Using Energy-Dispersive X-Ray Spectroscopy. *Appl. Phys. Lett.* **2013**, *102*, 173111.
(19) Lu, P.; Romero, E.; Lee, S.; MacManus-Driscoll, J. L.; Jia, Q. Chemical Quantification of Atomic-Scale EDS Maps under Thin Specimen Conditions. *Microsc. Microanal.* **2014**, *20*, 1782−1790.
(20) Lu, P.; Zhou, L.; Kramer, M. J.; Smith, D. J. Atomic-Scale Chemical Imaging and Quantification of Metallic Alloy Structures by Energy-Dispersive X-Ray Spectroscopy. *Sci. Rep.* **2014**, *4*, 3945.
(21) Niu, H. J.; Pitcher, M. J.; Corkett, A. J.; Ling, S.; Mandal, P.; Zanella, M.; Dawson, K.; Stamenov, P.; Batuk, D.; Abakumov, A. M.; Bull, C. L.; Smith, R. I.; Murray, C. A.; Day, S. J.; Slater, B.; Cora, F.; Claridge, J. B.; Rosseinsky, M. J. Room Temperature Magnetically Ordered Polar Corundum $GaFeO_3$ Displaying Magnetoelectric Coupling. *J. Am. Chem. Soc.* **2017**, *139*, 1520−1531.
(22) Roychowdhury, S.; Ghosh, T.; Arora, R.; Samanta, M.; Xie, L.; Singh, N. K.; Soni, A.; He, J.; Waghmare, U. V.; Biswas, K. Enhanced Atomic Ordering Leads to High Thermoelectric Performance in $AgSbTe_2$. *Science* **2021**, *371*, 722−727.
(23) Mohanty, D.; Sefat, A. S.; Li, J.; Meisner, R. A.; Rondinone, A. J.; Payzant, E. A.; Abraham, D. P.; Wood III, D. L.; Daniel, C. Correlating Cation Ordering and Voltage Fade in a Lithium−Manganese-Rich Lithium-Ion Battery Cathode Oxide: A Joint Magnetic Susceptibility and TEM Study. *Phys. Chem. Chem. Phys.* **2013**, *15*, 19496−19509.
(24) Rietveld, H. M. A Profile Refinement Method for Nuclear and Magnetic Structures. *J. Appl. Crystallogr.* **1969**, *2*, 65−71.
(25) Coelho, A. A. TOPAS and TOPAS-Academic : An Optimization Program Integrating Computer Algebra and Crystallographic Objects Written in C++. *J. Appl. Crystallogr.* **2018**, *51*, 210−218.
(26) Brown, I. D.; Altermatt, D. Bond-Valence Parameters Obtained from a Systematic Analysis of the Inorganic Crystal Structure Database. *Acta Crystallogr. B* **1985**, *41*, 244−247.
(27) Genevois, C.; Bazzaoui, H.; Boyer, M.; Ory, S.; Ledemi, Y.; Messaddeq, Y.; Pitcher, M. J.; Allix, M. Emergence of A-Site Cation Order in the Small Rare-Earth Melilites $SrREGa_3O_7$ (RE = Dy−Lu, Y). *Inorg. Chem.* **2021**, *60*, 12339−12354.
(28) Shannon, R. D. Revised Effective Ionic Radii and Systematic Studies of Interatomic Distances in Halides and Chalcogenides. *Acta Crystallogr. A* **1976**, *32*, 751−767.
(29) Stephens, P. W. Phenomenological Model of Anisotropic Peak Broadening in Powder Diffraction. *J. Appl. Crystallogr.* **1999**, *32*, 281−289.
(30) Sears, V. F. Neutron Scattering Lengths and Cross Sections. *Neutron News* **1992**, *3*, 26−37.
(31) Belokoneva, E. L.; Belov, N. V. Crystal Structure of Synthetic Ga,Ge-Helenite, $Ca_2Ga_2GeO_7$=$Ca_2Ga(GaGe)O_7$, and Its Comparison with the Structure of $Ca_3Ga_2Ge_4O_{14}$=$Ca_3Ge(Ga_2Ge)Ge_2O_{14}$. *Dokl. Akad. Nauk SSSR* **1981**, *260*, 1363−1366.
(32) Stadelmann, P. JEMS https://www.jems-swiss.ch/ (accessed 2022−03 -01).
(33) Dudka, A. P.; Mill', B. V. Accurate Crystal-Structure Refinement of $Ca_3Ga_2Ge_4O_{14}$ at 295 and 100K and Analysis of the Disorder in the Atomic Positions. *Crystallogr. Rep.* **2013**, *58*, 594−603.
(34) Chelstowski, D.; Witkowska, A.; Rybicki, J.; Padlyak, B.; Trapananti, A.; Principi, E. EXAFS Study of Glasses of the CaO−Ga_2O_3−GeO_2 System. *Opt. Appl.* **2003**, *33*, 125−132.
(35) Sarkar, A.; Eggert, B.; Witte, R.; Lill, J.; Velasco, L.; Wang, Q.; Sonar, J.; Ollefs, K.; Bhattacharya, S. S.; Brand, R. A.; Wende, H.; de Groot, F. M. F.; Clemens, O.; Hahn, H.; Kruk, R. Comprehensive Investigation of Crystallographic, Spin-Electronic and Magnetic Structure of $(Co_{0.2}Cr_{0.2}Fe_{0.2}Mn_{0.2}Ni_{0.2})_3O_4$: Unraveling the Suppression of Configuration Entropy in High Entropy Oxides. *Acta Mater.* **2022**, *226*, No. 117581.

https://doi.org/10.1021/acs.inorgchem.2c01173
Inorg. Chem. 2022, 61, 9339−9351

Supporting Information for:

"Stabilization of the trigonal langasite structure in $Ca_3Ga_{2-2x}Zn_xGe_{4+x}O_{14}$ ($0 \leq x \leq 1$) with partial ordering of three isoelectronic cations characterized by a multi-technique approach"

Haytem Bazzaoui[a], Cécile Genevois[a], Dominique Massiot[a], Vincent Sarou-Kanian[a], Emmanuel Veron[a], Sébastien Chenu[b], Přemysl Beran[c,d], Michael J. Pitcher[a*] and Mathieu Allix[a*]

[a] *CEMHTI, CNRS UPR 3079, 1d Avenue de la Recherche Scientifique, 45071 Orléans, France.*
[b] *Rennes Institute of Chemical Sciences, UMR CNRS 6226, Beaulieu Campus, 263 Av. Général Leclerc, 35042 Rennes, France*
[c] *Nuclear Physics Institute of the CAS, Hlavní 130, 250 68 Řež, Czech Republic*
[d] *European Spallation Source, ESS ERIC, Box 176, SE-22100 Lund, Sweden*
E-mail: mathieu.allix@cnrs-orleans.fr michael.pitcher@cnrs-orleans.fr

Contents

I. Solid-state synthesis of $Ca_3Ga_2Ge_4O_{14}$:

The feasibility of classic solid-state methods for the synthesis of $Ca_3Ga_2Ge_4O_{14}$ (x=0) was evaluated by in-situ PXRD. A reaction mixture was prepared from high purity reagents $CaCO_3$, Ga_2O_3 and GeO_2 which were ground in an agate mortar under ethanol. Once dried, the mixture was loaded into a platinum-lined corundum sample holder for variable temperature powder X-ray diffraction measurements (VT-PXRD). The reaction products at 1200 °C were a langasite type compound "$Ca_3Ga_2Ge_4O_{14}$" as the main phase, with a substantial amount of $CaGeO_3$ and Ga_2O_3 as secondary phases (see Figure I.1, below), indicating an incomplete reaction. The melting point of the mixture at ~1250°C precludes the use of higher temperatures, implying that several cycles of grinding and refiring at ~1200°C would be required to obtain a phase pure $Ca_3Ga_2Ge_4O_{14}$ ceramic in this system.

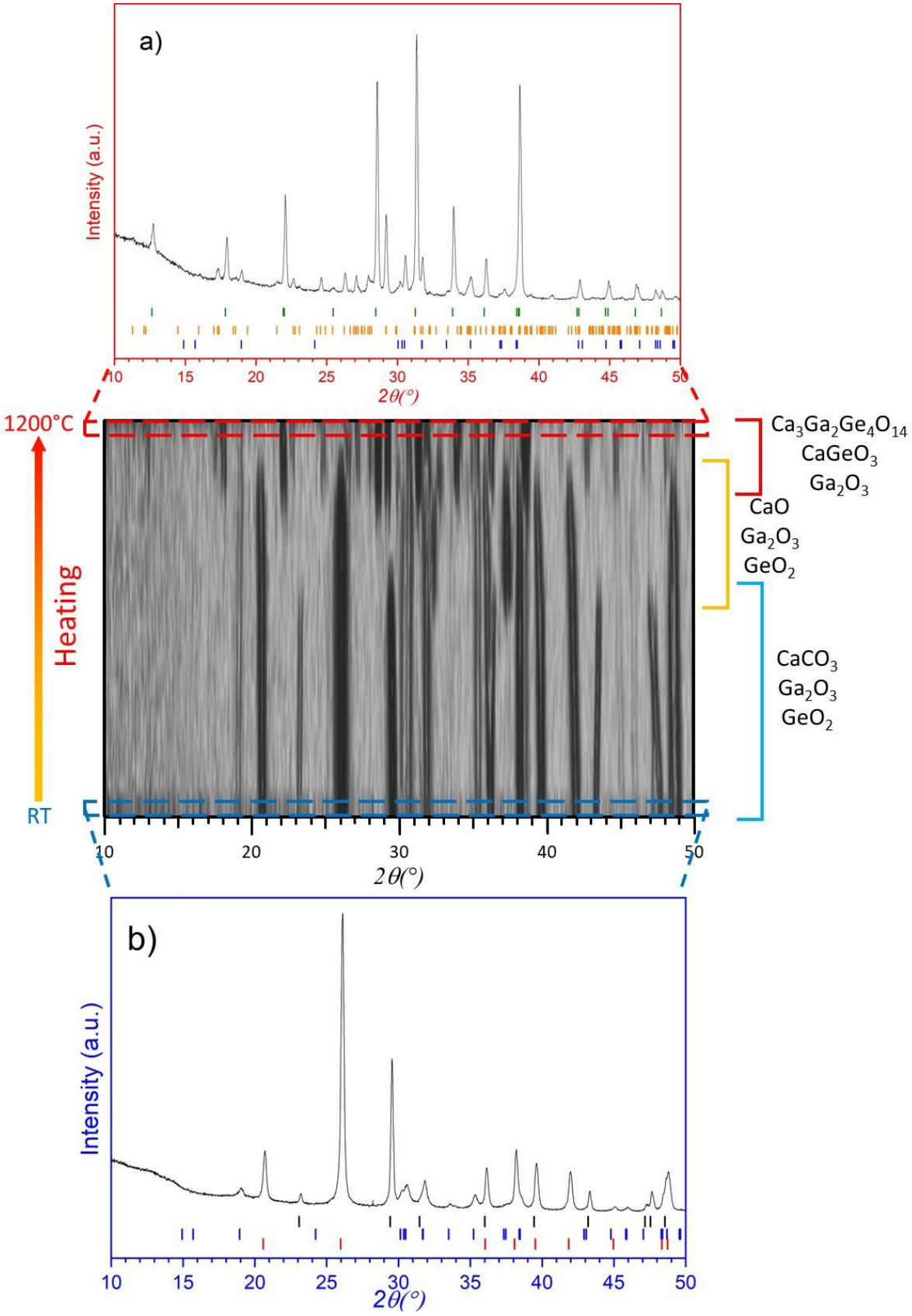

Figure I.1. In-situ powder X-ray diffraction (VT-PXRD) data of a $CaCO_3$-Ga_2O_3-GeO_2 mixture, with respect of $Ca_3Ga_2Ge_4O_{14}$ nominal composition, between room temperature and 1200°C. a) and b) inserts show the indexed diffraction patterns at room temperature and 1200°C, with the different color tickmarks corresponding to, $CaCO_3$ (black), Ga_2O_3 (blue), GeO_2 (red), $Ca_3Ga_2Ge_4O_{14}$ (green) and $CaGeO_3$ (orange).

II. ^{71}Ga NMR study of $Ca_3Ga_2Ge_4O_{14}$.

^{71}Ga NMR is a powerful tool to probe the Ga local structure in terms of coordination and also to provide a quantification of its different environments [1,2]. ^{71}Ga solid-state NMR spectroscopy was performed on the x = 0 member only ($Ca_3Ga_2Ge_4O_{14}$) at 20 T with a Bruker Avance Neo spectrometer equipped with a 0.7 mm magic angle spinning (MAS) double resonance Bruker probe-head. The powdered sample was spun at a MAS frequency of 100 kHz. Given the wide spectral broadening of the ^{71}Ga NMR environments, a radiofrequency field of 125 kHz was used, which corresponds to 90° and 180° central-transition selective pulses of 1 µs and 2 µs, respectively. A spin-echo experiment was recorded using a full echo acquisition (interpulse delay of 150 µs), a recycling delay of 2 s, and with 26,000 scans. Furthermore, a two-dimensional QPASS (Quadrupolar Phase-Adjusted Spinning Sidebands)[3] experiment was performed in order to improve the spectral resolution of the Ga environments by separating the overlapping spinning sidebands. Eight sets of timings (constant full duration of seven rotor periods) were needed for a proper separation, with a recycling delay of 2 s, and 8,000 scans per set of timings. The spectra were referenced to a 1 mol gallium nitrate solution.

As shown in Figure II.1 (below), the spectrum obtained from the spin-echo experiment lacks resolution because of overlapping spinning sidebands, even at ultra-high MAS frequency (100 kHz). The "spinning sidebands-free" QPASS spectrum allows to achieve ultimate spectral resolution and clearly identifies two contributions located at ca. 0 ppm and 100 ppm corresponding to 6-coordinated and 4-coordinated Ga respectively. However, the complexity of the QPASS experiment does not allow a precise quantification of the two Ga environments. The observed ^{71}Ga lineshapes have smoothed profiles as opposed to singularities expected for fully ordered crystalline phases, indicative of geometrical and chemical disorder of both Ga environments in the second coordination sphere.

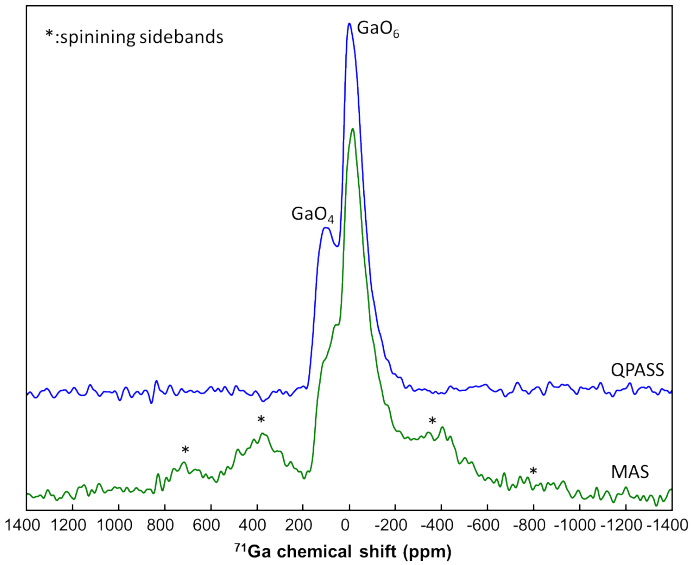

Figure II.1. ^{71}Ga NMR spectra acquired on sample of composition $Ca_3Ga_2Ge_4O_{14}$ (x=0) by a MAS spin echo (green) and a QPASS (blue) experiments, showing the two coordination types of Ga in the sample.

Table S1. Glass transition and crystallisation temperatures extracted from DSC measurements (data presented in Figure 2 of the main text).

	Glass transition temperature T_g(°C)	Exothermal peak onset point (crystallisation temperature T(°C)
$Ca_3Ga_2Ge_4O_{14}$ (x=0)	688°C	830°C
$Ca_3Ga_{1.5}Zn_{0.25}Ge_{4.25}O_{14}$ (x=0.25)	674°C	832°C
$Ca_3GaZn_{0.5}Ge_{4.5}O_{14}$ (x=0.5)	665°C	812°C
$Ca_3Ga_{0.5}Zn_{0.75}Ge_{4.75}O_{14}$ (x=0.75)	648°C	770°C
$Ca_3ZnGe_5O_{14}$ (x=1)	642°C	747°C

Table S2. Refined structural parameters obtained from SPD data collected at room temperature on $Ca_3Ga_2Ge_4O_{14}$ (x=0) (*P*321 space group, *a*= 8.072032(6) Å and *c*= 4.966435(5) Å) sample.

Atom	Position	x	y	z	Occ	B_{iso}
Ca	3e	0.42012(7)	0	0	1	0.96(1)
Ga1/Ge1	1a	0	0	0	0.4/0.6*	0.608(7)
Ga2/Ge2	3f	0.76255(3)	0	0.5	0.47/0.53*	0.679(5)
Ge3	2d	1/3	2/3	0.53090(8)	1	0.593(6)
O1	2d	1/3	2/3	0.1914(4)	1	1.21(2)[a]
O2	6g	0.4652(2)	0.3154(2)	0.3180(2)	1	1.21(2)[a]
O3	6g	0.2144(2)	0.0795(2)	0.7626(3)	1	1.21(2)[a]

*Fixed occupancy from [4]

[a]: constrained to refine to the same B_{iso} values.

Table S3. Refined structural parameters obtained from SPD data collected at room temperature on $Ca_3Ga_{1.5}Zn_{0.25}Ge_{4.25}O_{14}$ (x=0.25) (*P*321 space group, *a*= 8.05847(2) Å and *c*= 4.986577(14) Å) sample.

Atom	Position	x	y	z	Occ	B_{iso}
Ca	3e	0.41970(8)	0	0	1	1.02(1)
Ga1/Ge1/Zn1	1a	0	0	0	1*	1.04(1)
Ga2/Ge2/Zn2	3f	0.76349(4)	0	0.5	1*	0.90(1)
Ge3	2d	1/3	2/3	0.53149(10)	1	0.76(1)
O1	2d	1/3	2/3	0.1913(5)	1	1.40(3)[a]
O2	6g	0.4649(2)	0.3170(2)	0.3183(3)	1	1.40(3)[a]
O3	6g	0.2165(2)	0.0759(2)	0.7588(3)	1	1.40(3)[a]

*Site was set to be fully occupied without refining each atom occupancy

[a]: constrained to refine to the same B_{iso} values.

Table S4. Refined structural parameters obtained from SPD data collected at room temperature on $Ca_3GaZn_{0.5}Ge_{4.5}O_{14}$ (x=0.5) (*P*321 space group, *a*= 8.041920(12) Å and *c*= 4.999015(8) Å) sample.

Atom	Position	x	y	z	Occ	B_{iso}
Ca	3e	0.41956(8)	0	0	1	1.00(1)
Ga1/Ge1/Zn1	1a	0	0	0	1*	1.15(1)
Ga2/Ge2/Zn2	3f	0.76427(4)	0	0.5	1*	1.006(6)
Ge3	2d	1/3	2/3	0.52968(9)	1	0.844(7)
O1	2d	1/3	2/3	0.1867(5)	1	1.72(2)[a]
O2	6g	0.4650(2)	0.3164(2)	0.3208(3)	1	1.72(2)[a]
O3	6g	0.21624(19)	0.0756(2)	0.7547(3)	1	1.72(2)[a]

*Site was set to be fully occupied without refining each atom occupancy

[a]: constrained to refine to the same B_{iso} values.

Table S5. Refined structural parameters obtained from SPD data collected at room temperature on $Ca_3Ga_{0.5}Zn_{0.75}Ge_{4.75}O_{14}$ (x=0.75) (*P*321 space group, *a*= 8.03574(2) Å and *c*= 5.009068(17) Å) sample**.**

Atom	Position	x	y	z	Occ	B_{iso}
Ca	3e	0.41827(11)	0	0	1	0.92(2)
Ga1/Ge1/Zn1	1a	0	0	0	1*	1.26(2)
Ga2/Ge2/Zn2	3f	0.76488(6)	0	0.5	1*	0.971(1)
Ge3	2d	1/3	2/3	0.52939(14)	1	0.79(1)
O1	2d	1/3	2/3	0.1880(7)	1	1.26(4)[a]
O2	6g	0.4676(3)	0.3187(3)	0.3224(4)	1	1.26(4)[a]
O3	6g	0.2203(2)	0.0763(3)	0.7527(4)	1	1.26(4)[a]

*Site was set to be fully occupied without refining each atom occupancy

[a]: constrained to refine to the same B_{iso} values.

Table S6. Refined structural parameters obtained from SPD data collected at room temperature on $Ca_3ZnGe_5O_{14}$ (x=1) (*P*321 space group, *a*= 8.02913(3) Å and *c*= 5.014309(19) Å) sample. No strain modelled**.**

Atom	Position	x	y	z	Occ	B_{iso}
Ca	3e	0.41841(8)	0	0	1	1.16(1)
Zn1/Ge1	1a	0	0	0	1*	1.48(1)
Zn2/Ge2	3f	0.76499(4)	0	0.5	1*	1.154(7)
Ge3	2d	1/3	2/3	0.52849(11)	1	1.009(9)
O1	2d	1/3	2/3	0.1919(6)	1	1.95(3)[a]
O2	6g	0.4671(2)	0.3189(2)	0.3233(3)	1	1.95(3)[a]
O3	6g	0.22055(19)	0.0773(2)	0.7504(3)	1	1.95(3)[a]

*Site was put to be fully occupied without refining each atom occupancy

[a]: constrained to refine to the same B_{iso} values.

Table S7. Refined structural parameters obtained from SPD data collected at room temperature on $Ca_3ZnGe_5O_{14}$ (x=1) (*P*321 space group, *a*= 8.02916(2) Å and *c*= 5.014362(17) Å) sample. Modelled strain**.**

Atom	Position	x	y	z	Occ	B_{iso}
Ca	3e	0.41846(8)	0	0	1	1.15(1)
Zn1/Ge1	1a	0	0	0	1*	1.47 (1)
Zn2/Ge2	3f	0.76506(4)	0	0.5	1*	1.126(7)
Ge3	2d	1/3	2/3	0.52816(11)	1	0.999(8)
O1	2d	1/3	2/3	0.1926(5)	1	1.91(3)[a]
O2	6g	0.4676(2)	0.3195(2)	0.3230(3)	1	1.91(3)[a]
O3	6g	0.22065(19)	0.0772(2)	0.7502(3)	1	1.91(3)[a]

*Site was put to be fully occupied without refining each atom occupancy

[a]: constrained to refine to the same $_{Biso}$ values.

Table S8. Refined structural parameters obtained from SPD data collected at room temperature on $Ca_3ZnGe_5O_{14}$ (*C*2 space group, *a*= 13.91669(9) Å, b= 8.02315(5) Å, *c*= 5.01415(2) Å and β= 90.0759(4) °) sample. No strain modelled**.**

Atom	Position	x	y	z	Occ	B_{iso}
Ca1	2a	0.5	0.7623(5)	0	1	1.44(8)
Ca2	4c	0.2917(2)	0.3948(4)	0.0006(7)	1	1.02(4)
Zn1	1a	0.11841(10)	0.56943(16)	0.4969(4)	1	1.39(3)
Ge1	4c	0.33313(10)	0.6860(2)	0.47222(13)	1	0.96(1)
Ge2	2b	0.5	0.41986(18)	0.5	1	0.92(4)
Ge3	4c	0.5	0.1858(3)	0	1	1.00(1)
O1	4c	0.1177(4)	0.6953(9)	0.7829(10)	1	1.21(4)[a]
O2	4c	0.1611(6)	0.3732(11)	0.680(2)	1	1.21(4)[a]
O3	4c	0.4249(5)	0.5748(11)	0.3031(15)	1	1.21(4)[a]
O4	4c	0.4317(5)	0.3296(9)	0.7441(13)	1	1.21(4)[a]
O5	4c	0.3341(6)	0.6729(11)	0.8088(6)	1	1.21(4)[a]
O6	4c	0.0234(4)	0.4947(8)	0.2834(13)	1	1.21(4)[a]
O7	4c	0.2304(5)	0.5907(10)	0.3407(17)	1	1.21(4)[a]

[a]: constrained to refine to the same B_{iso} values.

Table S9. Refined structural parameters obtained from SPD data collected at room temperature on $Ca_3ZnGe_5O_{14}$ (*C*2 space group, *a*= 13.90286(11) Å, b= 8.03170(7) Å, *c*= 5.014276(16) Å and β= 89.9544(10) °) sample. Modelled strain**.**

Atom	Position	x	y	z	Occ	B_{iso}
Ca1	2a	0.5	0.7601(4)	0	1	0.45(6)
Ca2	4c	0.2903(2)	0.3895(5)	0.0005(8)	1	1.55(4)
Zn1	1a	0.11569(10)	0.55532(16)	0.5034(4)	1	1.25(3)
Ge1	4c	0.33367(13)	0.6757(3)	0.47220(10)	1	0.980(7)
Ge2	2b	0.5	0.4145(2)	0.5	1	1.07(5)
Ge3	4c	0.5	0.1800(4)	0	1	0.97(1)
O1	4c	0.1017(4)	0.7363(7)	0.7201(10)	1	1.46(3)[a]
O2	4c	0.1562(6)	0.3734(13)	0.674(2)	1	1.46(3)[a]
O3	4c	0.4298(6)	0.5696(13)	0.3262(18)	1	1.46(3)[a]
O4	4c	0.4377(4)	0.3391(9)	0.7873(9)	1	1.46(3)[a]
O5	4c	0.3344(7)	0.679(2)	0.8071(4)	1	1.46(3)[a]
O6	4c	0.0451(5)	0.4900(9)	0.2636(13)	1	1.46(3)[a]
O7	4c	0.2364(6)	0.5876(13)	0.3066(17)	1	1.46(3)[a]

[a]: constrained to refine to the same B_{iso} values.

Table S10. Atom Wyckoff positions in the hexagonal *P*321 structure and their equivalents in the monoclinic *C*2 cell.

Origin in *P*321		Analogue in *C*2	
Atom	Wyk. Pos.	Atom	Wyk. Pos.
Ca1	3f	Ca1	2a
		Ca2	4c
Ge1/Zn1	1a	Zn1	2a
Ge2/Zn2	3f	Ge1	4c
		Ge3	4c
Ge3	2d	Ge2	2b
O1	2d	O5	4c
O2	6g	O2	4c
		O3	4c
		O7	4c
O3	6g	O1	4c
		O4	4c
		O6	4c

Table S11. Extracted (refined) occupancies from the 2D EDS maps refinements in both zone1 and zone2, for the $Ca_3GaZn_{0.5}Ge_{4.5}O_{14}$ (x=0.5) composition**.**

	Site / Atom	1a	3f	2d
Zone1	Zn	0.19(6)	0.10(6)	0
	Ga	0.22(3)	0.26(3)	0
	Ge	0.59(3)	0.64(3)	1
Zone2	Zn	0.16(6)[a]	0.11(6)[a]	0
	Ga	0.25(3)[a]	0.25(3)[a]	0
	Ge	0.59(3)[a]	0.64(3)[a]	1

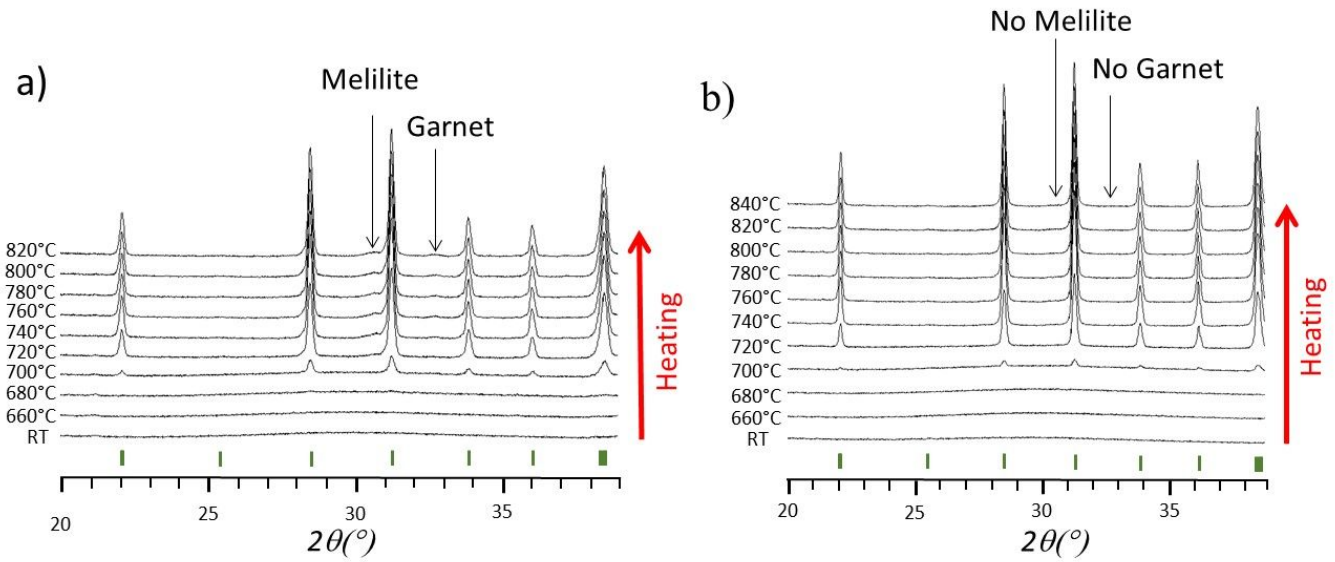

Figure S1. Variable temperature powder X-ray diffraction (VT-PXRD) measurements of, a) glass of composition $Ca_3Ga_2Ge_4O_{14}$ (x=0), b) glass of a slightly deviated composition from $Ca_3Ga_2Ge_4O_{14}$ (x=0) with an excess of 2.17% (%wt) of GeO2 added in the nominal composition. Green tickmarks represent the $Ca_3Ga_2Ge_4O_{14}$ indexation.

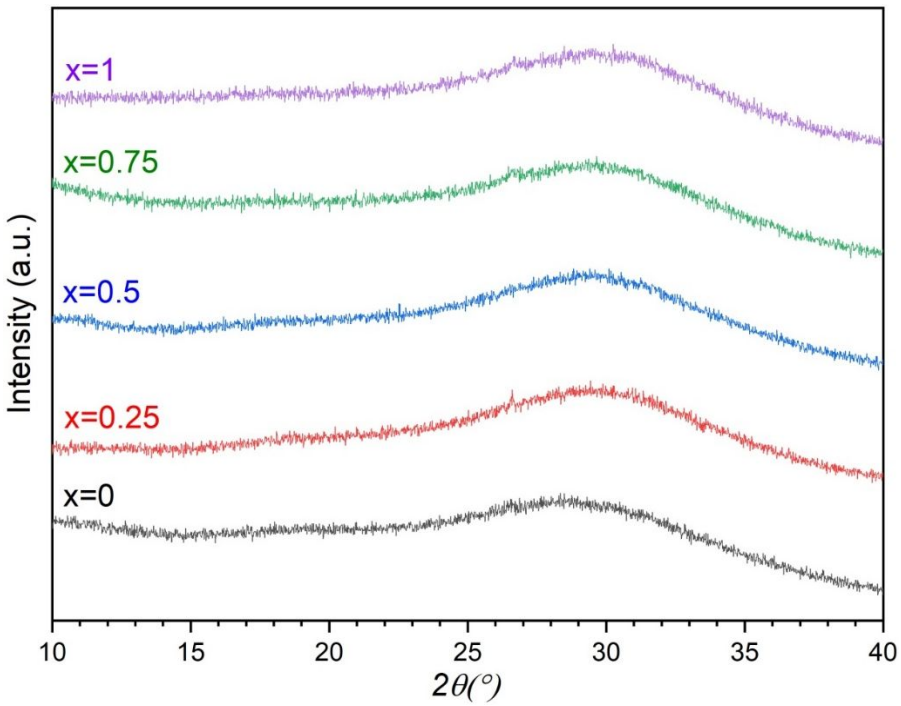

Figure S2. Laboratory X-ray powder diffraction data of $Ca_3Ga_{2-x}Zn_xGe_{4+x}O_{14}$ (x=0, 0.25, 0.5, 0.75, 1) glass samples synthesized by aerodynamic levitation coupled to laser heating (ADL).

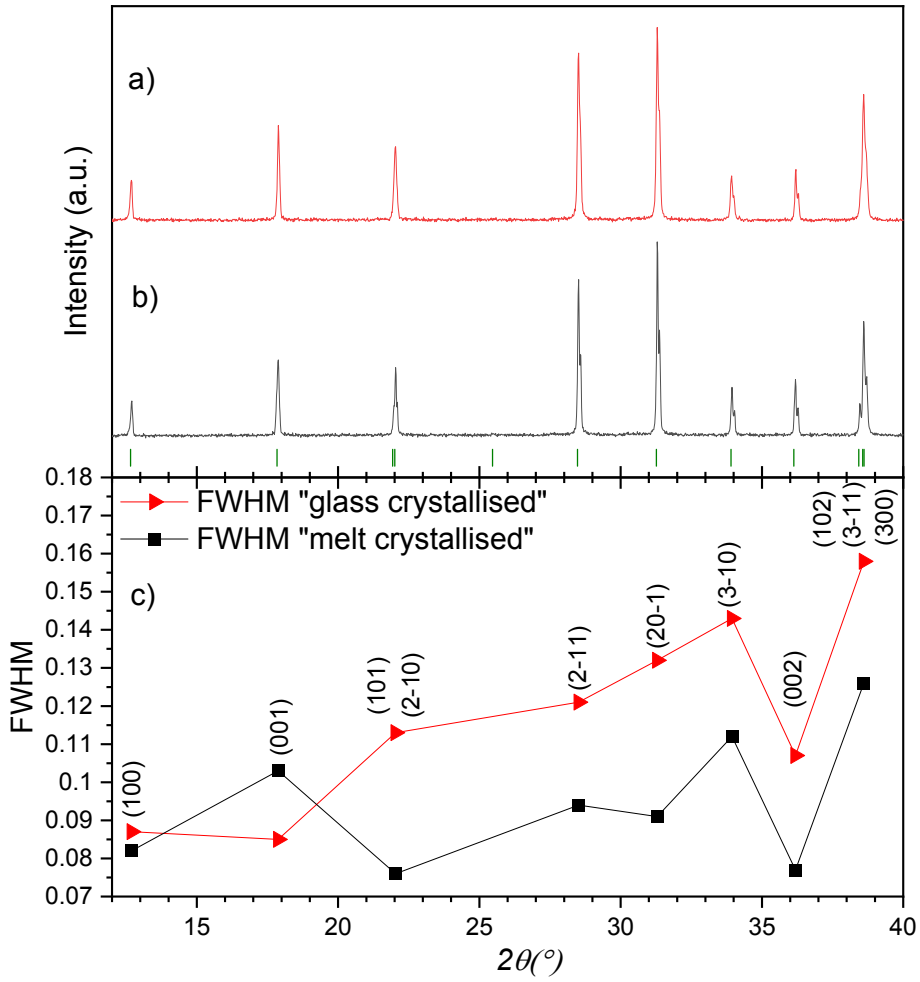

Figure S3. Crystallized $Ca_3Ga_2Ge_4O_{14}$ (x=0) sample from a) glass at 820°C in an open atmosphere furnace, b) molten liquid on the ADL montage, by turning the lasers off while the droplet is touching the nozzle. Green tick marks represent $Ca_3Ga_2Ge_4O_{14}$ indexation. c) the extracted FWHM's for each peak from a) and b).

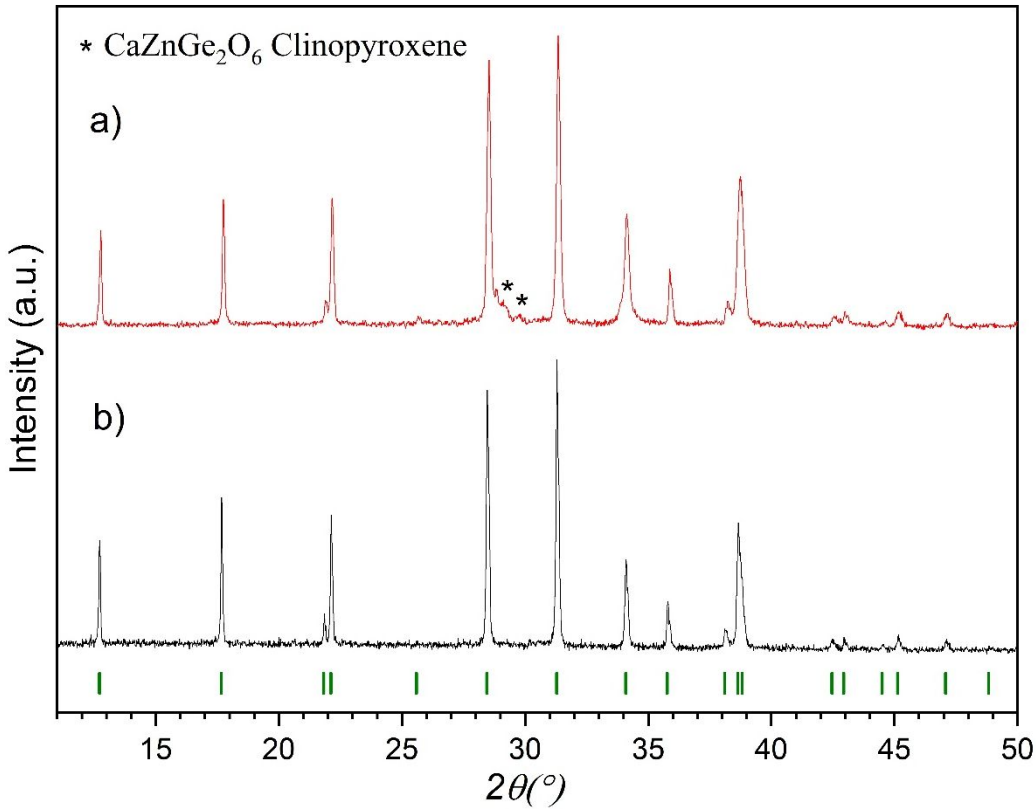

Figure S4. Lab powder X-ray diffraction data of two crystallized $Ca_3ZnGe_5O_{14}$ samples at 800°C under (a) powder form, (b) bulk form. Green tick marks represent $Ca_3ZnGe_5O_{14}$ indexation.

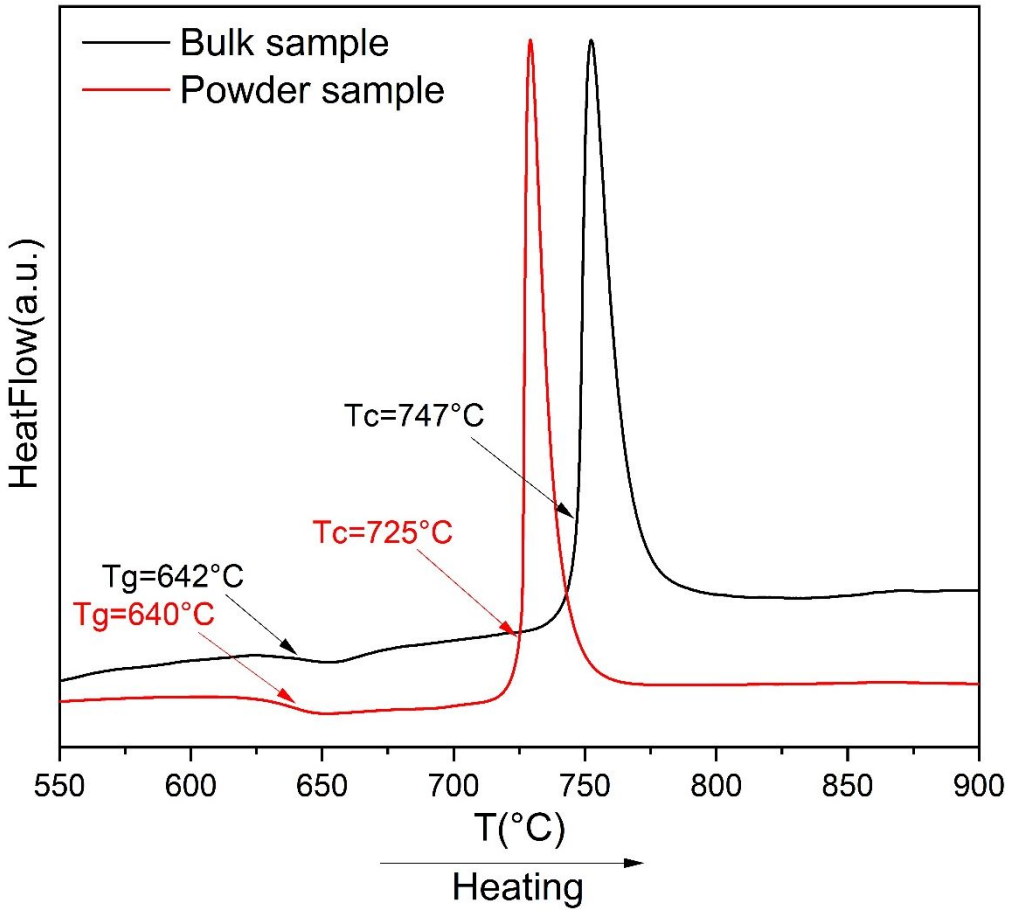

Figure S5. Comparison between a bulk and powder measured samples of the same composition $Ca_3ZnGe_5O_{14}$ (x=1) on the DSC.

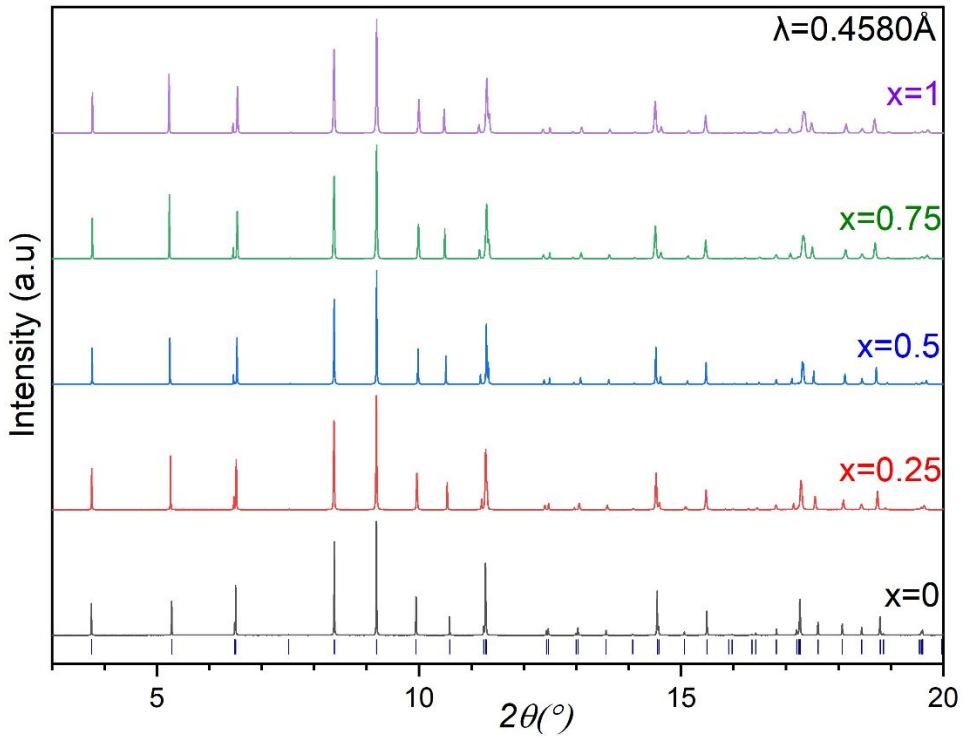

Figure S6. SPD data of $Ca_3Ga_{2-2x}Zn_xGe_{4+x}O_{14}$ x=0 (black), 0.25 (red), 0.5 (blue), 0.75 (green) and 1 (purple) compositions, with dark blue tickmarks corresponding to $Ca_3Ga_2Ge_4O_{14}$ indexation.

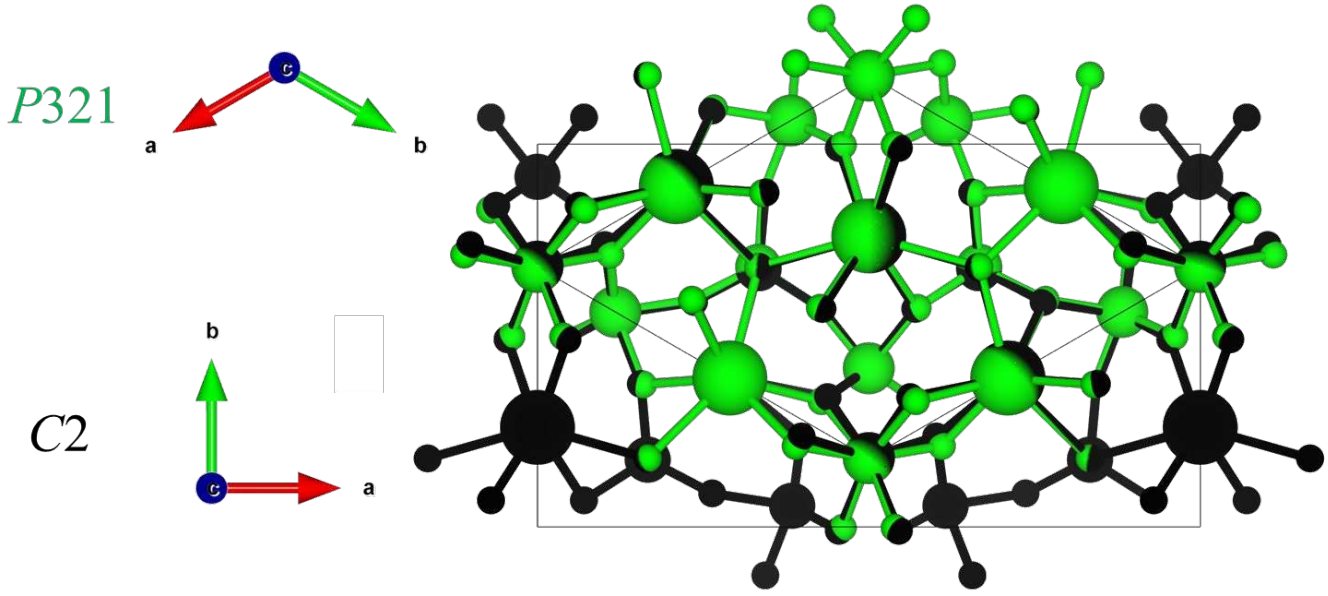

Figure S7. Overlay between Rietveld refined *C*2 (black atoms) and *P*321 (green atoms) structures for the $Ca_3ZnGe_5O_{14}$ (x=1) composition against SPD data, along the *c*-axis.

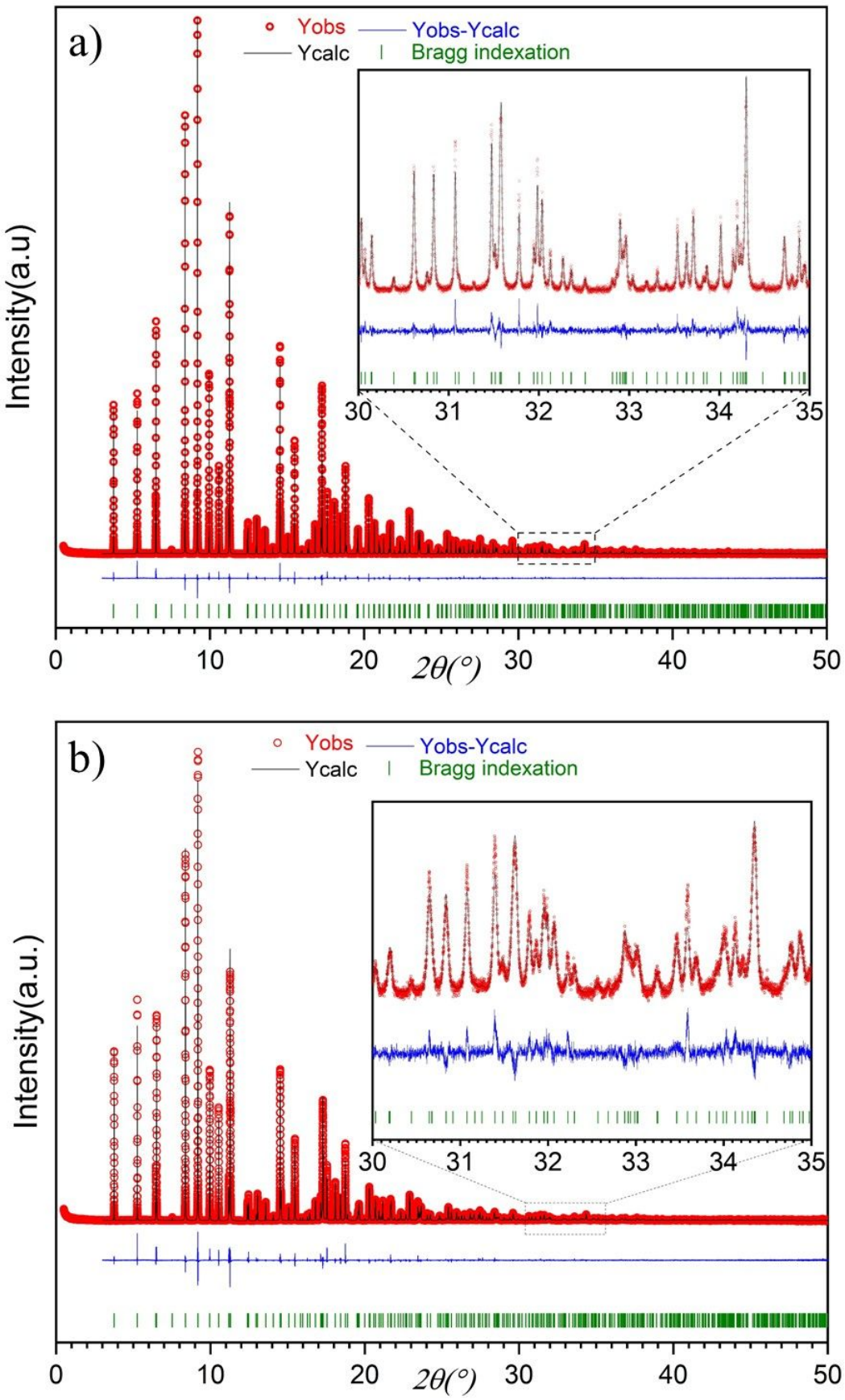

Figure S8. Rietveld refinement of a) $Ca_3Ga_2Ge_4O_{14}$ (x=0) (SPD data, R_p= 7.617% R_{wp}= 9.506%) and b) $Ca_3Ga_{1.5}Zn_{0.25}Ge_{4.25}O_{14}$ (x=0.25) (SPD data, R_p= 8.465% R_{wp}= 10.907%). Observed (red dot), calculated (black line), and difference (blue line) profiles are shown. The set of green vertical lines corresponds to reflection positions.

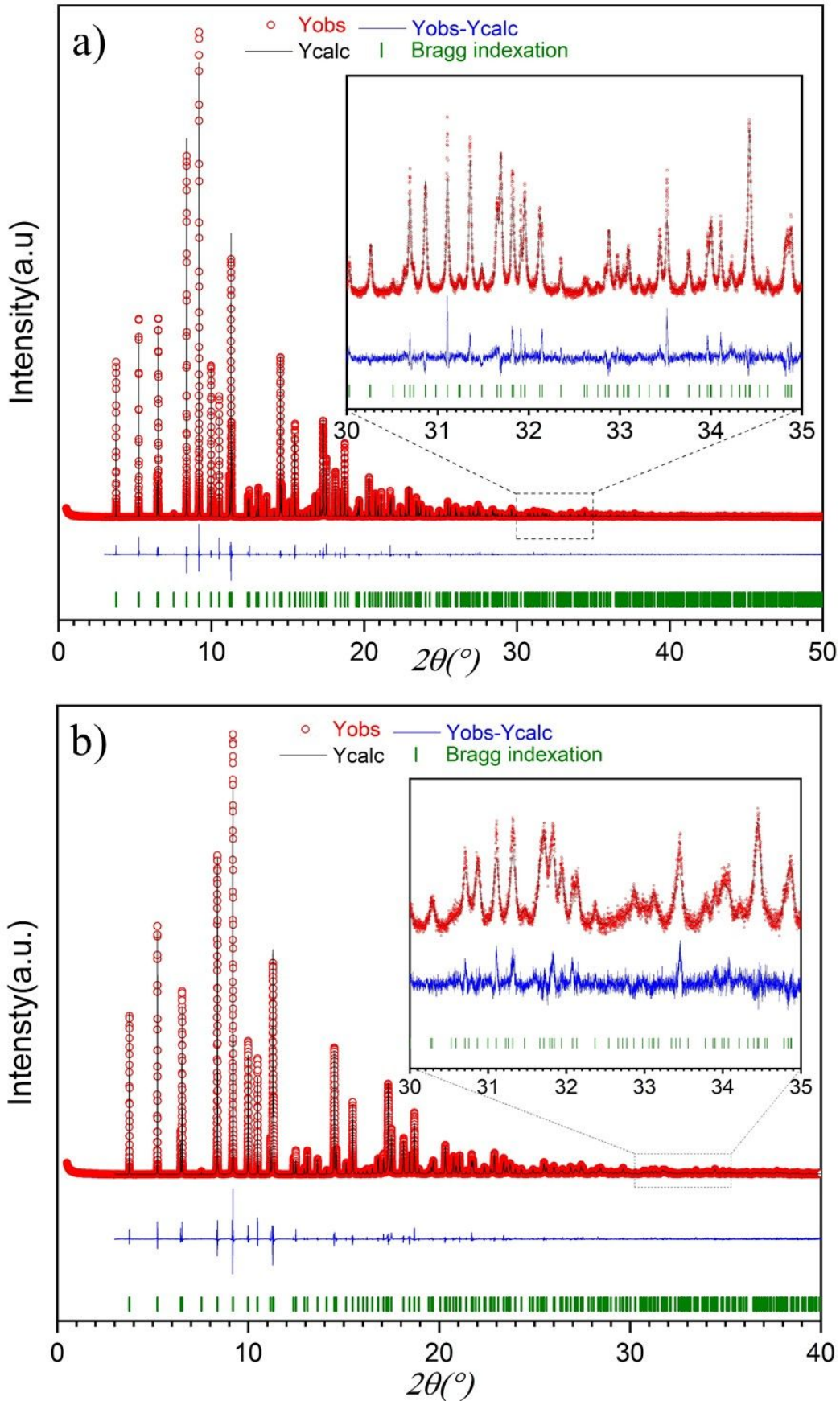

Figure S9. Rietveld refinement of a) $Ca_3GaZn_{0.5}Ge_{4.5}O_{14}$ (x=0.5) (SPD data, R_p= 7.617% R_{wp}= 9.506%) and b) $Ca_3Ga_{0.5}Zn_{0.75}Ge_{4.75}O_{14}$ (x=0.75) (SPD data, R_p= 8.465% R_{wp}= 10.907%). Observed (red dot), calculated (black line), and difference (blue line) profiles are shown. The set of green vertical lines corresponds to reflection positions.

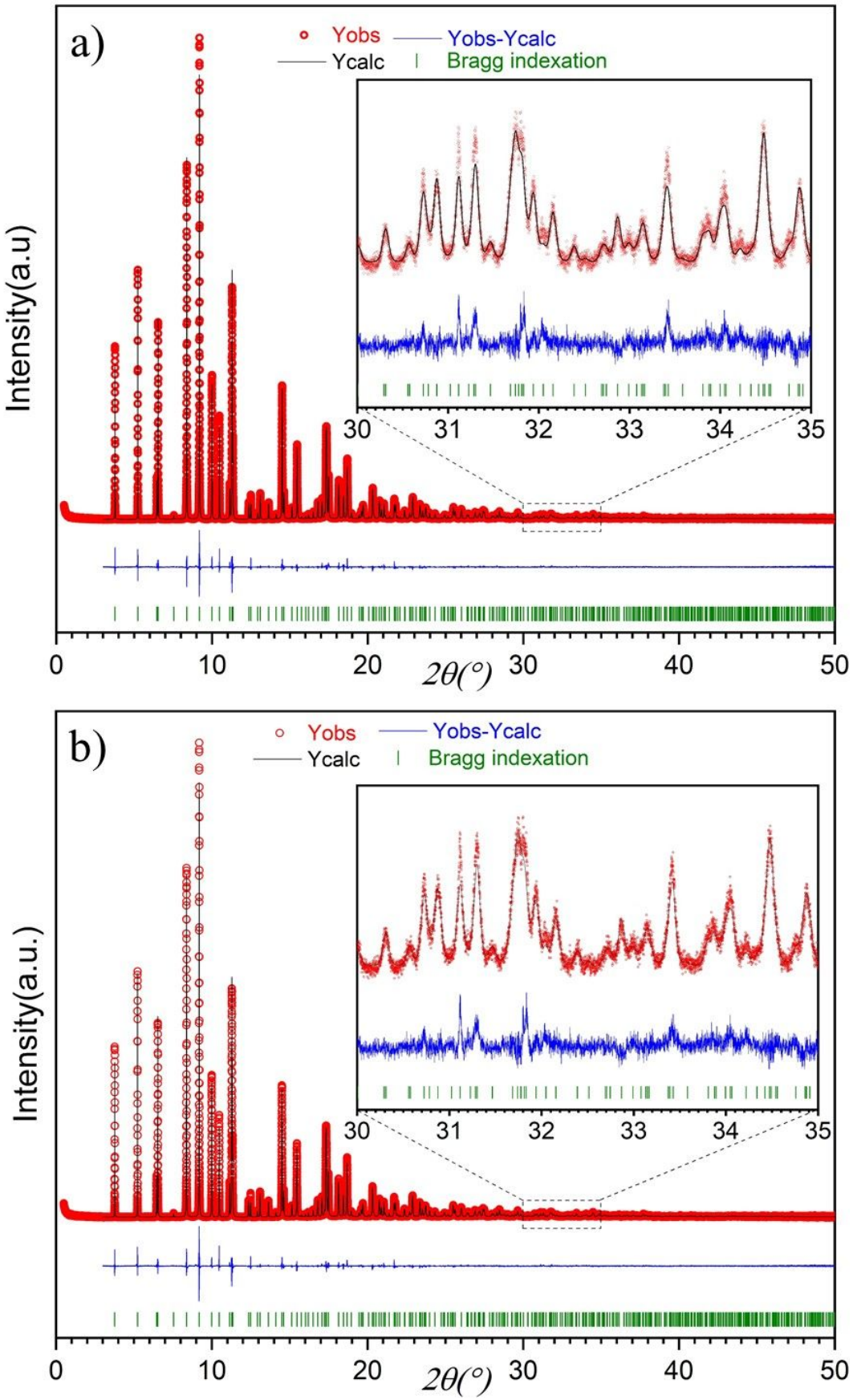

Figure S10 Rietveld refinement of $Ca_3ZnGe_5O_{14}$(x=1) SPD data against the hexagonal *P*321 cell, a) without strain (R_p= 7.18% R_{wp}= 8.93%), b) modelled strain (R_p= 7.02% R_{wp}= 8.75%). Observed (red dot), calculated (black line), and difference (blue line) profiles are shown. The set of green vertical lines corresponds to reflection positions.

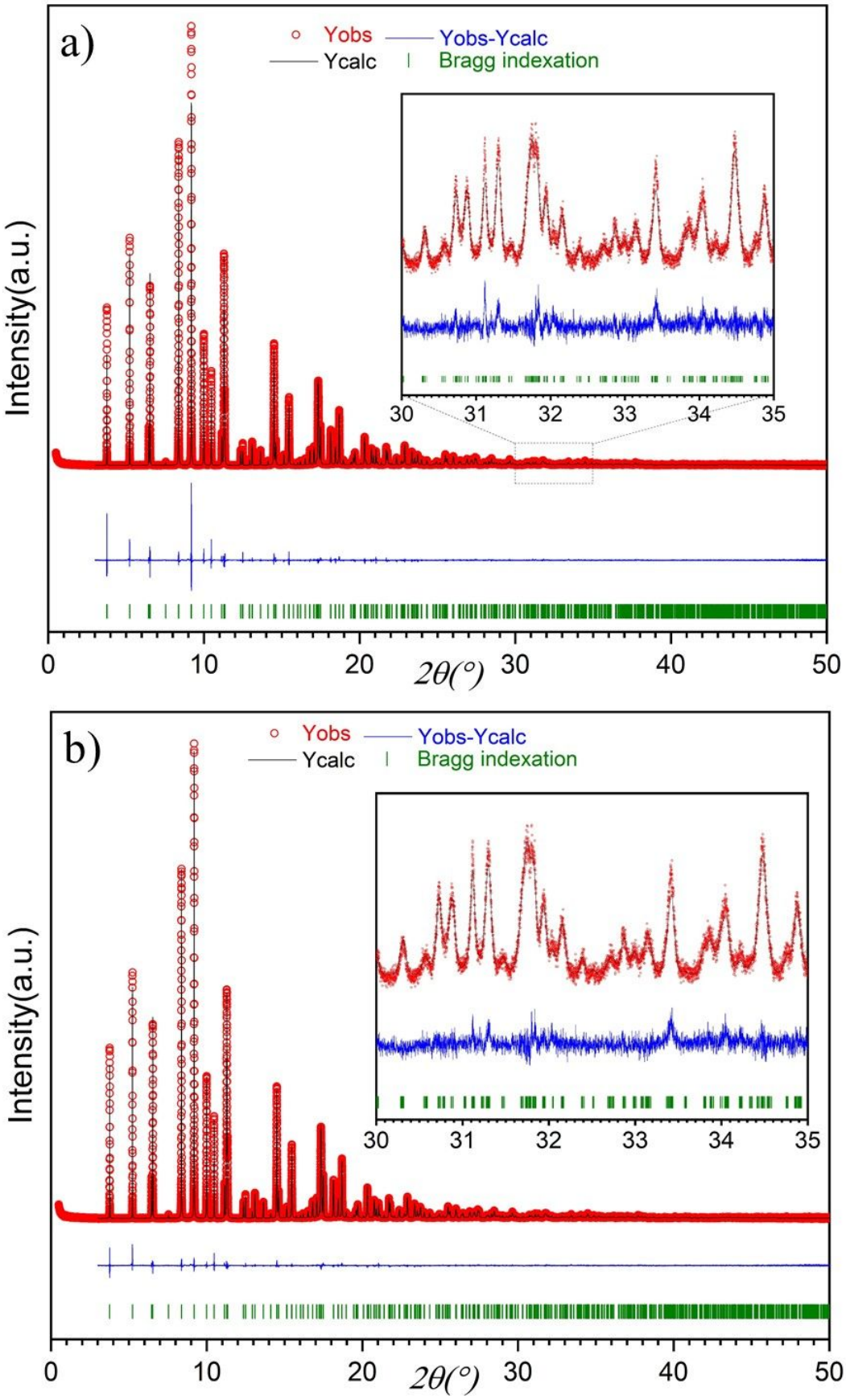

Figure S11. Rietveld refinement of $Ca_3ZnGe_5O_{14}$ (x=1) SPD data against the monoclinic *C*2 structure, a) without strain (R_p= 7.20% R_{wp}= 8.93%), b) modelled strain (R_p= 5.14% R_{wp}= 6.68%). Observed (red dot), calculated (black line), and difference (blue line) profiles are shown. The set of green vertical lines corresponds to reflection positions.

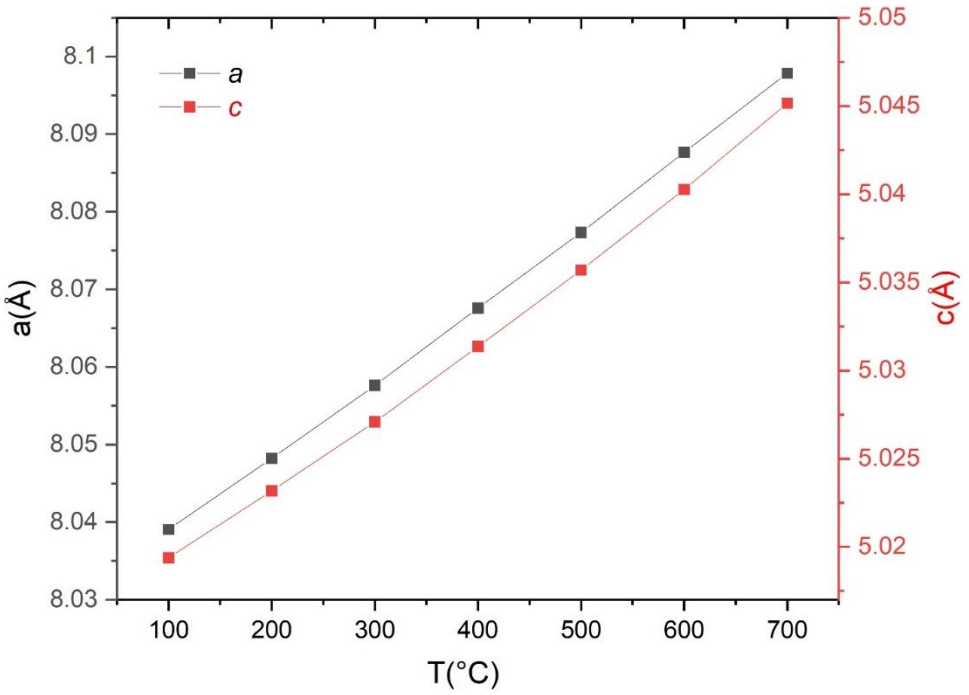

Figure S12. Cell parameters evolution of the $Ca_3ZnGe_5O_{14}$ sample *vs* temperature.

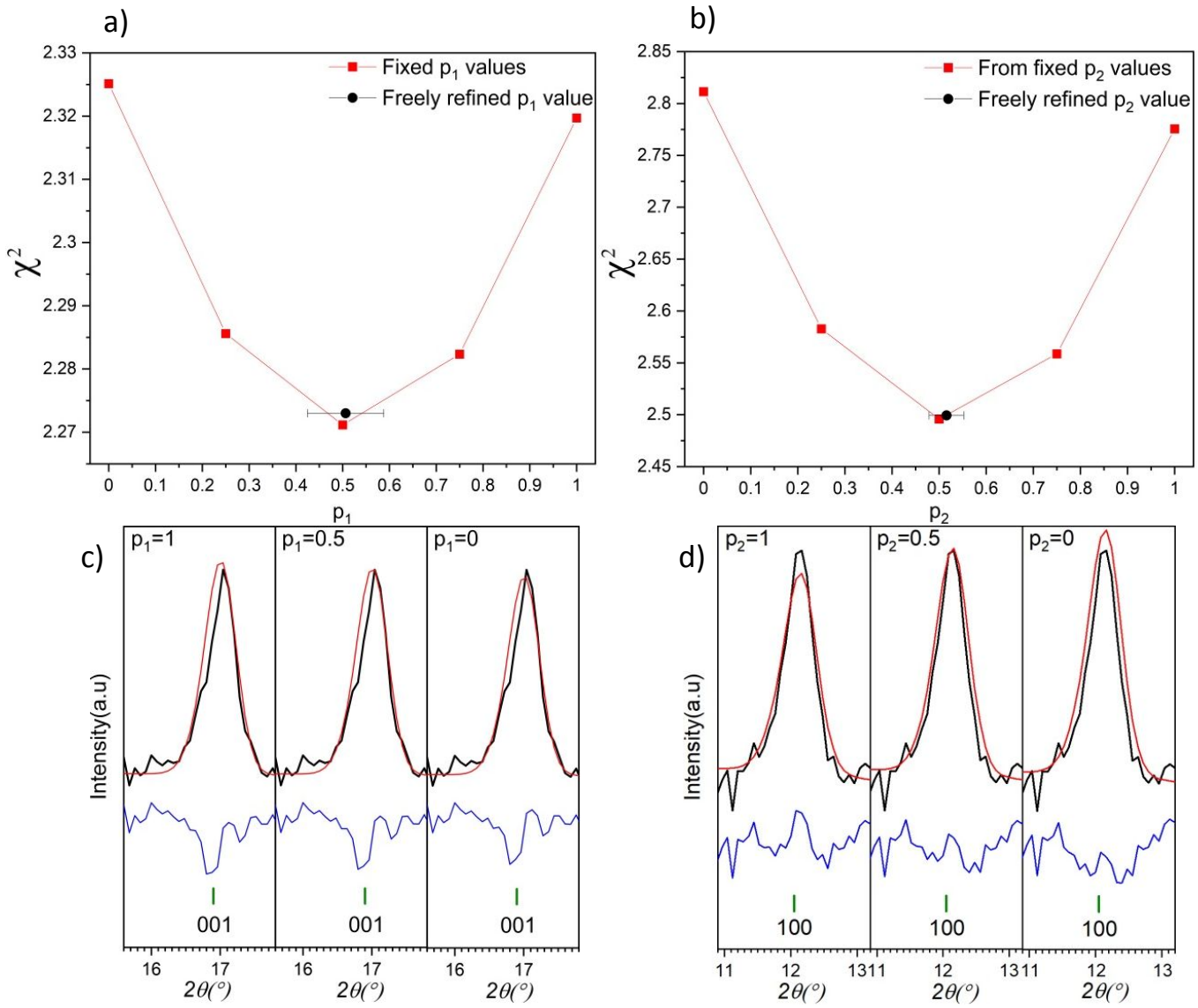

Figure S13. a), b) χ^2 evolution as a function of p_1 (Ga occupancy on the 1a site for x=0 compound), p_2 (Zn occupancy on the 1a site for x=1 compound). c), d) Rietveld fits (measured "black line", calculated "red line, difference "blue line" and indexation in green tick marks) zoomed view on the (001) and (100) for x=0 and x=1 compounds respectively for different fixed p_1 and p_2 values.

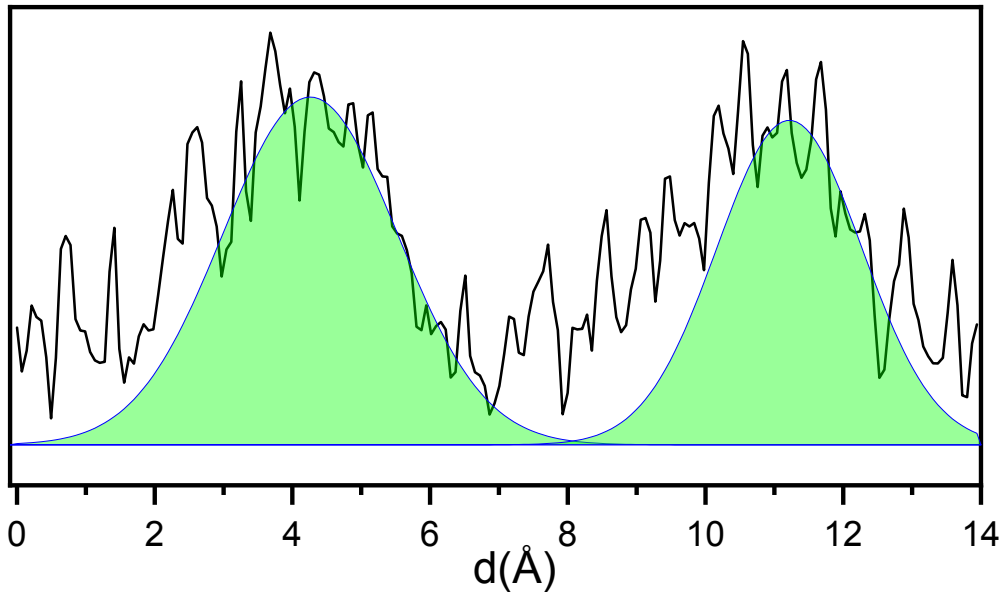

Figure S14. Refined signal of Zn from integrated area on the STEM-EDS raw maps with one Gaussian contribution from the 1a site position, where black curve, blue curve and green surface represents the raw integrated, calculated signals and the integrated area under the calculated curve.

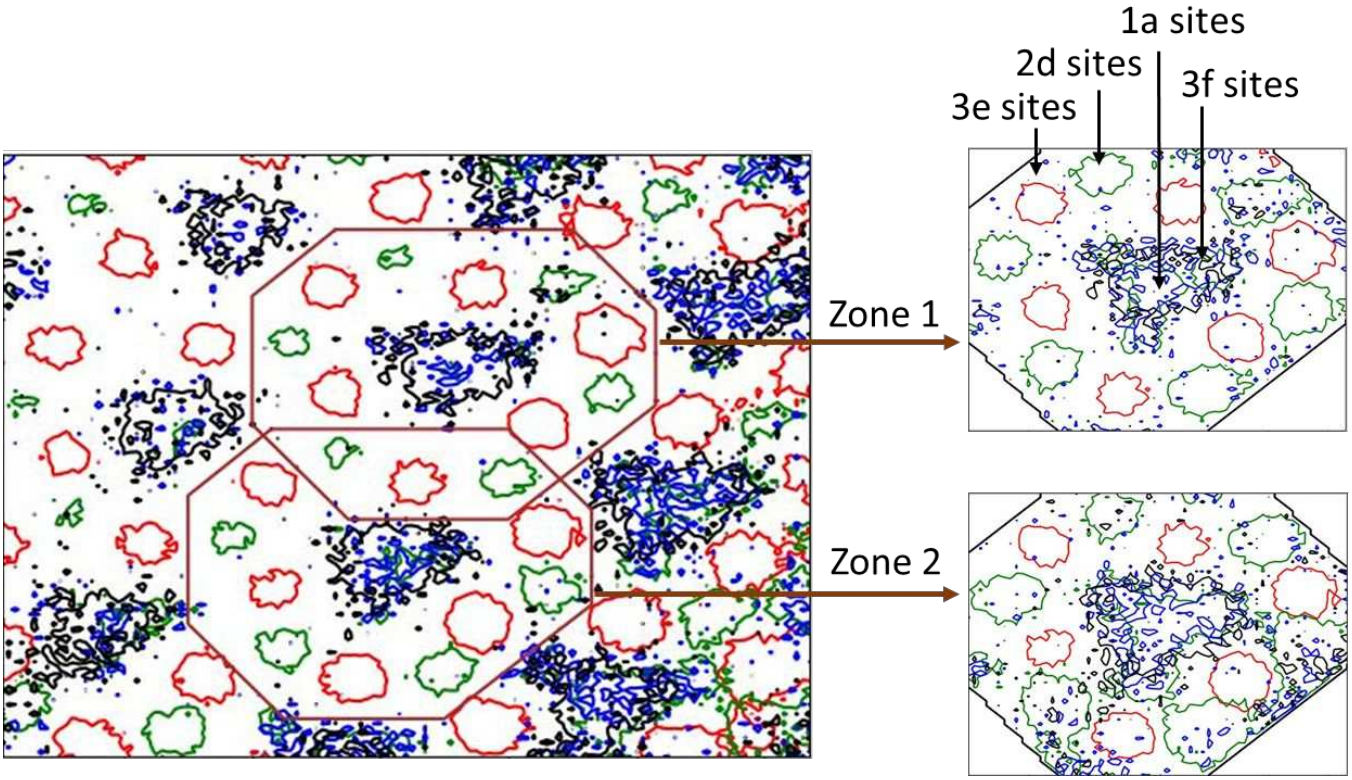

Figure S15. Overlay contour map of Ca (red), Ga (black), Ge (green) and Zn (blue) extracted from STEM-EDS raw data after the mask application.

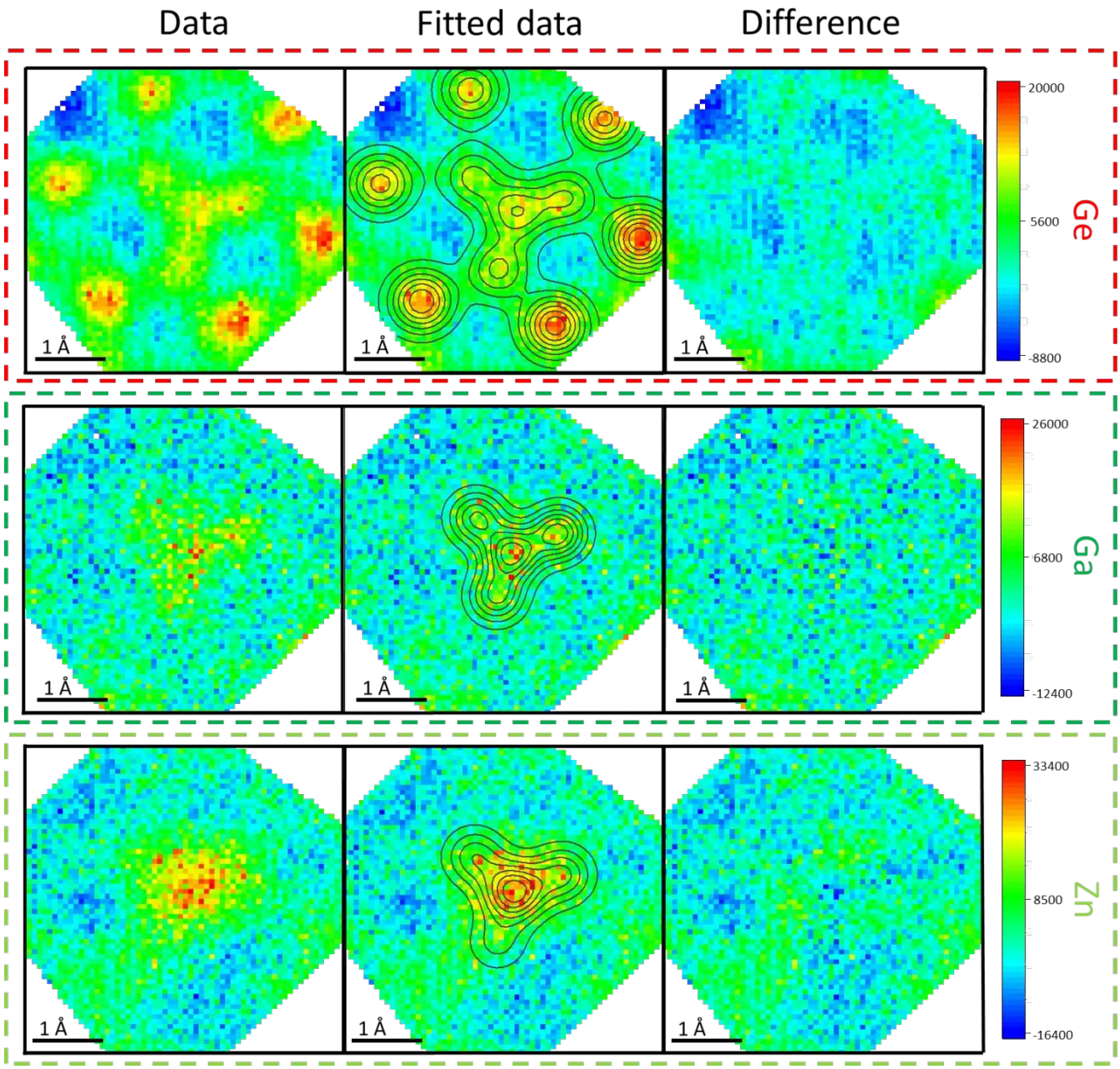

Figure S16. STEM-EDS 2D refinement plots of Ge, Ga and Zn from zone2 (zone 1 is shown in Figure 8 of the main text). The sample composition is $Ca_3GaZn_{0.5}Ge_{4.5}O_{14}$.

References:

(1) Massiot, D.; Vosegaard, T.; Magneron, N.; Trumeau, D.; Montouillout, V.; Berthet, P.; Loiseau, T.; Bujoli, B. ^{71}Ga NMR of Reference Ga_{iv}, Ga_{v}, and Ga_{vi} Compounds by MAS and QPASS, Extension of Galliumraluminum NMR Parameter Correlation. **1999**, 11.

(2) Fan, J.; Sarou-Kanian, V.; Yang, X.; Diaz-Lopez, M.; Fayon, F.; Kuang, X.; Pitcher, M. J.; Allix, M. $La_2Ga_3O_{7.5}$: A Metastable Ternary Melilite with a Super-Excess of Interstitial Oxide Ions Synthesized by Direct Crystallization of the Melt. *Chem. Mater.* **2020**, *32* (20), 9016–9025. https://doi.org/10.1021/acs.chemmater.0c03441.

(3) Massiot, D.; Montouillout, V.; Fayon, F.; Florian, P.; Bessada, C. Order-Resolved Sideband Separation in Magic Angle Spinning NMR of Half Integer Quadrupolar Nuclei. *Chem. Phys. Lett.* **1997**, *272* (3–4), 295–300. https://doi.org/10.1016/S0009-2614(97)88023-2.

(4) Mill, B. V.; Klimenkova, A. A.; Maximov, B. A.; Molchanov, V. N.; Pushcharovsky, D. Yu. Enantiomorphism of the $Ca_3Ga_2Ge_4O_{14}$ Compound and Comparison of the $Ca_3Ga_2Ge_4O_{14}$ and $Sr_3Ga_2Ge_4O_{14}$ Structures. *Crystallogr. Rep.* **2007**, *52* (5), 785–794. https://doi.org/10.1134/S1063774507050069.

Haytem BAZZAOUI

Synthèse et Caractérisation de Nouveaux Matériaux Oxydes par Cristallisation Complète et Congruente du verre ou du liquide fondu

Le développement de nouveaux matériaux à propriétés performantes est un axe majeur de la recherche actuelle. Au cours de cette thèse, de nouveaux matériaux hors équilibre ont été développés par des approches de synthèses innovantes : la cristallisation complète et congruente à partir du verre ou du liquide fondu. De hautes températures ont été atteintes par lévitation aérodynamique couplée à un chauffage par lasers CO_2. Les matériaux synthétisés visent des propriétés optiques et/ou de conductivités anioniques.

L'étude structurale des mélilites Sr*RE*Ga_3O_7 *RE*= [Dy – Lu, Y] synthétisées par cristallisation complète et congruente à partir d'un précurseur vitreux a permis de mettre en évidence une mise en ordre entre les cations Sr^{2+} et RE^{3+} sur trois sites cationiques, ce qui induit un triplement du paramètre *a* de la maille mélilite parent tétragonale, et donc la stabilisation d'une nouvelle maille orthorhombique. De plus, l'étude de la stabilité de cette structure orthorhombique à hautes températures en mode *in situ* a montré l'existence d'une transition de phase vers la maille parent tétragonale désordonnée de la mélilite. En revanche, l'étude du désordre chimique dans la solution solide de langasite $Ca_3Ga_{2-2x}Zn_xGe_{4+x}O_{14}$, un minéral lié à la famille de la mélilite et cristallisant sous une maille trigonale s'est avérée insuffisante par diffraction des rayons X et neutrons en raison de la présence de trois cations isoélectroniques (Ga^{3+}, Zn^{2+}, Ge^{4+}). Pour répondre à cette problématique, une analyse unique a été déployée : l'affinement de cartographies STEM-EDS 2D de chaque cation, permettant l'établissement d'un modèle de départ pour l'analyse Rietveld.

De nouveaux matériaux conducteurs anioniques ont été étudiés dans les solutions solides $La_{1+x}Ba_{1-x}Ga_3O_{7+x/2}$ et $La_xCa_{5-x}Ga_6O_{14+x/2}$. Ils cristallisent dans des structures mélilite ou dérivées. La première solution solide a été synthétisée par cristallisation à partir du liquide fondu à haute température et a révélé la rétention du polymorphe tétragonal de la mélilite avec la plus haute concentration en oxide interstitiel ($La_{1.725}Ba_{0.275}Ga_3O_{7.3625}$ x= 0.725). En outre, le composé $La_{1.6}Ba_{0.4}Ga_3O_{7.15}$ (x= 0.6) montre la plus haute valeur de conductivité anionique à 500°C, égalant les meilleurs conducteurs mélilites connus ($La_{1.64}Ca_{0.36}Ga_3O_{7.32}$ et $La_{1.54}Sr_{0.46}Ga_3O_{7.27}$). Finalement, l'étude de la deuxième solution solide a montré une substitution maximum x= 0.25 atteinte par réaction solide-solide. La complexité de cette étude repose sur la caractérisation structurale de ce composé qui a nécessité des calculs DFT pour identifier la structure la plus énergétiquement favorable.

Mots clés : Cristallisation du verre / liquide fondu à haute température, Nouveaux matériaux métastables, Matériaux hors équilibre, Analyse structurale par affinement Rietveld, Microscopie électronique en transmission à résolution atomique.

Synthesis and Characterisation of new Oxide Materials by full and Congruent Crystallisation from Glass or the Molten liquid

The development of new materials with high performing properties is a major theme in today's research. In this thesis, new out-of-equilibrium materials were developed by unique synthesis approaches: full and congruent crystallisation from glass or from an under-cooled melt. High temperatures were reached by aerodynamic levitation coupled to two CO_2 lasers. The synthesised materials target optical and/or ionic conductivity properties.

The structural study of the Sr*RE*Ga_3O_3 *RE*= [Dy – Lu, Y] melilites, synthesised by full and congruent crystallisation from glass precursors, characterised the ordering of Sr^{2+} and RE^{3+} cations over three distinct sites, inducing a tripling of the *a* cell parameter of the parent tetragonal melilite, leading to the stabilisation of a new orthorhombic cell. Moreover, the stability of this orthorhombic polymorph studied *in situ* against temperature, showed the occurrence of a phase transition to the parent fully disordered tetragonal melilite. In contrast, the cationic ordering in the $Ca_3Ga_{2-2x}Zn_xGe_{4+x}O_{14}$ langasite solid solution, a melilite-related mineral crystallising in a trigonal cell, could not be probed directly by diffraction methods (X-rays and neutrons) due to the presence of three isoelectronic cations (Ga^{3+}, Zn^{2+}, Ge^{4+}). In order to fulfil this task, a unique analysis approach was performed: refinement of atomic resolution 2D STEM-EDS maps for each cation.

Last, new ionic conductor materials were investigated in the melilite $La_{1+x}Ba_{1-x}Ga_3O_{7+x/2}$ and melilite-related $La_xCa_{5-x}Ga_6O_{14+x/2}$ solid solutions. The $La_{1+x}Ba_{1-x}Ga_3O_{7+x/2}$ series was synthesised by direct crystallisation of their under-cooled melts. The series retained its parent tetragonal structure up to $La_{1.725}Ba_{0.275}Ga_3O_{7.3625}$ (x= 0.725), which is the highest interstitial oxide concentration ever observed in this polymorph. Despite its lower carrier concentration, tetragonal $La_{1.6}Ba_{0.4}Ga_3O_{7.15}$ (x= 0.6) member was found to exhibit the highest conductivity values at 500°C, matching the best known melilite conductors $La_{1.64}Ca_{0.36}Ga_3O_{7.32}$ and $La_{1.54}Sr_{0.46}Ga_3O_{7.27}$. In contrast, the $La_xCa_{5-x}Ga_6O_{14+x/2}$ series revealed a much lower substitution limit of x= 0.25 attained by solid-state reaction, with a 100x enhancement in conductivity upon La doping. The low substitution rate posed major challenges for the structural characterisation of these compositions, which were addressed by combining maximum-entropy analysis of neutron diffractograms with DFT-based structure prediction.

Keywords: Crystallisation from glass / under-cooled melt at high temperatures, New metastable materials, Out of equilibrium materials, Structural analysis by Rietveld refinement, Atomic resolution transmission electronic microscopy.

CEMHTI-CNRS UPR3079
1D Avenue de la Recherche Scientifique
45071 Orléans Cedex 2